

Bramwell's Helicopter Dynamics

Bramwell's Helicopter Dynamics

Second edition

A. R. S. Bramwell
George Done
David Balmford



Oxford Auckland Boston Johannesburg Melbourne New Delhi

Butterworth-Heinemann
Linacre House, Jordan Hill, Oxford OX2 8DP
225 Wildwood Avenue, Woburn, MA 01801-2041
A division of Reed Educational and Professional Publishing Ltd



First published by Edward Arnold (Publishers) Ltd 1976
Second edition published by Butterworth-Heinemann 2001

© A. R. S. Bramwell, George Done and David Balmford 2001

All rights reserved. No part of this publication may be reproduced in any material form (including photocopying or storing in any medium by electronic means and whether or not transiently or incidentally to some other use of this publication) without the written permission of the copyright holder except in accordance with the provisions of the Copyright, Designs and Patents Act 1988 or under the terms of a licence issued by the Copyright Licensing Agency Ltd, 90 Tottenham Court Road, London, England W1P 0LP. Applications for the copyright holder's written permission to reproduce any part of this publication should be addressed to the publishers

British Library Cataloguing in Publication Data

Bramwell, A.R.S.

Bramwell's helicopter dynamics. – 2nd ed.

1 Helicopters – Aerodynamics

I Title II Done, George III Balmford, David IV Helicopter dynamics

629.1'33352

Library of Congress Cataloguing in Publication Data

Bramwell, A.R.S.

Bramwell's helicopter dynamics / A.R.S. Bramwell, George Done,
David Balmford.

–2nd ed.

p. cm.

Rev. ed. of: Helicopter dynamics. c1976

Includes index

ISBN 0 7506 5075 3

1 Helicopter-Dynamics 2 Helicopters-Aerodynamics I Done, George Taylor Sutton II Balmford, David III Bramwell, A.R.S. Helicopter dynamics

IV Title

TL716.B664 2001

629.133'352--dc21

00-049381

ISBN 0 7506 5075 3

Typeset at Replika Press Pvt Ltd, 100% EOU, Delhi 110 040, India
Printed and bound in Great Britain by Bath Press, Avon.



Contents

<i>Preface to the second edition</i>	<i>vii</i>
<i>Preface to the first edition</i>	<i>ix</i>
<i>Acknowledgements</i>	<i>xi</i>
<i>Notation</i>	<i>xiii</i>
1. Basic mechanics of rotor systems and helicopter flight	1
2. Rotor aerodynamics in axial flight	33
3. Rotor aerodynamics and dynamics in forward flight	77
4. Trim and performance in axial and forward flight	115
5. Flight dynamics and control	137
6. Rotor aerodynamics in forward flight	196
7. Structural dynamics of elastic blades	238
8. Rotor induced vibration	290
9. Aeroelastic and aeromechanical behaviour	319
<i>Appendices</i>	360
<i>Index</i>	371

Preface to the second edition

At the time of publication of the first edition of the book in 1976, Bramwell's *Helicopter Dynamics* was a unique addition to the fundamental knowledge of dynamics of rotorcraft due to its coverage in a single volume of subjects ranging from aerodynamics, through flight dynamics to vibrational dynamics and aeroelasticity. It proved to be popular, and the first edition sold out relatively quickly. Unfortunately, before the book could be revised with a view to producing a second edition, Bram (as he was known to his friends and colleagues) succumbed to a short illness and died. As well as leaving a sudden space in the helicopter world, his death left the publishers with their desire for further editions unfulfilled. Following an approach from the publishers, the present authors agreed, with considerable trepidation, to undertake the task of producing a second edition.

Indeed, being asked was an honour, particularly so for one of us (GD), since we had been colleagues together at City University for a short period of two years. However, although it may be one thing to produce a book from one's own lecture notes and published papers, it is entirely a different proposition to do the same when the original material is not your own, as we were to discover. It was necessary to try to understand why Bram's book was so popular with the helicopter fraternity, in order that any revisions should not destroy any of the vital qualities in this regard. One of the characteristics that we felt endeared the book to its followers was the way explanations of what are complicated phenomena were established from fundamental laws and simple assumptions. Theoretical expressions were developed from the basic mathematics in a straightforward and measured style that was particular to Bram's way of thinking and writing. We positively wished and endeavoured to retain his inimitable qualities and characteristics.

Long sections of the book are analytical, starting from fundamental principles, and do not change significantly in the course of time; however, we have tried to eradicate errors, printer's and otherwise, and improve explanations where considered necessary. There are also many sections that are largely descriptive, and, over the space of 25 years since the first edition, these had tended to become out of date, both in terms of the state-of-the-art and supporting references; thus, these have been updated. Opportunities, too, have been taken to expand the treatment of, and to include additional information in, the vibrational dynamics area, with both the additional and updated

viii Preface to the second edition

content introduced, hopefully, in such a way as to be compatible with Bram's style.

Another change which has taken place in the past quarter century is the now greater familiarity of the users of books such as this one with matrices and vectors. Hence, Chapter 1 of the first edition, which was aimed at introducing and explaining the necessary associated matrix and vector operations, has disappeared from the second edition. Also, some rather fundamental fluid dynamics that also appeared in this chapter was considered unnecessary in view of the material being readily available in undergraduate textbooks. What remained from the original Chapter 1 that was thought still necessary now appears in the Appendix. Readers familiar with the first edition will notice the inclusion of a notation list in the present edition. This became an essential item in re-editing the book, because there were many instances in the first edition of repeated symbols for different parameters, and different symbols for the same parameters, due to the fact that the much of the material in the original book was based on various technical papers published at different times. As far as has been possible, the notation has now been made consistent throughout all chapters; this has resulted in some of the least used symbols being changed.

Apart from the removal of the elementary material in the original Chapter 1, the overall structure of the book has not changed to any great degree. The order of the chapters is as before, although there has been some re-titling and compression of two chapters into one. Some of the sections in the last three chapters have been rearranged to provide a more natural development.

Since publication of the first edition, there have appeared in the market-place several excellent scientific textbooks on rotorcraft which cover some of the content of Bram's book to a far greater depth and degree of specialisation, and also other texts which are aimed at a broad coverage but at a lower academic level. However, the comprehensive nature of the subject matter dealt with in this volume should continue to appeal to those helicopter engineers who require a reasonably in-depth and authoritative text covering a wide range of topics.

Sherborne
Kew
2001

David Balmford
George Done

Preface to the first edition

In spite of the large numbers of helicopters now flying, and the fact that helicopters form an important part of the air strength of the world's armed services, the study of helicopter dynamics and aerodynamics has always occupied a lowly place in aeronautical instruction; in fact, it is probably true to say that in most aeronautical universities in Great Britain and the United States the helicopter is almost, if not entirely, absent from the curriculum. This neglect is also seen in the dearth of textbooks on the subject; it is fifteen years since the last textbook in English was published, and over twenty years have passed since the first appearance of Gessow and Myer's excellent introductory text *Aerodynamics of the Helicopter*, which has not so far been revised.

The object of the present volume is to give an up-to-date account of the more important branches of the dynamics and aerodynamics of the helicopter. It is hoped that it will be useful to both undergraduate and postgraduate students of aeronautics and also to workers in industry and the research establishments. In these days of fast computers it is a temptation to consign a problem to arithmetical computer calculation straightforwardly. While this is unavoidable in many complicated problems, such as the calculation of induced velocity, the important physical understanding is thereby often lost. Fortunately, most problems of the helicopter can be discussed adequately without becoming too involved mathematically, and it is usually possible to arrive at relatively simple formulae which are not only useful in preliminary design but which also enable a physical interpretation of the dynamic and aerodynamic phenomena to be obtained. The intention throughout this book, therefore, has been to try to arrive at useful mathematical results and 'working formulae' and at the same time to emphasize the physical understanding of the problem.

The first chapter summarizes some essential mechanics, mathematics, and aerodynamics which find application in later parts of the book. Apart from some recent research into the aerodynamics of the hovering rotor, discussed in Chapter 3, the next six chapters are really based on the pioneer work of Glauert and Lock of the 1920s and its developments up to the 1950s. In these chapters only simple assumptions about the dynamics and aerodynamics are made, yet they enable many important results to be obtained for the calculation of induced velocity, rotor forces and moments, performance, and the static and dynamic stability and control in both hovering and forward flight.

x Preface to the first edition

Chapter 8 considers the complicated problem of the calculation of the induced velocity and the rotor blade forces when the vortex wakes from the individual blades are taken into account. Simple analytical results are possible in only a few special cases and usually resort has to be made to digital computation. Aerofoil characteristics under conditions of high incidence and high Mach number for steady and unsteady conditions are also discussed.

Chapter 9 considers the motion of the flexible blade (regarded up to this point as a rigid beam) and discusses methods of calculating the mode shapes and frequencies for flapwise, lagwise, and torsional displacements for both hinged and hingeless blades.

The last three chapters consider helicopter vibration and the problems of aeroelastic coupling between the modes of vibration of the blade and between those of the blade and fuselage.

I should like to thank two of my colleagues: Dr M. M. Freestone for kindly reading parts of the manuscript and making many valuable suggestions, and Dr R. F. Williams for allowing me to quote his method for the calculation of the mode shapes and frequencies of a rotor blade.

A.R.S.B.

South Croydon, 1975

Acknowledgements

The authors would like to thank the persons and organisations listed below for permission to reproduce material for some of the figures in this book. Many such figures appeared in the first edition, and do so also in the second, the relevant acknowledgements being to: American Helicopter Society for Figs 3.25 to 3.32, 6.40, 6.47, 6.48, and 9.16; American Institute for Aeronautics and Astronautics for Figs 6.50, 6.51, and 6.52; Her Majesty's Stationery Office for Figs 3.6, 3.9, 4.7, 4.9, 4.10, and 6.11; A. J. Landgrebe for Figs 2.24 and 2.33; National Aeronautics and Space Administration for Figs 3.10, 3.11, 6.41, and 9.12; R.A. Piziali for Figs 6.24 and 6.25; Royal Aeronautical Society for Figs 4.15, 4.20, 6.19, 6.21, and 6.22; Royal Aircraft Establishment (now Defence Evaluation and Research Agency) for Figs 3.8, 6.31, 6.32, 6.33, 6.40, 6.42, 6.46, 7.3, 7.28, 8.30, and 8.31.

For figures that have appeared for the first time in the second edition, acknowledgements are also due to: GKN Westland Helicopters Ltd. for Figs 1.5(a), 1.5(b), 1.6(a), and 1.6(b), 6.37, 6.38, 7.28, 8.3 to 8.9, 8.12 to 8.18, 8.20 to 8.32, 9.13, 9.17 and 9.23; Stephen Fiddes for Fig. 2.37; Gordon Leishman of the University of Maryland for Figs 6.28 and 6.30; Jean-Jacques Philippe of ONERA for Figs 6.34, 6.35, and 6.36. In a few cases, the figure is an adaptation of the original.

We are also indebted to several other friends and colleagues for contributions provided in many other ways, ranging from discussions on content and provision of photographic and other material, through to highlighting errors, typographical and otherwise, arising in the first edition. These are Dave Gibbings and Ian Simons, formerly of GKN Westland Helicopters, Gordon Leishman of the University of Maryland and Gareth Padfield of the University of Liverpool.

Notation

A	Rotor disc area
A	Blade aspect ratio = R/c
A, B	Constants in solution for blade torsion mode
A, B, C	Moments of inertia of helicopter in roll, pitch and yaw, or of blade in pitch, flap and lag
A, B, C, D, E, F, G	Coefficients in general polynomial equation
A', B', C'	Moments of inertia of teetering rotor with built-in pitch and coning
A_{ij}, B_{ij}	ij th generalised inertia and stiffness coefficients
A_n	n th coefficient in periodic or finite series
A_j	Blade pitch j th input weighting (active vibration control)
A_1, B_1	Lateral and longitudinal cyclic pitch
$A_1, B_{1c}, C_1, D_1, E_1$	Coefficients in longitudinal characteristic equation
A_2, B_2, C_2, D_2, E_2	Coefficients in lateral characteristic equation
$\bar{A}_{ij}, \bar{B}_{ij}$	Normalised generalised coefficients = $A_{ij}, B_{ij}/0.5m\Omega^2R^3$
a	Lift curve slope of blade section
a	Distance from edge of vortex sheet
a	Offset of fixed pendulum point from rotor centre of rotation (bifilar absorber)
a, b, c, d, e	Square matrices, and column matrix (e) (Dynamic FEM)
a^*, b^*, c^*	Subsidiary square matrices (Dynamic FEM)
a_g	Acceleration of blade c.g.
a_T	Tailplane lift curve slope
a_0	Acceleration of origin of moving frame = $a_x\mathbf{i} + a_y\mathbf{j} + a_z\mathbf{k}$
a_0	Coning angle
a_1, b_1	Longitudinal and lateral flapping coefficients
a_0, a_1, a_2, b_1, b_2	Sine and cosine coefficients in equation for C_m
$\bar{a}_0, \bar{a}_1, \bar{b}_1$	Analogous to a_0, a_1, b_1 for hingeless rotor
B	Tip-loss factor (Prandtl) = R_e/R
\mathbf{B}	Vector of background vibration responses

B'_{1c}, C'_1	Coefficients B_{1c}, C_1 with speed derivatives neglected
\bar{B}_1	Laplace transform of B_1 (cyclic pitch)
b	Number of blades
b	Aerofoil semi-chord
b	Effective pendulum length (bifilar absorber)
C	Torsional moment of inertia per unit blade length
C, S	Cosine and sine multi-blade summation terms
C, F, G, H, S	Coefficients in solution for normal acceleration
$C(k)$	Theodorsen's function
C_D	Drag coefficient
C_H	H-force coefficient = $H/\rho A \Omega^2 R^2$
C_L	Lift coefficient
C_{LT}	Tailplane lift coefficient
C_T	Thrust coefficient based on disc area = $s t_c = T/\rho A \Omega^2 R^2$
C_M	Pitching moment coefficient
C_N	Normal force coefficient
\bar{C}_L	Equivalent $C_L = 3 \int_0^1 x^2 C_L dx$
C_l	Rolling moment coefficient of blade
C_m	Pitching moment coefficient of blade
C_{mf}	Pitching moment coefficient of fuselage = $M_f/\rho s A \Omega^2 R^3$
C_{ms}	Pitching moment coefficient due to hinge offset = $M_s/\rho s A \Omega^2 R^3$
C_p	Pressure coefficient
C_1, C_2, S_1, S_2	Coefficients in less usual solution for normal acceleration
C_1, D_1, F_1, G_1	Integrals of blade flapping mode shape functions (first and second moments, and powers)
C_ξ, F_β	Flap-lag cross coupling damping coefficients
c	Blade or aerofoil chord
c	Viscous damping coefficient
c	Offset of c.g. of oscillatory mass from pivot point (bifilar absorber)
c_{crit}	Critical damping coefficient = $2(k/m)^{-1/2}$
c_e	Equivalent chord
c_l	Linkage ratio on Bell stabilising bar
$c_n, d_n, e_n, f_n, g_n, h_n, j_n, k_n$	Coefficients relating to S_n, M_n, α_n, Z_n at blade station n (Myklestad)
c_0, c_n	Downwash factors (Mangler and Squire)
c_1, c_2, c_3, c_4	Constants determined from initial conditions
D	Drag of fuselage, or local blade section
D	Diameter of holes in fixed arm and oscillatory mass (bifilar absorber)
D, E, F	Blade or helicopter products of inertia

\bar{D}	Denominator in integral for ω_t
d	Drag factor, where blade drag = $d\Omega^2$
d	Diameter of pin connecting fixed arm and oscillatory mass (bifilar absorber)
d_0	Fuselage drag ratio = S_{FP}/sA
d_1, d_2	Bobweight arm lengths (DAVI)
E	Young's modulus
E_s	Modulus of rigidity or shear modulus
E_1	Generalised inertia of first flapping mode
E_1, E_2	Wake energy contributions
e	Rotor blade hinge offset, as fraction of R
e_A	Distance between blade centroid and elastic axis
e_1, e_2, e_3	Orthogonal unit vectors fixed in hub
F	Aerodynamic force on blade or helicopter, or general external force vector $= Xi + Yj + Zk$
\bar{F}	Ratio of Lock number equivalents for hingeless blade $= \gamma_2/\gamma_1$
F_R, F_I	Real and imaginary parts of L/L_q
F_y, F_z	Lagwise and flapwise forces acting on a blade section
F_ξ	Lag damping coefficient
f	Lateral distance of c.g. from shaft, as fraction of R
f	Function affecting the k correction factor $= 0.5b(1 - x)/\sin \phi$ (Prandtl vortex sheet model)
f	Bending flexibility matrix
$f(n), g(n)$	Generalised inertias for n th flap and lag bending modes
f_b	Factor dependent on number of blades
f_{in}	Forcing term assumed constant for i th step in n th mode
G	Centrifugal tension in blade
g	Gravitational constant
H	Rotor force component perpendicular to thrust axis (positive to rear) (H -force)
H	Total head pressure
H	Absolute angular momentum vector = $h_1\mathbf{i} + h_2\mathbf{j} + h_3\mathbf{k}$
$\bar{H}, \hat{H}, \hat{J}$	Non-dimensional quantities (air resonance)
H_B, H_D	Flap and pitch damping coefficients (Coleman and Stempin)
H_D	H -force referred to disc axes
H_P	H -force due to profile drag
H_i	H -force due to induced drag
H_0, H_1, H_2	Coefficients used in longitudinal response solution
H'_1, H'_5	Aerodynamic damping terms (Coleman and Stempin)

h	Height of hub above c.g. as fraction of R
h	Vertical spacing between vortex sheets (Loewy and Jones)
\mathbf{h}	Relative angular momentum vector
h'	Tail rotor height above c.g. based on wind axes $= h_t \cos \alpha_s - l_t \sin \alpha_s$
h_c	H-force coefficient = C_H/s
h_t	Tail rotor height above c.g., as fraction of R
h_1	Height of hub above c.g. based on wind axes $= h \cos \alpha_s - l \sin \alpha_s$
I	Second moment of area of blade section
I	Blade moment of inertia in both flap and lag (Southwell)
\mathbf{I}	The unit matrix
I_A, I_B	Non-dimensional inertia factors (Coleman and Stempin)
I_y, I_z	Second moments of inertia of blade section for lagwise and flapwise bending
I_β, I_θ	Blade flap and pitch moments of inertia
i, j, k	Unit vectors fixed in blade
i_A, i_B, i_C	Non-dimensional rolling, pitching and yawing inertias of helicopter
i_E	Non-dimensional roll-yaw inertia product term for helicopter
J	Modal error squared integral (Duncan)
J	Polar second moment of area of blade section
J	Performance index (active vibration control)
J_0, J_1	Bessel functions of first and second kinds (Miller)
j_1, j_2, j_3, j_4	Quantities dependent on first blade flapping mode shapes of hingeless blade
K	Induced velocity gradient (Glauert)
K	Stiffness between gearbox and fuselage (DAVI)
\bar{K}	Hingeless rotor blade constant = $\gamma_2 F_1/2$
$K(x)$	Elliptic integral
K'_θ	Stiffness of pitch control (Coleman and Stempin)
$K_0(ik), K_1(ik)$	Bessel functions of the second kind (Theodorsen)
k	Correction factor to induced velocity for number of blades (Prandtl and Goldstein)
k	Incremental correction factor to induced power relative to that for constant induced velocity
k	Frequency parameter = $nc/2V$ (Theodorsen), $= \omega b/\Omega R$ (Miller)
k	Blade structural constant = $EI/m\Omega^2 R^4$
k	Spring stiffness
k_A, k_B	Non-dimensional pitching and flapping radii of gyration $= c(A/M)^{1/2}, R(B/M)^{1/2}$
k_T	Correction factor to trim due to tailplane

k_i	Induced velocity ratio (axial flight) = v_i/v_2
k_s	Equivalent flap hinge stiffness for hingeless blade
k_β, k_ξ	Pitch/flap bending and pitch/lag bending coupling coefficients
k_θ	Stiffness of control system about feathering axis
k_ξ	Non-dimensional artificial lag damping
k_1, k_2	Wake constants (Landgrebe)
k_1, k_2	Constants associated with transient motion
k_A, k_B	Effective pitching and rolling stiffnesses (air resonance)
L	Blade sectional lift force
L	Lagrangian = $T - U$
L, M, N	Moments about $\mathbf{i}, \mathbf{j}, \mathbf{k}$ for a rigid body, or of helicopter in roll, pitch and yaw, or of blade in pitch, flap and lag
\bar{L}	Non-dimensional quantity (air resonance) = $2\bar{a}_0 \bar{J}$
L_A	Aerodynamic torsional moment
L_b	Lift due to bound circulation
L_e	Elastic moment in flap plane
L_q	Quasi-steady lift
L_v, L_p etc.	Rolling moment derivatives
L_0	Steady lift, and at instantaneous incidence
l	Distance forward of c.g. from shaft in terms of R
l	Position vector to vortex = $l_1 \mathbf{i} + l_2 \mathbf{j} + l_3 \mathbf{k}$
l'	Tail rotor arm based on wind axes = $l_t \cos \alpha_s + h_t \sin \alpha_s$
l_T	Tailplane arm, as fraction of R
l_b	Blade inertia to mass moment ratio (ground resonance) = $I/M_b r_g$
l_n	Length of n th beam element (Myklestad)
l_t	Tail rotor arm, as fraction of R
l_v, l_p etc.	Non-dimensional normalised rolling moment derivatives
l'_v, l'_p etc.	Non-dimensional rolling moment derivatives
l_I	Distance forward of c.g. from hub based on wind axes = $l \cos \alpha_s + h \sin \alpha_s$
M	Mass (general), chassis mass (ground resonance)
M	Bending moment
\mathbf{M}	Column vector of blade bending moments
$\bar{\mathbf{M}}$	Rotor figure of merit = Tv_i/P
M_A	Aerodynamic moment about flapping hinge, or hub
M_T	Pitching moment due to tailplane
M_b	Blade mass
M_c	Blade root bending moment coefficient = $M/\rho b c \Omega^2 R^4$
M_e	Elastic moment in lag plane
M_f	Pitching moment of fuselage
M_r	Moment of rotor forces about c.g.

M_s	Pitching moment per unit tilt of all the blades due to hinge offset
M_u, M_q , etc.	Pitching moment derivatives
M_1	Unit load bending moment
M_1, M_2	Combined rotor/gearbox, and fuselage mass (DAVI)
m	Mass, or mass per unit length
m	Frequency ratio (Miller) = ω/Ω
m_{bob}	Bobweight mass (DAVI)
m_u, m_q , etc.	Non-dimensional normalised pitching moment derivatives
m'_u, m'_q , etc.	Non-dimensional pitching moment derivatives
N_A	Aerodynamic lagging moment on a blade
N_i	Inertia lagging moment about real or virtual hinge
N_v, N_p , etc.	Yawing moment derivatives
$N_1, P_1, Q_1, R_1, S_1, T_1$	Relate to B_{1c}, C_1, D_1, E_1
$N_2, P_2, Q_2, R_2, S_2, T_2$	Relate to A_2, B_2, C_2, D_2, E_2
n	Offset hinge factor = $(1 - e)^3 (1 + e/3)$
n	Static load factor ('g')
n	Frequency of oscillation (Theodorsen), frequency/ Ω (Miller)
\bar{n}	Laplace transform of n (static load factor)
n_v, n_p , etc.	Non-dimensional normalised yawing moment derivatives
n'_v, n'_p etc.	Non-dimensional yawing moment derivatives
P	Power to drive blade, or rotor
P_i	Induced power
$P_i, Q_i, S_i, T_i, U_i, V_i$	Coefficients of periodic terms in expressions for lateral hub force components
P_{in}	Inertia force acting on chassis
P_{i0}	Induced power for constant induced velocity
P_p	Profile drag power
P_t	Tail rotor power
P_0	Induced power for constant induced velocity
$P_1(\psi), P_2(\psi)$	Periodic functions
p	Pressure
p	Roll angular velocity
p	Laplace variable
p	Chassis frequency, and aerofoil stall flutter frequency
\hat{p}	Non-dimensional roll velocity = p/Ω
$p(t), q(t)$	Forcing function components (Coleman)
p_l, p_u	Pressure on lower and upper sides of disc plane, or aerofoil surfaces
p_1, p_2	Pressure just ahead of actuator disc, and pressure in far wake
p_∞	Ambient pressure

\underline{Q}	Rotor torque
\bar{Q}	Volume flow through control volume sides, or flux
$Q(x)$	Blade torsion mode shape
Q_P	Torque due to rotor profile drag
Q_i	Induced rotor torque
$Q_1(x)$	First blade torsion mode shape
q	Pitching velocity
q	Local fluid velocity
\underline{q}	Induced velocity vector at a point on blade
\hat{q}	Non-dimensional pitching velocity = q/Ω
q_c	Torque coefficient = $Q/\rho s A \Omega^2 R^3$
q_r	Radial velocity component
q_z	Local fluid velocity in axial direction
q_ψ	Tangential velocity component
R	Rotor radius
R	Routh's discriminant
\underline{R}	Reaction forces at hinge = $R_1 \mathbf{e}_1 + R_2 \mathbf{e}_2 + R_3 \mathbf{e}_3$
R_D	Radius of blade drag centre from hub
R_{eff}	Effective blade radius (Prandtl)
R_0	Far wake radius
R_1, R_2	Control surface and far wake radii
r	Distance of blade element from hinge or axis of rotation
r	Radial wake coordinate
\underline{r}	Position vector = $x \mathbf{i} + y \mathbf{j} + z \mathbf{k}$
\bar{r}	Tip vortex radial coordinate (Landgrebe)
\underline{r}_g	Position vector of blade or system c.g. = $x_g \mathbf{i} + y_g \mathbf{j} + z_g \mathbf{k}$
r_1	Radial position of vortex filament on blade
S	Centrifugal force of blade
S	Shear force
$S(x)$	Flap bending mode shape
S_B	Projected side area of fuselage
S_{FP}	Fuselage equivalent flat plate area
S_T	Tailplane area
$S_1(x)$	First flap bending mode shape
s	Rotor solidity = $bc/\pi R$
s	Half width of vortex sheet, equivalent to half wing span
\underline{s}	Vortex axis vector = $s_1 \mathbf{i} + s_2 \mathbf{j} + s_3 \mathbf{k}$
s_p	Spacing of vortex sheets
s_t	Tail rotor solidity
\bar{s}_t	Normalised tail rotor solidity = $s_t A_t (\Omega R)_t / s A \Omega R$
T	Rotor thrust
T	Periodic time
T	Kinetic energy
\underline{T}	Moment of resultant external forces about O

xx Notation

T	Rotor/fuselage transfer matrix (active vibration control)
$T(x)$	Lag bending mode shape
$T_1(x)$	First lag bending mode shape
T_D	Thrust referred to disc axes
T_d	Time to double amplitude
T_f	Following time (inversely proportional to viscous damping) – (Bell bar)
T_h	Time to half amplitude
T_t	Tail rotor thrust
T_0	Thrust for constant v_i
t	Time
\hat{t}	Time non-dimensionalising factor = $W/g\rho s A \Omega R$
t_c	Thrust coefficient based on total blade area = $T/\rho s A \Omega^2 R^2$
t_{cD}	Thrust coefficient referred to disc axes
U	Velocity of wake normal to axis
U	Strain energy
U, V, W	Initial flight velocity components along x, y, z axes
U_B	Strain energy due to bending
U_G	Strain energy due to centrifugal tension
U_P	Component of air velocity relative to blade element perpendicular to plane of no-feathering
U_T	Component of air velocity relative to blade element tangential to plane of no-feathering
U_0, U_1, U_2	Coefficients used in longitudinal response solution
u, v, w	Perturbational velocities
u, v	Coleman coordinates
u', v'	Wake velocity components
$\bar{u}, \bar{v}, \bar{w}$	Laplace transforms of u, v, w (perturbational velocities)
$\hat{u}, \hat{v}, \hat{w}$	Non-dimensional perturbational velocities = $u/\Omega R, v/\Omega R, w/\Omega R$
u_{Fn}, v_{Fn}	Unit force constants relating to n th blade element (Myklestad)
u_{Mn}, v_{Mn}	Unit moment constants relating to n th blade element (Myklestad)
V	Forward velocity of helicopter or relative velocity far upstream of rotor
V	Forward velocity vector of helicopter
\bar{V}	Forward speed normalised on thrust velocity = V/v_0
\hat{V}	Forward speed normalised on tip speed = $V/\Omega R$
V'	Total velocity at the rotor
V_C	Rate of climb in axial flight, or axial velocity
\bar{V}_C	Climb speed normalised on induced velocity (actuator disc) = V_C/v_i
\bar{V}_T	Tail volume ratio = $S_T l_T / sA$

V_{des}	Descent velocity
\mathbf{v}	Absolute velocity vector
v_i	General induced velocity at rotor
v_{iT}	Downwash at blade tip (with linear distribution)
v_{i0}	Mean induced velocity
\mathbf{v}_{rel}	Relative velocity vector
\bar{v}_i	Induced velocity normalised on thrust velocity = v_i/v_0
v_0	Mean induced velocity in hover (thrust velocity)
\mathbf{v}_0	Velocity of origin of moving frame
v_2	Slipstream velocity in far wake
$v_{3/4}$	Induced velocity component at 3/4 chord point
W	Helicopter weight
W	Total relative flow velocity at blade section
W	Work done
W	Torque on blade element
\mathbf{W}	Total velocity vector at blade section
W_i	Vibration measurement weighting (active vibration control)
W_0, W_1, W_2	Coefficients used in longitudinal response solution
w	Velocity of wake sheets near rotor
w	Wake velocity
w	Induced velocity normal to disc, or aerofoil
w_D	Disc loading = T/A
w_P, w_Q	Induced velocity components normal to rotor at P, Q
w_b	Downward component of induced velocity due to bound vortices
w_c	Weight coefficient = $W/\rho s A \Omega^2 R^2$
w_s	Induced velocity component for shed part of wake
w_t	Downward component of induced velocity due to trailing vortex
X, Y, Z	General or aerodynamic force components
\mathbf{X}	Vector of higher harmonic control (HHC) inputs
$\bar{X}, \bar{Y}, \bar{Z}$	Mean hub force components
X_u, X_w , etc.	X force derivatives
x, y, z	Position coordinates (dimensional, or non-dimensionalised on R)
\bar{x}	Distance of datum point on aerofoil from mid-chord
x_k	General variable measured with respect to rotating k th blade
x_{kg}, y_{kg}	Coordinates of the k th blade relative to centre of hub (ground resonance)
x_{rg}, y_{rg}	Coordinates of rotor c.g. (ground resonance)
x_{st}	Static deflection of single degree of freedom system = F_0/k

x_u, x_w , etc.	Non-dimensional X force derivatives
x_1	Non-dimensional position of vortex filament on blade $= r_1/R$
Y, Z	Displacement of point on blade relative to axes rotating with blade
\mathbf{Y}	Vector of measurement vibration components (active vibration control)
Y_f	Fuselage side-force
Y_v, Y_p , etc.	Y force derivatives
Y_0, Y_1	Bessel functions of first and second kinds (Miller)
y_v, y_p , etc.	Non-dimensional Y force derivatives
\mathbf{Z}	Blade bending deflection vector
\mathbf{Z}_E	Elastic deflection vector of blade bending
\mathbf{Z}_R	Rigid body rotation deflection vector (about flapping hinge)
Z_u, Z_w , etc.	Z force derivatives
z	Distance along rotor axis
\bar{z}_T	Tip vortex axial coordinate (Langrebe)
z_u, z_w , etc.	Non-dimensional Z force derivatives
z_0	Wake coordinate
α	Incidence of blade section
α	Blade torsional stiffness constant $= \omega_0(CR/E_s J)^{1/2}$
$\bar{\alpha}$	Equivalent lag damping coefficient (Ormiston and Hodges)
α_D	Disc incidence
α_T	Tailplane incidence
α_{T0}	No lift setting of tailplane (with respect to fuselage)
α_i	Downwash angle relative to blade
α_i	Stiffening effect due to rotation $= (\omega_i^2 - \omega_{nr}^2)/\Omega^2$
α_i	Spanwise slope at RH end of i th element (Myklestad)
α_{nf}	Incidence with respect to plane of no-feathering
α_s	Rotor hub incidence (i.e. shaft tilt)
α_0	Incidence in the absence of induced velocity
α_0, α_1	Coefficients in polynomial expression for α
α_1, α_2	Amplitudes (Floquet)
$\alpha_1, \alpha_2, \alpha_3$	Lag hinge projected angles
β	Blade flapping angle, at hinge
$\bar{\beta}$	Analogous to β for hingeless rotor blade
β_s	Blade flapping, relative to shaft
β_{ss}	Side-slip angle
β_0	Built-in coning angle
χ	Wake angle
$\bar{\chi}$	Flap bending frequency difference term (air resonance) $= \lambda_1^2 - 1$

$\chi_i(t)$	<i>i</i> th generalised coordinate for lagwise bending
ξ	Blade lagging angle
ξ	Distance of vortex element from centre of aerofoil, based on semi-chord b
ξ, ζ	Aft and downwards position coordinates based on R and aligned with mean downwash angle (for defining tailplane position)
ξ_k	Lag angle of k th blade (ground resonance)
Δ	Stability quartic in Laplace variable p
Δ	Function of κ_β, κ_ξ
δ	Profile drag coefficient = $\delta_0 + \delta_1\alpha + \delta_2\alpha^2$
δ	Lateral deflection at a point on a beam
$\delta, \dot{\delta}$	Blade lag and chassis damping coefficients (ground resonance)
$\delta_1, \delta_2, \delta_3$	Flapping hinge projected angles
ε	Blade hinge offset factor = $M_b e x_g R^2 / B = 3e/2(1 - e)$
ε	Downwash angle at tailplane
ε	Phase angle
ε_0	Mean downwash angle at rotor = v_{i0} / V
$\varepsilon(x)$	Modal error function (Duncan)
ϕ	Shaft angle to vertical (roll of fuselage)
ϕ	Velocity potential, or real part of velocity potential
ϕ	Inflow angle at blade element = $\tan^{-1}(U_p/U_T)$
ϕ	Blade azimuth angle when vortex was shed
$\phi(x, z)$	Potential for plane steady flow past a cylinder (Sears)
$\phi_i(t)$	<i>i</i> th generalised coordinate for flapwise bending
Γ	Circulation, vortex strength
Γ	Blade rotating lag frequency in absence of Coriolis force coupling (ground resonance)
Γ_n	Amplitude of bound circulation (Miller)
Γ_{nc}, Γ_{ns}	In and out of phase components of Γ_n
Γ_q	Quasi-static circulation
Γ_1	Function of derivatives = $-m_q + \mu m_{B1}/z_{B1}$
γ	Lock's inertia number = $\rho acR^4/B$
γ	Vorticity (Theodorsen)
γ	Angular displacement of pendulum arm (bifilar absorber)
$\gamma(x)$	Assumed general blade bending mode shape (Lagrange)
γ_1, γ_2	Lock number equivalents for flexible blade
η	Contraction ratio of slipstream in hover
η	Transformed radial position coordinate (Mangler and Squire) = $(1-x^2)^{1/2}$

η	Non-dimensional chordwise position (thin aerofoil theory)
η, ζ	Coleman coordinates (ground resonance)
κ, κ_c	General blade lag, and chassis frequencies in terms of Ω
κ_β, κ_ξ	Functions of $\kappa_{\beta H}$, $\kappa_{\beta B}$ and $\kappa_{\xi H}$, $\kappa_{\xi B}$
$\kappa_{\beta H}, \kappa_{\xi H}$	Flap and lag stiffnesses of ‘hub springs’
$\kappa_{\beta B}, \kappa_{\xi B}$	Remainder of above stiffnesses outboard of feathering hinge
κ_l	First blade uncoupled natural rotating lag frequency in terms of Ω
$\frac{\Lambda}{\Lambda}$	Local wake helix angle
Λ_b	Wake constant (Landgrebe)
Λ_0	Bobweight arm length ratio = d_1/d_2 (DAVI)
λ	Far wake helix angle = $w/\Omega R_0$
λ	Mean inflow ratio relative to plane of no-feathering = $\sin \alpha_{nf} - \lambda_i$
λ	Rotating flap bending frequency in terms of Ω
λ, λ_n	General and n th eigenvalue in characteristic equation
λ'	General inflow ratio (function of ψ, r) = $(V \sin \alpha_{nf} - v_i)/\Omega R$
λ_D	Mean inflow ratio relative to disc plane = $\sin \alpha_D - \lambda_i$
λ_c	Climb inflow ratio = $V_c/\Omega R$ (axial flight), $\approx \sin \tau_c$ (forward flight)
λ_i	$v_{i0}/\Omega R$, or $v_{i1}/\Omega R$ for hovering flight
λ_{iT}	$v_{iT}/\Omega R$
$\lambda_{re}, \lambda_{im}$	Real and imaginary parts of eigenvalue λ
λ_l	First blade uncoupled natural rotating flap frequency in terms of Ω
μ	Constant determining natural undamped frequency of a non-rotating beam, from standard published results = $(m\omega_{nr}^2/EI)^{1/4}$
μ	Mass ratio (ground resonance) = $0.5bM_b/(M + bM_b)$
μ, μ_D	Advance ratios = $\hat{V} \cos \alpha_{nf}$, $\hat{V} \cos \alpha_D$
$\bar{\mu}$	Magnification factor = x_0/x_{st}
μ^*	Relative density parameter = $W/g\rho sAR$
μ_b	Bobweight mass ratio = m_{bob}/M_1 (DAVI)
ν	Helicopter pitching frequency ratio in terms of rotor revolutions
ν	Far wake velocity ratio
ν	Factor depending on disc tilt (Mangler and Squire) = $(1 - \sin \alpha_D)/(1 + \sin \alpha_D)$
ν	Lag bending frequency ratio
$\bar{\nu}$	Air resonance factor = $\gamma E_1/2$

\hat{v}	Incremental frequency term (Floquet) = $\gamma/16$
v_1	First blade uncoupled natural rotating torsional frequency in terms of Ω
v_1, v_2	Exponent constants (Floquet)
θ	Blade pitch or feathering angle
θ	Fuselage pitch attitude (shaft angle to vertical)
$\bar{\theta}$	Laplace transform of θ (fuselage pitch)
θ_{bar}	Angular displacement of Bell stabilising bar
θ_n	Amplitude of blade pitch variation at circular frequency n
θ_t	Tail-rotor collective pitch
θ_0	Collective pitch angle
θ_1	Blade twist (washout)
ρ	Ambient air density, or material density
ρ	Component of inflow angle = $\tan^{-1}(v_i/W)$
ρ_e	Degree of elastic coupling = $\kappa_\beta/\kappa_{\beta B} = \kappa_\xi/\kappa_{\xi B}$
ρ_m	Fuselage mass ratio = M_2/M_1 (DAVI)
σ	Solidity based on local radius = $bc/\pi r$
σ_g	Distance of c.g. of blade elemental strip behind flexural axis in terms of c
σ_1, σ_{-1}	Functions of lag frequency (ground resonance)
τ	Period of one rotor revolution
τ	Non-dimensional aerodynamic unit of time = t/\hat{t}
τ_c	Climb angle
τ_{des}	Angle of descent
Ω	Rotor or blade angular velocity
Ω	Angular velocity vector = $\omega_1 \mathbf{i} + \omega_2 \mathbf{j} + \omega_3 \mathbf{k}$
ω	Total wake swirl velocity
ω	Circular frequency
$\tilde{\omega}$	Normalised excitation frequency
ω_b	Component of ω due to bound circulation
ω_n	Natural frequency
ω_{nr}	Natural frequency of non-rotating blade
ω_t	Component of ω due to trailing vortices
ω_β	Uncoupled rotating flap natural frequency
ω_ξ	Uncoupled rotating lag natural frequency
ω_θ	Rotating torsional natural frequency
ω_0	Non-rotating torsional natural frequency
ψ	Azimuthal angular position of blade, or general angular coordinate

ψ	Imaginary part of velocity potential
ψ	Yaw displacement of helicopter (from steady state)
ψ_n	Angle between adjacent blades
ψ_w	Wake azimuth relative to blade
ζ	Non-dimensional damping factor = c/c_{crit}
ζ_{mean}	Weighted mean damping (stall flutter)
$\zeta_i(t)$	i^{th} generalised coordinate for blade torsion

Suffixes

The following suffixes refer to:

A	Aerodynamic
A, B, D, E	Inertia moments and products
D	Rotor disc (tip-path plane)
D	Drag
L	Lift
M	Moment
N	Normal force
P	Perpendicular
P	Profile drag
T	Tip of blade
T	Thrust
T	Tailplane
T	Tangential
b	Bound vorticity
c	Climbing
c	Coefficient
c	Chassis
e	Effective
f	Fuselage
g	Blade c.g., or c.g. of system of particles
h	On matrices indicates row is used to correspond to hinge
i	Induced
l, u	Lower and upper surfaces
kg	C.g. of k^{th} blade relative to hub (ground resonance)
nf	No feathering
nr	Non-rotating
p	Pressure
r	Radial direction
r	Root of blade
r	Rotor
rg	Rotor c.g. (ground resonance)
s	Shaft

s	Due to centrifugal force at blade hinge
s	Setting angle of tailplane
s	Shed part of wake
ss	Sideslip
t	Trailing vortices
t	Tail rotor
w	Wake
z	In z direction
β	Flap
ξ	Lag
θ	Pitch
ψ	In tangential direction
0	Generally modulus, or amplitude of
∞	At infinity

Basic mechanics of rotor systems and helicopter flight

1.1 Introduction

In this chapter we shall discuss some of the fundamental mechanisms of rotor systems from both the mechanical system and the kinematic motion and dynamics points of view. A brief description of the rotor hinge system leads on to a study of the blade motion and rotor forces and moments. Only the simplest aerodynamic assumptions are made in order to obtain an elementary appreciation of the rotor characteristics. It is fortunate that, in spite of the considerable flexibility of rotor blades, much of helicopter theory can be effected by regarding the blade as rigid, with obvious simplifications in the analysis. Analyses that involve more detail in both aerodynamics and blade properties are made in later chapters. The simple rotor system analysis in this chapter allows finally the whole helicopter trimmed flight equilibrium equations to be derived.

1.2 The rotor hinge system

The development of the autogyro and, later, the helicopter owes much to the introduction of hinges about which the blades are free to move. The use of hinges was first suggested by Renard in 1904 as a means of relieving the large bending stresses at the blade root and of eliminating the rolling moment which arises in forward flight, but the first successful practical application was due to Cierva in the early 1920s. The most important of these hinges is the *flapping* hinge which allows the blade to flap, i.e. to move in a plane containing the blade and the shaft. Now a blade which is free to flap experiences large Coriolis moments in the plane of rotation and a further hinge – called the *drag* or *lag* hinge – is provided to relieve these moments. Lastly, the blade can be *feathered* about a third axis, usually parallel to the blade span, to enable the blade pitch angle to be changed. A diagrammatic view of a typical hinge arrangement is shown in Fig. 1.1.

2 Bramwell's Helicopter Dynamics

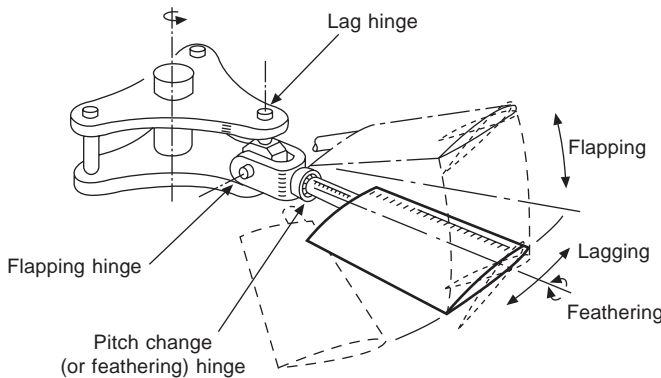


Fig. 1.1 Typical hinge arrangement

In this figure, the flapping and lag hinges intersect, i.e. the hinges are at the same distance from the rotor shaft, but this need not necessarily be the case in a particular design. Neither are the hinges always absolutely mutually perpendicular.

Consider the arrangement shown in Fig. 1.2. Let OX be taken parallel to the blade-span axis and OZ perpendicular to the plane of the rotor hub. Let OP represent either the flapping hinge axis or the lag hinge axis. The flapping hinge is referred to as the δ -hinge and the lag hinge as the α -hinge. We then define:

- the angle between OZ and the projection of OP onto the plane OYZ as δ_1 or α_1 ,
- the angle between OZ and the projection of OP onto the plane OXZ as δ_2 or α_2 ,
- the angle between OY and the projection of OP onto the plane OXY as δ_3 or α_3 .

These are the definitions in common use in industry. The most important angles in practice are α_2 , which leads to pitch resulting from lagging of the blade, and δ_3 , which couples pitch and flap, as follows.

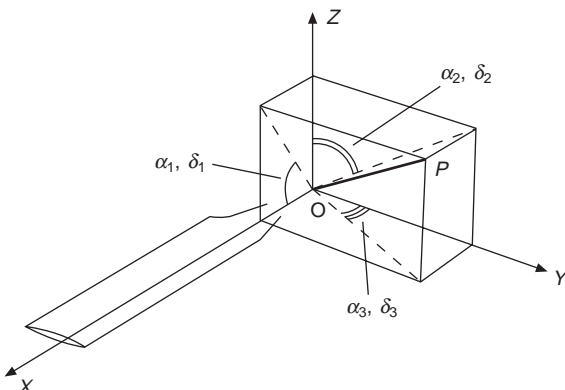


Fig. 1.2 Blade hinge angles

Referring to Fig. 1.3, when δ_3 is positive, positive blade flapping causes the blade pitch angle to be reduced. It will also be appreciated that, if the drag hinge is mounted outboard of the flapping hinge, movement about the lag hinge produces a δ_3 effect. If the blade moves through angle ξ_0 and flaps through angle β relative to the hub plane, the change of pitch angle $\Delta\theta$ due to flapping is found to be

$$\Delta\theta = -\tan \beta \tan(\delta_3 - \xi_0)$$

or for small angles

$$\Delta\theta = -\beta \tan(\delta_3 - \xi_0)$$

so $\Delta\theta$ is proportional to β .

The dynamic coupling of blade motions will be dealt with in more detail in Chapter 9.

The blades of two-bladed rotors are usually mounted as a single unit on a ‘see-saw’ or ‘teetering’ hinge, Fig. 1.4(a). No lag hinges are fitted, but the Coriolis root

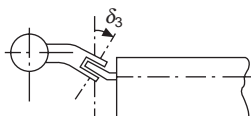
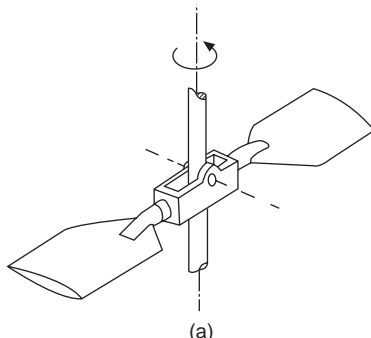
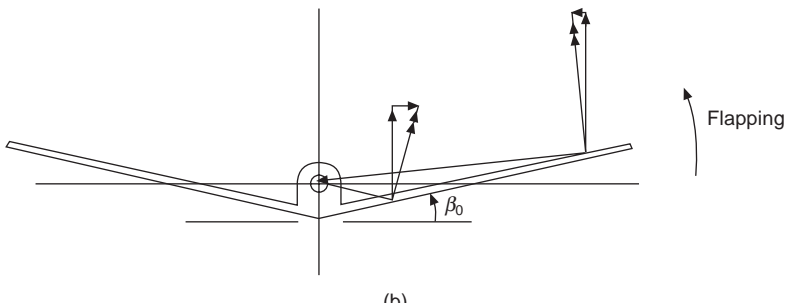


Fig. 1.3 The δ_3 -hinge



(a)



(b)

Fig. 1.4 (a) Teetering or see-saw rotor. (b) Underslung rotor, showing radial components of velocity on upwards flapping blade

4 Bramwell's Helicopter Dynamics

bending moments may be greatly reduced by ‘underslinging’ the rotor Fig. 1.4(b). It can be seen from the figure that, when the rotor flaps, the radial components of velocity of points on the upwards flapping blade below the hinge line are positive while those above are negative. Thus the corresponding Coriolis forces are of opposite sign and, by proper choice of the hinge height, the moment at the blade root can be reduced to second order magnitude. This assumes that a certain amount of pre-cone or blade flap, β_0 , is initially built in.

Although, as stated earlier, the adoption of blade hinges was an important step in the evolution of the helicopter, several problems are posed by the presence of hinges and the dampers which are also fitted to restrain the lagging motion. Not only do the bearings operate under very high centrifugal loads, requiring frequent servicing and maintenance, but when the number of blades is large the hub becomes very bulky and may contribute a large proportion of the total drag. Figure 1.5(a) shows a diagrammatic view of the Westland Wessex hub, on which, as may be observed, the flapping and lag hinges intersect. Figure 1.5(b) is a photograph of the same rotor hub, showing also the swash plate mechanism that enables the cyclic and collective pitch control (discussed in section 1.7).

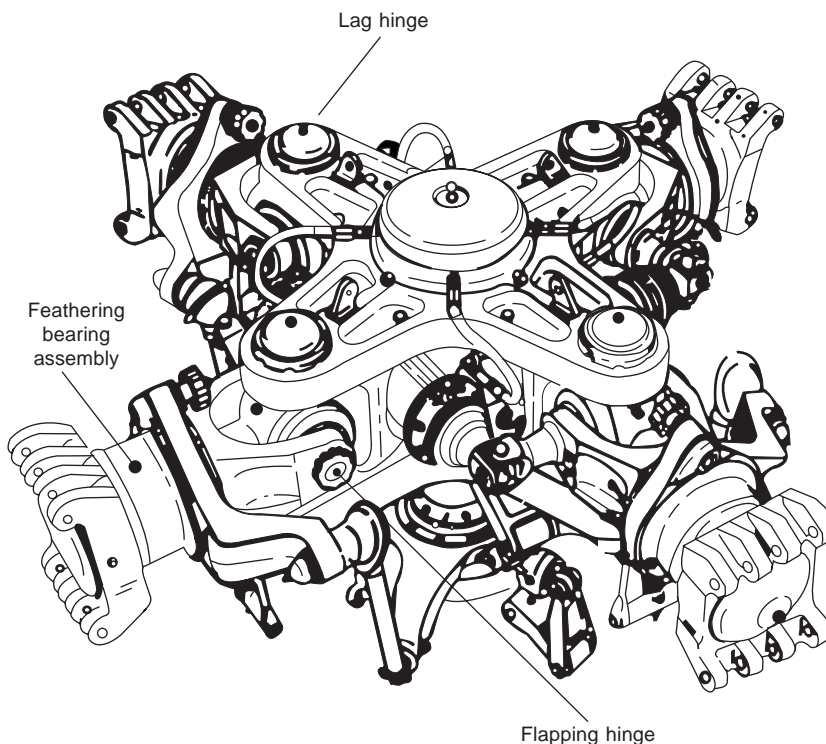


Fig. 1.5 (a) Diagrammatic view of Westland Wessex hub

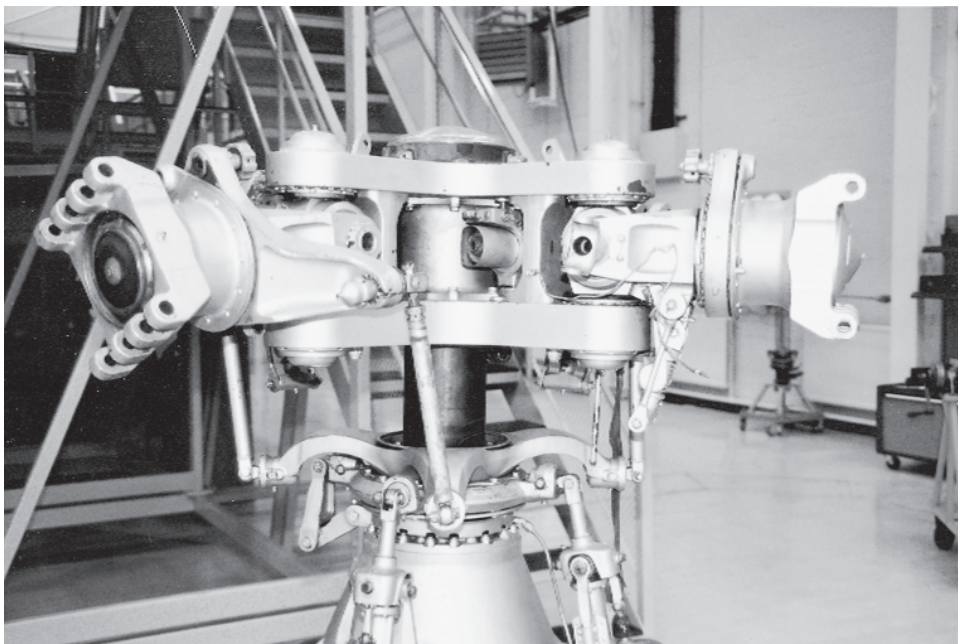


Fig. 1.5 (b) Photograph of Westland Wessex hub

More recently, improvements in blade design and construction enabled rotors to be developed which dispensed with the flapping and lagging hinges. These ‘hingeless’, or less accurately termed ‘semi-rigid’, rotors have blades which are connected to the shaft in cantilever fashion but which have flexible elements near to the root, allowing the flapping and lagging freedoms. Such a design is shown in Fig. 1.6(a) which is that of the Wesland Lynx helicopter. In this case, the flexible element is close in to the rotor shaft, with the feathering hinge between it and the flexible lag element, which is the furthest outboard. The diagram also indicates the attached lag dampers mentioned previously, and discussed in relation to ground resonance in Chapter 9, and a different, but less common, mechanism for changing the cyclic and collective pitch on the blades. A photograph of the same hub design, but with five blades, is shown in Fig. 1.6(b). Rotor hub designs for current medium to large helicopters commonly use a high proportion of composite material for the main structural elements, with elastomeric elements providing freedoms where only low stiffnesses are required (e.g. to allow blade feathering).

We now derive the equations of flapping, lagging, and feathering motion of the hinged blade – but assuming it to be rigid, as mentioned in the introduction. The motion of the hingeless blade will be considered in Chapter 7. Fortunately, except for the lagging motion, the equations can be derived with sufficient accuracy by treating each degree of freedom separately, e.g. in considering flapping motion it can be assumed that lagging and feathering do not occur.

6 Bramwell's Helicopter Dynamics

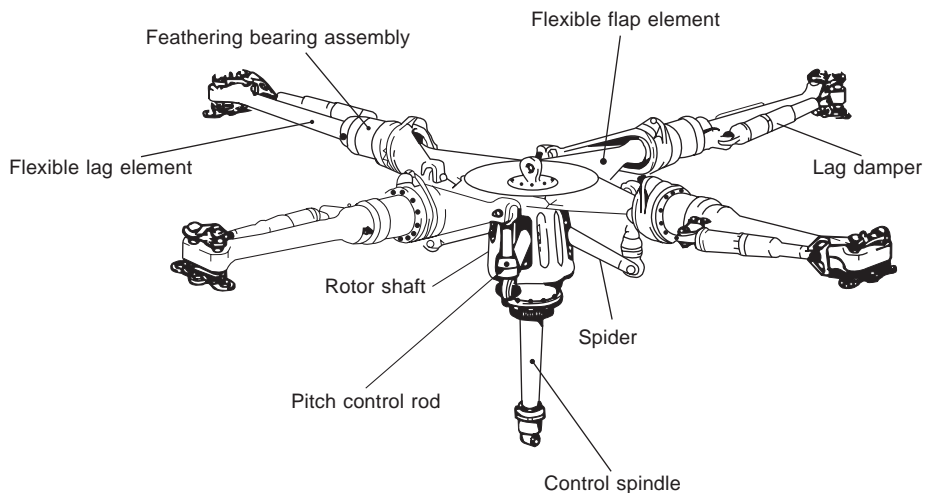


Fig. 1.6 (a) Diagrammatic view of Westland Lynx hub

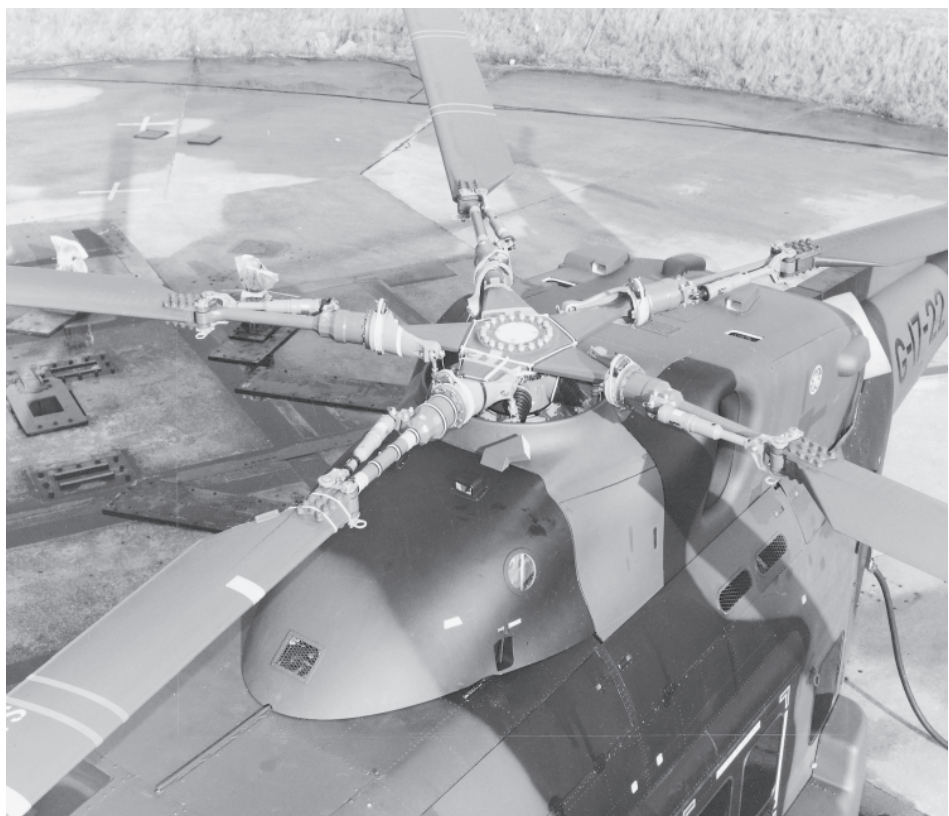


Fig. 1.6 (b) Photograph of Westland Lynx five-bladed hub

1.3 The flapping equation

Consider a single blade as shown in Fig. 1.7 and let the flapping hinge be mounted a distance eR from the axis of rotation. The shaft rotates with constant angular velocity Ω and the blade flaps with angular velocity $\dot{\beta}$. Take axes fixed in the blade, parallel to the principal axes, origin at the hinge, with the i axis along the blade span, the j axis perpendicular to the span and parallel to the plane of rotation, and the k axis completing the right-hand set. To a very good approximation the blade can be treated as a lamina.

Then, if A is the moment of inertia about i , and B the moment of inertia about j , the moment of inertia C about k is equal to $A + B$. The angular velocity components $\omega_1, \omega_2, \omega_3$ about these axes are

$$\omega_1 = \Omega \sin \beta, \quad \omega_2 = -\dot{\beta}, \quad \omega_3 = \Omega \cos \beta$$

The acceleration, \mathbf{a}_0 , of the origin is clearly $\Omega^2 eR$ and perpendicular to the shaft. Along the principal axes the components are

$$\{-\Omega^2 eR \cos \beta, \quad 0, \quad \Omega^2 eR \sin \beta\}$$

The position vector of the blade c.g. is $\mathbf{r}_g = x_g R i$, so that the components of $\mathbf{r}_g \times \mathbf{a}_0$ are

$$\{0, ex_g \Omega^2 R^2 \sin \beta, 0\}$$

The flapping motion takes place about the j axis, so putting the above values in the second of the ‘extended’ Euler’s equations derived in the appendix (eqn A.1.15), and using $A + B = C$, gives

$$B\ddot{\beta} + \Omega^2(B \cos \beta + M_b ex_g R^2) \sin \beta = M_A \quad (1.1)$$

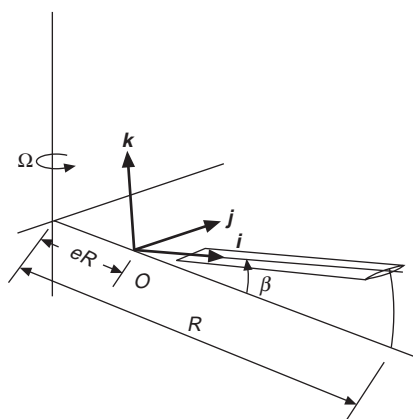


Fig. 1.7 Single flapping blade

8 Bramwell's Helicopter Dynamics

where $M_A = -M$ is the aerodynamic moment in the sense of positive flapping and M_b is the blade mass. For small flapping angles eqn 1.1 can be written

$$\ddot{\beta} + \Omega^2(1 + \varepsilon) \beta = M_A/B \quad (1.2)$$

where $\varepsilon = M_b e x_g R^2 / B$.

If the blade has uniform mass distribution, it can easily be verified that $\varepsilon = 3e/2(1 - e)$. A typical value of e is 0.04, giving ε as approximately 0.06.

The flapping equation (eqn 1.1) could also have been derived by considering an element of the blade of mass dm , and at a distance r from the hinge, to be under the action of a centrifugal force $(eR + r \cos \beta) \Omega^2 dm$ directed outwards and perpendicular to the shaft. The integral of the moment of all such forces along the blade is found to be the second term of eqn 1.1, i.e. $\Omega^2(B \cos \beta + M_b e x_g R^2) \sin \beta$. Regarding it as an external moment like M_A , this centrifugal moment (for small β) acts like a torsional spring tending to return the blade to the plane of rotation.

The other two extended Euler's equations (eqns A.1.17 and A.1.19) give

$$L = 0 \text{ and } N = -2B\Omega \dot{\beta} \sin \beta$$

These are the moments about the feathering and lag axes, respectively, which are required to constrain the blade to the flapping plane, or, in other words, $-L$ and $-N$ are the couples which the blade exerts on the hub due to flapping only. It can be seen that flapping produces no feathering inertia moment, but the in-plane moment $2B\Omega \dot{\beta} \sin \beta$ is often so large that it is usually relieved by the provision of a lag hinge or equivalent flexibility, as mentioned in section 1.2. This moment is the moment of the Coriolis inertia forces acting in the in-plane direction.

More generally, if the rotor hub is pitching with angular velocity q , Fig. 1.8, the angular velocity components of the blade are

$$\{q \sin \psi \cos \beta + \Omega \sin \beta, q \cos \psi - \dot{\beta}, -q \sin \psi \sin \beta + \Omega \cos \beta\}$$

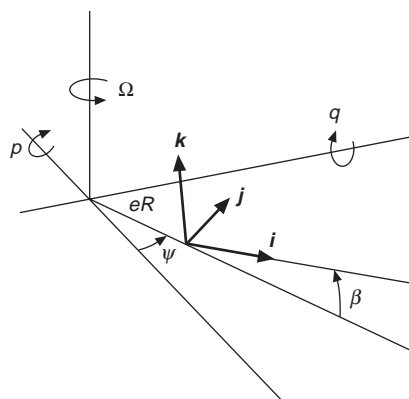


Fig. 1.8 Blade influenced by rotor hub pitching velocity q and rolling velocity p

where ψ is the *azimuth* angle of the blade, defined as the angle between the blade span and the rear centre line of the helicopter. The absolute accelerations of the hinge point O are the centripetal acceleration $\Omega^2 eR$ acting radially inwards and $eR(\dot{q} \cos \psi - 2q\Omega \sin \psi)$ acting normal to the plane of the rotor hub.

Inserting these values into eqn A.1.15 and neglecting q^2 , which is usually very small compared with Ω^2 , we finally obtain after some manipulation

$$\ddot{\beta} + \Omega^2(1 + \varepsilon)\beta = M_A/B - 2\Omega q(1 + \varepsilon) \sin \psi + \dot{q}(1 + \varepsilon) \cos \psi \quad (1.3)$$

The second term on the right is the gyroscopic inertia moment due to pitching velocity, and the third term is due to the pitching acceleration.

We now find that the feathering moment L is

$$L = A(2\Omega q \cos \psi + \dot{q} \sin \psi)$$

which means that the pitching motion produces a moment tending to twist the blade. The moment about the lag axis is hardly affected by the pitching motion, so that N remains as before.

When the rotor hub is rolling with angular velocity p , Fig. 1.8, the equivalent equation to 1.3 may be derived in like manner, and in this case the extra terms on the right-hand side can be shown to be $(1 + \varepsilon)(2\Omega p \cos \psi + \dot{p} \sin \psi)$.

1.4 The equation of lagging motion

We assume the flapping angle to be zero and that the blade moves forward on the lag hinge through angle ξ (Fig. 1.9). The angular velocity of the blade is $(\Omega + \dot{\xi})\mathbf{k}$ and $a_0 = -\Omega^2 eR(\cos \xi \mathbf{i} - \sin \xi \mathbf{j})$. Then the third of Euler's extended equations gives

$$C \ddot{\xi} + M_b e x_g \Omega^2 R^2 \sin \xi = N \quad (1.4)$$

or, for small ξ ,

$$\ddot{\xi} + \Omega^2 \varepsilon \xi = N/C \quad (1.5)$$

where ε , in this case, is $M_b e x_g R^2 / C$, eR being the drag-hinge offset distance.

It can easily be verified that if flapping motion is also included, the only important term arising is the moment $2B\Omega\beta\dot{\beta}$ calculated in the previous section. With a lag

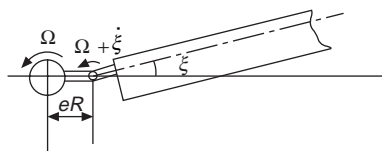


Fig. 1.9 Blade lagging

10 Bramwell's Helicopter Dynamics

hinge fitted, this moment can be regarded as an inertia moment and considered as part of N . Then, if N_A is taken as the aerodynamic lagging moment, together with any artificial damping which may be, and usually is, added, eqn 1.5 can be written finally as

$$\ddot{\xi} + \Omega^2 \varepsilon \xi - 2\Omega \beta \dot{\beta} = N_A/C \text{ (since } B \approx C) \quad (1.6)$$

The lagging motion produces no moment about the feathering axis, but the instantaneous angular velocity $\Omega + \dot{\xi}$ will affect the centrifugal and aerodynamic flapping moments and may have to be taken into account when considering coupled motion (see section 9.7).

1.5 Feathering motion

It is assumed that the flapping and lagging angles are zero and that the blade feathers through angle θ (Fig. 1.10). The angular velocity components about i , j , k are $\dot{\theta}$, $\Omega \sin \theta$, $\Omega \cos \theta$. The first of Euler's extended equations gives

$$A\dot{\theta} + A\Omega^2 \sin \theta \cos \theta = L \quad (1.7)$$

and, for the small feathering angles which normally occur, we can write

$$\ddot{\theta} + \Omega^2 \theta = L/A \quad (1.8)$$

The second and third of Euler's equations show that the feathering motion produces no flapping moment but a lagging moment of $-2A\dot{\theta}\Omega \sin \theta$. This latter moment is extremely small compared with the flapping Coriolis moment and can be neglected.

1.6 Flapping motion in hovering flight

The equation of blade flapping (1.2) is

$$d^2\beta/dt^2 + \Omega^2(1 + \varepsilon)\beta = M_A/B$$

It is convenient to change the independent variable from time to blade azimuth angle by means of $\psi = \Omega t$. Then since

$$d/dt = \Omega d/d\psi \quad \text{and} \quad d^2/dt^2 = \Omega^2 d^2/d\psi^2$$

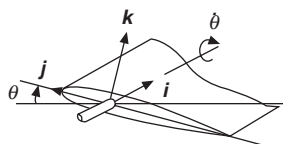


Fig. 1.10 Blade feathering

eqn 1.2 becomes

$$\frac{d^2\beta}{d\psi^2} + (1 + \varepsilon)\beta = M_A/B\Omega^2 \quad (1.9)$$

This equation is valid for any case of steady rectilinear flight including hovering. The problem is to express M_A as a function of ψ and then to solve the equation. We now consider some simple but important examples in hovering flight.

1.6.1 Disturbed flapping motion at constant blade pitch angle

We suppose that the blades are set at a constant blade pitch angle relative to the shaft and that the rotor is rotating steadily with angular velocity Ω . Since we are interested only in the character of the disturbed motion, the aerodynamic moment corresponding to the constant pitch angle will be ignored and attention will be concentrated on the aerodynamic moments arising from disturbed flapping motion.

Now, when a blade flaps with angular velocity $\dot{\beta}$, there is a relative downwash of velocity $r\dot{\beta}$ at a point on the blade distance r from the hinge. Assuming $\cos \beta = 1$, the chordwise component of wind velocity is $\Omega(r + eR)$, so that the local change of incidence $\Delta\alpha$ due to flapping is

$$\Delta\alpha = \frac{-r\dot{\beta}}{(r + eR)\Omega} = \frac{-x \frac{d\beta}{d\psi}}{x + e}$$

where $x = r/R$.

Assuming a constant lift slope a for the blade section, the lift on an element of blade is

$$dL = -\frac{1}{2}\rho ac\Omega^2 R^3(x + e)x(d\beta/d\psi)dx$$

The moment of this lift about the flapping hinge is rdL and the total aerodynamic moment, assuming the blade chord c to be constant, is

$$M_A = \int_0^{R(1-e)} rdL = -\frac{1}{2}\rho ac\Omega^2 R^4 \int_0^{(1-e)} x^2(x + e)(d\beta/d\psi)dx$$

giving

$$M_A/B\Omega^2 = -(\gamma/8)(1 - e)^3(1 + e/3)d\beta/d\psi$$

where $\gamma = \rho acR^4/B$ is called *Lock's inertia number*.

Writing n for $(1 - e)^3(1 + e/3)$, the flapping equation becomes

$$\frac{d^2\beta}{d\psi^2} + (n\gamma/8)d\beta/d\psi + (1 + \varepsilon)\beta = 0 \quad (1.10)$$

Equation 1.10 is the equation of damped harmonic motion with a natural undamped frequency $\Omega\sqrt{1 + \varepsilon}$. If ε is zero (no flapping hinge offset), the natural undamped frequency is exactly equal to the shaft frequency. Normally ε is about 0.06, giving an undamped flapping frequency about 3 per cent higher than the shaft frequency.

Taking a typical value of γ of 6 gives a value for $n\gamma/8$ of about 0.7. This means that the damping of the motion is about 35 per cent of critical, or that the *time-constant*

in terms of the azimuth angle is about 90° or $\frac{1}{4}$ of a revolution. Thus, the flapping motion is very heavily damped. It has already been remarked that the centrifugal moment acts like a spring, and we now see that flapping produces an aerodynamic moment proportional to flapping rate, i.e. in hovering flight the blade behaves like a mass–spring–dashpot system. In forward flight the damping is more complicated and includes a periodic component, but the notion of the blade as a second order system is often a useful one in a physical interpretation of blade motion.

1.6.2 Flapping motion due to cyclic feathering

Suppose that, in addition to a constant (collective) pitch angle θ_0 , the blade pitch is varied in a sinusoidal manner relative to the hub plane. The blade pitch θ can then be expressed as

$$\theta = \theta_0 - A_1 \cos \psi - B_1 \sin \psi \quad (1.11)$$

To simplify the calculations we will take $e = 0$, since the small values of flapping hinge offset normally employed have little effect on the flapping motion.

In calculating the flapping moment M_A , the induced velocity, or rotor downwash, to be discussed in Chapter 2, will be ignored. By a similar analysis to that above, the flapping moment is easily found to be given by

$$M_A/B\Omega^2 = \gamma(\theta_0 - A_1 \cos \psi - B_1 \sin \psi)/8$$

Substituting in eqn 1.9 leads to the steady-state solution

$$\beta = \gamma\theta_0/8 - A_1 \sin \psi + B_1 \cos \psi \quad (1.12)$$

The term $\gamma\theta_0/8$ represents a constant flapping angle and corresponds to a motion in which the blade traces out a shallow cone, and for this reason the angle is called the *coning angle*. If the induced velocity had been included, the coning angle would have been reduced somewhat. For our present purpose the exact calculation of the coning angle is unimportant. The terms $-A_1 \sin \psi + B_1 \cos \psi$ represent a tilt of the axis of the cone away from the shaft axis. Since ψ is usually measured from the rearmost position of the blade, i.e. along the axis of the rear fuselage, a positive value of B_1 denotes a forward (nose down) tilt of the cone, Fig. 1.11, while a positive value of A_1 denotes a sideways component of tilt in the direction of $\psi = 90^\circ$. The blade tips trace out the ‘base’ of the cone, which is often referred to as the *tip path plane* or as the *rotor disc*, Fig. 1.11.

In steady flight the blade motion must be periodic and is therefore capable of being expressed in a Fourier series as

$$\beta = a_0 - a_1 \cos \psi - b_1 \sin \psi - a_2 \cos 2\psi - b_2 \sin 2\psi - \dots \quad (1.13)$$

For the case in question,

$$a_0 = \gamma\theta_0/8, \quad a_1 = -B_1, \quad b_1 = A_1$$

$$a_2 = b_2 = \dots \text{ etc.} = 0$$

When the flight condition is steady, eqn 1.9 can always be solved by assuming the

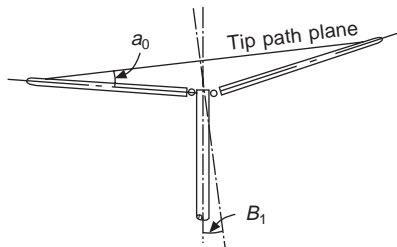


Fig. 1.11 Interpretation of flapping and feathering coefficients

form of eqn 1.13, substituting in the flapping equation, and equating coefficients of the trigonometric terms. This is a method we shall be forced to adopt when the flapping equation contains periodic coefficients, as will be the case in forward flight.

In terms of eqn 1.13, a_0 represents the coning angle and a_1 and b_1 represent respectively, a backward and sideways tilt of the rotor disc, the sideways tilt being in the direction of $\psi = 90^\circ$. The higher harmonics a_2, b_2, a_3, \dots , etc., which will have non-zero values in forward flight, can be interpreted as distortions or a ‘crinkling’ of the rotor cone. But although these harmonics can be calculated, the blade displacements they represent are only of the same order as those of the elastic deflections which, so far, have been neglected. Thus, it is inconsistent to calculate the higher harmonics of the rigid blade mode of motion without including the other deflections of the blade. Stewart¹ has shown that the higher harmonics are usually about one tenth of the values of those of the next order above.

Comparison of eqns 1.11 and 1.12 shows that the amplitude of the periodic flapping is precisely the same as the applied cyclic feathering and that the flapping lags the cyclic pitch by 90° . The phase angle is exactly what we might have expected, since the aerodynamic flapping moment forces the blade at its undamped natural frequency and, as is well known, the phase angle of a second order dynamic system at resonance is 90° whatever the damping. Further, the fact that the amplitude of flapping is exactly the same as the applied feathering has a simple physical explanation. Suppose that initially no collective or cyclic pitch were applied; the blades would then trace out a plane perpendicular to the rotor shaft. If cyclic pitch were then applied, and the blades remained in the initial plane of rotation, they would experience a cyclic variation of incidence and, hence, of aerodynamic moment. The moment would cause the blades to flap and, since, as we have found, blade flapping motion is stable, the blades must seek a new plane of rotation such that the flapping moment vanishes. This is clearly a plane in which there is no cyclic feathering and it follows from Fig. 1.12 that this plane makes the same angle to the shaft as the amplitude of the cyclic pitch variation. It is also obvious that the effect of applying cyclic pitch is precisely the same as if cyclic pitch had been absent but the shaft had been tilted through the same angle. Tilting the rotor shaft or, more precisely, the rotor hub plane, is the predominant method of controlling the rotor of an autogyro. Tilting the shaft of a helicopter is impossible if it is driven by a fuselage mounted engine, and the rotor must be controlled by cyclic feathering.

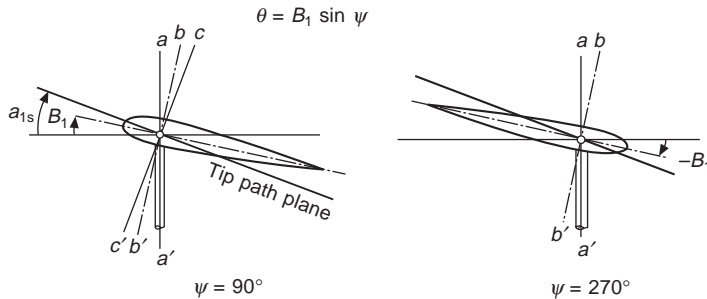


Fig. 1.12 Equivalence of flapping and feathering

The above discussion illustrates the phenomenon of the so-called ‘equivalence of feathering and flapping’; the interpretation is a purely geometric one. If flapping and feathering are purely sinusoidal, the amplitude of either depends entirely upon the axis to which it is referred. In Fig. 1.12, aa' is the shaft axis, bb' is the axis perpendicular to the blade chord, cc' the axis perpendicular to the tip path plane. If Fig. 1.12 shows the blade at its greatest pitch angle, bb' is clearly the axis relative to which the cyclic feathering vanishes and is called the *no-feathering axis*. Similarly cc' is the axis of no flapping.

Let a_{1s} be the angle between the shaft and the tip path plane and B_1 the angle between the shaft and the no-feathering axis. Viewed from the no-feathering axis the cyclic feathering is, by definition, zero but the angle of the tip path plane is $a_{1s} - B_1$. On the other hand, viewed from the tip path plane, the flapping is zero but the feathering amplitude is $B_1 - a_{1s}$. Thus feathering and flapping can be interchanged and either may be made to vanish by the appropriate choice of axis. The ability to select an axis relative to which either the feathering or flapping vanishes is useful in simplifying the analysis of rotor blade motion and for interpreting rotor behaviour. The coning angle a_0 and collective pitch θ_0 play no part in the principle of equivalence.

Strictly speaking, the principle of equivalence fails if the flapping hinges are offset, because the angle of the tip path plane will then no longer be the same as the amplitude of blade flapping, as a sketch will easily show. However, the size of the offset is usually so small that the equivalence idea can be generally applied. Offset hinges, as will be seen later, make an important contribution to the moments on the helicopter.

Another important feature of blade flapping motion can be deduced from the flapping equation. Assuming ε to be negligible, the flapping equation (eqn 1.9) can be written

$$\frac{d^2\beta}{d\psi^2} + \beta = M_A/B\Omega^2$$

in which β is defined relative to a plane perpendicular to the shaft axis.

Now, assuming that higher harmonics can be neglected, steady blade flapping can be expressed in the form

$$\beta = a_0 - a_1 \cos \psi - b_1 \sin \psi$$

and on substitution for β into the flapping equation above

$$M_A = B\Omega^2 a_0 = \text{constant}$$

Thus, for first harmonic motion, the blade flaps in such a way as to maintain a constant aerodynamic flapping moment. This does not necessarily mean that the blade thrust is also constant, since, except in hovering flight, the blade loading distribution varies with azimuth angle and the centre of pressure of the loading moves along the blade.

1.6.3 Flapping motion due to pitching or rolling

An important hovering flight case for which the response of the rotor can be calculated is pitching or rolling. Consider first the case of pitching at constant angular velocity q . The equation of motion, eqn 1.3, with $\varepsilon = 0$, is

$$\frac{d^2\beta}{dt^2} + \Omega^2\beta = M_A/B - 2\Omega q \sin \psi \quad (1.14)$$

Due to pitching and flapping, the velocity component normal to the blade at a point distance r from the hub is $r(q \cos \psi - \dot{\beta})$; with $\cos \beta = 1$ and neglecting a very small term in q , the chordwise velocity is Ωr . The corresponding change of incidence $\Delta\alpha$ is therefore

$$\Delta\alpha = (q \cos \psi - \dot{\beta})/\Omega = \hat{q} \cos \psi - d\beta/d\psi$$

where $\hat{q} = q/\Omega$.

The contribution to the flapping moment of the flapping velocity $\dot{\beta}$ has already been considered in section 1.6.1; by a similar calculation the moment due to the pitching velocity q is found to be

$$(M_A)_{\text{pitching}} = \rho ac\Omega^2 R^4 \hat{q} \cos \psi / 8 \quad (1.15)$$

Equation 1.14 now becomes

$$\frac{d^2\beta}{d\psi^2} + \frac{\gamma}{8} \frac{d\beta}{d\psi} + \beta = \frac{\gamma}{8} \hat{q} \cos \psi - 2\hat{q} \sin \psi \quad (1.16)$$

Assuming a steady-state solution, $\beta = a_0 - a_1 \cos \psi - b_1 \sin \psi$ gives

$$a_1 = -16\hat{q}/\gamma, \quad b_1 = -\hat{q} \quad (1.17)$$

Hence, when the shaft has a steady positive rate of pitch, the rotor disc tilts forward by amount $16\hat{q}/\gamma$ and sideways (towards $\psi = 270^\circ$) by amount \hat{q} . The longitudinal a_1 tilt is due to the gyroscopic moment on the blade, and the lateral b_1 tilt to the aerodynamic moment due to flapping. For typical values of γ , the lateral tilt is roughly half the longitudinal tilt.

The same result can be obtained in a somewhat different way by focusing attention on the rotor disc. If steady blade motion is assumed to occur, each blade behaves identically and the rotor can be regarded as a rigid body rotating in space with angular velocity components Ω about the shaft and q perpendicular to the shaft.

16 Bramwell's Helicopter Dynamics

According to elementary gyroscopic theory, the rotor will experience a precessing moment $bC\Omega q$ tending to tilt it laterally towards $\psi = 90^\circ$, bC being the moment of inertia of all the blades in the plane of rotation. In addition, there is the aerodynamic moment on the rotor due to its pitching rotation. Using eqn 1.15, we find that the total moment for *all* the blades is $bC\rho a\Omega^2 R^4 \hat{q}/16$ and is in the nose down sense. Now, these two moments must be in equilibrium with an aerodynamic moment produced by a cyclic pitch variation in the tip path plane, and the rotor achieves this by appropriate tilts a_1 and b_1 relative to the shaft. This cyclic pitch variation, by the arguments of section 1.6.1, is easily seen to be $-a_1 \sin \psi + b_1 \cos \psi$. By comparing this with eqn 1.11, the aerodynamic moment on one blade is seen to be $-B\Omega^2 \gamma(a_1 \sin \psi - b_1 \cos \psi)/8$. For *all* blades there would therefore be a steady moment $bB\Omega^2 \gamma b_1/16$ acting in the nose down sense and a moment $bB\Omega^2 \gamma a_1/16$ in the direction $\psi = 90^\circ$. For these moments to be equal and opposite to those above, we must have, as before,

$$a_1 = -16 \hat{q}/\gamma \quad \text{and} \quad b_1 = -\hat{q}$$

where we have taken $B = C$, since flapping and in-plane moments of inertia of the blade are almost identical – typically, $C \approx 1.003B$.

When the pitching rate q is not constant, eqn 1.3 becomes ($e = 0$)

$$\frac{d^2\beta}{d\psi^2} + \frac{\gamma}{8} \frac{d\beta}{d\psi} + \beta = \frac{\gamma}{8} \hat{q}(\psi) \cos \psi - 2\hat{q}(\psi) \sin \psi + \frac{d\hat{q}}{d\psi} \cos \psi \quad (1.18)$$

According to the theory of differential equations there is a solution in the form

$$\beta = a_0(\psi) - a_1(\psi) \cos \psi - b_1(\psi) \sin \psi \quad (1.19)$$

where, as indicated, the flapping coefficients are no longer constants, as in the previous cases, but functions of time or azimuth angle.

The case of sinusoidally varying pitching velocity, which is important in stability investigations, has been analysed by Sissingh² and Zbrozek³. Taking $q = q_0 \sin v\psi$ and substituting eqn 1.19 into eqn 1.18 gives, after equating coefficients of $\sin \psi$ and $\cos \psi$,

$$\begin{aligned} \frac{\gamma}{8} a_1 + 2 \frac{da_1}{d\psi} - \frac{\gamma}{8} \frac{db_1}{d\psi} - \frac{d^2 b_1}{d\psi^2} &= -2\hat{q}_0 \sin v\psi \\ \frac{\gamma}{8} \frac{da_1}{d\psi} + 2 \frac{d^2 a_1}{d\psi^2} + \frac{\gamma}{8} b_1 + 2 \frac{db_1}{d\psi} &= \hat{q}_0 v \cos v\psi \end{aligned}$$

The solutions for $a_1(\psi)$ and $b_1(\psi)$ are straightforward, but rather lengthy. Sissingh has shown that the tip path plane oscillates relative to the shaft, performing a beat motion out of phase with the shaft oscillation. Now, v is the ratio of the pitching frequency to the rotational frequency of the shaft and in typical disturbed motion is usually much less than 0.1. On this basis Zbrozek has shown that, to good approximations, the lengthy expressions for a_1 and b_1 can be reduced to

$$a_1 \approx -16 \hat{q}/\gamma + [(16/\gamma)^2 - 1] d\hat{q}/d\psi$$

$$b_1 \approx -\hat{q} + (24/\gamma) d\hat{q}/d\psi$$

Since a typical lateral or longitudinal stability oscillation is about 10 seconds, and the period of the rotor is about $\frac{1}{4}$ second (240 rev/min), v is about 0.025. With $\hat{q} = \hat{q}_0 \sin v\psi$, the second terms of a_1 and b_1 are quite small and by neglecting them Zbrozek's expressions for a_1 and b_1 become the same as for the steady case. Thus, in disturbed motion, both a_1 and b_1 are proportional to q , and the rotor responds as if the instantaneous values were steady. This is the justification for the 'quasi-steady' treatment of rotor behaviour in which the rotor response is calculated as if the continuously changing motion were a sequence of steady conditions. This assumption greatly simplifies stability and control investigations. The 'quasi-static' behaviour of the rotor might also have been expected from its response as a second order system. The impressed motion considered above corresponds to forcing at a very low frequency ratio, and it is well known that the response is almost the same as if the instantaneous value of the forcing function were applied statically.

If the rolling case is considered, with constant angular velocity and $\varepsilon = 0$ as in the pitching case, it can be shown that the equivalent to eqn 1.16 is

$$\frac{d^2\beta}{d\psi^2} + \frac{\gamma}{8} \frac{d\beta}{d\psi} + \beta = \frac{\gamma}{8} \hat{p} \sin \psi + 2\hat{p} \cos \psi \quad (1.16a)$$

in which $\hat{p} = p/\Omega$.

1.7 The cyclic and collective pitch control

The development of a satisfactory feathering mechanism was the last link in the creation of a successful helicopter and it enabled the rotor to be controlled without tilting the hub or shaft, as had been possible with the free-wheeling autogyro rotor. A brief description of the feathering mechanism is given below.

The principal feature of the feathering system is the swash plate mechanism, Fig. 1.13. This consists of two plates, of which the lower plate does not rotate with the shaft but can be tilted in any direction by the pilot's cyclic control. The upper plate rotates with the shaft but is constrained to remain parallel to the lower plate. It can be seen that if the swash plates are tilted the blade chord remains parallel to the swash plate and, as the blade rotates with the shaft, cyclic feathering takes place relative to

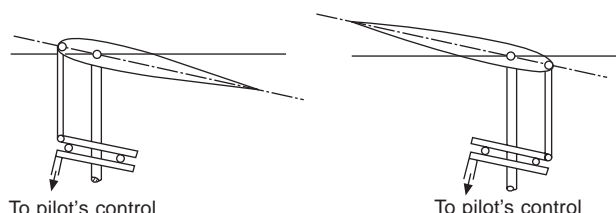


Fig. 1.13 Swash plate mechanism

18 Bramwell's Helicopter Dynamics

the plane perpendicular to the shaft. The swash plate is, of course, a plane of no-feathering, and the axis through the centre of the hub and perpendicular to the swash plates is the no-feathering axis. Figure 1.5(b) shows a typical swash plate control mechanism.

Other feathering mechanisms have been employed such as that in Fig. 1.6(a), but the one described above is used a majority of helicopters.

Collective (constant) pitch is applied by the collective lever which effectively raises or lowers the swash plate without introducing further tilt; this alters the pitch angle of all the blades by the same amount.

1.8 Lagging motion

The lagging-motion equation, eqn 1.6, is

$$\ddot{\xi} + \Omega^2 \varepsilon \xi - 2\Omega \beta \dot{\beta} = N/C$$

or

$$d^2\xi/d\psi^2 + \varepsilon \xi - 2\beta d\beta/d\psi = N/C\Omega^2 \quad (1.20)$$

where, as explained in section 1.4, the term $2\Omega\beta\dot{\beta}$ represents the Coriolis moment due to blade flapping.

In finding the free lagging motion, we assume the flapping motion to be absent and take N to be the aerodynamic (drag) moment of the blade about the lag hinge.

Let $d\Omega^2$ be the drag of the blade when it rotates at steady angular velocity Ω . The lagging motion increases the instantaneous angular velocity of the blade to $\Omega + \dot{\xi}$ and the drag can be assumed to be $d(\Omega + \dot{\xi})^2$. Since $\dot{\xi}$ is small compared with Ω , the drag is approximately $d\Omega^2 + 2d\Omega\dot{\xi}$. If R_D is the distance of the centre of drag of the blade from the hub, and assuming the lag hinge offset to be small,

$$N = -dR_D(\Omega^2 + 2\Omega\dot{\xi})$$

But $dR_D\Omega^3$ is the power, P say, required to drive one blade. Therefore

$$N = -(P/\Omega)(1 + 2\dot{\xi}/\Omega)$$

so that eqn 1.20 can be written

$$d^2\xi/d\psi^2 + (2P/C\Omega^3)d\xi/d\psi + \varepsilon \xi = -P/C\Omega^3 \quad (1.21)$$

Equation 1.21 is the equation of damped harmonic motion about a steady value $\xi = -P/C\Omega^3\varepsilon$. Typical values of $P/C\Omega^3$ and ε are 0.006 and 0.075 respectively, giving a steady value of ξ of about $4\frac{1}{2}^\circ$. The frequency of oscillation is 0.27Ω and the damping is only about 2 per cent of critical. The much lower damping of the lagging mode is due to the fact that the blade motion in this case is governed by the changes of drag, and not of incidence. This low natural damping is usually augmented by hydraulic or elastomeric damping to avoid potential instability problems.

1.9 Lagging motion due to flapping

It will be assumed that the lag hinges are parallel to the rotor shaft so that ξ represents a change of blade angle in the plane of the hub, as in the previous section. The flapping motion must also be taken relative to this plane, and we will assume it takes the form $\beta = a_0 - a_1 \cos \psi$. In some later work we will have to distinguish flapping relative to the shaft from that relative to the no-feathering axis by writing $\beta_s = a_{0s} + a_{1s} \cos \psi$.

Regarding the Coriolis moment due to flapping as a forcing function, and ignoring the damping, we rewrite eqn 1.20 as

$$\frac{d^2\xi}{d\psi^2} + \varepsilon\xi = 2\beta \frac{d\beta}{d\psi} + N/C\Omega^2 \quad (1.20a)$$

and we have to consider the meaning of the moment N in this case. Since the blade lift is perpendicular to the flow direction, the axis of the aerodynamic flapping moment must lie in the tip path plane, because this is the plane in which the blades move steadily. Thus there must be a component of the flapping moment about the lag hinge, and it is clear from Fig. 1.14 that this component is $-M_A a_1 \sin \psi$ and is equal to N .

But, we have seen that, for first harmonic flapping, and assuming zero flapping hinge offset, $M_A = B\Omega^2 a_0$, as explained in section 1.6.2. Therefore

$$N/C\Omega^2 = -a_0 a_1 \sin \psi$$

and, using the assumed form of $\beta = a_0 - a_1 \cos \psi$, then

$$2\beta \frac{d\beta}{d\psi} + N/C\Omega^2 = a_0 a_1 \sin \psi - a_1^2 \sin 2\psi$$

where, again, we have taken $B = C$. The solution to eqn 1.20a is

$$\xi = -[a_0 a_1 / (1 - \varepsilon)] \sin \psi + [a_1^2 / (4 - \varepsilon)] \sin 2\psi$$

The second term is generally smaller than the first and, since, ε is very small, to a fair approximation ξ can be written

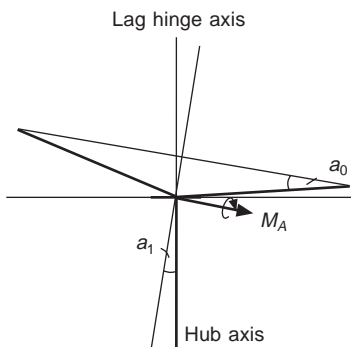


Fig. 1.14 Aerodynamic flapping moment component about lag hinge

$$\xi = -a_0 a_1 \sin \psi \quad (1.22)$$

Thus, the flapping motion forces a lagging motion which lags the flapping motion by 90° .

Equation 1.22 has a simple physical explanation. It can be seen from Fig. 1.15 that the blade movement about the lag hinge, i.e. in the hub plane, is simply steady motion of the blade in the tip path plane projected onto the hub plane. In other words, the ξ motion calculated above corresponds to uniform motion in the tilted rotor cone, and this is a result we should expect, for, since the flapping angle is constant relative to the tip path plane, there can be no Coriolis moments in this plane and the blade must rotate with constant angular velocity.

1.10 Feathering motion

For small pitch angles the blade feathering equation can be written

$$d^2\theta/d\psi^2 + \theta = L/A\Omega^2 \quad (1.23)$$

For free motion, $L = 0$, and the blade oscillates with shaft frequency. If θ is held constant, corresponding to collective pitch application, there will be a moment $A\Omega^2\theta$ trying to feather the blade into fine pitch. This moment is called the ‘feathering moment’ and must be resisted by the feathering mechanism. The fact that the natural

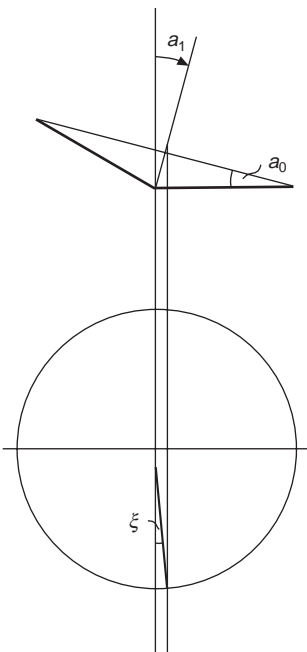


Fig. 1.15 Blade lagging motion due to flap

frequency of the feathering motion is exactly one cycle per revolution of the shaft – exactly as required – means that, except to overcome friction, no forces are necessary in the control links to maintain the motion.

The feathering moment $A\Omega^2\theta$ can be explained in terms of the centrifugal forces acting on the blade. In Fig. 1.16, AA' is a chord of the blade. Consider elementary masses at the leading and trailing edges of the blade. The centrifugal forces acting on these masses are inclined outwards and, therefore, have components in opposite directions. But the centrifugal force directions both lie in planes perpendicular to the shaft so that when the blade is pitched the opposite directed components exert a couple tending to feather the blade into fine pitch. Integrating this moment in the chordwise and spanwise directions can be shown to lead to $A\Omega^2\theta$.

As with the flapping motion, the centrifugal moment acts like a spring giving a frequency exactly equal to that of the shaft, but, again like the flapping motion, if the feathering motion is viewed from a plane passing through the chord, the feathering motion vanishes and the centrifugal moment in this plane also vanishes, Fig. 1.17.

1.11 Rotor forces and moments

So far we have derived the equations of blade flapping, lagging, and feathering and have considered some simple cases of blade motion to illustrate some of its dynamic properties. We now have to consider the effect of this blade motion on the helicopter as a whole. We shall derive expressions for the forces and moments on the helicopter

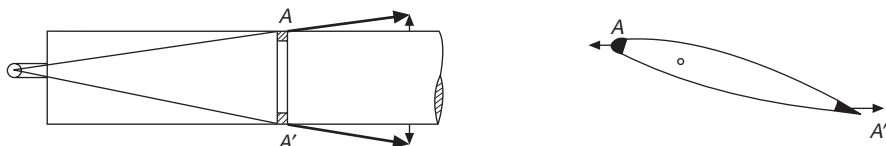


Fig. 1.16 Feathering moment

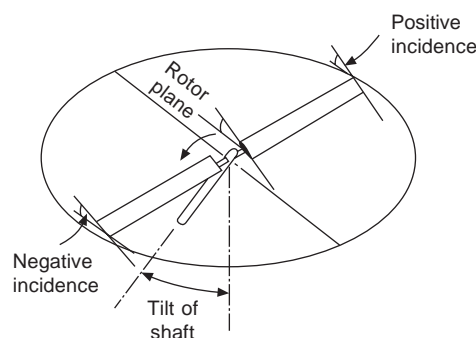


Fig. 1.17 Feathering in tip path plane due to rotor tilt

22 Bramwell's Helicopter Dynamics

and consider requirements for trimmed flight. These requirements will appear as the control angles necessary to establish a given flight condition analogous to the static stability analysis of the fixed wing aircraft.

In order to be able to write down the equations of motion of the helicopter in steady and accelerated flight, it is necessary to calculate the forces exerted by the blade on the hub. To do this we shall have to relate the motion expressed in terms of axes fixed in the blade to axes fixed in the rotating hub and then to axes fixed in the helicopter.

As before, let, i, j, k be the set of unit axes fixed in the blade. Let e_1, e_2, e_3 be a set of unit axes fixed in the rotating hub, Fig. 1.18.

When the blade is in its undeflected position, i.e. when there is no flapping or lagging, the blade axes coincide with the hub axes. Now, suppose the blade flaps through angle β about e_2 , bringing the blade axes into a position whose unit vectors are i_1, j_1, k_1 . The relationships between e_1, e_2, e_3 and i_1, j_1, k_1 are related through a rotation matrix transformation as

$$\begin{bmatrix} i_1 \\ j_1 \\ k_1 \end{bmatrix} = \begin{bmatrix} \cos \beta & 0 & \sin \beta \\ 0 & 1 & 0 \\ -\sin \beta & 0 & \cos \beta \end{bmatrix} \begin{bmatrix} e_1 \\ e_2 \\ e_3 \end{bmatrix} \quad (1.24)$$

The blade now rotates about the lag axis through angle ξ , bringing the unit vectors of the blade into their final positions i, j, k . The relationships between i, j, k and i_1, j_1, k_1 , are, in matrix form

$$\begin{bmatrix} i \\ j \\ k \end{bmatrix} = \begin{bmatrix} \cos \xi & \sin \xi & 0 \\ -\sin \xi & \cos \xi & 0 \\ 0 & 0 & 1 \end{bmatrix} \begin{bmatrix} i_1 \\ j_1 \\ k_1 \end{bmatrix} \quad (1.25)$$

The relationships between e_1, e_2, e_3 and i, j, k , are on multiplying the transformation matrices in eqns 1.24 and 1.25 together

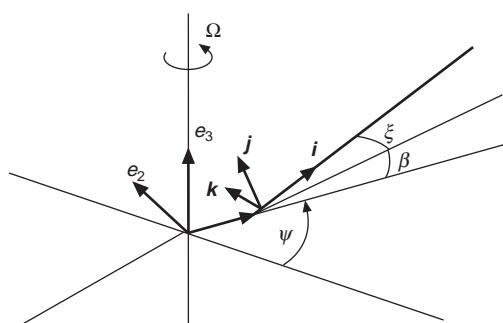


Fig. 1.18 Deflected rotating blade

$$\begin{bmatrix} \mathbf{i} \\ \mathbf{j} \\ \mathbf{k} \end{bmatrix} = \begin{bmatrix} \cos \xi \cos \beta & \sin \xi & \cos \xi \sin \beta \\ -\sin \xi \cos \beta & \cos \xi & -\sin \xi \sin \beta \\ -\sin \beta & 0 & \cos \beta \end{bmatrix} \begin{bmatrix} \mathbf{e}_1 \\ \mathbf{e}_2 \\ \mathbf{e}_3 \end{bmatrix} \quad (1.26)$$

The above relationships enable us to express quantities measured in one set of axes in terms of another set, and we shall need them for calculating the forces and moments on the helicopter.

Let the distance of the centre of gravity of the blade measured from the hinge be r_g . In terms of axes fixed in the blade the position vector of the c.g. is $\mathbf{r}_g = r_g \mathbf{i}$, and in terms of hub axes the position vector is

$$\mathbf{r}_g + eR\mathbf{e}_1 = r_g(\cos \beta \cos \xi \mathbf{e}_1 + \sin \xi \mathbf{e}_2 + \sin \beta \cos \xi \mathbf{e}_3) + eR\mathbf{e}_1$$

Expressing the absolute acceleration \mathbf{a}_g of the c.g. as $\mathbf{a}_g = a_1 \mathbf{e}_1 + a_2 \mathbf{e}_2 + a_3 \mathbf{e}_3$, the components, by applying the standard equations of the kinematics of a rigid body, are found to be

$$a_1 = r_g \frac{d^2}{dt^2} (\cos \beta \cos \xi) - 2r_g \Omega \frac{d}{dt} (\sin \xi) - \Omega^2 (r_g \cos \beta \cos \xi + eR) \quad (1.27)$$

$$a_2 = r_g \frac{d^2}{dt^2} (\sin \xi) + 2r_g \Omega \frac{d}{dt} (\cos \beta \cos \xi) - \Omega^2 r_g \sin \xi \quad (1.28)$$

$$a_3 = r_g \frac{d^2}{dt^2} (\sin \beta \cos \xi) \quad (1.29)$$

Now, let the aerodynamic force on the blade be \mathbf{F} and let \mathbf{R} be the force exerted by the hinge on the blade. If M_b is the blade mass, the equation of motion is

$$\mathbf{F} + \mathbf{R} = M_b \mathbf{a}_g \quad (1.30)$$

If $\mathbf{F} = F_1 \mathbf{e}_1 + F_2 \mathbf{e}_2 + F_3 \mathbf{e}_3$ and $\mathbf{R} = R_1 \mathbf{e}_1 + R_2 \mathbf{e}_2 + R_3 \mathbf{e}_3$,

$$\left. \begin{array}{l} R_1 = M_b a_1 - F_1 \\ R_2 = M_b a_2 - F_2 \\ R_3 = M_b a_3 - F_3 \end{array} \right\} \quad (1.31)$$

We now wish to resolve these rotating force components along axes fixed in the helicopter. In order to comply with the usual stability axes, we take a set of unit axes x, y, z , with the z axis pointing downwards along the negative direction of \mathbf{e}_3 , Fig. 1.19.

If X, Y, Z are the hub force components along the fixed axes, then, remembering that the force the blade exerts on the hub is $-\mathbf{R}$,

$$X = R_1 \cos \psi - R_2 \sin \psi$$

$$Y = -R_1 \sin \psi - R_2 \cos \psi$$

$$Z = R_3$$

These forces are time dependent, not only because of the $\sin \psi$ and $\cos \psi$ terms,

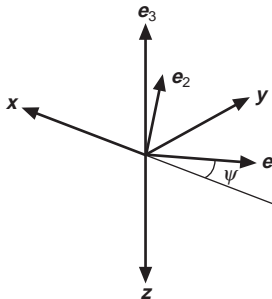


Fig. 1.19 Blade and helicopter axes

but because the aerodynamic force will also be a function of the azimuth angle. For performance and stability calculations we are interested in the time-averaged values. Consider the average value of X taken over a complete revolution. We have

$$\begin{aligned} \int_0^\tau X dt &= M_b \int_0^\tau a_1 \cos \psi dt - \int_0^\tau F_1 \cos \psi dt \\ &\quad - M_b \int_0^\tau a_2 \sin \psi dt + \int_0^\tau F_2 \sin \psi dt \end{aligned}$$

where τ is a complete period.

Now, from eqn 1.27, the first term of a_1 is $r_g d^2(\cos \beta \cos \xi)/dt^2$. Integrating twice by parts,

$$\begin{aligned} \int_0^\tau \frac{d^2}{dt^2} (\cos \beta \cos \xi) \cos \psi dt &= \left[\frac{d}{dt} (\cos \beta \cos \xi) \cos \psi \right]_0^\tau \\ &\quad + \Omega \left[\cos \beta \cos \xi \sin \psi \right]_0^\tau - \Omega \int_0^\tau \cos \beta \cos \xi \cos \psi dt \end{aligned}$$

If the other terms involving a_1 and a_2 are integrated in a similar way, we find that, if the motion is periodic, i.e. if the flight condition is steady, all the terms in the brackets vanish at the limits and all the remaining integrals cancel identically.

In other words, the mean values of all the inertia forces are zero and the only forces which remain are the aerodynamic forces. The vanishing of the inertia forces in steady unaccelerated flight might have been expected on physical grounds, but it is a common mistake to believe that this is not necessarily the case; the reason for this is that small angle approximations for the flapping and lagging angles are often made when resolving the inertia forces, and considerable residuals may remain, particularly as the centrifugal force is extremely large⁴.

The mean forces are therefore

$$(1/\tau) \int_0^\tau X dt = \bar{X} = -(1/\tau) \int_0^\tau F_1 \cos \psi dt + (1/\tau) \int_0^\tau F_2 \sin \psi dt \quad (1.32)$$

$$(1/\tau) \int_0^\tau Y dt = \bar{Y} = (1/\tau) \int_0^\tau F_1 \sin \psi dt + (1/\tau) \int_0^\tau F_2 \cos \psi dt \quad (1.33)$$

$$(1/\tau) \int_0^\tau Z dt = \bar{Z} = (1/\tau) \int_0^\tau F_3 dt \quad (1.34)$$

The force components \bar{X} and \bar{Y} in the plane of the hub give rise to pitching and rolling moments about the helicopter's centre of gravity. Further, the force at the offset hinge, in the direction of the shaft, also exerts pitching and rolling moments. This force has the same magnitude as Z , so that, if hR is the height of the hub above the c.g. and eR is the distance of the hinge from the shaft axis, the average rolling moment per blade on the helicopter is

$$\begin{aligned} L &= \bar{Y}hR + \frac{eR}{\tau} \int_0^\tau Z \sin \psi dt \\ &= \bar{Y}hR + \frac{M_b e x_g R^2}{\tau} \int_0^\tau \frac{d^2}{dt^2} (\sin \beta \cos \xi) \sin \psi dt - \frac{eR}{\tau} \int_0^\tau F_3 \sin \psi dt \\ &= \bar{Y}hR - \frac{M_b e x_g \Omega^2 R^2}{2\pi} \int_0^{2\pi} \sin \beta \cos \xi \sin \psi d\psi - \frac{eR}{2\pi} \int_0^{2\pi} F_3 \sin \psi d\psi \end{aligned} \quad (1.35)$$

in which $x_g R = r_g$.

Similarly, the pitching moment M per blade is

$$M = -\bar{X}hR - \frac{M_b e x_g \Omega^2 R^2}{2\pi} \int_0^{2\pi} \sin \beta \cos \xi \cos \psi d\psi - \frac{eR}{2\pi} \int_0^{2\pi} F_3 \cos \psi d\psi \quad (1.36)$$

The first integrals in L and M are the inertia couples which arise when the plane of a rotor with offset hinges is tilted relative to the shaft. If the flapping motion relative to the shaft is $\beta_s = a_0 - a_{1s} \cos \psi - b_{1s} \sin \psi$, then, for small β and ξ , these integrals are $\frac{1}{2} M_b e x_g \Omega^2 R^2 b_{1s}$ and $\frac{1}{2} M_b e x_g \Omega^2 R^2 a_{1s}$ respectively.

The second integrals in L and M are found to be very much smaller and can be neglected, so that to a good approximation

$$\begin{aligned} L &= \bar{Y}hR + \frac{1}{2} M_b e x_g \Omega^2 R^2 b_{1s} \\ &= \bar{Y}hR + \frac{1}{2} S e R b_{1s} \end{aligned} \quad (1.37)$$

and

$$M = -\bar{X}hR + \frac{1}{2} S e R a_{1s} \quad (1.38)$$

where $S = M_b x_g \Omega^2 R$ is the centrifugal force of the blade for zero offset, and approximately so for small offset.

For the small hinge offsets that are usual, the second terms of eqns 1.37 and 1.38 can be interpreted, in the case of two opposing blades, as the couple due to the displaced centrifugal force vectors, and these are parallel to the tip path plane which is the plane of steady rotation, Fig. 1.20. For small offsets, the inclination of the tip path plane is approximately equal to the flapping angle.

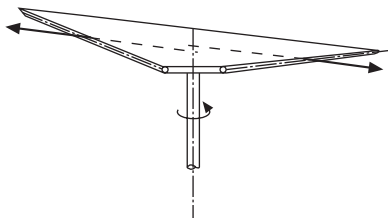


Fig. 1.20 Centrifugal force couple on tilted rotor with offset hinges

1.12 Rotor forces and choice of axes

In the previous section, the rotor force components were expressed in terms of a set of axes fixed in the helicopter. As explained there, such a formulation is necessary to study the forces and moments on the whole helicopter. However, it is more usual, and natural, when considering the rotor as a lifting device, to regard it as producing a thrust, defined along some convenient direction, together with small components of force in the other two perpendicular directions. For this purpose, three axes systems are in common use, as follows. The question as to which axis is the most useful depends upon the problem being considered, and will become apparent in the applications dealt with later, although some indications are given below.

1.12.1 The no-feathering or control axis

As explained in section 1.6.2, this is the axis normal to the plane of the swash plate. By definition, no cyclic feathering occurs relative to this axis, the blade pitch being the constant value supplied by the collective pitch application. Since the pitch angle is constant, the only other blade motion contribution to the local blade incidence is that due to the flapping. The no-feathering axis is often used to express the blade flapping, especially when blade aerodynamic forces are being established, since constant blade pitch at a section eases the mathematical development. The rotor aerodynamics and dynamics established in Chapter 3 are expressed using this axis system.

1.12.2 The tip path plane or disc axis

The tip path plane axis is the axis perpendicular to the plane through the blade tips and, for zero offset flapping hinges, it is therefore the axis of no flapping. The definition applies only to first harmonic motion since, when there are higher harmonics, the blades no longer trace out a plane. Of the higher harmonics, only the odd values affect the tilt of the disc, and these are usually extremely small compared with the first harmonics, as explained in section 1.6.2. Now, although there is no first harmonic flapping relative to the tip path plane, there will be cyclic feathering and the amount of feathering is exactly equal to the flapping relative to the no-feathering axis. Thus, in this case, the blade incidence will be determined from the collective pitch and the apparent feathering motion in the tip path plane.

When the flapping hinges are offset, the tip path plane axis is no longer the axis of no flapping, as can be easily seen from a diagram like Fig. 1.20 with exaggerated hinge offset. Strictly speaking, both feathering and flapping occur relative to the tip path plane but, provided the offset is small, as it usually is, the error in assuming that there is no flapping is negligible.

1.12.3 The shaft or hub plane axis

This axis is usually less convenient for calculating the rotor forces, as the blade incidence must be expressed in terms of both feathering and flapping. It is, nevertheless, a useful axis for dealing with hingeless rotors, since blade flapping relative to the hub is of prime importance. Indeed, the blade mechanics developed so far in the current chapter have been with reference to the shaft axis.

1.13 The rotor disc

In all the three cases discussed above, it is usual to call the force component along the axis, whichever of the above it is, the thrust T . The component perpendicular to this axis and pointing rearward is called the H force, and the third component, pointing sideways to starboard, is the Y force. Usually the Y force is very small and attention is mainly focused on the thrust and the H force, i.e. the longitudinal force components. Calculations and measurements show that the resultant rotor force is almost perpendicular to the tip path plane, usually pointing backwards slightly. It is for this reason that the tip path plane axis is useful since the resultant force is almost exactly equal to the thrust; the H force can be regarded as a kind of rotor drag.

Let us denote the thrust and the H force relative to the no-feathering axis by T and H respectively, and use the subscript D to denote the tip path plane (disc) axis and s to denote the shaft axis. Now the flapping and feathering angles are usually small – larger than 10° would be regarded as extreme values – so that, referring to Fig. 1.21, the approximate relations between the thrust and forces referred to the different axes are

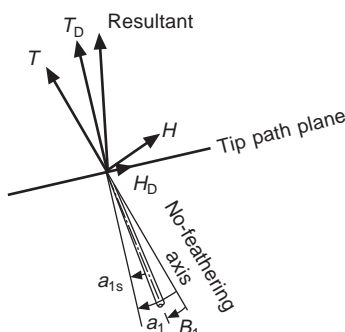


Fig. 1.21 Thrust and H -force vectors

$$T \approx T_D \approx T_s \quad (1.39)$$

$$H \approx H_D + T_D a_1 \approx H_s + T_s B_1 \quad (1.40)$$

where B_1 is the amplitude of the longitudinal cyclic pitch.

1.14 Longitudinal trim equations

The foregoing analysis in this chapter has provided the main features of rotor behaviour, and demonstrated the dependence of rotor forces on the various different parameters involved. By extending the analysis to include the helicopter fuselage whilst maintaining the simplified rotor model, it is possible to derive the equations of equilibrium in steady, uniform, trimmed flight. From this, the attitude of the fuselage may be determined. These exercises are done for longitudinal flight in this and the following section, and lateral control to trim is studied in the final section 1.16.

Referring to Fig. 1.22, and resolving forces in the vertical direction,

$$W + D \sin \tau_c = T \cos (\theta - B_1) - H \sin (\theta - B_1) \quad (1.41)$$

and, resolving horizontally,

$$D \cos \tau_c = -T \sin (\theta - B_1) - H \cos (\theta - B_1) \quad (1.42)$$

where θ is the angle between the vertical and shaft, positive nose up, and τ_c is the angle of climb. Since θ and B_1 are small angles, eqns 1.41 and 1.42 can be written approximately as

$$W + D \sin \tau_c \approx T \quad (1.43)$$

$$H + D \cos \tau_c \approx T(B_1 - \theta) \quad (1.44)$$

Since $D \sin \tau_c$ is very much smaller than W , then $T \approx W$.

The origin of moments O is defined as the point on the shaft met by the perpendicular from the c.g. If hR is the height of the hub above this point, and lR the distance of the

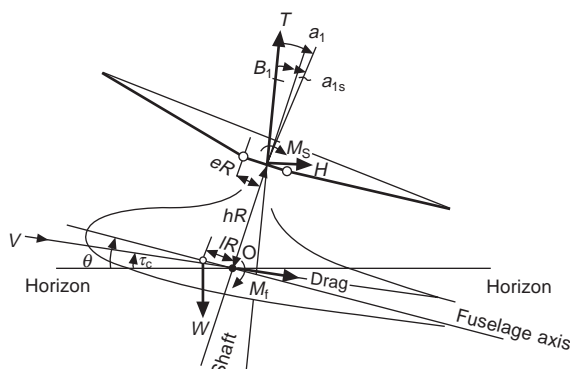


Fig. 1.22 Forces and moments in longitudinal plane

c.g. forward of this point, taking moments about O and making the small angle assumption gives

$$-WlR - ThRB_1 + HhR + M_f - M_s(B_1 - a_1) = 0 \quad (1.45)$$

where M_f is the fuselage pitching moment and $M_s = f_b SeR$ is the centrifugal moment per unit tilt of all the blades (eqn 1.38), and f_b is a factor depending on the number of blades.

Solving eqn 1.45 for B_1 gives

$$B_1 = (M_f - WlR + HhR + M_s a_1) / (ThR + M_s) \quad (1.46)$$

Equation 1.46 gives the longitudinal cyclic pitch required for trim. For very small or zero offset, we can put $M_s = 0$ and, since $T \approx W$, we have

$$B_1 = M_f / WhR - l/h + H/W \quad (1.47)$$

and, if the fuselage pitching moment $M_f = 0$,

$$B_1 = -l/h + H/W \quad (1.48)$$

The denominator of the right-hand side of eqn 1.46 represents the control moment for unit displacement of the rotor disc relative to the hub axis. The term ThR is the moment due to the tilt of the thrust vector, which is the only control moment acting if the hinges are centrally located ($e = 0$) or the rotor is of the see-saw type. M_s is the centrifugal couple due to the flapping hinge offset, section 1.11. We shall see in Chapter 4 that for a typical offset distance, $e = 0.04$ say, the total moment is more than doubled by the offset hinge contribution.

The importance of the offset hinge moment is that it not only augments the control power but is also independent of the thrust and can be designed to provide adequate control power in those flight conditions where the thrust is temporarily reduced, e.g. the ‘push-over’ manoeuvre or the transition from powered flight to autorotation.

Equation 1.48 has a simple physical interpretation: the longitudinal cyclic pitch B_1 must be such as to make the resultant rotor force pass through the helicopter’s centre of gravity, Fig. 1.23; the figure shows that $B_1 + l/h = \tan^{-1}(H/T) \approx H/W$, which is eqn 1.48.

If M_s and M_f are not zero, the resultant force vector no longer passes through the c.g. but must exert a moment about it in order to balance the M_s and M_f moments.

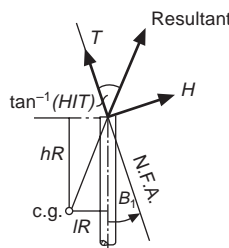


Fig. 1.23 Resultant rotor force vector

Expressed in terms of the tip path plane, eqn 1.47 becomes

$$B_1 = a_1 + H_D/W - l/h + M_f/WhR \quad (1.49)$$

Now H_D , the force component in the plane of the rotor disc, is usually quite small, so that for given values of l/h and M_f , the cyclic pitch to trim is roughly that required to eliminate the backward flapping of the rotor. This is a convenient way of interpreting the cyclic pitch to trim and shows the advantage of using the tip path plane as a reference plane in this case. With $M_f = 0$, Fig. 1.23 can be redrawn as Fig. 1.24.

1.15 The attitude of the helicopter

Since $T \approx W$, eqn 1.44 can be written

$$(D/W) \cos \tau_c + H/W = B_1 - \theta \quad (1.50)$$

Eliminating B_1 by means of eqn 1.46 gives

$$\theta = -\frac{D \cos \tau_c}{W} - \frac{H}{W} + \frac{M_f - WhR + HhR + M_s a_1}{WhR + M_s} \quad (1.51)$$

If M_s is negligible,

$$\theta = -(D/W) \cos \tau_c - l/h + M_f/WhR$$

Thus, for a given c.g. position and supposing M_f to be constant, the helicopter fuselage attitude is directly proportional to the drag and, hence, the square of the speed. Another important conclusion is that, unlike a fixed wing aircraft, the attitude depends very little on the angle of climb for, since the angle of climb is contained only in $\cos \tau_c$ even quite steep climbs have little effect on $(D/W) \cos \tau_c$ and therefore on θ .

1.16 Lateral control to trim

Referring to Fig. 1.25, resolving horizontally, with $T \approx W$ and ignoring the sideways pointing Y force,

$$W(A_1 + b_1 + \phi) + T_t = 0 \quad (1.52)$$

where T_t is the tailrotor thrust.

Taking moments about O, and for small angles of bank,

$$WfR + WhR(A_1 + b_1) + M_s(A_1 + b_1) + T_t h_t R = 0 \quad (1.53)$$

where fR is the lateral displacement of the c.g. and $h_t R$ is the tailrotor height.

Solving eqn 1.53 for A_1 gives

$$A_1 = -b_1 - \frac{WfR + T_t h_t R}{WhR + M_s} \quad (1.54)$$

which is the lateral cyclic pitch to trim.

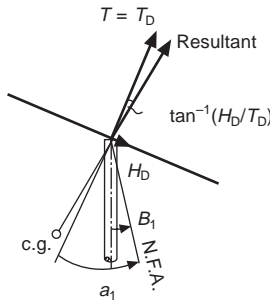


Fig. 1.24 Rotor force components in tip path (disc) plane

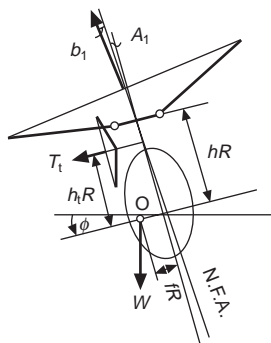


Fig. 1.25 Forces and moments in lateral plane

Eliminating A_1 from eqn 1.54 gives the trimmed bank attitude:

$$\phi = -\frac{T_t}{W} + \frac{WfR + T_t h_t R}{WhR + M_s} \quad (1.55)$$

If $M_s = 0$ (no offset hinge) and $h_t = h$, which is usually approximately true, then

$$\phi \approx f/h$$

which means that the c.g. lies vertically below the rotor, for the rotor thrust vector

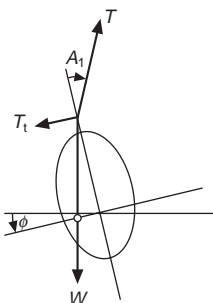


Fig. 1.26 Helicopter lateral attitude

32 Bramwell's Helicopter Dynamics

must be tilted relative to the vertical to balance the tailrotor side force and tilted away from the c.g. to balance the tailrotor moment, Fig. 1.26.

References

1. Stewart, W., 'Higher harmonics of flapping on the helicopter rotor', *Aeronautical Research Council CP 121*, 1952.
2. Sissingh, G. J., 'The frequency response of the ordinary rotor blade, the Hiller servo-blade and the Young-Bell stabilizer', *Aeronautical Research Council R&M 2860*, 1950.
3. Zbrozek, J. K., 'The simple harmonic motion of a helicopter rotor with hinged blades', *Aeronautical Research Council R&M 2813*, 1949.
4. Correspondence in *Aircraft Engineering*, September and November 1955.

Rotor aerodynamics in axial flight

2.1 Introduction

One of the most important aerodynamic problems of the helicopter is the determination of the loading of the rotor blades. For this purpose it is essential to know the local components of airflow at any station along the blade, and this in turn requires a knowledge of the air velocity induced by the lift of the blades. In developing the analysis, reference is made to well known and fundamental theorems, laws and equations in aerodynamics, which may be found in standard texts, such as Houghton and Carpenter¹.

An element of a rotor blade can be regarded as an elementary aerofoil and, in accordance with the Kutta–Zhukowsky theorem, there is a bound vortex of circulation Γ about the aerofoil which, in general, varies along the span. Now Helmholtz's theorem implies that a vortex cannot terminate in the interior of a fluid, and the vortex bounding the element continues as free vortex lines springing from the trailing edge of the element, Fig. 2.1(a). These free vortex lines are called *trailing vortices*. If Γ is the strength of the bound vortex of an element, and if $\Gamma + d\Gamma$ is the vortex strength of the neighbouring element, the neighbouring trailing vortices are in the

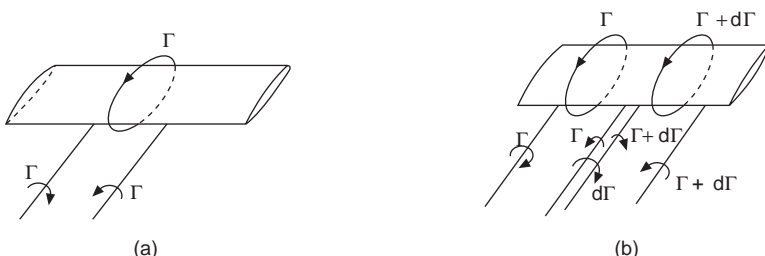


Fig. 2.1 Bound and trailing vortices

opposite sense and the *resultant* trailing-vortex strength is $d\Gamma$, Fig. 2.1(b). Thus, when the circulation varies along the span there is an associated distribution of trailing vortices forming a *vortex sheet* springing from the blade's trailing edge. In principle, once the distribution of vortex lines trailing from the rotor is determined, the induced velocity at a given point of the flow can be calculated by applying the Biot–Savart law to an element of the sheet and integrating over the sheet to obtain its total effect. The velocity distribution induced by the bound vortices and the vortex sheets of all the blades constitutes the rotor slipstream. Unfortunately, the geometry of the vortex sheet is extremely difficult to calculate, especially for the important case of the hovering rotor, since the flow through the rotor is determined largely by the velocities induced by the sheet itself; i.e. the sheet geometry and the velocity field it gives rise to are interdependent. In contrast, for a propeller operating under normal flight conditions, the velocities induced by the trailing vortices are found to be small compared with the relatively high axial velocity and can usually be regarded merely as perturbations to be superimposed on the otherwise uniform axial and rotational flow components.

We shall leave a detailed discussion of the flow pattern induced by the vortex wake until later in the chapter, since much useful information about the performance of the rotor can be gained from a simple flow pattern which can be treated by momentum methods. The method is known as the classical actuator disc theory.

2.2 Actuator disc theory

In the actuator disc analysis, the following assumptions are made.

- (i) The thrust is uniformly distributed over the rotor disc across which there is a sudden jump of pressure Δp . The uniform thrust distribution can be interpreted as an assumption that the rotor has an infinite number of blades.
- (ii) No rotation or ‘swirl’ is imparted to the flow. This is not a necessary restriction, since the effects of rotation can be included in the analysis². However, the problem becomes more complicated than is really justified, particularly as the swirl velocities in typical helicopter operation, as will be shown later, are usually negligible.
- (iii) The slipstream of the rotor is a clearly defined mass of moving air outside which the air is practically undisturbed.

A further assumption of the classic actuator disc theory is that the pressure in the ultimate slipstream is the same as the pressure of the surrounding undisturbed air. This assumption implies that the slipstream is like a jet whose velocity is unrelated to that of surrounding air, but the above description of the vortex wake generated by the rotor requires us to look at the assumption more critically. Since an element of the vortex sheet moves with the local velocity generated by the rest of the sheet, there is no normal flow component relative to the sheet itself. But this is also the boundary

condition for a solid surface moving through the fluid, so we deduce that the velocity field generated by the vortex sheet is the same as if the sheet were a rigid membrane whose constituent elements move with the local induced velocity. An important particular case has been considered by Betz³ who showed that for a certain blade loading, called the ‘ideal loading’, the power loss is a minimum and the trailing vortices lie on a helical surface of constant pitch which moves axially at constant velocity. This case is analogous to that for the minimum induced drag of a wing for which the span loading is known to be elliptic and the induced velocity along the span is constant. As mentioned above, the velocity field caused by the motion of the helical surface relative to the surrounding air constitutes the rotor ‘slipstream’. The formidable hydrodynamical problem of calculating this velocity field for a propeller having a finite number of blades was solved by Goldstein⁴ in 1929.

Actually, as will be discussed later, the ‘ideal’ blade loading does not occur in practice, and the vortex wake does not conform to the simple helical surface referred to above. Nevertheless, let us suppose that, close to the rotor at least, the wake consists of well defined sheets moving away from the rotor with constant velocity w ; Fig. 2.2 shows the sheet springing from one blade. Imagine an observer stationed at the point P and at rest relative to the undisturbed air. As the vortex sheets leave the blade and move downwards, the observer would be aware of a periodic flow. Now Bernoulli’s equation for unsteady flow is

$$p + \frac{1}{2}\rho q^2 + \rho \partial \phi / \partial t = \text{constant}$$

where q is the local fluid velocity and ϕ is the velocity potential of the flow. At a great distance from the wake both q and ϕ tend to zero and p approaches the ambient value p_∞ , therefore

$$p + \frac{1}{2}\rho q^2 + \rho \partial \phi / \partial t = p_\infty \quad (2.1)$$

This equation holds throughout the flow field, including points between the sheets, since only the sheets themselves represent regions for which the flow is not irrotational. If z denotes the distance along the rotor axis, r the radial distance, and ψ the angular co-ordinate of the point P, the periodicity of the flow enables us to write

$$\phi = f(z - wt, r, \psi)$$

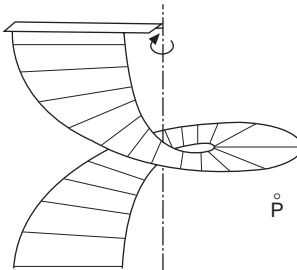


Fig. 2.2 Vortex sheet leaving blade

36 Bramwell's Helicopter Dynamics

because ϕ is constant for a point z_0 , r , ψ which moves with the wake, and $z_0 = z - wt$. Hence

$$\partial\phi/\partial t = -w\partial\phi/\partial z$$

But

$$\partial\phi/\partial z = q_z$$

where q_z is the fluid velocity component in the axial direction, therefore

$$p + \frac{1}{2}\rho q^2 - \rho w q_z = p_\infty \quad (2.2)$$

It will be shown shortly that the flow component in the axial direction is small compared with the rotor tip velocity, and this means that the vortex sheets are nearly parallel to the rotor plane and are also fairly close together. The flow about these sheets, as seen by the stationary observer, is indicated in Fig. 2.3.

Except near the edges of the sheets, where there may be a considerable radial flow, the velocity between the sheets is very nearly equal to the velocity of the sheets themselves, i.e. q_z and q are both approximately equal to w . Hence, for the rotor case, eqn 2.2 becomes

$$p = p_\infty + \frac{1}{2}\rho w^2 \quad (2.3)$$

showing that the pressure in the wake is generally higher than the ambient value p_∞ .

The above result can be obtained in another way. If the observer is moving with the sheets, the total head pressure at a point a great distance from the sheets is clearly $p_\infty + \frac{1}{2}\rho w^2$. Within the sheets, which are assumed to be almost parallel and close together, the flow is relatively at rest, but since the total head is constant, whether within the sheets or without, we have

$$p = p_\infty + \frac{1}{2}\rho w^2$$

as before.

The fact that the vortex sheet theory gives rise to an ‘overpressure’ in the wake has been remarked upon by Theordorsen,⁵ who derived eqn 2.2, but since his work was concerned with propellers in their normal operating state, for which the ‘overpressure’ is extremely small, its significance in relation to the helicopter rotor seems to have been overlooked.

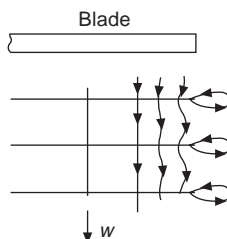


Fig. 2.3 Flow about adjacent vortex sheets

In practice, the helicopter blade is usually designed to give a favourable loading in forward flight and, as a result, the ‘ideal’ loading and helical wake is not achieved in hovering and axial flight. It appears⁶ that the wake pressure is somewhat overestimated by eqn 2.3, and one should expect a value which is somewhere between that given by eqn 2.3 and the ambient value p_∞ .

In the application of the classical actuator disc theory, we shall take an arbitrary value of the pressure in the final wake at first and then investigate the special case (i) where the wake pressure is equal to the ambient pressure p_∞ and (ii) the value given by eqn 2.3 above.

Let us take a *cylindrical* control surface surrounding a control volume whose radius is R_1 , which encloses the rotor, radius R , and its slipstream, Fig. 2.4. Although the slipstream does not extend upstream of the rotor, it is convenient to imagine that it does so for the purpose of applying momentum principles. Far upstream of the

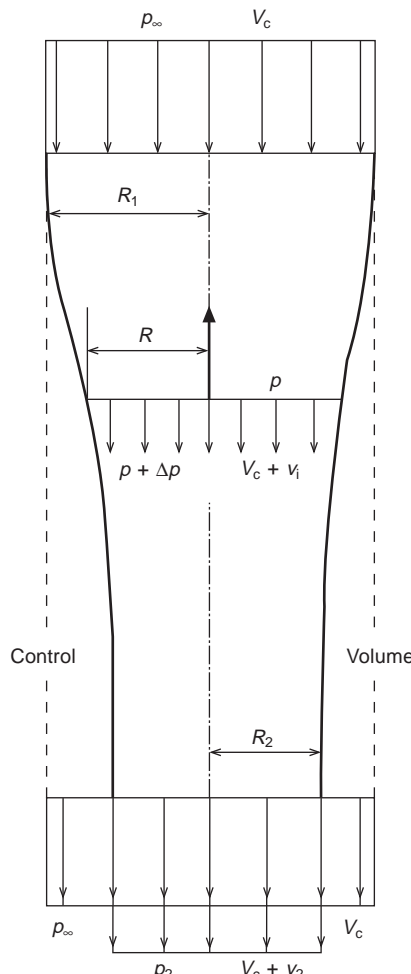


Fig. 2.4 Control volume for rotor in axial flight

38 Bramwell's Helicopter Dynamics

rotor, the air velocity relative to the rotor is the rate of climb V_c and the pressure is p_∞ . As the air approaches the rotor, the airspeed increases to $V_c + v_i$ at the rotor itself. Because the airflow is continuous there is no sudden change of velocity at the rotor, but there is a jump of pressure Δp which accounts for the rotor thrust $T = \Delta p A$, A being the rotor disc area πR^2 . The slipstream velocity continues to increase downstream of the rotor, reaching a value in the ultimate wake of $V_c + v_2$, where the slipstream radius is R_2 and the pressure p_2 .

Since the slipstream velocity is higher than the undisturbed axial velocity V_c , it is clear that the mass of fluid leaving the bottom end of the control volume exceeds that entering at the top. There must therefore be some flow through the cylindrical sides of the control surface. If this flux is denoted by \bar{Q} , we have

$$\begin{aligned}\bar{Q} &= \pi(R_1^2 - R_2^2)V_c + \pi R_2^2(V_c + v_2) - \pi R_1^2 V_c \\ &= \pi R_2^2 v_2\end{aligned}$$

Thus the total mass per unit time *entering* the control surface is

$$\rho \pi R_1^2 V_c + \rho \pi R_2^2 v_2$$

and the total mass *leaving* the surface is

$$\rho \pi(R_1^2 - R_2^2)V_c + \rho \pi R_2^2(V_c + v_2)$$

Since the flux entering the control surface consists of air having velocity V_c , the momentum per unit time entering the surface is

$$\rho V_c (\pi R_1^2 V_c + \pi R_2^2 v_2)$$

and the momentum per unit time leaving the surface is

$$\rho \pi(R_1^2 - R_2^2)V_c^2 + \rho \pi R_2^2(V_c + v_2)^2$$

Hence, the rate of change of momentum in the axial direction is

$$\begin{aligned}&\rho \pi(R_1^2 - R_2^2)V_c^2 + \rho \pi R_2^2(V_c + v_2)^2 - \rho \pi R_1^2 V_c^2 - \rho \pi R_2^2 V_c v_2 \\ &= \rho \pi R_2^2(V_c + v_2)v_2\end{aligned}$$

The total force in the axial direction acting on the control surface consists of the rotor thrust plus the pressure forces on the ends of the cylinder. Equating this force to the rate of change of momentum, we get

$$T + \pi R_1^2 p_\infty - \pi(R_1^2 - R_2^2)p_\infty - \pi R_2^2 p_2 = \rho \pi R_2^2(V_c + v_2)v_2$$

or
$$T = \rho \pi R_2^2(V_c + v_2)v_2 + \pi R_2^2(p_2 - p_\infty) \quad (2.4)$$

Continuity of the flow requires that

$$\rho(V_c + v_i)A = \rho(V_c + v_2)\pi R_2^2 \quad (2.5)$$

so that eqn 2.4 can be written

$$T/A = \Delta p = \rho(V_c + v_i)v_2 + (p_2 - p_\infty)(V_c + v_i)/(V_c + v_2) \quad (2.6)$$

Applying Bernoulli's equation to points upstream of the rotor gives

$$p_\infty + \frac{1}{2}\rho V_c^2 = p + \frac{1}{2}\rho(V_c + v_i)^2 \quad (2.7)$$

and for points downstream of the rotor

$$p + \Delta p + \frac{1}{2}\rho(V_c + v_i)^2 = p_2 + \frac{1}{2}\rho(V_c + v_2)^2 \quad (2.8)$$

Subtracting eqn 2.7 from eqn 2.8 gives

$$\Delta p = p_2 - p_\infty + \rho(V_c + \frac{1}{2}v_2)v_2 \quad (2.9)$$

and equating eqns 2.6 and 2.9 we have

$$\rho v_2(v_i - \frac{1}{2}v_2) = (p_2 - p_\infty)(v_2 - v_i)/(V_c + v_2) \quad (2.10)$$

Let us assume, as for the classical actuator disc, that the pressure in the final wake is the same as the ambient pressure, i.e. that $p_2 - p_\infty = 0$. Then, from eqn 2.10,

$$v_i = \frac{1}{2}v_2$$

irrespective of the axial velocity V_c of the rotor. Thus the increment of velocity at the rotor disc, which we usually refer to as the 'induced' velocity, is half the value in the ultimate wake. Putting this relationship, and $p_2 = p_\infty$, in eqn 2.6 we have

$$T = 2\rho A(V_c + v_i)v_i \quad (2.11)$$

from which the induced velocity may be calculated when the thrust is known. In particular, in hovering flight, $V_c = 0$ and

$$v_i = v_0 = \sqrt{T/2\rho A} \quad (2.12)$$

in which v_0 is termed the 'thrust velocity'.

If w_D is the *disc loading*, T/A , in N/m^2 , and ρ has the International Standard Atmosphere (ISA) value corresponding to sea-level,

$$v_i = v_0 = 0.64\sqrt{w_D}$$

A typical value of w_D is 250 N/m^2 , giving an induced velocity (thrust velocity) of 10.2 m/s .

To calculate the power being supplied by the rotor, we must consider the rate at which kinetic energy is being imparted to the air. The rate at which kinetic energy enters the control surface is

$$\frac{1}{2}(\rho\pi R_1^2 V_c + \rho\pi R_2^2 v_2)V_c^2$$

and the rate at which kinetic energy leaves the control surface is

$$\frac{1}{2}[\rho\pi(R_1^2 - R_2^2)V_c^3 + \rho\pi R_2^2(V_c + v_2)^3]$$

The power P delivered by the rotor is found to be

$$P = \rho A(V_c + v_i)(V_c + \frac{1}{2}v_2)v_2 + (p_2 - p_\infty)A(V_c + v_i) \quad (2.13)$$

in which the first term on the right-hand side is total rate of change of kinetic energy, the second term derives from rate of doing work by the pressures on the ends of the control volume, and the continuity relation, eqn 2.5, has been used.

With $p_2 = p_\infty$ and $v_i = \frac{1}{2}v_2$, we see from eqn 2.11 that

$$P = T(V_c + v_i) \quad (2.14)$$

The first term on the right of eqn 2.14 is the useful work done in climbing at speed V_c . The term Tv_i is the *induced power*, i.e. the work done producing the (unwanted) slipstream. In hovering flight,

$$P = Tv_i = T^{3/2}/\sqrt{(2\rho A)}$$

If the thrust of the helicopter is 45 000 N, with the disc loading of 250 N/m² referred to above, the induced power P_i is

$$\begin{aligned} P_i &= \frac{45\,000 \times 10.2}{1000} \text{ kW} \\ &= 453 \text{ kW} \end{aligned}$$

and this would represent about 60 per cent of the total power in hovering flight, the rest being used to overcome the blade drag and tailrotor and transmission losses. The induced power calculated above is a rather optimistic value because it has been assumed that the induced velocity is uniformly distributed over the disc and that this can be shown to be the optimum distribution. As we shall see shortly, for the induced velocity distributions likely to occur in practice, the induced power may be 10–15 per cent larger than the ‘ideal’ value just calculated.

The *contraction ratio* is the ratio of the radius of the final wake to that of the disc. The continuity equation gives at once

$$\begin{aligned} R_2/R &= \sqrt{(v_i/v_2)} \\ &= 1/\sqrt{2} \end{aligned}$$

when $p_2 = p_\infty$.

Now let us assume that the pressure in the ultimate slipstream is given from eqn 2.3 as

$$p_2 = p_\infty + \frac{1}{2}\rho v_2^2$$

where we have taken the wake velocity w to be the same as the local velocity increment v_2 . Then from eqn 2.10 we get

$$v_2^2 = v_i v_2 + \frac{1}{2}v_2^2 (V_c + v_i)/(V_c + v_2) \quad (2.15)$$

If we define $k_i = v_i/v_2$ and $\bar{V}_c = V_c/v_i$, eqn 2.15 can be written

$$\bar{V}_c = (3 - 2/k_i)/(1 - 2k_i)$$

In hovering flight, $\bar{V}_c = 0$, we find $k_i = \frac{2}{3}$, i.e. the final slipstream velocity is only $\frac{3}{2}$ times the induced velocity instead of twice the induced velocity when $p_2 = p_\infty$. As the axial velocity V_c increases, k_i varies as shown in Fig. 2.5.

It can be seen that $k_i \rightarrow \frac{1}{2}$ as the axial velocity increases indefinitely. In practice, however, \bar{V}_c is unlikely to exceed 2.

In general, the thrust is, from eqn 2.6,

$$\begin{aligned} T &= \rho A(V_c + v_i)v_2 + \frac{1}{2}\rho v_2^2 A(V_c + v_i)/(V_c + v_2) \\ &= \rho A(V_c + v_2)v_2 \end{aligned} \quad (2.16)$$

from eqn 2.15.

In particular, in hovering flight we find from eqn 2.16 that

$$v_i = \frac{2}{3} \sqrt{T/\rho A}$$

or, at sea-level, $v_i = 0.604 \sqrt{w_D}$ m/s when the disc loading w_D is given in N/m².

This result shows that the induced velocity is about 6 per cent lower, for a given disc loading, than when $p_2 = p_\infty$.

From eqn 2.13 the thrust power P is

$$\begin{aligned} P &= \rho A(V_c + v_i)(V_c + \frac{1}{2}v_2)v_2 + \frac{1}{2}\rho A v_2^2 (V_c + v_i) \\ &= \rho A(V_c + v_i)(V_c + v_2)v_2 \\ &= T(V_c + v_i) \end{aligned}$$

as in the previous case. However, as we have just seen, the induced velocity is less than for the case $p_2 = p_\infty$, so the induced power is correspondingly lower. In hovering flight we see that the induced power is about 6 per cent lower.

It was stated earlier that, in practice, it appears that the wake ‘overpressure’ is somewhat less than the ‘ideal’ value given by eqn 2.3; consequently the difference between the induced velocities and the induced powers for the two cases considered

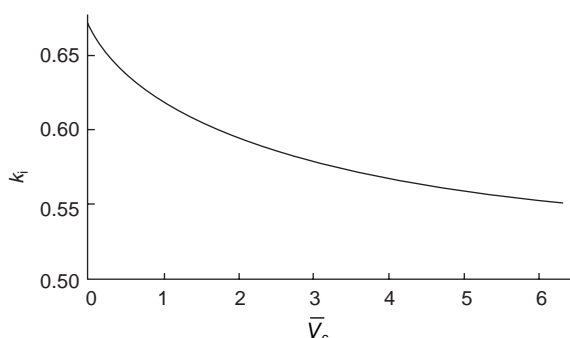


Fig. 2.5 Variation of final slipstream velocity factor with axial velocity factor

would be expected to be less than the 6 per cent calculated above. In what follows, it will be assumed that the wake pressure and the ambient pressure are equal, since the considerable simplification it affords justifies the acceptance of the fairly small inaccuracies just mentioned, particularly as it is not certain what the wake pressure should be. This assumption conforms, of course, to the classical actuator disc theory. One should be aware, therefore, that some of the quantities calculated by this theory differ by a few per cent from those calculated with a wake 'overpressure'. However, more exact rotor analyses, which require a knowledge of the geometry of the vortex wake and which will be discussed later in this chapter, will depend on the contraction ratio and the ratio of the velocity in the final wake to that at the rotor disc. As we have seen, the effect of the 'overpressure' on these quantities is considerable, although it is usually taken into account only indirectly through wake visualisation methods.

2.3 Vertical descent and the vortex ring state

The results obtained so far have been made possible only because it has been assumed that there has been a definite flow through the rotor with a well-defined slipstream. In vertical descent, however, it is clear that the relative upward flow will, if it becomes large enough, prevent a slipstream from forming, and some of the air will recirculate the rotor in what is known as the *vortex ring state*, Figs 2.6(a) and (b). The vortex ring state occurs when the rate of descent is of the same order as the induced velocity in hovering flight. It can also occur in forward flight and in either case leads to very high descent rates together with uncommanded pitch and roll excursions. Recovery is by reducing the collective pitch and attaining a forward flight velocity component, thereby moving the rotor into unrecirculated air. Flight tests describing the condition have been made by Brotherhood.^{7,8}

At higher rates of descent the recirculation ceases and a well defined slipstream develops again, but the wake widens after passing through the rotor and the vortex wake develops on the upper side of the rotor, Fig. 2.7(a). In contrast to the vertical-climb case, the air slows down on passing through the rotor and the condition is

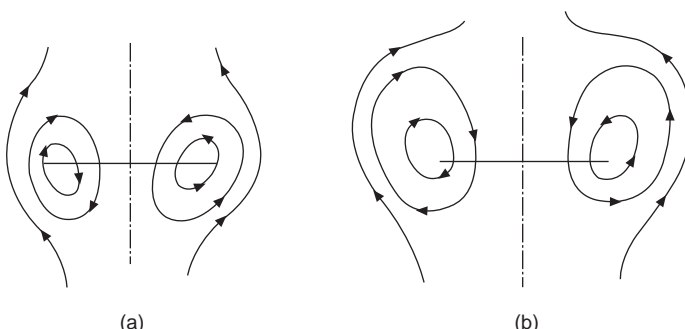


Fig. 2.6 Vortex ring flow in vertical descent: (a) slow rate of descent; (b) faster rate of descent

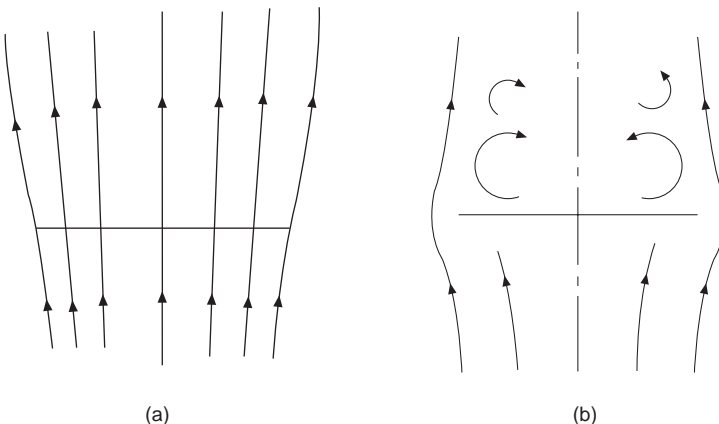


Fig. 2.7 (a) Windmill brake state; (b) Turbulent wake state

known as the *windmill brake state*. There is a transitional state between this and the vortex ring state in which the rotor acts rather like a bluff body, producing a turbulent wake downstream (i.e. on the upper side of the rotor). This is generally known as the *turbulent wake state* and is shown in Fig. 2.7(b).

In the absence of a well-defined slipstream, the momentum theory can no longer be readily applied, since the mass flow and velocity changes cannot be easily defined. A simple theoretical relationship between the induced velocity and the axial velocity of the rotor in such cases is no longer possible. We are then forced to obtain the induced velocity experimentally by inferring it from the results of the blade element theory, to be discussed in section 2.3, in connection with the measured rate of descent and blade collective pitch angle.

To calculate the induced velocity in hovering and climbing flight, we make use of eqn 2.11. Then, if v_0 is the induced velocity in hovering flight, or ‘thrust velocity’, we define

$$\bar{v}_i = v_i/v_0 \quad \text{and} \quad \bar{V}_c = V_c/v_0$$

so that eqn 2.11 can be written

$$\bar{v}_i(\bar{V}_c + \bar{v}_i) = 1 \quad (2.17)$$

For vertical descent velocities which are large enough for a slipstream to be developed again, i.e. the windmill-brake state, eqn 2.11 must be written as

$$2\rho A/V_c + v_i|v_i = T$$

the modulus sign indicating that the mass flow, represented by the term $V_c + v_i$, must be positive (which it is certain to be in climbing flight). The correct result for descending flight can be expressed as

$$2\rho A(V_c + v_i)v_i = -T$$

or, in non-dimensional form, as

$$\bar{v}_i(\bar{V}_c + \bar{v}_i) = -1 \quad (2.18)$$

From eqns 2.17 and 2.18, and using values of the induced velocity obtained from flight and wind tunnel tests for the vortex ring state, we can describe the complete curve of \bar{v}_i as a function of \bar{V}_c , Fig. 2.8.

The broken lines of Fig. 2.8 are the continuations of eqns 2.17 and 2.18 into regions for which the vortex ring state renders them invalid. Of particular interest is the state of 'ideal autorotation' in which there is zero mean flow through the rotor so that $V_c = -v_i$. This is given by the intersection of the curve of \bar{v}_i against V_c with the line $\bar{v}_i = -\bar{V}_c$, shown chain-dotted in Fig. 2.8. We find that this occurs when $\bar{V}_c = -1.8$. The condition of 'ideal autorotation' is equivalent to the motion of a circular plate broadside on to the stream which destroys the momentum of the air approaching it. The thrust of the rotor in this condition can be equated to the drag of such a disc, so that, if C_D is the drag coefficient,

$$T = C_D \frac{1}{2} \rho V_c^2 A = 2 \rho A v_0^2$$

or

$$C_D = 4/\bar{V}_c^2$$

Substituting the value of \bar{V}_c found above, we have

$$C_D = 4/(1.8)^2 = 1.23$$

which is close to the drag coefficient of a circular plate. Thus, in 'ideal autorotation' the rotor behaves rather like a parachute.

2.4 The swirl velocity

So far the rotational or 'swirl' velocity has been omitted from the calculations. Since

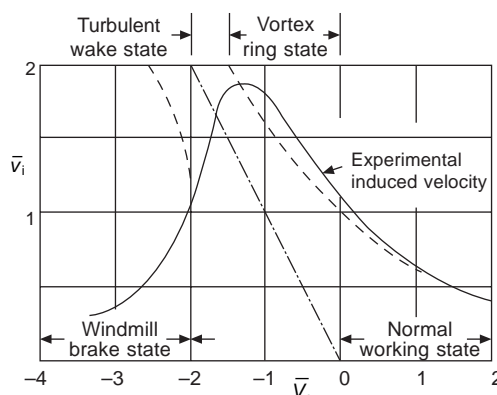


Fig. 2.8 Variation of induced velocity in vertical flight

the flow upstream of the rotor is irrotational, there can be no swirl ahead of the rotor disc. Behind the rotor disc there are two contributions to the swirl velocity: that due to the bound circulation about the blades and that due to the spiral vortex lines forming the slipstream, Fig. 2.9. Let the swirl angular velocity contributions be denoted by ω_b and ω_t respectively. Ahead of the rotor we have $\omega_b + \omega_t = 0$ or $\omega_b = -\omega_t$. On passing through the disc the contribution from the bound circulation changes sign, while the contribution from the trailing vortices remains the same; hence, behind the disc the total angular velocity is $\omega = -\omega_b + \omega_t = 2\omega_t$. This value remains constant in the slipstream because no extra circulation is added; we should also expect the swirl velocity to remain constant from the fact that the bound vorticity contribution diminishes as we go away from the disc but the trailing vortex contribution steadily increases from its value at the disc to twice that value in the ultimate slipstream since, for any point there, the vortex lines are doubly infinite.

To relate the swirl velocity to the thrust on the rotor disc, consider axes fixed in the advancing and rotating rotor blade. With respect to these axes the flow is steady and, since the flow is irrotational, except at the vortex lines leaving the blade, the constant in Bernoulli's equation must be the same everywhere. Let q_z , q_r , q_ψ be the velocity components of the air relative to *fixed* axes situated in the rotor disc, and let the rotor rotate with angular velocity Ω , Fig. 2.10. The velocity components relative to a given point on the blade are q_z , q_r , $q_\psi - \Omega r$. At a great distance ahead of the rotor, the velocity components relative to the same point of the blade are $q_z = V_c$, $q_r = 0$, $q_\psi = -\Omega r$. Also, $p = p_\infty$. Bernoulli's equation for the flow which applies everywhere, is

$$p_\infty + \frac{1}{2}\rho V_c^2 = p + \frac{1}{2}\rho q_z^2 + \frac{1}{2}\rho q_r^2 + \frac{1}{2}\rho(q_\psi - \Omega r)^2$$

Let p_1 be the pressure just in front of the disc; since there is no swirl in front of the disc $q_\psi = 0$, hence

$$p_\infty + \frac{1}{2}\rho V_c^2 = p_1 + \frac{1}{2}\rho(q_z^2 + q_r^2 + \Omega^2 r^2) \quad (2.19)$$

Just behind the disc the pressure will have jumped to $p_1 + \Delta p$, the axial velocity will be unchanged, and the radial velocity will have changed sign since we shall have

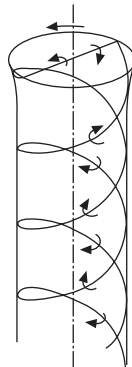


Fig. 2.9 Spiral vortices in axial flight

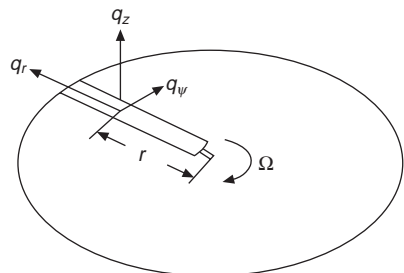


Fig. 2.10 Velocity components relative to blade

passed through the vortex sheet leaving the blade. (For an infinite number of blades, the radial velocity will be zero.) Thus, behind the disc we have

$$p_\infty + \frac{1}{2}\rho V_c^2 = p_1 + \Delta p + \frac{1}{2}\rho(q_z^2 + q_r^2 + q_\psi^2 - 2q_\psi\Omega r + \Omega^2 r^2) \quad (2.20)$$

Subtracting eqn 2.19 from eqn 2.20 gives

$$\Delta p = \rho q_\psi(\Omega r - \frac{1}{2}q_\theta) \quad (2.21)$$

If we write $q_\psi = \omega r$, eqn 2.21 can be expressed as

$$\Delta p = \rho\omega(\Omega - \frac{1}{2}\omega)r^2 \quad (2.22)$$

The total head pressure just ahead of the disc and relative to axes fixed in the disc is

$$H = p_1 + \frac{1}{2}\rho(q_z^2 + q_r^2)$$

Just behind the disc we have

$$H + \Delta H = p_1 + \Delta p + \frac{1}{2}\rho(q_z^2 + q_r^2 + q_\psi^2)$$

giving

$$\begin{aligned} \Delta H &= \Delta p + \frac{1}{2}\rho q_\psi^2 \\ &= \Delta p + \frac{1}{2}\rho\omega^2 r^2 \end{aligned} \quad (2.23)$$

Thus, the change in total head pressure exceeds the jump in static pressure across the disc by a term representing the kinetic energy of the swirl of the slipstream.

To get some idea of the swirl velocity, $q_\psi = \omega r$, in a typical case, let us note that eqn 2.22 can be expressed in terms of the disc loading as

$$\Delta p = w_D = \rho\omega(\Omega - \frac{1}{2}\omega)r^2 \quad (2.24)$$

and take the values $w_D = 250 \text{ N/m}^2$, $\Omega = 25 \text{ rad/s}$ and $r = 6 \text{ m}$. For sea-level density we find $\omega = 0.23 \text{ rad/s}$ and $q_\psi = 1.38 \text{ m/s}$. Since the induced velocity in hovering for this disc loading has been found to be 10.2 m/s, the angle of flow relative to the rotor axis is 7.8° . We also see that the second term in eqn 2.23 is only about $\frac{1}{2}$ per cent larger than Δp ; this justifies the neglect of the swirl velocity in the earlier analysis.

2.5 Blade element theory in vertical flight

The relationship developed in the previous sections between the thrust and the induced velocity requires that either the thrust or the induced velocity is known. We now consider the lift characteristics of the blade regarded as an aerofoil to obtain a further relationship between thrust and induced velocity, thereby enabling both to be evaluated. The calculations follow closely the standard methods of aerofoil theory but the rotor

analysis is simplified considerably because the blade incidence and inflow angles are usually so small that the familiar small angle approximations may be made.

Consider an element of blade of chord c with width dr at a radius r from the axis of rotation. The geometric pitch angle of the blade element relative to the plane of rotation is θ , the climbing speed is V_c , and the local induced velocity is v_i . The direction of the flow relative to the blade makes an angle ϕ (usually called the *inflow angle*) with the plane of rotation, Fig. 2.11, and ϕ is given by

$$\tan \phi = (V_c + v_i)/\Omega r$$

or, for small ϕ ,

$$\phi = (V_c + v_i)/\Omega r$$

The lift on the blade elements is

$$\begin{aligned} dL &= \frac{1}{2}\rho W^2 C_L c dr \\ &\approx \frac{1}{2}\rho \Omega^2 r^2 C_L c dr \end{aligned}$$

since, for small ϕ , $W^2 \approx \Omega^2 r^2$.

Let us suppose that the lift slope a of the section is constant so that, if the section incidence α is measured from the no-lift line, we can write

$$C_L = a\alpha = a(\theta - \phi)$$

Empirical data suggests a lift slope of about 5.7. The elementary lift is now

$$dL = \frac{1}{2}\rho \Omega^2 r^2 a(\theta - \phi) c dr$$

Since ϕ is usually a small angle, we can write $dL \approx dT$, where dT is the elementary thrust, the force perpendicular to the plane of rotation. The total thrust is therefore

$$T = \frac{1}{2}\rho ab\Omega^2 \int_0^R c(\theta - \phi)r^2 dr \quad (2.25)$$

where b is the number of blades.

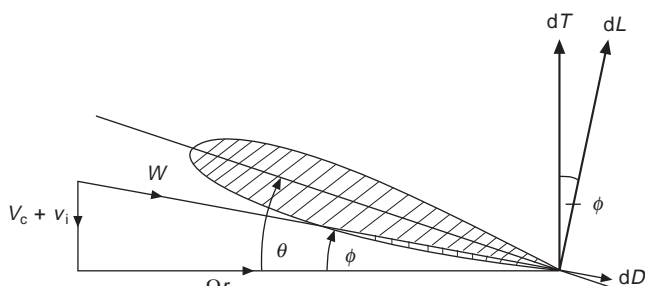


Fig. 2.11 Force components on blade

Defining

$$\lambda_c = V_c/\Omega R, \quad \lambda_i = v_i/\Omega R, \quad x = r/R$$

eqn 2.25 can be written

$$T = \frac{1}{2} \rho a b \Omega^2 R^3 \int_0^1 c [\theta x^2 - (\lambda_c + \lambda_i) x] dx \quad (2.26)$$

If the chord, induced velocity, and 'collective' pitch angle θ are constant along the blade, eqn 2.26 can be integrated easily to give

$$T = \frac{1}{2} \rho a c b \Omega^2 R^3 [\frac{1}{3} \theta_0 - \frac{1}{2} (\lambda_c + \lambda_i)] \quad (2.27)$$

where θ_0 is the constant (collective) pitch angle.

Defining a thrust coefficient by

$$t_c = T / \rho s A \Omega^2 R^2$$

where $s = bc/\pi R$ is the rotor solidity, eqn 2.27 gives

$$t_c = (a/4)[2\theta_0/3 - (\lambda_c + \lambda_i)] \quad (2.28)$$

In American work, the thrust coefficient is usually defined by

$$C_T = T / \rho A \Omega^2 R^2$$

so that the two thrust coefficients are related by $t_c = C_T/s$.

From the momentum theory, the induced velocity and the thrust are related by

$$T = 2\rho A (V_c + v_i) v_i \quad (2.11)$$

which can be written in non-dimensional form as

$$\lambda_i^2 + \lambda_c \lambda_i - \frac{1}{2} s t_c = 0 \quad (2.29)$$

the positive root being the correct one to take. With λ_c being given, eqns 2.28 and 2.29 can be solved for t_c if θ_0 is known, or the required pitch angle θ_0 can be calculated if t_c is given. In hovering flight we have simply

$$t_c = (a/4)(2\theta_0/3 - \lambda_i) \quad (2.30)$$

and

$$s t_c = 2 \lambda_i^2 \quad (2.31)$$

Equations 2.28 and 2.29 have been obtained on the assumption that the blade pitch and chord were constant along the blade and that the downwash velocity had the constant 'momentum' value given by eqn 2.11. Modern helicopter blades usually have constant chord and approximately linear twist, and, if we assume that a linear variation of induced velocity is quite a good approximation to that obtaining in practice, eqn 2.26 can again be integrated quite easily. Let us write the local blade pitch as $\theta_0 - \theta_1 x$ and the local induced velocity as $v_i = v_{iT} x$, where θ_1 is the blade

'washout' angle and v_{iT} is the downwash velocity at the blade tip. Then eqn 2.26 integrates to give

$$t_c = \frac{a}{4} \left[\frac{2}{3} \left(\theta_0 - \frac{3}{4} \theta_1 \right) - \lambda_c - \frac{2}{3} \lambda_{iT} \right] \quad (2.32)$$

where $\lambda_{iT} = v_{iT}/\Omega R$.

Now it is generally accepted that eqn 2.11 can be expressed in differential form as

$$dT = 4\pi r \rho v_i (V_c + v_i) dr \quad (2.33)$$

where $2\pi r dr$ is the area of the annulus of width dr over which the thrust dT is distributed. It can be shown⁹ that eqn 2.33 is not strictly valid but it has given successful results in airscrew work and may be regarded as sufficiently accurate for most purposes. It appears to be true¹⁰ for the linearised problem in which we take $V_c + v_i \approx V_c$ and $dT = 4\pi r \rho v_i V_c dr$. Then putting $v_i = v_{iT}x$ in eqn 2.33 and integrating gives

$$T = \rho \pi R^2 (v_{iT}^2 + 4v_{iT}V_c/3)$$

or, in coefficient form,

$$\lambda_{iT}^2 + 4\lambda_{iT}\lambda_c/3 - st_c = 0 \quad (2.34)$$

Numerical solutions of eqn 2.34 show that the values of λ_{iT} are very nearly equal to $\sqrt{2}\lambda_i$ (λ_i being the constant momentum value of eqn 2.29) for a wide range of λ_c and is exactly equal to $\sqrt{2}\lambda_i$ for the hovering condition ($\lambda_c = 0$). Thus, when we assume the induced velocity is linear, which, as we have said, is good approximation to real conditions, v_{iT} can be replaced with good accuracy by $\sqrt{2}\lambda_i$. Substituting for λ_{iT} in eqn 2.32 gives

$$t_c = \frac{a}{4} \left[\frac{2}{3} \left(\theta_0 - \frac{3}{4} \theta_1 \right) - \lambda_c - \frac{2\sqrt{2}}{3} \lambda_i \right] \quad (2.35)$$

But $\theta_0 - \frac{3}{4}\theta_1$ is the blade pitch angle at $\frac{3}{4}R$ and $2\sqrt{2}/3 = 0.943$; hence, if we take θ_0 as the value of θ at the $\frac{3}{4}$ radial position and approximate $2\sqrt{2}/3$ by unity, we can use the simple equations 2.28 and 2.29 or 2.30 and 2.31 for all cases. These approximations mean that the thrust will be underestimated by about 2 or 3 per cent relative to eqns 2.32 and 2.34, but, since the blade lift slope and the actual induced velocity will not be known precisely, further refinement is hardly justified.

It can easily be verified that if the blade planform also has linear taper, eqn 2.28 still holds, with the exception of some very small terms, if the chord is taken as that at $\frac{3}{4}R$ as well as the blade pitch angle.

A useful relationship between the thrust coefficient and the blade lift coefficient can be obtained since, for constant blade chord,

$$T = \frac{1}{2} \rho b c \Omega^2 R^3 \int_0^1 x^2 C_L dx$$

or

$$t_c = \frac{1}{2} \int_0^1 x^2 C_L \, dx \\ = \bar{C}_L / 6 \quad (2.36)$$

where

$$\bar{C}_L = 3 \int_0^1 x^2 C_L \, dx$$

If the lift coefficient is constant along the blade, then

$$t_c = C_T/s = C_L/6$$

Usually the rotor operates at a mean C_L of between 0.35 and 0.6, giving typical values of t_c within the range of 0.06 to 0.1.

The rotor torque can be calculated in a similar way to the rotor thrust. From Fig. 2.11, the torque dQ of a blade element about the axis of rotation is

$$dQ = r(dD + \phi \, dL) \\ = \frac{1}{2}\rho\Omega^2 r^3 c(\delta + \phi \, C_L)dr \quad (2.37)$$

where δ is the local blade section drag coefficient. If δ is assumed to be constant, eqn 2.37 can be integrated to give

$$Q = \delta\rho b c \Omega^2 R^4 / 8 + \frac{1}{2}\rho b c \Omega^2 R^4 \int_0^1 x^3 \phi C_L \, dx \quad (2.38)$$

Defining a torque coefficient q_c by

$$q_c = Q/\rho s A \Omega^2 R^3$$

eqn 2.37 can then be written in coefficient form as

$$q_c = \delta/8 + \frac{1}{2} \int_0^1 x^3 \phi C_L \, dx \quad (2.39)$$

Assuming constant induced velocity, $\phi = (\lambda_c + \lambda_i)/x$, so that eqn 2.39 becomes, on using eqn 2.36,

$$q_c = \delta/8 + (\lambda_c + \lambda_i)t_c \quad (2.40)$$

For the special case of hovering flight, $\lambda_c = 0$,

$$q_c = \delta/8 + \lambda_i t_c \\ = \delta/8 + \sqrt{(s/2)t_c^{3/2}} \quad (2.41)$$

The first term of eqn 2.41 represents the torque required to overcome the profile drag; the second represents the torque to overcome the induced drag of the blades. It can be seen that the second term is the non-dimensional form of the hovering power calculated in section 2.1 from energy and momentum considerations.

Using momentum principles we can find the effect of a non-uniform induced

velocity distribution on the induced power. Let us assume that eqn 2.14 holds in differential form; then in hovering flight we can write

$$dP = dT v_i = 4\pi r \rho v_i^3 dr$$

where v_i is the local induced velocity. If we take the linear induced velocity distribution $v_i = v_{iT}x$, we have

$$dP = 4\pi R^2 \rho v_{iT}^3 x^4 dx$$

so that

$$P = 4\pi R^2 \rho v_{iT}^3 / 5 \quad (2.42)$$

The thrust from momentum considerations is

$$\begin{aligned} T &= 4\pi \rho R^2 \int_0^1 v_{iT}^2 x^3 dx \\ &= \rho \pi R^2 v_{iT}^2 \end{aligned} \quad (2.43)$$

If the induced velocity v_i is *constant*, we have, for the corresponding thrust T_0 ,

$$T_0 = 2\rho \pi R^2 v_i^2 \quad (2.44)$$

Comparing eqns 2.43 and 2.44 we see that for the thrusts to be the same we must have

$$v_{iT}^2 = 2v_i^2$$

Then

$$P = 8\sqrt{2}\rho \pi R^2 v_i^3 / 5$$

and, if P_0 is the induced power when the induced velocity is constant,

$$P_0 = 2\rho \pi R^2 v_i^3$$

Hence

$$P/P_0 = 4\sqrt{2}/5 = 1.131$$

that is, when the induced velocity is linear, the induced power is about 13 per cent higher than if the induced velocity were constant; the latter condition corresponding to the least induced power for a given thrust. For the linear induced velocity, the torque coefficient would be

$$q_c = \delta/8 + 1.13\sqrt{(s/2)} t_c^{3/2} \quad (2.45)$$

A typical value assumed for δ is 0.012. With typical values of 0.05 and 0.08 for the solidity and thrust coefficient respectively, the two terms of q_c are 0.0015 and 0.00403, showing that the induced power is more than two and a half times the profile drag power.

52 Bramwell's Helicopter Dynamics

Tests on aerofoils with rotor blade type of construction show that δ depends considerably on incidence and can be represented in the form

$$\delta = \delta_0 + \delta_1 \alpha + \delta_2 \alpha^2 \quad (2.46)$$

Bailey¹¹ has suggested the values

$$\delta = 0.0087 - 0.0216\alpha + 0.4\alpha^2 \quad (\alpha \text{ in radians})$$

and has used them in the calculation of thrust, H -force, and torque coefficients in hovering and vertical flight. The expressions which had to be calculated were very lengthy and the results were given in tabular form. They are to be found in the book by Gessow and Myers.¹² Since, however, Bailey used constant induced velocity in his calculations, it is rather doubtful whether the results he obtained would have been much better than if δ had been assumed constant because, in forward flight especially, the induced velocity differs considerably from the constant mean value, with correspondingly large variations in local blade incidence.

Another parameter of great importance is Mach number, especially for current helicopters which operate at higher tip speeds than formerly. With Mach number and induced velocity properly taken into account, the calculations of thrust and torque become more complicated; consideration of Mach number effects is provided in Chapter 6. However, equations 2.28 and 2.45 give acceptable accuracy for many performance problems.

2.6 Calculation of the inflow angle

When making rotor calculations, it is often useful to know the inflow angle when the rotor geometry and operating conditions are given. We saw in the last section that the elementary thrust dT on an annulus of the rotor disc, when there are b blades, is

$$dT = \frac{1}{2} \rho abc \Omega^2 r^2 (\theta - \phi) dr \quad (2.47)$$

where it has been supposed that the local lift coefficient is given by $C_L = a\alpha$.

Now

$$\phi = (V_c + v_i)/\Omega r$$

so that eqn 2.47 can be written

$$dT = \frac{1}{2} \rho abc \Omega^2 r^2 [\theta - (V_c + v_i)/\Omega r] dr \quad (2.48)$$

Momentum theory applied to the annulus gives

$$dT = 4\pi\rho(V_c + v_i)v_i r dr$$

and on eliminating dT from eqn 2.48 we have

$$v_i^2 + \left(V_c + \frac{abc\Omega}{8\pi} \right) v_i - \frac{abc\Omega^2 r}{8\pi} \left(\theta - \frac{V_c}{\Omega r} \right) = 0 \quad (2.49)$$

Writing $\lambda_i = v_i/\Omega R$ and $\lambda_c = V_c/\Omega R$, as before, and putting $\sigma = bc/\pi r$, where σ is the solidity based on the local radius, eqn 2.49 becomes

$$\lambda_i^2 + \left(\lambda_c + \frac{a\sigma x}{8} \right) \lambda_i - \frac{a\sigma x}{8} \left(\theta - \frac{\lambda_c}{x} \right) = 0 \quad (2.50)$$

In eqn 2.50 σ and θ are variables, so that variable twist and taper can be taken into account. In hovering flight $\lambda_c = 0$ and eqn 2.50 reduces to

$$\lambda_i^2 + (a\sigma x/8)\lambda_i - (a\sigma x^2/8)\theta = 0 \quad (2.51)$$

Since $\phi = v_i/\Omega r = \lambda_i/x$, eqn 2.51 can be written as

$$\phi^2 + (a\sigma/8)\phi - (a\sigma/8)\theta = 0$$

or

$$\phi^2 = (a\sigma/8)(\theta - \phi) \quad (2.52)$$

Hence, given the local blade pitch angle and solidity, the local value of ϕ can be calculated and then used in eqns 2.25 and 2.38 to obtain the thrust and torque. Further, $\theta - \phi$ is the local blade incidence and $a(\theta - \phi)$ the local blade lift coefficient.

As an example of the use of eqn 2.52, let us consider a three-bladed rotor whose pitch angle at the blade root is 12° and whose blades have a washout* of 5° . The blade has a radius of 25 ft (7.6 m) and a constant chord of 1.5 ft (0.46 m). The lift slope of the blade section is assumed to be 5.7. Table 2.1 shows how the required quantities vary along the span, ϕ being obtained as the solution of eqn 2.52.

From eqn 2.36 it can be seen that we can calculate the thrust coefficient by the integration of $x^2 C_L$, which is proportional to the blade aerodynamic loading. The variation of $x^2 C_L$ along the blade span is shown in Fig. 2.12. On integration we find that $t_c = 0.0639$.

Let us compare this value with the thrust coefficient calculated from eqns 2.30 and 2.31. Eliminating λ_i gives the following quadratic in $t_c^{1/2}$:

$$t_c = (a/4)[2\theta_0/3 - \sqrt{(st_c/2)}] \quad (2.53)$$

and the pitch angle to be used is the value of θ at $\frac{3}{4}R$, i.e. 7.5° as discussed in

Table 2.1 Variation of ϕ , α and C_L with blade section radius

$x = r/R$	0.3	0.5	0.7	0.8	0.9	1
θ rad	0.178	0.158	0.136	0.126	0.115	0.105
σ	0.191	0.114	0.082	0.0715	0.0636	0.0573
ϕ	0.102	0.0795	0.0639	0.0585	0.0531	0.0483
$\alpha = (\theta - \phi)^\circ$	4.36	4.49	4.13	3.86	3.54	3.24
$C_L = a(\theta - \phi)$	0.434	0.447	0.411	0.385	0.353	0.324

* A twisted rotor blade or wing is said to have ‘washout’ when the incidence of the tip section is less than that of the root.

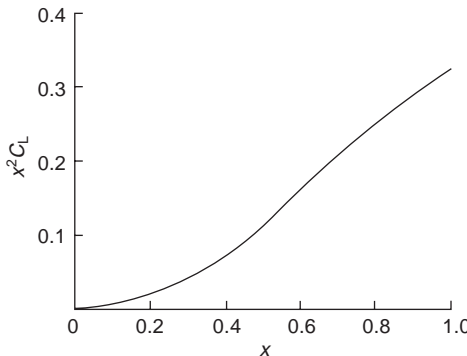


Fig. 2.12 Non-dimensional blade loading as a function of span

section 2.4. Solving eqn 2.53, with $s = 0.0573$, gives $t_c = 0.0638$, which agrees extremely well with the previous result and shows that the simple analysis gives an accuracy well within that of the assumed value for the lift slope.

2.7 The optimum rotor

It was stated in the last section that the lowest induced power occurs when the induced velocity is uniform over the disc. The optimum rotor would be one designed so that this state was achieved and, in addition, the angle of attack would be chosen so that the section would be operating at the most efficient lift coefficient, which is not necessarily at the highest C_L/C_D ratio.

In hovering flight, the pitch angle of a blade element is

$$\begin{aligned}\theta &= \alpha + v_i/\Omega r \\ &= \alpha + \lambda_i/x\end{aligned}\quad (2.54)$$

where v_i is constant. The angle of attack α is also the constant value chosen as the most efficient. Thus the pitch angle can be considered as consisting of a constant part and a part which varies inversely with blade radius.

Now the thrust on an annulus of the rotor from the blade element theory is

$$dT = \frac{1}{2} \rho \Omega^2 r^2 a \alpha c dr$$

and from momentum theory

$$dT = 4\pi \rho r v_i^2 dr$$

Equating these differential thrusts shows that to ensure constant induced velocity the chord must vary inversely with the radius. Thus, the optimum rotor must be twisted in accordance with eqn 2.54 and tapered inversely as the radius. The latter requirement would result in an unusual blade shape and one that would be difficult to construct. Departures from the optimum blade, which usually means only that the

chord is kept constant, do not result in a serious loss of efficiency; usually the amount is about 2 to 3 per cent more power for a given thrust. The subject is dealt with in some detail by Gessow and Myers¹². The reader is recommended to compare an optimum rotor with one of the same solidity having, say, constant chord and twist differing from the optimum.

The equivalent chord c_e of a rotor on a *thrust* basis is defined as

$$\begin{aligned} c_e &= \frac{\int_0^1 cx^2 dx}{\int_0^1 x^2 dx} \\ &= 3 \int_0^1 cx^2 dx \end{aligned} \quad (2.55)$$

and on a *torque* basis

$$c_e = 4 \int_0^1 cx^3 dx \quad (2.56)$$

These are the values of the chord for which constant-chord blades would yield the same thrust and torque as a tapered blade, for the same radius and incidence distribution.

2.8 The efficiency of a rotor

The efficiency of any device should indicate the measure of the success with which that device performs its duty. It is reasonable to want a hovering rotor to produce the most thrust for the least power; that is, to make the ratio T/P as large as possible. This simple criterion has been objected to on the grounds that T/P is not a dimensionless quantity. The standard measure of efficiency adopted in helicopter work is the *figure of merit* \bar{M} defined by

$$\bar{M} = T v_i / P$$

where v_i is the mean momentum induced velocity in hover. Since $T v_i$ is the ideal induced power, the figure of merit is the ratio of the induced power to the total power. Since $P = T v_i + P_p$, where P_p is the profile drag power, the figure of merit can also be written as

$$\bar{M} = T v_i / (T v_i + P_p)$$

and, in non-dimensional form, as

$$\bar{M} = \sqrt{(s/2) t_c^{3/2} / q_c}$$

It could well be argued that the figure of merit so defined is even less satisfactory than the ratio T/P , because for constant thrust a high value can be achieved by increasing the induced velocity (by reducing the radius, say), thereby increasing the

56 Bramwell's Helicopter Dynamics

total power, which is the opposite of the desired effect. The reason for this rather unsatisfactory feature of the figure \bar{M} is that the induced power is regarded rather like the 'useful work' of standard airscrew theory and takes no account of the fact that induced power is no more desirable than profile power.

The difficulty of defining an efficiency factor for the helicopter is that many parameters are involved and some of them cannot be arbitrarily varied because of structural and mechanical as well as aerodynamic limitations. Nevertheless, some useful conclusions can be drawn from an examination of the thrust/power ratio. Let us write this ratio as

$$\frac{T}{P} = \frac{T}{T^{3/2}/\sqrt{(2\rho A)} + \delta\rho s A \Omega^3 R^3/8} \quad (2.57)$$

The first term in the denominator of eqn 2.57 is the induced power, and the second term is the profile drag power.

Suppose the rotor radius is kept constant and the thrust is kept constant in such a way as to keep the incidence at a favourable value. This means that the mean lift coefficient and, hence, t_c is kept constant. But since $T = t_c \rho s A \Omega^2 R^2$, we must have $s\Omega^2$ constant, so the only variable term in T/P is the profile drag power, which must therefore be proportional to Ω . Thus T/P can be increased by reducing Ω , which also requires s to increase; or, in other words, we need a low rotor speed and high solidity if the radius is to be kept constant.

Suppose now we fix the thrust, solidity, and tip speed ΩR and vary the rotor radius. Differentiating eqn 2.57 with respect to A gives

$$\frac{\partial}{\partial A} \left(\frac{T}{P} \right) = T \frac{\delta\rho s \Omega^3 R^3/8 - T/2\sqrt{2\rho A}^{3/2}}{[\delta\rho s \Omega^3 R^3/8 + T^{3/2}/\sqrt{(2\rho A)}]^2} = 0, \text{ for maximum } T/P$$

$$\text{i.e. } \delta\rho s A \Omega^3 R^3/8 = \frac{1}{2}T/\sqrt{(2\rho A)}$$

that is, the profile power is half the induced power for maximum T/P . The figure of merit for this condition is $\frac{2}{3}$.

Finally, for a given tip speed, solidity, disc area, and drag coefficient, we can write

$$\frac{T}{P} = \frac{1}{\Omega R} \frac{t_c}{\delta/8 + \sqrt{(s/2)t_c^{3/2}}}$$

To find the optimum thrust coefficient we have

$$\frac{\partial}{\partial t_c} \left(\frac{T}{P} \right) = \frac{1}{\Omega R} \frac{\delta/8 + \sqrt{(s/2)t_c^{3/2}} - \frac{3}{2}t_c^{3/2}\sqrt{(s/2)}}{[\delta/8 + \sqrt{(s/2)t_c^{3/2}}]^2} = 0$$

$$\text{or } \frac{1}{2}\sqrt{(s/2)t_c^{3/2}} = \delta/8$$

and, as above, the profile power is half the induced power and the figure of merit is again $\frac{2}{3}$. If we take as typical values $s = 0.05$ and $\delta = 0.012$, we find the optimum value of t_c to be 0.072.

2.9 Ground effect on the lifting rotor

When a rotor hovers near the ground, the presence of the ground has a considerable effect on the induced-velocity distribution over the rotor and, hence, on the thrust and power. At the ground the vertical component of velocity must vanish, and we can expect that over the rotor the induced velocity would be less than in free air. The reduction of induced velocity results in a proportionate reduction of induced power for a given thrust and since, as we saw earlier, the induced power may be at least two thirds of the total power, the improvement in performance may be quite remarkable; indeed, some of the earlier, underpowered, helicopters could hover only with the help of the ground.

A theoretical treatment of ground effect has been made by Knight and Hefner¹³. It was assumed that the circulation along the blade was constant, so that a vortex trailed from the blade tip having the same circulation as that round the chord. The spiral vortices from each blade were assumed to form a uniform vortex cylinder reaching the ground. Now, it is well known that the presence of a plane ground can be represented by an appropriate image system such that the flow normal to the plane vanishes, which is the required boundary condition. In this case the image system is a cylinder of opposite vorticity, Fig. 2.13. It is clear that the effect of the image system is to produce an upflow tending to reduce the induced velocity at the rotor. The treatment is very similar to that for a fixed wing flying near the ground, which may be represented by a simplified horse-shoe vortex and its image system.

The ratio of the induced velocity to that which would have occurred in free air is shown in Fig. 2.14 as a function of the radial position and the ratio of rotor height, h , to rotor radius. The ratio of the corresponding powers is given in Fig. 2.15 as a function of thrust coefficient and rotor height. A typical value of the ratio of the rotor height to rotor radius when the helicopter is on the point of taking off is about 0.3,

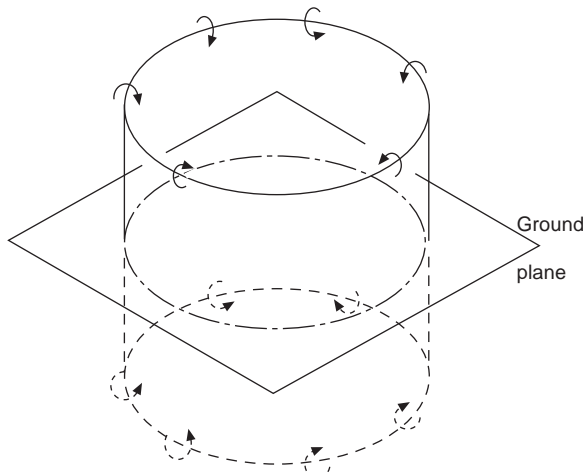


Fig. 2.13 Reflection of tip vortex in ground plane

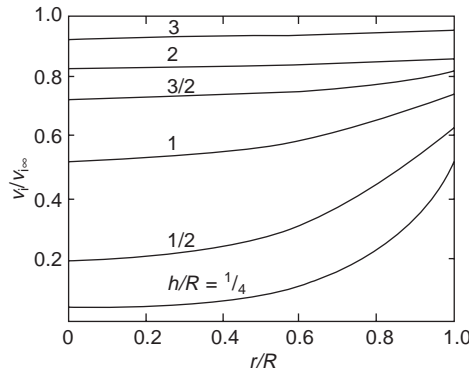


Fig. 2.14 Ground effect on mean induced velocity

and it can be seen from Fig. 2.15 that the induced power is about half that which would have occurred in free air, representing a reduction of about a third of the total power.

The same improvement in performance can be presented in another way. From a number of tests on model rotors, Zbrozek¹⁴ has derived curves of the thrust that can be produced for a given power and has expressed the results as the ratio of the thrust in ground effect to the thrust in free air as a function of the rotor height and thrust coefficient, Fig. 2.16.

Hovering in ground effect (IGE) confers considerable operational benefits at high altitude when the power available may not be sufficient to hover out of ground effect (OGE). A take-off at altitude, for example, may be initiated followed by transition to forward flight IGE until a speed is reached such that the power required becomes less than the power available (see Chapter 4) and a climb out may be performed.

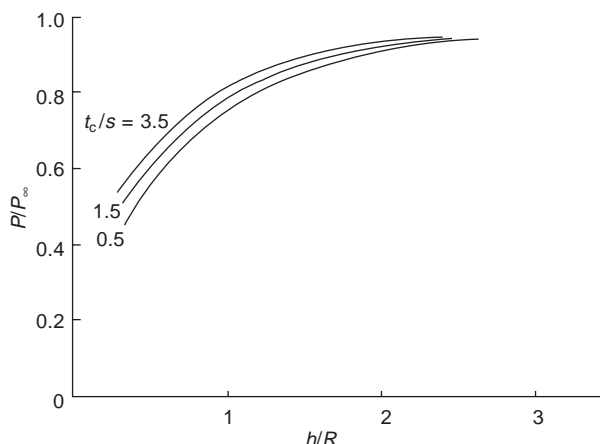


Fig. 2.15 Ground effect on induced power

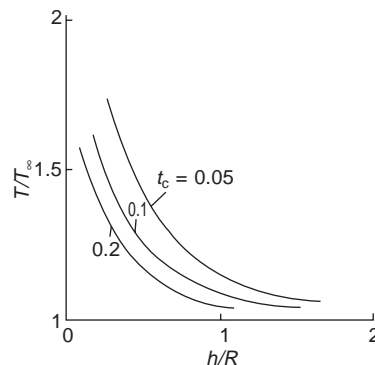


Fig. 2.16 Ground effect on thrust

2.10 Rotor wake models

As stated at the beginning of this chapter, since the only flow through the rotor in hovering flight is due to the velocity field created by the bound vortices and the trailing vortex sheets, and since the distribution of the trailed vorticity is determined by this velocity field, the problem of calculating the flow becomes extremely complex and a purely analytical solution is not feasible.

A hierarchy of methods of analysis has developed of which the simplest is the uniform or rigid wake model, mentioned at the start of this chapter. This consists of a helical surface representing a vortex sheet trailed from each blade and moving axially at constant velocity. From the point of view of an observer on the rotating blade, the wake configuration remains fixed. A more refined model is that of the prescribed wake which embodies improvements to the wake description and velocity field, including those that have been observed from experiment. The most refined of all models is that of the free wake, whose configuration interacts with and is consistent with the velocity field. These are now considered in more detail.

2.10.1 The rigid wake and the methods of Goldstein, Lock, and Theodorsen

We referred earlier to the theorem of Betz which states that the induced power of an airscrew or rotor is least when the vortex wake springing from the blades moves axially as if it were a rigid helical surface. A proof of Betz's theorem has been given by Theodorsen⁵.

To appreciate the implications of this result we consider the analogous but much simpler problem of a fixed wing and its vortex wake. It is well known that the induced drag of a wing is least when the induced velocity of the wing is constant along the span, in which case the spanwise loading is elliptical. Sufficiently far behind the wing the induced velocity becomes independent of the rearward distance, and such a flow can be produced by a two-dimensional strip whose width is equal to the span and which moves perpendicular to its plane with velocity w , Fig. 2.17. The circulation about the wing, corresponding to this optimum case, can be evaluated by

calculating the line integral C_1 joining the points P and P' which are, respectively, just above and just below the wing, Fig. 2.17. Now, since the flow is irrotational, the line integral C_1 is equal to the line integral C_2 , and this integral is equal to the difference of potential between the points P and P', which are equidistant from the tip of the strip, Fig. 2.18. The velocity potential, and hence circulation Γ , for a two-dimensional strip moving normal to itself is found to be elliptical with a maximum value $\Gamma_0 = 2ws$ at the wing centre, $2s$ being the width of the sheet (and the wing span). For the wing itself, however, the maximum circulation should be given by $\Gamma_0 = 4ws$, since the wing and its trailing wake represent only half the assumed two-dimensional strip, and the induced velocity for a given circulation is half the two-dimensional value.

The corresponding problem for the rotor is to find the velocity potential for a series of helical vortex sheets, Fig. 2.19, one for each blade, moving with constant velocity w relative to the otherwise undisturbed air. Once this problem has been solved, the effect of the number and relative spacing of the sheets on the blade circulation can be investigated. It is also possible to determine the relationship between the induced velocity at the blade and the mean velocity between the sheets.

The formidable problem presented by this motion was eventually solved by Goldstein⁴ in 1929, but here we shall merely describe a simpler method due to Prandtl¹⁵, especially as Prandtl's result has been used to calculate the rotor blade 'tip loss'. Prandtl's method, which contains all the essentials of Goldstein's problem, was to replace the curved sheets of the helical surface by a series of two-dimensional sheets on the

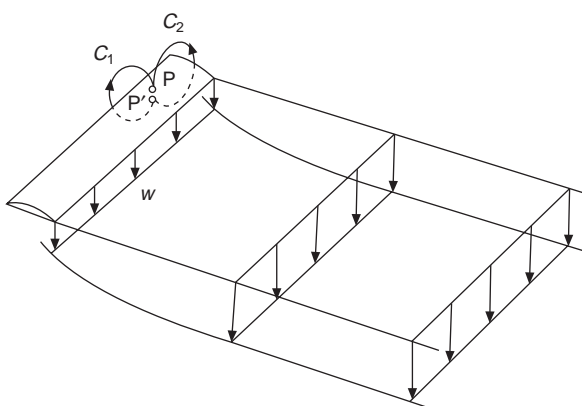


Fig. 2.17 Induced velocity distribution behind elliptically loaded wing

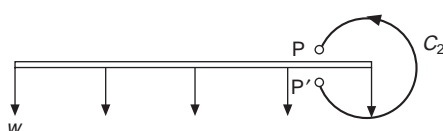


Fig. 2.18 Circulation about wing

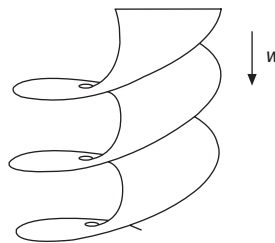


Fig. 2.19 Vortex sheet arrangement near rotor blade

assumption that the radius of curvature of the outer parts of the sheets is so large that they can be considered as doubly infinite straight strips, Fig. 2.20.

Before considering the flow about these sheets, let us rewrite the thrust equations for an element of a blade in terms of the local circulation about the element. Let the induced velocity at the blade element be v_i , the axial velocity be V_c , and the overall resultant velocity be W , Fig. 2.21.

For an infinite number of blades the thrust on an annulus of radius r and width dr is, from momentum considerations,

$$dT = 2\pi r \rho (V_c + v_i \cos \phi) 2v_i \cos \phi dr \quad (2.58)$$

where we have assumed that the induced velocity in the far wake is twice that at the disc.

From blade element theory we also have

$$dT = dL \cos \phi = \frac{1}{2} b W^2 \rho C_L c \cos \phi dr \quad (2.59)$$

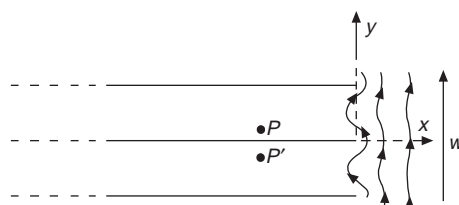


Fig. 2.20 Two-dimensional flow about vortex sheets

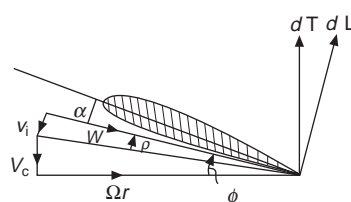


Fig. 2.21 Velocity and force components at a blade element

62 Bramwell's Helicopter Dynamics

where dL is the lift on the element, b is the number of blades, and C_L is the local lift coefficient.

Now, from the Kutta–Zhukowsky theorem,

$$\frac{1}{2}\rho W^2 C_L c = \rho W \Gamma \quad (2.60)$$

where Γ is the circulation about the element. Then from eqns 2.58, 2.59, and 2.60 we obtain

$$dT = \rho b W \Gamma \cos \phi \, dr$$

But from Fig. 2.21 we see that

$$W \sin \phi = V_c + v_i \cos \phi$$

so that on eliminating dT we finally get

$$v_i = b\Gamma/4\pi r \sin \phi \quad (2.61)$$

which gives a relationship between the local induced velocity and the circulation when the number of blades is infinite.

Returning now to Prandtl's representation of the vortex sheets, Fig. 2.20, let the infinite array of sheets move relative to the surrounding air with velocity w . The complex potential of such a flow is known* to be

$$\phi + i\psi = \frac{ws}{\pi} \cos^{-1} e^{\frac{i\pi z}{s_p}} \quad (2.62)$$

where s_p is the spacing of the sheets, which is easily seen to be given by

$$s_p = (2\pi r/b) \sin \phi \quad (2.63)$$

It can be verified that eqns 2.62 and 2.63 satisfy the requirements of the problem.

Now consider the points P and P' just above and just below one of the sheets ($x < 0$), Fig. 2.20. The required circulation, as explained earlier, is equal to the difference of potential between these points. Then taking, for simplicity, the sheet on the x axis, on which $\psi = 0$, the potential difference across the sheet at a distance a from the edge of the sheet is easily found from eqn 2.62 to be

$$\begin{aligned} \phi_P - \phi_{P'} &= \Gamma = \frac{2ws}{\pi} \cos^{-1} e^{\frac{-\pi a}{s_p}} \\ &= wsk \end{aligned}$$

where

$$k = \frac{2}{\pi} \cos^{-1} e^{\frac{-\pi a}{s_p}}$$

* ϕ in eqn 2.62 is the standard symbol for velocity potential and should not be confused with the inflow angle.

Hence,

$$w = \Gamma/s_p k$$

Now, if we can take the induced velocity at the blade to be half this value, i.e. if we suppose $v_i = \frac{1}{2}w$, we have, on substituting from eqn 2.63 for s_p

$$v_i = b\Gamma/4\pi rk \sin \phi \quad (2.64)$$

This is precisely the same expression as eqn 2.61 except for the factor k , which can be regarded as a correction factor for the number of blades. Since k is always less than unity, the induced velocity for a given circulation is always larger the fewer the number of blades. Put in another way, there is a loss of circulation near the blade tips when the number of blades is finite.

If a is interpreted as the distance $R - r$ from the blade tips and s is based on the value at the blade tip, k can be written as

$$\begin{aligned} k &= \frac{2}{\pi} \cos^{-1} e^{\frac{-b(1-x)}{\sin \phi}} \\ &= \frac{2}{\pi} \cos^{-1} e^{-f} \end{aligned} \quad (2.65)$$

where $f = \frac{1}{2}b(1-x)/\sin \phi$. This relationship is shown plotted in Fig. 2.22.

Goldstein's more exact analysis for the helical vortex sheets resulted in an equation identical with eqn 2.64 but k did not have the simple form of eqn 2.65. Goldstein's values of k , which are a function of the number of blades, the radial position of the element in question, and the inflow angle ϕ , are given in Fig. 2.23.

Proceeding with the rotor analysis, we see from Fig. 2.21, that

$$\begin{aligned} \tan \rho &= v_i/W \\ &= bcC_L/8\pi rk \sin \phi \end{aligned}$$

from eqns 2.60 and 2.64, or

$$\tan \rho = \sigma C_L/8k \sin \phi \quad (2.66)$$

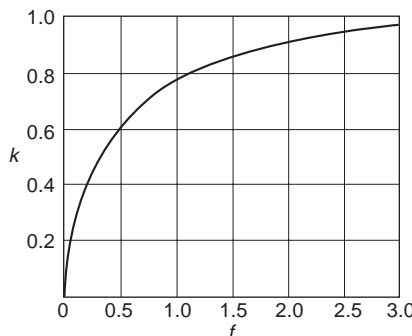


Fig. 2.22 Variation of circulation factor as function of f

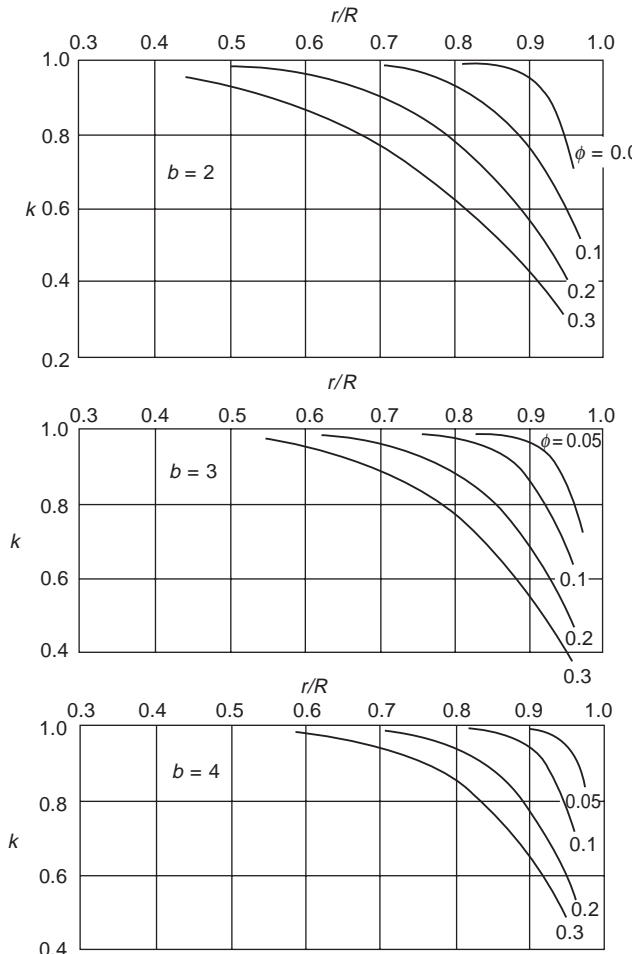


Fig. 2.23 Goldstein circulation factors

In hovering flight $\rho = \phi$ and, since $C_L = a(\theta - \phi)$, eqn 2.66 becomes

$$8k\phi^2 = \sigma a(\theta - \phi) \quad (2.67)$$

which is precisely the same as eqn 2.52 except for the factor k .

The value of k in eqn 2.64 has been derived on the assumption that the ideal wake conditions exist, and this, in turn, implies a certain range of blade loadings depending on the inflow angle and number of blades. Hence, any calculations using these values of k are strictly valid only for these particular loadings. Lock¹⁶, however, widened the range of application by assuming that the values of k would apply with reasonable accuracy to any practical load distributions.

The rigid wake analysis of Goldstein implies a certain variation of the inflow angle ϕ with respect to the radius; Lock's assumption allows us to use ϕ freely, just as we did for the calculations shown in Table 2.1.

Let us apply the Goldstein–Lock analysis to the rotor whose induced velocity and local lift coefficient were calculated in section 2.5. This time we solve eqn 2.67 with the appropriate value of k instead of taking it as unity. Actually, as ϕ is unknown, the correct value of k cannot be found immediately, but let us first calculate ϕ with $k = 1$ (corresponding to an infinite number of blades) and then find k from Fig. 2.22; if necessary we can use the new value of ϕ to obtain a better value of k , and so on. The convergence is usually very rapid. For the case under consideration, k becomes worth considering only for radial distances greater than $0.9 R$. The results of the calculations are shown in Table 2.2.

For the small inflow angles, i.e. the small vortex sheet spacings, which normally occur in practice, it might be expected that Prandtl's much simpler analysis would be adequate. The same calculations were made using Prandtl's formula and the results are compared with those of the Goldstein–Lock analysis, Table 2.2, from which it can be seen that the differences are indeed very small.

The effect on the blade loading distribution $x^2 C_L$ is shown in Fig. 2.24, and the loss of thrust, or 'tip loss', amounts to about $4\frac{1}{2}$ per cent of the total thrust. The loss would be larger for two blades and less for four or more blades. The figure also shows clearly that the difference between the Prandtl and the Goldstein–Lock analyses is very small.

2.10.2 The tip loss factor

The above calculations show how we can estimate the loss of thrust near the blade

Table 2.2 Variation of factor k and inflow angle ϕ near blade tip

	x	0.9	0.95	0.96	0.97
Goldstein	k	0.97	0.85	0.79	0.68
	ϕ	0.0536	0.0532	0.0540	0.0567
Prandtl	k	0.97	0.85	0.81	0.73
	ϕ	0.0536	0.0532	0.0537	0.0551

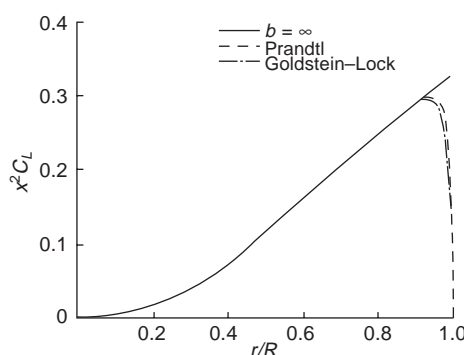


Fig. 2.24 Calculations of tip effect

tips. It would clearly be desirable to have a means of calculating the tip loss which is simpler than the strip analysis described above. For this purpose Prandtl devised a tip loss factor which gave the ratio of the mean induced velocity over the rotor to an effective velocity at the blades themselves.

If the number of blades were infinite, the vortex sheets would be indefinitely close together and all the air between them would be carried down with the sheets. The air outside the sheets would remain at rest. When the number of blades is finite, however, the spaces between the sheets allows some of the air to escape upwards round the edges so that, for a given velocity of the sheets, the average downwash velocity is somewhat less than at the sheets themselves, and this latter velocity corresponds to the induced velocity at the blades. Expressed in another way, if a finite-bladed rotor carries a given thrust, the mean induced velocity at the blades is higher than the value of the induced velocity calculated on the basis of infinite blades.

Prandtl regarded the defect of mean velocity as equivalent to a shortening of the lengths of the sheets, i.e. of a reduction of the radius of the blades from R to an effective value R_{eff} . By finding the ratio between the mean velocity between the sheets and the velocity of the sheets themselves, Prandtl showed¹⁷ that

$$R - R_{\text{eff}} = (1.386/b)xR \sin \phi$$

or

$$R_{\text{eff}}/R \approx 1 - (1.386/b) \sin \phi \quad (2.68)$$

since, near the tip, x can be taken as unity.

For hovering flight it is usual to take

$$\sin \phi = \lambda_i = \sqrt{(C_T/2)} \quad (2.69)$$

so that to a good approximation eqn 2.68 can be written as

$$R_{\text{eff}}/R = B = 1 - \sqrt{C_T/b} \quad (2.70)$$

This expression, and others similar to it, has often been used to determine the 'tip loss factor' B . For the three-bladed rotor considered earlier, B is about 0.980.

Now the idea of Prandtl's tip loss factor is to represent the increased induced velocity at the blades by calculating the mean induced velocity from the simple momentum theory but based on a reduced radius $R_{\text{eff}} = BR$. The tip loss factor is intended to apply only to the calculation of the induced velocity, but in most textbooks and in many technical papers it has been interpreted as meaning that the outer portion of the blade $R - R_{\text{eff}}$ is incapable of carrying lift. This means that the thrust integral would be written

$$T = \int_0^{BR} (dT/dr) dr = \int_0^B (dT/dx) dx$$

Clearly this interpretation is quite different from the one intended by Prandtl. If the upper limit of the integral of eqn 2.26 is B instead of unity, we have, for constant induced velocity and hovering flight,

$$T = \frac{1}{2}b\rho ac\Omega^2 R^3 (B^3\theta_0/3 - B^2\lambda_i/2)$$

giving

$$t_c = (aB^2/4)(2B\theta_0/3 - \lambda_i) \quad (2.71)$$

instead of

$$t_c = (a/4)(2\theta_0/3 - \lambda_i) \quad (2.28)$$

Using the values for θ_0 and λ_i of section 2.5, we find that eqn 2.71 leads to a reduction of thrust of about 7.7 per cent compared with the thrust given by eqn 2.28. Thus the use of B as an upper limit to the thrust integral considerably overestimates the ‘tip loss’. In addition, the expressions for thrust and other rotor quantities become very complicated when the upper limit B is applied to the forward flight cases. A much simpler method of accounting for the tip loss is to apply the reduced radius to the calculation of the induced velocity in the manner conceived by Prandtl. Thus the induced velocity is simply increased by $1/B^2$ and the expression for the thrust coefficient becomes

$$t_c = (a/4)(2\theta_0/3 - \lambda_i/B^2) \quad (2.72)$$

This expression gives a thrust reduction of 4 per cent, which is quite close to the value of $4\frac{1}{2}$ per cent from the strip theory.

It is suggested that eqn 2.72 should be used as the simplest and most accurate method of allowing for tip loss. In forward flight the value of B given by eqn 2.70 no longer applies, as the vortex wake is skewed relative to the rotor disc which makes it necessary to adopt a different analysis.

2.10.3 Theodorsen's theory

The analyses of Prandtl and Goldstein–Lock described above can be justly criticised in that the wake contraction has not been taken into account. It was assumed that the induced velocity in the wake was twice that at the rotor disc but that the wake was a uniform helix having the same diameter as the rotor. Because of this restriction, the analysis was assumed to apply to ‘light loadings’. Theodorsen⁵ was the first to make an attempt to take the wake contraction into account. On the assumption that the ideal helical wake was being created, Theodorsen used Goldstein’s circulation results to establish relationships between the power (or thrust) of the propeller and the far wake parameters. By considering the efficiency of a blade element, the ratio of the induced velocity in the wake to that at the propeller could be found and the slipstream contraction could also be calculated. Thus, with the helix angle and diameter of the final wake known, the corresponding values of the induced velocity and helix angle at the blade could be found. From Goldstein’s results the ideal circulation and, hence, the required blade geometry could then be calculated. Actually, Theodorsen’s method works in the reverse sense to that of Goldstein–Lock, as he begins with the final wake and calculates the (ideal) propeller which generates it.

Later, in 1969, Theodorsen¹⁸ extended his method to the analysis of static propellers and hovering rotors. The full theory is given in his paper and the book previously referred to, but the results for hovering flight are interesting and are given in the

figures below. In these figures the common parameter is Λ_0 , the tangent of the wake helix angle, defined by

$$\Lambda_0 = w/\Omega R_0$$

where w is the velocity of the far wake and R_0 is its radius. With $C_T (= st_c)$ assumed known for the rotor, Λ_0 can be read off from Fig 2.25. Then, from Figs 2.26 and 2.27 we can find the contraction ratio η and v , the ratio of the final wake velocity to that at the rotor. Since for most helicopters C_T is not likely to exceed 0.01, it can be seen that η will vary only between about 0.816 and 0.835 and v from about 1.5 to 1.65. The theory depends on the assumption that the ideal wake exists; as we noted in section 2.1, however, these values may be different for the non-uniform wakes likely to occur in practice.

In his 1969 paper, Theodorsen does not explain how his results for hovering flight were to be used, but it is reasonable to assume that they would be applied in the same way as for the conventional propeller described in his book. Theodorsen's consideration of the wake contraction is not complete, however. The implication of his method is that, although the local wake helix angle and induced velocity are correctly estimated, the wake at the propeller is still assumed to be cylindrical since the theory makes use

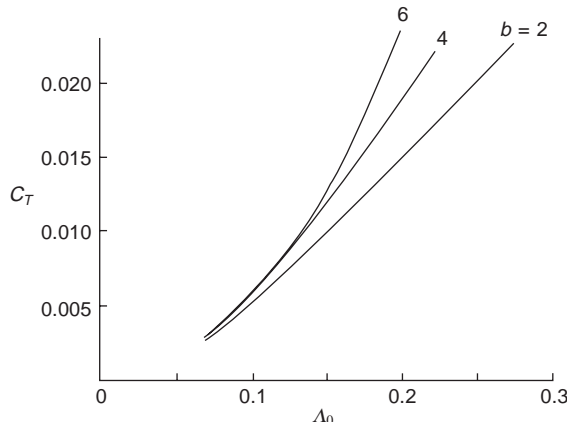


Fig. 2.25 Thrust coefficient as a function of wake helix angle (i.e. velocity)

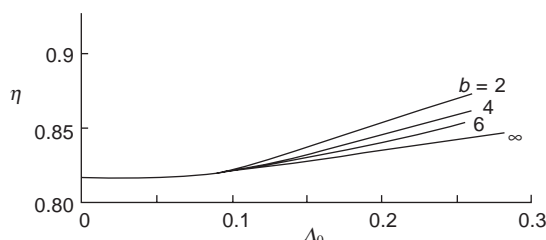


Fig. 2.26 Contraction ratio as a function of wake velocity

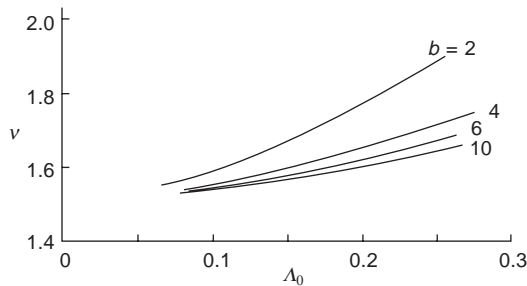


Fig. 2.27 Induced velocity ratio as a function of wake velocity

of Goldstein's results, Fig. 2.28. This is probably quite justified for the conventional propeller, since not only does the contraction amount to only a few per cent at most but also the high axial velocity means that the contraction is complete only at a considerable distance from the disc. For the hovering rotor, however, it is known that the contraction is usually complete within a rotor diameter, and the curved part of the contracting wake lies close enough to the blades to have a considerable influence on the incidence near the tips, Fig. 2.29.

Unfortunately, although the amount of contraction, as we have just seen, can be obtained quite easily, the calculation of the *rate* of contraction in the neighbourhood of the rotor is very complicated and certainly cannot be found in closed form as with Theodorsen's other results. To obtain reliable information we need to make use of experimental data, to be combined, if possible, with theory. These methods are described in a later section.

2.10.4 The prescribed wake

The Goldstein-Lock theory assumes that the wake is a uniform or rigid helix. In hovering and vertical flight of low axial velocity, the flow through the rotor is dominated by the induced velocity which, as we have seen, is not generally uniform over the rotor and in the wake. The vortex elements springing from the blade are

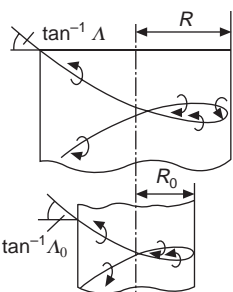


Fig. 2.28 Wake parameters in Theodorsen's calculations (propeller theory)

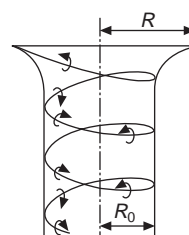


Fig. 2.29 Wake contraction for a hovering rotor

therefore transported downwards at different rates, rather than at a constant rate, as assumed by the rigid wake model.

The reduction in bound circulation about the blade towards the tip as shown in Fig. 2.23, which is quite rapid for the lower inflow angles, implies a concentration of trailed vorticity here, that quickly rolls up to form a concentrated vortex emanating from near the tip. Typically, the bound circulation also reduces inboard, but at a lesser rate²⁰ (in radial terms) and this leads to a trailing vortex sheet of opposite sign to that of the tip vortex. The wake model shown in Fig. 2.30 consisting of an assembly of discrete vortex elements can be considered to form a suitable representation, which may be used to evaluate the induced velocity.

An initial calculation of the vertical induced velocity is made using momentum theory. The vertical displacements of the vortex elements are then calculated, consistent with the assumed induced velocity, and the pattern of the vortex wake is therefore defined. Then, by applying the Biot–Savart law to the individual elements, the induced velocity at the rotor disc can be calculated by summing the contributions of all the elements.

Langrebe¹⁹ has made such calculations and compared them with those obtained from the simple momentum theory, Fig. 2.31. It can be seen that the difference

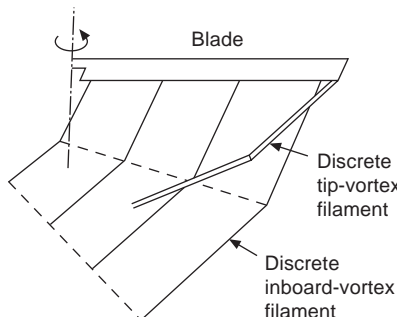


Fig. 2.30 Vortex wake representation (after Landgrebe)

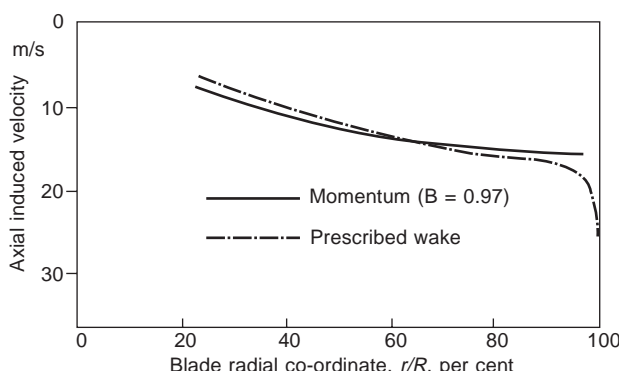


Fig. 2.31 Comparison of induced velocity by momentum and prescribed wake methods

between the methods is quite small, in spite of the fact that the uniform helical wake assumes quite a different loading distribution from those occurring in practice. The indications are that Lock's assumption, which is that Goldstein's results for a uniform helix can still be applied when the blade loading is not ideal, gives quite accurate results.

The wake geometries of the theoretical methods described so far fail to take into account completely the contraction of the wake and other distortions of the wake when the blade loading does not conform to the ideal distribution. In the mid-1950s, Gray^{21,22}, from the results of smoke studies, concluded that the wake from a blade consisted of strong tip vortex and an inner vortex sheet of opposite sense. This arrangement is shown diagrammatically in Fig. 2.32.

It was observed that the outer part of the sheet moves faster than the inner part, with the result that the sheet becomes more and more inclined to the rotor plane, and that the outer part of the sheet moves faster than the tip vortex.

Landgrebe's¹⁹ later series of smoke tests confirmed Gray's results and also confirmed that cross-sections of the tip vortices do not necessarily occur at the ends of the corresponding sheet. It was also observed that the tip vortex from a blade moves downwards relatively slowly until it passes beneath the following blade, from which point it moves down more rapidly.

These results were confirmed by the experiments of Tangler *et al.*²³, who investigated the wake pattern by methods of flow visualisation and hot-wire anemometry. These tests indicated very clearly the movement of the tip vortices and the way in which they eventually interact and diffuse after maximum wake contraction has occurred. The ultimate wake appears to be unstable and moves downstream in a confused manner. The instability of a helicopter wake was implied by the results of Levy and Forsdyke²⁴, who investigated the motion of a helical vortex. They showed that the

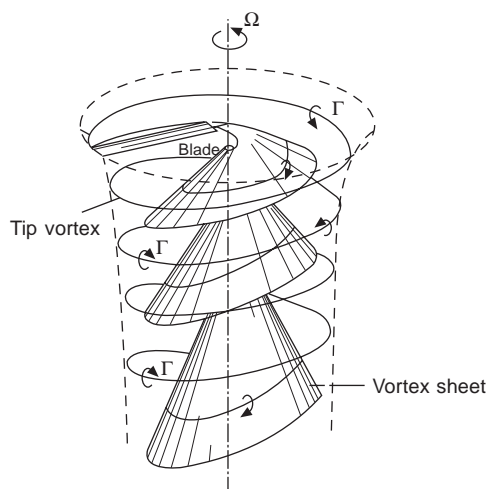


Fig. 2.32 Landgrebe's calculation of wake velocity in hovering flight

vortex would be stable only if the tangent of the helix pitch angle were greater than 0.3; in general this is not satisfied by a hovering helicopter rotor.

The axial and radial co-ordinates normalised on R of the tip vortex, derived from Landgrebe's results for a particular case, are shown in Fig. 2.33 and for two radial positions of the inner sheet in Fig. 2.34. The change of downward velocity of the tip velocity just referred to is seen in Fig. 2.33 as a sudden change of slope of the axial displacement.

Landgrebe reduced these results to formulae giving the radial and axial co-ordinates of a tip vortex in terms of the azimuth angle, and corresponding results for the inner sheets. For example, the axial displacement of the tip vortex is given by

$$\begin{aligned}\bar{z}_T &= k_1 \psi_w, \quad \text{for } 0 \leq \psi_w \leq 2\pi/b \\ &= (\bar{z}_T)_{\psi_w = 2\pi/b} + k_2(\psi_w - 2\pi/b), \quad \text{for } \psi_w > 2\pi/b\end{aligned}$$

where ψ_w is the wake azimuth angle relative to the blade,

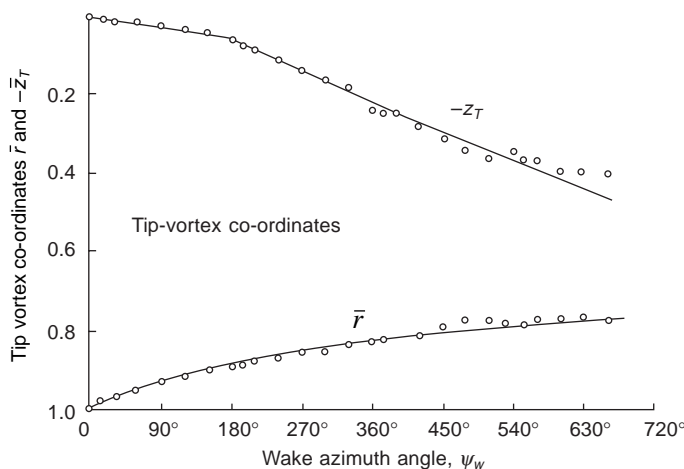


Fig. 2.33 Tip vortex co-ordinates as a function of wake azimuth angle

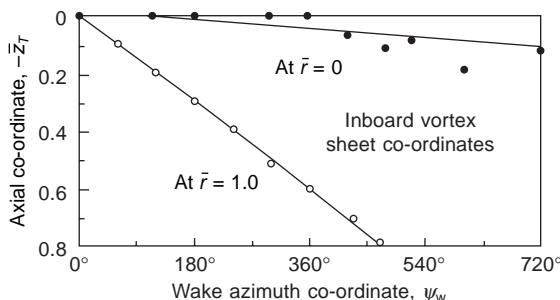


Fig. 2.34 Inboard vortex sheet co-ordinates (after Landgrebe)

$$k_1 = -0.25(t_c + 0.001\theta_1),$$

and

$$k_2 = -(1 + 0.01\theta_1)\sqrt{C_T},$$

where θ_1 is the blade twist in degrees, and $C_T = st_c$ in which s is the solidity.

The formula for the radial co-ordinate of the tip vortex is

$$\bar{r} = 0.78 + 0.22 e^{-\bar{\Lambda}\psi_w}$$

$$\text{where } \bar{\Lambda} = 0.145 + 27C_T$$

The two formulae define the boundary of the wake, at least for the part near the rotor which remains stable, and form the basis for an experimentally prescribed wake. It is interesting to note that Landgrebe's results indicate a final slipstream contraction ratio of 0.78, which is closer to the value of 0.816 predicted by Theodorsen's ideal wake theory than to the 0.707 of the classical momentum theory.

These experiments show how rapidly the wake contracts under the rotor. Using the results given in Fig. 2.33 we can draw the wake boundary for that case, as shown below in Fig. 2.35. It can be seen that the contraction is practically complete within only about half a rotor radius, most of it occurring within a distance of 20 per cent of the radius.

The importance of these figures is that they show that the vortices at the boundary of the slipstream are displaced well inboard of the blade tip while still close to the rotor. This means that the inwardly displaced vortices induce an *upwash* in the tip region instead of the strong downwash which would occur if the wake contraction were small or occurred relatively slowly as with the conventional propeller.

Landgrebe calculated the blade incidence distribution using the wake geometry deduced from the smoke tests and found that the upwash results in a sharp rise of incidence just inboard of the tip, Fig. 2.36. Because of the high Mach numbers occurring at the tip, even in hovering flight, locally high incidences are very undesirable, since they may lead to shock stall with corresponding loss of lift and increase of drag. Further, the locally high tip incidence increases the spanwise loading gradient and intensifies the already strong tip vortex.

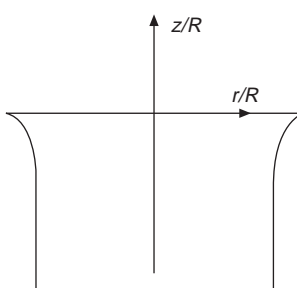


Fig. 2.35 Contraction of rotor wake using Fig. 2.33 results

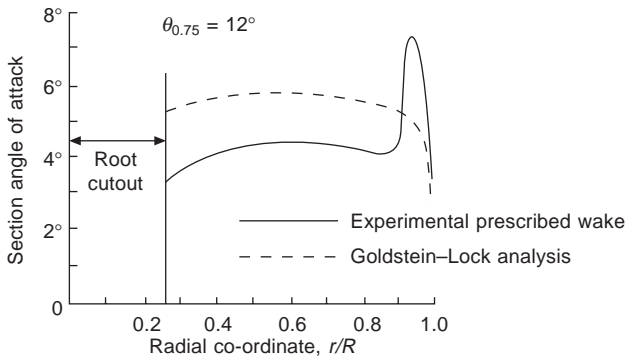


Fig. 2.36 Effect of experimental prescribed wake (Landgrebe) on incidence distribution

2.10.5 Free wake analysis

Amongst the earliest work on free wakes in the hover is that of Clark and Leiper.²⁵ An initial wake geometry was assumed which is based on the mean induced velocity calculated from the simple momentum theory. The wake is broken into a number of straight vortex filaments whose strengths are determined by the bound circulation distribution. Using the Biot–Savart law, the induced velocity components due to these filaments are then computed and the initially assumed velocity field is modified accordingly. The positions of the vortex elements, which ‘float’ with the fluid, are modified in turn to conform with the velocity field. The induced velocity at the blade and the bound-circulation distribution are also recalculated. The process is allowed to iterate until satisfactory convergence has been achieved, indicating that the wake geometry is consistent with the velocity field it induced. The calculations were considerably simplified by defining a ‘far wake’ as that part of the wake beyond a distance corresponding to two rotor revolutions and representing this far wake by a stack of stepped vortex rings approximating to a helix whose spacing is determined by the number of blades and mean local induced velocity.

The calculations of Clark and Leiper clearly identified the wake features found experimentally by Landgrebe¹⁹, namely, that the outer trailing vortices roll up quickly to form a strong tip vortex, while the inner vortices move downwards as a vortex sheet which becomes progressively more inclined to the rotor plane. Their model also showed that the initial position of the tip vortex depends strongly on the number of blades; if the number of blades is high, the tip vortex remains roughly in the plane of the rotor until it becomes close to the succeeding blade, when it is convected downwards. As stated before, this feature had been noted by Landgrebe and is indicated by the change of slope of \bar{Z}_T in Fig. 2.33.

The later model of Favier *et al.*²⁶ was similar to that of Clark and Leiper in that a rigid far wake was assumed (semi-infinite circular vortex cylinder beyond $\psi = 10\pi/b$, and a constant pitch helix between $\psi = 5\pi/b$ and $10\pi/b$). A free wake was assumed from the blade to $\psi = 2\pi/b$ and a prescribed wake based on Landgrebe¹⁹ from here to the start of the rigid wake. This confirmed the experimental observations previously mentioned.

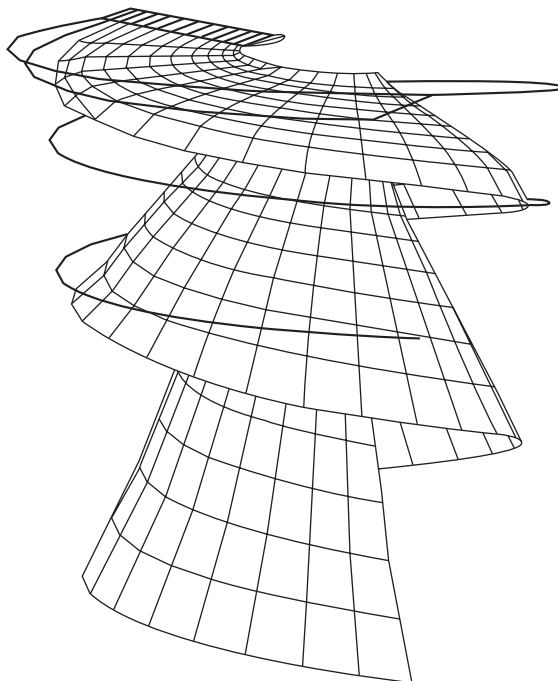


Fig. 2.37 Converged wake geometry for Caradonna and Tung²⁸ rotor (from Brown and Fiddes²⁷)

The free wake model of Brown and Fiddes²⁷ develops a three turn free wake from a constant pitch helical wake using a relaxation process, with the influence of the far wake being accounted for. An interesting feature is the merging of adjacent vortices according to a criterion in order to prevent mutual orbiting. The method was validated against the experimental results of Carradonna and Tung²⁸ on a constant chord, untwisted, two-bladed rotor. The converged wake geometry is shown in Fig. 2.37. In this case, a panel method was used on the blade itself, rather than a lifting line or single bound vortex.

References

1. Houghton, E. L. and Carpenter P. W., *Aerodynamics for engineering students*, London, Edward Arnold, 1993.
2. Durand, W. F. (ed.), *Aerodynamic theory*, vol. IV, section L, New York, Dover Publications, 1963.
3. Betz, A., *Schraubenpropellers mit geringstem Energieverlust*, Gottinger Nachrichten, 1919, p. 193.
4. Goldstein, S., 'On the vortex theory of screw propellers', *Proc. Roy. Soc.*, **123**, 1929.
5. Theodorsen, T., *Theory of propellers*, New York, McGraw-Hill, 1948.
6. Bramwell, A. R. S., 'A note on the static pressure in the wake of a hovering rotor', *Res. Memo. City Univ. Lond. Aero.* 73/3, 1973.

76 Bramwell's Helicopter Dynamics

7. Brotherhood, P., 'Flow through a helicopter rotor in vertical descent', *Aeronautical Research Council R&M 2735*, 1949.
8. Brotherhood, P., 'Flight measurements of the stability and control of a Westland "Whirlwind" helicopter in vertical descent', *RAE TR 68021*, 1968.
9. Goorjian, P. M., 'An invalid equation in the general momentum theory of the actuator disc', *AIAAJ*, **10**(4) 1972.
10. Bramwell, A. R. S., 'Some remarks on the induced velocity field of a lifting rotor and on Glauert's formula', *Aeronautical Research Council CP 1301*, 1974.
11. Bailey, F. R., jnr, 'A simplified theoretical method of determining the characteristics of a lifting rotor in forward flight', *NACA Rep. 716*, 1941.
12. Gessow, A. and Myers, Garry C., jnr, *Aerodynamics of the helicopter*, New York, Ungar, 1952.
13. Knight, M. and Hefner, R. A., 'Analysis of ground effect on the lifting airscrew', *NACA TN 835*, 1941.
14. Zbrozek, J. K., 'Ground effect on the lifting rotor', *Aeronautical Research Council R&M 2347*, 1947.
15. Prandtl, L., Appendix to Betz, A., *ibid*.
16. Lock, C. N. H., 'The application of Goldstein's theory to the practical design of airscrews', *Aeronautical Research Council R&M 1377*, 1931.
17. Durand, W. F., *ibid*, pp. 264, 265.
18. Theodorsen, T., 'Theory of static propellers and helicopter rotors', *Proc. 25th Annual National Forum American Helicopter Society 236*, 1969.
19. Landgrebe, A. J., 'Analytical and experimental investigation of helicopter rotor and hover performance and wake geometry characteristics', *USAAMRDL TR 71-24*, 1971.
20. Johnson, W., 'Airloads and wake models for a comprehensive helicopter analysis,' *Vertica*, **14**(3), pp. 255–300, 1990.
21. Gray, R. B., 'An aerodynamic analysis of a single-bladed rotor in hovering and low speed forward flight as determined from smoke studies of the vorticity distribution in the wake', *Princeton Univ. Aeronaut. Eng. Rep. 356*, 1956.
22. Gray, R. B., 'Vortex modeling for rotor aerodynamics – the Alexander A. Nikolsky Lecture', *J. Amer. Helicopter Soc.*, **37**(1), 1992.
23. Tangler, James L., Wohlfield, Robert M. and Miley, Stan J., 'An experimental investigation of vortex stability, tip shapes, compressibility and noise for hovering model rotors', *NASA Contractor Rep. NASA CR - 2305*, 1973.
24. Levy, M. A. and Forsdyke, A. C., 'The steady motion and stability of a helical vortex', *Proc. Roy. Soc. Series A*, vol. 120, 1928.
25. Clark, D. R. and Leiper, A. C., 'The free wake analysis – a method for the prediction of helicopter hovering performance', *J. Amer. Helicopter Soc.*, **15**(1), pp. 3–11, Jan. 1970.
26. Favier, D., Nsi Mba, M., Barbi, C. and Maresca, C., 'A free wake analysis for hovering rotors and advancing propellers', *Vertica*, **11**(3), pp. 493–511, 1987.
27. Brown, K. D. and Fiddes, S. P., 'New developments in rotor wake methodology', Paper No. 14, *22nd European Rotorcraft Forum*, 17–19 Sept. 1996, Brighton, U.K.
28. Carradonna, F. X. and Tung, C., 'Experimental and analytical studies of a model helicopter rotor in hover', *Vertica*, **5**, pp. 149–161, 1981.

Rotor aerodynamics and dynamics in forward flight

3.1 Introduction

In this chapter we examine firstly the aerodynamics of the rotor in forward flight and then the dynamics. In order to be able to determine blade lift, drag and flapping moment, and, ultimately, rotor performance, it is necessary, as with axial flight, to determine the induced velocity in forward flight. Fortunately, for many important problems a detailed description of the induced velocity distribution is not necessary, and much useful work can be done by treating the rotor as a lifting surface with an infinite number of blades. The dynamics of the blades and rotor are equally susceptible to simple approaches based on straightforward ideas of induced velocity, aerofoil characteristics and blade modelling. The effects of blade flexibility and more comprehensive induced velocity distributions are dealt with in later chapters, as is a discussion of the peculiarities of blade-section characteristics undergoing continually changing conditions.

3.2 Induced velocity in forward flight

The first proposal for calculating the induced velocity for a rotor carrying a given thrust was due to Glauert¹. He regarded the rotor as an elliptically loaded circular wing to which lifting-line wing theory could be applied, and proposed that a mean induced velocity v_{i0} could be obtained from the formula

$$v_{i0} = T/2\rho AV' \quad (3.1)$$

where, if V is the relative velocity far upstream of the rotor, the total velocity at the rotor $V' = \sqrt{V^2 \cos^2 \alpha_D + (V \sin \alpha_D - v_{i0})^2}$, A is the rotor area, and α_D is the rotor disc incidence.

Although a general proof of this formula has never been given, its validity was

justified on the grounds that in hovering flight it reduces to the momentum formula, eqn 2.12, while in forward flight, when $V' \approx V$, it assumes the same form as for the induced velocity of an elliptically loaded wing. The formula appears to be true, however, for all loading distributions in the 'high-speed case'².

Glauert's eqn 3.1 can be interpreted by imagining a circular jet of air of velocity V having the same diameter as the rotor, flowing past and around the rotor and being deflected downwards so that far downstream it has an induced velocity component normal to the rotor disc of $2v_{i0}$, Fig. 3.1. This interpretation, and the fact that eqn 3.1 reduces to the 'momentum' formula of hovering flight, may lead one to think that the formula is obvious from momentum considerations: it should be appreciated, however, that the flow depicted in Fig. 3.1 is quite fictitious and that eqn 3.1 is far from obvious. More will be said about this point later in section 3.5.

Equation 3.1 can be expressed as a unique curve if, as in Chapter 2, we define $v_0 = \sqrt{(T/2\rho A)}$ as the 'thrust velocity'. Then, for $\alpha_D = 0$ and if

$$\bar{v}_{i0} = v_{i0}/v_0 \text{ and } \bar{V} = V/v_0$$

eqn 3.1 can be written

$$\bar{v}_{i0}^4 + \bar{V}^2 \bar{v}_{i0}^2 - 1 = 0 \quad (3.2)$$

This equation is shown plotted in Fig. 3.2.

The dotted line shows the relations $\bar{v}_{i0} = 1/\bar{V}$, which for $\bar{V} > 1$ lies extremely close to the true result. This implies that, for forward speeds greater than about 10 m/s, the induced velocity is much smaller than the forward speed and is equivalent to an approximation to eqn 3.1 in the form

$$v_{i0} = T/2\rho AV \quad (3.3)$$

Although eqn 3.1 provides a very simple and useful formula for the estimation of the mean induced velocity, it was appreciated by Glauert that the induced velocity over the rotor is far from uniform. From aerofoil and wing theory one would expect

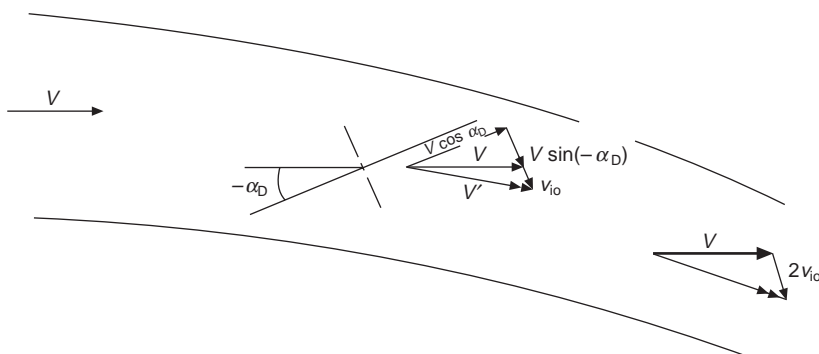


Fig. 3.1 Flow interpretation of Glauert's formula (showing disc incidence α_D as negative for normal helicopter flight case)

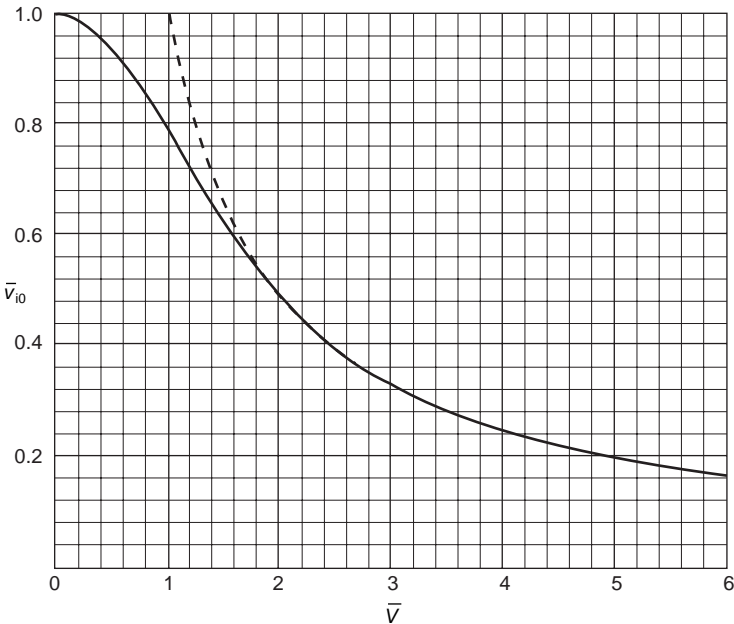


Fig. 3.2 Non-dimensional induced velocity as a function of forward speed

an upwash at the leading edge of the rotor and an increase of induced velocity towards the trailing edge. Accordingly, Glauert proposed a second formula:

$$v_i = v_{i0}(1 + Kx \cos \psi) \quad (3.4)$$

where v_i is the general induced velocity and v_{i0} is the induced velocity at the rotor centre (and also the mean induced velocity), taken as the value given by eqn 3.1, $x = r/R$, and K is a factor chosen to be slightly greater than unity. A typical value taken for K is 1.2, so that on the longitudinal axis ($\psi = 0$ or π) there is an upwash at the leading edge and a linear increase of induced velocity towards the trailing edge; in fact, the value of K denotes the slope of the induced velocity distribution along the longitudinal axis.

An attempt to calculate the longitudinal induced velocity distribution and to find a theoretical value of K was made by Coleman, Feingold, and Stempin. Their analysis was based on the fact that a rotor carrying a uniform load and moving through the air at an angle to its plane leaves behind a vortex wake in the form of an elliptical cylindrical shell, Fig. 3.3.

This cylindrical shell can be regarded as a continuous distribution of vortex rings whose planes are parallel to the rotor plane and whose 'strength' is determined by the magnitude of the load and the forward speed of the rotor. By applying the Biot-Savart law to the cylindrical wake, the induced velocity could be obtained in the form of a double integral. The integral could not be evaluated at a general point of the rotor disc, but an exact expression was obtained for points on the longitudinal axis. However, even this result was quite complicated and expressible only in the form of elliptical

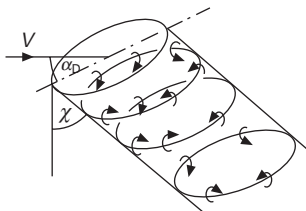


Fig. 3.3 Vortex ring representation of rotor wake in forward flight

integrals. A number of longitudinal distributions depending on the wake angle χ are shown in Fig. 3.4. It can be seen that the induced velocity distribution is not exactly linear but can be taken as approximately so over most of the rotor diameter. The slope of the ratio v_i/v_{i0} at the rotor centre was found from the analysis to be $\tan(\chi/2)$, so that Glauert's formula, eqn 3.4, could be written as

$$v_i = v_{i0}(1 + x \tan(\chi/2) \cos \psi) \quad (3.5)$$

Since $\chi \leq 90^\circ$, this approximation to the slope fails to give the required upwash at the leading edge of the rotor, although giving some dependence on the wake angle.

Another result obtained by Coleman *et al.* is that, since the vortex rings composing the wake lie at an angle to the wake axis, there will be a component of induced velocity causing the wake to move downwards normal to its axis and that, in the ultimate wake, this component of wake velocity is $2v_{i0} \tan(\chi/2)$. Also, if the disc incidence is α_D , the above result leads to the following relationship between the mean induced velocity and the ultimate wake angle

$$v_{i0}/V = \cos(\chi + \alpha_D)/2 \tan(\chi/2) \quad (3.6)$$

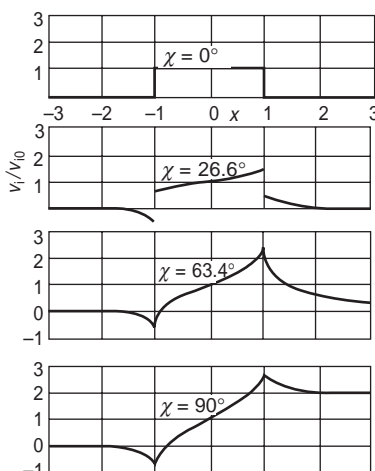


Fig. 3.4 Longitudinal induced velocity distribution for uniformly loaded rotor

3.3 The method of Mangler and Squire

One of the more complete induced velocity calculations in which the rotor is treated as a lifting surface with a pressure jump is that of Mangler and Squire.⁴ They considered a rotor loading distribution which closely resembled that of a typical rotor and succeeded in obtaining an exact solution for the induced velocity for any point on the rotor. Their method was quite different from Coleman's and it will be instructive to discuss it in some detail.

If the induced velocity field is regarded as a small perturbation superimposed upon an otherwise uniform velocity field, and if the x axis is taken along the direction of the uniform velocity V , Euler's equations of motion for an elemental volume of fluid (e.g. Ref. 1, Chapter 2, p. 150) can be linearised to read

$$V\partial u/\partial x = - (1/\rho) \partial p/\partial x \quad (3.7)$$

$$V\partial v/\partial x = - (1/\rho) \partial p/\partial y \quad (3.8)$$

$$V\partial w/\partial x = - (1/\rho) \partial p/\partial z \quad (3.9)$$

Differentiating eqns 3.7 to 3.9 with respect to x , y , z respectively and then adding gives

$$V \frac{\partial}{\partial x} \left(\frac{\partial u}{\partial x} + \frac{\partial v}{\partial y} + \frac{\partial w}{\partial z} \right) = - \frac{1}{\rho} \left(\frac{\partial^2 p}{\partial x^2} + \frac{\partial^2 p}{\partial y^2} + \frac{\partial^2 p}{\partial z^2} \right)$$

But, by continuity,

$$\partial u/\partial x + \partial v/\partial y + \partial w/\partial z = 0$$

so that

$$\frac{\partial^2 p}{\partial x^2} + \frac{\partial^2 p}{\partial y^2} + \frac{\partial^2 p}{\partial z^2} = 0 \quad (3.10)$$

Hence, we have the rather interesting result that for small disturbances the pressure field satisfies Laplace's equation. The first part of the problem, then, is to find a solution of Laplace's equation which also satisfies the given pressure discontinuity across the rotor disc. Secondly, having obtained such a solution for p , any one of the induced velocity components can be calculated by integrating the appropriate one of eqns 3.7 to 3.9. Thus, if the disturbance far in front of the rotor is assumed to be zero, the velocity component w normal to the flight direction is given by

$$w = -(1/\rho V) \int_{\infty}^x (\partial p/\partial z) dx \quad (3.11)$$

where x corresponds to the chosen point P in the field. The integration, in this case, is performed with the values of y and z appropriate to the path of integration; e.g. if the path of integration were in the plane of the rotor, z would be zero and y would be constant and have the value corresponding to the field point P.

The other two velocity components, u and v , would be obtained by similar integrations.

Although the method has been illustrated here by the use of Cartesian co-ordinates for the sake of simplicity, Mangler and Squire used elliptical co-ordinates since they allowed the boundary conditions to be satisfied more easily and because these functions give the necessary discontinuity across the disc. In boundary problems of this kind, the solution appears as a multiply infinite series; in this case the solution for the pressure at the rotor disc appears as an infinite series of pressure mode 'shapes' which have to be chosen to match some prescribed pressure distribution corresponding to the rotor loading. It was found that the first two pressure shapes at the disc plane were given by

$$(p_l - p_u)_1 = \frac{3}{4}\rho V^2 C_T \sqrt{1-x^2}$$

$$(p_l - p_u)_2 = -\frac{1}{2}\rho V^2 C_T (1 - 5x^2/2) \sqrt{1-x^2}$$

and a particular linear combination gives

$$(p_l - p_u)/\rho V^2 C_T = 15x^2 \sqrt{1-x^2}/8 \quad (3.12)$$

This distribution is shown in Fig. 3.5 and is such that the load vanishes at the edge and the middle of the rotor, thereby representing a typical rotor loading very well. It was indeed fortunate that a reasonable loading shape could be obtained by using only the first two pressure functions as, even with these, the calculations of the induced velocity were very lengthy. Examples of the results of the calculations are shown in Figs 3.6 and 3.7. It can be seen that the longitudinal variation of induced velocity is far from being linear and that there is actually an upwash over a small portion of the rear half of the rotor as well as at the leading edge. It can also be seen that the downwash is very strong near the outer edges of the rear half of the rotor, reaching values three or four times greater than the mean. The downwash distribution is symmetric about the longitudinal axis.

Mangler and Squire also succeeded in expressing their results in the form of a Fourier series, i.e. as

$$v_i = 4v_{i0} \left[\frac{1}{2}c_0 - \sum_{n=1}^{\infty} c_n(\eta, \alpha_D) \cos n\psi \right] \quad (3.13)$$

where

$$c_0 = 15\eta(1-\eta^2)/8 \quad (3.14)$$

and for $n \geq 2$, and even,

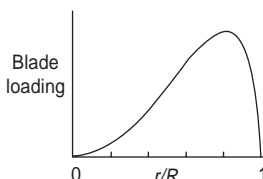


Fig. 3.5 Rotor loading assumed by Mangler

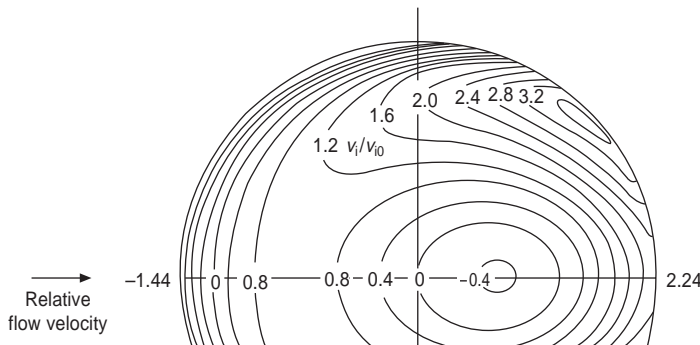


Fig. 3.6 Induced velocity distribution according to Mangler's theory, $\alpha_D = 15^\circ$

$$c_n = (-1)^{(n-2)/2} \frac{15}{8} \left[\frac{\eta + n}{n^2 - 1} \cdot \frac{9\eta^2 + n^2 - 6}{n^2 - 9} + \frac{3\eta}{n^2 - 9} \right] \\ \times \left(\frac{1 - \eta}{1 + \eta} \right)^{n/2} \left(\frac{1 - \sin \alpha_D}{1 + \sin \alpha_D} \right)^{n/2} \quad (3.15)$$

and $c_1 = -\frac{15\pi}{256} (5 - 9\eta^2)(1 - \eta^2)^{1/2} \left(\frac{1 - \sin \alpha_D}{1 + \sin \alpha_D} \right)^{1/2}$

$$c_3 = \frac{45\pi}{256} (1 - \eta^2)^{3/2} \left(\frac{1 - \sin \alpha_D}{1 + \sin \alpha_D} \right)^{3/2}$$

where $\eta^2 = 1 - x^2$.

For odd values of $n \geq 5$, $c_n = 0$. The use of the mean induced velocity in eqn 3.13 (as given by eqn 3.3) should not be taken to imply that eqn 3.13 may be used at the hover or for slow speeds, since the Mangler and Squire theory assumed that $v_i \ll V$.

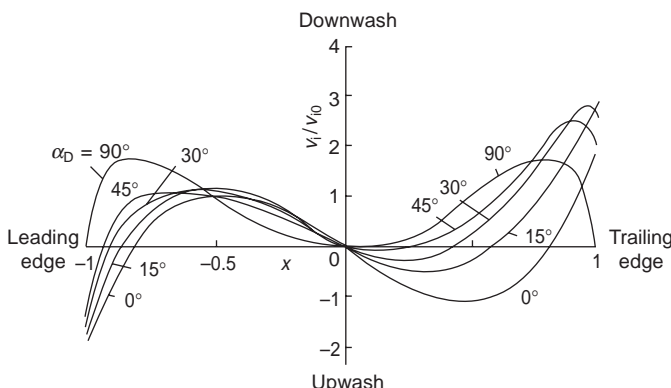


Fig. 3.7 Longitudinal induced velocity distribution according to Mangler's theory

3.4 Flight and wind tunnel tests

A series of pioneering attempts to measure the induced velocity in forward flight was made in 1948 by the UK Royal Aircraft Establishment⁵ (now part of DERA, the Defence Evaluation and Research Agency). Smoke generators were suspended from a slow flying fixed-wing aircraft in front of the helicopter, a Sikorsky Hoverfly, and



Fig. 3.8 Flow pattern as revealed by smoke filaments in forward flight. Speed 53 mph. Plane of smoke filaments $0.4R$ to starboard

were arranged to emit a band of smoke filaments which lay in a vertical plane. Figure 3.8 shows a typical example photograph taken by a third aircraft flying in formation with the other two. Tests were conducted at a number of different speeds, and with the plane of the filaments intersecting the rotor at various radii between $0.25R$ and $0.4R$ on the advancing side.

The smoke filaments gave a broad picture of the flow through the rotor but were not really distinct enough to show the velocity distribution in detail. Figure 3.9 shows the induced velocity distribution along the longitudinal axis as deduced from the deflection of the smoke filaments. The results would appear to indicate that the distribution is roughly linear, but it is also clear from the photographs that the filaments become too diffused to show the details predicted by Mangler and Squire's theory. The photograph clearly shows, however, an interesting phenomenon: the series of 'whorls' appearing behind the tailrotor are the cross-sections of the trailing vortices shed by the individual rotor blades cut by the plane of the smoke filaments.

A comprehensive and more easily controlled series of tests was conducted in a wind tunnel by Heyson and Katzoff⁶. The method used was to place a grid of wool tufts in a number of positions in the vicinity of the rotor and to record the tuft deflections. An analysis of the deflections gave the induced-velocity field and it was found that the theoretical distribution of Mangler and Squire was largely confirmed. Heyson and Katzoff also made numerical calculations of the induced velocity field by using the same basic uniform loading model as Coleman *et al.* but superimposing them linearly to obtain symmetrical loadings having arbitrary radial distributions. Examples of the induced velocity distributions along the longitudinal axis found by

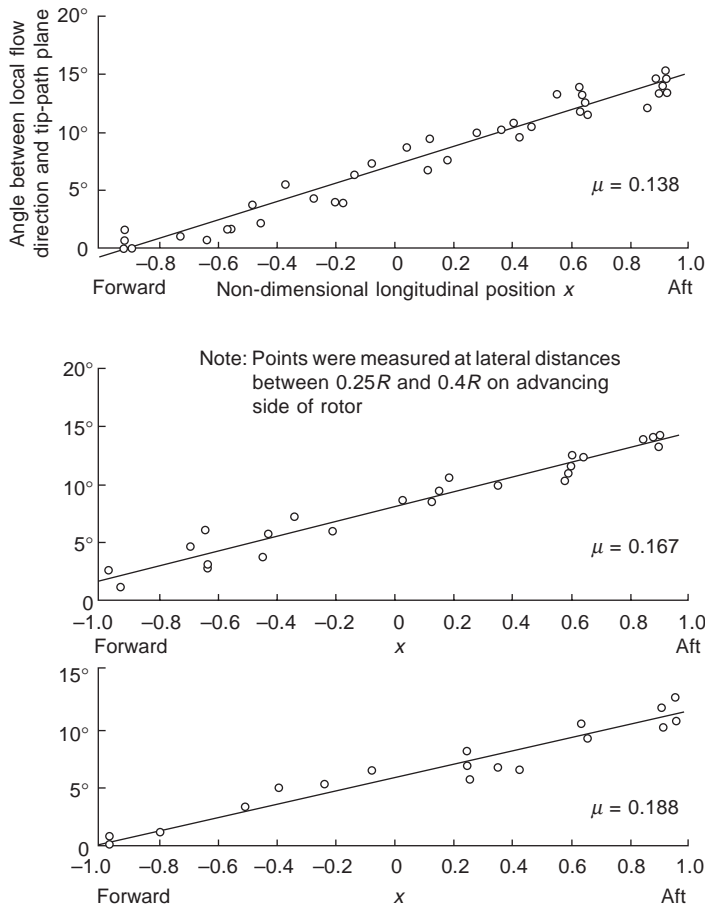


Fig. 3.9 Longitudinal induced velocity distribution obtained from smoke photographs

Heyson and Katzoff and compared with that of Mangler and Squire are shown in Fig. 3.10.

Heyson and Katzoff also investigated the velocity field behind the rotor and found it to be remarkably similar to that of a circular wing, showing two distinct trailing vortices. An example of the tuft pattern at a distance of about one diameter behind the rotor, as seen by an observer looking forward through the grid, is shown in Fig. 3.11.

Katzoff has obtained some useful symmetry relationships between the induced velocity components for a uniform load. By superimposing a skew-symmetric wake on the original one, Fig. 3.12, a two-dimensional elliptic wake is created by means of which the following relationships can be deduced.

- If P and Q are two points within the rotor disc and symmetrically located on either side of the lateral axis, the sum of the induced velocity components w_P and w_Q , normal to the rotor plane, is equal to the normal component of the induced velocity within the wake. Since this is constant, it follows that $w_P + w_Q$ is

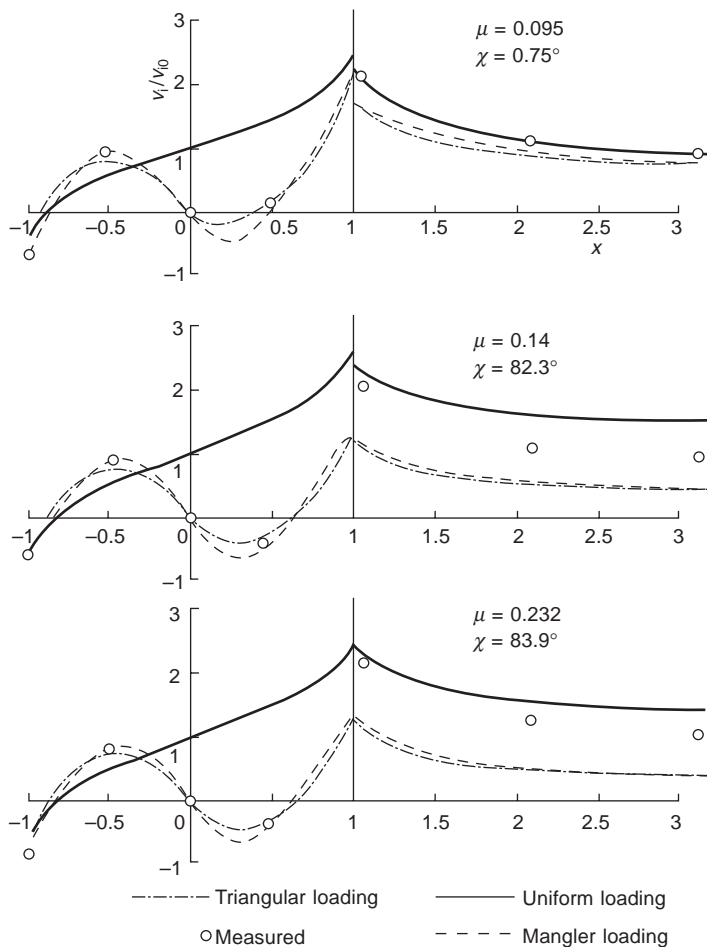


Fig. 3.10 Longitudinal induced velocity distribution obtained from wind tunnel tests for different values of μ

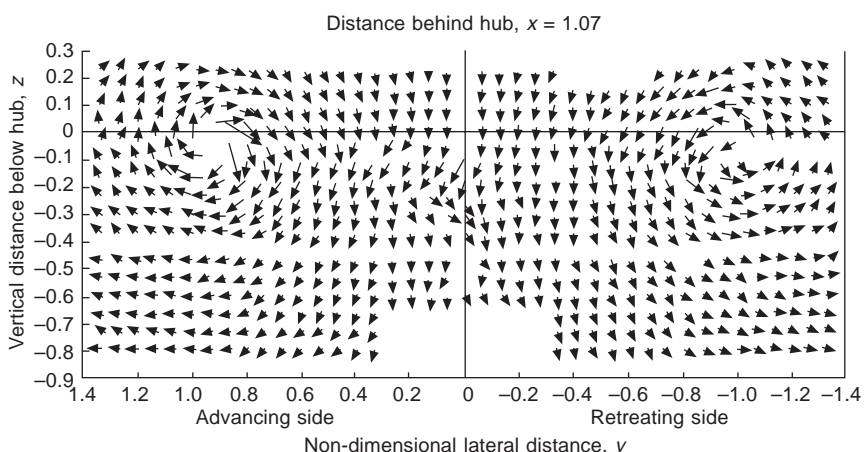


Fig. 3.11 Vortex pattern behind rotor

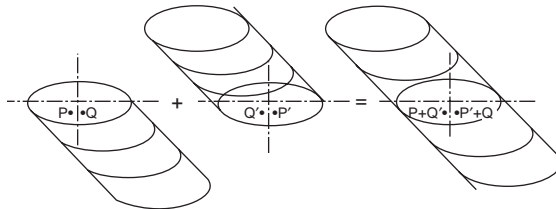


Fig. 3.12 Symmetry relations for induced velocity in forward flight

constant everywhere over the disc and, therefore, that the induced velocity distribution at the rotor is skew-symmetric with respect to the lateral axis.

- (ii) If P and Q are symmetrically located about the lateral axis but lie outside the disc, we have

$$w_P + w_Q = v' \sin \chi$$

where v' is the longitudinal component of velocity in the ellipse plane at the point corresponding to either P or Q, Fig. 3.13.

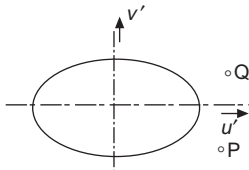


Fig. 3.13 Symmetry relations for induced velocity in forward flight

The components of velocity u' and v' about the elliptic wake arise from the self-induced motion of the wake itself through the surrounding air. If the velocity of the wake normal to its axis is U , we have seen that Coleman *et al.* have found U to be given by

$$U = 2v_{i0} \tan(\chi/2)$$

where v_{i0} is the induced velocity at the rotor centre (which is also the value along the lateral axis) and χ is the angle between the wake and the rotor plane. On the lateral axis, $w_P = w_Q = w$, say, and, by calculating the flow about the ellipse², we find that on the lateral axis outside the rotor

$$w = v_{i0} [1 - x(x^2 - \sin^2 \chi)^{-1/2}] \quad (3.16)$$

where $x = r/R$. This variation is shown in Fig. 3.14.

On the lateral axis, therefore, there is a strong upwash outside the rotor disc as opposed to the downwash on the inside. The upwash also exists forward of the lateral axis and for some distance behind it, but a downwash appears further to the rear at a point depending on the incidence of the rotor.

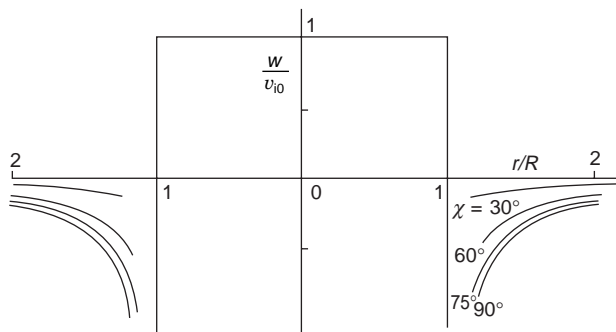


Fig. 3.14 Induced velocity near uniformly loaded rotor on the lateral axis

3.5 General remarks on the forward flight case

We have seen that the mean induced velocity in forward flight can be given by Glauert's formula

$$v_i = T/2\rho AV' \quad (3.1)$$

and that it can be expressed in a form which resembles the 'momentum' formula of climbing and hovering flight. Now, we assumed in Chapter 2 that this relationship could be expressed in the differential form

$$dT = 4\pi r \rho (V_c + v_i) v_i dr$$

and that from this expression the induced velocity for non-uniform loadings could be derived. However, the axial flight case, which includes the conventional propeller, is a special one for two reasons, namely,

- (i) the induced velocity is in the same direction as the general flow, and
- (ii) because of the symmetry of this, the flow is confined to well defined concentric shells for which the mass flow can easily be calculated.

Under these circumstances, momentum principles can be confidently applied and have been used already to obtain a number of results. But in forward flight neither of these two conditions applies. We have already seen that, in the linearised problem of the lifting rotor, the pressure field satisfies Laplace's equation. In particular, it can be shown² that for the uniformly loaded rotor the pressure at any point is proportional to the solid angle which the rotor disc subtends at that point. Further, the *acceleration* and pressure gradient fields, for the linearised case, both have precisely the same form as the velocity field of a vortex ring. Suppose, for simplicity, that the rotor is moving in its own plane and that we wish to find the component of induced velocity w normal to the rotor disc. As we have already seen, w can be calculated by the integral in eqn 3.11. The interpretation of this integral is that we are integrating the

component of pressure gradient normal to the rotor along a path in the plane of the disc. The shape of this pressure gradient component along the longitudinal axis of the rotor is shown in Fig. 3.15.

Starting from a point to the left of Fig. 3.15, and a great distance from the leading edge, we see that the pressure gradient is upward so that, if w is zero a long way in front of the rotor, integration results in a gradual increase of upwash as the rotor is approached. Just behind the leading edge the pressure gradient reverses and the upwash diminishes until a downwash develops at a point between the leading edge and the rotor centre, gradually increasing as the trailing edge is approached. Proceeding further to the right, the pressure gradient becomes positive again as the trailing edge is passed, gradually reducing the downwash until it becomes exactly twice that at the rotor centre.

What has just been described is the qualitative evaluation of the downwash corresponding to the case $\chi = 90^\circ$ calculated by Coleman *et al.* and presented in Fig. 3.4. In fact, the integration for this case can be performed analytically and gives simply

$$w = - \frac{\Delta p}{4\pi\rho V} [2\pi \mp 4xK(x)] \quad \begin{aligned} & 1 > x > 0 \\ & -1 < x < 0 \end{aligned}$$

$$w = - \frac{\Delta p}{4\pi\rho V} [2\pi \mp K(1/x)] \quad \begin{aligned} & 1 < x < \infty \\ & -1 > x > -\infty \end{aligned}$$

where Δp is the pressure step across the disc, x is normalised with respect to the rotor radius, and $K(x)$ is the complete elliptical integral of the first kind. This agrees with the more general result of Coleman *et al.*

It is clear that, unlike the axial case, the induced velocity at a particular point in forward flight depends not merely on the local loading but on the way in which the pressure gradient varies along the path of integration, which for the linearised analysis is determined only by the rotor-disc incidence. Of course, in any given flight condition,

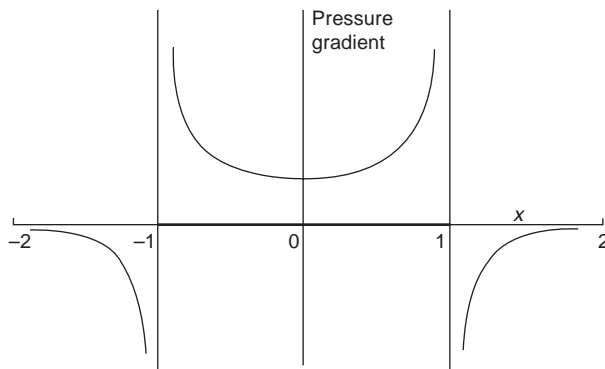


Fig. 3.15 Pressure gradient along longitudinal axis of uniformly loaded rotor

the rotor thrust must be accountable in terms of the momentum changes in the air, but care must be taken to ensure that all the forces acting on the air are properly taken into account when applying the principle.

3.6 Induced power in forward flight

We saw in Chapter 2 that for a uniformly loaded rotor carrying a thrust T the induced power is Tv_i , where v_i is the mean induced velocity. When the loading is non-uniform, the induced power is always higher than this ‘ideal’ value. In particular, for an axially symmetric loading the increase is about 13 per cent. A figure of about 15 per cent greater than the ‘ideal’ value is generally accepted to account for the non-uniformities of loading and induced velocity in both axial and forward flight.

We now inquire as to whether this factor for forward flight is valid when we note from Figs 3.6 and 3.7 the considerable distortion of the induced velocity field for these cases.

As in the axial case, to find the induced power we calculate the energy being supplied to the slipstream by the passage of a uniformly loaded rotor. In forward flight the energy of the slipstream consists of two distinct contributions:

- (i) the energy of the flow in the cylindrical wake (this is the only source of energy in the axial case);
- (ii) the energy imparted to the air outside the cylindrical wake due to the movement of the wake through it. (We saw earlier in this chapter that the wake moves normal to itself with velocity $2v_{i0} \tan(\chi/2)$.)

If E_1 and E_2 are the two contributions per unit length of wake, the power expended, P , is $V(E_1 + E_2)$, and this is the induced power. The mass flow through the wake at the rotor is $\rho\pi R^2 v_i \cos \chi$, since $\pi R^2 \cos \chi$ is the cross-sectional area of the wake. The absolute velocity of the air in the ultimate wake is $2v_i \sec^2(\chi/2)$, as discussed earlier, so that

$$E_1 = 2\rho v_i^2 \pi R^2 \cos \chi \sec^2(\chi/2)$$

By considering the kinetic energy of the air outside the elliptic wake, it can be shown² that

$$E_2 = 2\rho v_i^2 \pi R^2 \tan^2(\chi/2)$$

for which we find that

$$P = Tv_i$$

as in hovering and axial flight.

The extension of the above calculation to arbitrary loadings is much more difficult, even when the relationship between the loading and the induced velocity is known

completely, as in the work of Mangler and Squire referred to earlier. The case of the rotor in high speed flight ($\chi = 90^\circ$) carrying Mangler's loading can be calculated quite easily², however, and the result shows that the induced power is about 1.17 times greater than if the induced velocity were uniform.

One can also calculate the induced power by considering the in-plane component of the blade thrust vector which is tilted backwards by the induced velocity, as is considered in classical blade element theory, Chapter 2. If Δp is the axisymmetrical radial pressure distribution, the thrust carried on an annulus of width dr is

$$dT = 2\pi r \Delta p dr$$

and this thrust is shared by the b blades of the rotor. The elementary induced torque is

$$dQ_i = r dT v_i / \Omega r = (v_i / \Omega) dT$$

where v_i is the induced velocity at a given blade. The corresponding induced power is

$$\begin{aligned} dP_i &= \Omega dQ_i = v_i dT \\ &= 2\pi r \Delta p v_i dr \end{aligned}$$

From Mangler and Squire's work, and also the work of Coleman *et al.*, for axisymmetrical pressure loadings the induced velocity can be expressed as

$$v_i = 4v_{i0} \left[\frac{1}{2}c_0 - \sum_{n=1}^{\infty} c_n \cos n\psi \right]$$

as in eqn 3.13 and where $2v_{i0}c_0$ is the same as the induced velocity in axial flight for the same loading. Because of the cosine terms, the *mean* value of the power with respect to azimuth depends only on the first term of the series and we have

$$\begin{aligned} P_i &= 4\pi v_{i0} \int_0^R \Delta p c_0 r dr \\ &= 4\pi v_{i0} R^2 \int_0^1 \Delta p(x) c_0(x) x dx \end{aligned}$$

Thus, when the rotor loading is axisymmetrical, the induced power can be calculated from a knowledge only of the induced velocity distribution in axial flight fast enough for linearisation to apply. For the particular case of Mangler and Squire's loading, we find

$$\begin{aligned} P_i &= (225/8)Tv_{i0} \int_0^1 x^5 (1 - x^2) dx \\ &= (75/64)Tv_{i0} = 1.172Tv_{i0} \\ &= (1 + k)P_{i0} \end{aligned}$$

say, where P_{i0} is the induced power for constant induced velocity. This value agrees with that given earlier. It should be noted that the rotor disc loading is proportional to $x^2\sqrt{1-x^2}$ which implies a *blade thrust* loading proportional to $x^3\sqrt{1-x^2}$.

If a similar analysis for hovering flight is made, i.e. if we assume that $\Delta p = 2\rho v_i^2$ instead of $2\rho V_c v_i$ as in the calculations above, we find that Mangler and Squire's distribution gives $1+k = 1.11$. Hence, the induced power is 11 per cent higher than the ideal power in hovering flight, rising to about 17 per cent at high forward speed.

If $\Delta p = Cx^n$ (implying a blade thrust loading proportional to x^{n+1}), we easily find that

$$1+k = (1 + \frac{1}{2}n)^{3/2} / (1 + \frac{3}{4}n) \text{ when } \mu = 0$$

and

$$1+k = (1 + \frac{1}{2}n)^2 / (1+n) \text{ at high } \mu$$

These relationships are shown in Fig. 3.16.

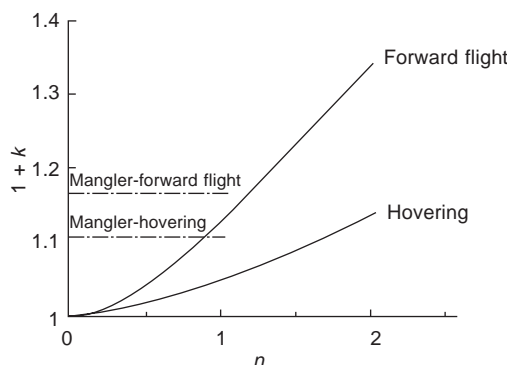


Fig. 3.16 Induced power factor as a function of radial pressure distribution exponent

3.7 Velocity components at the blade

Before being able to calculate the forces and moments on a blade, it is necessary to know the velocity components of the air relative to any point of the blade. In the following sections the blade will be assumed to be a rigid beam with a flapping hinge, and only simple ideas of induced velocity and aerofoil characteristics will be used. The analysis follows closely the classical work of Glauert¹ and Lock⁷, and, because the mathematical development is eased, the no-feathering axis system will be used.

We take as our *final* reference axes a set of right-hand axes fixed in the blade as

was shown in Fig. 1.18. It is sufficient to assume for the calculation of the aerodynamic forces that the flapping hinge offset is zero. The only velocity component affected by the flapping hinge offset is that due to blade flapping, but, since the hinge offset is usually only a few per cent of the blade radius, the error in assuming it to be zero is negligible. Taking the upward direction as positive, Fig. 3.17, and taking unit vectors i_1, j_1, k_1 , with k_1 along the no-feathering axis and i_1 sideways, the forward velocity V of the helicopter can be expressed as

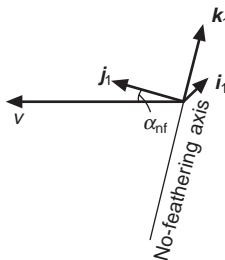


Fig. 3.17 Blade axes

$$V = V \cos \alpha_{\text{nf}} j_1 - V \sin \alpha_{\text{nf}} k_1$$

The blade is itself rotating with angular velocity Ω and it lies at an azimuth angle ψ with respect to the rearward direction of the helicopter, Fig. 3.18. The blade, at present, lies in the no-feathering plane. Taking a new unit axes system i_2, j_2, k_2 , with i_2 and j_2 defined as in Fig. 3.18, the helicopter's forward velocity can now be written as

$$V = -V \cos \alpha_{\text{nf}} \cos \psi i_2 + V \cos \alpha_{\text{nf}} \sin \psi j_2 - V \sin \alpha_{\text{nf}} k_2$$

since $k_1 = k_2$.

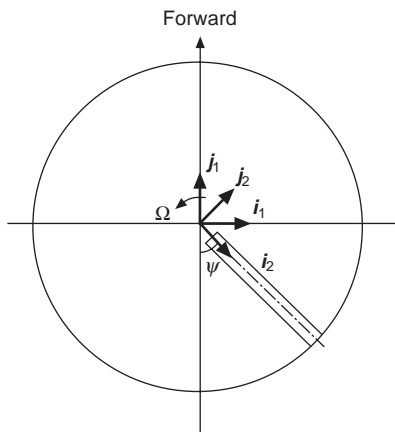


Fig. 3.18 View in plane of no feathering

The rotational motion of the blade will add a velocity component Ωr at a blade section radius r , in the direction j_2 ; then, writing W for the total velocity vector at this section, we have

$$W = -V \cos \alpha_{\text{nf}} \cos \psi i_2 + (V \cos \alpha_{\text{nf}} \sin \psi + \Omega r) j_2 - V \sin \alpha_{\text{nf}} k_2$$

Now let the blade flap through angle β about j_2 into the final blade position represented by the axes i, j, k , Fig. 3.19. The relationship between the sets of axes i_2, j_2, k_2 and i, j, k is the same as in eqn 1.24, i.e.

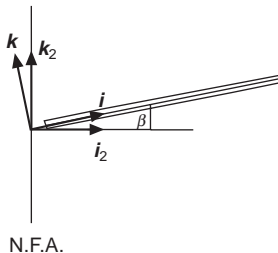


Fig. 3.19 Flapped blade

$$\begin{bmatrix} i \\ j \\ k \end{bmatrix} = \begin{bmatrix} \cos \beta & 0 & \sin \beta \\ 0 & 1 & 0 \\ -\sin \beta & 0 & \cos \beta \end{bmatrix} \begin{bmatrix} i_2 \\ j_2 \\ k_2 \end{bmatrix}$$

Using this transformation, W can be written

$$\begin{aligned} W = & -(V \cos \alpha_{\text{nf}} \cos \psi \cos \beta + V \sin \alpha_{\text{nf}} \sin \beta) i + (V \cos \alpha_{\text{nf}} \sin \psi + \Omega r) j \\ & + (V \cos \alpha_{\text{nf}} \cos \psi \sin \beta - V \sin \alpha_{\text{nf}} \cos \beta) k \end{aligned}$$

To complete the calculation of the velocity components we must add the contributions due to flapping $r\dot{\beta}j$ and the relative wind due to the induced velocity $-v_i k$. Thus, the components of *relative* wind along and perpendicular to the blade section are:

$$i \text{ direction: } V \cos \alpha_{\text{nf}} \cos \psi \cos \beta + V \sin \alpha_{\text{nf}} \sin \beta \quad (3.17)$$

$$j \text{ direction: } -V \cos \alpha_{\text{nf}} \sin \psi - \Omega r \quad (3.18)$$

$$k \text{ direction: } -V \cos \alpha_{\text{nf}} \cos \psi \sin \beta + V \sin \alpha_{\text{nf}} \cos \beta - r\dot{\beta} - v_i \quad (3.19)$$

It is generally assumed that the spanwise component of velocity in the i direction can be neglected. It is also usual to denote the component that is tangential to the plane of no feathering, or j direction (eqn 3.18), by U_T , taken as positive when it blows from leading to trailing edge, and the k direction or perpendicular component in eqn 3.19 by U_P . Then for small values of β , U_P and U_T can be written

$$U_P = -V\beta \cos \alpha_{nf} \cos \psi + V \sin \alpha_{nf} - r\dot{\beta} - v_i \quad (3.20)$$

$$U_T = V \cos \alpha_{nf} \sin \psi + \Omega r \quad (3.21)$$

We now define

$$\lambda' = (V \sin \alpha_{nf} - v_i)/\Omega R$$

where v_i may be a function of azimuth and radius, and

$$\mu = (V \cos \alpha_{nf})/\Omega R$$

U_P and U_T can then be written as

$$\begin{aligned} U_P &= \Omega R (\lambda' - x\dot{\beta}/\Omega - \mu\beta \cos \psi) \\ &= \Omega R(\lambda' - x \frac{d\beta}{d\psi} - \mu\beta \cos \psi) \end{aligned} \quad (3.22)$$

and

$$U_T = \Omega R (x + \mu \sin \psi) \quad (3.23)$$

Since U_T lies in the no-feathering plane, the local incidence α of the blade can be written (Fig. 3.20)

$$\alpha = \theta + \phi$$

where

$$\phi = \tan^{-1}(U_P/U_T) \approx U_P/U_T \quad (3.24)$$

since ϕ is a small angle except, perhaps, near the blade root.

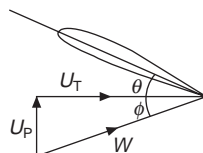


Fig. 3.20 Velocity components at a blade section

When $0 < \psi < 180^\circ$ the blade is said to be ‘advancing’, and the half of the rotor disc defined by this range of azimuth angle is referred to as the ‘advancing’ side of the rotor disc; in this region the relative wind due to the rotational speed of the blade is increased by a component of the forward speed. Similarly, in the azimuth range $180^\circ < \psi < 360^\circ$ the blade is said to be ‘retreating’ and to lie in the ‘retreating’ half of the disc; in this region the forward speed component reduces the relative chordwise wind.

It is clear that over some part of the retreating blade the forward speed component will be greater than that due to the rotational speed, i.e. the relative flow will be from the trailing edge to the leading edge. Referring to eqn 3.23, this occurs when

$x + \mu \sin \psi < 0$ and this inequality defines a circular region whose diameter is μR , Fig. 3.21. This region is known as the ‘reverse flow region’. Since the incidence of the blade is defined in relation to leading edge to trailing edge flow, it is obvious that the calculation of the lift and flapping moment in this region must be treated with some care. Fortunately, the contribution from this region is usually very small, e.g. for $\mu = 0.3$ the area of the reverse flow region is only $2\frac{1}{4}$ per cent of the total rotor area and the velocities there will also be small. The dynamic pressure in the reverse flow region is low; thus, below values of μ of about 0.4, and bearing in mind that an advance ratio of 0.5 represents a practical maximum for current helicopters, the effect of the reverse flow on rotor thrust and other performance contributors may be neglected, as is done in the following sections.

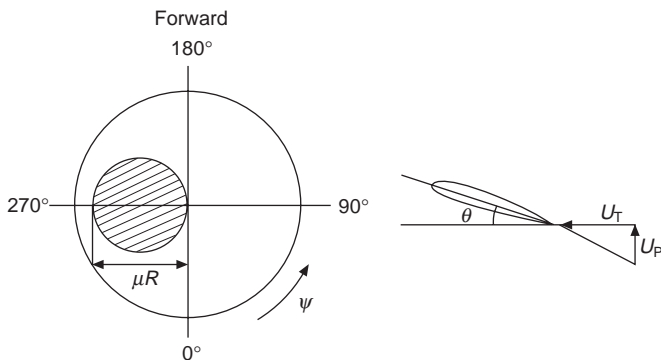


Fig. 3.21 Reversed flow region

3.8 Calculation of the rotor thrust

The lift dL on an element of the blade is given by

$$dL = \frac{1}{2}\rho W^2 C_L c \, dr \quad (3.25)$$

and, if the thrust dT is taken as the component of the resultant force along the no-feathering axis (Fig. 3.22),

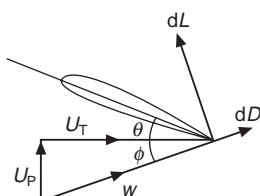


Fig. 3.22 Lift and drag components at a blade section

$$\begin{aligned} dT &= (dL \cos \phi + dD \sin \phi) \cos \beta \\ &\approx dL \end{aligned}$$

Also, having ignored the spanwise component of the induced velocity,

$$W^2 = U_P^2 + U_T^2 \approx U_T^2$$

since U_P is usually much smaller than U_T .

Assuming constant lift slope a , we can write

$$C_L = a\alpha$$

as in Chapter 2, where a generally has a value of about 5.7.

The elementary thrust is therefore

$$\begin{aligned} dT &= \frac{1}{2}a\rho U_T^2 (\theta + U_P/U_T)c dr \\ &= \frac{1}{2}a\rho (\theta U_T^2 + U_P U_T)c dr \\ &= \frac{1}{2}a\rho\Omega^2 R^2 [\theta(x + \mu \sin \psi)^2 + (\lambda' - x d\beta/d\psi - \mu\beta \cos \psi) \\ &\quad \times (x + \mu \sin \psi)]c dr \end{aligned} \quad (3.26)$$

Before eqn 3.26 can be integrated, β and λ' must first be expressed as functions of ψ . Assuming steady flight conditions, β can be expressed as

$$\beta = a_0 - a_1 \cos \psi - b_1 \sin \psi - a_2 \cos 2\psi - b_2 \sin 2\psi - \dots \quad (3.27)$$

so that

$$d\beta/d\psi = a_1 \sin \psi - b_1 \cos \psi + 2a_2 \sin 2\psi - 2b_2 \cos 2\psi - \dots \quad (3.28)$$

Let us take Mangler and Squire's series for the induced velocity, i.e. let

$$v_i = 4v_{i0} [\frac{1}{2}c_0 + \sum_{n=1}^{\infty} c_n(x, \alpha_D) \cos n\psi] \quad (3.29)$$

In this, we assume that the expression holds equally for the no-feathering plane as for the plane it actually applies to, which most nearly corresponds to the tip path plane.

To find the total rotor thrust we calculate the average thrust of a blade taken round the disc and multiply by the number of blades. To do this it is easier first to average the elementary thrust, given by eqn 3.26, with respect to azimuth and then integrate along the blade. The average value of dT over the azimuth range $0 < \psi < 360^\circ$ is found to be

$$dT = \frac{1}{2}\rho ac\Omega^2 R^3 [\theta(x^2 + \frac{1}{2}\mu^2) + x\hat{V} \sin \alpha_{nf} - 2xc_0\lambda_i + \frac{1}{2}\mu^2 b_2] dx \quad (3.30)$$

where $\lambda_i = v_{i0}/\Omega R$, v_{i0} being the mean induced velocity, and $\hat{V} = V/\Omega R$.

Assuming for simplicity that the chord c and pitch angle θ are constant along the blade, integration of eqn 3.30 along the blade gives

$$T = \frac{1}{4} \rho a c \Omega^2 R^3 \left[\frac{2}{3} \theta_0 (1 + 3\mu^2/2) + \hat{V} \sin \alpha_{nf} - \lambda_i + \frac{1}{4} \mu^2 b_2 \right]$$

since, from eqn 3.14

$$\begin{aligned} \int_0^1 c_0 x \, dx &= (15/8) \int_0^1 \eta (1 - \eta^2) x \, dx \\ &= (15/8) \int_0^1 x^3 \sqrt{1 - x^2} \, dx \\ &= \frac{1}{4} \end{aligned}$$

It is easy to show that we could have obtained exactly the same result if eqns 3.1 or 3.4 had been used for the induced velocity. Then defining

$$\lambda = \hat{V} \sin \alpha_{nf} - \lambda_i \quad (3.31)$$

the thrust for b blades becomes

$$T = \frac{1}{4} b \rho a c \Omega^2 R^3 \left[\frac{2}{3} \theta_0 (1 + 3\mu^2/2) + \lambda \right] \quad (3.32)$$

where we have neglected the very small term in b_2 .

Defining a thrust coefficient by

$$t_c = T / \rho s A \Omega^2 R^2$$

eqn 3.42 gives

$$t_c = \frac{a}{4} \left[\frac{2}{3} \theta_0 (1 + 3\mu^2/2) + \lambda \right] \quad (3.33)$$

Current blades are usually without taper so that it is justifiable to integrate eqn 3.30 on the assumption that the chord is constant. Most blades have considerable twist, however, but in Chapter 2 we found that for linear twist the thrust equation in hovering flight was still valid provided the pitch angle θ_0 at $\frac{3}{4}$ radius was taken. Since the thrust equation in forward flight involves only a small extra term in μ^2 , taking the $\frac{3}{4}$ -radius pitch angle for θ_0 should be a very good approximation in this case too. For a tapering blade the chord can also be taken as that at $\frac{3}{4}$ radius when defining the rotor solidity.

3.9 The in-plane H -force

Referring to Fig. 3.23, the force component dH perpendicular to the no-feathering axis and in the rearward direction is

$$dH = (dD \cos \phi - dL \sin \phi) \sin \psi - (dL \cos \phi + dD \sin \phi) \sin \beta \cos \psi \quad (3.34)$$

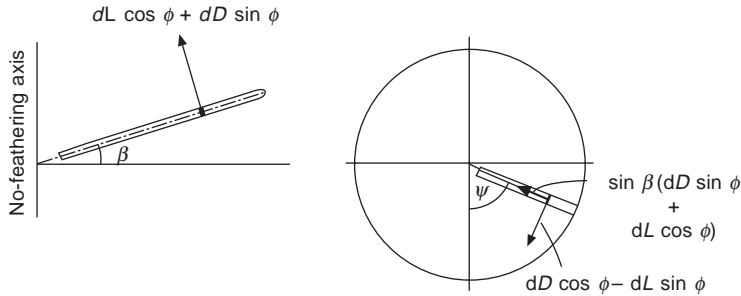


Fig. 3.23 Force components in plane of rotor

For small ϕ and β , eqn 3.34 becomes

$$dH = dD \sin \psi - dL(\beta \cos \psi + \phi \sin \psi) \quad (3.35)$$

The first term of eqn 3.35 can be regarded as the profile drag contribution to H , while the bracketed term can be regarded as the ‘induced’ component arising from the inclination of the lift vector.

The profile drag term H_P , found by averaging the first term of eqn 3.35 round the disc, is

$$H_P = (b/2\pi) \int_0^R \int_0^{2\pi} \frac{1}{2} \rho U_T^2 \delta c \sin \psi d\psi dr \quad (3.36)$$

Assuming the profile drag coefficient δ and chord c to be constant, we find

$$H_P = \frac{1}{4} \rho b c \delta \mu \Omega^2 R^3$$

The elementary ‘induced’ component is

$$\begin{aligned} dH_i &= -dL(\beta \cos \psi + \phi \sin \psi) \\ &= -\frac{1}{2} \rho a U_T^2 (\theta_0 + U_P/U_T) [\beta \cos \psi + (U_P/U_T) \sin \psi] c dr \\ &= -\frac{1}{2} \rho a [(\theta_0 U_T^2 + U_P U_T) \beta \cos \psi + (\theta_0 U_P U_T + U_P^2) \sin \psi] c dr \end{aligned}$$

The mean value for b blades is

$$\begin{aligned} H_i &= -(b/2\pi) \int_0^R \int_0^{2\pi} \frac{1}{2} \rho a c [(\theta_0 U_T^2 + U_P U_T) \beta \cos \psi \\ &\quad + (\theta_0 U_P U_T + U_P^2) \sin \psi] d\psi dr \end{aligned} \quad (3.37)$$

Mangler and Squire’s expression for the induced velocity can be used here but the analysis becomes rather complicated and, since the terms involving the induced velocity are fairly small, it is convenient to assume it to be constant. Then substituting for U_P , U_T and β from eqns 3.22, 3.23, and 3.27, in which harmonic terms of higher order than one have been ignored in β , and replacing λ' by λ we find for H

$$H = \frac{1}{2} \rho abc \Omega^2 R^3$$

$$\times \left[\frac{\mu\delta}{2a} + \frac{1}{3} a_1 \theta_0 + \frac{3}{4} \lambda a_1 - \frac{1}{2} \mu \lambda \theta_0 + \frac{1}{4} \mu a_1^2 - \frac{1}{6} a_0 b_1 + \frac{1}{4} \mu a_0^2 \right] \quad (3.38)$$

We shall see in section 3.12 that, when the induced velocity is constant,

$$b_1 = \frac{4\mu a_0/3}{1 + \frac{1}{2}\mu^2}$$

Ignoring the small term in μ^2 in the denominator, the last two terms in eqn 3.38 reduce to $\mu a_0^2/36$, which is very small compared with the other terms and may be neglected. The coefficient form of the H -force can then be written finally as

$$h_c = C_H/s = \frac{H}{\rho s A \Omega^2 R^2} = \frac{a}{2} \left[\frac{\mu\delta}{2a} + \frac{1}{3} a_1 \theta_0 + \frac{3}{4} \lambda a_1 - \frac{1}{2} \mu \theta_0 \lambda + \frac{1}{4} \mu a_1^2 \right] \quad (3.39)$$

3.10 The rotor torque, Q

The torque dQ about the no-feathering axis on a blade element is, Fig. 3.23,

$$dQ = r(dD \cos \phi - dL \sin \phi)$$

or

$$dQ = \frac{1}{2} \rho U_T^2 \delta cr dr - \frac{1}{2} \rho U_T^2 C_L \phi cr dr$$

The first term denotes the torque due to the profile drag. Calling this Q_P we have, for b blades,

$$\begin{aligned} Q_P &= (b/2\pi) \int_0^R \int_0^{2\pi} \frac{1}{2} \rho U_T^2 \delta cr d\psi dr \\ &= (b/2\pi) \rho c \Omega^2 R^4 \int_0^1 \int_0^{2\pi} \delta(x + \mu \sin \psi)^2 x d\psi dx \\ &= \rho bc \delta \Omega^2 R^4 (1 + \mu^2)/8 \end{aligned} \quad (3.40)$$

assuming the chord and drag coefficient to be constant.

The mean induced torque Q_i is

$$\begin{aligned} Q_i &= -(b/2\pi) \int_0^R \int_0^{2\pi} \frac{1}{2} \rho U_T^2 C_L \phi cr d\psi dr \\ &= -(\rho abc/4\pi) \int_0^R \int_0^{2\pi} (\theta_0 U_P U_T + U_P^2) r d\psi dr \end{aligned}$$

The integrand can be expanded and averaged as for the H -force but this is not

necessary and it is more convenient and instructive to proceed as follows. The integrand, including the scalar term $\frac{1}{2}\rho ac$, can be written

$$\frac{1}{2}\rho ac(\theta_0 U_P U_T + U_P^2)r = \frac{1}{2}(\rho ac/\Omega)(\theta_0 U_P U_T + U_P^2)(U_T - V \cos \alpha_{nf} \sin \psi)$$

since, from eqn 3.21,

$$\Omega r = U_T - V \cos \alpha_{nf} \sin \psi$$

or

$$r = (U_T - V \cos \alpha_{nf} \sin \psi)/\Omega$$

Hence

$$\begin{aligned} & \frac{1}{2}\rho ac(\theta_0 U_P U_T + U_P^2)r dr \\ &= \frac{1}{2} \frac{\rho ac U_P}{\Omega} (\theta_0 U_T^2 + U_P U_T) dr - \frac{1}{2} \frac{\rho ac V \cos \alpha_{nf}}{\Omega} (\theta_0 U_P U_T + U_P^2) \sin \psi dr \\ &= \frac{U_P}{\Omega} dT - \frac{1}{2} \frac{\rho ac V \cos \alpha_{nf}}{\Omega} (\theta_0 U_P U_T + U_P^2) \sin \psi dr \end{aligned}$$

But, from the previous sections,

$$\begin{aligned} \frac{1}{2}\rho ac (\theta_0 U_P U_T + U_P^2) \sin \psi dr &= -dH_i - \frac{1}{2}\rho ac (\theta_0 U_T^2 + U_P U_T) \beta \cos \psi dr \\ &= -dH_i - dT \beta \cos \psi \end{aligned}$$

so that

$$\begin{aligned} & \frac{1}{2}\rho ac (\theta_0 U_P U_T + U_P^2)r dr \\ &= \frac{U_P}{\Omega} dT + (dT \beta \cos \psi + dH_i) \frac{V \cos \alpha_{nf}}{\Omega} \\ &= \frac{dT}{\Omega} \left(V \sin \alpha_{nf} - v_{i0} - \Omega r \frac{d\beta}{d\psi} \right) + dH_i \frac{V \cos \alpha_{nf}}{\Omega} \end{aligned} \quad (3.41)$$

since $U_P = V \sin \alpha_{nf} - v_{i0} - \Omega r d\beta/d\psi - V \cos \alpha_{nf} \beta \cos \psi$.

Now

$$\int_0^R r dT d\beta/d\psi = M_A d\beta/d\psi$$

and from eqn (1.2) for zero flapping hinge offset

$$M_A = B \Omega^2 (d^2 \beta_s / d\psi^2 + \beta_s) = B \Omega^2 (d^2 \beta / d\psi^2 + \beta)$$

in which β_s is used temporarily to indicate that eqn (1.2) was derived for flapping defined relative to a plane perpendicular to the shaft axis. The second equality is easily derived using $a_1 = a_{1s} + B_1$ and $b_1 = b_{is} + A_1$.

Therefore the mean value of $-\int_0^R r dT d\beta/d\psi$ with respect to azimuth is

$$\begin{aligned}
& -\frac{B\Omega^2}{2\pi} \int_0^{2\pi} \left(\frac{d^2\beta}{d\psi^2} + \beta \right) \frac{d\beta}{d\psi} d\psi \\
&= -\frac{B\Omega^2}{4\pi} \left[\int_0^{2\pi} \frac{d}{d\psi} \left(\frac{d\beta}{d\psi} \right)^2 d\psi + \int_0^{2\pi} \frac{d}{d\psi} (\beta^2) d\psi \right] \\
&= -\frac{B\Omega^2}{4\pi} \left[\left[\left(\frac{d\beta}{d\psi} \right)^2 \right]_0^{2\pi} + [\beta^2]_0^{2\pi} \right] \\
&= 0
\end{aligned}$$

Since the terms in the brackets are periodic and are therefore identical at the limits. The other terms multiplying dT and dH_i in eqn 3.41 are constants so that

$$\begin{aligned}
Q_i &= - \left[\frac{T}{\Omega} (V \sin \alpha_{nf} - v_{i0}) + H_i \frac{V \cos \alpha_{nf}}{\Omega} \right] \\
&= -(T\lambda + H_i\mu)R
\end{aligned}$$

and the total torque is

$$\begin{aligned}
Q &= Q_p + Q_i \\
&= \rho b c \delta \Omega^2 R^4 (1 + \mu^2)/8 - (T\lambda + H_i\mu)R \\
&= \rho b c \delta \Omega^2 R^4 (1 + 3\mu^2)/8 - (T\lambda + H\mu)R
\end{aligned} \tag{3.42}$$

The torque coefficient is

$$\begin{aligned}
q_c &= Q / \rho b c R \Omega^2 R^3 = Q / \rho s A \Omega^2 R^3 \\
&= \delta(1 + 3\mu^2)/8 - \lambda t_c - \mu h_c
\end{aligned} \tag{3.43}$$

The term $-(\lambda t_c + \mu h_c)$ might have been expected on physical grounds since it is the scalar product, in non-dimensional form, of the resultant rotor force and resultant flow through the rotor, i.e. it represents the work done by the rotor in producing the rotor force. The first term of eqn 3.43 represents, of course, the torque required to overcome the profile drag.

Equation 3.43 has been derived on the assumption that the spanwise velocity component can be neglected. While this is a reasonable assumption for the calculation of the lift, Bennett⁸ has argued that this does not apply to the drag which depends on the resultant velocity over the blade. From Bennett's calculations, the profile drag contribution to the torque should be written as $\delta(1 + n\mu^2)/8$, where n has the following values

μ	0	0.3	0.6	1
n	4.5	4.58	4.66	4.67

From similar calculations, Stepniewski⁹ proposes the expression $\delta(1 + 4.7\mu^2)/8$.

We should also consider the increase of induced power due to the non-uniformity of the induced velocity by introducing the factor k as discussed in Chapter 3. The expression for the torque coefficient then becomes

$$q_c = \delta(1 + 4.7\mu^2)/8 - \lambda t_c - \mu h_c + k\lambda_i t_c \quad (3.44)$$

3.11 Blade flapping

The aerodynamic flapping moment dM_A about the hinge due to the elementary lift is

$$\begin{aligned} dM_A &= r dL = \frac{1}{2} \rho a U_T^2 \left(\theta + \frac{U_p}{U_T} \right) cr dr \\ &= \frac{1}{2} \rho a c \Omega^2 R^4 \\ &\times \left[\theta(x + \mu \sin \psi)^2 + \left(\lambda' - x \frac{d\beta}{d\psi} - \mu \beta \cos \psi \right) (x + \mu \sin \psi) \right] x dx \end{aligned} \quad (3.45)$$

Expanding eqn 3.45 and integrating, assuming constant pitch angle, gives

$$\begin{aligned} M_A &= \frac{1}{2} \rho a c \Omega^2 R^4 \\ &\times \left[\theta_0 \left(\frac{1}{4} + \frac{2}{3} \mu \sin \psi + \frac{1}{2} \mu^2 \sin^2 \psi \right) + \int_0^1 x^2 \lambda' dx - \frac{1}{4} \frac{d\beta}{d\psi} - \frac{1}{3} \mu \beta \cos \psi \right. \\ &\left. + \mu \sin \psi \int_0^1 x \lambda' dx - \frac{1}{3} \mu \frac{d\beta}{d\psi} \sin \psi - \frac{1}{2} \mu^2 \beta \sin \psi \cos \psi \right] \end{aligned} \quad (3.46)$$

It can easily be shown that for hovering flight the assumption of linear taper leads to the same flapping moment as eqn 3.46, provided the pitch angle is taken as that at $0.8R$ (cf. $0.75R$ in the calculation of the thrust). This value will be changed slightly when variable induced velocity is included, but it will be assumed that in calculations involving a twisted blade it will be sufficiently accurate to use eqn 3.46 with the collective pitch angle taken as that at $0.8R$.

To evaluate the inflow integrals in eqn 3.46 we again use Mangler and Squire's induced velocity distribution (eqn 3.13), considering the first harmonic only. Then

$$\begin{aligned} \int_0^1 \lambda' x^2 dx &= \int_0^1 x^2 \hat{V} \sin \alpha_{nf} dx - 2\lambda_i \int_0^1 c_0 x^2 dx + 4\lambda_i \cos \psi \int_0^1 c_1 x^2 dx \\ &= \frac{1}{3} \hat{V} \sin \alpha_{nf} - \frac{15}{4} \lambda_i \int_0^1 x^4 \sqrt{(1 - x^2)} dx \\ &- \frac{15\pi}{64} \lambda_i v^{1/2} \cos \psi \int_0^1 (9x^2 - 4)x^3 dx \end{aligned}$$

$$= \frac{1}{3} \hat{V} \sin \alpha_{nf} - \frac{15\pi}{128} \lambda_i - \frac{15\pi}{128} \lambda_i v^{1/2} \cos \psi$$

in which $v = (1 - \sin \alpha_D)/(1 + \sin \alpha_D)$.

To a reasonable approximation this integral may be expressed as

$$\int_0^1 \lambda' x^2 dx = (\lambda - 1.1v^{1/2} \lambda_i \cos \psi)/3$$

The second integral in eqn 3.46 is

$$\begin{aligned} \int_0^1 x \lambda' dx &= \int_0^1 x \hat{V} \sin \alpha_{nf} dx - (15/4) \lambda_i \int_0^1 x^3 \sqrt{(1 - x^2)} dx \\ &\quad - \frac{15\pi}{64} \lambda_i v^{1/2} \cos \psi \int_0^1 (9x^2 - 4)x^2 dx \\ &= \frac{1}{2} \hat{V} \sin \alpha_{nf} - \frac{1}{2} \lambda_i - \frac{7\pi}{64} \lambda_i v^{1/2} \cos \psi \\ &= \frac{1}{2} (\lambda - 0.69 \lambda_i v^{1/2} \cos \psi) \end{aligned}$$

Hence,

$$\begin{aligned} M_A &= \frac{1}{8} \rho a c \Omega^2 R^4 \left[\theta_0 \left(1 + \frac{8}{3} \mu \sin \psi + 2\mu^2 \sin^2 \psi \right) \right. \\ &\quad \left. + \frac{4}{3} \lambda - 1.46 v^{1/2} \lambda_i \cos \psi - \frac{d\beta}{d\psi} - \frac{4}{3} \mu \beta \cos \psi + 2\mu \lambda \sin \psi \right. \\ &\quad \left. - \frac{4}{3} \mu \frac{d\beta}{d\psi} \sin \psi - \mu^2 \beta \sin 2\psi - 0.69 \mu \lambda_i v^{1/2} \sin 2\psi \right] \quad (3.47) \end{aligned}$$

The flapping equation of a centrally hinged blade relative to a plane perpendicular to the shaft axis has been found in Chapter 1 to be

$$d^2\beta_s/d\psi^2 + (1 + \varepsilon)\beta_s = M_A/B\Omega^2 \quad (1.9)$$

As before, with β defined from the no-feathering plane, the equation can be shown to be exactly similar in form, i.e.

$$d^2\beta/d\psi^2 + (1 + \varepsilon)\beta = M_A/B\Omega^2$$

Then, on using eqn 3.47 and rearranging, we obtain the differential equation of flapping in the form

$$\frac{d^2\beta}{d\psi^2} + \frac{\gamma}{8} \left(1 + \frac{4}{3} \mu \sin \psi \right) \frac{d\beta}{d\psi} + \left[1 + \varepsilon + \frac{\gamma}{8} \left(\frac{4}{3} \mu \cos \psi + \mu^2 \sin 2\psi \right) \right] \beta$$

$$\begin{aligned}
 &= \frac{\gamma}{8} \left[\theta_0 \left(1 + \frac{8}{3} \mu \sin \psi + 2\mu^2 \sin^2 \psi \right) + \frac{4}{3} \lambda - 1.46v^{1/2} \lambda_i \cos \psi \right. \\
 &\quad \left. + 2\mu\lambda \sin \psi - 0.69\mu\lambda_i v^{1/2} \sin 2\psi \right] \tag{3.48}
 \end{aligned}$$

Equation 3.48 is a linear equation with periodic coefficients and there is no known solution in closed form. Moreover, as discussed in section 3.7, it is valid only for the advancing region $0 < \psi < 180^\circ$, since in the reverse flow area the lift and flapping moment are incorrectly evaluated. For the speeds typical of present day helicopters, however, this results in negligible error, as was stated earlier.

The free motion of the blade is found by putting the terms on the right-hand side of eqn 3.48 equal to zero. The flapping equation is then

$$\frac{d^2\beta}{d\psi^2} + \frac{\gamma}{8} \left(1 + \frac{4}{3} \mu \sin \psi \right) \frac{d\beta}{d\psi} + \left[1 + \varepsilon + \frac{\gamma}{8} \left(\frac{4}{3} \mu \cos \psi + \mu^2 \sin 2\psi \right) \right] \beta = 0 \tag{3.49}$$

Considerable attention has been given to this equation, since its solution answers the important question of the stability of the flapping motion. In hovering flight, $\mu = 0$, as we have seen already, the equation reduces to one with constant coefficients, eqn 1.10, and it was found that the corresponding motion is heavily damped. It is reasonable to expect that the damping would remain high for low values of μ but further investigation is required to find the effect of the periodic terms for high values of μ . As we shall see shortly, the denominator of one of the flapping coefficients of steady motion is the term $1 - \mu^2/2$, indicating that infinite flapping amplitudes might be expected to occur at $\mu = \sqrt{2}$.

Several attempts to solve eqn 3.49 analytically have been made, notably by Glauert and Shone,¹⁰ Bennett,¹¹ Horvay,¹² Shutler and Jones,¹³ and Lowis.¹⁴ Of these, only Lowis has attempted to take the reverse flow area into account. The others indicate that the flapping motion appears to be stable for $\mu < 1$ but their results are not really valid for values of μ greater than about 0.7 because of the neglect of the reverse-flow region. The last three authors make use of Floquet's theorem, which states that an equation of the type eqn 3.49 has a solution of the form

$$\beta = \alpha_1 e^{v_1 \psi} P_1(\psi) + \alpha_2 e^{v_2 \psi} P_2(\psi) \tag{3.50}$$

where $\alpha_1, \alpha_2, v_1, v_2$ are constants and $P_1(\psi), P_2(\psi)$ are periodic functions of period 2π . Hovering flight is a special case of eqn 3.50 with solution

$$\beta = e^{-\hat{v}\psi} [\alpha_1 \sin (1 - \hat{v}^2)^{1/2} \psi + \alpha_2 \cos (1 - \hat{v}^2)^{1/2} \psi]$$

where $\hat{v} = \gamma/16$.

The stability of the motion is determined by the values of v_1 and v_2 , which may not be real, and the investigations mentioned have been directed to finding their values.

An exact analytical determination is not possible, and v_1 and v_2 must be evaluated numerically for a range of flight parameters. Lowis found an approximate method of taking the reverse flow region into account which amounted merely to changing the sign of γ in eqn 3.49 over a range of ψ in the retreating region depending on the value of μ . His results showed that flapping instability occurs for μ in the range 2.2 to 2.8, depending on the inertia number γ .

Another method of dealing with eqn 3.49 is to use computational methods. The reversed-flow area and periodic coefficients can be easily and exactly taken into account. Of course, the output gives the flapping *response* to a given set of conditions, which does not provide as much information as the values of v_1 and v_2 . Nevertheless, by suitably choosing the initial conditions, the response can give an adequate picture of the flapping behaviour and stability. Investigations of this kind have been made by Wilde and Bramwell¹⁵ and Sissingh¹⁶. The results obtained by Wilde and Bramwell for $\gamma = 6$ and $\varepsilon = 0$ are shown in Fig. 3.24; they agree closely with the results of Lowis and Sissingh.

3.12 The flapping coefficients

In the previous section the free blade motion was discussed; we now wish to find the forced blade motion, that is, the steady motion in forward flight corresponding to a given collective pitch angle, tip speed ratio, and inflow ratio – these conditions completely define the operating state of the rotor. To do this we assume that the transient response is stable and that, as in previous sections, the forced blade motion is periodic and can be expressed as

$$\beta = a_0 - a_1 \cos \psi - b_1 \sin \psi - a_2 \cos 2\psi - b_2 \sin 2\psi - \dots$$

remembering that β is defined relative to the plane of no-feathering.

This expression is substituted into eqn 3.48 and, assuming that it represents a solution, the coefficients of the terms in $\sin \psi$, $\cos \psi$, ... on the left- and right-hand sides of eqn 3.48 can be equated. If we consider only the constant term and the two first harmonic terms, we obtain, after manipulation of terms such as $\sin \psi$, $\sin 2\psi$, etc.,

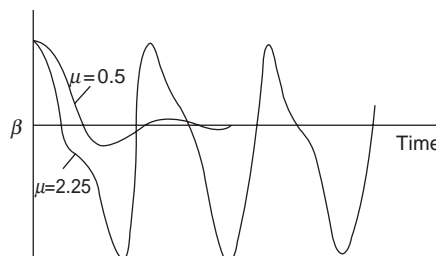


Fig. 3.24 Blade flapping response at high tip speed ratios

$$a_0 = \frac{\gamma}{8(1 + \varepsilon)} \left[\theta_0(1 + \mu^2) + \frac{4}{3}\lambda \right] \quad (3.51)$$

$$a_1 = \frac{2\mu(4\theta_0/3 + \lambda)}{1 - \mu^2/2} + \frac{8}{\gamma} \cdot \frac{\varepsilon}{1 - \mu^2/2} b_1 \quad (3.52)$$

$$b_1 = \frac{4(\mu a_0 + 1.1v^{1/2}\lambda_i)/3}{1 + \mu^2/2} - \frac{8}{\gamma} \cdot \frac{\varepsilon}{1 + \mu^2/2} a_1 \quad (3.53)$$

If Glauert's formula, eqn 3.4, for the induced velocity had been used instead of Mangler and Squire's, the values of a_0 and a_1 would be unaltered but it would have been found that

$$b_1 = \frac{4(\mu a_0 + 1.75K\lambda_i)/3}{1 + \mu^2/2} - \frac{8}{\gamma} \cdot \frac{\varepsilon}{1 + \mu^2/2} a_1 \quad (3.54)$$

For typical values of flapping hinge offset the terms in ε are usually negligible except, perhaps, in the equations for b_1 (eqns 3.53 and 3.54) at high values of μ . When $\varepsilon = 0$, the formulae reduce to their classical forms:

$$a_0 = \frac{\gamma}{8} \left[\theta_0(1 + \mu^2) + \frac{4}{3}\lambda \right] \quad (3.55)$$

$$a_1 = \frac{2\mu(4\theta_0/3 + \lambda)}{1 - \mu^2/2} \quad (3.56)$$

$$b_1 = \frac{4(\mu a_0 + 1.1v^{1/2}\lambda_i)/3}{1 + \mu^2/2} \quad (3.57)$$

The case of constant induced velocity is found by putting $v_i = v_{i0}$ in eqn 3.13, whence it is seen that the term involving $v^{1/2}$ in eqns 3.53 and 3.57 is absent. Alternatively, letting $K = 0$ in eqn 3.54 leads to the same result.

Higher order flapping coefficients can be obtained by considering higher harmonics of the flapping motion, but it is found that the coefficients appear explicitly as the solutions of an infinite chain of simultaneous equations and cannot be evaluated easily. Stewart¹⁷ has extracted the coefficients up to the fourth harmonic and has shown that their magnitudes decrease very rapidly with order of harmonic. As a rough rule it was found that the magnitude of a coefficient was about one tenth of the value of that of the next lower harmonic. The calculation of the higher harmonics, as has been mentioned in Chapter 1, is somewhat academic since the effects of the higher modes of blade bending are at least as great as these harmonics of the first (rigid) blade mode.

However, it should be noted here that the higher harmonic terms do become important when considering rotor induced vibration (see Chapter 8). The simple rigid blade flapping model used in the current analysis may be seen to give rise to first and

second harmonic forcing terms on the right-hand side of eqn 3.48 (or 1Ω and 2Ω terms, to use the terminology adopted in Chapter 8), but in a more general case with a flexible blade flapping model, forcing terms are generated over a wide range of harmonics.

3.13 Force and torque coefficients referred to disc axes

It is useful to obtain expressions for the force and torque coefficients when referred to the tip path plane axis (or rotor-disc axis) instead of the no-feathering axis. In Chapter 1, section 1.13, we saw that, since the angle between these two axes is the small flapping angle a_1 , we have the relationships

$$T_D \approx T$$

$$H_D \approx H - Ta_1$$

For the tip-speed and inflow ratios we also have

$$\mu_D = \hat{V} \cos \alpha_D \approx \mu$$

$$\lambda_D = \hat{V} \sin \alpha_D - \lambda_i \approx \lambda + \mu a,$$

where T_D , H_D , μ_D , and λ_D are referred to the tip path plane.

Substituting for λ in eqns 3.55 to 3.57 for the flapping coefficients, we have for a_1

$$a_1 = \frac{2\mu(4\theta_0/3 + \lambda_D - \mu a_1)}{1 - \mu^2/2}$$

remembering that this is still with reference to the plane of no-feathering. On solving for a_1 we get

$$a_1 = \frac{2\mu(4\theta_0/3 + \lambda_D)}{1 + 3\mu^2/2} \quad (3.60)$$

The coning angle a_0 becomes

$$a_0 = \frac{\gamma}{8} \left[\theta_0 (1 + \mu^2) + \frac{4}{3} \lambda_D - \frac{4}{3} \mu a_1 \right]$$

and on substituting eqn 3.60 we have

$$a_0 = \frac{\gamma}{8} \left[\theta_0 \frac{1 - 19\mu^2/18 + 3\mu^4/2}{1 + 3\mu^2/2} + \frac{4}{3} \lambda_D \frac{1 - \mu^2/2}{1 + 3\mu^2/2} \right] \quad (3.61)$$

The lateral flapping coefficient b_1 remains unaltered:

$$b_1 = \frac{4(\mu a_0 + 1.1v^{1/2}\lambda_i)/3}{1 + \mu^2/2} \quad (3.57)$$

The thrust coefficient can be written

$$t_{cD} = t_c = \frac{a}{4} \left[\frac{2}{3} \theta_0 (1 + 3\mu^2/2) + \lambda_D - \mu a_1 \right] \quad (3.62)$$

and on substituting for a_1 we have

$$t_{cD} = \frac{a}{4} \left[\frac{2}{3} \theta_0 \frac{1 - \mu^2 + 9\mu^4/4}{1 + 3\mu^2/2} + \lambda_D \frac{1 - \mu^2/2}{1 + 3\mu^2/2} \right] \quad (3.63)$$

The H -force coefficient takes the simple form

$$h_{cD} = \frac{1}{4}\mu\delta + \frac{a\lambda_D}{4} [\frac{1}{2}a_1 - \mu\theta_0] \quad (3.64)$$

which can also be written as

$$h_{cD} = \frac{1}{4}\mu\delta + \frac{a\mu\lambda_D}{4} \left[\frac{(\theta_0/3)(1 - 9\mu^2/2)}{1 + 3\mu^2/2} + \frac{\lambda_D}{1 + 3\mu^2/2} \right] \quad (3.65)$$

Finally, the torque coefficient can easily be seen to have the same form as eqn 3.43, that is

$$q_c = \delta(1 + 3\mu^2)/8 - \lambda_D t_{cD} - \mu h_{cD} \quad (3.66)$$

On considering the resultant blade flow velocity and induced power coefficient we also have the same result as eqn 3.44, i.e.

$$q_c = \delta(1 + 4.7\mu^2)/8 - \lambda_D t_{cD} - \mu h_{cD} + k\lambda_i t_c \quad (3.67)$$

3.14 Comparison with experiment

In order to arrive at fairly simple formulae for the force and flapping coefficients, a number of simplifying assumptions were made in the analysis and it is important to test the accuracy of the results by comparisons with experimental data. Squire *et al.*¹⁸ have conducted wind tunnel tests on a 3.65 m diameter rotor and compared the results with theoretical values. Generally speaking, the agreement was found to be good. Since the ranges of parameters in Squire's tests were arbitrary, many of the combinations were outside the range of normal helicopter operations. Much more recently, Harris¹⁹ has conducted tests on a 1.53 m diameter rotor which contains a large number of cases in which the collective pitch was adjusted so that the thrust coefficient was kept constant at a value typical of steady flight. Thus, the variation of μ in the tests corresponded to a helicopter changing its forward speed under conditions of trim. Harris also measured the coning angle and other quantities not considered in Squire's tests.

The force and flapping coefficients contain two quantities, namely, the blade lift

slope a and the drag coefficient δ , which are not known for a particular rotor although, of course, in the absence of data, reasonable assumptions can be made. In the tests described by Harris, the thrust and torque were measured over a range of collective pitch angles at a nominal tip speed ratio of 0.08. Now we saw earlier in this chapter that the mean induced velocity can be found from

$$v_{i0} = T/2\rho AV$$

which can be expressed as

$$\lambda_i = st_c/2\mu$$

provided $\bar{V} > 1$, or as $\mu > \lambda_i$, _{hov}. This inequality is satisfied for the tests made at $\mu = 0.08$ referred to above.

The thrust coefficient can be written from eqn 3.33 as

$$t_c = \frac{a}{4} \left[\frac{2}{3} \theta_0 (1 + 3\mu^2/2) + \mu \alpha_{nf} - \frac{st_c}{2\mu} \right]$$

$$\text{or } t_c \left(1 + \frac{as}{8\mu} \right) = \frac{a}{4} \left[\frac{2}{3} \theta_0 (1 + 3\mu^2/2) + \mu \alpha_{nf} \right]$$

Differentiating with respect to θ_0 gives

$$\frac{\partial t_c}{\partial \theta_0} = \frac{a(1 + 3\mu^2/2)/6}{1 + as/8\mu}$$

With μ and solidity s known, the slope of the thrust coefficient with collective pitch depends only on the blade lift slope a . Thus a can be determined from the slope of a graph of thrust coefficient against collective pitch. Figure 3.25 shows such data from Harris's tests, from which we obtain $\partial t_c / \partial \theta_0 = 0.523$ and $a = 5.5$. The variation of q_c against collective pitch is shown in Fig. 3.26. When $t_c = 0$ we have $q_c = \delta/8$ (since μh_c is extremely small) and from the figure we find that $\delta/8 = 0.0018$, giving $\delta = 0.0144$.

With a and δ deduced from the tests we can now calculate force, torque, and

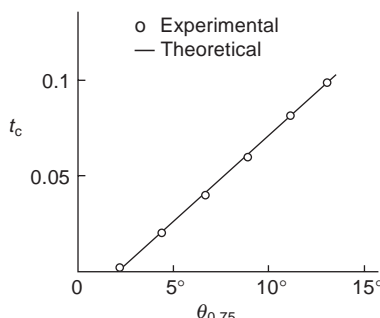


Fig. 3.25 Thrust coefficient as a function of collective pitch

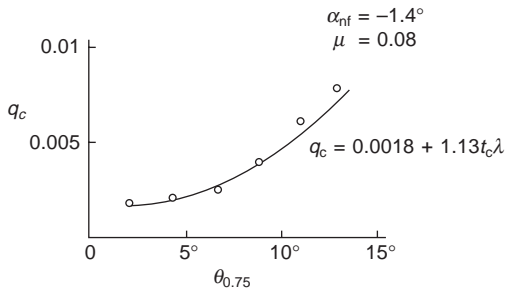


Fig. 3.26 Torque coefficient as a function of collective pitch

flapping coefficients. These are shown in Figs 3.27 to 3.31, together with the corresponding measured values.

It can be seen from Figs 3.27 and 3.26 that the agreement between theoretical and measured values of thrust and torque is very good; the slight discrepancy at larger values of collective pitch in the case of q_c probably indicates that the value of the profile drag coefficient δ should be higher in this region. The theoretical values of h_c , on the other hand, show less good agreement with experiment, Fig. 3.28, but it should be noted that, unlike t_c , h_c represents only a small component of the resultant rotor force and that the expression for h_c does not take into account the effects of the variable induced velocity since, as was mentioned in section 3.9, this would result in a very complicated analysis. It is easy to account for the effect of the induced velocity on the total power, however, since we need only apply a factor to the induced power, as discussed earlier in this chapter. As can be seen from Fig. 3.29, the agreement between the estimated and measured torque coefficients is excellent.

Agreement between the theoretical and experimental values of the flapping angles is less satisfactory. The theoretical value of the coning angle a_0 , as one would expect, is zero at the value of collective pitch angle for which the thrust also vanishes, and it is not understood why the measured values show a significant coning angle at this point or why the slope with collective-pitch angle is less than the theoretical value, Fig. 3.30. Fortunately, since the coning angle plays very little part in performance and stability estimations, the discrepancy is not serious.

Comparison between theoretical and experimental values of the backward flapping angle a_1 , Fig. 3.31, displays a tendency previously observed²⁰ in connection with

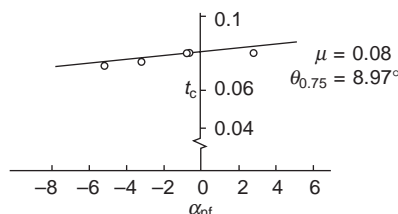
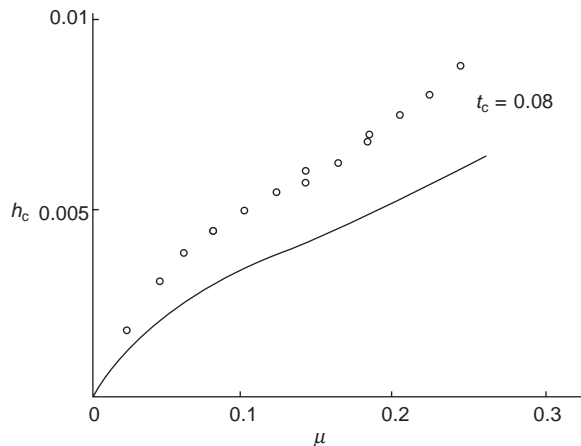
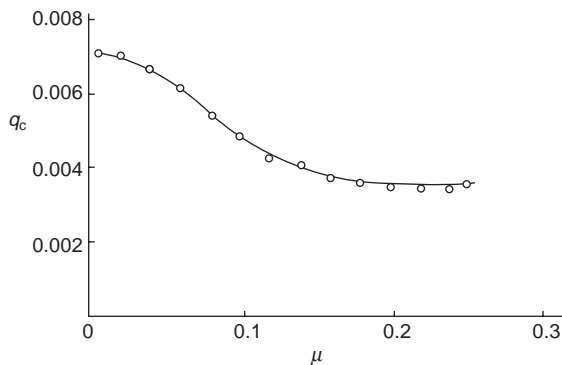
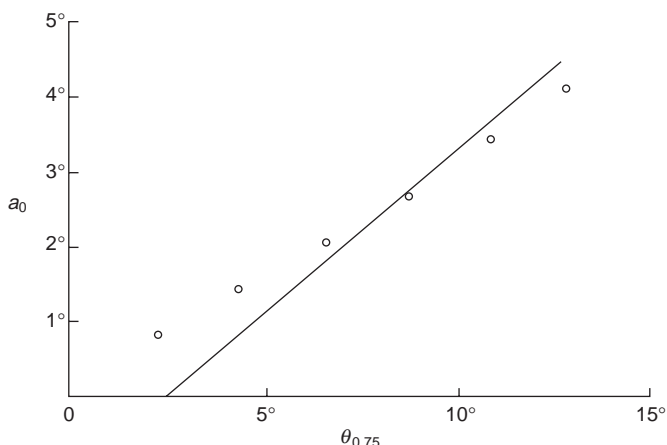


Fig. 3.27 Thrust coefficient as a function of shaft angle

**Fig. 3.28** H -force coefficient as a function of tip speed ratio**Fig. 3.29** Torque coefficient as a function of tip speed ratio**Fig. 3.30** Coning angle as a function of collective pitch

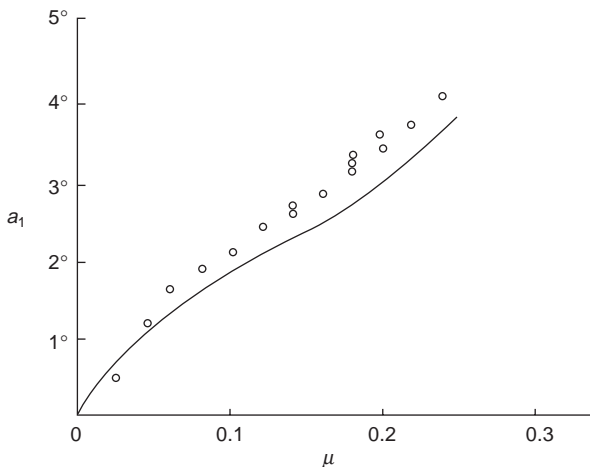


Fig. 3.31 Longitudinal flapping as a function of tip speed ratio

Squire's results, namely, that the theoretical values underestimate the actual flapping angle by about 10 to 20 per cent. This is probably due to the simplifying assumptions made for the induced velocity distribution.

The longitudinal induced velocity distribution has a very pronounced influence on the sideways flapping angle b_1 . As was discussed in section 3.12, the sideways flapping can be attributed to two effects: the incidence variation due to coning and that due to the longitudinal induced velocity distribution. As can be seen from Fig. 3.32, nearly all of the sideways flapping at low speeds is due to the longitudinal induced velocity distribution, and calculations depend strongly on the assumptions made. Harris¹⁹ has considered a number of simple expressions which have been used for representing the longitudinal induced velocity distribution but none of them shows the 'peakiness' evinced by the measured values. Equation 3.53 appears to give the best agreement of those expressions examined.

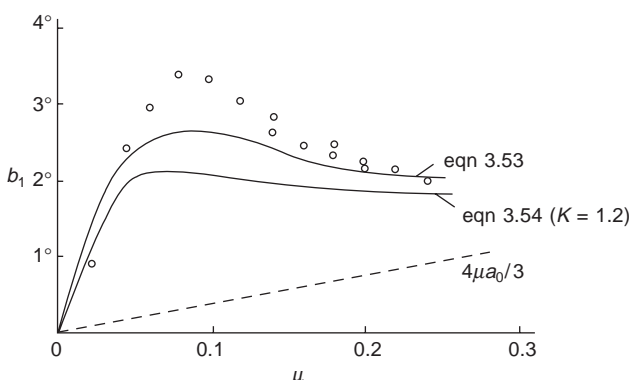


Fig. 3.32 Lateral flapping as a function of tip speed ratio

References

1. Glauert, H., 'A general theory of the autogyro', *Aeronautical Research Council R&M 1111*, 1926.
2. Bramwell, A. R. S., 'Some remarks on the induced velocity field of a lifting rotor and on Glauert's formula', *Aeronautical Research Council CP 1301*, 1974.
3. Coleman, R. P., Feingold, A. M. and Stempin, C. W., 'Evaluation of the induced velocity field of an idealized helicopter rotor', *NACA ARR L5E10*, 1947.
4. Mangler, K. W. and Squire, H. B., 'The induced velocity field of a rotor,' *Aeronautical Research Council R&M 2642*, 1950.
5. Brotherhood, P. and Stewart, W., 'An experimental investigation of the flow through a helicopter in forward flight', *Aeronautical Research Council R&M 2734*, 1949.
6. Heyson, H. H. and Katzoff, S., 'Induced velocities near a lifting rotor with non-uniform disc loading', *NACA Rep. 1319*, 1958.
7. Lock, C. N. H. 'Further developments of autogyro theory', *Aeronautical Research Council R&M 1127*, 1927.
8. Bennett, J. A. J., 'Rotary wing aircraft', *Aircraft Engineering*, March 1940.
9. Stepniewski, W. Z., 'Basic aerodynamics and performance of the helicopter', *AGARD Lect. Ser. 63*, 1973.
10. Glauert, H. and Shone, G., 'The disturbed motion of the blades of a gyroplane', *Aeronautical Research Council Paper 993*, 1933.
11. Bennett, J. A. J., 'Rotary wing aircraft', *Aircraft Engineering*, May 1940.
12. Horvay, G., 'Rotor blade flapping motion', *Q. Appl. Math.*, July 1947.
13. Shutler, A. G. and Jones, J. P., 'The stability of rotor blade flapping motion', *Aeronautical Research Council R&M 3178*, 1958.
14. Lowis, O. J., 'The effect of the reverse flow on the stability of rotor blade flapping motion at high tip speed ratios', *Aeronautical Research Council Paper 24 431*, 1963.
15. Wilde, E., Bramwell, A. R. S. and Summerscales, R., 'The flapping behaviour of a helicopter rotor at high tip speed ratios', *Aeronautical Research Council CP 877*, 1966.
16. Sissingh, G. J., 'Lifting rotors operating at high speeds and advance ratios', *AGARD Conf. Proc. CP-22*, paper 5 (part II), 1967.
17. Stewart, W., 'Higher harmonics of flapping on the helicopter rotor', *Aeronautical Research Council CP 121*, 1952.
18. Squire, H. B., Fail, R. A. and Eyre, R. C. W., 'Wind tunnel tests on a 12 ft helicopter rotor', *Aeronautical Research Council CP 2695*, 1949.
19. Harris, F. D., 'Articulated rotor blade flapping motion at low advance ratio', *J. Amer. Helicopter Soc.*, January 1972.
20. Bramwell, A. R. S., 'Stability and control of the single rotor helicopter', *Aeronautical Research Council R&M 3104*, 1959.

Trim and performance in axial and forward flight

4.1 Introduction

Having obtained formulae for the rotor forces and blade flapping motion in Chapter 3, we are now in a position to solve the trim equations derived in Chapter 1. In Chapter 1 it was possible to draw some general conclusions relating to trimmed flight with little specific reference to the values of the flight parameters such as collective pitch, inflow ratio, and so on. We now seek a method which enables us to calculate these quantities for a given helicopter under given steady-flight conditions. These values are necessary, not only because one wishes to know the control displacements required to maintain a given flight condition, but because these, and other, parameters are needed for performance and stability calculations.

Having solved the trim equations, one can then calculate the corresponding power and establish relationships between a given set of flight conditions and the power required to achieve them. It is also of interest to calculate such quantities as the maximum speed, maximum rate of climb, etc., and for this purpose it is easier to consider the maximum power available to the rotor and to solve an energy equation. If the trim and energy equations are based on the same set of assumptions, it is, of course, merely a matter of convenience as to which ones are used to obtain the desired quantities.

The following analysis and discussion will be based on the comparatively simple formulae derived in Chapter 3. The reader is reminded that these formulae are only approximate and that their derivation has been made possible only by making a number of simplifying assumptions, the chief of which are that the lift slope and drag coefficient of the blade section are constant, and that blade stall does not occur. The introduction of more complicated aerodynamic data, in which the lift and drag are both arbitrary functions of incidence and Mach number, requires the use of computational methods for solution of the trim equations and calculation of performance. However, the simplified equations are often adequate for all but the most advanced

design work and have the important advantage that they enable a physical interpretation of helicopter flight to be made easily.

4.2 Helicopter trim in forward flight

In Chapter 1 the longitudinal and lateral trim equations were derived. Because of the asymmetry of the helicopter, e.g. the presence of a tailrotor in a single rotor helicopter, the longitudinal and lateral equations should, strictly speaking, be solved simultaneously; indeed, in a very thorough analysis of helicopter trim, Price¹ finds that the various trim parameters are related through no less than fourteen equations. However, the complicated process of having to satisfy such a large number of equations simultaneously is not necessary in practice, especially as the accuracy of some of the aerodynamic data would hardly justify such detail. The longitudinal and lateral equations will therefore be treated as separate groups and solved independently of one another.

Now it was stated in Chapter 1 that the resultant rotor force is almost perpendicular to the rotor tip path plane, i.e. the H -force is small when the rotor force components are referred to the tip path plane axes. Because of this fact these axes are very useful for investigating helicopter trim, as it is much easier, when using the corresponding force coefficients, to establish the rotor incidence α_D and thence to obtain the other parameters.

4.2.1 Longitudinal trim

Referring to Fig. 4.1, we can write the trim equations given in Chapter 1, eqns 1.41 and 1.42, with reference the tip path plane or disc axes.

Resolving forces vertically and horizontally we have

$$T_D \cos (\alpha_D + \tau_c) - H_D \sin (\alpha_D + \tau_c) = W + D \sin \tau \quad (4.1)$$

$$T_D \sin (\alpha_D + \tau_c) + H_D \cos (\alpha_D + \tau_c) = -D \cos \tau \quad (4.2)$$

Now the angle $\alpha_D + \tau$ is the inclination of the rotor-disc plane to the horizontal and

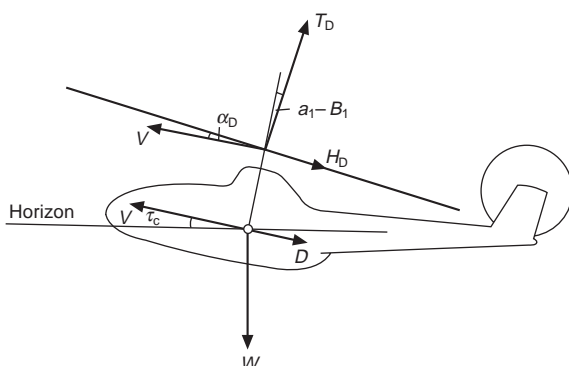


Fig. 4.1 Forces and moments in longitudinal plane

is usually a small angle in steady flight. Thus the usual small angle assumptions can be applied to eqns 4.1 and 4.2 which then become, approximately,

$$T_D \approx T = W + D \sin \tau_c \quad (4.3)$$

$$T(\alpha_D + \tau_c) + H_D = -D \cos \tau_c \quad (4.4)$$

where the term $H_D \sin (\alpha_D + \tau_c)$ has been neglected. The angle of climb τ_c might not be a small angle.

Let the helicopter fuselage drag D be written as

$$D = \frac{1}{2} \rho V^2 S_{FP} \quad (4.5)$$

where S_{FP} is the so-called equivalent flat plate area.

Then expressing eqns 4.3 and 4.4 in coefficient form by dividing through by $\rho s A \Omega^2 R^2$ gives

$$t_{cD} = w_c + \frac{1}{2} \hat{V}^2 d_0 \sin \tau_c \quad (4.6)$$

and

$$t_{cD}(\alpha_D + \tau_c) + h_{cD} = -\frac{1}{2} \hat{V}^2 d_0 \cos \tau_c \quad (4.7)$$

where w_c is a weight coefficient, $d_0 = S_{FP}/sA$, and $\hat{V} = V/\Omega R$.

Solving eqn 4.7 for α_D gives

$$\alpha_D = -(\frac{1}{2} \hat{V}^2 d_0 \cos \tau_c + h_{cD}) / t_{cD} - \tau_c \quad (4.8)$$

t_{cD} having been obtained from eqn 4.6. Unless the rotor-disc incidence is unusually large, it is usual to take $t_{cD} = w_c$. With this approximation, the only unknown quantity in eqn 4.8 is h_{cD} . Now, from numerical calculations, it appears that the most important term of h_{cD} is the first one of eqns 3.64 or 3.65, i.e. the term representing the rotor profile drag. Therefore as a good first approximation to h_{cD} we can write

$$h_{cD} = \frac{1}{4} \mu \delta \quad (4.9)$$

and obtain, from eqn 4.8, the first approximation to α_D .

The inflow ratio can now be calculated from

$$\begin{aligned} \lambda_D &= \hat{V} \sin \alpha_D - \lambda_i \\ &= \mu_D \tan \alpha_D - \lambda_i \end{aligned}$$

or, approximately,

$$\lambda_D = (\mu \alpha)_D - \lambda_i \quad (4.10)$$

To obtain λ_i we can use the values of \bar{v}_i of Fig. 3.2 which applies when $\alpha_D \approx 0$. Now

$$\lambda_i = \bar{v}_i \frac{v_0}{\Omega R} \quad (4.11)$$

and

$$\bar{V} = \hat{V} \frac{\Omega R}{v_0} \approx \mu_D \frac{\Omega R}{v_0} \quad (4.12)$$

where $v_0 = \sqrt{(T/2\rho A)}$ is the mean induced velocity in hovering flight or ‘thrust velocity’, and $\mu_D = \hat{V} \cos \alpha_D$. Then, if $v_0/\Omega R$ is computed, \bar{V} can be obtained from eqn 4.12 and, with \bar{v}_i being read off from Fig. 3.2, λ_i can be finally calculated from eqn 4.11.

With λ_D now known, or rather a first approximation to it, and taking $t_{cD} = w_c$, eqn 3.63 can be solved for the collective pitch angle θ_0 . These values of λ_D and θ_0 enable a better approximation to h_{cD} to be calculated from eqn 3.64 (or 3.65) and new values of α_D and λ_D to be obtained from eqns 4.8 and 4.10 respectively. In most cases, however, the improved value of h_{cD} makes very little difference to α_D , as indicated by the numerical example below, which also indicates the usefulness of the disc axes for these calculations. Finally, the flapping coefficients can be calculated.

Example. To illustrate the procedure just described, we shall calculate the trim of a four-bladed helicopter in level flight at sea level at tip speed ratio 0.3. The helicopter is represented by the following data:

$$W = 45\,000 \text{ N}, \text{ solidity } s = 0.05, \quad R = 8 \text{ m}, \quad h = 0.25$$

$$\delta = 0.013, \quad \Omega R = 208 \text{ m/s}, \quad S_{FP} = 2.3 \text{ m}^2, \quad b = 4, \quad a = 5.7$$

Blade data: $M_b = 74.7 \text{ kg}$; in terms of R , $x_g = 0.45$, $e = 0.04$

It will be assumed that the fuselage pitching moment, M_f , including, possibly, a tailplane, is zero.

The above data give

$$sA = 10 \text{ m}^2, \quad d_0 = 0.23, \quad w_c = 0.085, \quad \frac{1}{2}\mu^2 d_0 = 0.0104 \quad v_0 = 9.6 \text{ m/s}$$

The first approximation to h_{cD} is $\frac{1}{4}\mu\delta = 0.000\,975$, and hence

$$\begin{aligned} \alpha_D &= -(\frac{1}{2}\mu^2 d_0 + h_{cD})/w_c \\ &= -0.134 = -7.67^\circ \end{aligned}$$

Now $v_0/\Omega R = 0.0462$, so that $\bar{V} = \mu\Omega R/v_0 = 6.50$. From Fig. 3.2 or eqn 3.2 we find $\bar{v}_{i0} = 0.154$, from which $\lambda_i = \bar{v}_{i0}v_0/\Omega R = 0.0071$.

Then, from eqn 4.10,

$$\lambda_D = -0.0473$$

Solving eqn 3.63 for θ_0 gives

$$\theta_0 = 0.1824 = 10.5^\circ$$

To obtain a better value of h_{cD} we need an estimate of a_1 . From eqn 3.60, and using the above values of θ_0 and λ_D , we find

$$a_1 = 0.104 = 5.93^\circ$$

and, using eqn 3.64 or 3.65, we calculate h_{cD} , giving

$$h_{cD} = 0.001172$$

This value is about 20 per cent greater than the first approximation, $\frac{1}{4}\mu\delta$, but the new value of λ_D using this revised value of h_{cD} is

$$\lambda_D = -0.0479$$

which is close to one per cent of the first value. The small difference in λ_D using the recalculated value of h_{cD} is also found at other values of μ , suggesting that the original approximation to h_{cD} leads to sufficiently accurate values of λ_D and θ_0 . In any case, it is very unlikely that the fuselage drag, upon which λ_D and α_D depend strongly, would be known accurately enough to justify ‘exact’ calculations of the H -force.

From eqns 3.61, 3.57, and 3.66, we find

$$a_0 = 0.066 = 3.78^\circ, \quad b_1 = 0.037 = 2.1^\circ$$

$$q_c = 0.00579$$

The total power required at this speed is therefore 638 kW.

To calculate the cyclic pitch to trim, we write eqn 1.45 in terms of force components related to disc axes, i.e.

$$-WfR - T_D hRB_1 + (H_D + T_D a_1)hR + M_f - M_s(B_1 - a_1) = 0$$

Putting $T_D = W$ and solving for B_1 gives

$$B_1 = a_1 + (M_f + H_D hR - WfR)/(WhR + M_s) \quad (4.13)$$

$$= a_1 + (C_{mf} + h_{cD} h - w_c f)/(w_c h + C_{ms}) \quad (4.14)$$

where $C_{mf} = M_f/\rho sA\Omega^2 R^3$

and $C_{ms} = M_s/\rho sA\Omega^2 R^3 = \frac{1}{2}bSeR/\rho sA\Omega^2 R^3$

or $C_{ms} = bM_b x_g e / 2\rho sAR$

since $S = M_b r_g \Omega^2$.

The pitching moment M_f of the basic fuselage is not likely to be known very accurately. The rather unstreamlined shape of most helicopter fuselages and the fact that the fuselage lies in the complicated downwash pattern of the rotor makes it difficult to make estimates of the pitching moment. Also, because of the problem of correctly representing the downwash, it is difficult to obtain reliable wind tunnel measurements of the pitching moment. The contribution from a tailplane, however, can be estimated comparatively accurately, although it depends on the fuselage incidence, which is not known in advance. A method for calculating the tailplane moment will be given later in the chapter.

For the purpose of illustrating the calculation of the trim, we assume $C_{m_f} = 0$. From the data given we find also that

$$t_{c_D} h = w_c h = 0.0214 \quad \text{and} \quad C_{m_s} = 0.0274$$

The two quantities above represent the control moment contributions, expressed in non-dimensional form, referred to in section 1.14, i.e. the thrust moment and the centrifugal couple due to the flapping hinge offset, which has been taken as $e = 0.04$. It can be seen that this typical value of flapping hinge offset results in a total control moment which is more than double that due to the thrust alone.

Equation 4.14 provides the longitudinal cyclic pitch angle B_1 to trim for different c.g. positions and to calculate the fuselage attitude θ , we can write eqn 3.50 in terms of the disc axes as

$$(D/W) \cos \tau_c + H_D/W + T_D a_1/W = B_1 - \theta$$

or, in non-dimensional form, as

$$\theta = B_1 - a_1 - h_{c_D}/w_c - \frac{1}{2}\mu^2 d_0/w_c$$

A negative sign for θ indicates that the fuselage is in a nose-down attitude. Except at low speeds, by far the largest term in the equation for θ is the fuselage drag term $\frac{1}{2}\mu^2 d_0/w_c$.

Values of B_1 and θ for three different values of f (c.g. position) are shown in Table 4.1.

The variation of longitudinal trim parameters with tip speed ratio in the range 0 to 0.35 are shown in Figs 4.2 to 4.6. The effects of hinge offset and c.g. position are shown in Figs 4.5 and 4.6 for B_1 and fuselage attitude θ .

The variation of λ with μ , Fig. 4.2, displays the reduction of the thrust velocity part of the induced velocity at the higher speeds, shown by the broken line, and then the gradually increasing total inflow due to the forward tilt of the rotor disc required to overcome the helicopter drag (full line).

Table 4.1 Values of cyclic pitch B_1 and fuselage pitch attitude θ for different c.g. positions

f	0	0.01	0.02
C.g. position	On shaft	7.9 cm fwd	15.8 cm fwd
B_1°	6.32	5.31	4.31
θ°	-7.45	-8.45	-9.45

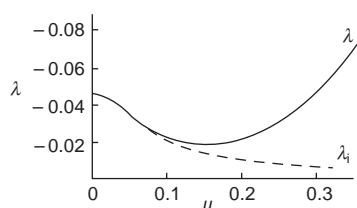


Fig. 4.2 Inflow ratio in trimmed flight

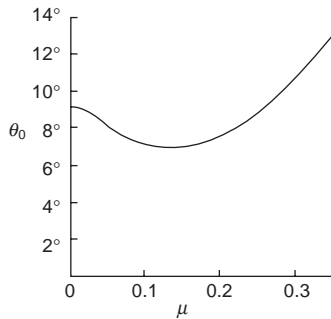


Fig. 4.3 Collective pitch variation in trimmed flight

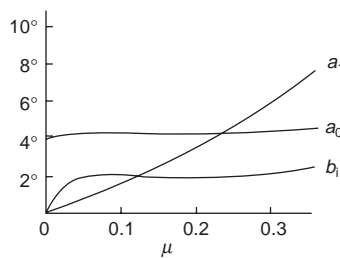


Fig. 4.4 Flapping angles in trimmed flight

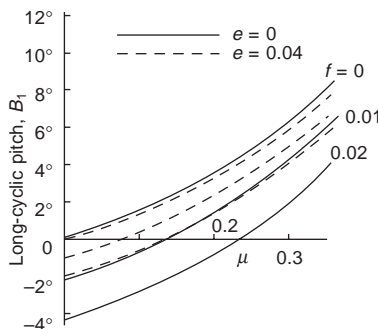


Fig. 4.5 Longitudinal pitch angle to trim

In order that the thrust should be kept constant the collective pitch angle θ_0 , as follows from eqn 3.33, must vary in almost exactly the same way as λ , and this can also be seen in Fig. 4.3.

As might be expected, at constant rotor thrust the coning angle a_0 is practically constant over the entire speed range, Fig. 4.4, while the longitudinal flapping angle a_1 varies roughly linearly with speed.

The variation of longitudinal cyclic pitch B_1 required for trim is shown in Fig. 4.5 for three c.g. positions and for the flapping offsets represented by $e = 0$ and $e = 0.04$.

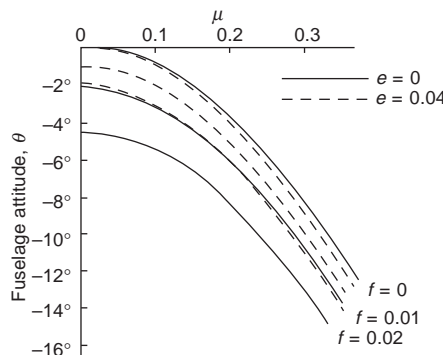


Fig. 4.6 Fuselage angle in trimmed flight

Referring to eqn 4.14, we see that if $C_{m_f} = 0$ and if the c.g. is on the shaft ($f = 0$), B_1 differs from a_1 only by the small term in h_{CD} , and that the difference becomes smaller the larger the hinge offset or hub couple. Our previous calculations show that, at $\mu = 0.3$, the difference between B_1 and a_1 is only 0.36° for the offset $e = 0.04$; for zero offset, $e = 0 = C_{ms}$ and the difference is 0.79° .

With zero hinge offset, the effect of moving the c.g. is merely to change the amount of cyclic pitch to trim by the ratio of c.g. distances f/h , as explained in section 1.14. According to eqn 4.14, with $h = 0.25$ a forward c.g. displacement of 7.9 cm ($f = 0.01$) requires a change of cyclic pitch of -2.3° in hovering flight, and since the H -force term is always small, this change of cyclic pitch is roughly constant over the entire speed range, as can be seen in Fig. 4.5.

With a flapping hinge offset of 31.5 cm ($e = 0.04$), the cyclic pitch change for the same c.g. shift is much smaller since the control moment, as we have seen earlier, is more than doubled by the addition of the offset hinge moment so that a given external moment requires a correspondingly smaller amount of cyclic pitch movement to maintain trim, resulting in a lessened fuselage attitude, Fig. 4.6. Expressed in another way, and as clearly illustrated in Fig. 4.5, the existence of a hub couple, such as would be obtained from offset hinges or hingeless blades, allows a much larger c.g. travel for a given cyclic pitch range. The amount of cyclic pitch available is usually limited by the rotor tilt allowed by the helicopter geometry, and early helicopters, which had little or no flapping hinge offset, had only a small c.g. travel. For this reason the fuselages of these helicopters tended to be rather wide, since the load carried had to be confined within limited longitudinal dimensions. The larger c.g. range of more recent helicopters with comparatively large hinge offsets, or with hingeless blades, allows a more slender fuselage design.

Since wind-tunnel measurements of rotor forces and flapping motion generally show good agreement with theoretical values, any discrepancy between measured and theoretical values of the longitudinal cyclic pitch to trim is usually attributed to incorrect estimates of the fuselage pitching moment, since this is the only moment contribution which is likely to be seriously in error. An example of theoretical and flight test values of the longitudinal cyclic pitch angle to trim for the Sikorsky S-51 is shown in Fig. 4.7.

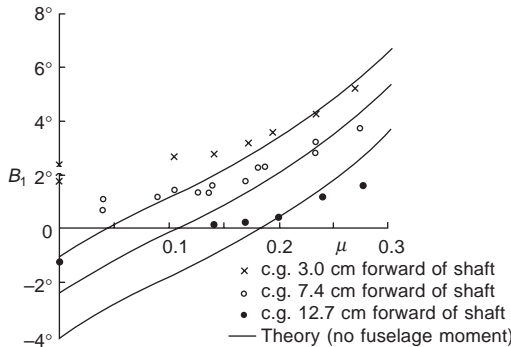


Fig. 4.7 Measured longitudinal control to trim; Sikorsky S-51, level flight 172 rev/min

4.2.2 Effect of tailplane on trim

Let us suppose that the pitching moment of the tailplane can be calculated in isolation from the fuselage on which it is mounted. The fuselage datum line for referring angles is a line perpendicular to the rotor hub axis. If the no-lift line of the tailplane makes an angle α_{T0} to the datum line it can be seen from Fig. 4.8 that the tailplane incidence α_T is given by

$$\alpha_T = \alpha_D + B_1 - a_1 + \alpha_{T0} - \varepsilon = \theta - \tau_c + \alpha_{T0} - \varepsilon$$

where ε is the downwash angle at the tailplane relative to the undisturbed flow.

If S_T is the tailplane area, a_T is the lift slope and $l_T R$ is the tail arm, the pitching moment M_T is

$$M_T = -\frac{1}{2}\rho V^2 S_T l_T R a_T (\alpha_D + B_1 - a_1 + \alpha_{T0} - \varepsilon)$$

If this moment can be added independently to the basic fuselage pitching moment M_f , the equation for the longitudinal cyclic pitch to trim, eqn 4.13, can be modified to become

$$B_1 = a_1 + \frac{M_f + H_D h R - W f R + M_T}{W h R + M_s}$$

$$= a_1 + \frac{C_{m_f} + h_{c_D} h - w_c f - \frac{1}{2} \mu^2 \bar{V}_T a_T (\alpha_D + B_1 - a_1 + \alpha_{T0} - \varepsilon)}{w_c h + C_{m_s}}$$

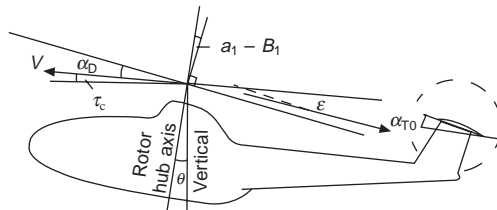


Fig. 4.8 Determination of tailplane incidence

where $\bar{V}_T = S_T l_T / sA$ is the tail volume ratio.

This equation can be arranged to give

$$B_1 = a_1 + \frac{C_{m_f} + h_{c_D} h - w_c f - \frac{1}{2} \mu^2 \bar{V}_T a_T (\alpha_D + \alpha_{T_0} - \varepsilon)}{k_T (w_c h + C_{m_s})} \quad (4.15)$$

where $k_T = 1 + \frac{1}{2} \mu^2 \bar{V}_T a_T / (w_c h + C_{m_s})$. The equation may be compared with eqn 4.14 for the no-tailplane case.

To see the effect of the tailplane on the trim of our example helicopter, let us take $\alpha_{T_0} = 12^\circ$, $\bar{V}_T = 0.1$, $a_T = 3.5$, and let the distance of the tailplane below the hub be 1.25 m ($= 0.156R$). For the appropriate values of the downwash angle ε , we use the charts below, Figs 4.9 and 4.10, taken from Reference 2, which summarise the results of Heyson and Katzoff referred to in Chapter 3. As described there, the downwash pattern behind the rotor consists of two distinct trailing vortices. The mean downwash angle ε_0 , based on the mean induced velocity, is used to define the axis of reference for longitudinal and normal position coordinates ξ and ζ (positive aft and downwards from the rotor hub, and non-dimensionalised on R) of which the downwash, v_i , is a function. Vertical downwash distributions are provided for two positions aft of the rotor hub.

Taking the case $\mu = 0.3$, as before, we have

$$\begin{aligned} \varepsilon_0 &= v_{i0}/V = \lambda_i/\hat{V} \approx \lambda_i/\mu \\ &= 0.024 = 1.38^\circ \end{aligned}$$

and

$$\xi = l_T = 1.2$$

Referring to Fig. 4.8, the vertical displacement of the trailing vortices at the non-dimensional distance $\xi = 1.2$ behind the rotor is $1.2(\varepsilon_0 - \alpha_D)R = 1.2(0.024 + 0.134)R = 0.19R$ below the rotor plane. Since the distance of the tailplane below the rotor is $0.142R$ (having taken account of the small angle $a_1 - B_1$), the tailplane is $0.048R$ above the ζ axis. Using the $\xi = 1.07$ case in Fig. 4.9 as being the closest to the desired $\xi = 1.2$, with $\zeta = +0.048$, we find $v_i/v_{i0} = 1.8$. Thus, the downwash angle at the tailplane is $1.8 \times 1.38^\circ = 2.48^\circ$.

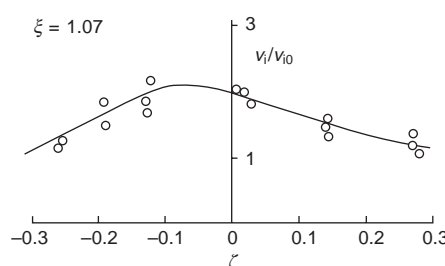


Fig. 4.9 Vertical distribution of induced velocity at $\xi = 1.07$ behind rotor

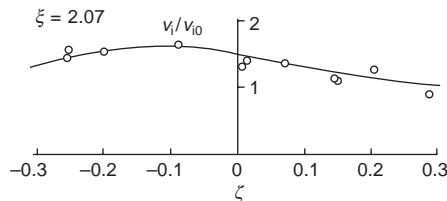


Fig. 4.10 Vertical distribution of induced velocity at $\xi = 2.07$ behind rotor

From the data given previously, we find that $\alpha_D + \alpha_{T_0} - \epsilon = 1.85^\circ$ and $k_T = 1.32$, so that, from eqn 4.15,

$$B_1 - a_1 = -0.19^\circ$$

whereas, without the tailplane,

$$B_1 - a_1 = 0.36^\circ$$

Figure 4.11 shows the effect of the given tailplane on the longitudinal trim. The full line shows the previously calculated tailplane case with the c.g. on the shaft and with $e = 0.04$, as shown in Fig. 4.5. The two broken lines show the cyclic pitch to trim for two tailplane settings of 12° and 15° . At low speeds the large downwash angle causes the tailplane incidence to be negative and the consequent download requires a small forward application of the stick to trim, relative to the tailless case. At higher speeds the downwash angle increases, the tailplane incidence tends to become positive and a backward stick movement is required. At still higher speeds the increasingly nose down attitude acquired by the fuselage causes the tailplane incidence to reduce again, and the slope of the trim curve rapidly increases. For a fixed tailplane the trend indicated in Fig. 4.11 is quite general.

4.2.3 Lateral control to trim

One of the forces contributing to the lateral trim of the helicopter is the tailrotor thrust T_t . Assuming that the tailrotor thrust moment is the only moment balancing the main rotor torque, we have

$$T_t = Q/l_t R$$

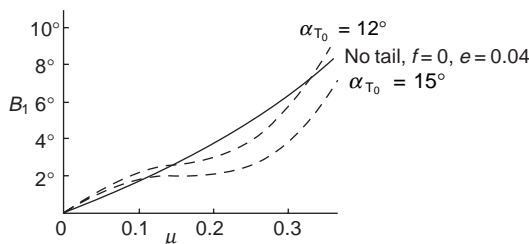


Fig. 4.11 Effect of tailplane on longitudinal control to trim

where $l_t R$ is the distance of the tailrotor from the c.g. of the helicopter. Calculation of the torque coefficient at $\mu = 0.3$ from eqn 3.67 gives

$$q_c = 0.00632 \quad \text{or} \quad Q = 25800 \text{ Nm}$$

If the tailarm is 11 m, the tailrotor thrust is

$$T_t = 2340 \text{ N}$$

From the parameters already calculated, and from eqn 3.53 we find

$$b_1 = 2.24^\circ$$

For the lateral cyclic pitch to trim, eqn 1.53 can be written in non-dimensional form as

$$A_1 = -b_1 - \frac{w_c f_1 + (T_t/W) t_c h_t}{t_c h + C_{m_s}} \quad (4.16)$$

and the lateral tilt ϕ of the fuselage is

$$\phi = -b_1 - A_1 - T_t/W \quad (4.17)$$

If we take $f_1 = 0$, i.e. no lateral displacement of the c.g., and $h_t = 0.2$, we find

$$A_1 = -3.34^\circ \quad \text{and} \quad \phi = -1.98^\circ$$

The lateral trim quantities b_1 , A_1 , and ϕ are shown in Fig. 4.12.

Although there may be a contribution from the fin and fuselage, it will be supposed, for illustration, that the tailrotor thrust is the only agency balancing the main rotor torque. The calculation of the rotor torque is discussed in the next section.

If the solidity, rotor area, and tip speed of the tailrotor are denoted by s_t , A_t and $(\Omega R)_t$ respectively, the corresponding thrust coefficient is defined by

$$t_{c_t} = T_t / \rho s_t A_t (\Omega R)_t^2$$

Let us suppose that the tailrotor axis is perpendicular to the flight direction, i.e. the incidence of the no-feathering axis of the tailrotor is zero. The only contribution to the inflow ratio λ_t is the induced velocity ratio λ_{it} , which can be calculated from

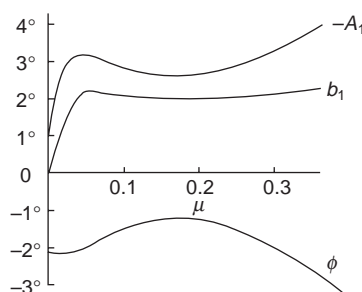


Fig. 4.12 Lateral control angles to trim

$$\lambda_{it} = \sqrt{(s_t t_{c_t}/2)}, \text{ in hovering flight}$$

and

$$\lambda_{it} = s_t t_{c_t}/2\mu_t, \text{ for } \mu_t > 0.05$$

Usually, the tip speeds of the main rotor and the tailrotor are the same, i.e. μ_t can be taken as μ .

To calculate the collective pitch we can use eqn 3.33, where t_c is referred to the no-feathering axis, and obtain

$$\theta_{0t} = \frac{3}{2(1 + 3\mu^2/2)} \left(\frac{4}{a} t_{c_t} - \lambda_{it} \right) \quad (4.18)$$

Taking $s_t = 0.1$, $R_t = 1.4$ m, $(\Omega R)_t = \Omega R = 208$ m/s, the tailrotor collective-pitch angle to trim has been calculated and is shown in Fig. 4.13. The high values at hovering and low speed are partly due to the high solidities typical of tailrotors resulting in somewhat higher induced velocities than the main rotor.

4.3 Helicopter performance in forward flight

It is now possible to estimate the performance of the helicopter in forward flight, this being the performance at a specific flight condition, or point on the flight envelope. This should not be confused with the mission performance, which is aimed at assessing the overall ability of the helicopter to complete a particular operational mission that consists of a series of inter-related tasks.

The trim calculations of the previous sections give all the information needed for calculating the power required for a given flight condition; in fact, using eqn 3.66, the torque and power were calculated from the values of θ_0 and λ was obtained from the trim equations. For the performance alone, however, calculation of the trim parameters is not necessary. A form of the torque equation for performance calculations more convenient than eqn 3.66 can be obtained by considering the balance of forces along the flight path in conjunction with eqn 3.66.

Referring to Fig. 4.1, we see that

$$T_D \sin \alpha_D + H_D \cos \alpha_D + W \sin \tau_c + D = 0$$

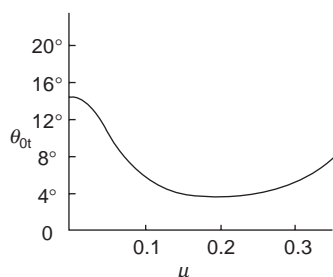


Fig. 4.13 Tailrotor pitch angle to trim

Multiplying by $\hat{V} = V/\Omega R$ and remembering that $\hat{V} \sin \alpha_D = \lambda_D + \lambda_i$ gives

$$(\lambda_D + \lambda_i)T_D + \mu H_D + W\hat{V} \sin \tau_c + D\hat{V} = 0$$

which can be written in non-dimensional form as

$$\lambda_D t_{c_D} + \mu h_{c_D} = -(\lambda_i t_{c_D} + w_c \hat{V} \sin \tau_c + \frac{1}{2} \hat{V}^3 d_0)$$

Substituting for $\lambda_D t_{c_D} + \mu h_{c_D}$ in eqn 3.66 gives

$$q_c = \delta(1 + 3\mu^2)/8 + \lambda_i t_{c_D} + w_c \hat{V} \sin \tau_c + \frac{1}{2} \hat{V}^3 d_0 \quad (4.19)$$

This expression for the torque coefficient can be regarded as the non-dimensional form of an energy equation; the first term represents the power required to overcome the profile drag of the blades, the second represents the induced power, the third is the power required for climbing, and the last term is the power required to overcome the fuselage drag. Of course, eqn 4.19 could have been derived from energy considerations directly, but it is instructive to derive it from the balance of forces.

Equation 4.19 has been derived from eqn 3.66 on the assumption that the induced velocity was constant. Since the induced power in eqn 4.19 appears as a separate term, it is a simple matter to include the effect of non-uniform induced velocity, as mentioned in the previous chapter. Now, as we saw in Chapter 3, the induced power can be expressed as $(1 + k)P_{i0}$, where P_{i0} is the 'ideal' induced power for a constant induced velocity distribution defined by $v_{i0}T$ and which, in non-dimensional form, is represented by the second term of eqn 4.19. Values of k for the Mangler and Squire induced velocity distribution were given in Fig. 3.16. Thus, the contribution of the induced power to the torque coefficient can be expressed more accurately by $(1 + k)\lambda_i t_{c_D}$. Further, we have yet to include the torque which must be provided to the tailrotor. The tailrotor is driven by a shaft geared to the main rotor, but the torque supplied to the shaft depends on the inclination of the tailrotor axis to the fuselage. Thus, for example, it is possible to incline the axis so that the tailrotor autorotates and for no power to be necessary at the tailrotor, causing a drag force which, in turn, would require a forward tilt of the main rotor to trim it, with a corresponding increase of power to be developed at the main rotor shaft. It can easily be verified that the amount of power required at the tailrotor shaft, plus the work which must be done to overcome the tailrotor force, is independent of the tailrotor shaft angle. As we have found with the main rotor, the power absorbed can be expressed simply as that which would be needed to overcome the profile drag of the blades and the induced power. Hence, the power P_t required for the tailrotor is

$$P_t = \left[\frac{\delta_t}{8}(1 + 3\mu_t^2) + \lambda_{it} t_{ct} \right] \rho s_t A_t (\Omega R)_t^3$$

and the effective increment to the mainrotor torque coefficient is

$$q_{c_t} = \left[\frac{\delta_t}{8} (1 + 3\mu_t^2) + \lambda_{it} t_{c_t} \right] \frac{s_t A_t (\Omega R)_t^2}{s A (\Omega R)^3}$$

Now it is reasonable to assume that, as the tip speeds of the tailrotor and the main rotor are usually equal, the terms in the square bracket have roughly the same values as those of the main rotor, although, as we saw earlier, λ_{it} may be rather higher than in hovering flight. Hence, the power to be attributed to the tailrotor is, to a good approximation, $s_t A_t / s A$ times that of the main rotor. Thus, a simple way to calculate the tailrotor power is merely to increase the mainrotor power by the fraction $s_t A_t / s A$ whose value is typically about 0.06. As a percentage of the *total* power, the tailrotor power varies from about 6 per cent in hovering to about 3 per cent at high speed.

The torque coefficient can finally be written as

$$q_c = \left[\frac{\delta}{8} (1 + 3\mu^2) + (1 + k) \lambda_i t_{c_D} \right] \left(1 + \frac{s_t A_t}{s A} \right) + w_c \hat{V} \sin \tau_c + \frac{1}{2} \hat{V}^3 d_0 \quad (4.20)$$

The required power P is calculated from $\Omega Q = q_c \rho s A \Omega^3 R^3$ and is shown for the example helicopter in level flight in Fig. 4.14. The four contributions to the power are shown by the broken lines, the value of the induced power factor k being taken as 0.17.

Suppose the maximum installed power of our example helicopter is 900 kW. It can be seen from Fig. 4.14 that the maximum excess power occurs at $\mu = 0.154$ (32 m/s) and is 496 kW. This gives a maximum rate of climb of 11 m/s.

The maximum forward speed occurs when the installed power and the required power are equal; the intersection of the two curves in Fig. 4.14 occurs at $\mu = 0.358$, i.e. at 74.8 m/s.

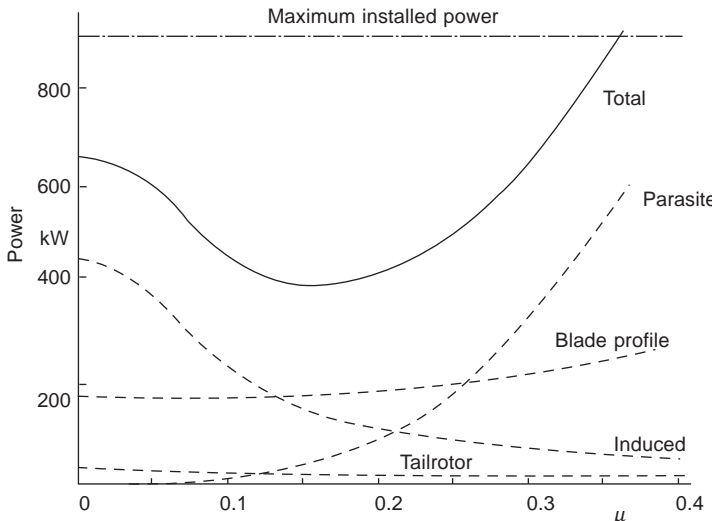


Fig. 4.14 Variation of power with forward speed

4.3.1 Fuselage parasite drag

The figure for the parasite drag of our example helicopter is a value, typical for its weight, of production helicopters. The flat plate parasite drag of a number of helicopters as a plot of equivalent flat plate area is shown against gross weight in Fig. 4.15. The points define fairly well a typical curve of drag against weight. A second curve is shown which is based on aerodynamically clean experimental helicopters. This latter curve represents the lowest drag which can reasonably be achieved in helicopter design, although it falls far short of best fixed wing practice. It is clear that the particular basic shape which must be adopted by helicopter fuselages, and the fact that the helicopter is normally expected to fulfil a variety of roles, means that it is unable to reach the degree of aerodynamic refinement which is possible in fixed wing practice. In fact, both helicopter drag curves are roughly proportional to $W^{1/2}$, instead of $W^{2/3}$ as might have been expected, which is an indication of a large amount of separation drag. The drag curve of the much cleaner fixed wing aircraft is more nearly proportional to $W^{2/3}$.

A breakdown of the fuselage parasite drag is shown in the table below.

Component	Percentage drag
Basic fuselage with protuberances	20 to 40
Landing gear or fairing	6 to 25
Rotor pylon and hub	35 to 50
Tailrotor and tail surfaces	5 to 15

The drag of the rotor pylon and hub represents a high proportion of the overall drag, and this is therefore an area where drag reduction leads to considerable benefit; hence the appearance of hub and pylon fairings on the larger and faster helicopters.

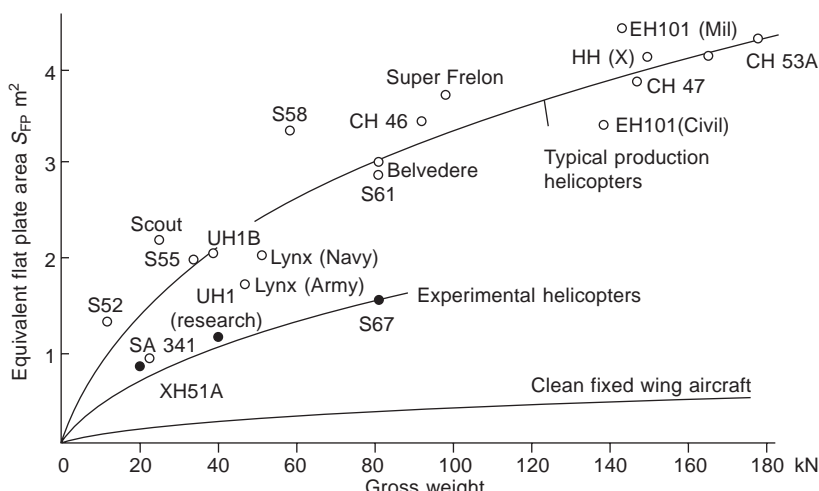


Fig. 4.15 Parasite drag of helicopters

Interference drag plays a significant role, because on a helicopter there are a number of separate aerodynamic ‘shapes’ in close proximity whose pressure distributions and boundary layers can interact with each other. Hub and pylon fairings are designed to minimise interference drag in addition to reducing the basic parasitic drag contribution of these components, the upper cambered shape of the former being a result³.

Also, larger and faster helicopters tend to utilise retractable landing gear, which leads to the lower figure in the above table.

4.3.2 Analytical estimation of performance

Except at very low speeds (when the disc incidence may not always be small) we can put $\hat{V} = \mu$ and $\lambda_i = st_c/2\mu$; also, writing λ_c for $\hat{V} \sin \tau_c$, eqn 4.20 can be expressed as

$$q_c = \left[\frac{\delta}{8} (1 + 3\mu^2) + \frac{1}{2}(1 + k) \frac{st_c^2}{\mu} \right] \left(1 + \frac{s_t A_t}{sA} \right) + \lambda_c t_c + \frac{1}{2}\mu^3 d_0 \quad (4.21)$$

where q_c is the torque coefficient corresponding to the given power.

The expression for q_c can be used to calculate either the torque and power for a given flight condition or, as described below, the maximum speed and rate of climb for a given torque.

To find the maximum level speed ($\lambda_c = 0$) for a given power, i.e. given q_c , we have to solve the quartic in μ expressed by eqn 4.21. Now at high speed we note that the induced power is small; therefore, neglecting this term and the term $3\mu^2$ of the profile drag, we find as a first approximation to μ , μ_1 say,

$$\mu_1^3 = \frac{2[q_c - \delta(1 + s_t A_t/sA)/8]}{d_0}$$

The value of q_c corresponding to the maximum power (900 kW) is 0.00834. Then, with the previously given values of δ and d_0 , we find

$$\mu_1^3 = 0.0561 \quad \text{or} \quad \mu_1 = 0.383$$

With this value of μ , we calculate the terms previously neglected to give the second approximation μ_2 as

$$\mu_2^3 = 0.0468 \quad \text{or} \quad \mu_2 = 0.36$$

which is extremely close to the correct value. Thus, the iteration provides the required maximum value in two steps.

To find the maximum rate of climb we must satisfy the condition

$$\partial \lambda_c / \partial \mu = 0$$

This condition leads to

$$6d_0\mu^4 + [3\delta\mu^3 - 2(1 + k)st_c^2] \left(1 + \frac{s_t A_t}{sA} \right) = 0 \quad (4.22)$$

To solve this equation for μ we note from Fig. 4.14 that the blade profile drag contributes little to the slope of the power curve (which led to eqn 4.22), so that for a first approximation μ_1 we can neglect the second term of eqn 4.22 and obtain

$$\mu_1^4 = \frac{(1+k)st_c^2}{3d_0} \left(1 + \frac{s_t A_t}{sA} \right)$$

From our data we find

$$\mu_1^4 = 0.000642$$

or

$$\mu_1 = 0.159$$

For the second approximation, a value for the second term is calculated using μ_1 , giving

$$\mu_2^4 = 0.000642 - 0.000117 = 0.000525$$

or

$$\mu_2 = 0.152$$

This agrees with the value obtained graphically and, again, the iteration leads to a satisfactory answer in two steps. This value of μ is substituted into eqn 4.21 and the equation is solved for λ_c , giving the required rate of climb.

4.3.3 Autorotative forward flight

Autorotation is defined as self-sustained rotation of the rotor in the absence of applied torque, i.e. when $Q = q_c = 0$. The work to be done to overcome the rotor and fuselage drag must be obtained at the expense of the potential energy of the helicopter. Level flight autorotation is impossible, and steady flight can be achieved only by descending. To find the rate of descent at a given forward speed we simply put $q_c = 0$ in eqn 4.21 and solve for λ_c at the appropriate value of μ . Thus

$$\lambda_c = -\frac{\delta}{8t_c}(1+3\mu^2) + \frac{1}{2}(1+k)\frac{st_c}{\mu} + \frac{1}{2}\mu^3\frac{d_0}{t_c} \quad (4.23)$$

and the rate of descent V_{des} is given by

$$V_{\text{des}} = -\lambda_c \Omega R$$

The angle of descent τ_{des} is clearly

$$\tau_{\text{des}} = \tan^{-1} (V_{\text{des}}/V) \quad (4.24)$$

The rate and angle of descent of our example helicopter is shown in Figs 4.16 and 4.17.

It can be seen from eqns 4.21 and 4.23 that the rate of descent is proportional to the torque coefficient in level flight; in fact, the rate of descent curve, Fig. 4.16, is

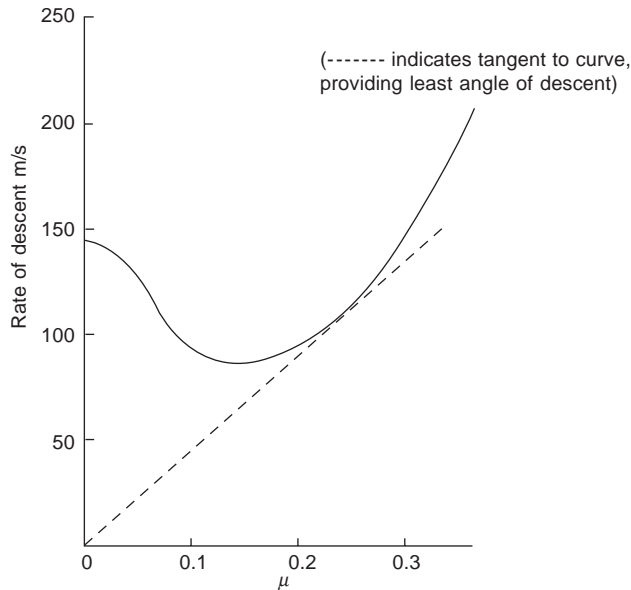


Fig. 4.16 Rate of descent in autorotation

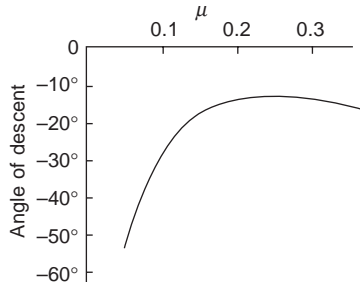


Fig. 4.17 Angle of descent in autorotation

merely the power curve, Fig. 4.14, drawn to a different scale. Thus, the minimum rate of descent occurs at the same speed as the minimum power in level flight.

From eqn 4.24 the condition for least angle of descent is given by

$$\frac{d\tau_{des}}{dV} = \frac{\cos^2 \tau_{des}}{V^2} \left(V \frac{dV_{des}}{dV} - V_{des} \right) = 0$$

i.e. $dV_{des}/dV = V_{des}/V$

Except at low speeds, when the disc angle may be quite large, this condition can be written as

$$d\lambda_c/d\mu = \lambda_c/\mu$$

and the solution can be found by the point at which the line drawn from the origin makes a tangent to the curve of λ_c against μ or of V_{des} against μ , as shown in Fig. 4.16.

In autorotation there must be a flow up through the rotor disc so that the total moment, or torque, of the blade forces is zero. Figure 4.18 shows the forces on a blade section with the resultant force dR perpendicular, or nearly perpendicular, to the plane of rotation. It can be seen that the resultant velocity vector W must be inclined upwards relative to the plane of rotation in order that there should be a component of lift to balance the blade drag.

It is clear that in autorotation the collective pitch will be lower than in forward flight. To find the collective pitch angle to trim it is best to use eqn 3.66, putting $q_c = 0$ and neglecting the small term in μh_{cD} , giving

$$\lambda_D = \delta(1 + 3\mu^2)/8t_{cD} \quad (4.25)$$

Since $t_{cD} = w_c$, λ_D can easily be calculated from eqn 4.25 and then substituted in eqn 3.63 to obtain θ_0 . The collective pitch variation with μ is shown in Fig. 4.19. The fact that it is practically constant follows from the need for an almost constant flow through the rotor to maintain zero torque, as can be seen from an inspection of eqn 4.25.

4.3.4 General remarks on performance estimation

The performance estimations discussed in this chapter have been based on very simple assumptions, particularly with regard to the aerodynamic properties of the

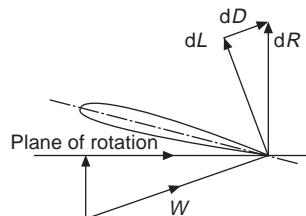


Fig. 4.18 Forces on aerofoil in autorotation

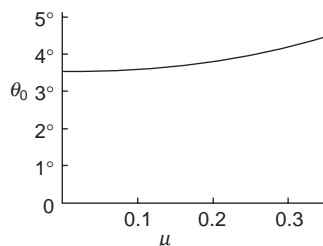


Fig. 4.19 Collective pitch to trim in autorotation

blades. One of the most important, and which has allowed a particularly simple analysis, is the assumption of constant blade section drag coefficient even though, as we shall discuss in detail in Chapter 6, the local incidence may vary over a wide range and enter the stall region.

An early attempt to consider the dependence of the drag coefficient δ on the incidence α was that of Bailey (1941)⁴, who assumed that

$$\delta = 0.0087 - 0.0216\alpha + 0.4\alpha^2$$

This expression was inserted into the same sort of analysis as presented in Chapter 3, using a tip loss factor $B = 0.97$, $\gamma = 15$, and an arbitrary amount of linear twist. The induced velocity was assumed to be constant.

As might be expected, the expressions for the force, torque, and flapping coefficients were quite complicated, partly on account of the presence of the tip-loss factor B .

For performance estimation, Bailey and Gustafson⁵ calculated the induced, fuselage, and tailrotor power contributions in a manner similar to that described in this chapter, but for the profile power Bailey's results were used by expressing them in chart form for zero blade twist. However, in order to use the charts it was still necessary to find the trim values of θ_0 and λ and also to interpolate between charts. Although Bailey's analysis would appear to contain a more accurate representation of the blade drag, it is doubtful if it justifies the extra complexity or even gives a more reliable value of the profile power; for example, the inclusion of the tip loss factor leads to many terms in B^4 and B^5 so that a bad choice of the value of B can clearly make a considerable difference to the final result. In any case, the value of B normally assumed is based on hovering flight theory and is not applicable to forward flight.

This illustrates the case against too great an expenditure of effort in estimating the performance of the rotor, as can be seen also by referring to Fig. 4.20. The figure shows the effective L/D ratio of the complete helicopter plotted against the L/D ratio

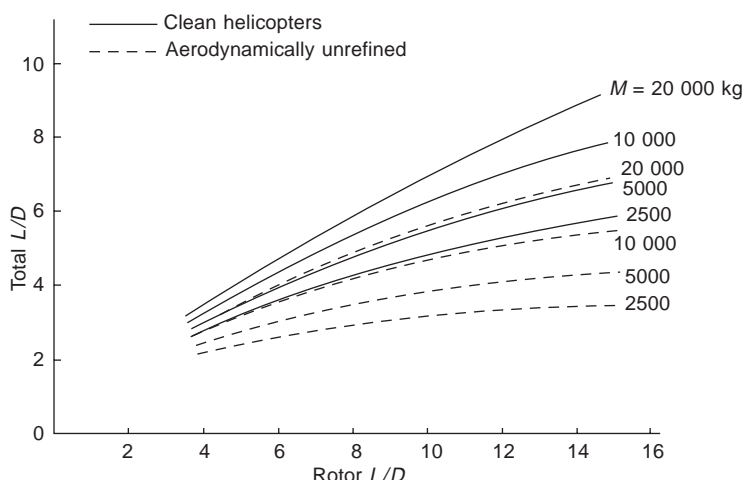


Fig. 4.20 Effect of L/D of rotor on L/D of complete helicopter

of the rotor alone. The effective drag has been calculated from the power expended, P , by

$$D = P/V$$

giving

$$L/D = VW/P = VW/(P_p + P_i + P_t + P_f)$$

where P_p , P_i , P_t , and P_f are, respectively, the blade profile drag and the induced, tailrotor, and fuselage power contributions.

At cruising speeds, i.e. for tip speed ratios of between, say, 0.25 and 0.35, it can be calculated from the data of Fig. 4.14 that the L/D ratio for the rotor alone of our example helicopter varies from about 7 to 10. Figure 4.20 shows that, at these values, a comparatively large increase of the L/D ratio of the rotor would be needed to produce a significant increase in the L/D ratio of the complete helicopter, especially at low values of the gross weight.

Thus, there is a limit to the expenditure of effort that ought reasonably to be spent in either making calculations of the rotor power or effecting real improvements in rotor performance through aerodynamic refinement.

What has been said above applies strictly to the calculation of the *performance* of the helicopter, by which we mean the estimation of the power for a given flight condition or the flight range possible for a given installed power. The high speed performance of modern helicopters, however, is far more likely to be restricted by the vibration and increase of control loads due to blade stall and compressibility than through lack of power. It is in this area that the aerodynamics of the rotor must be considered in sufficient detail to be able to design a rotor in which these undesirable effects are reduced to a minimum. The simple rotor force and flapping analysis of the previous chapter is no longer adequate, and more advanced methods are necessary. The complicated aerodynamics which need to be considered in these flight conditions will be described in Chapter 6.

References

1. Price, H. L., 'Rotor dynamics and helicopter stability', *Aircraft Engineering* March to July 1963.
2. Bramwell, A. R. S., 'Part I – the longitudinal stability and control of the tandem rotor helicopter. Part II – the lateral stability and control of the tandem rotor helicopter,' *Aeronautical Research Council R&M 3223*, 1961.
3. Stroub, R. H., Young, L. A., Graham, D. R. and Louie, A. W., 'Investigation of generic hub fairing and pylon shapes to reduce hub drag, Paper No. 2.9, 13th European Rotorcraft Forum, Arles, 8–11 Sept. 1987.
4. Bailey, F. J., jnr, 'A simplified theoretical method of determining the characteristics of a lifting rotor in forward flight', *NACA Rep. 716*, 1941.
5. Bailey, F. J., jnr and Gustafson, F. B., 'Charts for the estimation of the characteristics of a helicopter rotor in forward flight. I – profile drag-lift ratio for untwisted rectangular blades', *NACA ACR L4H07*, 1944.

Flight dynamics and control

5.1 Introduction

At first sight, the study of helicopter flight dynamics and control may seem very complicated, since each blade possesses degrees of freedom in addition to those of the fuselage. Fortunately, apart from some special cases of helicopter dynamic stability such as the phenomenon of air resonance to be considered in Chapter 9 a knowledge of the motion of the individual blades is not required, and for calculating the forces and moments in disturbed flight it is sufficient to consider only the behaviour of the rotor as a whole.

The simplifying assumptions which have enabled helicopter dynamics of flight and dynamic stability to be handled in ‘classical’ form are due mainly to the original work of Hohenemser¹ and Sissingh². These assumptions are as follows.

- (i) In disturbed flight the rotor behaves as if the motion were a sequence of steady conditions, i.e. the accelerations of the helicopter are small enough to have a negligible effect on the rotor response. This assumption was justified in Chapter 1 where it was shown that the rotating blade could be represented by a second order system having a natural frequency which is the same as the rotor angular frequency; typical disturbed motion corresponds to forcing the blade at a very low frequency ratio so that the rotor responds as if the instantaneous disturbance were being applied steadily.

The rotor can thus be regarded as responding instantaneously to speed and angular rates, just as is generally assumed for the fixed wing aircraft.

- (ii) The rotor speed remains constant. This assumption is justified because not only is the rotor speed controlled by the engine, but the changes of torque under normal steady flight conditions are quite small. In autogyro flight neither of these two conditions applies, and the rotor angular velocity variations may be quite considerable.
- (iii) Lateral and longitudinal motions are uncoupled and can be treated independently of one another, as is normally the case with the fixed wing aircraft. Now, we

have seen that the rotor tilts sideways with forward speed, and we shall meet other examples in which the lateral and longitudinal responses are coupled. Nevertheless, it is assumed that the effects of coupling are quite small, and, for the present purpose of studying the flight dynamics at a particular speed and configuration, may be ignored.

Before dealing with the flight dynamics and the dynamic stability problem analytically, let us consider the physical effects of velocity and angular rate disturbances on the helicopter.

5.1.1 Forward speed disturbance

We have seen in Chapters 3 and 4 that, for constant collective pitch and inflow ratio λ , the backward flapping angle a_1 of the disc is almost exactly proportional to forward speed. Figure 3.31, for example, shows that, even when θ_0 and λ vary in trimmed flight, a_1 is still roughly linear with forward speed, and it follows that when the forward speed is increased the rotor tilts back by an amount which is almost independent of the original flight speed; a typical value is 1° for about 10 m/s. It is found that the in-plane H -force, whose steady value is already very small, changes very little so it can be assumed that the rotor thrust force tilts back with the disc, Fig. 5.1.

The tilt of the thrust vector gives a backward force component, relative to the original flight direction, and a nose up pitching moment. The thrust also changes but, unlike the fixed wing aircraft, the change may be positive or negative depending on the flight speed; for example, at high forward speed, when the disc will be tilted forward at quite a large angle, a change of forward speed increases the flow through the disc, reducing the blade incidence and causing a loss of thrust. Of course, if in trimmed flight the thrust vector does not pass through the helicopter c.g., the change of thrust will also contribute to the pitching moment, but it is usually found that the total moment is dominated by the thrust tilt just described. With offset hinges or hingeless blades there is an additional moment due to the disc tilt alone, as discussed in Chapter 1. The fuselage drag also provides a substantial contribution to the backward force, particularly at high speed.

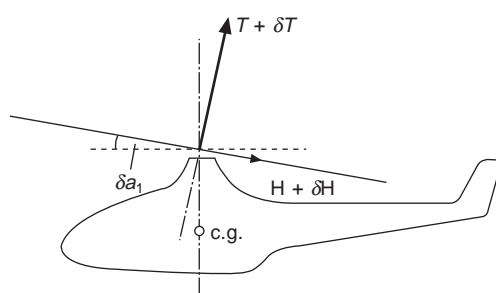


Fig. 5.1 Rotor force and flapping in disturbed flight

5.1.2 Vertical speed (incidence) disturbance

An upward (positive) velocity of the surrounding air mass imposed on the helicopter increases the incidence of all the blades, and there is a consequent increase of the total lift. The helicopter can be regarded as having a lift slope like a fixed wing aircraft, but, as we saw in Chapter 3, the local blade lift is proportional to the term $U_p U_T$ and, since the vertical velocity increases U_p by a constant amount, the change of lift depends on the chordwise velocity component U_T which is laterally asymmetric and has a maximum on the advancing side of the disc. Because of the 90° phase lag, this results in a backward tilt of the rotor disc producing a backward force component and a nose up pitching moment. The effect increases roughly linearly with speed and is zero in hovering flight. Thus, the helicopter rotor is unstable with respect to incidence and becomes progressively more so as forward speed increases. A tailplane is often fitted to provide positive incidence stability, but it is really effective only in the upper half of the speed range.

5.1.3 Pitching angular velocity disturbance

Imagine the helicopter to be pitching with constant angular velocity q and that the rotor is in equilibrium and pitching in space at the same rate. The rotor can then be regarded as a gyroscope which will therefore be subjected to a precessing moment tending to tilt it sideways. Because of the 90° response lag the rotor actually tilts in the longitudinal plane, causing longitudinal forces and moments. Now we know that a tilt of the rotor relative to the shaft produces cyclic pitch variations in the tip path (disc) plane and a consequent aerodynamic moment. The rotor disc will therefore tilt such that the aerodynamic moment is in equilibrium with the precessing moment. It is found that the nose up pitching of the helicopter produces a nose down tilt of the rotor. The corresponding nose down moment is in a favourable sense, i.e. it opposes the disturbance. We find that in this angular motion the rotor force does not remain perpendicular to the disc: the change of H -force is quite large and tilts the resultant force vector in the opposite direction to that of the disc, thereby reducing the moment. Under conditions of large inflow ratio, such as rapid climb, the sign of the moment may even be reversed. The destabilising effect of the H -force is less important when the moment is augmented by the presence of offset hinges or hingeless blades.

In addition to the precessing moment mentioned above, the pitching motion causes aerodynamic incidence changes which result in a lateral tilt of the rotor and therefore of lateral forces and moments (section 1.6.3). Typically, the lateral tilt is about half the longitudinal tilt. This is another example of the coupling between lateral and longitudinal motion.

The above discussion applies equally well to rolling motion and we see that rolling causes a moment in opposition to the motion, i.e. there is ‘damping in roll’, as with a fixed wing aeroplane, but for a given size of aircraft the helicopter roll damping is usually much weaker.

5.1.4 Sideslip disturbance

When the helicopter sideslips, i.e. when there is a component of wind relative to the undisturbed flight direction, it appears to the rotor as if the relative wind speed were unchanged but that it comes from a different direction. Thus the direction of maximum flapping of the rotor is merely rotated through the angle of sideslip and, as we shall see later, the change of sideways rotor flapping angle b_1 depends directly on the backward flapping angle a_1 and vice-versa. Since a_1 is usually much larger than b_1 , the main result is a sideways tilt of the rotor away from the side wind. There is therefore a rolling moment opposing the sideslip, corresponding to the dihedral effect of the fixed wing aircraft. Further, the blades of the tailrotor experience a change of incidence and the tailrotor acts like a fin producing favourable 'weathercock' stability.

5.1.5 Yawing disturbance

Yawing velocity causes a change of incidence at the tailrotor and, again, produces a favourable 'fin' effect – or 'damping in yaw'.

Summarising the above physical description of the effects of the disturbances, we can expect that the nose up pitching moments which arise with forward and vertical speed changes will result in longitudinal characteristics very different from those of the fixed wing aeroplane. On the other hand it is rather remarkable that, although the lateral force and moments arise in quite a different way from those of the conventional aeroplane, they have similar signs and we shall see that the stability characteristics are similar.

The dynamic stability analysis which now follows is formulated at the same level as the equivalent fixed wing analysis in standard undergraduate texts, and is subject to similar assumptions and approximations. For a fully comprehensive text on helicopter flight dynamics the reader is referred to Padfield³. The analysis begins with the longitudinal motion.

5.2 The longitudinal equations of motion

The equations of motion of a rigid body referred to axes fixed in the body are derived in Appendix A2. We found that the assumption of small disturbances enabled the inertia terms to be linearised and the lateral and longitudinal dynamic terms to be uncoupled. We have now to choose a suitable initial orientation of the axes in undisturbed flight. Several axes systems were discussed in Chapter 1, but none of them appears to have any particular advantage as an initial set for describing the dynamic stability. At the same time, the rotor forces have no special relationship with the undisturbed flow direction, as is the case with the conventional aeroplane, so the initial flight direction (wind axes) offers no advantage in expressing the aerodynamic forces. However, wind axes at least remove the terms qW_0 and pW_0 from the force equations A.2.12 and A.2.13 and have the advantage of being thoroughly established in fixed wing aircraft work.

We shall therefore use wind axes to describe the stability equations, i.e. in undisturbed flight the x axis is directed parallel to the flight path, with the z axis pointing downwards and the y axis pointing to starboard.

The linearised equations of longitudinal motion are therefore

$$(W/g)\dot{u} = -W\theta \cos \tau_c + \Delta X \quad (5.1)$$

$$(W/g)\dot{w} = -(W/g)V\dot{\theta} = -W\theta \sin \tau_c + \Delta Z \quad (5.2)$$

$$B\ddot{\theta} = \Delta M \quad (5.3)$$

where ΔX , ΔZ , ΔM are the aerodynamic force and moment increments in disturbed flight, Fig. 5.2, $\dot{\theta} = q$, and τ_c is the climb angle.

Since the disturbances in u , w , and q are supposed to be small, the force and moment increments can be written as the first terms of a Taylor series, i.e. ΔX can be written as

$$\begin{aligned} \Delta X &= \frac{\partial X}{\partial u}u + \frac{\partial X}{\partial w}w + \frac{\partial X}{\partial q}q + \frac{\partial X}{\partial B_1}B_1 + \frac{\partial X}{\partial \theta_0}\theta_0 \\ &= X_u u + X_w w + X_q q + X_{B_1} B_1 + X_{\theta_0} \theta_0 \end{aligned} \quad (5.4)$$

where u , w , etc. are understood to be differential quantities. B_1 and θ_0 are the cyclic and collective pitch control terms respectively. Similar expressions can be written for ΔZ and ΔM . The terms X_u , X_w , etc., are called aerodynamic derivatives in fixed wing aircraft work, but the term is less appropriate here because the force and moment increments are due to rotor disc tilt as well as to changes in aerodynamic forces. The derivatives are regarded as constants in disturbed motion. The variables B_1 and θ_0 are due to pilot (or possibly autostabiliser) action and are specified functions of time or of the other variables.

The stability eqns 5.1 to 5.3 can be written as

$$(W/g)\dot{u} - X_u u - X_w w - X_q q + W\theta \cos \tau_c = X_{B_1} B_1 + X_{\theta_0} \theta_0 \quad (5.5)$$

$$-Z_u u + (W/g)\dot{w} - Z_w w - Z_q q - (W/g)V\dot{\theta} + W\theta \sin \tau_c = Z_{B_1} B_1 + Z_{\theta_0} \theta_0 \quad (5.6)$$

$$-M_u u - M_w w - M_q q + B\ddot{\theta} = M_{B_1} B_1 + M_{\theta_0} \theta_0 \quad (5.7)$$

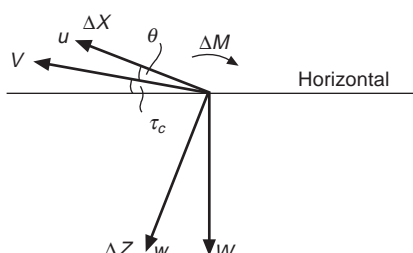


Fig. 5.2 Longitudinal force components in longitudinal plane

Apart from the form of the control terms, the equations are identical to those of the fixed wing aircraft. The term $M_{\dot{w}}\dot{w}$ allows for the effect of 'downwash lag' on the tailplane, if fitted, as in the fixed wing aircraft work.

5.2.1 Non-dimensionalisation of the equations

The fixed wing scheme of non-dimensionalisation can conveniently be used for the helicopter, but the following reference quantities are more useful:

- (i) the rotor blade radius R is the unit of length,
- (ii) the rotor tip speed ΩR is the unit of speed,
- (iii) the blade area $s\pi R^2 = sA$ is the reference area, where $s = bc/\pi R$ is the rotor solidity.

Let us define the following non-dimensional quantities:

$$\hat{u} = u/\Omega R$$

$$\hat{w} = w/\Omega R$$

$$\hat{q} = q/\Omega$$

The non-dimensional aerodynamic unit of time is defined by

$$\tau = t/\hat{t}$$

where $\hat{t} = W/g\rho s A \Omega R$.

Note that

$$\hat{q} \neq d\theta/d\tau; \quad \hat{q} = \frac{1}{\Omega \hat{t}} \frac{d\theta}{d\tau}$$

The helicopter longitudinal relative density parameter μ^* is defined by

$$\mu^* = W/g\rho s A R = \Omega \hat{t}$$

and the non-dimensional moment of inertia i_B is defined by

$$i_B = B/(WR^2/g)$$

Finally we define the non-dimensional derivatives as

$$\begin{array}{lll} x_u = X_u/\rho s A \Omega R, & x_w = X_w/\rho s A \Omega R, & x'_q = X_q/\rho s A \Omega R^2 \\ z_u = Z_u/\rho s A \Omega R, & z_w = Z_w/\rho s A \Omega R, & z'_q = Z_q/\rho s A \Omega R^2 \\ m'_u = M_u/\rho s A \Omega R^2, & m'_w = M_w/\rho s A \Omega R^2, & m'_q = M_q/\rho s A \Omega R^3 \\ x_{B_1} = X_{B_1}/\rho s A \Omega^2 R^2, & m'_{\dot{w}} = M_{\dot{w}}/\rho s A R^2 & m'_{B_1} = M_{B_1}/\rho s A \Omega^2 R^3 \\ x_{\theta_0} = X_{\theta_0}/\rho s A \Omega^2 R^2, & z_{B_1} = Z_{B_1}/\rho s A \Omega^2 R^2, & m'_{\theta_0} = M_{\theta_0}/\rho s A \Omega^2 R^3 \\ & z_{\theta_0} = Z_{\theta_0}/\rho s A \Omega^2 R^2, & \end{array}$$

Then dividing the force eqns 5.5 and 5.6 by $\rho sA\Omega^2R^2$ and the moment eqn 5.7 by $\rho sA\Omega^2R^3$ we have the non-dimensional form of the stability equations as

$$\frac{d\hat{u}}{d\tau} - x_u \hat{u} - x_w \hat{w} - \frac{x'_q}{\mu^*} \frac{d\theta}{d\tau} + w_c \theta \cos \tau_c = x_{B_l} B_l + x_{\theta_0} \theta_0 \quad (5.8)$$

$$-z_u \hat{u} + \frac{d\hat{w}}{d\tau} - z_w \hat{w} - \left(\hat{V} + \frac{z'_q}{\mu^*} \right) \frac{d\theta}{d\tau} + w_c \theta \sin \tau_c = z_{B_l} B_l + z_{\theta_0} \theta_0 \quad (5.9)$$

$$\begin{aligned} -\frac{\mu^*}{i_B} m'_u \hat{u} - \frac{\mu^*}{i_B} m'_w \hat{w} - \frac{m'_w}{i_B} \frac{d\hat{w}}{d\tau} + \frac{d^2\theta}{d\tau^2} - \frac{m'_q}{i_B} d\theta \\ = \frac{\mu^*}{i_B} m'_{B_l} B_l + \frac{\mu^*}{i_B} m'_{\theta_0} \theta_0 \end{aligned} \quad (5.10)$$

in which $w_c = W/\rho sA\Omega^2R^2$.

The above system of non-dimensionalisation, based on the original work of Bryant and Gates⁴, was intended to display the mass and inertia parameters represented by μ^* and i_B . However, in practice, the slight advantage does not justify the somewhat unwieldy notation and we propose here to write m_u for $\mu^* m'_u / i_B$, $x_q = x'_q / \mu^*$ etc. It was for this reason that a ‘dash’ was applied to some of the non-dimensional derivatives above, indicating that the final forms for these derivatives had yet to be defined.

Since, also, the non-dimensional variables \hat{u} and \hat{w} appear only in combination with the non-dimensional derivatives, which are written in lower case letters, there should be no ambiguity if \hat{u} and \hat{w} are written simply as u and w . Then the final non-dimensional form of the equations can be written as

$$\frac{du}{d\tau} - x_u u - x_w w - x_q \frac{d\theta}{d\tau} + w_c \theta \cos \tau_c = x_{B_l} B_l + x_{\theta_0} \theta_0 \quad (5.11)$$

$$-z_u u + \frac{dw}{d\tau} - z_w w - (\hat{V} + z_q) \frac{d\theta}{d\tau} + w_c \theta \sin \tau_c = z_{B_l} B_l + z_{\theta_0} \theta_0 \quad (5.12)$$

$$-m_u u - m_w w - m_{\dot{w}} \frac{dw}{d\tau} + \frac{d^2\theta}{d\tau^2} - m_q \frac{d\theta}{d\tau} = m_{B_l} B_l + m_{\theta_0} \theta_0 \quad (5.13)$$

5.3 Longitudinal dynamic stability

To study the longitudinal dynamic stability, the controls are assumed fixed. It is worth noting here that in comparing the stability of a helicopter with that of a fixed wing aircraft, the concept of static stability is not as meaningful because of the relative lack of importance of the c.g. position in determining the longitudinal behaviour of the helicopter. Neither is the concept of stick-free stability, due to the inherent instability with respect to incidence at low speeds (section 5.1.2), and lack of a natural force feedback to the pilot’s controls that relates to longitudinal control (as in the case for fixed wing aircraft).

Thus we put $B_1 = \theta_0 = 0$, remembering that, in the equations, B_1 and θ_0 are variations from the trim values. We also find that z_q is always zero and that x_q is negligibly small.

Equations 5.11, 5.12, and 5.13 are linear differential equations with constant coefficients, and to solve them we put*

$$u = u_0 e^{\lambda\tau}, \quad w = w_0 e^{\lambda\tau}, \quad \theta = \theta_0 e^{\lambda\tau}$$

where u_0 , w_0 , θ_0 , and λ are constants.

Substituting in eqns 5.11, 5.12, and 5.13 and cancelling throughout by $e^{\lambda\tau}$ we obtain

$$(\lambda - x_u) u_0 - x_w w_0 + w_c \theta_0 \cos \tau_c = 0 \quad (5.14)$$

$$-z_u u_0 + (\lambda - z_w) w_0 - (\hat{V}\lambda - w_c \sin \tau_c) \theta_0 = 0 \quad (5.15)$$

$$-m_u u_0 - (\lambda m_{\dot{w}} + m_w) w_0 + (\lambda^2 - m_q \lambda) \theta_0 = 0 \quad (5.16)$$

For non-trivial and consistent values of u_0 , w_0 , θ_0 it is necessary for the determinant of the coefficients in eqns 5.14, 5.15, and 5.16 to be zero, i.e. for

$$\begin{vmatrix} \lambda - x_u & -x_w & w_c \cos \tau_c \\ -z_u & \lambda - z_w & -(\hat{V}\lambda - w_c \sin \tau_c) \\ -m_u & -(\lambda m_{\dot{w}} + m_w) & \lambda^2 - m_q \lambda \end{vmatrix} = 0$$

Expanding this determinant leads to the characteristic equation

$$A_1 \lambda^4 + B_{1c} \lambda^3 + C_1 \lambda^2 + D_1 \lambda + E_1 = 0 \quad (5.17)$$

where

$$A_1 = 1$$

$$B_{1c} = N_1 - m_q - \hat{V}m_{\dot{w}} \dagger \quad (5.18)$$

$$C_1 = P_1 - N_1 m_q - Q_1 m_{\dot{w}} - \hat{V}m_w \quad (5.19)$$

$$D_1 = S_1 m_u - P_1 m_q - R_1 m_{\dot{w}} - Q m_w \quad (5.20)$$

$$E_1 = T_1 m_u - R_1 m_w \quad (5.21)$$

and

$$N_1 = -x_u - z_w \quad (5.22)$$

* Care must be taken not to confuse θ_0 here with the collective pitch angle; from this point down to eqn (5.16) θ_0 refers to the maximum amplitude of pitch θ of the whole aircraft.

† B_{1c} as a coefficient of the characteristic equation is distinct from B_1 , the longitudinal cyclic pitch angle.

$$P_1 = x_u z_w - x_w z_u \quad (5.23)$$

$$Q_1 = -\hat{V}x_u - w_c \sin \tau_c \quad (5.24)$$

$$R_1 = -w_c(z_u \cos \tau_c - x_u \sin \tau_c) \quad (5.25)$$

$$S_1 = w_c \cos \tau_c - \hat{V}x_w \quad (5.26)$$

$$T_1 = -w_c(z_w \cos \tau_c - x_w \sin \tau_c) \quad (5.27)$$

the suffix 1 denoting longitudinal coefficients.

Equation 5.17 will have four roots $\lambda_1, \lambda_2, \lambda_3, \lambda_4$ which may be either real or complex. Thus the general solution for u can be written

$$u = c_1 e^{\lambda_1 \tau} + c_2 e^{\lambda_2 \tau} + c_3 e^{\lambda_3 \tau} + c_4 e^{\lambda_4 \tau} \quad (5.28)$$

where the constants c_1, c_2, c_3 , and c_4 can be determined from the initial conditions. Solutions for w and θ can be written in the same way.

Since we are concerned here only with the stability of the motion, we need consider only the values of λ .

When λ is real and positive, $e^{\lambda \tau}$ increases without limit and the motion is known as a *divergence*, Fig. 5.3.

When λ is real and negative, $e^{\lambda \tau}$ decreases steadily to zero and the motion is known as a *subsidence*, Fig. 5.3.

When λ is complex it can be written as

$$\lambda = \lambda_{re} \pm i\lambda_{im}$$

since the complex roots always appear as conjugate pairs.

The mode of motion corresponding to this pair of roots can be expressed as

$$u = k_1 e^{\lambda_{re} \tau} \sin \lambda_{im} \tau + k_2 e^{\lambda_{re} \tau} \cos \lambda_{im} \tau \quad (5.29)$$

If λ_{re} is positive, the motion is a divergent oscillation, Fig. 5.4; if λ_{re} is negative, the motion is a convergent or damped oscillation.

The rate at which these motions subside or diverge is determined from the real values or real parts of λ . It is usual to express this rate as the time to halve or to double the amplitude of the motion. It can easily be seen that the time to half amplitude T_h is given by

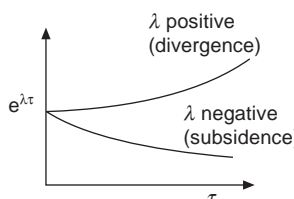
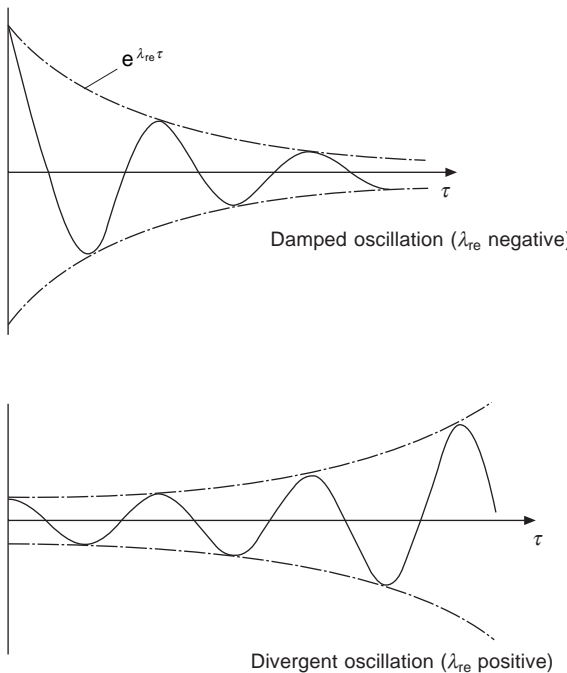


Fig. 5.3 Divergence and subsidence

**Fig. 5.4** Damped and divergent oscillations

$$T_h = \ln 2\hat{t}/(-\lambda) = 0.693\hat{t}/(-\lambda) \quad (5.30)$$

when λ is real and negative or

$$T_h = 0.693\hat{t}/(-\lambda_{re}) \quad (5.31)$$

when λ is complex and λ_{re} is negative.

The time to double amplitude, T_d , is given by

$$T_d = 0.693\hat{t}/\lambda \quad (5.32)$$

for real and positive λ

$$\text{or } T_d = 0.693\hat{t}/\lambda_{re} \quad (5.33)$$

when λ is complex and λ_{re} positive.

From eqn 5.29 it can be seen that the periodic time, T , is given by

$$\lambda_{im}\tau = \lambda_{im}T/\hat{t} = 2\pi$$

i.e.

$$T = 2\pi\hat{t}/\lambda_{im} \quad (5.34)$$

5.4 Calculation of the derivatives

The main contributions to the incremental forces and moments arise from the rotor, as discussed at the beginning of this chapter. We have also assumed, with good justification, that the rotor forces and moments, like those of the fixed wing aircraft, depend only on the instantaneous values of speed, incidence, and rate of pitch. To calculate the derivatives, then, it is necessary only to resolve the rotor forces onto the chosen axes and perform straightforward differentiation on the expressions for force and flapping in Chapter 3. Some of the fuselage contributions can be calculated with fair confidence, particularly those of the tailplane.

As far as the rotor calculations are concerned it does not matter whether tip path plane (disc) axes or no-feathering axes are used but, as we found in Chapter 3, the H -force is usually very small when the rotor forces are expressed in terms of either set of axes, and this is an aid in the physical appreciation of the problem. We shall therefore use disc axes in general in our analysis but occasionally use no-feathering axes when it makes the differentiation easier.

Referring to Fig. 5.5, let α_D be the disc incidence in steady flight. In disturbed flight the longitudinal flapping increases by amount δa_1 and the incidence of the wind axes is $\alpha \approx w/V$. Resolving the thrust and in-plane force along the wind axes, we get

$$\begin{aligned}\delta X &= -(T_D + \delta T_D) \sin(\alpha_D + \delta a_1) - (H_D + \delta H_D) \cos(\alpha_D + \delta a_1) - T_D \sin \alpha_D \\ &\quad - H_D \cos \alpha_D \\ &\approx -T_D \delta a_1 - \delta T_D \alpha_D - \delta H_D\end{aligned}$$

since α_D and δa_1 are small angles.

Also

$$\begin{aligned}\delta Z &= -(T_D + \delta T_D) \cos(\alpha_D + \delta a_1) + (H_D + \delta H_D) \sin(\alpha_D + \delta a_1) \\ &\quad + T_D \cos \alpha_D - H_D \sin \alpha_D \\ &\approx -\delta T_D + \delta H_D \alpha_D + H_D \delta a_1 \\ &\approx -\delta T_D\end{aligned}$$

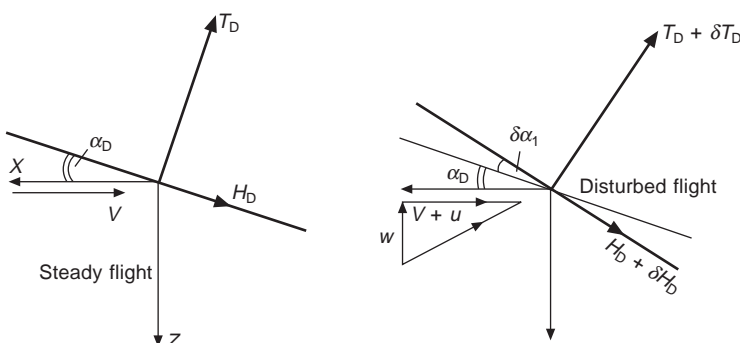


Fig. 5.5 Longitudinal forces and flapping in disturbed flight

since the terms in H_D are very small.

Then

$$X_u = \frac{\partial X}{\partial u} = -T_D \frac{\partial a_1}{\partial u} - \alpha_D \frac{\partial T_D}{\partial u} - \frac{\partial H}{\partial u} \quad (5.35)$$

$$Z_u = \frac{\partial Z}{\partial u} = -\frac{\partial T_D}{\partial u} \quad (5.36)$$

$$X_w = \frac{\partial X}{\partial w} = -T_D \frac{\partial a_1}{\partial w} - \alpha_D \frac{\partial T_D}{\partial w} - \frac{\partial H_D}{\partial w} \quad (5.37)$$

$$Z_w = \frac{\partial Z}{\partial w} = -\frac{\partial T_D}{\partial w} \quad (5.38)$$

$$X_q = \frac{\partial X}{\partial q} = -T_D \frac{\partial a_1}{\partial q} - \alpha_D \frac{\partial T_D}{\partial q} - \frac{\partial H_D}{\partial q} \quad (5.39)$$

$$Z_q = \frac{\partial Z}{\partial q} = -\frac{\partial T_D}{\partial q} \quad (5.40)$$

Now, since the disc makes a small angle to the x axis, we can write

$$\frac{d}{du} = \frac{1}{\Omega R} \frac{d}{d\hat{u}} \approx \frac{1}{\Omega R} \frac{d}{d\mu_D} \approx \frac{1}{\Omega R} \frac{d}{d\mu}$$

Then

$$x_u = \frac{X_u}{\rho s A \Omega R} = -t_c \frac{\partial a_1}{\partial \mu} - \alpha_D \frac{\partial t_c}{\partial \mu} - \frac{\partial h_{cD}}{\partial \mu} \quad (5.41)$$

and similarly

$$z_u = -\frac{\partial t_c}{\partial \mu} \quad (5.42)$$

$$x_w = -t_c \frac{\partial a_1}{\partial \hat{w}} - \alpha_D \frac{\partial t_c}{\partial \hat{w}} - \frac{\partial h_{cD}}{\partial \hat{w}} \quad (5.43)$$

$$z_w = -\frac{\partial t_c}{\partial \hat{w}} \quad (5.44)$$

$$x_q = -t_c \frac{\partial a_1}{\partial \hat{q}} - \alpha_D \frac{\partial t_c}{\partial \hat{q}} - \frac{\partial h_{cD}}{\partial \hat{q}} \quad (5.45)$$

$$z_q = -\frac{\partial t_c}{\partial \hat{q}} \quad (5.46)$$

To calculate the moment derivatives, we see from Fig. 5.6 that the moment of the rotor forces δM_r about the c.g. is

$$\begin{aligned} \delta M_r &= (-\delta X \cos \alpha_s + \delta Z \sin \alpha_s) lR + (\delta Z \cos \alpha_s + \delta X \sin \alpha_s) hR \\ &= -h_1 R \delta X + l_1 R \delta Z \end{aligned}$$

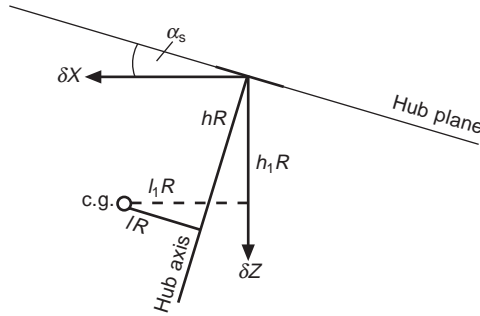


Fig. 5.6 Force components contributing to longitudinal moment

where

$$\begin{aligned} h_1 &= h \cos \alpha_s - l \sin \alpha_s \\ &\approx h - l\alpha_s \end{aligned}$$

and

$$\begin{aligned} l_1 &= l \cos \alpha_s + h \sin \alpha_s \\ &\approx l + h\alpha_s \end{aligned}$$

α_s being the incidence of the rotor hub axis in trimmed flight.

In addition to the moment of the forces there is the hub moment due to offset hinges or hingeless blades, $M_s \delta a_1$, and the fuselage pitching moment δM_f . Hence the total moment increment is

$$\delta M = -h_1 R \delta X + l_1 R \delta Z + M_s \delta a_1 + \delta M_f$$

from which

$$M_u = -h_1 R X_u + l_1 R Z_u + M_s \frac{\partial a_1}{\partial u} + (M_u)_f \quad (5.47)$$

$$M_w = -h_1 R X_w + l_1 R Z_w + M_s \frac{\partial a_1}{\partial w} + (M_w)_f \quad (5.48)$$

$$M_q = -h_1 R X_q + l_1 R Z_q + M_s \frac{\partial a_1}{\partial q} + (M_q)_f \quad (5.49)$$

which, in non-dimensional form, become

$$m'_u = -h_1 x_u + l_1 z_u + C_{m_s} \frac{\partial a_1}{\partial \mu} + (m_u)_f \quad (5.50)$$

$$m'_w = -h_1 x_w + l_1 z_w + C_{m_s} \frac{\partial a_1}{\partial \hat{w}} + (m_w)_f \quad (5.51)$$

$$m'_q = -h_1 x_q + l_1 z_q + C_{m_s} \frac{\partial a_1}{\partial \hat{q}} + (m_q)_f \quad (5.52)$$

with

$$m_u = \frac{\mu^*}{i_B} m'_u, \quad m_w = \frac{\mu^*}{i_B} m'_w, \quad m_q = -\frac{m'_q}{i_B}$$

The moment derivatives can also be expressed in terms of the thrust and in-plane forces. It can easily be verified that

$$\delta M = -(l - ha_{1s})R\delta T + hR(T\delta a_1 + \delta H) + M_s\delta a_1 + \delta M_f$$

where $a_{1s} = a_1 - B_1$, which is a small angle.

Then

$$m'_u = -(l - ha_{1s}) \frac{\partial t_c}{\partial \mu} + h \left(t_c \frac{\partial a_1}{\partial \mu} + \frac{\partial h_{cD}}{\partial \mu} \right) + C_{m_s} \frac{\partial a_1}{\partial \mu} + (m_u)_f \quad (5.53)$$

$$m'_w = -(l - ha_{1s}) \frac{\partial t_c}{\partial \hat{w}} + h \left(t_c \frac{\partial a_1}{\partial \hat{w}} + \frac{\partial h_{cD}}{\partial \hat{w}} \right) + C_{m_s} \frac{\partial a_1}{\partial \hat{w}} + (m_w)_f \quad (5.54)$$

$$m'_q = -(l - ha_{1s}) \frac{\partial t_c}{\partial \hat{q}} + h \left(t_c \frac{\partial a_1}{\partial \hat{q}} + \frac{\partial h_{cD}}{\partial \hat{q}} \right) + C_{m_s} \frac{\partial a_1}{\partial \hat{q}} + (m_q)_f \quad (5.55)$$

5.4.1 The rotor force and flapping derivatives

To complete the calculation of the sets of force and moment derivatives above, we need the basic rotor force and flapping derivatives $\partial t_c / \partial \mu$, $\partial a_1 / \partial \hat{w}$, ..., etc. Now one of the important variables in the expressions for t_c , h_c and a_1 is the inflow ratio λ (or λ_D), and it will be useful to find its derivatives first.

In order to do this, it will be assumed that the inflow remains constant for the purpose of subsequent differentiation. In fact, the thrust coefficient, for example, has an effect on the inflow via the lift deficiency function familiar in fixed wing aircraft aerodynamic theory. This can be developed (see Johnson⁵) to provide a relationship between local (elemental) momentum theory and local elemental lift which leads to expressions for pitch and roll. These are dependent on the coefficients of an expression for the local induced velocity coefficient which depends on radial position and harmonically on azimuth angle. Pitt and Peters⁶, and Peters and Ha Quang⁷ have formalised this 'dynamic inflow' approach and demonstrated its applicability in the flight mechanics of manoeuvring flight.

However, the present development is aimed at a more elementary level, and thus the inflow, as mentioned above, will be held constant whilst differentiating to obtain the derivatives. Since t_{cD} and t_c are almost identical, it is convenient to use eqn 3.33 for the relation between the thrust coefficient and the inflow ratio; i.e. starting from

$$t_c = \frac{a}{4} \left[\frac{2}{3} \theta_0 (1 + 3\mu^2/2) + \lambda \right] \quad (3.33)$$

where λ is referred to the no-feathering axis, we differentiate with respect to μ to obtain

$$(4/a)\partial t_c/\partial \mu = 2\mu\theta_0 + \partial \lambda/\partial \mu \quad (5.56)$$

Now, for small α_{nf}

$$\lambda = \mu\alpha_{nf} - \lambda_i$$

where λ_i is the mean ‘momentum’ inflow ratio, therefore

$$\partial \lambda/\partial \mu = \alpha_{nf} - \partial \lambda_i/\partial \mu \quad (5.57)$$

since α_{nf} remains constant with changes of μ .

In non-dimensional form, eqn 3.1 can be written (for small α_D)

$$\lambda_i = st_c/2(\hat{V}^2 + \lambda_i^2)^{1/2}$$

so that

$$\frac{\partial \lambda_i}{\partial \mu} = \frac{s}{2(\hat{V}^2 + \lambda_i^2)^{1/2}} \frac{\partial t_c}{\partial \mu} - \frac{st_c}{2(\hat{V}^2 + \lambda_i^2)^{3/2}} \left(\hat{V} + \lambda_i \frac{\partial \lambda_i}{\partial \mu} \right)$$

since $\partial/\partial \mu \approx \partial/\partial \hat{V}$, or

$$\frac{\partial \lambda_i}{\partial \mu} = \frac{\lambda_i}{t_c} \frac{\partial t_c}{\partial \mu} - \frac{4\hat{V}\lambda_i^3}{s^2 t_c^2} - \frac{4\lambda_i^4}{s^2 t_c^2} \frac{\partial \lambda_i}{\partial \mu} \quad (5.58)$$

Further, the induced velocity in hovering flight, or ‘thrust velocity’ v_0 (Chapter 2) is related to the thrust coefficient by

$$v_0^2 = \frac{1}{2}st_c\Omega^2 R^2$$

so that eqn 5.58 can also be written as

$$\frac{\partial \lambda_i}{\partial \mu} = \frac{\lambda_i}{t_c} \frac{\partial t_c}{\partial \mu} - \bar{V}\bar{v}_i^3 - \bar{v}_i^4 \frac{\partial \lambda_i}{\partial \mu} \quad (5.59)$$

where $\bar{V} = V/v_0$ and $\bar{v}_i = v_i/v_0$, and \bar{v}_i can be taken from the chart, Fig. 3.2.

Then, from eqns 5.56, 5.57 and 5.59, we find,

$$\frac{\partial \lambda_i}{\partial \mu} = \frac{2\mu\theta_0 + \alpha_{nf} - (4t_c/a\lambda_i) \bar{V}\bar{v}_i^3}{1 + (4t_c/a\lambda_i)(1 + \bar{v}_i^4)} \quad (5.60)$$

For $\mu > 0.08$ (See sections 3.2 and 3.14)

$$\lambda_i \approx st_c/2\mu \quad \text{and} \quad \bar{v}_i^4 \ll 1$$

and eqn 5.60 can be written

$$\frac{\partial \lambda_i}{\partial \mu} = \frac{2\mu\theta_0 + \alpha_{nf} - 4t_c/a\mu}{1 + 8\mu/as} \quad (5.61)$$

The incidence, α_{nf} can be written alternatively as $\alpha_D - a_1$.

With $\partial \lambda_i/\partial \mu$ known, it is now possible to obtain $\partial t_c/\partial \mu$. Eliminating $\partial \lambda_i/\partial \mu$ from eqn 5.59 using eqn 5.60 gives

$$\frac{\partial t_c}{\partial \mu} = \frac{2\mu\theta_0 + \alpha_D - a_1 + \bar{V}\bar{v}_i^3/(1+\bar{v}_i^4)}{4/a + (\lambda_i/t_c)/(1+\bar{v}_i^4)} \quad (5.62)$$

and for $\mu > 0.08$ this simplifies to

$$\frac{\partial t_c}{\partial \mu} = \frac{2a\mu}{8\mu + as} (2\mu\theta_0 + \alpha_D - a_1 + st_c/2\mu^2) \quad (5.63)$$

We note that $\partial\lambda_i/\partial\mu$ and $\partial t_c/\partial\mu$ are both zero in hovering flight.

To find $\partial a_1/\partial\mu$ it is convenient to use the expression for a_1 with λ referred to the no-feathering axis, eqn 3.56

$$a_1 = \frac{2\mu(4\theta_0/3 + \lambda)}{1 - \mu^2/2} \quad (3.56)$$

Differentiating with respect to μ and rearranging gives

$$\frac{\partial a_1}{\partial \mu} = \frac{a_1}{\mu} - \frac{2\mu}{1 - \mu^2/2} \frac{\partial \lambda}{\partial \mu} \quad (5.64)$$

When μ is zero, eqn 5.64 reduces to

$$\partial a_1 / \partial \mu = 8\theta_0/3 + 2\lambda \quad (5.65)$$

To calculate $\partial h_{cD}/\partial\mu$ we differentiate eqn 3.64; numerical examples show, however, that only the profile drag term is of any importance, and we have simply

$$\partial h_{cD} / \partial \mu = \frac{1}{4} \quad (5.66)$$

When considering derivatives with respect to the vertical velocity w , the component of flow through the rotor must be expressed as $\lambda_i - \hat{w}$ before differentiating. This expression of the flow component is not valid if the flight path is steep, for then the z axis, i.e. the w direction, makes a considerable angle to the rotor axis. However, steep flight paths are possible in only a narrow range at low forward speed and overall provide no practical restriction. The induced velocity ratio must then be written

$$\lambda_i = st_c/2[\hat{V}^2 + (\lambda_i - \hat{w})^2]^{1/2} \quad (5.67)$$

where \hat{w} is made zero after differentiation.

Differentiating eqn 5.67 with respect to \hat{w} gives

$$\begin{aligned} \frac{\partial \lambda_i}{\partial \hat{w}} &= \frac{s}{2(\hat{V}^2 + \lambda_i^2)^{1/2}} \frac{\partial t_c}{\partial \hat{w}} - \frac{st_c(\partial \lambda_i / \partial \hat{w} - 1)\lambda_i}{2[\hat{V}^2 + (\lambda_i - \hat{w})^2]^{3/2}} \\ &= \frac{\lambda_i}{t_c} \frac{\partial t_c}{\partial \hat{w}} + \frac{4\lambda_i^4}{s^2 t_c^2} \left(1 - \frac{\partial \lambda_i}{\partial \hat{w}}\right) \\ &= \frac{\lambda_i}{t_c} \frac{\partial t_c}{\partial \hat{w}} + \bar{v}_i^4 \left(1 - \frac{\partial \lambda_i}{\partial \hat{w}}\right) \end{aligned} \quad (5.68)$$

Writing $\lambda = \hat{V} \sin \alpha_{\text{nf}} - \lambda_i$

$$\frac{\partial \lambda}{\partial \hat{w}} = \hat{V} \cos \alpha_{\text{nf}} \frac{\partial \alpha_{\text{nf}}}{\partial \hat{w}} - \frac{\partial \lambda_i}{\partial \hat{w}}$$

But, except for steep flight paths, it is clear from Fig. 5.7 that the change of incidence $\delta\alpha_{\text{nf}}$ of the no-feathering axis due to the disturbance w is

$$\delta\alpha_{\text{nf}} = w/V$$

i.e.

$$\frac{\partial \alpha_{\text{nf}}}{\partial \hat{w}} = 1/\hat{V}$$

Thus, providing α_{nf} is not too large (so that $\cos \alpha_{\text{nf}} \approx 1$),

$$\frac{\partial \lambda}{\partial \hat{w}} = 1 - \frac{\partial \lambda_i}{\partial \hat{w}} \quad (5.69)$$

Since

$$\lambda_D = \lambda + \mu a_1$$

the derivative of λ_D is

$$\frac{\partial \lambda_D}{\partial \hat{w}} = \frac{\partial \lambda}{\partial \hat{w}} + \mu \frac{\partial a_1}{\partial \hat{w}} \quad (5.70)$$

Differentiating eqn 3.33

$$\begin{aligned} \frac{\partial t_c}{\partial \hat{w}} &= \frac{a}{4} \frac{\partial \lambda}{\partial \hat{w}} \\ &= \frac{a}{4} \left(1 - \frac{\partial \lambda_i}{\partial \hat{w}} \right) \end{aligned} \quad (5.71)$$

Hence, from eqn 5.68,

$$\frac{\partial \lambda_i}{\partial \hat{w}} = \frac{(a/4)\lambda_i/t_c + \bar{v}_i^4}{1 + (a/4)\lambda_i/t_c + \bar{v}_i^4} \quad (5.72)$$

so that

$$\frac{\partial \lambda}{\partial \hat{w}} = \frac{1}{1 + (a/4)\lambda_i/t_c + \bar{v}_i^4} \quad (5.73)$$

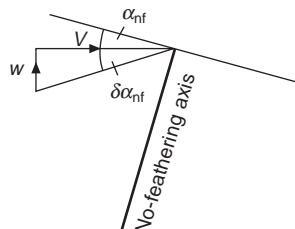


Fig. 5.7 Change of incidence of no-feathering axis

and

$$\frac{\partial t_c}{\partial \hat{w}} = \frac{a}{4} \frac{1}{1 + (a/4)\lambda_i/t_c + \bar{v}_i^4} \quad (5.74)$$

Differentiating eqn 3.56 gives

$$\begin{aligned} \frac{\partial a_1}{\partial \hat{w}} &= \frac{2\mu}{1 - \mu^2/2} \frac{\partial \lambda}{\partial \hat{w}} \\ &= \frac{2\mu}{(1 - \mu^2/2)(1 + (a/4)\lambda_i/t_c + \bar{v}_i^4)} \end{aligned} \quad (5.75)$$

Then, from eqn 5.70,

$$\frac{\partial \lambda_D}{\partial \hat{w}} = \frac{1}{1 + (a/4)\lambda_i/t_c + \bar{v}_i^4} \cdot \frac{1 + 3\mu^2/2}{1 - \mu^2/2} \quad (5.76)$$

and so we have from eqn 3.64

$$\frac{\partial h_{cD}}{\partial \hat{w}} = \frac{a}{4(1 + (a/4)\lambda_i/t_c + \bar{v}_i^4)} \left(\frac{1}{2}a_1 - \mu\theta_0 + \frac{\mu\lambda_D}{1 - \mu^2/2} \right) \quad (5.77)$$

The derivatives 5.74, 5.75, and 5.77 can be simplified for most of the speed range. For $\mu = 0$, $\bar{v}_i = 1$ and $st_c = 2\lambda_i^2$, and we have

$$\partial t_c / \partial \hat{w} = -z_w = 2a\lambda_i / (16\lambda_i + as) \quad (5.78)$$

and

$$\partial a_1 / \partial \hat{w} = \partial h_{cD} / \partial \hat{w} = 0$$

For $\mu > 0.08$, $\bar{v}_i \approx 0$ and $st_c = 2\mu\lambda_i$, and we have

$$\frac{\partial t_c}{\partial \hat{w}} = -z_w = \frac{2a\mu}{8\mu + as} \quad (5.79)$$

$$\frac{\partial a_1}{\partial \hat{w}} = \frac{16\mu^2}{(1 - \mu^2/2)(8\mu + as)} \quad (5.80)$$

and

$$\frac{\partial h_{cD}}{\partial \hat{w}} = \frac{4a\mu^2}{8\mu + as} \frac{\theta_0(1 - 9\mu^2/2)/6 + \lambda_D}{1 - \mu^2/2} \quad (5.81)$$

5.4.2 The q-derivatives

In the equation for the thrust coefficient,

$$t_c = \frac{a}{4} \left[\frac{2}{3} \theta_0 (1 + 3\mu^2/2) + \lambda \right] \quad (3.33)$$

all the terms are independent of the pitch rate q ; therefore

$$\partial t_c / \partial \hat{q} = -z_q = 0$$

Now a rate of pitch applied to the rotor shaft gives rise to extra aerodynamic and inertia terms in the flapping equation. According to eqn 1.16 we must add the terms $\gamma \hat{q} \cos \psi / 8 - 2\hat{q} \sin \psi$ to the right-hand side of eqn 3.48. Then we find, from examination of the various harmonic terms, that the longitudinal flapping Δa_1 due to the rate of pitch is

$$\Delta a_1 = -\frac{16}{\gamma} \cdot \frac{\hat{q}}{1 - \mu^2/2}$$

or

$$\frac{\partial a_1}{\partial \hat{q}} = -\frac{16}{\gamma} \cdot \frac{1}{1 - \mu^2/2} \quad (5.82)$$

We find that the aerodynamic incidence changes represented by the term $2\hat{q} \sin \psi$ cause sideways flapping given by

$$\frac{\partial b_1}{\partial \hat{q}} = -\frac{1}{(1 + \mu^2/2)} \quad (5.83)$$

Also, from eqn 3.51, it follows that

$$\partial a_0 / \partial \hat{q} = 0 \quad (5.84)$$

Due to the pitching motion, the normal velocity at the rotor blade becomes modified to

$$U_P = \Omega R(\lambda_D - \mu a_0 \cos \psi + x\hat{q} \cos \psi)$$

Using this expression in the calculation of the in-plane force H_D , we find for its coefficient

$$h_{cD} = \frac{1}{4} \mu \delta - \frac{a}{4} \left[\frac{1}{3} a_0 b_1 - \frac{1}{2} \mu a_0^2 + \frac{1}{3} a_0 \hat{q} - \frac{1}{2} a_1 \lambda_D + \mu \theta_0 \lambda_D + \frac{1}{8} \mu b_1 \hat{q} \right] \quad (5.85)$$

or, in terms of λ (referred to the no-feathering axis),

$$h_{cD} = \frac{1}{4} \mu \delta - \frac{a}{4} \left[\frac{1}{3} a_0 b_1 - \frac{1}{2} \mu a_0^2 + \frac{1}{3} a_0 \hat{q} - \frac{1}{2} a_1 \lambda - \frac{1}{2} \mu a_1^2 + \mu \theta_0 \lambda + \mu^2 \theta_0 a_1 + \frac{1}{8} \mu b_1 \hat{q} \right] \quad (5.86)$$

In these expressions for h_{cD} we have not cancelled the first two terms in the brackets, as in eqn 3.39. Then differentiating eqn 5.86, using eqns 5.83 and 5.84, and remembering that $\partial \lambda / \partial \hat{q} = 0$, gives

$$\begin{aligned} \frac{\partial h_{cD}}{\partial \hat{q}} = & -\frac{a}{4} \left[\frac{-a_0/3}{(1 + \mu^2/2)} + \frac{1}{3} a_0 - \frac{1}{2} \lambda \frac{\partial a_1}{\partial \hat{q}} - \mu a_1 \frac{\partial a_1}{\partial \hat{q}} + \mu^2 \theta_0 \frac{\partial a_1}{\partial \hat{q}} \right. \\ & \left. + \frac{1}{8} \mu b_1 - \frac{\mu \hat{q}}{8(1 + \mu^2/2)} \right] \end{aligned}$$

Typically \hat{q} is very small compared with a_0 , a_1 , b_1 and the final term in this

expression may be neglected. Assuming that \hat{q} does not alter the induced velocity unduly, then the same assumptions that followed eqn 3.38 may be made, leading to

$$\frac{\partial h_{c_D}}{\partial \hat{q}} = \frac{a}{4} \left[\frac{1}{2} \lambda + \mu a_1 - \mu^2 \theta_0 \right] \frac{\partial a_1}{\partial \hat{q}} - \frac{a}{12} \frac{\mu^2 a_0}{(1 + \mu^2/2)}$$

Again, the final term involving μ^2 can be shown to be small compared with the bracketed term and may be neglected, leading to

$$\frac{\partial h_{c_D}}{\partial \hat{q}} = - \frac{4a}{\gamma(1 - \mu^2/2)} \left[\frac{1}{2} \lambda + \mu a_1 - \mu^2 \theta_0 \right] \quad (5.87)$$

Since $\partial t_c / \partial \hat{q}$ is zero, eqn 5.55 becomes

$$m'_q = - \frac{4ah}{\gamma(1 - \mu^2/2)} \left[\frac{2}{3} \theta_0 + \frac{3}{2} \lambda + \mu a_1 \right] - \frac{16 C_{m_s}}{\gamma(1 - \mu^2/2)} + (m_q)_f \quad (5.88)$$

Equation 5.87 displays the ‘Amer effect’⁸, i.e. the considerable and destabilising change of the in-plane force during pitching, the terms in the square bracket of eqn 5.87 adding to those of t_c , eqn 3.33. In hovering flight these extra terms reduce the effect of the thrust tilt by about 25–30 per cent; in climbing flight (large λ) the reduction is much greater.

5.4.3 The tailplane derivatives

The derivative (m_u)_T If M_T is the pitching moment due to the tailplane, then, in the notation of Chapter 4, section 4.2.2

$$M_T = -\frac{1}{2} \rho V^2 S_T l_T R C_{L_T} \quad (5.89)$$

and

$$\frac{\partial M_T}{\partial u} = -\rho V S_T l_T R \left[C_{L_T} + \frac{1}{2} V \frac{\partial C_{L_T}}{\partial u} \right]$$

The tailplane lift coefficient can be expressed as

$$C_{L_T} = a_T (\alpha_{T_0} + \theta - \tau - \varepsilon)$$

from section 4.2.2. Then

$$V \frac{\partial C_{L_T}}{\partial u} = -a_T V \frac{\partial \varepsilon}{\partial u}$$

and, since $\varepsilon = v_i/V$,

$$\begin{aligned} V \frac{\partial \varepsilon}{\partial u} &= \frac{\partial v_i}{\partial V} - \frac{v_i}{V} \\ &= \frac{\partial \lambda_i}{\partial \mu} - \frac{\lambda_i}{\mu} \end{aligned}$$

where v_i is evaluated at the tailplane by the method discussed in Chapter 4.

Hence

$$\frac{\partial M_T}{\partial u} = -\rho V S_T l_T R \left[C_{L_T} + \frac{1}{2} a_T \left(\frac{\partial \lambda_i}{\partial \mu} - \frac{\lambda_i}{\mu} \right) \right]$$

which in non-dimensional form is

$$(m_u)'_T = -\mu \bar{V}_T \left[C_{L_T} + \frac{1}{2} a_T \left(\frac{\partial \lambda_i}{\partial \mu} - \frac{\lambda_i}{\mu} \right) \right] \quad (5.90)$$

The derivative $(m_w)_T$ Differentiating eqn 5.89 with respect to w gives

$$\frac{\partial M_T}{\partial w} = -\frac{1}{2} \rho V^2 S_T l_T R \frac{\partial C_{L_T}}{\partial w}$$

$$\text{and } \frac{\partial C_{L_T}}{\partial w} = \frac{a_T}{V} \left(1 - \frac{\partial \epsilon}{\partial \alpha} \right) = \frac{a_T}{V} \left(1 - \frac{\partial \lambda_i}{\partial w} \right)$$

Hence

$$(m_w)'_T = -\frac{1}{2} \mu \bar{V}_T a_T \left(1 - \frac{\partial \lambda_i}{\partial \hat{w}} \right) \quad (5.91)$$

Here again, the downwash term is evaluated at the tailplane.

The derivative $(m_q)_T$ For a steady pitching rate q the change of incidence at the tailplane is

$$\Delta \alpha_T = l_T R q / V$$

and the moment change is

$$\Delta M = -\frac{1}{2} \rho a_T V S_T l_T^2 R^2 q$$

Therefore

$$(M_q)_T = -\frac{1}{2} \rho a_T V S_T l_T^2 R^2$$

In non-dimensional form,

$$(m_q)'_T = -\frac{1}{2} a_T \mu \bar{V}_T l_T \quad (5.92)$$

The derivative $(m_{\dot{w}})_T$ This is the moment derivative arising from the time taken for the changes of downwash to reach the tailplane, and may be calculated in the same manner as for the fixed wing aircraft. It appears that for the small tailplanes typical of most helicopters this derivative is of little importance. According to Bramwell⁹ the derivative is

$$(m_{\dot{w}})'_T = -\frac{1}{2} a_T \bar{V}_T l_T \frac{\partial \lambda_i}{\partial \hat{w}} \quad (5.93)$$

5.4.4 Summary of longitudinal derivatives

For convenience, all the longitudinal derivatives are collected together below:

$$x_u = -t_c \frac{\partial a_1}{\partial \mu} - \alpha_D \frac{\partial t_c}{\partial \mu} - \frac{\partial h_{cD}}{\partial \mu} \quad (5.41)$$

$$z_u = -\frac{\partial t_c}{\partial \mu} \quad (5.42)$$

$$x_w = -t_c \frac{\partial a_1}{\partial \hat{w}} - \alpha_D \frac{\partial t_c}{\partial \hat{w}} - \frac{\partial h_{cD}}{\partial \hat{w}} \quad (5.43)$$

$$z_w = -\frac{\partial t_c}{\partial \hat{w}} \quad (5.44)$$

Since $\partial t_c / \partial \hat{q}$ is identically zero, $z_q = 0$ and

$$x_q = -t_c \frac{\partial a_1}{\partial \hat{q}} - \frac{\partial h_{cD}}{\partial \hat{q}}$$

but x_q is negligible as a *force* derivative, although it should be included in the moment derivative m'_q .

$$m'_u = -h_1 x_u + l_1 z_u + C_{m_s} \frac{\partial a_1}{\partial \mu} + (m_u)_f \quad (5.50)$$

$$= -(l - ha_{1s}) \frac{\partial t_c}{\partial \mu} + h \left(t_c \frac{\partial a_1}{\partial \mu} + \frac{\partial h_{cD}}{\partial \mu} \right) + C_{m_s} \frac{\partial a_1}{\partial \mu} + (m_u)_f \quad (5.53)$$

$$m'_w = -h_1 x_w + l_1 z_w + C_{m_s} \frac{\partial a_1}{\partial \hat{w}} + (m_w)_f \quad (5.51)$$

$$= -(l - ha_{1s}) \frac{\partial t_c}{\partial \hat{w}} + h \left(t_c \frac{\partial a_1}{\partial \hat{w}} + \frac{\partial h_{cD}}{\partial \hat{w}} \right) + C_{m_s} \frac{\partial a_1}{\partial \hat{w}} + (m_w)_f \quad (5.54)$$

$$m'_q = -h_1 x_q + C_{m_s} \frac{\partial a_1}{\partial \hat{q}} + (m_q)_f \quad (5.52)$$

$$= h \left(t_c \frac{\partial a_1}{\partial \hat{q}} + \frac{\partial h_{cD}}{\partial \hat{q}} \right) + C_{m_s} \frac{\partial a_1}{\partial \hat{q}} + (m_q)_f \quad (5.55)$$

The tailplane derivatives, which may be the only contributions capable of being calculated for the fuselage, are

$$(m_u)'_T = -\mu \bar{V}_T \left[C_{L_T} + \frac{1}{2} a_T \left(\frac{\partial \lambda_i}{\partial \mu} - \frac{\lambda_i}{\mu} \right) \right] \quad (5.90)$$

$$(m_w)'_T = -\frac{1}{2} \mu a_T \bar{V}_T \left(1 - \frac{\partial \lambda_i}{\partial \mu} \right) \quad (5.91)$$

$$(m_q)'_T = -\frac{1}{2}\mu a_T \bar{V}_T l_T \quad (5.92)$$

$$(m_{\dot{w}})'_T = -\frac{1}{2}a_T \bar{V}_T l_T \frac{\partial \lambda_i}{\partial \hat{w}} \quad (5.93),$$

Other derivative terms which are used in the above are

$$\frac{\partial \lambda}{\partial \mu} = \alpha_{nf} - \frac{\partial \lambda_i}{\partial \mu} = \alpha_D - \alpha_1 - \frac{\partial \lambda_i}{\partial \mu} \quad (5.57)$$

$$\frac{\partial \lambda_i}{\partial \mu} = \frac{2\mu\theta_0 + \alpha_{nf} - (4t_c/a\lambda_i)\bar{V}\bar{v}_i^3}{1 + (4/a)(t_c/\lambda_i)(1 + \bar{v}_i^4)} \quad (5.60)$$

$$\frac{\partial t_c}{\partial \mu} = \frac{2\mu\theta_0 + \alpha_{nf} + \bar{V}\bar{v}_i^3/(1 + \bar{v}_i^4)}{4/a + (\lambda_i/t_c)/(1 + \bar{v}_i^4)} \quad (= 0 \text{ when } \mu = 0) \quad (5.62)$$

$$\frac{\partial t_c}{\partial \mu} \approx \frac{2a\mu}{8\mu + as} \left(2\mu\theta_0 + \alpha_{nf} + \frac{st_c}{2\mu^2} \right) \quad (\text{for } \mu > 0.08) \quad (5.63)$$

$$\frac{\partial a_1}{\partial \mu} = \frac{a_1}{\mu} - \frac{2\mu}{1 - \mu^2/2} \cdot \frac{\partial \lambda}{\partial \mu} \quad (5.64)$$

$$\frac{\partial h_{cD}}{\partial \mu} = \frac{1}{4}\delta \quad (5.66)$$

$$\frac{\partial t_c}{\partial \hat{w}} = \frac{a}{4} \cdot \frac{1}{1 + (a/4)\lambda_i/t_c + \bar{v}_i^4} \quad (5.74)$$

$$\frac{\partial t_c}{\partial \hat{w}} = \frac{2a\lambda_i}{16\lambda_i + as} \quad \text{when } \mu = 0 \quad (5.78)$$

$$\frac{\partial t_c}{\partial \hat{w}} \approx \frac{2\mu}{8\mu + as} \quad (\text{for } \mu > 0.08) \quad (5.79)$$

$$\frac{\partial a_1}{\partial \hat{w}} = \frac{2\mu}{(1 - \mu^2/2)(1 + (a/4)\lambda_i/t_c + \bar{v}_i^4)} \quad (5.75)$$

$$\frac{\partial a_1}{\partial \hat{w}} \approx \frac{16\mu^2}{(1 - \mu^2/2)(8\mu + as)} \quad (\text{for } \mu > 0.08) \quad (5.80)$$

$$\frac{\partial h_{cD}}{\partial \hat{w}} = \frac{a}{4(1 + (a/4)\lambda_i/t_c + \bar{v}_i^4)} \left(\frac{1}{2}a_1 - \mu\theta_0 + \frac{\mu\lambda_D}{1 - \mu^2/2} \right) \quad (5.77)$$

$$\frac{\partial h_{cD}}{\partial \hat{w}} = \frac{4a\mu^2}{8\mu + as} \frac{\theta_0(1 - 9\mu^2/2)/6 + \lambda_D}{1 - \mu^2/2} \quad (\text{for } \mu > 0.08) \quad (5.81)$$

$$\frac{\partial t_c}{\partial q} = 0,$$

$$\frac{\partial a_1}{\partial \hat{q}} = -\frac{16}{\gamma} \cdot \frac{1}{1 - \mu^2/2} \quad (5.82)$$

$$\frac{\partial h_{c_D}}{\partial \hat{q}} = \frac{a}{4} \left[\frac{1}{2} \lambda + \mu a_1 - \mu^2 \theta_0 \right] \frac{\partial a_1}{\partial \hat{q}} \quad (5.87)$$

5.5 The longitudinal stability characteristics

The longitudinal derivatives for the example helicopter of Chapter 4 have been calculated and are shown in Fig. 5.8. But, before discussing the stability over the whole speed range, let us examine the hovering case since, although the analysis is very much simplified by the absence of a number of derivatives, the stability characteristics are typical of most of the flight range.

The stability derivatives for the hovering case (c.g. on shaft axis) are

$$\begin{array}{lll} x_u = -0.032 & x_w = 0 & x_q = 0 \\ z_u = 0 & z_w = -0.52 & z_q = 0 \\ m'_u = 0.016 & m'_w = 0 & m'_q = -0.099 \end{array}$$

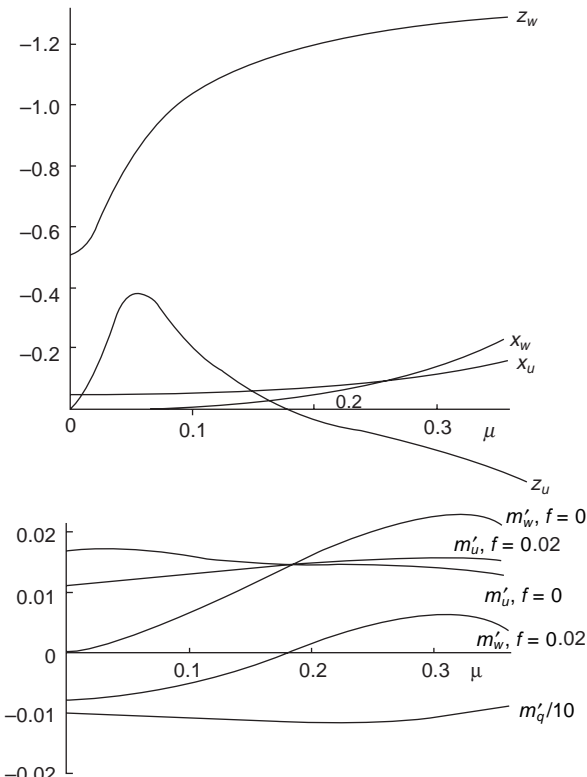


Fig. 5.8 Typical variation of helicopter derivatives with speed

The relative density parameter $\mu^* = 47.6$ and $\hat{t} = 1.82$ seconds.

Taking $i_B = 0.11$ as the non-dimensional longitudinal moment of inertia gives

$$m_u = 6.8, \quad m_w = 0, \quad m_q = -0.90$$

In hovering flight $\hat{V} = \tau_c = 0$ and, since $z_u = 0$ also, we see at once from eqn 5.15 that the vertical motion is uncoupled from the pitching and fore-and-aft motion, and eqn 5.15 gives

$$\lambda - z_w = 0$$

or

$$\lambda = -0.52$$

indicating a heavily damped subsidence. The other modes of motion are determined from

$$\begin{vmatrix} \lambda - x_u & w_c \\ -m_u & \lambda^2 - m_q\lambda \end{vmatrix} = 0$$

or $\lambda^3 - (x_u + m_q)\lambda^2 + x_u m_q \lambda + m_u w_c = 0 \quad (5.94)$

This is the characteristic equation for hovering flight; it could also have been derived from the characteristic quartic, of course, which would have given the root $\lambda = z_w$. Inserting the numerical values above gives

$$\lambda^3 + 0.93\lambda^3 + 0.029\lambda + 0.58 = 0$$

which has the solution

$$\lambda_1 = -1.26, \quad \lambda_{2,3} = 0.165 \pm 0.65i$$

The real root represents a heavily damped subsidence, whose amplitude is halved in one second, and the complex roots represent a divergent oscillation with a period of 17.5 seconds and whose amplitude doubles in 7.1 seconds.

The motions corresponding to the roots of the characteristic cubic, eqn 5.94, involve attitude and speed changes only; the vertical motion in hovering flight, as we have seen, is independent of these two degrees of freedom. To get some idea of the nature of these modes of motion we substitute the values of λ back into the equations of motion from which the roots originated, i.e. eqns 5.14 and 5.16, with w absent and $\tau_c = 0$, giving

$$\begin{aligned} (\lambda - x_u) u_0 + w_c \theta_0 &= 0 \\ -m_u u_0 + (\lambda^2 - m_q \lambda) \theta_0 &= 0 \end{aligned}$$

Since the characteristic equation expresses the consistency of these equations, either can be used to find the ratio u_0/θ_0 for the root in question. Then from eqn 5.16 we have, using the numerical values of the derivatives,

$$u_0/\theta_0 = (\lambda^2 + 0.9\lambda)/6.8$$

Taking the real root $\lambda = -1.26$ gives

$$u_0/\theta_0 = 0.0655$$

In dimensional terms this represents a subsidence in which there is a forward speed change of 1 m/s for every 4.3° of nose up attitude. It is difficult to attach a physical meaning to this mode.

The complex root $\lambda = 0.165 + 0.65i$ gives

$$u_0/\theta_0 = -0.036 + 0.117i$$

Reverting to dimensional values, this result shows that speed changes of about 0.5 m/s accompany attitude changes of 1° . The complex ratio u_0/θ_0 can be represented by rotating vectors, and we see that the speed leads the attitude by about 107° . The physical interpretation of this motion is as follows, Fig. 5.9. Imagine the hovering helicopter to experience a small horizontal velocity disturbance Fig. 5.9(a). The relative airspeed causes the rotor to tilt backwards and exert a nose up pitching moment on the helicopter. A nose up attitude then begins to develop, and the backward component of rotor thrust decelerates the helicopter until its forward motion is arrested. At this point (b) the disc tilt and rotor moment vanish but the nose up attitude remains so that backward motion begins, causing the rotor to tilt forwards and exert a nose down moment (c). Following this, a nose down attitude is attained (d) which accelerates the helicopter forward and returns it to the situation (a). The cycle then begins again but, as we have found analytically, the motion is unstable and its amplitude increases steadily.

The unstable motion described above is due entirely to the characteristic backward flapping of the rotor with forward speed, although the rate of divergence is reduced by the favourable damping in pitch m_g . If it were possible for m_u to be negative, i.e. for the rotor to flap forward with speed, it follows that the last term of eqn 5.94 would be negative, implying a positive real root and a pure divergence, which is even less desirable. Zbrozek¹⁰ investigated the effects of configuration changes on the dynamic stability but found that no reasonable departure from the conventional helicopter shape would significantly improve the stability. In particular, the c.g. position, which is of great importance in the stability of the fixed wing aircraft, has no effect on the stability of the hovering helicopter. For the helicopter with zero offset hinges and zero fuselage moment, the rotor force vector must pass through the c.g., as we saw in Chapter 1, so that moving the c.g. merely has the effect of changing the fuselage attitude without altering the pitching moments. When the flapping hinges are offset, or if the blades are hingeless, a hub moment can be exerted and it is no longer

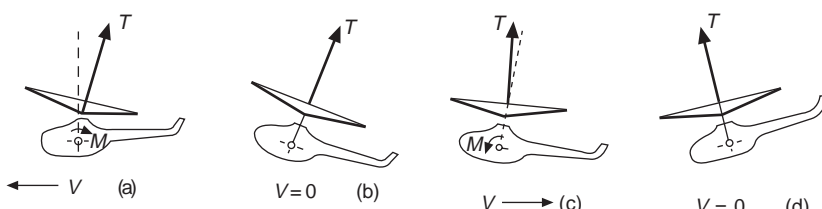


Fig. 5.9 Disturbed longitudinal motion of helicopter

necessary for the rotor force to pass through the c.g., so that changes of rotor force can contribute to the pitching and rolling moments. But, as we saw earlier, in hovering flight the thrust changes due to forward speed, $\partial t_c / \partial \mu$, and to pitching rate, $\partial t_c / \partial \hat{q}$, are both zero and, although $\partial t_c / \partial \hat{w} \neq 0$, inspection of the coefficients of the quartic, eqns 5.18 to 5.21, shows that when $\hat{V} = 0$ the m_w derivative can make no contribution. Thus, in hovering flight, it is true for all types of helicopter that movement of the c.g. has no effect on the dynamic stability.

5.5.1 Forward flight

The roots of the stability quartic, eqn 5.17, have been calculated for the speed range $\mu = 0$ to $\mu = 0.35$ and are shown in root-locus form in Fig. 5.10 for the two cases, c.g. on the shaft ($l = 0$) and forward c.g. ($l = 0.02$). On the scale of this figure, the large negative roots (corresponding to $\lambda = -1.26$ of the hovering case) cannot be shown but, since they represent the most stable mode, they are of least significance. The most important roots are those representing the unstable oscillation and it can be seen that, for the case $l = 0$, the destabilising effect of the positive m_w becomes more important as the speed increases; if higher speeds had been considered it would have been found that the two complex branches of the curve would have met on the real axis and then moved in opposite directions along this axis, implying two real roots and at least one divergent mode.

The effect of setting the c.g. forward of the shaft is shown by the case $l = 0.02$ ($lR = 13$ cm). Here the moment generated by the rotor thrust is stabilising and opposes the moment due to the rotor tilt. Although the aircraft remains unstable, the

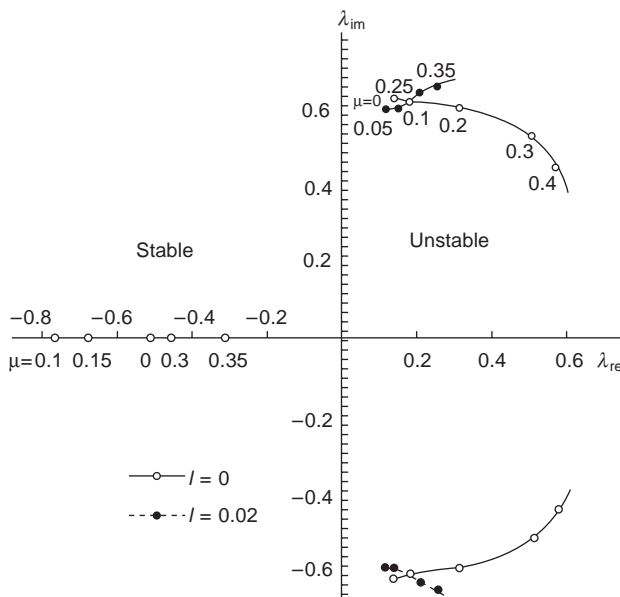


Fig. 5.10 Root-locus plot for typical single rotor helicopter

deterioration of stability with increase of speed is much reduced. As we have noted before, to obtain a moment contribution due to change of thrust requires a continuous hub moment to be exerted on the fuselage in order for the rotor force vector to be displaced from the c.g., and this can be achieved with offset hinges or hingeless blades. But a constant moment exerted on the fuselage implies a fluctuating load on the rotating hub, and problems of fatigue limit the amount that can be tolerated. Thus, although setting the c.g. forward of the shaft with offset or hingeless rotors improves the stability, the improvement is restricted by the necessity to keep loads low enough to avoid fatigue failure.

5.5.2 The effect of a tailplane

The effect of a tailplane on the stability of the helicopter has been calculated by considering the tailplane referred to in Chapter 4, i.e. one having a tail volume of 0.1 and a lift slope of 3.5. The derivatives $(m_w)'_T$ and $(m_q)'_T$ were calculated from eqns 5.91 and 5.92 respectively; for the purpose of illustration, $(m_u)_T$ was taken as zero since it depends on the rigging angle, which can be arbitrarily chosen, and $(m_{\dot{w}})'_T$ was neglected. The results for the case $l = 0$ are shown in Fig. 5.11, together with the tailless case for comparison. It can be seen that in the upper half of the speed range the beneficial effects of the tailplane become large enough to confer positive stability. As the speed increases, the two negative roots coalesce to form two complex branches whose values indicate a well-damped rapid oscillation.

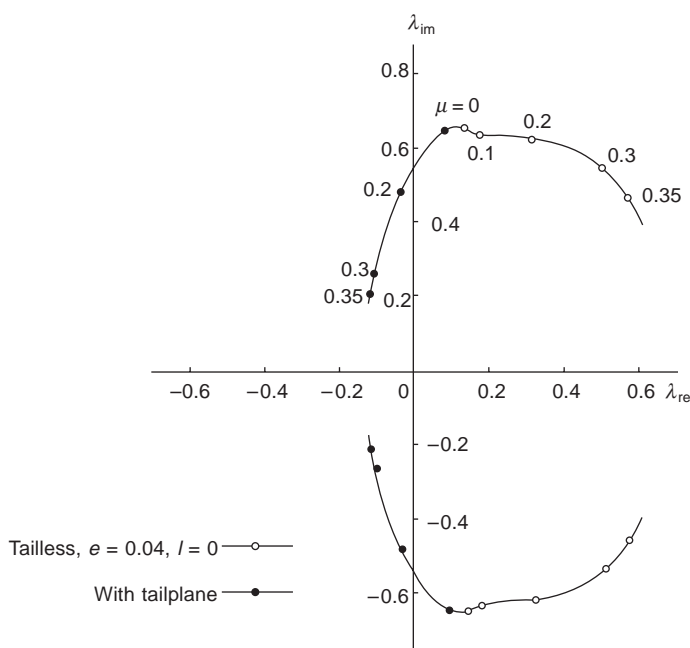


Fig. 5.11 Effect of tailplane on stability roots

5.5.3 The effect of hingeless rotors

The full analysis of the hingeless rotor will be made in Chapter 7, but to discuss its effect on helicopter stability it need only be assumed that, like the rotor with offset flapping hinges, the hingeless rotor can exert a longitudinal moment proportional to the tilt of the disc a_{1s} (relative to the shaft) and a lateral moment proportional to the sideways tilt b_{1s} . For illustration we shall take a hingeless rotor which, for a given rotor tilt, can exert a hub moment five times greater than that of the 4 per cent offset hinges of our example helicopter. In Chapter 7 it will be found that, under a given set of conditions, the flapping of a hingeless rotor is almost identical to that of a hinged one. Thus, all the rotor forces and flapping derivatives will be the same as before and it is necessary only to increase terms such as $C_{m_s} \partial a_1 / \partial \mu$ (eqn 5.53) to $5C_{m_s} \partial a_1 / \partial \mu$ to represent the hub moments of a hingeless rotor. This has been applied to the moment derivatives calculated earlier (and shown in Fig. 5.8).

For hovering flight, the characteristic cubic of our example helicopter becomes

$$\lambda^3 + 3.41\lambda^2 + 0.11\lambda + 1.95 = 0$$

whose roots are

$$\lambda_1 = -3.54 \quad \text{and} \quad \lambda_{2,3} = 0.065 \pm 0.74i$$

The subsidence is even more heavily damped than previously. Then divergence of the oscillation is a little milder, and the period has decreased from 17.5 seconds to 15.4 seconds.

The roots of the quartic have been calculated for forward flight and are shown in Fig. 5.12. Also shown is the same hingeless helicopter fitted with the tailplane of the previous example. It can be seen that the instability, as might have been expected, is intensified by the hingeless blades and that at the top speeds the unstable oscillation degenerates into two purely divergent motions, indicated by the two positive real roots. The tailplane reduces the severity of the instability but for our case is unable to provide positive stability. Setting the c.g. forward would further improve the stability, but we are again faced with the objection that this would involve the fluctuating hub moments and associated fatigue problems.

The longitudinal dynamic stability of the hingeless rotor helicopter is therefore generally inferior to that of the helicopter with flapping hinges of small offset, and worsens at high speed. Autostabilisation is generally incorporated to bring about an improvement. In mitigation of the inferior stability is the fact that the larger hub moments allow much greater control power to be achieved.

As is well known, the longitudinal stability quartic of the fixed wing aircraft splits up into two quadratics whose coefficients are related in a very simple way to the coefficients of the quartic, leading to a simple physical interpretation of the motion. Unfortunately this is not so for the helicopter. We have already seen that in hovering flight the interaction of the pitching and horizontal motions leads to a characteristic cubic equation, and this is further complicated by coupling with the vertical motion as speed increases.

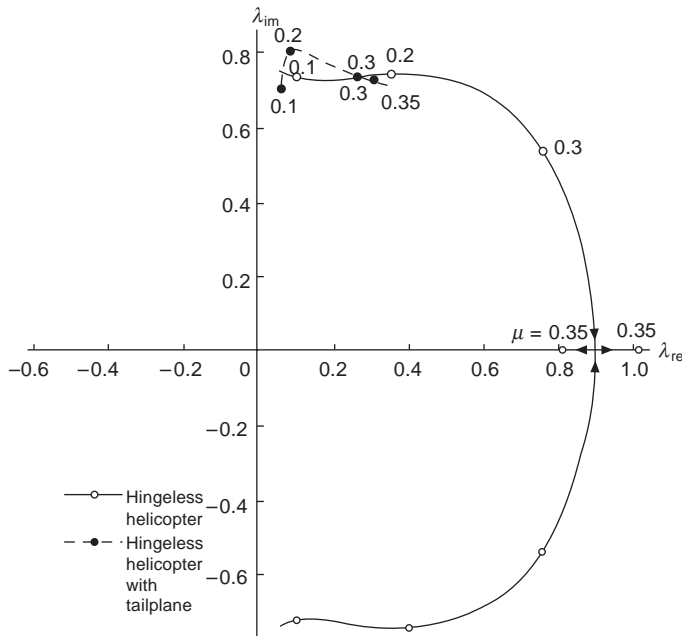


Fig. 5.12 Stability roots of helicopter with hingeless blades

5.6 Lateral dynamic stability

5.6.1 The equations of motion

Writing the lateral equations of motion A.2.13, A.2.15 and A.2.17 in the same manner as for the longitudinal equations, we have

$$(W/g)\dot{v} - Y_v v - Y_p p + (W/g)Vr - Y_r r - W\phi \cos \tau_c - W\psi \sin \tau_c \\ = Y_{A_l} A_l + Y_{\theta_t} \theta_t \quad (5.95)$$

$$-L_v v + A\dot{p} - L_p p - E\dot{r} - L_r r = L_{A_l} A_l + L_{\theta_t} \theta_t \quad (5.96)$$

$$-N_v v - E\dot{p} - N_p p + C\dot{r} - N_r r = N_{A_l} A_l + N_{\theta_t} \theta_t \quad (5.97)$$

The variables are defined as shown in Fig. 5.13; A_l and θ_t are the lateral cyclic and tailrotor collective pitch angles respectively.

The non-dimensional derivatives are defined by:

$y_v = Y_v / \rho s A \Omega R$, y_p and y_r are found to be negligibly small.

$$l'_v = L_v / \rho s A \Omega R^2, \quad n'_v = N_v / \rho s A \Omega R^2$$

$$l'_p = L_p / \rho s A \Omega R^3, \quad l'_r = L_r / \rho s A \Omega R^3$$

$$n'_p = N_p / \rho s A \Omega R^3, \quad n'_r = N_r / \rho s A \Omega R^3$$

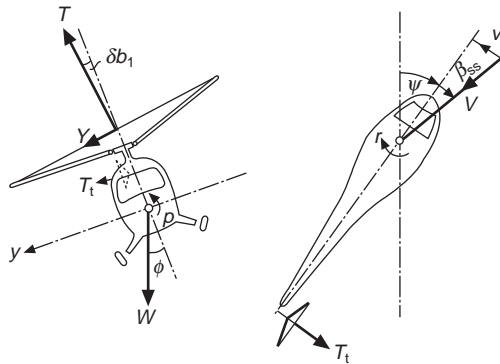


Fig. 5.13 Nomenclature diagram for lateral stability

$$l'_{A_l} = L_{A_l} / \rho s A \Omega^2 R^3$$

$$l'_{\theta_t} = L_{\theta_t} / \rho s A \Omega^2 R^3$$

$$n'_{A_l} = N_{A_l} / \rho s A \Omega^2 R^3,$$

$$n'_{\theta_t} = N_{\theta_t} / \rho s A \Omega^2 R^3$$

$$y_{A_l} = Y_{A_l} / \rho s A \Omega^2 R^3,$$

$$\gamma_{\theta_t} = Y_{\theta_t} / \rho s A \Omega^2 R^2$$

The non-dimensional moments and products of inertia are defined by

$$i_A = A/mR^2, \quad i_c = C/mR^2, \quad i_E = E/mR^2$$

and μ^* and \hat{t} are the same as for the longitudinal case.

The non-dimensional forms of the equations of motion are then

$$\frac{dv}{d\tau} - y_v v - w_c \phi \cos \tau_c + \hat{V} \frac{d\psi}{dt} - w_c \psi \sin \tau_c = y_{A_l} A_l + y_{\theta_t} \theta_t \quad (5.98)$$

$$-l_v v + \frac{d^2 \phi}{d\tau^2} - l_p \frac{d\phi}{d\tau} - \frac{i_E}{i_A} \frac{d^2 \psi}{d\tau^2} - l_r \frac{d\psi}{d\tau} = l_{A_l} A_l + l_{\theta_t} \theta_t \quad (5.99)$$

$$-n_v v - \frac{i_E}{i_C} \frac{d^2 \phi}{d\tau^2} - n_p \frac{d\phi}{d\tau} + \frac{d^2 \psi}{d\tau^2} - n_r \frac{d\psi}{d\tau} = n_{A_l} A_l + n_{\theta_t} \theta_t \quad (5.100)$$

where $l_v = \mu^* l'_v / i_A$, $l_p = l'_p / i_A, \dots$, $n_v = \mu^* n'_v / i_C$, $n_p = n'_p / i_C, \dots$,

5.6.2 Stick-fixed dynamic stability

Putting the control displacements A_l and θ_t to zero and assuming solutions of the form

$$v = v_0 e^{\lambda \tau}, \quad \phi = \phi_0 e^{\lambda \tau}, \dots, \text{etc.}$$

leads to the vanishing of the determinant

$$\begin{vmatrix} \lambda - y_v & -w_c \cos \tau_c & \hat{V}\lambda - w_c \sin \tau_c \\ -l_v & y^2 - l_p\lambda & -(i_E/i_A)\lambda^2 - l_r\lambda \\ -n_v & -(i_E/i_C)\lambda^2 - n_p\lambda & \lambda^2 - n_r\lambda \end{vmatrix} = 0$$

and to the characteristic frequency equation

$$\lambda(A_2\lambda^4 + B_2\lambda^3 + C_2\lambda^2 + D_2\lambda + E_2) = 0 \quad (5.101)$$

where

$$A_2 = 1 - i_E^2/i_A i_C \quad (5.102)$$

$$B_2 = -y_v(1 - i_E^2/i_A i_C) - N_2 \quad (5.103)$$

$$C_2 = y_v N_2 + P_2 + l_v(i_E/i_C)\hat{V} + n_v\hat{V} \quad (5.104)$$

$$D_2 = y_v P_2 + l_v Q_2 - n_v R_2 \quad (5.105)$$

$$E_2 = l_v S_2 - n_v T_2 \quad (5.106)$$

and

$$N_2 = l_p + n_r + (i_E/i_C)l_r + (i_E/i_A)n_p \quad (5.107)$$

$$P_2 = l_p n_r - l_r n_p \quad (5.108)$$

$$Q_2 = n_p \hat{V} - w_c \cos \tau_c \quad (5.109)$$

$$R_2 = l_p \hat{V} - w_c \sin \tau_c \quad (5.110)$$

$$S_2 = n_p w_c \sin \tau_c + n_r w_c \cos \tau_c \quad (5.111)$$

$$T_2 = l_p w_c \sin \tau_c + l_r w_c \cos \tau_c \quad (5.112)$$

the suffix 2 denoting the lateral coefficients.

The zero root of eqn 5.101 implies that the aircraft has no preference for a particular heading.

5.6.3 The lateral stability derivatives

Referring to Fig. 5.13 the side force ΔY in disturbed lateral motion will be

$$\Delta Y = T\delta b_1 + \delta T_t + \delta Y_f$$

where δT_t and δY_f are the incremental tailrotor and fuselage forces respectively. We assume that in lateral motion the main rotor thrust remains constant and that, apart from rolling motion, the force in the plane of the rotor disc remains very small.

In general, the helicopter longitudinal axis will be inclined to the wind axes, Fig. 5.14, and the effective tailrotor height $h'_t R$ and the rearward distance $l'_t R$ from the c.g. are related to the datum distances by

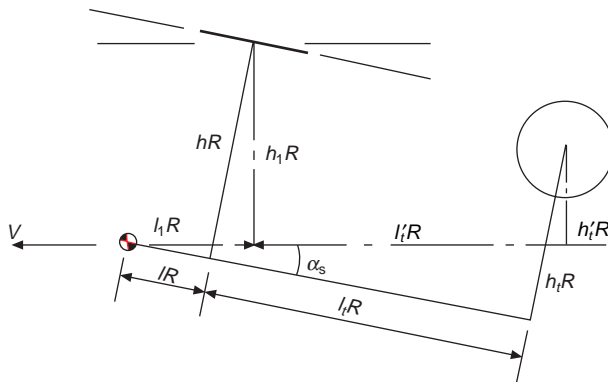


Fig. 5.14 Moment arms for calculating lateral moments

$$\begin{aligned} h_t'R &= (h_t \cos \alpha_s - l_t \sin \alpha_s)R \\ &\approx (h_t - l_t \alpha_s)R \end{aligned} \quad (5.113)$$

and

$$\begin{aligned} l_t'R &= (l_t \cos \alpha_s + h_t \sin \alpha_s)R \\ &\approx l_t R \end{aligned} \quad (5.114)$$

The rolling moment will consist of the moment of the main rotor thrust and side force, the hub moment due to rotor tilt, and the moment of the tailrotor thrust, i.e.

$$\Delta L = h_1 R T \delta b_1 + h_1 R \delta Y + M_s \delta b_1 + h_t' R \delta T_t$$

It will be assumed that the contribution of the fuselage to the rolling moment is negligible.

The yawing moment contributions will arise from changes in the tailrotor thrust and the fuselage and fin. Thus

$$\Delta N = -l_t' R \delta T_t + \delta N_f$$

The sideslip, rolling, and yawing disturbances all give rise to axial velocity components at the tailrotor, and the associated thrust changes can be calculated from the relations already obtained from the main rotor. Thus, if we denote any of these velocity components by w , we have

$$\partial T / \partial v = -\partial T / \partial w$$

In the rolling motion, $w \equiv -h_t' R p$, and

$$\frac{\partial T_t}{\partial p} = -h_t' R \frac{\partial T}{\partial w}$$

and for yawing, since $w \equiv l_t' R r$,

$$\frac{\partial T_t}{\partial r} = l'_t R \frac{\partial T}{\partial w}$$

Then

$$L_v = h_l R \left(T \frac{\partial b_1}{\partial v} + \frac{\partial Y}{\partial v} \right) - h'_t R \frac{\partial T}{\partial w} + M_s \frac{\partial b_1}{\partial v} \quad (5.115)$$

$$L_p = h_l R \left(T \frac{\partial b_1}{\partial p} + \frac{\partial Y}{\partial p} \right) - h'^2 R^2 \frac{\partial T}{\partial w} + M_s \frac{\partial b_1}{\partial p} \quad (5.116)$$

$$L_r = h'_t l'_t R^2 \frac{\partial T}{\partial w} \quad (5.117)$$

$$N_v = l'_t R \frac{\partial T}{\partial w} + (N_v)_f \quad (5.118)$$

$$N_p = h'_t l'_t R^2 \frac{\partial T}{\partial w} + (N_p)_f \quad (5.119)$$

$$N_r = -l'^2 R^2 \frac{\partial T}{\partial w} + (N_r)_f \quad (5.120)$$

To calculate $\partial b_1 / \partial v$ we recall that, when a rotor is placed in a stream of air of velocity V , the rotor tilts backwards with angle a_1 and sideways with angle b_1 with reference to the plane of no-feathering (Chapter 3). The resultant tilt is therefore $(a_1^2 + b_1^2)^{1/2}$ at angle $\psi_0 = \tan^{-1}(b_1/a_1)$ towards the advancing blade, ψ_0 being measured from the rearmost position of the blade. Then, when a small side wind blows, the relative wind appears to come from a new direction, making sideslip angle $\beta_{ss} = v/(V \cos \alpha_{nf})$ to the original direction, in the no-feathering plane. Thus, the resultant flapping will be of the same magnitude but rotated through angle β_{ss} so that the new sideways flapping will be

$$\begin{aligned} b_1 + \delta b_1 &= (a_1^2 + b_1^2)^{1/2} \sin(\psi_0 - \beta_{ss}) \\ &= (a_1^2 + b_1^2)^{1/2} (\sin \psi_0 \cos \beta_{ss} - \sin \beta_{ss} \cos \psi_0) \\ &= b_1 - a_1 \beta_{ss}, \text{ for small } \beta_{ss}. \end{aligned}$$

Therefore

$$\delta b_1 = -a_1 \beta_{ss} = -a_1 v / (V \cos \alpha_{nf})$$

and so

$$\partial b_1 / \partial \hat{v} = -a_1 / \mu \quad (5.121)$$

where $\hat{v} = v/\Omega R$.

It should be noted that the sign of $\partial b_1 / \partial \hat{v}$ depends on the sense of rotation of the rotor, and this should be allowed for in the derivation of any formulae; but a little consideration shows that the rotor always tilts away from the component of relative wind so that there should be no confusion about the appropriate sign of the forces and moments due to sideways flapping. In this work the rotor is supposed to be rotating in an anticlockwise direction when viewed from above, i.e. positive sideways flapping is directed to starboard.

By the same reasoning, the side wind will always cause a sideways component of the longitudinal in-plane H -force, and it is easy to see that

$$\partial Y / \partial v = - H_D / V \cos \alpha_D$$

remembering that we are considering forces in the plane of the disc.

The non-dimensional form is

$$\partial y_c / \partial \hat{v} = - h_c / \mu \approx - \frac{1}{4} \delta$$

in which $y_c = Y / \rho s A \Omega^2 R^2$ and the inflow contribution to h_c is ignored (see eqn 3.64). The calculation of the rolling moment due to the rate of roll p follows a similar procedure to that described for the pitching moment, and we find that the non-dimensional rolling moment derivative due to the rotor forces is

$$(l_p)_r = h_l (t_c + a\lambda_D / 8) \partial b_1 / \partial \hat{v} \quad (5.123)$$

in which $\partial y_c / \partial b_1 \equiv \partial h_c / \partial a_1 = a\lambda_D / 8$ from eqn 3.64. Also, if the extra terms due to \hat{p} from eqn 1.16a are added to the right-hand side of eqn 3.48, and an examination is made of the various harmonic terms (as in the pitching case), then it can be shown that

$$\partial b_1 / \partial \hat{p} = - 16 / \gamma (1 + \mu^2 / 2) \quad (5.124)$$

It has been shown¹¹ that the fuselage contribution to the side force can be expressed approximately as

$$(y_v)_f = - 0.3 \mu S_B / sA \quad (5.125)$$

where S_B is the projected side area of the fuselage.

The non-dimensional forms of all the lateral derivatives are

$$y_v = - t_c \frac{a_1}{\mu} - \frac{1}{4} \delta - \bar{s}_t \frac{\partial t_c}{\partial \hat{w}} - 0.3 \mu \frac{S_B}{sA} \quad (5.126)$$

$$l'_v = - (h_l t_c + C_{m_s}) \frac{a_1}{\mu} - h'_t \bar{s}_t \frac{\partial t_c}{\partial \hat{w}} \quad (5.127)$$

$$l'_p = - \frac{16 [h_l (t_c + a\lambda_D / 8) + C_{m_s}]}{\gamma (1 + \mu^2 / 2)} - h'^2_t \bar{s}_t \frac{\partial t_c}{\partial \hat{w}} \quad (5.128)$$

$$l'_r = h'_t l'_v \frac{\partial t_c}{\partial \hat{w}} \quad (5.129)$$

$$n'_v = l'_t \bar{s}_t \frac{\partial t_c}{\partial \hat{w}} + (n_v)'_f \quad (5.130)$$

$$n'_p = h'_t l'_t \bar{s}_t \frac{\partial t_c}{\partial \hat{w}} + (n_p)'_f \quad (5.131)$$

$$n'_r = -l'^2_t \bar{s}_t \frac{\partial t_c}{\partial \hat{w}} + (n_r)'_f \quad (5.132)$$

where $\bar{s}_t = s_t A_t (\Omega R)_t / s A \Omega R$. But, usually, $(\Omega R)_t \approx \Omega R$; hence $\bar{s}_t = s_t A_t / s A$.

The fuselage derivatives are not likely to be known accurately except, perhaps, the contribution of the fin. In the example below, the fuselage moment derivatives have been taken as zero.

5.7 The lateral stability characteristics

The lateral stability derivatives for the example helicopter have been calculated and are shown in Fig. 5.15, taking

$$l_t = 1.2 \quad \text{and} \quad h_t = 0.1$$

and considering level flight, $\tau_c = 0$.

The non-dimensional moments of inertia are taken to be

$$i_A = 0.033, \quad i_C = 0.11, \quad i_E = 0$$

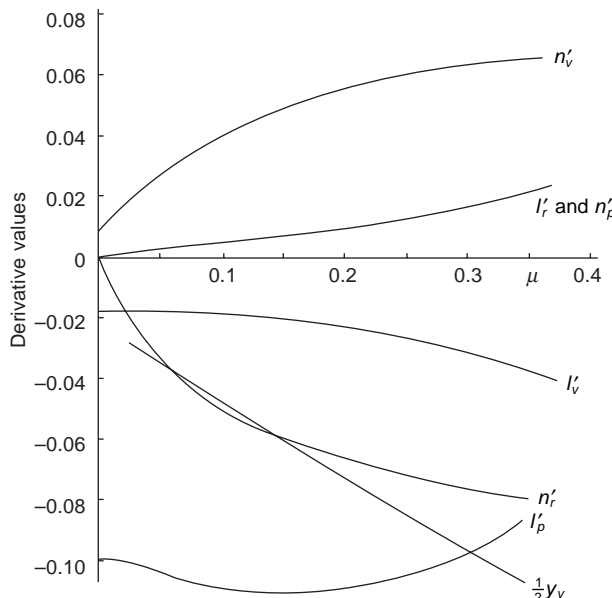


Fig. 5.15 Lateral derivatives for typical single rotor helicopter

Now we found for the longitudinal hovering case that, in addition to the speed being zero, some of the longitudinal derivatives were also zero, and this led to a great simplification. Strictly speaking this is not so for the lateral case, because the yawing and rolling motions are coupled by the tailrotor, and this coupling is represented by the derivatives l_r and n_p . However, if we assume that l_r is negligible – if, for example, the tailrotor shaft were on the roll axis – the resulting motion would be analogous to the longitudinal case, with the corresponding characteristic equation

$$(\lambda - n_r)[\lambda^3 - (y_v + l_p)\lambda^2 + y_v l_p \lambda - l_v w_c] = 0 \quad (5.133)$$

The root $\lambda = n_r$ indicates that the yawing motion is independent of the sideways and rolling motion. The cubic is analogous to the longitudinal equation, eqn 5.94, but we should note that the moment of inertia in roll is much lower than in pitch, with a consequent increase in the numerical values of the coefficients.

The numerical values of the lateral derivatives are

$$n_r = -0.25, \quad y_v = -0.052$$

$$l'_p = m'_q = -0.099, \quad l_p = -3.0$$

$$l'_v = -m'_u = -0.016, \quad l_v = -23$$

The characteristic cubic is

$$\lambda^3 + 3.05\lambda^2 + 0.16\lambda + 1.96 = 0$$

with roots

$$\lambda = -3.19 \quad \text{and} \quad \lambda = 0.07 \pm 0.78i$$

Substitution of the real root $\lambda = -3.19$ back into the equations of motion shows that it corresponds to an almost pure rolling motion, i.e. it can be regarded as the ‘damping-in-roll’ root. This motion is heavily damped with a time to half amplitude of less than half a second. The complex root represents a divergent oscillation of period 14.8 seconds which doubles amplitude in 18 seconds. The yawing motion previously mentioned has a time to half amplitude of about 5 seconds.

5.7.1 Forward flight

The quartic eqn 5.101 has been solved for a range of μ , and the roots are shown in the root-locus plot of Fig. 5.16. It can be seen that the mildly unstable oscillation in hovering flight very soon becomes stable and becomes progressively more so as the speed increases. The increase of the imaginary part of the root indicates that the period of the oscillation steadily becomes shorter. The mode shape of the oscillation at the higher speeds shows that $\psi \approx -\beta_{ss} = -\hat{v}/\mu$, i.e. the helicopter ‘weathercocks’ with very little sideways translation, and the motion is similar to the ‘Dutch roll’ oscillation of the conventional aeroplane. By neglecting the rolling that occurs and using the above approximation, it follows from eqn 5.100 that the time of oscillation of the ‘Dutch roll’ oscillation is approximately

$$T = 2\pi\hat{v}/\sqrt{(\mu n_v)}$$

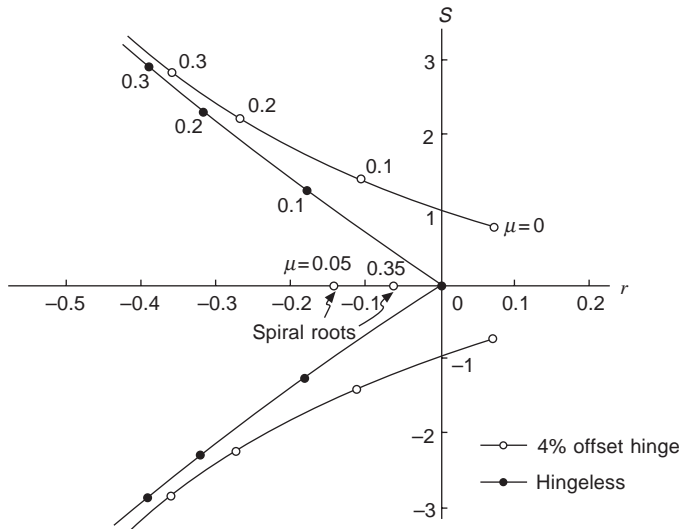


Fig. 5.16 Root-locus plot of lateral stability

We also find that the quartic has a small root given approximately by

$$\lambda = -E_2/D_2$$

which corresponds to the 'spiral root' and, as we have already seen, a large negative root which corresponds to almost pure damping in roll. Thus, except for fairly low speeds, where the characteristic hover mode is dominant, the lateral stability modes of the helicopter are similar to those of the conventional aircraft. This is rather remarkable when it is considered that, apart from the tailrotor, which would be expected to act like a fin, the forces and moments from a helicopter rotor arise in quite a different manner to those of the aerodynamic surfaces of a fixed wing aircraft.

5.7.2 The effect of hingeless rotors

As with the longitudinal case, we represent the hingeless rotor by increasing the hub moment of the 4 per cent offset hinge of our example helicopter by a factor of five. This increases the moment derivatives l_p and i_v , since they arise almost entirely from the main rotor, but not the ‘weathercock’ derivative n_n .

The characteristic equation for hovering flight becomes

$$\lambda^3 + 11.2\lambda^2 + 0.59\lambda + 6.48 = 0$$

whose roots are

$$\lambda_1 = -11.2 \text{ and } \lambda_{2,3} = \pm 0.76i$$

The subsidence is now very heavily damped and the previously unstable oscillation has now become neutrally stable with a period of 15.2 seconds, which is almost identical to the period of the longitudinal motion.

It is interesting to note that increasing the rotor hub ‘stiffness’ (hub moment per unit rotor tilt) is equivalent to decreasing the moment of inertia. It happens that increasing the hub moment five times in the longitudinal case produces almost the same effect as changing from the longitudinal to lateral moments of inertia, and we see that the cubic equations for these cases are numerically very similar.

Let us decrease the moment of inertia so that it approaches zero. It can easily be seen that the cubic characteristic equation, eqn 5.133, then degenerates to the quadratic

$$\lambda^2 - y_v \lambda - (l_v/l_p)w_c = 0$$

whose roots are

$$\lambda = \frac{1}{2}y_v \pm \sqrt{\left[\frac{1}{4}y_v^2 + (l_v/l_p)w_c\right]}$$

This represents a lightly damped oscillation whose period, ignoring the y_v term, is

$$T = 2\pi\hat{f}\sqrt{(l_p/l_v w_c)}$$

This, in our notation, is Hohenemser’s formula¹ for the period of oscillation in hovering flight. For the longitudinal case the period is

$$T = 2\pi\hat{f}\sqrt{(-m_q/m_u w_c)}$$

For the case considered,

	Time of oscillation (seconds)	
	Exact	Hohenemser
Longitudinal (4% offset)	17.5	14.2
Longitudinal (hingeless)	15.4	15.1
Lateral (4% offset)	14.8	14.2
Lateral (hingeless)	15.2	15.0

Thus, for high control power or low inertia, Hohenemser’s formula gives quite accurate results.

The stability in forward flight with the hingeless rotor, Fig. 5.16, shows that, unlike the longitudinal case, the lateral stability is generally improved compared with the aircraft with 4 per cent offset hinges.

5.8 Autostabilisation

We have seen that the helicopter is unstable both laterally and longitudinally in hovering flight and that the longitudinal instability becomes worse with increase of forward speed, particularly when the rotor has hingeless blades. We have also seen that a tailplane is really effective only in the upper half of the speed range and that, since the unstable characteristics of the rotor also deteriorate with speed, the tailplane may be incapable of making the machine completely stable.

Although adequate control power is usually available to correct disturbances, an unstable aircraft will require continuous correction and will be tiring to fly for long periods, even in quite calm weather. Furthermore, in some conditions, such as flying on instruments, an unstable aircraft could be quite dangerous and it is clearly desirable to provide some form of artificial stabilisation to make good the inherent deficiencies.

The stabilisation devices in common use fall into two categories:

- (i) a mechanical/gyro device which is an integral part of the rotor system, as used on Bell and Hiller helicopters;
- (ii) automatic flight control systems using feedback control based on signals from sensors such as attitude or rate gyros.

5.8.1 Mechanical/gyro devices

The simple Bell stabilising bar embodies the essentials of all mechanical/gyro devices. The Bell bar is basically a bar pivoted to the rotor shaft, Fig. 5.17, and provided with viscous damping. The bar behaves like a gyroscope with lag damping.

The bar is linked to the blade so that a tilt of the bar relative to the shaft causes a change of pitch of the rotor blade.

Since the bar can pivot relative to the shaft, its equation of motion is precisely the same form as that of the blade under the excitation of gyroscopic and inertia moments, eqn 1.16. Thus, if θ_{bar} is the angular displacement of the bar, its equation of motion is

$$\ddot{\theta}_{\text{bar}} + (2/T_f)\dot{\theta}_{\text{bar}} + \Omega^2\theta_{\text{bar}} = -2\Omega q \sin \psi + \dot{q} \cos \psi$$

in which the viscous damping is conveniently represented by the ‘following’ time T_f , or the time taken for a sudden displacement of the bar to diminish by 63 per cent. The last term of eqn 1.16 is negligibly small in practice and so the equation above can also be written

$$d^2\theta_{\text{bar}}/d\psi^2 + (2/T_f\Omega)d\theta_{\text{bar}}/d\psi + \theta_{\text{bar}} = -2\hat{q} \sin \psi \quad (5.134)$$

Let c_l be the linkage ratio such that

$$\theta = c_l\theta_{\text{bar}} \quad (5.135)$$

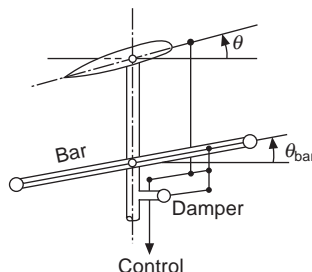


Fig. 5.17 Bell stabilising bar

so that, if c_l is unity, one degree of the tilt of the bar produces one degree of blade pitch. Since the bar does not affect the collective pitch, eqn 5.135 can be written in the form

$$c_l \theta_{\text{bar}} = -A_1 \sin \psi - B_1 \cos \psi \quad (5.136)$$

where the cyclic pitch amplitudes A_1 and B_1 are functions of time.

Substituting eqn 5.136 in 5.134 and equating coefficients of $\sin \psi$ and $\cos \psi$ gives

$$A_1'' + (2/T_f \Omega) A_1' + 2B_1' + (2/T_f \Omega) B_1 = 2c_l \hat{q} \quad (5.137)$$

and

$$2A_1' + (2/T_f \Omega) A_1 - B_1'' - (2/T_f \Omega) B_1' = 0 \quad (5.138)$$

where the dashes denote differentiation with respect to ψ .

The free motion corresponding to eqns 5.137 and 5.138 is found to consist of a high frequency ‘nutation’ mode, of no practical interest, and a significant low frequency mode. An approximation to this latter mode can be obtained by ignoring the A_1 terms, giving

$$dB_1/d\psi + (1/T_f \Omega) B_1 = c_l \hat{q} \quad (5.139)$$

A similar relationship exists between the lateral cyclic pitch A_1 and the rate of roll p .

In terms of aerodynamic time, eqn 5.139 can be written as

$$dB_1/d\tau + (\hat{t}/T_f) B_1 = c_l d\theta/d\tau \quad (5.140)$$

Then considering hovering flight, the equations of stick fixed longitudinal motion are

$$\begin{aligned} du/d\tau - x_u u + w_c \theta &= 0 \\ -m_u u + d^2 \theta/d\tau^2 - m_q d\theta/d\tau - m_{B_1} B_1 &= 0 \\ c_l d\theta/d\tau - dB_1/d\tau - (\hat{t}/T_f) B_1 &= 0 \end{aligned}$$

The characteristic equation of this motion can be written as

$$(\lambda + \hat{t}/T_f)\{\text{hovering cubic}\} - c_l m_{B_1} \lambda (\lambda - x_u) = 0 \quad (5.141)$$

where the ‘hovering cubic’ is the uncontrolled characteristic equation, eqn 5.94. The control derivative m_{B_1} is the moment coefficient for unit cyclic pitch change; and therefore, for our example helicopter, $m_{B_1} = -0.0214$ (zero offset).

The quartic, eqn 5.141, has been solved for a large range of values of the following time T_f/\hat{t} and the two linkage ratios $c_l = \frac{1}{2}$ and $c_l = 1$. The roots indicate a heavily damped oscillation of short period and a lightly damped oscillation of long period, which can be regarded as the original undamped stick-fixed motion modified by the presence of the bar. The roots of this latter oscillation are shown in Fig. 5.18. It can be seen that the amount of stabilisation provided by the bar is rather limited.

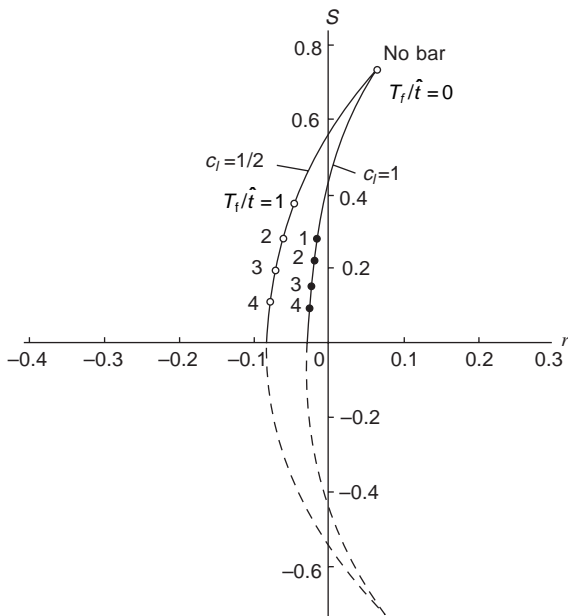


Fig. 5.18 Effect of Bell stabilising bar on lateral stability roots

The Hiller stabilising bar is similar to the Bell bar, except that small aerofoils on the bar provide aerodynamic damping in place of the viscous damping. A further difference is that the pilot controls the bar directly, which acts as a servo control between the stick and the rotor blades. By their nature, Bell and Hiller stabilising bars are well adapted to the two-bladed teetering rotors which are a characteristic of these helicopters.

5.8.2 Automatic flight control systems

Some automatic flight control systems (AFCS) are specifically designed to deal with the basic instability inherent in conventional helicopters. The latter implies continuous pilot activity on the controls in order to fly uncomplicated manoeuvres or even simply straight and level, which can be tiring over long periods. The stability augmentation system (SAS) described briefly in (a) below is designed to address this problem. The automatic stabilisation system (ASE) described in (b) below is aimed at maintaining a desired manoeuvre attitude and therefore normally operates over a shorter time period. More detailed descriptions of these and other types of AFCS fitted to helicopters may be found in McLean¹² and Pallett and Coyle¹³. Generally, these systems are fitted to the larger and more expensive machines, the application of mechanical gyro devices such as the Bell and Hiller bars being confined to the smaller helicopters. The latter tend to confer only a limited improvement of stability and can add considerably to the drag of the rotor head, whilst the former offers a more flexible means of stabilisation and is accommodated completely within the airframe.

(a) SAS (stability augmentation system)

The SAS is designed to maintain the helicopter at the datum to which it has been trimmed. It uses a simple feedback control in which a rate gyro senses pitch rate, for example, which, on integration, provides a correcting input at the swash plate (if this is the means of rotor control). Within the feedback loop, however, there is a so-called ‘leaky integrator’ path parallel with the output from the rate gyro, the effect of these parallel paths being equivalent to that of a phase-lag network. The leaky integrator path leads to a signal proportional to the angle through which the helicopter has been disturbed; this initially provides an input to the swash plate that counteracts the angular disturbance. In the longer term, the input decays or ‘leaks away’, so that if the helicopter does not respond to the corrective action, or the pilot holds the new attitude, then the final angular position becomes the new equilibrium state.

(b) ASE (automatic stabilisation equipment)

The ASE is designed to control a desired attitude, e.g. pitch or roll. The attitude angles are sensed from a gyro and these, and their rates which are found by differentiation, are summed in appropriate proportions, together with signals from the cyclic stick (control) position and the c.g. trim system. The latter centres the gyro to a datum corresponding to successive new flight conditions. The signal from the stick is used to cancel the gyro signal when the pilot demands a manoeuvre, otherwise the attitude control would hold the original datum and oppose the manoeuvre demanded.

5.9 Control response

We now consider the behaviour of the helicopter in response to the pilot’s control input and to vertical gusts. A detailed account of the motion following these disturbances would be out of place here, and the discussion will be limited to those features of helicopter response which are usually regarded as being the most important. These are

- (a) the normal acceleration in response to a cyclic pitch displacement,
- (b) the normal acceleration in response to a vertical gust,
- (c) the pitching and rolling response to cyclic pitch displacements.

Response to collective pitch changes will not be considered, since it is not normally regarded as a ‘short-term’ control, although it may be possibly used in an auto-stabilisation system.

Detailed knowledge of the control response is essential for determining the flying qualities of a helicopter, and subsequent assessment of how these relate to the separately identifiable tasks within a flying mission. An extensive treatment of the topic is provided in Padfield³.

In order to proceed with this limited study of the control response, the force and moment derivatives with respect to cyclic and collective pitch applications are now found.

5.9.1 The B_1 control derivatives

The application of longitudinal cyclic pitch tilts the no-feathering axis in the longitudinal plane and produces precisely the same effect as if the cyclic stick had been kept fixed and the incidence of the helicopter had been reduced by the same amount, i.e.

$$\Delta B_1 = -\Delta \alpha = -(1/\mu) \Delta \hat{w}$$

or

$$\frac{\partial}{\partial B_1} = -\mu \frac{\partial}{\partial \hat{w}}$$

Thus

$$\frac{\partial t_c}{\partial B_1} = -\mu \frac{\partial t_c}{\partial \hat{w}} \quad (5.142)$$

$$\frac{\partial h_{cp}}{\partial B_1} = -\mu \frac{\partial h_{cp}}{\partial \hat{w}} \quad (5.143)$$

$$\frac{\partial a_1}{\partial B_1} = -\mu \frac{\partial a_1}{\partial \hat{w}} \quad (5.144)$$

the w derivatives being given by eqns 5.79 to 5.81.

In obtaining the force and moment derivatives we have to allow for the fact that the no-feathering axis moves relative to the shaft when cyclic pitch is applied. Thus, the X force must be written

$$\begin{aligned} X &= -T \sin \alpha_D - H_D \cos \alpha_D \\ &= -T \sin (\alpha_s + a_1 - B_1) - H_D \cos(\alpha_s + a_1 - B_1) \end{aligned}$$

where α_s is the incidence of the shaft (rotor hub axis)

Then

$$\begin{aligned} \frac{\partial X}{\partial B_1} &= X_{B_1} = -\frac{\partial T}{\partial B_1} \sin \alpha_D - T \cos \alpha_D \left(\frac{\partial a_1}{\partial B_1} - 1 \right) \\ &\quad + \frac{\partial H_D}{\partial B_1} \cos \alpha_D + H_D \sin \alpha_D \left(\frac{\partial a_1}{\partial B_1} - 1 \right) \end{aligned} \quad (5.145)$$

$$\approx -\frac{\partial T}{\partial B_1} \alpha_D + T \left(1 + \mu \frac{\partial a_1}{\partial \hat{w}} \right) - \frac{\partial H_D}{\partial B_1} \quad (5.146)$$

In non-dimensional form,

$$x_{B_1} = \frac{X_{B_1}}{\rho s A \Omega^2 R^2} = \frac{\partial t_c}{\partial B_1} \alpha_D + t_c \left(1 + \mu \frac{\partial a_1}{\partial \hat{w}} \right) - \frac{\partial h_{cp}}{\partial B_1} \quad (5.147)$$

Similarly

$$z_{B_1} = -\partial t_c / \partial B_1 = -uz_w \quad (5.148)$$

The moment derivative is

$$m'_{B_1} = -h_1 x_{B_1} + l_1 z_{B_1} - C_{m_s} \left(1 + \mu \frac{\partial a_1}{\partial \hat{w}} \right) \quad (5.149)$$

which can also be written as

$$m'_{B_1} = -(l - h a_{1s}) \frac{\partial t_c}{\partial B_1} - (t_c h + C_{m_s}) \left(1 + \mu \frac{\partial a_1}{\partial \hat{w}} \right) + h \frac{\partial h_{c_D}}{\partial B_1} \quad (5.150)$$

Numerical examples show that the terms in h_{c_D} can be neglected. The force and moment derivatives for our example helicopter have been calculated and are shown in Fig. 5.19.

5.9.2 The θ_0 control derivatives

Differentiating eqn 3.33 with respect to θ_0 gives

$$\frac{\partial t_c}{\partial \theta_0} = \frac{a}{4} \left[\frac{2}{3} (1 + 3\mu^2/2) + \frac{\partial \lambda}{\partial \theta_0} \right]$$

But

$$\lambda = \mu \alpha_{nf} - \lambda_i$$

therefore

$$\partial \lambda / \partial \theta_0 = - \partial \lambda_i / \partial \theta_0$$

since μ and α_{nf} are independent of θ_0 .

Taking as before

$$\lambda_i = st_c / 2\sqrt{(\hat{V}^2 + \lambda_i^2)}$$

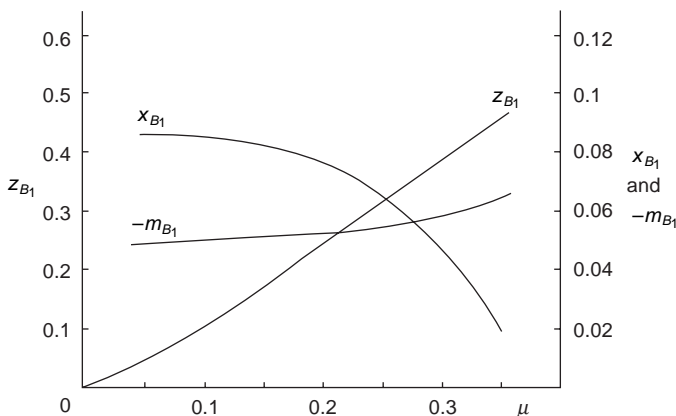


Fig. 5.19 Control derivatives (cyclic pitch)

we have

$$\begin{aligned}\frac{\partial \lambda_i}{\partial \theta_0} &= \frac{s}{2\sqrt{(\hat{V}^2 + \lambda_i^2)}} \frac{\partial t_c}{\partial \theta_0} - \frac{st_c \lambda_i}{2(\hat{V}^2 + \lambda_i^2)^{3/2}} \frac{\partial \lambda_i}{\partial \theta_0} \\ &= \frac{\lambda_i}{t_c} \frac{\partial t_c}{\partial \theta_0} - \bar{v}_i^4 \frac{\partial \lambda_i}{\partial \theta_0}\end{aligned}$$

or

$$(1 + \bar{v}_i^4) \frac{\partial \lambda_i}{\partial \theta_0} = \frac{\lambda_i}{t_c} \frac{\partial t_c}{\partial \theta_0} \quad (5.151)$$

giving finally

$$\frac{\partial t_c}{\partial \theta_0} = \frac{a}{6} \cdot \frac{1 + 3\mu^2/2}{1 + (a\lambda_i/4t_c)(1 + \bar{v}_i^4)} \quad (5.152)$$

For $\hat{V} = \mu = 0$ we have approximately

$$\frac{\partial t_c}{\partial \theta_0} = \frac{4}{3} \cdot \frac{a\lambda_i}{8\lambda_i + as} \quad (5.153)$$

and for $\mu > 0.08$

$$\frac{\partial t_c}{\partial \theta_0} = \frac{4}{3} a\mu \frac{1 + 3\mu^2/2}{8\mu + as} \quad (5.154)$$

From

$$\begin{aligned}a_1 &= \frac{2\mu(4\theta_0/3 + \lambda)}{1 - \mu^2/2} \\ \frac{\partial a_1}{\partial \theta_0} &= \frac{2\mu}{1 - \mu^2/2} \left[\frac{4}{3} + \frac{\partial \lambda}{\partial \theta_0} \right] \\ &= \frac{2\mu}{1 - \mu^2/2} \left[\frac{4}{3} - \frac{\partial \lambda_i}{\partial \theta_0} \right]\end{aligned}$$

Since $\partial a_1/\partial \theta_0$ is obviously zero when $\mu = 0$, it is sufficient to consider only the simpler case $\mu > 0.08$. Then from eqns 5.151 and 5.152 we find

$$\frac{\partial \lambda_i}{\partial \theta_0} = \frac{2}{3} as \frac{1 + 3\mu^2/2}{8\mu + as} \quad (5.155)$$

giving

$$\frac{\partial a_1}{\partial \theta_0} = \frac{8\mu/3}{1 - \mu^2/2} \left[1 - \frac{\frac{1}{2}as(1 + 3\mu^2/2)}{8\mu + as} \right] \quad (5.156)$$

Finally, differentiating eqn 3.64

$$\begin{aligned}\frac{\partial h_{c_D}}{\partial \theta_0} &= \frac{\partial}{\partial \theta_0} \left(\frac{a \lambda_D a_1}{8} \right) - \frac{\partial}{\partial \theta_0} \left(\frac{a \mu \lambda_D \theta_0}{4} \right) \\ &= \frac{a}{8} \left[\left(a_1 \frac{\partial \lambda_D}{\partial \theta_0} + \lambda_D \frac{\partial a_1}{\partial \theta_0} \right) - 2\mu \left(\lambda_D + \theta_0 \frac{\partial \lambda_D}{\partial \theta_0} \right) \right]\end{aligned}\quad (5.157)$$

Since

$$\lambda_D = \mu(\alpha_{nf} + a_1) - \lambda_i$$

$$\frac{\partial \lambda_D}{\partial \theta_0} = \mu \frac{\partial a_1}{\partial \theta_0} - \frac{\partial \lambda_i}{\partial \theta_0}$$

so that eqn 5.157 can be calculated in conjunction with eqns 5.155 and 5.156.

The force and moment derivatives are

$$x_{\theta_0} = -t_c \frac{\partial a_1}{\partial \theta_0} - \alpha_D \frac{\partial t_c}{\partial \theta_0} - \frac{\partial h_{c_D}}{\partial \theta_0} \quad (5.158)$$

$$z_{\theta_0} = -\frac{\partial t_c}{\partial \theta_0} \quad (5.159)$$

$$m'_{\theta_0} = -h_1 x_{\theta_0} + l_1 z_{\theta_0} - C_{m_s} \frac{\partial a_1}{\partial \theta_0} \quad (5.160)$$

which can also be expressed as

$$m'_{\theta_0} = -(l - ha_{1s}) \frac{\partial t_c}{\partial \theta_0} + (t_c h + C_{m_s}) \frac{\partial a_1}{\partial \theta_0} + h \frac{\partial h_{c_D}}{\partial \theta_0} \quad (5.161)$$

Again, the terms in h_{c_D} are negligibly small. The θ_0 derivatives for our example helicopter are shown in Fig. 5.20.

5.9.3 Control response in forward flight

As mentioned earlier, response to collective pitch variation will not be considered, so the non-dimensional equations of motion reduce to

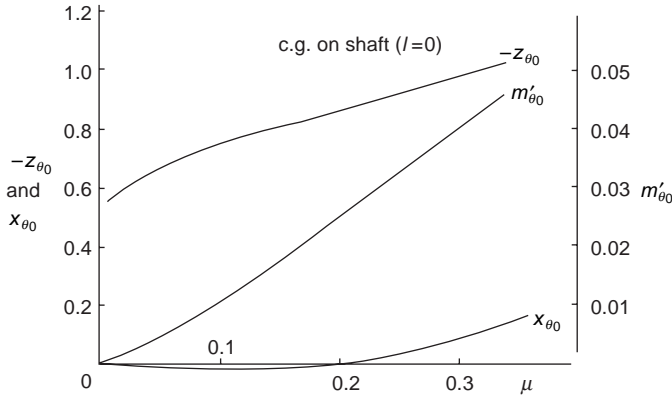
$$du/d\tau - x_u u - x_w w + w_c \theta \cos \tau_c = x_{B_1} B_1(\tau) \quad (5.162)$$

$$-z_u u + dw/d\tau - z_w w - \hat{V} d\theta/d\tau + w_c \theta \sin \tau_c = z_{B_1} B_1(\tau) \quad (5.163)$$

$$-m_u u - m_w w - m_{\dot{w}} dw/d\tau + d^2 \theta/d\tau^2 - m_q d\theta/d\tau = m_{B_1} B_1(\tau) \quad (5.164)$$

in which θ here is the fuselage pitch attitude change.

The cyclic pitch displacement B_1 is a function of time, either as a prescribed control input by the pilot or, as we discussed earlier in the section on autostabilisation,

**Fig. 5.20** Control derivatives (collective pitch)

related to some of the other variables through a control law. We have already considered an example of the latter case in the section on stabilising bars.

Many of the control displacements which result in responses giving useful information enable the above equations to be conveniently solved by the Laplace transformation. Denoting the Laplace transforms of u , w , and θ by \bar{u} , \bar{w} and $\bar{\theta}$ and supposing the aircraft to be initially in trim, the transformed equations of motion become

$$(p - x_u)\bar{u} - x_w\bar{w} + w_c\bar{\theta} \cos \tau_c = x_{B_l}\bar{B}_1 \quad (5.165)$$

$$-z_u\bar{u} + (p - z_w)\bar{w} - (\hat{V}p - w_c \sin \tau_c)\bar{\theta} = z_{B_l}\bar{B}_1 \quad (5.166)$$

$$-m_u\bar{u} - (pm_{\dot{w}} + m_w)\bar{w} + (p^2 - m_q p)\bar{\theta} = m_{B_l}\bar{B}_1 \quad (5.167)$$

Solving for \bar{u} , \bar{w} and $\bar{\theta}$ gives

$$\bar{u}/\bar{B}_1 = x_{B_l}/(p^3 + U_2 p^2 + U_{1P} + U_0)/\Delta \quad (5.168)$$

$$\bar{w}/\bar{B}_1 = z_{B_l}(p^3 + W_2 p^2 + W_1 p + W_0)/\Delta \quad (5.169)$$

$$\bar{\theta}/\bar{B}_1 = m_{B_l}(H_2 p^2 + H_1 p + H_0)/\Delta \quad (5.170)$$

where

$$\Delta = p^4 + B_{1C}p^3 + C_1p^2 + D_1p + E_1 \text{ (the stability quartic)}$$

and

$$U_2 = -(z_w + m_q + \hat{V}m_{\dot{w}}) + x_w \frac{z_{B_l}}{x_{B_l}}$$

$$U_1 = z_w m_q - \hat{V}m_w + m_{\dot{w}} w_c \sin \tau_c + (\hat{V}x_w - w_c \cos \tau_c) \frac{m_{B_l}}{x_{B_l}}$$

$$-(x_w m_q + m_{\dot{w}} w_c \cos \tau_c) \frac{z_{B_l}}{x_{B_l}}$$

$$U_0 = m_w w_c \sin \tau_c - m_w w_c \cos \tau_c \frac{z_{B_1}}{x_{B_1}} + (z_w \cos \tau_c - x_w \sin \tau_c) w_c \frac{m_{B_1}}{x_{B_1}}$$

$$W_2 = -x_u - m_q + z_u \frac{x_{B_1}}{z_{B_1}} + \hat{V} \frac{m_{B_1}}{z_{B_1}}$$

$$W_1 = x_u m_q - (z_u m_q - \hat{V} m_w) \frac{x_{B_1}}{z_{B_1}} - (\hat{V} x_u + w_c \sin \tau_c) \frac{m_{B_1}}{z_{B_1}}$$

$$W_0 = m_u w_c \cos \tau_c - m_u w_c \sin \tau_c \frac{x_{B_1}}{z_{B_1}} + (z_u w_c \cos \tau_c - x_u w_c \sin \tau_c) \frac{m_{B_1}}{z_{B_1}}$$

$$H_2 = 1 + m_{\dot{w}} \frac{z_{B_1}}{m_{B_1}}$$

$$H_1 = -x_u - z_w + (m_u + z_u m_{\dot{w}}) \frac{x_{B_1}}{m_{B_1}} + (m_w - x_w m_{\dot{w}}) \frac{z_{B_1}}{m_{B_1}}$$

$$H_0 = x_u z_w - x_w z_u + (z_u m_w - z_w m_u) \frac{x_{B_1}}{m_{B_1}} + (x_w m_u - x_u m_w) \frac{z_{B_1}}{m_{B_1}}$$

Equations 5.168, 5.169, and 5.170 are the transfer functions of the variables u , w , and θ in relation to the control input B_1 .

Let us use the equations to find the normal acceleration due to a sudden increase of cyclic pitch B_1 . The increment of acceleration can be expressed as ‘ g ’ units and

$$ng = V \frac{d\theta}{dt} - \frac{dw}{dt}$$

or, in non-dimensional form, taking $\hat{V} = \mu$, as

$$n = \frac{1}{w_c} \left(\mu \frac{d\theta}{d\tau} - \frac{dw}{d\tau} \right) \quad (5.171)$$

The Laplace transform of eqn 5.171 is

$$\bar{n} = \frac{p}{w_c} (\mu \bar{\theta} - \bar{w})$$

and for the input of cyclic pitch

$$\bar{B}_1 = B_1/p$$

so that

$$\bar{n} = \frac{B_1}{w_c} \left(\mu \frac{\bar{\theta}}{\bar{B}_1} - \frac{\bar{w}}{\bar{B}_1} \right) \quad (5.172)$$

Usually the solution of $\Delta = 0$ consists of two real roots and a complex pair, and the inverse of eqn 5.172 then takes the form

$$n = F + Ge^{\lambda_1 \tau} + He^{\lambda_2 \tau} + e^{\lambda_{re} \tau} [C \cos \lambda_{im} \tau + S \sin \lambda_{im} \tau] \quad (5.173)$$

with similar solutions for u , w , and θ . For the less usual solution of two complex roots, the inverse of n takes the form

$$n = F + e^{\lambda_{re1} \tau} (C_1 \cos \lambda_{im_1} \tau + S_1 \sin \lambda_{im_1} \tau) + e^{\lambda_{re2} \tau} (C_2 \cos \lambda_{im_2} \tau + S_2 \sin \lambda_{im_2} \tau)$$

In the above two equations, F , G , H , C , C_1 , etc. are constants that are determined by the initial conditions.

The normal acceleration in response to a step input of longitudinal cyclic pitch has been calculated for our example helicopter ($e = 0.04$), for $\mu = 0.3$, and is shown by the full line of Fig. 5.21. Now, in a manouevre of this kind it would not be expected that the stick would be held fixed for more than about three seconds, because the pilot would want to retrim the aircraft into a new steady state. During such a relatively short time interval, the forward speed would be expected to change very little and it would seem reasonable to omit the speed terms, i.e. the u - and X -force derivatives, from the response equations. The result of doing this is shown by the broken line of Fig. 5.21, and it can be seen that the error in omitting these terms is quite small. The simplification to the response equations is, however, considerable. The normal acceleration can then be written as

$$\begin{aligned} n &= \frac{1}{w_c} \left(\mu \frac{d\theta}{dt} - \frac{dw}{dt} \right) \\ &= -\frac{1}{w_c} (z_{B_1} B_1 + z_w w) \end{aligned} \quad (5.174)$$

from, the simplified eqn 5.163.

Then, for a step input of cyclic pitch,

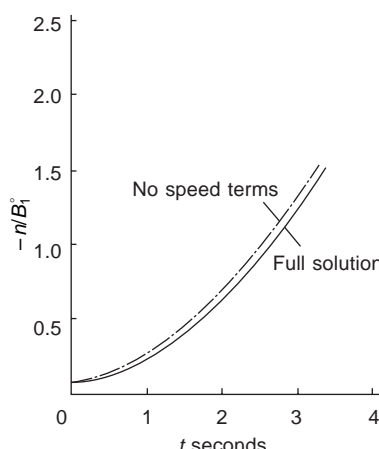


Fig. 5.21 Time history of normal acceleration in response to sudden change of cyclic pitch

$$\bar{n} = -\frac{z_{B_1} \bar{B}_1}{w_c} \left(\frac{1}{p} + z_w \frac{p + \Gamma_1}{p^2 + B'_1 p + C'_1} \right) \quad (5.175)$$

where $\Gamma_1 = -m_q + \mu m_{B_1}/z_{B_1}$ and B'_{1c} and C'_1 are the quartic coefficients B_{1c} and C_1 with the speed derivatives neglected.

The response calculations presented in Figs 5.22 to 5.24 have been made using eqn 5.175.

Figure 5.22 compares the response of our example helicopter ($e = 0.04$) with a hingeless helicopter which, as before, is assumed to have a hub moment five times larger than that of the 4 per cent offset flapping hinge. It can be seen that the greater control power and the increased instability result in a rapid increase of acceleration, and the roots of $p^2 + B'_{1c}p + C'_1 = 0$ indicate this growth to be rapidly divergent.

A peculiarity of helicopter normal acceleration is the sudden jump of acceleration which occurs with the initial application of cyclic pitch. This is due to the force produced by the sudden change of rotor disc incidence which is roughly proportional to speed.

Fitting the tailplane considered earlier to both helicopters, Figs 5.23 and 5.24, shows that the rate of increase of acceleration reaches a maximum and then begins to decrease.

5.9.4 Control response in hovering flight

Another important flying quality of the helicopter is the rolling response in hovering flight, particularly in relation to accurate manoeuvring near the ground. We shall assume that we need consider only pure rolling, in which case the equations of motion reduce simply to

$$\frac{d^2\phi}{dt^2} - l_p \frac{d\phi}{dt} = l_{A_1} A_1 \quad (5.178)$$

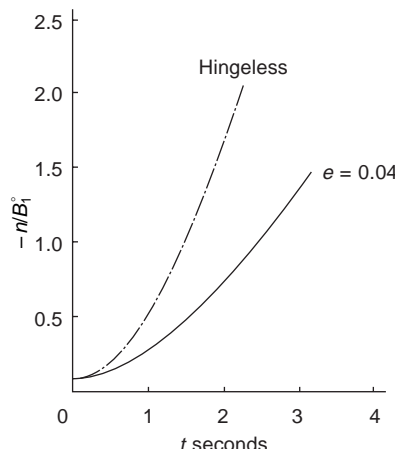


Fig. 5.22 Time history of normal acceleration for hingeless helicopter

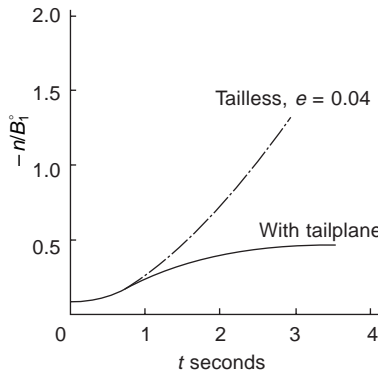


Fig. 5.23 Effect of tailplane on longitudinal response (articulated rotor)

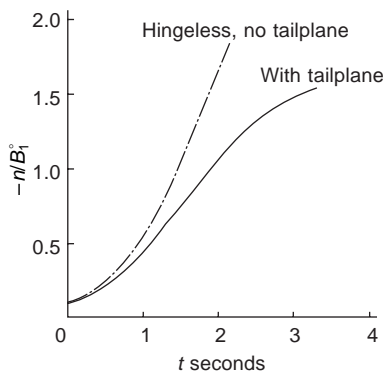


Fig. 5.24 Effect of tailplane on longitudinal response (hingeless rotor)

The rolling response to a sudden application of cyclic pitch A_1 is

$$\frac{d\phi}{d\tau} = -\frac{l_{A_1}}{l_p}(1 - e^{-l_p \tau})A_1$$

Numerical values for our example helicopter with 4 per cent hinges and of helicopters with zero offset and with a hingeless rotor are shown in Fig. 5.25.

It can be seen that the high roll damping of the hingeless helicopter enables it to reach a constant rate of roll within less than a second, whereas the helicopter with zero flapping hinge offset has not reached a steady rate by even four seconds. It is interesting to note that, for a given amount of cyclic pitch, the final rates of roll are the same. This is because the control power, represented by l_{A_1} , and the roll damping l_p vary in roughly the same proportion, and it is the ratio between them that determines the final rate of roll. Pilots have described the response of the hingeless helicopter as 'crisp', whereas some would say of the helicopter with zero hinge offset that it 'lags' the application of control. The probable explanation for this is that the roll damping of the latter helicopter is so weak that, roughly speaking, control application demands



Fig. 5.25 Rate of roll in response to sudden application of lateral control

roll acceleration which is, so to speak, two stages in advance of the roll angle which is usually the required response. Thus, since a steady state is not reached in a fairly short time, considerable anticipation is required of the pilot in order to check the rolling motion and prevent overshooting the required bank angle. The control of the hingeless helicopter is said to command roll rate because of the high damping.

An indication of the pilot's action required to achieve a 20° angle of bank in 2 seconds is shown in Fig. 5.26 for the hingeless helicopter and for one with zero flapping hinge offset. The roll manoeuvre demanded is assumed to be given by

$$\phi = 1.25[\cos(3\pi/2)t - 9 \cos(\pi/2)t + 8]^\circ$$

The quantities $d^2\phi/dt^2$ and $d\phi/d\tau$ are therefore known and inserted in eqn 5.178 to obtain the lateral control A_1 directly.

It can be seen that for the helicopter with zero offset hinges the manoeuvre is only about one quarter completed when the stick begins to move in the opposite direction, and is barely half completed before considerable opposite stick has to be applied to check the rolling motion and settle into the required bank angle. The hingeless helicopter, on the other hand, requires very little opposite stick to achieve the same manoeuvre. The amount of stick movement required is not only much less but is smoother than that of the helicopter with zero offset. This response would be regarded as very satisfactory, and is one of the benefits of the hingeless rotor.

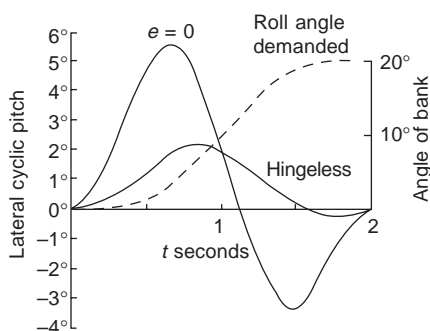


Fig. 5.26 Lateral cyclic pitch to achieve given roll manoeuvre

5.9.5 Response to vertical gusts

In this section we shall describe briefly the response of a helicopter to a sharp vertical gust. A thorough investigation taking into account the time taken for the rotor to enter the gust and the subsequent blade bending and flapping response would be very lengthy. We shall assume that the rotor takes a negligible time to enter the gust completely and, as in the section on forward flight response, we shall assume that changes of forward speed are negligible, at least for the important initial response. We shall also neglect the flapping motion of the blades.

The effect of meeting an up-gust, as far as the calculation of the blade forces and moments is concerned, is identical to the effect of a downward velocity of the complete helicopter; i.e. if the gust has velocity w_g , the vertical force due to the gust alone is $Z_w w_g$ and the pitching moment is $M_w w_g$.

The non-dimensional equations of motion corresponding to level flight are therefore

$$\frac{dw}{d\tau} - z_w w - \mu \frac{d\theta}{d\tau} = z_w w_g \quad (5.179)$$

$$-m_{\dot{w}} \frac{dw}{d\tau} - m_w w + \frac{d^2\theta}{d\tau^2} - m_q \frac{d\theta}{d\tau} = m_{\dot{w}} \frac{dw_g}{d\tau} + m_w w_g \quad (5.180)$$

The increment of normal acceleration ng is given, as before, by

$$ng = \frac{g}{w_c} \left(\mu \frac{d\theta}{d\tau} - \frac{dw}{d\tau} \right)$$

or

$$n = - \frac{z_w}{w_c} (w_g + w) \quad (5.181)$$

from eqn 5.179.

By comparing eqn 5.181 with eqn 5.174, the Laplace transformation of the response to a sharp-edged gust is

$$\bar{n} = - \frac{z_w w_g}{w_c} \left(\frac{1}{p} + z_w \frac{p + \Gamma_1}{p^2 + B'_{lc} p + C'_1} \right) \quad (5.182)$$

Equation 5.182 has been solved for the cases of the helicopter with 4 per cent flapping hinge offset and one with a hingeless rotor, both with and without a tailplane, and the results for $\mu = 0.3$ are shown in Figs 5.27 and 5.28.

Both tailless helicopters are unstable, as has been shown before, and we see that, apart from a slight initial drop, the normal acceleration increases indefinitely, the hingeless helicopter diverging more rapidly due to the larger, positive, value of m_w . When a tailplane is fitted, the response is improved and the normal acceleration of the helicopter with offset hinges subsides quite quickly. The hingeless helicopter at this forward speed is just about neutrally stable, and the normal acceleration remains practically constant. At higher forward speeds, the hingeless helicopter becomes unstable and the normal acceleration diverges.

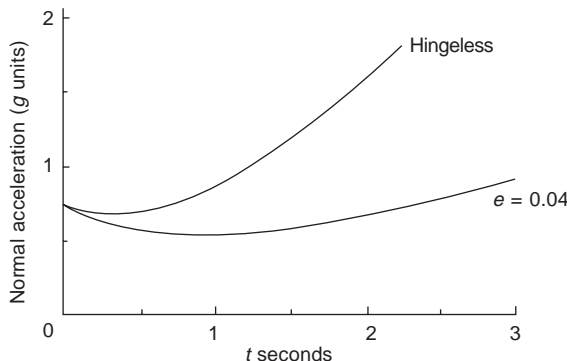


Fig. 5.27 Longitudinal acceleration in response to sharp-edged vertical gust for a tailless helicopter

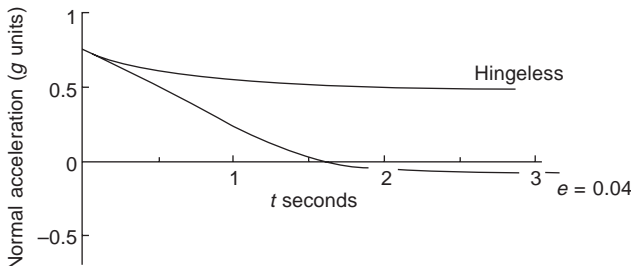


Fig. 5.28 Effect of tailplane on gust response

It is sometimes said that, because helicopter blades can flap or bend, the rotor is effectively self-alleviating with regard to the gust loads. There is a grain of truth in this as far as the *initial* load is concerned because, while the blades are accelerating, the reaction at the hinge will usually be less than the sudden change of lift*. But we know that the blade flapping response is extremely rapid and can be regarded as practically complete within about $\frac{1}{4}$ second, so that after that time the lift load will be fully transmitted to the hub and airframe. This extremely short time interval is insignificant compared with the total response time, and justifies the assumption that the blade flapping motion can be ignored. Furthermore, the rather academic example of a sharp-edged gust represents the worst case; the more realistic 'ramp' type of gust would give the blades even more time to reach equilibrium before the maximum gust velocity is reached.

It is interesting to compare the *initial* acceleration response of the helicopter with that of the fixed wing aircraft. If w_g is the initial gust velocity, the normal acceleration is given by

*If the centre of lift coincides with the centre of percussion of the blade the *initial* hinge reaction will be zero.

$$ng = \frac{-Z_w w_g}{W/g}$$

for the helicopter and for the fixed-wing aircraft.

For the helicopter,

$$n = -\frac{z_w \rho s A \Omega R w_g}{w_c \rho s A \Omega^2 R^2} = -\frac{z_w w_g}{w_c \Omega R}$$

and for the fixed-wing aircraft

$$n = -z_w \rho \frac{S}{W} V w_g$$

For the helicopter we can take $z_w = -2a\mu/(8\mu + as)$, and for the fixed wing aircraft $z_w = -\frac{1}{2}a$, where a in the latter case is the lift slope of the complete aircraft.

Let us compare our example helicopter (hinged or hingeless) with a fixed wing aircraft whose wing loading W/S is 1450 N/m^2 and whose lift slope is 4. Then, if w_g is 10.5 m/s (standard gust velocity), the initial acceleration for both aircraft is as shown in Fig. 5.29.

That the normal acceleration of the helicopter is practically constant is easily seen physically since, for even quite high forward speeds, the rotor lift is dominated by the (constant) rotational speed of the rotor, so the effect of a given vertical gust is almost independent of speed. On the other hand, the response of the fixed wing aircraft increases with speed.

5.9.6 The longitudinal characteristic quartic coefficients E_1 and C_1

The coefficient E_1 . Consider a helicopter changing from one trimmed speed to another, the collective pitch remaining fixed. For small changes of speed from level flight, the resulting angle of climb or descent will be quite small, corresponding to the ‘gliding flight’ of classical fixed wing stability theory.

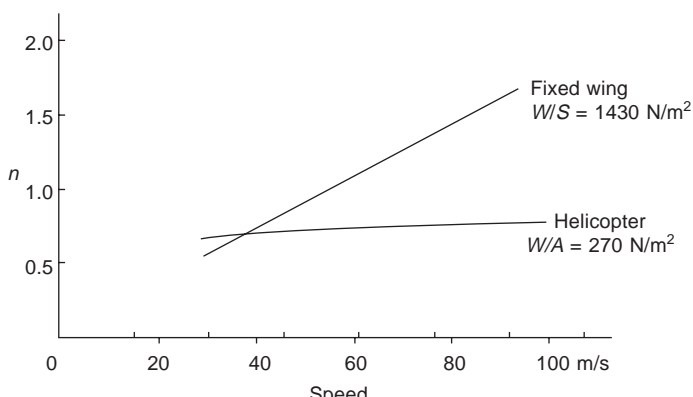


Fig. 5.29 Comparison of helicopter and fixed wing aircraft response to vertical gust

The pitching moment under these conditions will be a function of the tip speed ratio μ , the (non-dimensional) vertical velocity w , and the longitudinal cyclic pitch B_1 . Since the helicopter is supposed to be in trim, we must have $C_m(\mu, w, B_1) = 0$ at all speeds. Therefore

$$\frac{dC_m}{d\mu} = \frac{\partial C_m}{\partial \mu} + \frac{\partial C_m}{\partial w} \frac{dw}{d\mu} + \frac{\partial C_m}{\partial B_1} \frac{dB_1}{d\mu} = 0$$

Since the thrust will be practically constant, we also have

$$\frac{dt_c}{d\mu} = \frac{\partial t_c}{\partial \mu} + \frac{\partial t_c}{\partial w} \frac{dw}{d\mu} + \frac{\partial t_c}{\partial B_1} \frac{dB_1}{d\mu} = 0$$

In terms of the aerodynamic derivatives, these two equations can be written approximately as

$$m_u + m_w \frac{dw}{d\mu} + m_{B_1} \frac{dB_1}{d\mu} = 0$$

and

$$z_u + z_w \frac{dw}{d\mu} + z_{B_1} \frac{dB_1}{d\mu} = 0$$

Eliminating $dw/d\mu$ gives

$$\frac{dB_1}{d\mu} = \frac{m_w z_u - m_u z_w}{m_{B_1} z_w - m_w z_{B_1}}$$

Now, when calculating the control derivatives, we found that $z_{B_1} = -\mu z_w$, so that

$$\begin{aligned} \frac{dB_1}{d\mu} &= \frac{m_w z_u - m_u z_w}{z_w (m_{B_1} + \mu m_w)} \\ &= \frac{E_1}{z_w t_c (m_{B_1} + \mu m_w)} \end{aligned}$$

from eqns 5.21, 5.25, and 5.27, with $t_c = 0$.

Thus, the rate of change of cyclic pitch to trim with forward speed is proportional to the constant term in the stability quartic, i.e. it is a measure of the static stability of the helicopter. The result is analogous to that of the fixed wing aircraft. Now, in the theory of the static stability of subsonic aircraft it is usual to regard m_u as zero, so that the static stability is entirely determined by the sign of m_w , which is proportional to $\partial C_m / \partial C_L$. But $\partial C_m / \partial C_L$ is proportional to the distance of the c.g. from the *neutral point*, and for this reason $-\partial C_m / \partial C_L$ is called the ‘static margin’. Thus the static stability of the fixed wing aircraft is related simply to a quantity which has a clear physical meaning. Unfortunately, as we have seen, in helicopter work there is no such simple parameter which directly controls the static and dynamic stability. Both types of stability are affected by a number of quantities over which the designer has only limited powers of variation. At low speeds m_w is small, and the static stability is dominated by m_u which, although positive, is responsible for the helicopter’s characteristic divergent oscillation. At high speeds the static stability is often improved, because m_u has changed very little and m_w , although being much larger and positive

(i.e. in the unstable sense), is usually associated with a positive z_u . When a tailplane is fitted to improve the dynamic stability, at the high speeds for which z_u is usually positive, the combination $z_u m_w$ is such as to decrease the value of E_1 . Thus the desirability of a positive static stability is not as straight/forward for the helicopter as it is with a fixed wing aircraft.

The coefficient C_1 . Consider a helicopter performing a pull-up manoeuvre at constant speed in a vertical plane, Fig. 5.30. It will be assumed that the flight path is circular and the helicopter is in trim. The pitching moment will be a function of the vertical velocity w , the rate of pitch q , and the cyclic pitch B_1 ; i.e. in the trimmed manoeuvre we have $C_m(w, q, B_1) = 0$ with w and q being dependent on ng , the excess normal acceleration. Therefore

$$\frac{dC_m}{dn} = \frac{\partial C_m}{\partial w} \frac{dw}{dn} + \frac{\partial C_m}{\partial q} \frac{dq}{dn} + \frac{\partial C_m}{\partial B_1} \frac{dB_1}{dn} = 0$$

or
$$\frac{dB_1}{dn} = - \frac{(\partial C_m / \partial w) dw/dn + (\partial C_m / \partial q) dq/dn}{\partial C_m / \partial B_1} \quad (5.183)$$

where, in eqn 5.183, w and q have been non-dimensionalised (section 5.2). Then, if ΔT is the increase of thrust in the manoeuvre, we have

$$ng = \frac{\Delta T}{W/g}$$

or

$$n = \frac{(\partial T / \partial w) w \Omega R}{W} = - \frac{z_w}{w_c} w$$

so that

$$\frac{dw}{dn} = - \frac{w_c}{z_w}$$

Now

$$q = \frac{ng}{V\Omega}$$

therefore
$$\frac{dq}{dn} = \frac{g}{V\Omega} = \frac{w_c}{\mu\mu^*}$$

Substituting in eqn 5.183 and expressing in derivative form gives

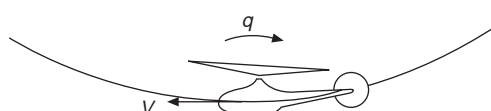


Fig. 5.30 Helicopter in vertical pull-up

$$\begin{aligned}\frac{dB_1}{dn} &= \frac{m'_w w_c/z_w - m'_q w_c/\mu\mu^*}{m'_{B_1}} \\ &= \frac{\mu m_w - z_w m_q}{\mu z_w m_{B_1}} \\ &\propto C'_1\end{aligned}$$

Hence, as with the fixed wing aircraft, the rate of change of control angle to trim with normal acceleration is proportional to C'_1 , i.e. the value of C_1 when the forward velocity terms have been neglected. Now we have seen that the normal acceleration response to either a longitudinal control input or a vertical gust depends on the value of C'_1 ; if it is positive the motion is stable (since the coefficient B'_{lc} is always positive), and if it is negative the response is divergent. Thus the slope of the control angle to trim in a pull-up gives a direct indication of the normal acceleration response. Again, as with the static stability, the c.g. position has little influence on the slope of the control angle with acceleration, but we note that C'_1 is not confounded by the presence of forward velocity derivatives and its value can be directly affected by a tailplane. Thus, with a large enough tailplane, one can always ensure that C'_1 is positive, although the tailplane may have to be inconveniently large to suppress the inherent instability of the hingeless rotor at high speeds. However we should note that a large tailplane (negative m_w) with a positive z_u may lead to static *instability*, as indicated in the discussion relating to E_1 .

References

1. Hohenemser, K., 'Dynamic stability of a helicopter with hinged rotor blades', *NACA Tech. Memo. 907*, 1939.
2. Sissingh, G. J., 'Contributions to the dynamic stability of rotary wing aircraft with articulated blades', *Air Material Command Trans. F-TS-690-RE*, August 1946.
3. Padfield, G. D., *Helicopter flight dynamics*, Blackwell Science, 1996.
4. Bryant, L. W. and Gates, S. B., 'Nomenclature for stability coefficients', *Aeronautical Research Council R&M 1801*, 1937.
5. Johnson, W., *Helicopter theory*, Princeton Univ. Press, Princeton NJ, 1980.
6. Pitt, D. M. and Peters, D. A., 'Rotor dynamic inflow derivatives and time constants from various inflow models', Paper No. 55, 9th European Rotorcraft Forum, Stresa, Italy, 13–15 Sept. 1983.
7. Peters, D. A. and HaQuang, N., 'Dynamic inflow for practical applications', *J. Amer. Helicopter Soc.*, **33**(4), pp. 64–68, Oct. 1988.
8. Amer, K. B., 'Theory of helicopter damping in pitch or roll and a comparison with flight measurements', *NACA Tech. Note 2136*, 1950.
9. Bramwell, A. R. S., 'Longitudinal stability and control of the single rotor helicopter', *Aeronautical Research Council R&M 3104*, 1959.
10. Zbrozek, J. K., 'Introduction to the dynamic longitudinal stability of the single rotor helicopter', *RAE Rep. Aero. 2248*, 1948.
11. Bramwell, A. R. S., 'The lateral stability and control of the tandem-rotor helicopter', Part II *Aeronautical Research Council R&M 3223*, 1961.
12. McLean, D., *Automatic flight control systems*, Prentice-Hall, 1990.
13. Pallett, E. H. J. and Coyle, S., *Automatic flight control*, Blackwell Science, 1993 (4th edition).

Rotor aerodynamics in forward flight

6.1 Introduction

In Chapter 3 we gave some methods for calculating the induced velocity in forward flight on the assumption that the rotor could be regarded as a lifting surface. These methods give simple expressions for the induced velocity which can be incorporated into the equations for calculating the rotor forces and blade flapping and which eventually lead to fairly simple formulae for these forces and moments. We have so far used only ‘linear’ aerofoil characteristics, e.g. a linear lift slope without stall and a constant drag coefficient.

We now consider the fact that, as in hovering flight dealt with in Chapter 2, vortex wakes spring from the individual blades and form a complicated downwash pattern as the vortex elements spiral downwards below the rotor plane. We also consider the aerofoil characteristics under conditions of high Mach number and changing incidence.

6.2 The vortex wake

Consider the blade in steady forward flight. As in hovering flight the circulation, in general, varies along the span and, in consequence, vortex lines leave the trailing edge and spiral downwards beneath the rotor. In addition, however, and as we saw in Chapter 3, both the incidence and chordwise velocity vary over wide ranges in forward flight causing timewise changes of incidence at a given radial position. In accordance with Kelvin’s theorem each change of circulation at the blade must result in a counter vortex being shed in the wake. Thus, in forward flight the vortex wake also includes vortex lines which lie in the spanwise direction. These are referred to as ‘shed’ vortices, to distinguish them from the ‘trailing’ vortex lines arising from the spanwise circulation variation. The trailing vortices themselves are of varying strength due to the timewise variation in the bound circulation in forward flight. The vortex wake from a blade can be represented as in Fig. 6.1.

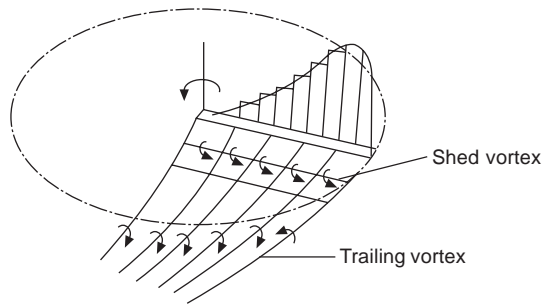


Fig. 6.1 Shed and trailing vortices from lifting blade

Let us look at a small portion of the wake in more detail. Consider an element of the blade of span dr . The local circulation is Γ , and trailing vortices of this strength leave the ends of this element, Fig. 6.2. If the rate of change of circulation is $\partial\Gamma/\partial t$, the circulation at an instant dt before would have been $\Gamma - (\partial\Gamma/\partial t)dt$, and the change will have resulted in a spanwise vortex element or filament of strength $(\partial\Gamma/\partial t)dt$ being shed behind the element, as shown in Fig. 6.2. Since the strength of the bound circulation at the earlier instant was $\Gamma - (\partial\Gamma/\partial t)dt$, the arrangement of vortex filaments can be represented in the form shown in Fig. 6.3, i.e. the vortex wake can be regarded as an assembly of infinitesimal vortex rings. The distribution of vortex rings is equivalent to a layer of doublets whose axes are perpendicular to the vortex sheet, and Baskin¹ has used this to develop an induced velocity theory.

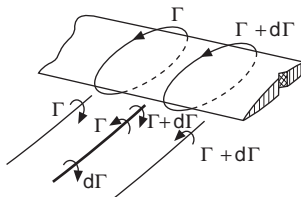


Fig. 6.2 Spanwise change of bound circulation

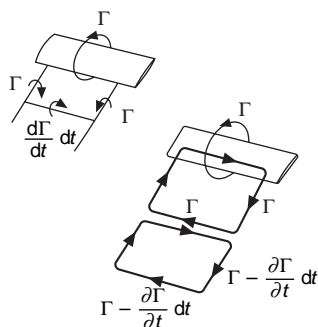


Fig. 6.3 Modelling of vortex wake

The total induced velocity at a point P on a given blade of the rotor will be the combined effect of the velocities induced by the trailing and shed vortices of all the blades and of the bound vortices of all the blades except the one in question. If Γ is the strength of a vortex element whose length is ds , and \mathbf{l} is the displacement vector between the element and the point P , Fig. 6.4, the Biot–Savart law gives for the corresponding increment of induced velocity

$$d\mathbf{q} = \frac{\Gamma}{4\pi} \cdot \frac{\mathbf{l} \times d\mathbf{s}}{l^3} \quad (6.1)$$

Using this formula it would appear straightforward, in principle, to integrate the contributions mentioned above. Unfortunately, as we also saw in the hovering case, the vortices interact with one another and the wake pattern becomes very complicated. This means that we are unsure of the positions of the vortex elements, particularly in the more distant parts of the wake, or, in other words, \mathbf{l} in eqn 6.1 is not known for certain. Due to the forward flight case not having the axial symmetry of vertical flight, the pattern of vortex interaction is different because, except at low speeds, the flow through the rotor is determined largely by the component of forward flight speed which is, of course, constant over the disc. Let us suppose that the induced velocity is small compared with the forward speed (corresponding to a lightly loaded rotor at high forward speed) and ignore the distortions due to vortex interaction. To include partially the effect of the induced velocity we can calculate the ‘momentum’ value and add it to the component of the forward speed perpendicular to the rotor disc. The trailing vortex lines then lie on the surfaces of skewed cylinders. This represents, in effect, a rigid wake model by analogy with that for hovering flight. The plan and side views of a trailing vortex line are shown in Figs 6.5 and 6.6.

If the x axis lies along the direction of motion and in the plane of the rotor, and the z axis points upwards perpendicular to the rotor plane, as shown in Figs 6.5 and 6.6, the co-ordinates of a trailing vortex element which was shed when the blade azimuth angle was ϕ are

$$x = -r_1 \cos \phi - Vt \cos \alpha_D, \quad y = x_1 R \sin \phi, \quad z = Vt \sin \alpha_D - v_i t$$

where t is the time taken for the blade to rotate from ϕ to ψ . Since $\psi - \phi = \Omega t$, we have

$$x = -r_1 \cos \psi - (V \cos \alpha_D / \Omega)(\psi - \phi) = -r_1 \cos \psi - \mu_D R(\psi - \phi)$$

$$y = x_1 R \sin \phi$$

$$z = (V \sin \alpha_D - v_i)(\psi - \phi) / \Omega = \lambda_D R(\psi - \phi)$$

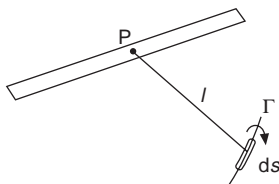
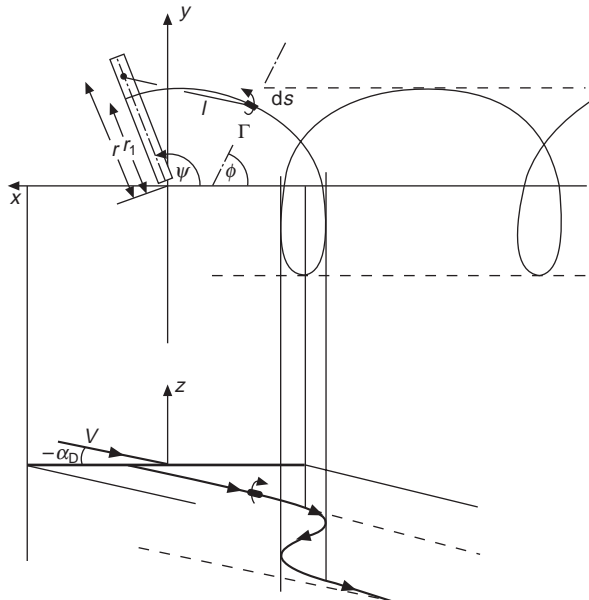


Fig. 6.4 Induced velocity at P



Figs 6.5 and 6.6 Plan and side views of vortex filament

where $\mu_D = V \cos \alpha_D / \Omega R$, $\lambda_D = (V \sin \alpha_D - v_i) / \Omega R$, $x_1 = r_1/R$

It can be seen that the plan view of a trailing vortex filament, under the given assumptions, is a cycloid, and the side view shows the constant downward displacement of the cycloid.

Returning to eqn 6.1, let

$$\mathbf{l} = l_1 \mathbf{i} + l_2 \mathbf{j} + l_3 \mathbf{k}$$

and

$$ds = ds_1 \mathbf{i} + ds_2 \mathbf{j} + ds_3 \mathbf{k}$$

where $\mathbf{i}, \mathbf{j}, \mathbf{k}$ are unit vectors along the *x*, *y*, *z*, axes. Then, if w_t denotes the downward component of induced velocity due to a trailing vortex of strength Γ

$$dw_t = \frac{\Gamma}{4\pi} \frac{l_1 ds_2 - l_2 ds_1}{l^{3/2}} \quad (6.2)$$

where

$$l^2 = l_1^2 + l_2^2 + l_3^2$$

Then, measuring ds in the direction away from the blade,

$$ds_1 = -dx = -R(x_1 \sin \phi + \mu_D) d\phi$$

$$ds_2 = -dy = -x_1 R \cos \phi d\phi$$

From Figs 6.5 and 6.6 we see that, relative to the blade from which the vortex element originated,

$$l_1 = r \cos \psi - r_1 \cos \phi + \mu_D R(\psi - \phi)$$

$$\begin{aligned}l_2 &= -R(x \sin \psi - x_1 \sin \phi) \\l_3 &= \lambda_D R(\psi - \phi)\end{aligned}$$

The blade in question will also be affected by the trailing vortices of the preceding blades. The above equations still apply provided we allow for the appropriate phase shift in the translational terms of l_1 , l_2 , l_3 . Thus, more generally,

$$\left. \begin{aligned}l_1 &= R[x \cos \psi - x_1 \cos \phi + \mu_D(\psi - \phi + (2\pi/b)n)] \\l_2 &= -R(x \sin \psi - x_1 \sin \phi) \\l_3 &= \lambda_D R(\psi - \phi + (2\pi/b)n)\end{aligned}\right\} \quad (6.3)$$

where $n = 0, 1, 2, \dots, b - 1$, and b is the number of blades.

Now the appropriate value of Γ of the trailing vortex filament is the *change* of circulation (Fig. 6.2) over an element of the span dr , i.e. $(\partial\Gamma/\partial r)dr$. Then, integrating along the trailing vortices from infinity up to the blade and along the span and summing for all the blades, we have

$$\begin{aligned}w_t = \frac{1}{4\pi R} \sum_{n=0}^b \int_0^1 \int_{-\infty}^{\psi_n} \left[\frac{x_1 + xx_1 \cos(\psi - \phi) + \mu_D(x \sin \psi - x_1 \sin \phi)}{\bar{D}^{3/2}} \right. \\ \left. + \frac{\mu_D \{\psi - \phi - (2\pi/b)n\} \cos \phi}{\bar{D}^{3/2}} \right] \frac{\partial \Gamma}{\partial x_1} dx_1 d\phi \quad (6.4)\end{aligned}$$

where $\psi_n = (2\pi/b)n$, $n = 0, 1, 2, \dots, b - 1$

$$\begin{aligned}\text{and } \bar{D} &= x^2 + x_1^2 - 2xx_1 \cos(\psi - \phi) + (\mu_D^2 + \lambda_D^2)\{\psi - \phi + (2\pi/b)n\}^2 \\ &\quad + 2\mu_D\{\psi - \phi - (2\pi/b)n\}(x \cos \psi - x_1 \cos \phi)\end{aligned}$$

To calculate the induced velocity w_b from the bound vortices of each blade, consider two blades separated by angle ψ_n , as shown in Fig. 6.7.

The co-ordinates of a bound vortex element Γ_n are

$$x_1 = -r_1 \cos(\psi + \psi_n), \quad y_1 = r_1 \sin(\psi + \psi_n)$$

Hence, for the elementary line

$$ds_1 = -dr_1 \cos(\psi + \psi_n), \quad ds_2 = dr_1 \sin(\psi + \psi_n)$$

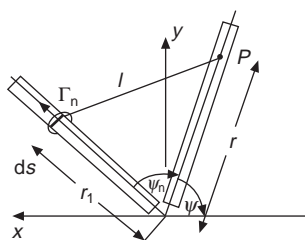


Fig. 6.7 Effect of bound circulation on succeeding blade

and the components of the line joining the line element to a point on the reference blade are

$$l_1 = -r \cos \psi + r_1 \cos (\psi + \psi_n)$$

$$l_2 = r \sin \psi - r_1 \sin (\psi + \psi_n)$$

Then, noting that this calculation does not include the reference blade, $n = 0$, the total contribution of the bound vorticity to the downwash at P is

$$w_b = \frac{1}{4\pi R} \sum_{n=1}^{b-1} \int_0^1 \frac{x \sin \psi_n \Gamma_n(x_1)}{(x^2 + x_1^2 - 2xx_1 \cos \psi_n)^{3/2}} dx_1 \quad (6.5)$$

According to Miller², the contribution of the bound vortices is usually extremely small.

Finally, calculating the induced velocity component w_s for the shed part of the wake, we have, see Fig. 6.8,

$$ds_1 = -dr_1 \cos \psi_0, \quad ds_2 = dr_1 \sin \psi_0$$

The values of l_1, l_2, l_3 are the same as those of eqn 6.3; hence, integrating in both the azimuthwise and spanwise directions gives

$$w_s = \frac{1}{4\pi R} \sum_{n=0}^{b-1} \int_0^1 \int_{-\infty}^{\psi_n} \frac{x \sin(\psi - \phi) - \mu_D R(\psi - \phi) \sin \phi}{D^{3/2}} \frac{\partial \Gamma_n}{\partial \phi} d\phi dx_1 \quad (6.6)$$

The upper limit of the inner integral in eqn 6.6, must be treated with care. In integral eqn 6.4, the azimuthwise integration is taken up to the span axis of the blade since, in calculating the effect of the trailing vortices, it is reasonable to neglect chordwise velocity variations and apply the idea of lifting line theory to the high aspect ratio blade. The shed wake integral, on the other hand, really demands lifting surface techniques since the chordwise vorticity distribution behind the aerofoil induces a considerable chordwise velocity distribution as well as difficulties of singularities in the region of the trailing edge. This matter will be dealt with in more detail in section 6.2.2.

The induced velocity contributions given by eqns 6.4, 6.5, and 6.6 must now be related to the circulation which gave rise to them. If W is the resultant chordwise velocity at the blade, the local loading is

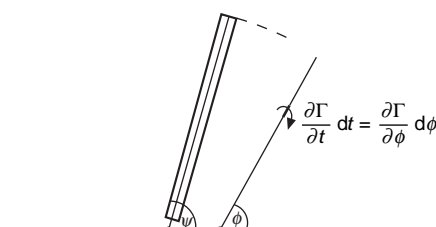


Fig. 6.8 Shed vortex element

$$\frac{dL}{dr} = \frac{1}{2} \rho W^2 C_L c \quad (6.7)$$

and the Kutta–Zhukowsky relation is

$$\frac{dL}{dr} = \rho WT$$

Equating eqns 6.7 and 6.8 gives

$$\Gamma = \frac{1}{2} WC_L c$$

Let us suppose that the lift slope is constant. Then

$$C_L = a\alpha$$

and writing

$$\alpha = \alpha_0 + \alpha_i$$

where α_0 is the incidence in the absence of the induced velocity and α_i is the downwash angle relative to the blade, we have

$$\Gamma = \frac{1}{2} a(\alpha_0 + \alpha_i) Wc$$

But

$$\alpha_i \approx w/W$$

therefore

$$\Gamma = \frac{1}{2} aW\alpha_0 c + \frac{1}{2} ac(w_t + w_b + w_s) \quad (6.9)$$

where w_t , w_b , w_s are given by eqns 6.4, 6.5, and 6.6.

Equation 6.9 is the *integral equation* for the circulation of the reference blade. Although the equation has been simplified by the assumption of a rigid wake, no standard method exists for solving it. One possible way which suggests itself is to assume a simple induced velocity distribution, such as a uniform or Glauert type, and make a first approximation to the circulation. From this approximation the integrals eqns 6.4 to 6.6 are calculated, and new values of Γ are obtained from eqn 6.9. The process is repeated until satisfactory convergence has been obtained. It cannot be certain that convergence will always occur.

It is not necessary, of course, to develop an integral equation such as eqn 6.9. Some methods begin by assuming a prescribed wake model based upon experimental data or reasonable physical arguments and performing piecewise calculations of their contributions to the induced velocity, as discussed in the following section.

6.2.1 Prescribed wake model development

One of the first attempts to depart from the idea of the rotor as a lifting surface, and to use reasonable physical arguments to model the vortex wakes from individual blades in such a way as to make the problem tractable, was that of Willmer³. The main feature that allowed effective computation, particularly in view of the speed of

computers at that time, was his principle of ‘rectangularisation’. Consider the trailing wake from two successive blades, Fig. 6.9. Willmer argued that the radius of curvature of the sheets is large enough (especially for the important outer parts of the blade) for the sheets to be regarded as straight. Actually this is the same assumption as the one made by Prandtl in his method of calculating ‘tip loss’ in hovering flight, section 2.10.1.

Under ‘rectangularisation’, the trailing wakes, Fig. 6.9, are replaced by those shown in Fig. 6.10. The wake attached to the reference blade is assumed to be a straight sheet extending back to infinity, while those of the other blades are assumed to be doubly infinite sheets placed so that the straight vortex lines are tangential to the curved wakes where they pass under the reference blade. Part of the problem in Willmer’s work was to determine the appropriate positions of the wakes of the blades. Any number of parts of the original curved wake could be included, and the choice made depended on the required accuracy. Once the numbers and positions of the sheets had been chosen, the induced velocity at the reference blade could be calculated by an extension of Glauert’s wing theory. It should be noted that this does not imply that the vortex wake is regarded as a number of discrete vortices, as is sometimes thought, but that the vortex wake is continuous and conditions are satisfied at a number of points along the span (method of collocation). Unfortunately, because the loading of a rotor blade is very different from the elliptic, or near elliptic, loading of the conventional fixed wing, a larger number of spanwise points are needed for acceptable accuracy. A comparison of the calculation of the blade thrust by Willmer’s method with that of experiment and of the theory using constant induced velocity for

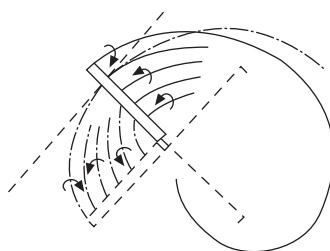


Fig. 6.9 Plan view of successive vortex sheets

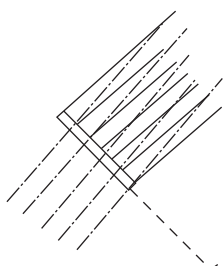


Fig. 6.10 ‘Rectangularisation’ of vortex sheet

$\mu = 0.08$ is shown in Fig. 6.11. Although the agreement with experiment can only be described as fair, it is clear that the new model provided a great improvement on the theory using constant induced velocity and went far to explain the large thrust variations which often lead to large vibration at low values of μ .

Two important defects of the work were that it took no account of shed vorticity and, related to this, it assumed that the strength of the trailing vortex elements were constant along their length.

6.2.2 The shed vorticity

The question of shed vorticity and investigations into suitable representations of the vortex wake have been considered by Miller^{2,4}. Since Miller and others have given considerable attention to the effect of the shed wakes, it may be useful to give a short account of the methods of calculation here.

Consider an aerofoil, Fig. 6.12, whose incidence is changing. Any change of circulation about the aerofoil must be accompanied by a corresponding vortex or vorticity of the opposite sense in the wake, since Kelvin's theorem requires that the total circulation in a circuit containing the aerofoil and the wake must remain constant with time. Thus, an aerofoil whose incidence is continually changing must deposit a sheet of vorticity in the wake whose local strength is related to the time history of rate of change of circulation. Now, the presence of vorticity in the wake plays a part in satisfying the Kutta-Zhukowsky condition at the trailing edge of the aerofoil, so that the circulation about the aerofoil is different from what would have been the case had the vorticity been absent. Also, since the motion we are discussing is unsteady, there

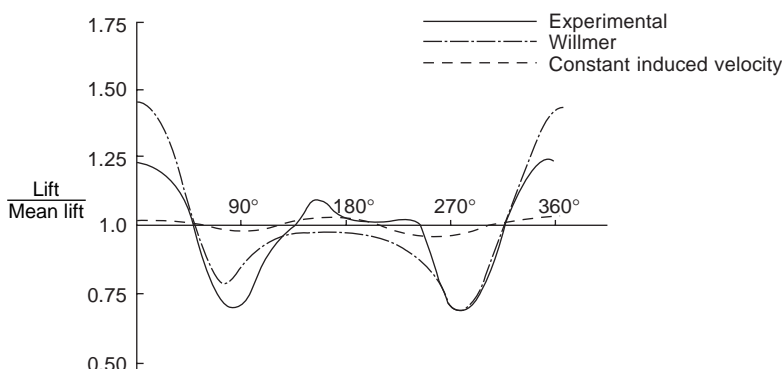


Fig. 6.11 Variation of blade loading with azimuth angle

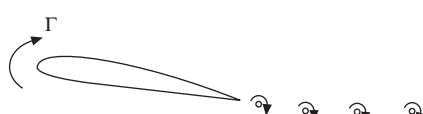


Fig. 6.12 Vortices shed by aerofoil changing its incidence

is an extra pressure, or ‘virtual mass’, term which relates to the acceleration of the air particles in the flow about the aerofoil.

The most important case of unsteady motion is a sinusoidal variation of incidence. The first complete theory was given by Theodorsen⁵, who showed that for an aerofoil whose incidence is changing by performing a sinusoidal vertical (heaving) motion, the lift L as a fraction of the steady lift L_0 at the instantaneous incidence is given by

$$L/L_0 = C(k) + \frac{1}{2}i(k) \quad (6.10)$$

where $C(k)$ is Theodorsen’s function and k is the frequency parameter $nc/2V$, n being the frequency of oscillation and c the aerofoil chord. Theodorsen’s function is defined by

$$C(k) = K_1(ik)/[K_0(ik) + K_1(ik)]$$

where $K_0(ik)$ and $K_1(ik)$ are Bessel functions of the second kind.

For an aerofoil oscillating about its mid-chord, the corresponding result is

$$L/L_0 = \frac{1}{2} [i + (i + 2/k)C(k)] \quad (6.11)$$

These results can be expressed in vector form as shown in Figs 6.13 and 6.14.

The results eqns 6.10 and 6.11 can be obtained in a number of ways⁶ but, since the ‘method of vortices’ is closely related to the ideas being discussed in this chapter, it will be described briefly below.

Corresponding to changes of circulation $d\Gamma$ about the aerofoil, vortex elements of strength $\gamma b d\xi$, equal and opposite to the circulation, are deposited in the wake, γ being the vorticity and ξ the distance of the element from the centre of the aerofoil, non-dimensionalised in terms of the semi-chord b , Fig. 6.15.

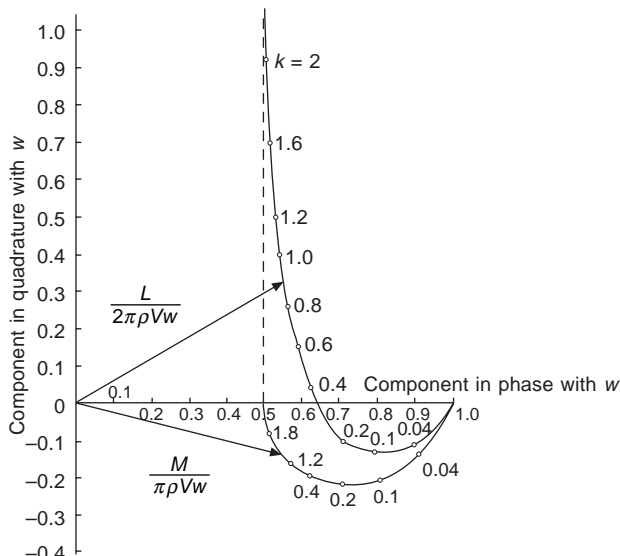


Fig. 6.13 Amplitude and phase of lift and moment of aerofoil oscillating in heave

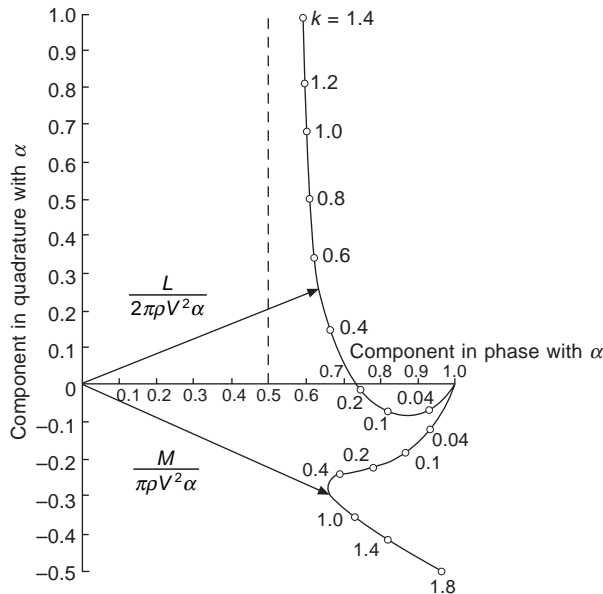


Fig. 6.14 Amplitude and phase of lift and moment of aerofoil oscillating in pitch

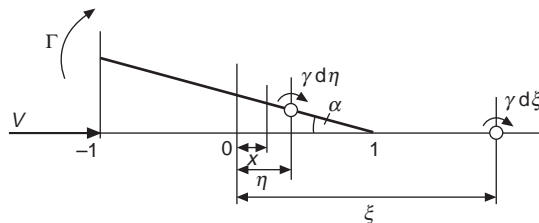


Fig. 6.15 Shed vortex elements

In particular, for a given increment of time dt , the change of circulation is $d\Gamma$ and a vortex element $-V\gamma dt$ is shed at the trailing edge. Since γ is a function of both time and distance, we can write

$$\frac{d\Gamma}{dt} = -V\gamma(l, t) \quad (6.12)$$

and since the total amount of vorticity shed in the wake must be equal to the total circulation about the aerofoil, we also have the relation

$$\Gamma(t) = -b \int_1^\infty \gamma(\xi, t) d\xi \quad (6.13)$$

From thin aerofoil theory⁷, the chordwise vorticity distribution can be expressed as

$$\gamma(x) = A_0 \tan\left(\frac{1}{2} \cos^{-1}\eta\right) + \sum_{n=1}^{\infty} A_n \sin n(\cos^{-1}\eta) \quad (6.14)$$

The assumed form, eqn 6.14, automatically satisfies the Kutta–Zhukowsky condition at the trailing edge. The induced velocity at x due to a vortex element on the aerofoil at η is

$$dv(x) = \frac{\gamma(\eta, t) d\eta}{2\pi(x - \eta)} \quad (6.15)$$

Substituting the series eqn 6.14 for γ and integrating across the chord from -1 to $+1$, gives

$$v(x) = -\frac{1}{2}A_0 - \sum_{n=1}^{\infty} \frac{1}{2}A_n \cos n(\cos^{-1}\eta)$$

where we make use of the well known result

$$\int_0^\pi \frac{\cos n\phi}{\cos \phi - \cos(\cos^{-1}\eta)} d\phi = \pi \frac{\sin n(\cos^{-1}\eta)}{\sin(\cos^{-1}\eta)} \quad (6.16)$$

Let us suppose that, in addition to its forward velocity V , the aerofoil has a vertical (heaving) velocity of \dot{z} at a point about which the aerofoil is also rotating, Fig. 6.16.

The relative air velocity normal to the chord at x due to the motion is

$$u(x) = \alpha \dot{V} + \dot{z} - \dot{\alpha} b(\bar{x} - x)$$

The induced velocity at x due to a vortex element in the wake is

$$dw(x) = \frac{\gamma d\xi}{2\pi(\xi - x)}$$

and the velocity at x induced by the entire wake is

$$w(x) = \int_1^\infty \frac{\gamma d\xi}{2\pi(\xi - x)}$$

Since there can be no flow perpendicular to the chord, we must have

$$u(x) + v(x) + w(x) = 0$$

or

$$-\frac{1}{2}A_0 - \frac{1}{2} \sum_{n=1}^{\infty} A_n \cos n(\cos^{-1}\eta) + [\alpha \dot{V} + \dot{z} - \dot{\alpha} b(\bar{x} - x)] + \int_1^\infty \frac{\gamma d\xi}{2\pi(\xi - x)} = 0 \quad (6.17)$$

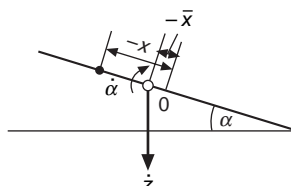


Fig. 6.16 Aerofoil oscillating in heave

Now eqn 6.16 can also be expressed as

$$\int_0^\pi \frac{\cos n\phi}{\xi - \cos \phi} d\phi = \frac{\pi[\xi - \sqrt{(\xi^2 - 1)}]^n}{\sqrt{(\xi^2 - 1)}}$$

so that the Fourier coefficients A_n occurring in eqn 6.17 are easily found to be

$$\left. \begin{aligned} A_0 &= \frac{1}{\pi} \int_1^\infty \frac{\gamma d\xi}{\sqrt{(\xi^2 - 1)}} + 2(\alpha V + \dot{z} - \dot{\alpha} b \bar{x}) \\ A_1 &= \frac{2}{\pi} \int_1^\infty \left[\frac{\xi}{\sqrt{(\xi^2 - 1)}} - 1 \right] \gamma d\xi + 2b\dot{\alpha} \\ A_n &= \frac{2}{\pi} \int_1^\infty \frac{\xi - \sqrt{(\xi^2 - 1)}}{\sqrt{(\xi^2 - 1)}} \gamma d\xi \end{aligned} \right\} \quad (6.18)$$

The linearised Bernoulli equation gives for the pressure difference between the upper and lower surfaces

$$p_l - p_u = 2p \left(\frac{\partial \phi}{\partial t} + V \frac{\partial \phi}{\partial x} \right) \quad (6.19)$$

In terms of the vorticity on the aerofoil, the velocity potential is

$$\phi(x) = \frac{1}{2}b \int_{-1}^x \gamma dx$$

so that

$$\frac{\partial \phi}{\partial x} = \frac{1}{2}b\gamma$$

and

$$\frac{\partial \phi}{\partial t} = \frac{1}{2}b \frac{\partial}{\partial t} \int_{-1}^x \gamma dx$$

The lift on the aerofoil is

$$L = b \int_{-1}^{+1} (p_l - p_u) dx$$

Substituting for the pressure difference from eqn 6.19 and the vorticity from eqn 6.14 leads to

$$L = \rho\pi b \left[\frac{1}{2}b \frac{\partial}{\partial t} (A_0 - \frac{1}{2}A_2) + b \frac{\partial}{\partial t} (A_0 + \frac{1}{2}A_1) + V(A_0 + \frac{1}{2}A_1) \right] \quad (6.20)$$

The circulation about the aerofoil is

$$\Gamma = b \int_{-1}^{+1} \gamma dx = b\pi(A_0 + \frac{1}{2}A_1) \quad (6.21)$$

From eqns 6.18 and 6.21, the first two terms in the bracket of eqn 6.20 can be written as

$$\begin{aligned}
 \frac{1}{2}b \frac{\partial}{\partial t} (A_0 - \frac{1}{2}A_2) + \frac{1}{\pi} \frac{\partial \Gamma}{\partial t} &= \frac{b}{\pi} \frac{\partial}{\partial t} \int_1^\infty \frac{1 - \xi^2 + \xi\sqrt{(\xi^2 - 1)}}{\sqrt{(\xi^2 - 1)}} \gamma d\xi \\
 &\quad + b(\dot{\alpha}V + \ddot{z} + \dot{\alpha}b\bar{x}) + \frac{1}{\pi} \frac{\partial \Gamma}{\partial t} \\
 &= \frac{b}{\pi} \frac{\partial}{\partial t} \int_1^\infty \gamma \xi d\xi - \frac{b}{\pi} \frac{\partial}{\partial t} \int_1^\infty \sqrt{(\xi^2 - 1)} \gamma d\xi \\
 &\quad - b(\dot{\alpha}V + \ddot{z} + \dot{\alpha}b\bar{x}) + \frac{1}{\pi} \frac{\partial \Gamma}{\partial t} \tag{6.22}
 \end{aligned}$$

Now, each element of vorticity in the wake is carried backwards with velocity V , so the vorticity must be of the form

$$\gamma(\xi, t) = f(t - b\xi/V)$$

Since, for a given element of vorticity, $t - b\xi/V$ is constant, it follows that

$$d\gamma = \frac{\partial \gamma}{\partial t} dt + \frac{\partial \gamma}{\partial \xi} d\xi = 0$$

and

$$dt - \frac{b}{V} d\xi = 0$$

i.e.

$$\frac{\partial \gamma}{\partial t} = -\frac{V}{b} \frac{\partial \gamma}{\partial \xi} \tag{6.23}$$

in the wake.

Differentiating under the integral sign and making use of eqn 6.23, we find

$$\begin{aligned}
 \frac{\partial}{\partial t} \int_1^\infty \gamma \xi d\xi - \frac{\partial}{\partial t} \int_1^\infty \sqrt{(\xi^2 - 1)} \gamma d\xi \\
 &= -\frac{V}{b} \int_1^\infty \frac{\partial \gamma}{\partial \xi} \xi d\xi + \frac{V}{b} \int_1^\infty \sqrt{(\xi^2 - 1)} \frac{\partial \gamma}{\partial \xi} d\xi \\
 &= -\frac{V}{b} [\gamma \xi]_1^\infty + \frac{V}{b} \int_1^\infty \gamma d\xi + \frac{V}{b} [\gamma \sqrt{(\xi^2 - 1)}]_1^\infty \\
 &\quad - \frac{V}{b} \int_1^\infty \frac{\gamma \xi}{\sqrt{(\xi^2 - 1)}} d\xi \\
 &= -\frac{V}{b} \{[\xi - \sqrt{(\xi^2 - 1)}]\gamma(\xi, t)\}_1^\infty + \frac{V}{b} \int_1^\infty \gamma d\xi \\
 &\quad - \frac{V}{b} \int_1^\infty \frac{\gamma \xi}{\sqrt{(\xi^2 - 1)}} d\xi,
 \end{aligned}$$

on integrating by parts.

Now $\xi - \sqrt{(\xi^2 - 1)} = 1/[\xi + \sqrt{(\xi^2 - 1)}]$, from which it follows that, since $\gamma(\xi, t)$ is finite, the term in the bracket vanishes at the upper limit. At the lower limit the term in the bracket is equal to $(V/b)\gamma(1, t)$. This term cancels identically with the last term of the eqn 6.22, so that

$$\begin{aligned} & \frac{1}{2}b \frac{\partial}{\partial t} (A_0 - \frac{1}{2}A_2) + \frac{1}{\pi} \frac{\partial \Gamma}{\partial t} + V(A_0 + \frac{1}{2}A_1) \\ &= \frac{V}{\pi} \int_1^\infty \gamma d\xi - \frac{V}{\pi} \int_1^\infty \frac{\gamma \xi}{\sqrt{(\xi^2 - 1)}} d\xi + b(\dot{\alpha}V + \ddot{z} - \ddot{\alpha}b\bar{x}) + V(A_0 + \frac{1}{2}A_1) \\ &= VA_0 + Vb\dot{\alpha} + b(\dot{\alpha}V + \ddot{z} - \ddot{\alpha}b\bar{x}) \end{aligned}$$

on eliminating the integrals by means of eqn 6.18. The lift can then be written as

$$L = 2\pi\rho Vb[\alpha V + \dot{z} + \dot{\alpha}b(\frac{1}{2} - \bar{x})] + \rho Vb \int_1^\infty \frac{\gamma d\xi}{\sqrt{(\xi^2 - 1)}} + \pi\rho b^2(\dot{\alpha}V + \ddot{z} - \alpha b\bar{x}) \quad (6.24)$$

The first term is the ‘quasi-steady’ lift which alone would occur if the motion were steady, the second term represents the lift due to the vortex wake, and the third term is the lift due to the fluid inertia or ‘apparent mass’. Denoting the quasi-steady lift by L_q we have

$$\begin{aligned} L_q &= 2\pi\rho Vb[\alpha V + \dot{z} + \dot{\alpha}b(\frac{1}{2} - \bar{x})] \\ &= \int_1^\infty \left[\frac{\xi + 1}{\sqrt{(\xi^2 - 1)}} - 1 \right] \gamma d\xi \end{aligned}$$

on eliminating Γ and $A_0 + \frac{1}{2}A_1$ from eqns 6.13, 6.18, and 6.21. It then follows that eqn 6.24 can be written

$$L = L_q \cdot \frac{\int_1^\infty \frac{\gamma \xi d\xi}{\sqrt{(\xi^2 - 1)}}}{\int_1^\infty \frac{\gamma \xi d\xi}{\sqrt{(\xi^2 - 1)}} + \int_1^\infty \frac{\gamma d\xi}{\sqrt{(\xi^2 - 1)}}} + \pi\rho b^2(\dot{\alpha}V + \ddot{z} - \ddot{\alpha}b\bar{x}) \quad (6.25)$$

For sinusoidal motion, the lift can be expressed as $L = L_0 e^{i\omega t}$ and the vorticity in the wake, as was discussed earlier, must be of the form

$$\begin{aligned} \gamma(\xi, t) &= \gamma_0 e^{i\omega(t - b\xi/v)} \\ &= \gamma_0 e^{i\omega t} e^{-ik\xi} \end{aligned}$$

where $k = \omega b/V$ is the ‘reduced frequency’.

The ratio of integrals occurring in eqn 6.25 then becomes

$$\begin{aligned}
& \frac{\int_1^\infty \frac{\gamma \xi d\xi}{\sqrt{(\xi^2 - 1)}}}{\int_1^\infty \frac{\gamma \xi d\xi}{\sqrt{(\xi^2 - 1)}} + \int_1^\infty \frac{\gamma d\xi}{\sqrt{(\xi^2 - 1)}}} = \frac{\int_1^\infty \frac{\gamma \xi d\xi}{\sqrt{(\xi^2 - 1)}}}{\int_1^\infty \sqrt{\frac{\xi + 1}{\xi - 1}}} \\
&= \frac{\int_1^\infty \frac{\xi}{\sqrt{(\xi^2 - 1)}} e^{-ik\xi} d\xi}{\int_1^\infty \sqrt{\frac{\xi + 1}{\xi - 1}} e^{-ik\xi} d\xi} \\
&= C(k), \text{ Theodorsen's function, referred to earlier.}
\end{aligned}$$

The lift can now be written

$$L = C(k) L_q + \pi \rho b^2 (\dot{\alpha} V + \ddot{z} - \ddot{\alpha} b \bar{x}) \quad (6.26)$$

The pitching moment about the point of rotation $x = \bar{x}$ is found to be

$$M = bC(k)(\frac{1}{2} + \bar{x})L_q + \pi \rho b^3 [\bar{x}\ddot{z} - V\dot{\alpha}(\frac{1}{2} - \bar{x}) - b\ddot{\alpha}(\frac{1}{8} + \bar{x}^2)] \quad (6.27)$$

In particular, the lift in purely *rotational* harmonic motion about the mid-chord can be written as

$$L = \pi \rho V b^2 \dot{\alpha} + 2\pi \rho V^2 b(1 + ik/2)C(k)\alpha \quad (6.28)$$

and for *heaving* motion as

$$L = \pi \rho b^2 \ddot{z} + 2\pi \rho V b C(k) \dot{z} \quad (6.29)$$

In both cases the term proportional to $C(k)$ is due to the bound circulation.

If L_0 is the steady lift at the *instantaneous* incidence the values of L/L_0 can easily be shown to reduce to the forms of eqns 6.10 and 6.11.

It is interesting now to consider the velocity component $v_{3/4}$ at the $\frac{3}{4}$ -chord point due to the aerofoil motion. For aerofoil rotations about the mid-chord, we have

$$v_{3/4} = \alpha V + \frac{1}{2} b \dot{\alpha}$$

For harmonic motion, $\alpha = \alpha_0 e^{i\omega t}$, and

$$v_{3/4} = \dot{\alpha} V (1 + ik/2)$$

If L_b denotes the lift due to the bound circulation, i.e. that part of the lift proportional to $C(k)$, we see from eqn 6.28 that

$$L_b = 2\pi \rho V b C(k) v_{3/4}$$

For the *heaving* motion we have simply

$$v_{3/4} = \dot{z}$$

and, again, from eqn 6.29,

$$L_b = 2\pi\rho VbC(k)v_{3/4}$$

Thus, in both cases, it appears that the part of the lift arising from the bound circulation is proportional to the ‘downwash’ at the $\frac{3}{4}$ -chord point. For this reason, the $\frac{3}{4}$ -chord point is known as the ‘rear aerodynamic centre’ and is the appropriate chordwise position to consider when lifting-line techniques are used in cases such as those described above, where the chordwise variation of velocity may be important.

The effect of shed vorticity in the special case of hovering flight has been investigated by Loewy⁸ and Jones⁹. Although hovering flight is usually regarded as a symmetrical flight state, any disturbed blade motion will give rise to periodic lift forces and the generation of a shed vortex wake in addition to the trailing vortices. The work of Loewy and Jones was based on two-dimensional analysis which one would expect to overestimate the effects somewhat, since the shed vortex lines in practice extend only the length of the span. The mathematical model used is as indicated in Fig. 6.17. The shed wake pattern is imagined to consist of the semi-infinite wake attached to the blade and a vertical array of doubly infinite wakes representing those of other blades and of the previous passages of the reference blade. The vertical spacing h between each sheet is determined from the mean flow through the rotor. If the effect of the lower sheets is averaged over the blade chord (lifting-line assumption), the lift on the blade is then

$$L = \rho Vb \int_1^\infty \frac{\gamma d\xi}{\sqrt{(\xi^2 - 1)}} + \rho Vb \sum_{n=1}^{\infty} \int_{-\infty}^{+\infty} \frac{\gamma \xi d\xi}{n^2 h^2 + \xi^2} + L_0 + \rho \pi \ddot{z} b^2$$

which is the same as eqn 6.24 except for the addition of the second term which denotes the contribution of those sheets below the blade. For oscillations which are integer frequencies of the rotor speed, Miller found that

$$\frac{L}{L_q} = C(k, m, h) = \frac{J_1 - iY_1}{J_1 - iY_1 + Y_0 + iJ_0 + [2i/e^{hk} e^{2i\pi m} - 1]} \equiv F_R + iF_I \quad (6.30)$$

where J_0 , Y_0 , J_1 , Y_1 are Bessel functions of the first and second kinds, of orders zero and unity and argument k ; $m = \omega/\Omega$ and $k = \omega b/\Omega R$. Figure 6.18 shows the comparison of eqn 6.30 with Loewy’s exact lifting-surface results. The agreement is extremely good for F_R but there is poor agreement for the phase shift represented by F_I . However as pointed out by Miller, typical values of h are greater than unity and the error is fairly small.

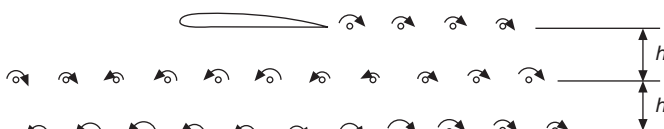


Fig. 6.17 Vortex sheets shed by oscillating aerofoil in hover

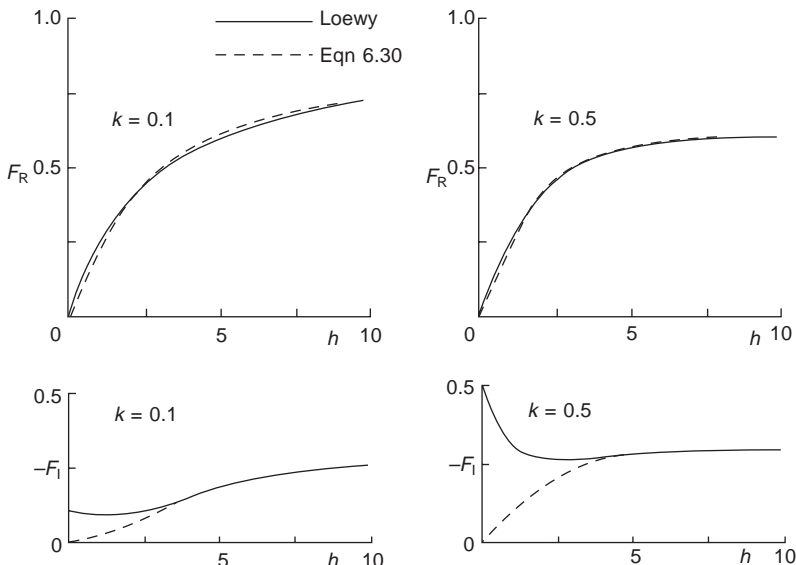


Fig. 6.18 Comparison between exact and approximate oscillatory parameters

The case of an infinite number of blades leads to a particularly simple result. The shed vorticity is then uniformly distributed vertically, and Miller found that, if the frequency is $n\Omega$, the induced velocity at the aerofoil becomes

$$w = \frac{inbc\Gamma_n e^{in\Omega t}}{8\pi^2 R\lambda} \int_0^\infty \int_{-\infty}^{+\infty} \frac{e^{inc\xi/2R}}{z^2 + \xi^2} d\xi dz$$

where λ is the mean inflow ratio and Γ_n is the amplitude of the bound circulation. From the blade element theory, if $\theta = \theta_n e^{in\Omega t}$ is the blade pitch variation we have

$$\Gamma = \pi\Omega R c(\theta - w/\Omega R)$$

since the quasi-static circulation is $\Gamma_q = \pi\Omega R c\theta_n$.

Elimination of w and writing $s = bc/\pi R$ leads finally to

$$C = 1/(1 + s\pi/4\lambda)$$

Thus, in this approximation, C is independent of the frequency. The analysis is unable to predict the phase shift. Comparison of this method with Loewy's results shows very good agreement for values of h below 5, i.e. for typical values of h occurring in practice.

Miller extended the approximate analysis just discussed to the three-dimensional vertical flight case. It was assumed that the circulation was constant along the blade, so that the trailing vortex wake consisted only of a tip vortex and a vortex along the rotor axis. Applying the above approximations to the integrals 6.4 and 6.6 leads to the result

$$w = (b/4\pi\lambda R)(\Gamma_{ns} \sin n\psi + \Gamma_{nc} \cos n\psi)$$

when the bound circulation is given by

$$\Gamma_n = \Gamma_{ns} \sin n\psi + \Gamma_{nc} \cos n\psi$$

The lift deficiency function C turns out to be exactly that of the previous analysis, namely,

$$C = 1/(1 + s\pi/4\lambda)$$

It is interesting to note that, although the contribution of the shed wake in this case is smaller on account of the finite length of the vortex lines, this is exactly compensated for by the effect of the trailing vortex lines which, in the two-dimensional case, were omitted.

The values of the lift deficiency function indicate that the effective lift slope of the blade is much reduced and, under some conditions, could approach zero. This implies correspondingly reduced damping of the blade flapping motion.

Because of the good agreement between Miller's approximate two-dimensional analysis and the exact analysis of Loewy, Miller argued that for calculations of the forward flight case it is reasonable to consider both the shed and trailing wakes in two parts: a 'near' shed wake which corresponds to the first quadrant of the wake and a 'far' wake consisting of the remainder. Furthermore, the 'near' wake could be regarded as straight and extended back to infinity, as was assumed by Willmer. It was supposed that the classical two-dimensional unsteady theory of Theodorsen could be applied to account for the shed vorticity in this section of the wake. For the treatment of the shed vorticity in the far wake, it was assumed that the chordwise variation of velocity at the blade could be neglected and that only a mean velocity need be considered, as in Miller's two-dimensional analysis. Calculations showed that, above $\mu = 0.2$, the far wake has little effect and the values of F_R and $-F_I$ approach those of the classical two-dimensional theory. The results suggested that a good approximation could be obtained by simply 'fairing' the results found for the hovering case to those of the two-dimensional aerofoil theory, Fig. 6.19.

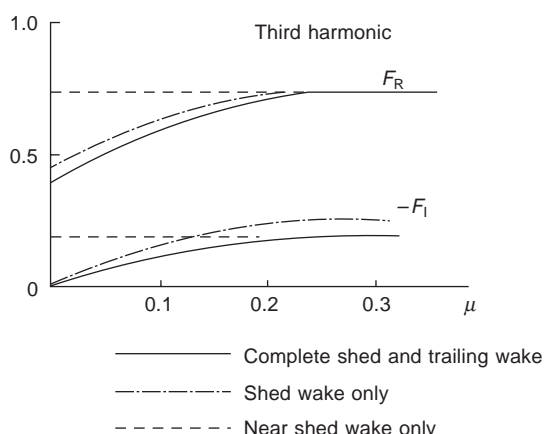


Fig. 6.19 Variation of oscillatory parameters in forward flight

Calculations made by assuming infinite straight vortex filaments for the spiral trailing vortices in the integral 6.4 showed little loss of accuracy but a great reduction of computer time.

Calculations also showed that good accuracy was retained even when the trailing wake was assumed to consist of only two discrete vortices, one springing from the tip and another a little inboard of the mid-span. Such a vortex system has indeed been found by Tararine¹⁰ from smoke tests, Fig. 6.20.

Comparison of Miller's calculations with experimental air loads is shown in Figs 6.21 and 6.22.

The peak loading at an azimuth angle of about 90° is due to the tip vortex of the preceding blade. This peak travels down the blade as it advances from 90° to 180° , and can be detected in Figs 6.21 and 6.22. It might be thought that the peak could be reduced by increasing the number of blades, but, although the vortex strength is reduced, so are the blade spacings, with the result that the vortices pass closer to the blade in question. According to Miller, the peak loading is influenced very little by the number of blades.

A further conclusion of Miller's work is that almost all the harmonic content of the air loads is contained in harmonics above the second, and they are derived from the effects of the far wake. These harmonics are practically independent of blade flapping motion.

As was stated earlier, Miller's work was based on the assumption of a rigid wake.

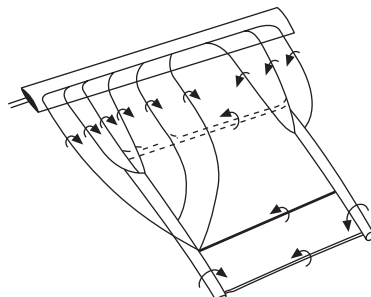


Fig. 6.20 Representation of shed and trailing vortices (after Tararine)

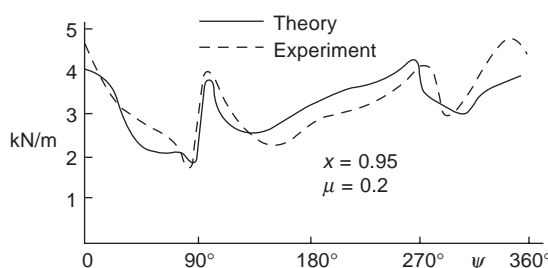


Fig. 6.21 Blade loading variation with azimuth angle

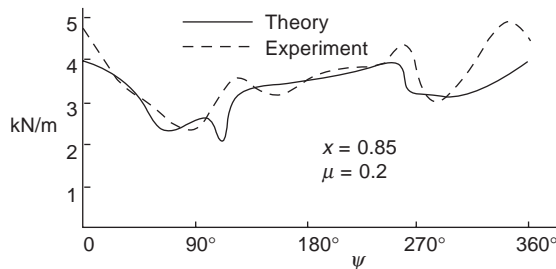


Fig. 6.22 Blade loading variation with azimuth angle

6.2.3 Free wake model development

In the 1960s, Cornell Aeronautical Laboratory carried out a programme of work aimed at improving the understanding of, and the ability to model, the wake of a helicopter in steady state flight. As part of this, Piziali¹¹ proposed a wake model that embodied the shed and trailing vorticity in the form of a mesh of straight line vortex filaments, as shown in Fig. 6.23. This occupied the near wake adjacent to the blade, whilst the far wake was modelled simply by concentrated root and tip vortices, the former being deleted for some studies. The mesh part of the wake could be truncated at any chosen position downstream. Initial studies in the forward flight case placed the wake mesh points on an undistorted skewed helix (i.e. a rigid wake), but later models allowed distortions from this to occur for a fixed length of time, the distorted wake being maintained thereafter. Blade flapping bending modes were included in the programme, and the calculated loading, blade response, and corresponding induced velocity were interdependent and were calculated iteratively until all quantities were self-consistent.

Like Miller, Piziali gave great attention to the unsteady aerodynamic characteristics due to the shed wakes. To test the validity of the finite element representation of the shed vorticity, the calculations were made for the two-dimensional aerofoil and compared

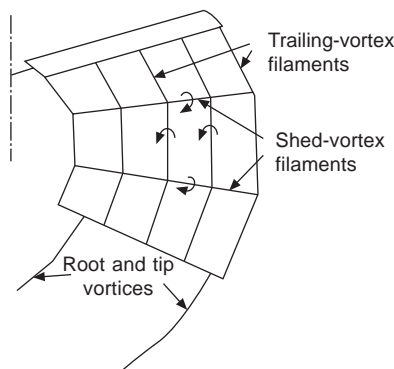


Fig. 6.23 Piziali's wake model

with the classical exact theory discussed in the previous section. It was found that, unless the interval between successive vortex lines was much smaller than was really practical for the computational capabilities that were then current, agreement was rather poor, but by advancing the shed wake towards the aerofoil by about 70 per cent of a complete interval the agreement was greatly improved. In a later paper by Piziali, a smoothing routine was employed to simulate a continuous wake from a number of finite elements. Comparisons of measured loadings with those from Piziali's method are shown in Figs 6.24 and 6.25.

In the free wake model of Landgrebe¹², the basic rotor wake is similar to that described above, but the vortex elements are allowed to take up positions determined by the free stream velocity and the induced velocity of all the other elements. Only the bound and trailing vortices were considered in the calculations; the shed vorticity was accounted for by using two-dimensional unsteady aerofoil data.

One of the difficulties of representing the wake by discrete vortex elements is that infinite velocities occur at the vortex itself. To overcome this, Landgrebe supposed that the vortex had a core within which the induced velocity can be neglected. The core size assumed by Landgrebe was 1 per cent of the rotor radius. Other investigators have assumed that the velocity within the core varies linearly with radial distance

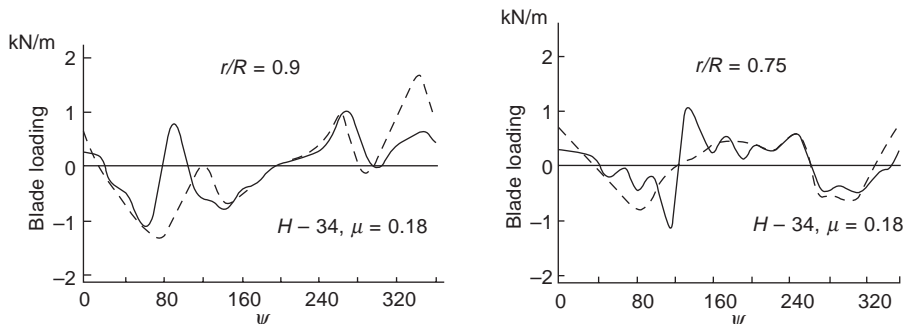


Fig. 6.24 Blade loading variation with azimuth angle

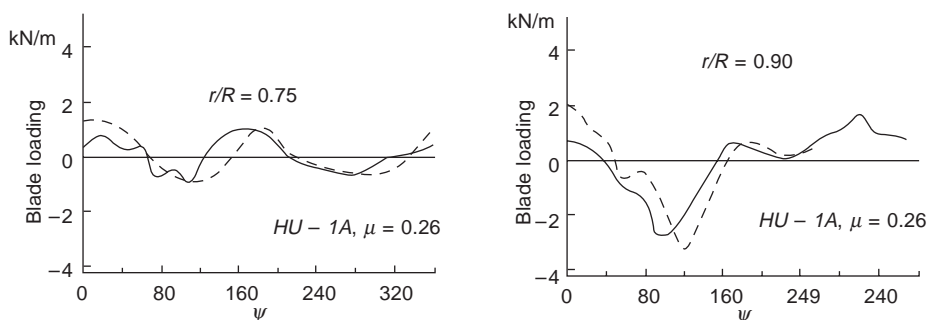


Fig. 6.25 Blade loading variation with azimuth angle

(i.e. as if the core were solid). Measurements conducted to investigate the structure of the tip vortex have been described by Cook¹³.

In order to reduce the computational time and expense, not all the vortex elements were assumed to be free to convect in accordance with the local velocities. Computation was greatly reduced by assuming that the positions of the vortex elements beyond a certain distance from the point of interest remained the same as in the original prescribed wake which formed the starting point of the calculations. An example of Landgrebe's calculations is given in Fig. 6.26, which shows the axial displacement of the tip vortex filament compared with the 'classical' rigid wake uniform displacement. Another example is the theoretical wake boundary at low μ compared with that from a smoke visualisation study, Fig. 6.27. It can be seen that the vortex filaments at the front of the disc lie very close to the disc. This might have been expected from the Glauert or Mangler distributions, since they predict a slight upwash at the leading edge of the disc. Landgrebe's calculations also showed that the wake boundary rolls up, eventually forming two large vortices very similar to those observed by Heyson and Katzoff, as described in Chapter 3.

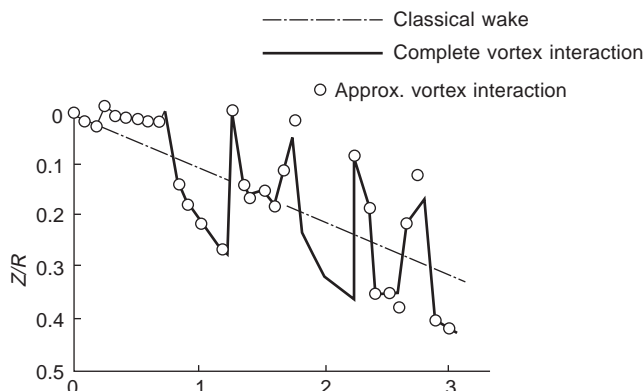


Fig. 6.26 Displacement of tip vortex in forward flight

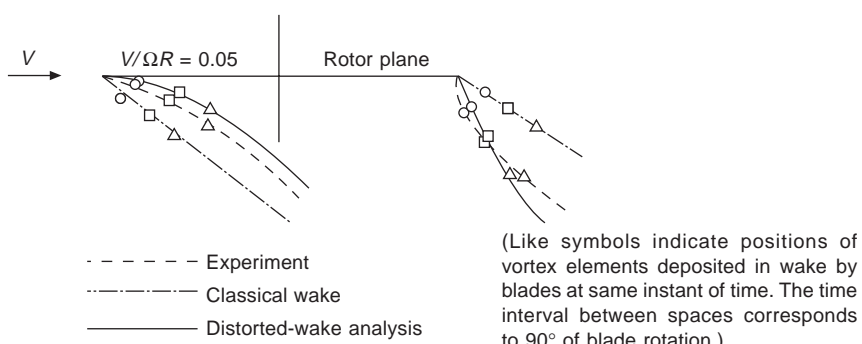


Fig. 6.27 Displacement of wake boundary

The pioneering studies of Piziali, Landgrebe and associates, together with those of Clark and Leiper, for hovering flight, and others of that era laid the foundations for much subsequent wake modelling research. The main difficulties that had to be overcome, once computational power became sufficient, were largely numerical, such as instability and/or poor convergence. In order to avoid such problems, Bagai and Leishman¹⁴ used a relaxation method, as opposed to a time-stepping approach, which enforces periodicity as a boundary condition and specifies that the trailing vortex filaments be attached to the blades as an initial condition. The basic model was similar to that in Fig. 6.23. An improvement over an existing free wake modelling code was demonstrated and comparisons made with existing experimental data. Perspective views of the computed rotor wake in the hover and in forward flight shown in Fig. 6.28; the rolling up of the wake boundaries downstream at the faster forward flight speeds is clearly seen.

The advent of computational fluid dynamics, or CFD, has brought with it a steady advance in the complexity of flows that can be analysed. However, the computation of the complete flow field around a helicopter in forward flight, which may include interaction with the fuselage and tail surfaces, remains an outstanding problem with current computing capabilities. A brief account of the difficulties of using the various CFD approaches is given by Coppens *et al.*¹⁵ in the introduction to an account of a time-marching method of computing the rotor wake.

Figure 6.28 for the forward flight cases shows the rotor blades passing close to tip vortices shed by preceding blades; this proximity, which is termed blade–vortex interaction, or BVI, leads to impulsive loading and noise problems. It is particularly severe in descending forward flight, such as during an approach to landing, when the rotor tends to fly through its own wake. The plan view of a typical pattern of BVI is shown in Fig. 6.29 (from Tangler¹⁶) for a two-bladed rotor at an advance ratio of 0.145. Four interactions are shown on the advancing side and three on the retreating

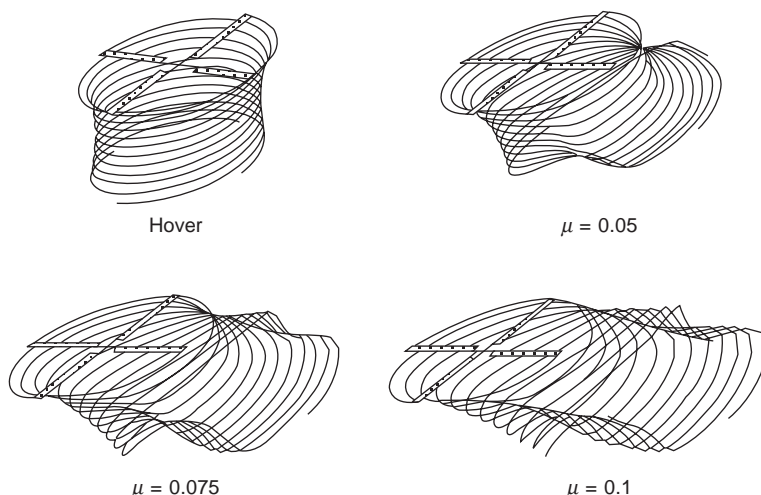


Fig. 6.28 Perspective views of computed rotor wake (Bagai and Leishman¹⁴)

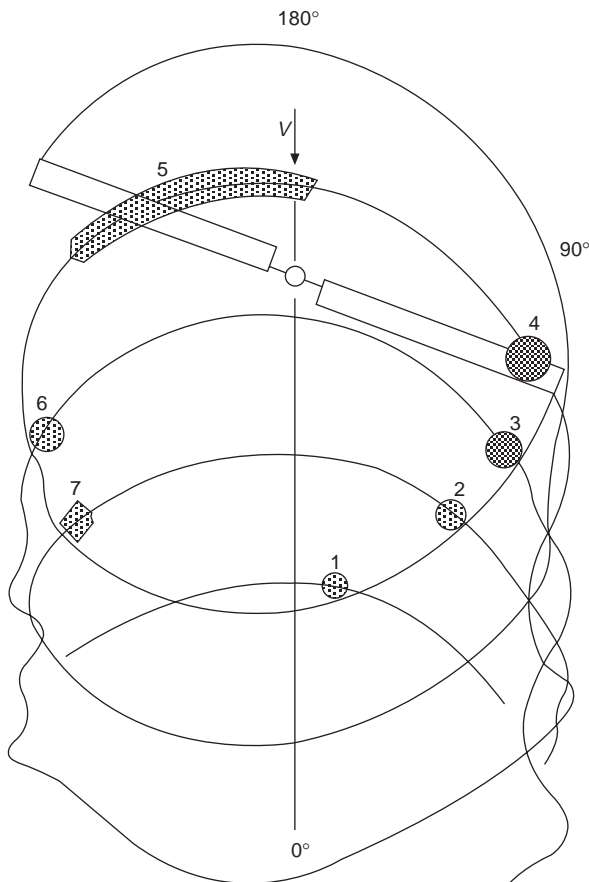


Fig. 6.29 Plan view of blade-vortex interactions (from Tangler¹⁶)

side. The strength of each interaction is dependent on the strength of the tip vortex, the vortex core size, the instantaneous angle between the blade and the vortex at the interaction, and the normal separation between the two, or the ‘miss’ distance. When the rotor is in descending flight, the miss distance can become quite small.

On the advancing side, the approach of a blade section to a preceding vortex is as shown in Fig. 6.30, with a typical resulting lift coefficient history indicated (adapted from Leishman¹⁷). On the retreating side, the rotation direction of the vortex with respect to the blade is reversed, and the lift coefficient history is similarly affected. Since the lift change occurs over a very small period of time, it is practically impulsive, leading to two predominant effects. One is that of blade loading, which possesses a high frequency content, and the other is that of acoustic radiation, or noise.

The introduction of the improved wake modelling described earlier has allowed the problems of BVI to be defined more accurately and solutions proposed with a greater degree of confidence. The impulsive blade loading problem is a problem because it leads to undesired structural vibration, but a possible solution can be provided by use of higher harmonic control, or HHC. In this approach, higher than

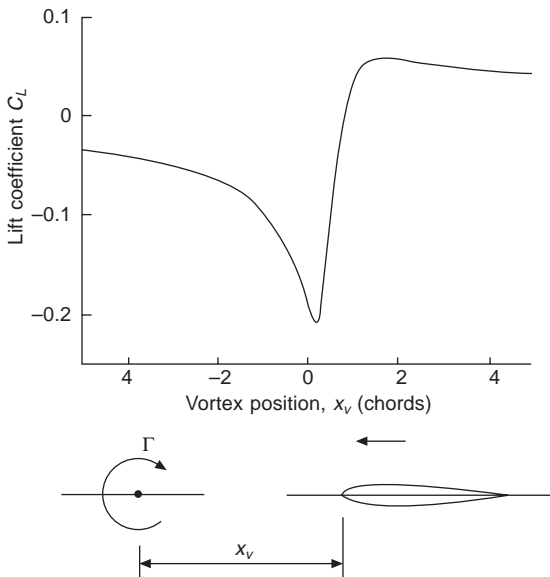


Fig. 6.30 Lift coefficient time history (adapted from Leishman¹⁷)

once-per-revolution input is introduced to the pitch control by means of subsidiary signals to the actuators below the swash plate. An alternative scheme allows for the signals to be fed to supplementary actuators positioned between the swash plate and the blades, this being termed individual blade control, or IBC. Practical tests on both arrangements applied to a four-bladed wind tunnel rotor model are described by Kube and Schultz¹⁸, and these cover both vibration and noise aspects.

Considerable effort has been expended in studying noise propagation from helicopters, since commercial viability is strongly affected by environmental acceptability. Schmitz and Yu¹⁹ provided a comprehensive review of theoretical and experimental studies as an aid to understanding the problems, and Lowson²⁰ suggested the way forward towards achieving quieter helicopters. From the point of view of the observer on the ground, the most recognisable component of sound radiation is that of ‘blade slap’, which tends to occur at slow to medium speeds with the helicopter in descending flight. The interaction which normally provides the predominant effect is number 4 in Fig. 6.29, for which the miss distance is small and the intersection angle is highly oblique. For a four-bladed rotor, this occurs at an azimuth angle of about 60°, and leads to a directional preference for the radiated sound pressure level, as described by Ehrenfried *et al.*²¹ in experimental tests and by Lowson²² from fundamental considerations.

6.3 Aerofoil characteristics in forward flight

We saw in Chapter 3 that the blade encounters a wide range of conditions in forward

flight. The incidence of the retreating blade increases with tip speed ratio so that the stalling angle may be reached, particularly on the important outer section of the blade, while on the advancing blade the Mach number may reach values at which the compressibility drag rise begins. These varying conditions may be conveniently shown in a ‘figure-of-eight’ diagram, as in Fig. 6.31, which shows the α -Mach number relationship at the radial position $x = 0.913$ for a ‘Wessex’ rotor flying at $\mu = 0.32$. The hovering case would be represented by one point on the diagram.

As μ increases, the ‘figure-of-eight’ gradually expands, extending into regions of higher C_L and higher M . To test whether the aerofoil will encounter stall and compressibility drag rise, one can plot on the same diagram the α - M boundaries for these conditions. For the NACA 0012, which is the aerofoil on the ‘Wessex’, the boundaries are shown in Fig. 6.32, together with the α - M variation of Fig. 6.31. It can be seen that the α - M loop passes well into the stall region on the retreating blade and well into the drag-rise region on the advancing blade. The effects on the pressure distribution of the NACA 0012 aerofoil have been examined in detail by Pearcey *et al.*²³ and they show that the flow is supersonic over some part of the aerofoil for almost the complete azimuth cycle of the blade. This is indicated in Fig. 6.32 by the fact that the α - M loop lies entirely beyond the supercritical boundary. Pressure distributions at the azimuth angles $\psi = 112^\circ$, and $\psi = 237^\circ$ are shown in Fig. 6.33. Pearcey found that the stall following $\psi = 237^\circ$ is precipitated by shock induced separation, the Mach

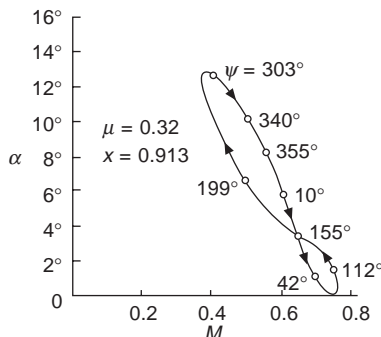


Fig. 6.31 ‘Figure-of-eight’ variation of incidence and Mach number

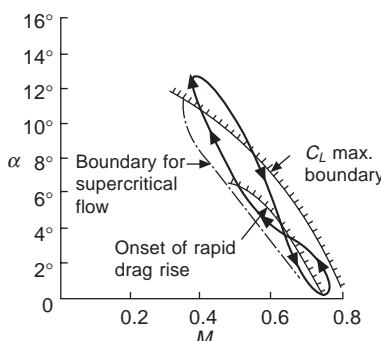


Fig. 6.32 Stall and compressibility boundary

number near the leading edge being about 1.4 although the free stream Mach number is only 0.4. There is then a collapse of the pressure distribution until reattachment occurs when the blade reaches its most rearmost position ($\psi = 360^\circ$).

The conditions described above relate to a section near to the blade tip, and impose constraints on the performance of the helicopter. Improvements can be gained through appropriate design of the tip to alleviate the adverse effects on both advancing and retreating sides, and through design of the aerofoil shape itself in the tip region and inboard of the tip. The NACA 0012 aerofoil was not designed with helicopter use in mind and is not ideal for operating under the extreme conditions described above.

In pursuit of the alleviation of the most undesirable transonic effects on the advancing side, tip shapes other than straight rectangular have been investigated and are currently in use. A comprehensive study by Desopper *et al.*²⁴ was based on a series of computational and experimental studies at ONERA. Preliminary work (including that of other researchers) indicated that the intensity of the transonic flow was reduced for a large azimuthal sector of the advancing blade side by using a constant 30 degree sweptback tip, and hence the power required to drive the rotor was also decreased. However, a strong expansion observed on the outboard part of this tip limited the total benefit to be gained. A sweptback tip having a progressively increasing angle of sweep, i.e. a parabolic leading edge, was found to eliminate, or at least delay, this expansion, hence providing a further gain.

A systematic study of blade tip shapes was then undertaken covering analytical and experimental studies, which provided ample verification. The tip shapes considered in the former are shown in Fig. 6.34 and the pressure contours computed using a three-dimensional unsteady transonic small perturbation method are shown in Fig. 6.35. The parabolic swept tip (PF2) indicates a significant decrease in supercritical flow intensity, this being borne out by experiment as indicated in Fig. 6.36 (the FL5 tip is similar to PF2 except that there is no discontinuity in sweepback angle at the start of the parabolic tip section).

On the retreating side of the rotor disc, the main performance limiting factor is that of stall, or to use a more appropriate term, dynamic stall. The stalling characteristics of an aerofoil subject to rapidly changing or dynamic conditions is markedly different from that operating in steady conditions, as will be described later. The maximum value of C_L under dynamic conditions that can be attained determines the stall boundary, and blade design aimed at increasing this value can lead to a significant improvement in performance.

Research conducted by the UK Royal Aircraft Establishment (RAE), now the Defence,

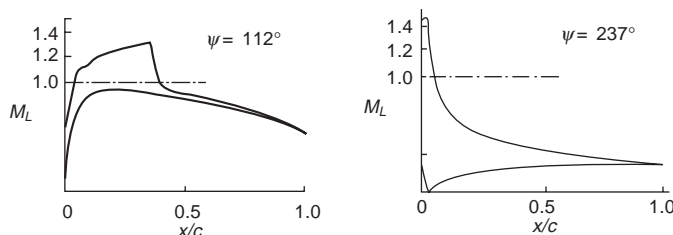


Fig. 6.33 Chordwise pressure distribution (showing local Mach number)

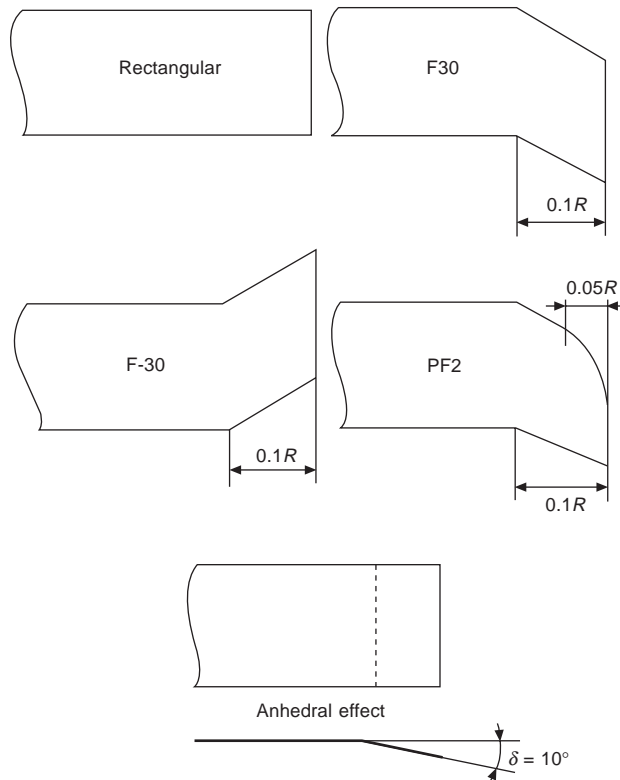


Fig. 6.34 Different tip shapes, ONERA non-lifting unsteady calculations²⁴

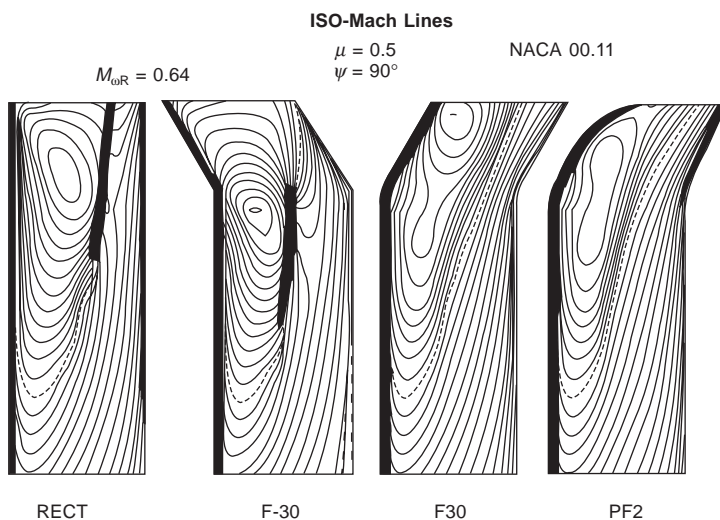


Fig. 6.35 Study of different tip shapes, non-lifting unsteady calculations, pressure contours²⁴

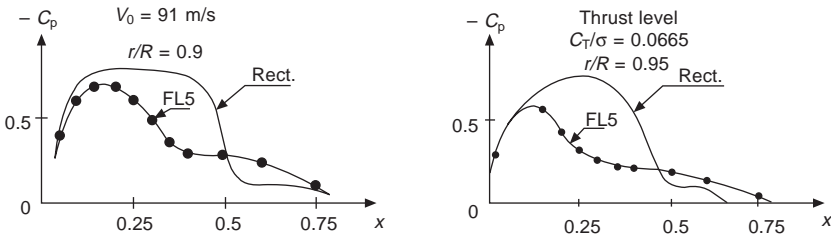


Fig. 6.36 Measured pressure distributions on the upper side of rectangular and parabolic swept (FL5) blade tips²⁴

Evaluation and Research Agency (DERA), with GKN Westland Helicopters led to the BERP (British Experimental Rotor Programme) rotor design²⁵. The blade has a sweptback paddle-shaped tip, as shown in Fig. 6.37, which is its most obvious observable characteristic. However, the design of the blade as a whole and the aerofoil sections selected are also vital features. Flight tests on rectangular blades had shown that the high incidence performance required on the retreating side was not needed over the whole span, but the requirements could not be relaxed between 65 and 95 per cent radius. Thus, if a thin section were used near the tip to avoid advancing blade Mach number constraints, this would have an adverse effect on the retreating blade stall performance, even though a more appropriate, i.e. thicker, aerofoil section were used inboard.

As will be seen in a later paragraph, the BERP tip confers a high incidence capability independent of these considerations, and allows the conflicting requirements on the advancing and retreating side of the rotor to be met independently. The BERP blade uses an aerofoil (RAE 9645) between 65 and 85 per cent of blade radius that produces a high dynamic $C_{L\max}$ for good stall performance. However, it also gives rise to a high nose down pitching moment which would be undesirable were it not counteracted by using a different section, RAE 9648, inboard of 65 per cent radius. This has a reflexed trailing edge and a nose up pitching moment characteristic; being inboard, its lower stalling angle is not so important. The BERP tip is swept and its increased chord provides it with a lower thickness to chord ratio than just inboard (without decreasing the actual blade thickness), thereby avoiding the shock on the upper side and consequent pitching moment change when the blade is advancing.

When the blade is retreating, a tip vortex is initiated from the outermost part of the tip at low angles of incidence, but when at high angles of incidence, the vortex starts at the point where the chord changes, i.e. at the start of the parabolic leading edge. It acts rather in the same manner as the bound vortex on a narrow delta wing aircraft, e.g. Concorde, maintaining a flow on the upper surface of the aerofoil at a high incidence and delaying stall (see Fig. 6.38).

The forward extension of the leading edge at the start of the parabolic sweepback allows the pitching moment caused by a normal geometric sweep of the tip to be minimised.

6.4 Aerofoil characteristics when oscillating at conditions of high incidence

So far the discussion of rotor characteristics and the calculations made have assumed



Fig. 6.37 The BERP blade

that the characteristics of the aerofoil sections of the blade are the same as those measured in two-dimensional steady flow. Provided the theoretical values of incidence do not exceed about 12° anywhere over the rotor disc, theoretical and experimental values of rotor forces and flapping motion are generally in good agreement. However, it was observed in, for example, the wind tunnel tests of Squire *et al.*²⁶ that, for a given collective pitch angle, the slope of the curve of the thrust coefficient with shaft incidence decreased when the shaft angle exceeded a certain value. It was assumed that, in this region, stall was occurring on the retreating blade and that the stall area

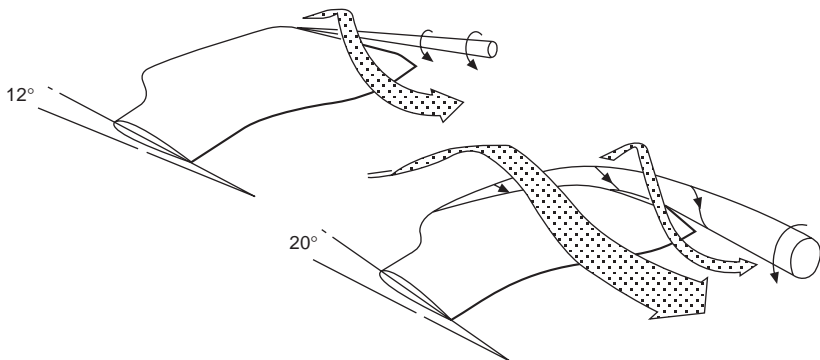


Fig. 6.38 Tip vortex at high incidence on BERP tip

was increasing with increase of shaft incidence. At that time the introduction of aerodynamic data which included the stall was not possible, as it required computer facilities which were not available until the 1960s. When such data was included in rotor theory, it was rather surprising to find that the slope of the thrust coefficient in the stalled region was much less than that given by experiment²⁷, Fig. 6.39. The phenomenon had also been reported by Harris *et al.*²⁸, Fig. 6.40.

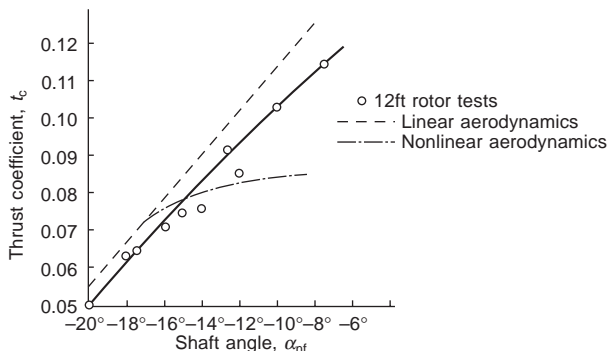


Fig. 6.39 Thrust coefficient as a function of shaft angle (RAE tests)

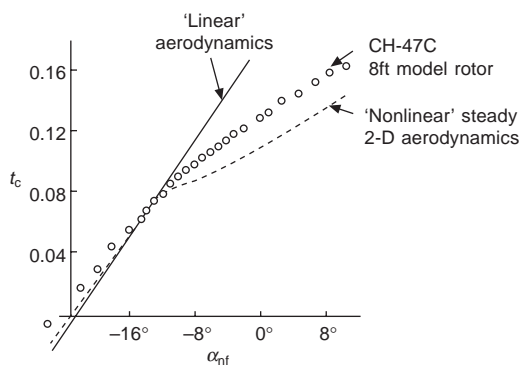


Fig. 6.40 Thrust coefficient as a function of shaft angle (Boeing-Vertol tests)

It was also found that the calculated torque was considerably higher than the experimental values. It was therefore concluded that the rotor blade did not stall in the same manner as when under two-dimensional steady conditions. This notion was reinforced by analysis of the wind tunnel tests of Meyer and Falabella²⁹ and the flight-test data of Scheiman³⁰ which indicated values of lift coefficient far in excess of the maximum steady values, as in Fig. 6.41, which shows the results from the tests of Meyer and Falabella. The C_L contours for calculations made with the steady two-dimensional data and uniform induced velocity distribution are shown in Fig. 6.42 where it can be seen that the magnitudes and shapes of the C_L values and contours are quite different from those of Meyer and Falabella.

Now, it has been known for some considerable time³¹ that, when a wing is changing its incidence, the stalling angle and associated lift may be different from that in steady flow. In particular, when the aerofoil is oscillating about a mean incidence above that of the steady-state stall, the lift coefficient may exceed the steady-state

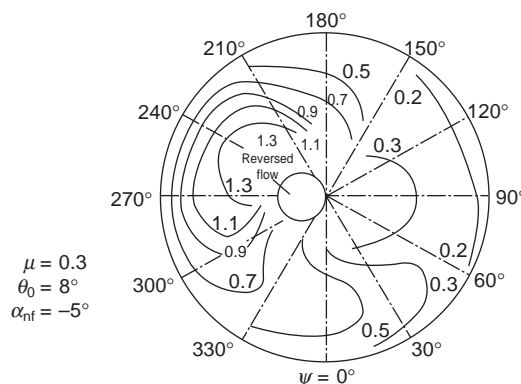


Fig. 6.41 C_L contours derived from wind tunnel tests (Meyer and Falabella)

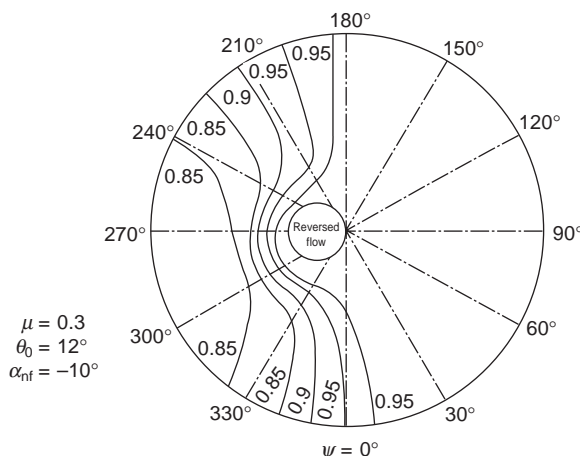


Fig. 6.42 Computed C_L contours using two-dimensional steady aerofoil data

value when the incidence is increasing and fall below it when the incidence is decreasing. Further results have been given by Halfman *et al.*³² for flutter investigations, but valuable data for helicopter applications were first given by Carta³³, who reported oscillation tests on a NACA 0012 aerofoil. A typical result of Carta's tests is shown in Fig. 6.43. The aerofoil in this case was oscillated at 4 Hz (typical rotor frequency) with an amplitude of 6° about a mean incidence of 12°.

It can be seen that under these conditions the lift coefficient varies by as much as 0.5 from the steady values, and the difference may often be far greater. In the papers by Bramwell *et al.*²⁷ and Harris *et al.*²⁸, attempts were made to express the oscillating aerofoil data of the kind shown in Fig. 6.42 in numerical or mathematical form and apply it to rotor force calculations. In Bramwell's paper the difference between the steady and unsteady lift coefficients was superimposed on the experimentally derived hovering aerofoil characteristics ('synthesised' data); in Harris's paper the values were superimposed on two-dimensional steady aerofoil data in which the C_L was corrected for the local sweep angle. The improvement in the calculated performance is shown in Figs 6.44 and 6.45. The former also paid attention to the C_L contours over the disc. Figure 6.46 shows the contours obtained by superimposing oscillating aerofoil

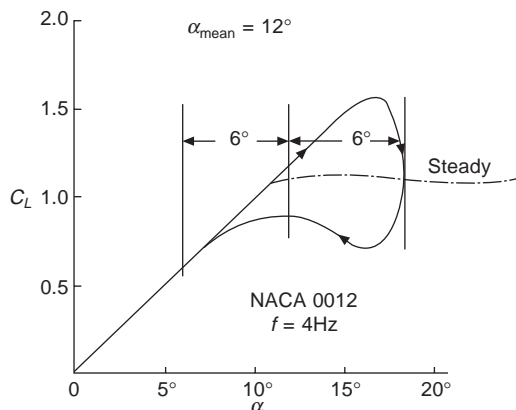


Fig. 6.43 Hysteresis loop for aerofoil oscillating above stall

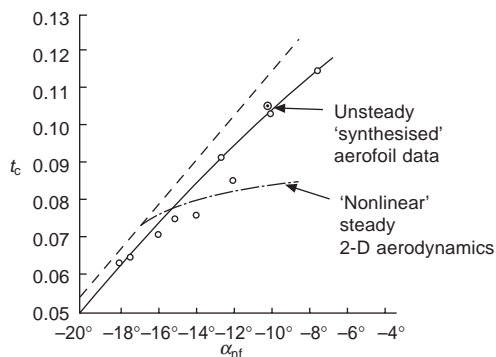


Fig. 6.44 Effect of applying oscillating aerofoil data to rotor calculations (RAE)

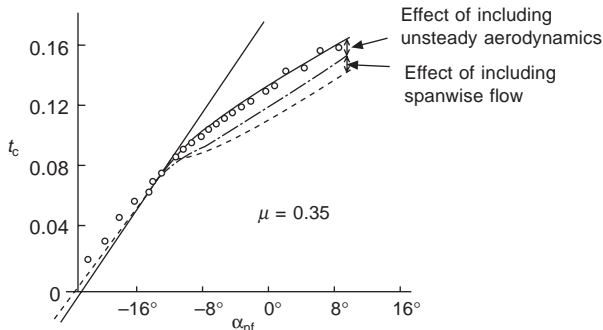


Fig. 6.45 Effect of applying oscillating aerofoil data to rotor calculations (Boeing-Vertol)

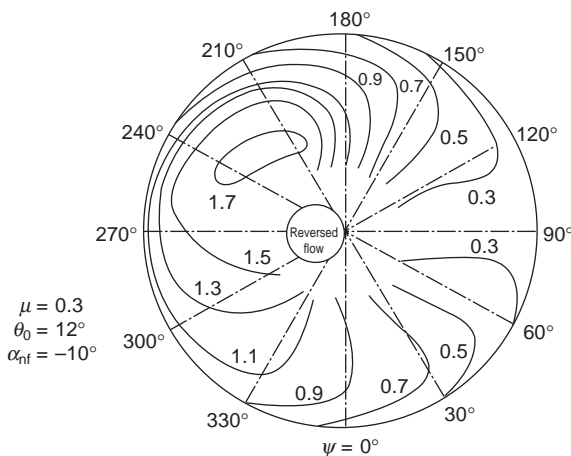


Fig. 6.46 Effect of applying oscillating aerofoil data on C_L contours

data on the synthesised aerofoil characteristics; these should be compared with those of Figs 6.41 and 6.42. Although the test conditions were not exactly the same as those of the calculations, the figures show that the use of oscillating aerofoil data results in contours whose appearance resembles those of the rotor tests far more closely than the steady two-dimensional calculations.

Since the work of Carta, many others have investigated the unusual aerofoil behaviour which occurs at high incidence under unsteady conditions, notably Ham and Garelick³⁴, and McCroskey and Fisher³⁵. From the analysis of chordwise pressure distributions on the blade, it is seen that, as the blade moves into the retreating region, the rapid rate of increase of incidence allows the aerofoil section to exceed the normal steady stall incidence without signs of a flow breakdown; i.e. there is still a large suction peak near the leading edge. As pointed out by Carta, this may be due, in part at least, to the apparent increase of camber due to the rotation of the aerofoil. As the incidence increases further, a vortex is formed and shed from the leading edge and moves backwards across the aerofoil at a speed somewhat less than the local flow speed. The effect of the vortex is to produce a suction peak in the mid-chord region, resulting

in a large nose down pitching moment. The lift continues to grow even after the leading edge suction has started to collapse. After this, the aerofoil moves into a condition of deep stall and the tests show that torsion flutter may occur. When the blade reaches approximately the rear of the disc, where the blade incidence is greatly reduced, the flow returns to the steady pattern of low incidence. The aerofoil's chordwise pressure distributions in the sequence described are sketched in Fig. 6.47, with typical values of C_N and incidence at four azimuth angles on the retreating blade.

McCroskey and Fisher³⁵ have observed that the relationship between the normal force and pitching moment coefficients in their model helicopter measurements and those of the two-dimensional aerofoil measurements of Ham and Garelick³⁴ are

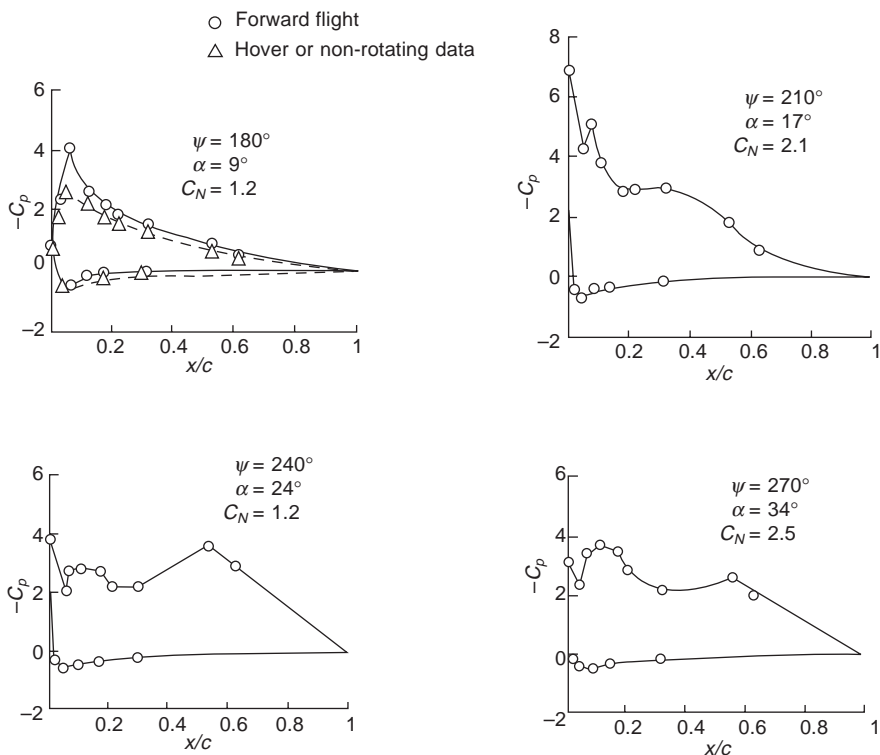


Fig. 6.47 Chordwise pressure distributions at high incidence

remarkably similar. Figure 6.48 shows the variation of C_N and C_M with blade azimuth angle for the point $r/R = 0.75$ on the rotor blade, and the corresponding values from the two-dimensional tests for similar values of the incidence α and of $\dot{\alpha}$.

From the similarity of the curves, it can be inferred that the performance of the blade section at high incidence has little to do with the three-dimensional rotating environment and that the section characteristics can be obtained with sufficient accuracy from unsteady two-dimensional aerofoil tests.

The particular flow states mentioned above can be identified on Fig. 6.48; thus, for the model rotor results (full line), for ψ increasing from 90° , the normal force coefficient increases to beyond the maximum steady state value (about 1.5) until $\psi = 210^\circ$.

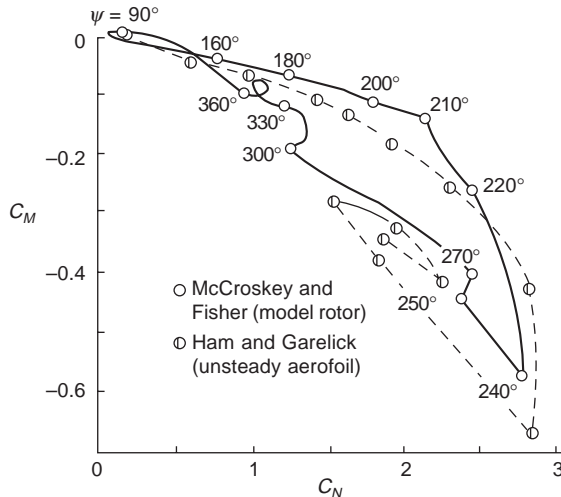


Fig. 6.48 Variation of pitching moment and normal force coefficients with azimuth angle

Beyond this azimuth angle, C_N continues to increase but accompanied by a significant nose down pitching moment; this is associated with the shedding and movement rearwards of the concentrated vorticity from the leading edge region. After $\psi = 240^\circ$, C_N decreases corresponding to the aerofoil being fully stalled, and the vortex having passed clear of the trailing edge. At about 360° , the flow re-attaches.

This sequence of events has been modelled by Leishman and Beddoes³⁶ and validated through comparison with experiment following initial work by Beddoes³⁷ to produce a practical and versatile design tool. For the attached flow in the initial phase, the changing normal force and moment are modelled indicially using lift and moment deficiency functions, rather as for fixed wing theory in relation to gusts and other time-dependent conditions. Leading edge separation occurs when C_N achieves a critical value which is dependent on local Mach number; however, there is a lag or time delay in unsteady flow which allows C_N to reach higher than normal static values. This delay is determined empirically and has been found to be largely independent of aerofoil shape.

Subsequently, the vortex which separates from the leading edge is transported downstream causing the centre of pressure also to move rearwards. Meanwhile, the vortex itself generates lift which dissipates (exponentially) as fast as it accumulates, until the vortex passes clear of the trailing edge, whereupon the lift (or C_N) decays rapidly to a value appropriate to fully separated flow, assuming the angle of incidence is still sufficiently high. The speed of convection of the vortex downstream is derived from a large body of experimental data involving dynamic stall over a wide range of Mach numbers.

The indicial approach has been further implemented by Leishman³⁸ to account for arbitrary motion of a rotor blade section, as well as encounters with gusts or interactions with vortices shed by other blades.

6.5 The boundary layer on a rotating blade

The first attempt at calculating the boundary layer on a rotating blade was made by Fogarty³⁹ in 1951 for the case of hovering flight. Fogarty made use of a theorem of Sears⁴⁰ which states that if $\phi_1(x, z)$ is the potential for plane steady flow past the cylinder in a parallel stream at unit speed, then the potential ϕ for flow about the cylinder when rotating at angular velocity Ω is

$$\phi = \Omega y [\phi_1(x, z) - x] \quad (6.31)$$

It was also shown that the velocity components u_1, v_1, w_1 , relative to the blade are, Fig. 6.49,

$$u_1 = \Omega y \frac{\partial \phi_1}{\partial x}$$

$$v_1 = \Omega [\phi_1(x, z) - 2x]$$

$$w_1 = \Omega y \frac{\partial \phi_1}{\partial z}$$

Thus the velocity components u_1 and w_1 in the plane of the cylinder are the same as those of steady plane flow about the cylinder in a stream of velocity Ωy . The spanwise component v_1 , which is independent of the radial distance, can be found directly from the plane flow potential ϕ_1 . These relationships establish the appropriate boundary conditions outside the boundary layer.

The equations used are the familiar Navier–Stokes equations referred to co-ordinates rotating with the blade, Fig. 6.49. If the usual boundary layer approximations are made, and certain terms are neglected on account of the high aspect ratio of the blade, we have for the boundary layer equations

$$u \frac{\partial u}{\partial x} + w \frac{\partial u}{\partial z} - \Omega^2 x = - \frac{1}{\rho} \frac{\partial p}{\partial x} + \nu \frac{\partial^2 u}{\partial z^2}$$

$$u \frac{\partial v}{\partial x} + w \frac{\partial v}{\partial z} + 2\Omega u - \Omega^2 y = - \frac{1}{\rho} \frac{\partial p}{\partial y} + \nu \frac{\partial^2 v}{\partial z^2}$$

$$\frac{\partial p}{\partial z} = 0$$

together with the continuity equation

$$\frac{\partial u}{\partial x} + \frac{\partial w}{\partial z} = 0$$

To find the pressure gradients $\partial p / \partial x$ and $\partial p / \partial y$ we use Bernoulli's equation for the external potential flow, i.e.

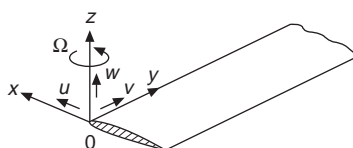


Fig. 6.49 Co-ordinates of rotating blade

$$p/\rho + \frac{1}{2}(u_1^2 + v_1^2) = \frac{1}{2}\Omega^2(x^2 + y^2) + \text{constant}$$

Then, neglecting the small terms $v_1\partial v_1/\partial x$ and $v_1\partial v_1/\partial y$, we have approximately

$$\frac{1}{\rho} \frac{\partial p}{\partial x} = \Omega^2 x - u_1 \frac{\partial u_1}{\partial x}$$

$$\frac{1}{\rho} \frac{\partial p}{\partial y} = \Omega^2 y - u_1 \frac{\partial u_1}{\partial y}$$

so that, on substituting for the pressure gradients, the boundary layer equations are

$$u \frac{\partial u}{\partial x} + w \frac{\partial u}{\partial z} = u_1 \frac{\partial u_1}{\partial x} + v \frac{\partial^2 u}{\partial z^2} \quad (6.32)$$

$$u \frac{\partial v}{\partial x} + w \frac{\partial v}{\partial z} + 2u\Omega = u_1 \frac{\partial u_1}{\partial y} + v \frac{\partial^2 v}{\partial z^2} \quad (6.33)$$

$$\partial u/\partial x + \partial w/\partial z = 0$$

together with the boundary conditions

$$u = v = w = 0 \quad \text{for } z = 0$$

$$u \rightarrow u_1 = \Omega y \frac{\partial \phi_1}{\partial x}, \quad v \rightarrow v_1 = \Omega[\phi_1(x, z) - 2x]$$

$$w \rightarrow w_1 = \Omega y \frac{\partial \phi_1}{\partial z}, \quad \text{for } z \rightarrow \infty$$

We notice that eqn 6.32 is the same as the boundary layer equation for two-dimensional plane flow and may therefore be solved by any of the known methods. Having solved this equation for u and w , we can obtain v from the solution of eqn 6.33. This has been done by Fogarty for the case of a flat plate and the section defined by $z = kx(1 - x^2)$. The results for the flat plate are shown in Fig. 6.50.

The importance of Fogarty's results is that the spanwise flow, or 'centrifugal pumping', is usually very small. As an example, let us take a point at a radial distance of 6 m from the hub. Since the chord will be about 0.5 m at most, let us take $x = 0.3$ m.

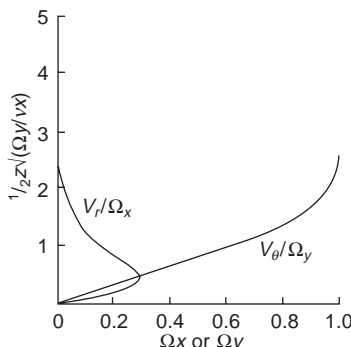


Fig. 6.50 Velocity distributions in laminar boundary layer

Then, if Ω is 25 rad/s, $\Omega x = 7.5$ m/s and the largest spanwise velocity is about $7.5 \times 0.3 = 2.25$ m/s, compared with the free stream chordwise velocity of 150 m/s. The spanwise flow becomes considerable only near the hub, where x/y is no longer a small quantity. Thus, for the conventional rotor blade the spanwise, or secondary, flow appears to be insignificant, although it might be important for wide blades such as marine propellers.

McCroskey *et al.*⁴¹ have calculated the details for a turbulent boundary layer, the results of which are shown in Fig. 6.51. We see that the spanwise flow is even smaller, due mainly to the larger stresses in the turbulent layer.

McCroskey and Yaggy⁴² have extended the theorem of Sears to the forward flight case and have made calculations on the basis of Fogarty's laminar flow theory in hovering flight. The calculations show that the spanwise flow is dominated by the spanwise component of forward speed, as the example in Fig. 6.52 shows.

The chordwise flow is affected by several terms which are additional to those arising in the hovering case. Generally, the effects represented by these terms are favourable with regard to the delay of laminar separation, particularly in the retreating quadrant 180° to 270°. This may be another reason for the improved performance of the rotor blade compared with steady two-dimensional aerofoil characteristics although, as we saw in the previous section, it seems that it is the unsteady motion which is largely responsible for the peculiar behaviour of the aerodynamic characteristics at high incidence.

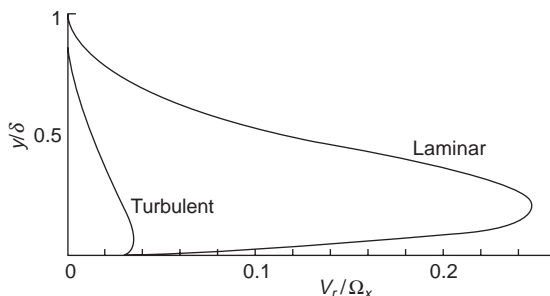


Fig. 6.51 Velocity distribution in turbulent boundary layer

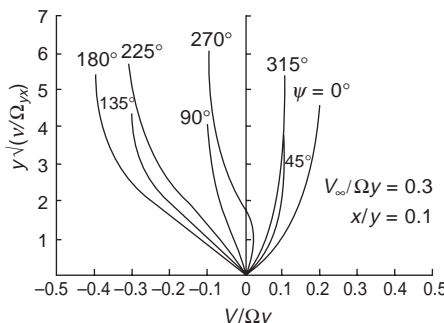


Fig. 6.52 Laminar boundary profiles in forward flight

References

- Mil, M. L., Nekrasov, A. V., Braverman, A. S., Grodko, L. N. and Leykand, M. A., *Helicopters – calculation and design*, Vol. I ‘Aerodynamics’, *NASA Tech. Transl. NASA TT F-494*, 1967 (see p. 244 for ‘Vortex Theory of V. E. Baskin’).
- Miller, R. H., ‘Unsteady air loads on helicopter rotor blades’, *J. Roy. Aeronautical Soc.*, April 1964.
- Willmer, M. A. P. ‘The loading of helicopter blades in forward flight’, *Aeronautical Research Council R&M 3318*, 1959.
- Miller, R. H., ‘Rotor blade harmonic air loading’, *AIAA J.*, **2**(7), July 1964.
- Theodorsen, T., ‘General theory of aerodynamic instability and the mechanism of flutter’, *NACA Tech. Rep. 496*, 1935.
- Van de Vooren, A. I., *AGARD Manual on Aeroelasticity*, part II, Chapter 2, 1960.
- Glauert, H., *Aerofoil and airscrew theory*, London, Camb. Univ. Press, 1959.
- Loewy, R. G., ‘A two-dimensional approach to the unsteady aerodynamics of rotary wings’, *J. Aerospace Sci.*, **24**, 1957, pp. 82–98.
- Jones, J. P., ‘The influence of the wake on the flutter and vibration of rotor blades’, *Aeronaut. Q.*, **9**, August 1958.
- Tararine, S., ‘Experimental and theoretical study of local induced velocities over a rotor disc’, *CAL/TRECOM Symposium*, Buffalo N.Y., June 1963.
- Piziali, R. A., ‘Method for the solution of aeroelastic response for rotating wings’, *J. Sound and Vibration*, **4**(3), 1966.
- Landgrebe, A. J., ‘An analytical method for predicting rotor wake geometry’ *J. Amer. Helicopter Soc.*, **14**(4), October 1969.
- Cook, C. V., ‘The structure of the rotor blade tip vortex’, *AGARD Conf. Proc. CP-111*, 1972.
- Bagai, A. and Leishman, J. G., ‘Rotor free-wake modeling using a pseudo-implicit technique – including comparisons with experimental data’, *J. Amer. Helicopter Soc.*, **40**(3), 1995.
- Coppens, G., Costes, M., Leroy, P. and Devinant, P., ‘Computation of helicopter rotor wake using a high order panel method’, Paper No. AE11, 24th European Rotorcraft Forum, Marseilles, France, Sept. 1998.
- Tangler, J. L., ‘Schlieren and noise studies of rotors in forward flight’, Paper No. 33-05, 33rd American Helicopter Society Annual National Forum, Washington, DC, 1977.
- Leishman, J. G., ‘Aeroacoustics of blade–vortex interaction using indicial aerodynamics and the acoustic analogy’, Paper No. 80, 22nd European Rotorcraft Forum, Brighton, UK, 17–19 Sept. 1996.
- Kube, R. and Schultz, K.-J., ‘Vibration and BVI noise reduction by active rotor control: HHC compared to IBC’, Paper No. 85, 22nd European Rotorcraft Forum, Brighton, UK, 17–19 Sept. 1996.
- Schmitz, F. H. and Yu, Y. H., ‘Helicopter impulsive noise: theoretical and experimental status’, *J. Sound and Vibration*, **109**(3), pp. 361–422, 1986.
- Lowson, M. V., ‘Progress towards quieter civil helicopters’, *Aeronautical J.*, June/July 1992.
- Ehrenfried, K., Geissler, W., Seelhorst, U. and Vollmers, H., ‘Combined numerical and experimental investigations of BVI-noise generation and radiation from the HART-test campaign’, Paper No. I-2, 21st European Rotorcraft Forum, St Petersburg, 30 Aug–1 Sept. 1995.
- Lowson, M. V., ‘Directionality of helicopter BVI noise’, Paper No. I-10, 21st European Rotorcraft Forum, St Petersburg, 30 Aug–1 Sept. 1995.
- Pearcey, H. H., Wilby, P. G., Riley, M. J. and Brotherhood, P., ‘The derivation and verification of a new rotor profile on the basis of flight phenomena; aerofoil research and flight tests’, *AGARD Conf. Proc. CP-111*, 1972.
- Desopper, A., Lafon, P., Ceroni, P. and Philippe, J. J., ‘Ten years of rotor flow studies at ONERA’, *J. Amer. Helicopter Soc.*, **34**(1), 1989.

25. Perry, F. J., Wilby, P. G. and Jones, A. F., 'The BERP rotor – how does it work, and what has it been doing lately?' *Vertiflite*, Spring, 1998.
26. Squire, H. B., Fail, R. A. and Eyre, R. C. W., 'Wind tunnel tests on a 12 ft diameter helicopter rotor', *Aeronautical Research Council R&M 2695*, 1949.
27. Bramwell, A. R. S., Wilde, E. and Johnstone, J. B. B., 'Comparison of theoretical and experimental determination of helicopter rotor characteristics with particular reference to high blade incidence conditions', *RAE Rep. 66139*, 1966.
28. Harris, F. D., Tarzanin, F. T. and Fisher, R. K., 'Rotor high speed performance, theory vs. test', *J. Amer. Helicopter Soc.*, July 1970.
29. Meyer, J. R. and Falabella, G., 'An investigation of the experimental aerodynamic loading on a model helicopter rotor blade', *NACA TN 2953*, 1953.
30. Scheiman, James, 'A tabulation of helicopter rotor blade differential pressures, stresses and motions in forward flight', *NASA TM X-952*, March 1964.
31. Farren, W. S., 'Reaction on a wing whose angle of incidence is changing rapidly', *Aeronautical Research Council R&M 1648*, 1935.
32. Halfman, R. L., Johnson, H. C. and Haley, S. M., 'Evaluation of high angle of attack aerodynamic derivative data and stall flutter prediction technique', *NACA TN 2533*, 1951.
33. Carta, F. O., 'Experimental investigation of the unsteady aerodynamic characteristics of NACA 0012 airfoil', *United Aircr. Lab. Rep. M-1283-1*, August 1960.
34. Ham, N. D. and Garellick, M. S., 'Detailed stall oscillations in helicopter rotors', *J. Amer. Helicopter Soc.*, **13**(2), 1968.
35. McCroskey, W. J., and Fisher, R. K., jnr, 'Detailed aerodynamic measurements on a model rotor in the blade stall regime', *J. Amer. Helicopter Soc.*, Vol. 17, no. 1, 1972.
36. Leishman, J. G. and Beddoes, T. S., 'A semi-empirical model for dynamic stall', *J. Amer. Helicopter Soc.*, **34**(3), 1989.
37. Beddoes, T. S., 'A synthesis of unsteady aerodynamic effects including stall hysteresis', Paper No. 17, 1st European Rotorcraft Forum, Southampton, UK, Sept. 1975.
38. Leishman, J. G., 'Modeling of subsonic unsteady aerodynamics for rotary wing applications', *J. Amer. Helicopter Soc.*, **35**(1), 1990.
39. Fogarty, L. E., 'The laminar boundary layer on a rotating blade', *J. Aeronaut. Sci.*, **18**(3), 1951.
40. Sears, W. R., 'Potential flow around a rotating cylinder', *J. Aeronaut. Sci.*, Vol. 17, no. 3, 1950.
41. McCroskey, W. J., Nash, J. F., and Hicks, J. G., 'Turbulent boundary layer flow over a rotating flat plate blade', *AIAA J.* **9**(1) 1971.
42. McCroskey, W. J. and Yaggy, P. F., 'Laminar boundary layers on helicopter rotors in forward flight', *AIAA J.* **6**(10), 1968.

Structural dynamics of elastic blades

7.1 Introduction

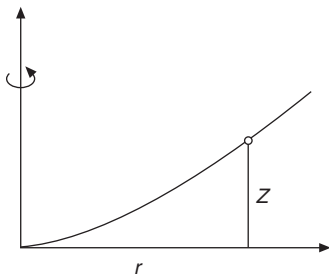
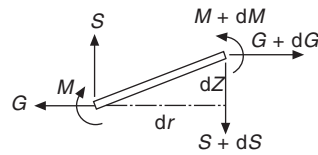
In previous chapters the rotor blade has been assumed to be rigid, and this assumption has been adequate to provide the solution to a number of important helicopter problems with acceptable accuracy. A rotor blade is of course very flexible, and a number of problems arise which make it necessary to study the effects of flexibility on blade motion. For example, we need to know whether the motion of the blade significantly affects the estimated performance and rotor blade loading; what stresses occur in the deformed blade; and whether the frequencies of the blade motion coincide with the frequencies of the aerodynamic forcing loads. The problem of blade flexibility is a very complex one, for not only has the blade several degrees of freedom but the aerodynamic loading depends strongly on the blade shape. However, for the purpose of illustration, we shall consider the flapwise, torsional, and lagwise motions of the blade separately, and try to draw some general conclusions. For the far more complicated problem of coupled motion between the degrees of freedom only a brief discussion will be given and the reader will be referred to specialist papers.

7.2 Free vibrations of rotor blades

7.2.1 Flapwise bending

We define flapwise bending as deflection of the blade in a plane perpendicular to the rotor hub plane, Fig. 7.1.

Let Z be the displacement of an element of the blade above the flapping plane and r the distance from the axis of rotation. Consider the motion of this element under the forces acting on it, Fig. 7.2; S is the local shear force, M the bending moment, and G the centrifugal tension in the blade.

**Fig. 7.1** Blade flapwise bending**Fig. 7.2** Forces on blade element

The equilibrium of the blade element requires that

$$dG + m\Omega^2 r dr = 0 \quad (7.1)$$

$$dS + m dr \frac{\partial^2 Z}{\partial t^2} = 0 \quad (7.2)$$

$$G dZ + S dr - dM = 0 \quad (7.3)$$

From eqn 7.1 we get at once

$$G = \int_r^R m\Omega^2 r dr$$

and eqns 7.2 and 7.3 give

$$\frac{\partial S}{\partial r} = -m \frac{\partial^2 Z}{\partial t^2} \quad (7.4)$$

$$\frac{\partial M}{\partial r} = G \frac{\partial Z}{\partial r} + S \quad (7.5)$$

Differentiating eqn 7.5 and substituting eqn 7.4 we get

$$\frac{\partial^2 M}{\partial r^2} = \frac{\partial}{\partial r} \left(G \frac{\partial Z}{\partial r} \right) + \frac{\partial S}{\partial r} = \frac{\partial}{\partial r} \left(G \frac{\partial Z}{\partial r} \right) - m \frac{\partial^2 Z}{\partial t^2}$$

But elementary bending theory gives

$$M = EI \frac{\partial^2 Z}{\partial r^2}$$

so that we have, finally, for the equation of bending

$$\frac{\partial^2}{\partial r^2} \left(EI \frac{\partial^2 Z}{\partial r^2} \right) - \frac{\partial}{\partial r} \left(G \frac{\partial Z}{\partial r} \right) + m \frac{\partial^2 Z}{\partial t^2} = 0 \quad (7.6)$$

Equation 7.6 represents the free motion of the blade *in vacuo*.

Let the solution of eqn 7.6 take the form

$$Z = S(r)\phi(t) \quad (7.7)$$

where $S(r)$ is a function of r alone and $\phi(t)$ is a function of t alone. Substituting eqn 7.7 into eqn 7.6 gives

$$\frac{d^2(EI d^2S/dr^2)/dr^2 - d(G dS/dr)/dr}{mS(r)} = \frac{d^2\phi/dt^2}{\phi(t)} \quad (7.8)$$

Now, the left-hand side of eqn 7.8 is a function of r only and the right hand side is a function of t only. Since the two sides are always equal they must be equal to a constant. The constant has dimensions T^{-2} and it is convenient to write it as $\lambda^2\Omega^2$. Thus, we have

$$\frac{d^2}{dr^2} \left(EI \frac{d^2S}{dr^2} \right) - \frac{d}{dr} \left(G \frac{dS}{dr} \right) + m\lambda^2\Omega^2 S = 0 \quad (7.9)$$

and

$$\frac{d^2\phi}{dt^2} - \lambda^2\Omega^2\phi = 0 \quad (7.10)$$

Let us write $z = Z/R$, $x = r/R$, and $\psi = \Omega t$. Then eqns 7.9 and 7.10 become

$$\frac{d^2}{dx^2} \left(EI \frac{d^2S}{dx^2} \right) - R^2 \frac{d}{dx} \left(G \frac{dS}{dx} \right) - m\lambda^2\Omega^2 R^4 S = 0 \quad (7.11)$$

and

$$\frac{d^2\phi}{d\psi^2} + \lambda^2\phi = 0 \quad (7.12)$$

The boundary conditions to be satisfied are as follows.

(a) *Hinged blade (including flapping hinge offset)*

At $x = e$ (at flapping hinge)

$$S = 0$$

$$d^2S/dx^2 = 0 \quad (\text{zero bending moment})$$

At $x = 1$ (blade tip)

$$d^2S/dx^2 = 0 \quad (\text{zero bending moment})$$

$$d^3S/dx^3 = 0 \quad (\text{zero shear force})$$

(b) *Hingeless blade*

At $x = 0$

$$S = 0$$

$$dS/dx = 0 \quad (\text{zero slope})$$

At $x = 1$

$$\frac{d^2S}{dx^2} = 0$$

$$\frac{d^3S}{dx^3} = 0$$

Equation 7.7 will be a solution of eqn 7.6 provided $S(x)$ and $\phi(\psi)$ satisfy eqns 7.11 and 7.12 and the appropriate boundary conditions.

There is an infinite number of solutions of eqn 7.11 since λ is not a fixed number but can be adjusted to satisfy the equation in association with the appropriate boundary conditions. These solutions represent the blade shape and are called *normal modes* on account of the orthogonal property to be proved in section 7.3.

Equation 7.12 is the equation of simple harmonic motion, and the infinite number of discrete values of λ determine the frequencies $\omega = \lambda\Omega$ of the corresponding mode shape. λ_n is therefore the ratio of the blade natural frequency ω_n to the shaft rotational frequency Ω for the n th mode shape.

It can easily be verified that when there is no flapping offset, i.e. $e = 0$, a solution of eqn 7.11 is $S(x) = x$, with $\lambda = 1$, that is, the first normal mode shape of the centrally hinged blade is a straight line whose flapwise frequency is exactly equal to the rotational frequency of the shaft. This is the ‘rigid’ blade shape already assumed in the previous chapters. If $e \neq 0$, the mode shape is not exactly a straight line, although for typical values of e it is very close to it.

Methods for calculating the blade mode shapes and frequencies are dealt with below. Figure 7.3 shows the first four shapes for a typical helicopter blade.

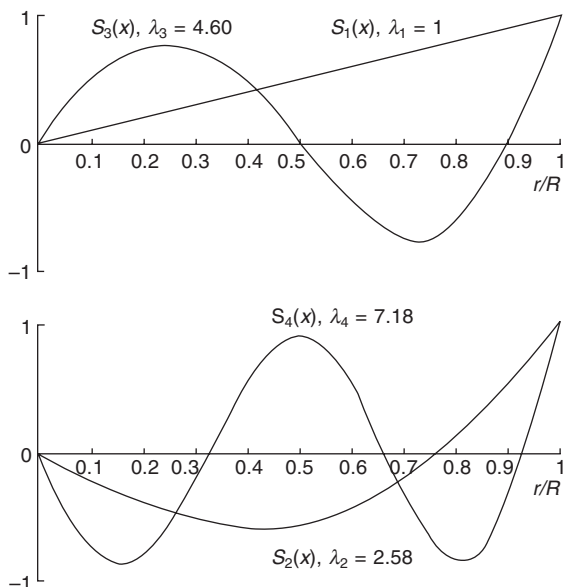


Fig. 7.3 Mode shapes of typical helicopter blade

7.2.2 Calculation of blade mode shapes and frequencies

We must now attempt to solve eqn 7.11 in order to obtain the blade mode shapes $S_n(x)$ and associated frequencies $\lambda_n \Omega$. In general, both the blade elastic stiffness EI and mass distribution m will be complicated functions of the radial station x , and it is obvious that a simple analytical solution of the blade bending equation is out of the question. Typical spanwise variations of stiffness and mass for a uniform blade are shown in Fig. 7.4.

It can be seen that over the greater part of the blade the stiffness and mass distributions are practically constant, but that near the blade root large and often discontinuous changes occur because of the root attachment.

Now it is well known that for a uniform *non-rotating* beam there is an exact closed solution of the mode equation and that other exact solutions exist for some particular mass and stiffness distributions. However, there is no known closed solution for the *rotating* beam, even for the apparently simple case of constant mass and stiffness, the equation of which is given below, eqn 7.13:

$$k^2 \frac{d^4 z}{dx^4} - \frac{1}{2} \frac{d}{dx} \left[(1 - x^2) \frac{dz}{dx} \right] - \lambda_n^2 z = 0 \quad (7.13)$$

where $k^2 = EI/m\Omega^4$ is constant.

The mode shapes and frequencies of a rotating uniform blade for $k^2 = 0.0055$ have been calculated and are shown in Fig. 7.5. The broken lines show the mode shapes and frequencies for a non-rotating blade of the same thickness (standard results for a uniform vibrating beam). It is perhaps a little surprising to note that the effect of rotation is quite small, which suggests that the non-rotating mode shapes might serve as useful approximations in the calculation of the rotating modes.

The lack of an exact solution of eqn 7.13 is unfortunate because, although the mass and stiffness distributions might not be representative of a practical blade, it would be very useful for testing the accuracy of approximate methods of solution.

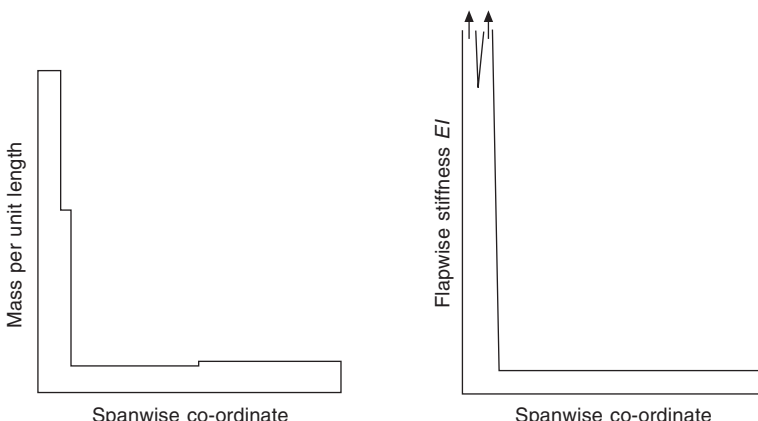


Fig. 7.4 Mass and stiffness distributions of a typical uniform blade

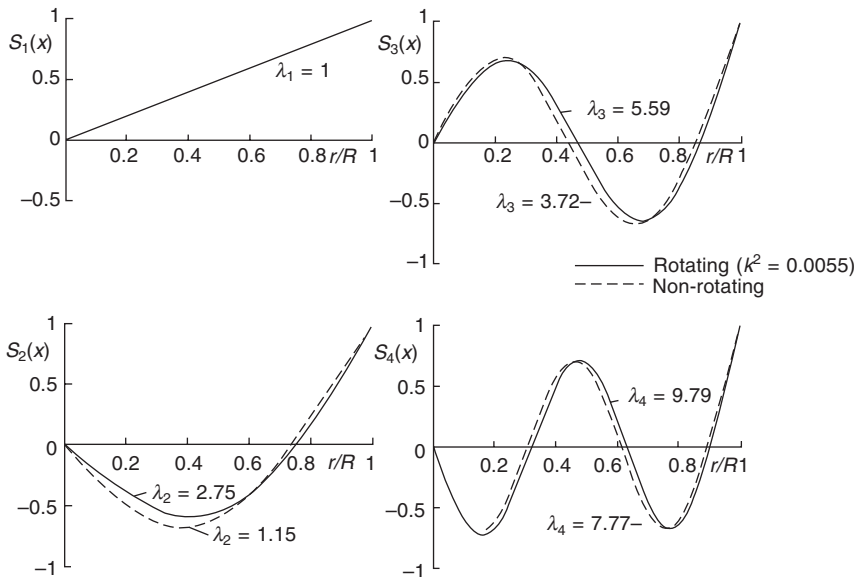


Fig. 7.5 Mode shapes of rotating and non-rotating uniform blade

The approximate methods usually used fall under two main headings:

- (i) method of assumed modes,
- (ii) method of lumped parameters.

7.2.2.1 Method of assumed modes

This method consists of choosing a finite sequence of functions which, preferably, approximate to the expected mode shapes and satisfy the appropriate boundary conditions. This latter requirement is not essential, however, since it is always possible to include restraint conditions in the analysis.

We shall consider three methods employing assumed modes:

- (a) Lagrange's equations
- (b) Rayleigh–Ritz procedure,
- (c) Galerkin's method.

(a) Lagrange's equations

Let the sequence of functions which are to be used to approximate to the blade shape be

$$\gamma_1(x), \gamma_2(x), \dots, \gamma_i(x), \dots, \gamma_n(x)$$

and let the displacement be

$$z(x, \psi) = \sum_{i=1}^n \gamma_i(x) \phi_i(\psi)$$

It will be assumed that the functions $\gamma_i(x)$ satisfy the boundary conditions.

Then

$$\partial z / \partial \psi = \sum_{i=1}^n \gamma_i(x) \phi'_i(x)$$

and the kinetic energy T in term of blade axes (see section 7.3.2) is therefore

$$\begin{aligned} T &= \frac{1}{2} \Omega^2 R^3 \sum_{i=1}^n \sum_{j=1}^n \phi'_i \phi'_j \int_0^1 m \gamma_i \gamma_j \, dx \\ &= \sum_{i=1}^n \sum_{j=1}^n A_{ij} \phi''_i \phi''_j \end{aligned} \quad (7.14)$$

$$\text{where } A_{ij} = \frac{1}{2} \Omega^2 R^3 \int_0^1 m \gamma_i \gamma_j \, dx$$

is a generalised mass or inertia coefficient.

It should be noted that the orthogonal properties do not apply to the integral of eqn 7.14 since the functions $\gamma_i(x)$ themselves are not exact solutions of the blade bending equation, eqn 7.11.

The strain and potential energy U is, as will be seen from eqn 7.92.

$$\begin{aligned} U &= \frac{1}{2R} \sum_{i=1}^n \sum_{j=1}^n \phi_i \phi_j \int_0^1 \left(EI \frac{d^2 \gamma_i}{dx^2} \cdot \frac{d^2 \gamma_j}{dx^2} + R^2 G \frac{d\gamma_i}{dx} \frac{d\gamma_j}{dx} \right) dx \\ &= \sum_{i=1}^n \sum_{j=1}^n B_{ij} \phi_i \phi_j \end{aligned}$$

$$\text{where } B_{ij} = \frac{1}{2R} \int_0^1 \left(EI \frac{d^2 \gamma_i}{dx^2} \frac{d^2 \gamma_j}{dx^2} + R^2 G \frac{d\gamma_i}{dx} \frac{d\gamma_j}{dx} \right) dx$$

is a generalised stiffness coefficient (including both structural and centrifugal stiffening effects).

Then applying Lagrange's equations eqn 7.95, with $\partial W / \partial \phi_n = 0$, gives

$$\sum_{j=1}^n A_{ij} \phi''_j + \sum_{j=1}^n B_{ij} \phi_j = 0 \quad (7.15)$$

If $\phi_j = \phi_{j0} \sin \lambda_j \psi$, eqn 7.15 becomes

$$\sum_{j=1}^n (B_{ij} - \lambda_j^2 A_{ij}) \phi_{j0} = 0 \quad (7.16)$$

As a simple example, let us calculate the first two mode shapes and frequencies of a centrally hinged uniform blade and suppose that the deflection amplitude can be expressed as

$$\gamma_0 = \phi_{10} \gamma_1 + \phi_{20} \gamma_2$$

where

$$\gamma_1(x) = x \text{ and } \gamma_2(x) = 10x^3/3 - 10x^4/3 + x^5$$

It can easily be seen that the functions satisfy the boundary conditions of a centrally hinged blade. Then evaluating the integrals A_{ij} and B_{ij} we get

$$\bar{A}_{11} = \frac{1}{3}, \quad \bar{A}_{12} = \bar{A}_{21} = \frac{16}{63}, \quad \bar{A}_{22} = \frac{1304}{6237}$$

$$\bar{B}_{11} = \frac{1}{3}, \quad \bar{B}_{12} = \bar{B}_{21} = \frac{16}{63}, \quad \bar{B}_{22} = \frac{80}{21}k^2 + \frac{1850}{6237}$$

the bars denoting that the integrals have been divided by $\frac{1}{2}m\Omega^2R^3$, and where $k^2 = EI/m\Omega^2R^4$. In this case the tension G is $\frac{1}{2}m\Omega^2R^3(1 - x^2)$. substituting in eqn 7.16 gives, in matrix form,

$$\begin{bmatrix} \frac{1}{3} & \frac{16}{63} \\ \frac{16}{63} & \frac{80}{21}k^2 + \frac{1850}{6237} \end{bmatrix} \begin{bmatrix} \phi_{10} \\ \phi_{20} \end{bmatrix} - \begin{bmatrix} \frac{1}{3}\lambda^2 & \frac{16}{63}\lambda^2 \\ \frac{16}{63}\lambda^2 & \frac{1304}{6237}\lambda^2 \end{bmatrix} \begin{bmatrix} \phi_{10} \\ \phi_{20} \end{bmatrix} = 0$$

or

$$\begin{bmatrix} \frac{1}{3}(\lambda^2 - 1) & \frac{16}{63}(\lambda^2 - 1) \\ \frac{16}{63}(\lambda^2 - 1) & \frac{1304}{6237}\lambda^2 - \frac{80}{21}k^2 - \frac{1850}{6237} \end{bmatrix} \begin{bmatrix} \phi_{10} \\ \phi_{20} \end{bmatrix} = 0$$

The frequency equation is found by putting the determinant of the square matrix to zero. If we take $k^2 = 0.004$ as a typical value, the determinant gives

$$\begin{vmatrix} \lambda^2 - 1 & 0.7619(\lambda^2 - 1) \\ \lambda^2 - 1 & 0.8232\lambda^2 - 1.2279 \end{vmatrix} = 0$$

or

$$(\lambda^2 - 1)(\lambda^2 - 7.5988) = 0$$

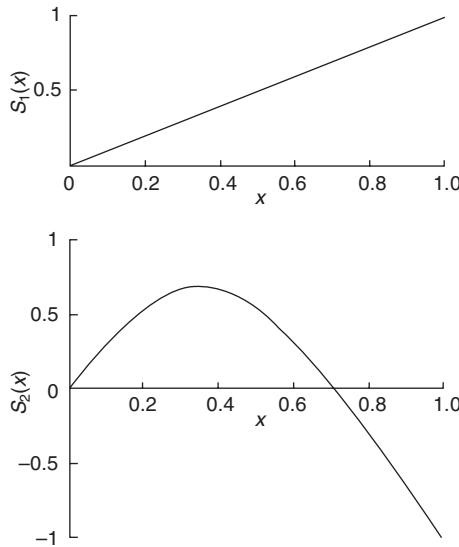
This equation gives $\lambda = 1$, a value we should expect since $\gamma_1 = x$ is known to be an exact solution, and $\lambda = 2.757$. We cannot find the absolute amplitudes of the modes but only the ratio of the amplitudes. Taking the second equation of the matrix form of eqn 7.16 gives

$$(\lambda^2 - 1)\phi_{10} + (0.8232\lambda^2 - 1.2279)\phi_{20} = 0$$

When $\lambda = 1$, we have $\phi_{20}/\phi_{10} = 0$, i.e. if $\phi_{10} \neq 0$, $\phi_{20} = 0$ indicating that in the oscillation whose frequency is Ω the mode shape consists entirely of the function $\gamma = x$. This is, again, just what we should expect, as $\gamma = x$ is an exact solution of the flapping equation. The higher frequency 2.757Ω gives $\phi_{10}/\phi_{20} = -0.759$ and the corresponding mode shape can be written

$$S_2(x) = -3.15x + 4.15x^3(10/3 - 10x/3 + x^2)$$

The two modes are shown in Fig. 7.6. The accuracy of the mode shapes and frequencies improves with the number of functions chosen, the lower modes being improved the most. In general, the stiffness and mass distribution will be such as to require numerical integration of the integrals A_{ij} and B_{ij} .

**Fig. 7.6** Normal mode shapes*(b) The Rayleigh–Ritz procedure*

It can be shown¹ from the calculus of variations that a function satisfying the fourth order linear differential equation

$$\frac{d^2}{dx^2} \left(EI \frac{d^2 S}{dx^2} \right) - R^2 \frac{d}{dx} \left(G \frac{dS}{dx} \right) - m\lambda^2 \Omega^2 R^4 S = 0 \quad (7.11)$$

in association with either set of boundary conditions for the hinged or hingeless blade, is a function which gives a stationary value to the integral

$$L = \frac{1}{2R} \int_0^1 \left[m\lambda^2 \Omega^2 R^4 S^2 - EI \left(\frac{d^2 S}{dx^2} \right)^2 - R^2 G \left(\frac{dS}{dx} \right)^2 \right] dx \quad (7.17)$$

It will be seen from energy considerations (eqns 7.87, 7.89 and 7.91) that \$L\$, termed the Lagrangian, is the difference between the kinetic and strain energies in a given mode of motion, i.e.

$$L = T - U$$

The Rayleigh–Ritz procedure is to assume a finite series of approximation functions

$$S_n(x) = A_1 \gamma_1(x) + A_2 \gamma_2(x) + \dots + A_i \gamma_i + \dots + A_n \gamma_n$$

where the terms \$\gamma_i\$ satisfy the boundary conditions, and substitute the series into eqn 7.17. Since \$A_1, A_2, \dots\$, etc. can be arbitrarily varied, the condition that \$L\$ should have stationary values is

$$\frac{\partial L}{\partial A_1} = \frac{\partial L}{\partial A_2} = \dots = \frac{\partial L}{\partial A_i} = \dots = \frac{\partial L}{\partial A_n}$$

giving \$n\$ equations for the evaluation of the terms \$A_i\$.

We find that this gives exactly the same set of equations as we obtained by the Lagrange method of the previous section. It is worth mentioning, however, that the Rayleigh–Ritz method can be applied to problems, e.g. static equilibrium, to which the Lagrange equations would not normally be applicable.

The Rayleigh–Ritz method is a generalization of the application of Rayleigh's principle² that the frequencies corresponding to the solutions of eqn 7.11 have *stationary* values. This means that, if the chosen functions differ from the exact solutions S_i by small quantities of the first order, the calculated frequencies will be in error by only small quantities of the second order. Thus, it can be expected that quite a poor approximation to the true mode shape will give a good approximation to the frequency.

Now, when a system oscillates in a normal mode with frequency $\omega_i = \lambda_i \Omega$, each part of the system oscillates in phase or in antiphase with every other part of the system. Thus we can write for a typical displacement in a normal mode

$$\begin{aligned} Z &= \gamma_i(x) \sin(\omega_i t + \varepsilon) \\ &= \gamma_i(x) \sin(\lambda_i \psi + \varepsilon) \end{aligned}$$

Then the kinetic energy T of the system, as will be seen from eqn 7.87, is

$$\begin{aligned} T &= \frac{1}{2} \Omega^2 R^3 \int_0^1 m \left(\frac{\partial \gamma}{\partial \psi} \right)^2 dx \\ &= \frac{1}{2} \lambda_i^2 \Omega^2 R^3 \cos^2(\lambda_i \psi + \varepsilon) \int_0^1 m y^2(x) dx \end{aligned}$$

and from eqns 7.89 and 7.91 the potential energy of the rotating blade is

$$\begin{aligned} U &= U_B + U_G \\ &= \frac{1}{2R} \sin^2(\lambda_i \psi + \varepsilon) \int_0^1 EI \left(\frac{d\gamma_i}{dx} \right)^2 dx + \frac{1}{2} R \sin^2(\lambda_i \psi + \varepsilon) \int_0^1 G \left(\frac{d\gamma_i}{dx} \right)^2 dx \end{aligned}$$

In this simple harmonic motion the maximum kinetic energy must equal the maximum potential energy. Thus the coefficients of $\cos^2(\lambda_i \psi + \varepsilon)$ and $\sin^2(\lambda_i \psi + \varepsilon)$ can be equated giving

$$\lambda_i^2 \Omega^2 = \frac{\int_0^1 EI (d^2 \gamma_i / dx^2)^2 dx + R^2 \int_0^1 G (d\gamma_i / dx)^2 dx}{R^4 \int_0^1 m \gamma_i^2 dx} \quad (7.18)$$

Then, if a mode shape $\gamma_i(x)$ is assumed which is reasonably near an exact mode, eqn 7.18 gives the corresponding frequency. The use of the Rayleigh method is usually confined to the calculation of the lowest frequency, since the corresponding mode shape will probably be comparatively simple and a good guess can usually be made.

Equation 7.18 has been used by Southwell³ to obtain a relationship to the non-

rotating frequency of the blade and its natural frequency under rotation. Equation 7.18 can be written

$$\omega_i^2 = \lambda_i^2 \Omega^2 = \omega_{nr}^2 + \frac{1}{R^2} \cdot \frac{\int_0^1 G(d\gamma_i/dx)^2 dx}{\int_0^1 m\gamma_i^2 dx} \quad (7.19)$$

where ω_{nr} is the non-rotating frequency of the blade.

Now

$$\begin{aligned} G &= \int_r^R m\Omega^2 r dr \\ &= \Omega^2 R^2 \int_x^1 mx dx \end{aligned}$$

therefore

$$\int_0^1 G \left(\frac{d\gamma_i}{dx} \right)^2 dx = \Omega^2 R^2 \int_0^1 \int_x^1 mx dx \left(\frac{d\gamma_i}{dx} \right)^2 dx$$

The integral on the right-hand side can be transformed to read

$$\Omega^2 R^2 \int_0^1 mx \int_0^x \left(\frac{d\gamma_i}{dx} \right)^2 dx dx$$

and eqn 7.19 can finally be expressed as

$$\omega_i^2 = \omega_{nr}^2 + \alpha_i \Omega^2 \quad (7.20)$$

where ω_{nr} is the natural frequency of the non-rotating blade and

$$\alpha_i = \frac{\int_0^1 mx \int_0^x (d\gamma_i/dx)^2 dx dx}{\int_0^1 m\gamma_i^2 dx} \quad (7.21)$$

Equation 7.20 is Southwell's formula.

To consider a specific case, let us use Southwell's formula to calculate the first bending frequency of a uniform blade hinged at the root ($k^2 = 0.004$) having the mode shape found earlier, namely

$$S_2(x) = -3.15x + 4.15x^3(10/3 - 10x/3 + x^2)$$

Substituting in eqn 7.21 with m constant we find

$$\alpha_2 = 8.241$$

α_1 being unity and corresponding to the rigid blade mode. The frequency of the non-rotating blade is obtained from the standard results⁴ for a pinned-free non-rotating uniform beam, which give

$$\begin{aligned}\omega_{nr}^2 &= \mu^4 EI/m \\ &= \mu^4 R^4 k^2 \Omega^2\end{aligned}$$

where μ is a constant given in the above reference.

If we take $\Omega = 25$ rad/s, then $k^2 \Omega^2 = 2.5$ and the value of $(\mu R)^4$ is 237.7. Hence

$$\omega_{nr}^2 = 594.3$$

and Southwell's formula for this case is therefore

$$\omega_2^2 = 594.3 + 8.241\Omega^2$$

The frequency at $\Omega = 25$ rad/s is 3.031Ω , which is higher than the value we calculated before but this is to be attributed to the fact that the assumed mode shape, which was based on only two functions, differs considerably from the more exact value, and the departure from the true shape is equivalent to the imposition of constraints which effectively increase the stiffness.

Southwell's formula is very useful for showing the effect of the rotor speed on the natural frequency of the blade. Strictly speaking, α_i is not constant because the mode shape would be expected to change slightly with Ω . However, assuming α_i constant, we see from eqn 7.20 that as the rotational speed becomes very large we have

$$\omega_i \rightarrow \Omega^{\sqrt{\alpha_i}}$$

The curves of eqn 7.20 for the various modes are often plotted in conjunction with a 'spoke' diagram, Fig. 7.7. One can see at a glance if there are any natural frequencies of the blade which coincide with a harmonic of the rotor speed, indicating the possibility of resonance.

(c) The Galerkin method

We start with the blade bending equation

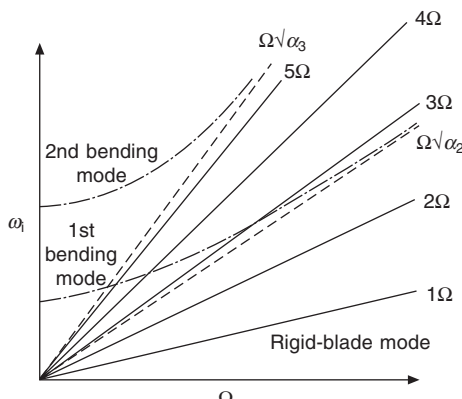


Fig. 7.7 'Spoke' diagram of bending frequencies

$$\frac{d^2}{dx^2} \left(EI \frac{d^2 S_n}{dx^2} \right) - R^2 \frac{d}{dx} \left(G \frac{dS_n}{dx} \right) - m\lambda_n^2 \Omega^2 R^4 S_n = 0 \quad (7.11)$$

and suppose as before, that

$$S_n(x) = A_1 \gamma_1(x) + A_2 \gamma_2(x) + \dots + A_i \gamma_i(x) + \dots + A_n \gamma_n(x) \quad (7.22)$$

We now substitute for $S_n(x)$ in eqn 7.11, multiply each term by γ_i , integrate from 0 to 1, and equate the result to zero. When i is made to take the successive values 1, 2, ..., n , we obtain n simultaneous equations which determine the coefficients A_i .

Duncan has shown⁵ that this process is equivalent to finding the error $\varepsilon(x)$ which results from substituting the approximate solution eqn 7.22 into eqn 7.11 and finding the stationary values of the integral

$$J \equiv \int_0^1 \varepsilon^2 dx$$

by satisfying the condition

$$\partial J / \partial A_i = 0$$

The Galerkin process can be regarded as a ‘least-squares’ fit of the assumed solution eqn 7.22 to the exact solution of eqn 7.11.

Duncan has also shown⁶ that the Galerkin and Rayleigh–Ritz methods, and therefore the Lagrange method, are all equivalent in linear problems, but notes that the Galerkin method can be extended to non-linear and non-conservative problems.

The application of the Galerkin method differs from the other two in that the integrals to be calculated are those derived from the terms in the differential equation 7.11, instead of those to be found in eqns 7.88 and 7.90. This means that in the Galerkin method the integrand of the elastic terms involves differential coefficients of the stiffness, and this may be a disadvantage if the stiffness undergoes sudden changes.

Figure 7.8 shows the rigid mode and the first bending mode when the first four functions

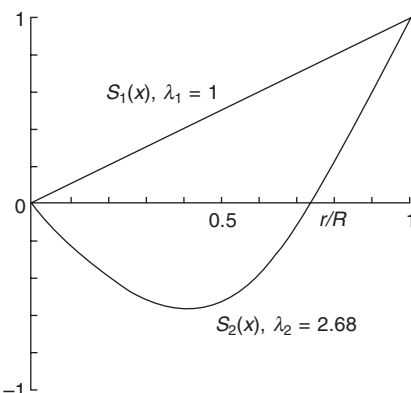


Fig. 7.8 Rigid and first bending modes and frequencies of a uniform beam

$$\gamma = x, \quad \gamma_i = (i+2)(i+3)x^{i+1}/6 - i(i+3)x^{i+2}/3 + i(i+1)x^{i+3}/6 \quad i = 2, 3, 4$$

are used to calculate the mode shapes and frequencies of a uniform beam.

7.2.2.2 Method of lumped parameters

We now consider two methods of analysis which are described as ‘lumped-parameter’ methods. In this technique the continuous blade is represented by a number of discrete segments, so that the partial differential equation of blade bending is replaced by a set of simultaneous ordinary differential equations.

The two methods to be described are

- (a) the Myklestad method,
- (b) the dynamic finite element method.

(a) The Myklestad method

This is a development of the Holzer⁷ method which was originally used for the calculation of torsional oscillations but was later extended and modified by Myklestad for the calculation of lateral beam vibrations.

Consider the deflected blade, Fig. 7.9 divided into a number of concentrated masses between which the elastic properties remain unaltered. The n th element and the forces acting on it are shown in Fig. 7.10.

With reference to Figs 7.11 and 7.12 we also define the following elastic coefficients in relation to the application of a unit force and of a unit moment.

Assuming the elastic properties are constant over the element, the four coefficients can be expressed as

$$\begin{aligned} u_{Fn} &= l_n^3/6(EI)_n & v_{Fn} &= l_n^2/2(EI)_n \\ u_{Mn} &= l_n^2/2(EI)_n & v_{Mn} &= l_n/(EI)_n \end{aligned}$$

We now imagine the blade to be forced to vibrate with harmonic motion of frequency ω . This adds an inertia force $m_{n+1}\omega^2 Z_{n+1}$ to the element, and the equilibrium of the element leads to the following relations:

$$G_{n+1} = G_n + m_{n+1}\Omega^2 r_{n+1} \quad (7.23)$$

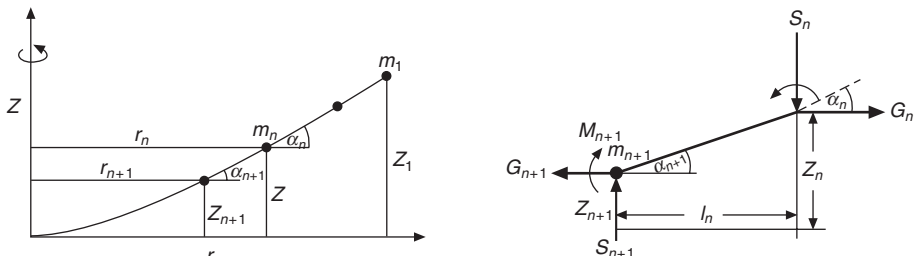


Fig. 7.9 Distributed-mass representation of helicopter blade (Myklestad)

Fig. 7.10 Forces on blade element (Myklestad method)

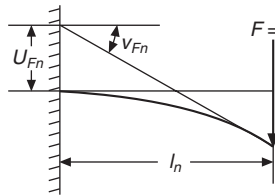


Fig. 7.11 Definition of unit load coefficients

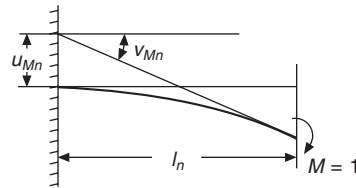


Fig. 7.12 Definition of unit moment coefficients

$$S_{n+1} = S_n - m_{n+1}\omega^2 Z_{n+1} \quad (7.24)$$

$$M_{n+1} = M_n - S_n l_n + G_n (Z_n - Z_{n+1}) \quad (7.25)$$

$$\alpha_{n+1} = \alpha_n (1 + G_n v_{Fn}) - S_n v_{Fn} + M_n v_{Mn} \quad (7.26)$$

$$Z_{n+1} = Z_n - (l_n + u_{Fn} G_n) \alpha_n + u_{Fn} S_n - u_{Mn} M_n \quad (7.27)$$

We obtain at once from eqn 7.23

$$G_n = \sum_{i=1}^n m_i \Omega^2 r_i \quad (7.28)$$

and eliminating $Z_n - Z_{n+1}$ between eqns 7.25 and 7.27 gives

$$M_{n+1} = M_n (1 + u_{Mn} G_n) - S_n (l_n + u_{Fn} G_n) + G_n (l_n + u_{Fn} G_n) \quad (7.29)$$

For a given value of ω , these recurrence relations enable us to calculate S , M , α and Z at any point along the blade in terms of the corresponding values at one end. Thus, for example, the boundary conditions at the blade tip are

$$S_1 = m_1 \omega^2; \quad M_1 = 0; \quad \alpha_1 = \alpha_{10}, \text{ say}; \quad Z_1 = 1$$

It may seem that the first boundary condition contradicts the requirement of zero shear force at the tip, but it must be remembered that the mass of the last element is concentrated at the tip so that it really represents an average condition for the element. The last two boundary conditions are arbitrary and merely define the scale of the blade displacement. It can easily be seen that, at any given station, S , M , α , and Z must be of the form

$$S_n = c_n + d_n \alpha_{10} \quad (7.30)$$

$$M_n = e_n + f_n \alpha_{10} \quad (7.31)$$

$$\alpha_n = g_n + h_n \alpha_{10} \quad (7.32)$$

$$Z_n = j_n + k_n \alpha_{10} \quad (7.33)$$

where c_n , d_n , ..., etc. are numbers* which depend on the blade station in question.

* Recurrence relations expressing these numbers in terms of the original constants and tabulation methods for the calculation procedure are given in detail in reference 7 and need not be given here.

Now at the blade root the displacement is zero. Thus, if the suffix r denotes the root,

$$Z_r = j_r + k_r \alpha_{10}$$

or $\alpha_{10} = -j_r/k_r$

The remaining root boundary condition to be satisfied is either

$$M_r = 0, \quad \text{for the hinged blade}$$

or

$$\alpha_r = 0, \quad (\text{or, possibly, a known non-zero value}) \text{ for the hingeless blade.}$$

For the first case, we have from eqn 7.31, after substituting for α_{10} ,

$$M_r = (e_r k_r - j_r f_r)/k_r = 0$$

Now the term in the bracket is a function of the assumed value of the frequency ω . Thus, if a range of values of ω is taken, a natural frequency occurs every time the function becomes zero, Fig. 7.13. For such a value of ω , the mode shape, defined by the values of Z_n , can be determined from eqn 7.33.

Similarly, for the hingeless blade, we have from eqn 7.32

$$\alpha_r = (g_r k_r - h_r j_r)/k_r = 0$$

and, again, we seek the values of ω which make the function in the bracket zero.

Now, in the methods described earlier, if it is required to calculate, say, the fifth mode and frequency, it may be necessary to take at least ten functions and solve the resulting ten simultaneous equations to obtain reasonable accuracy for the fifth and lower modes. In the Myklestad method, however, each mode can be calculated independently of the others, although a certain amount of ‘searching’ may be necessary to locate the appropriate zero.

The Myklestad method described above refers only to pure flapwise bending. An extension of the method has been given by Isakson and Eisley⁸ which includes the effect of coupling between the bending and torsional modes of vibration. Their analysis, however, is far too lengthy to be included here, and the reader is referred to the original paper.

(b) The dynamic finite element method⁹

As in the Myklestad method described in the previous section, the blade is divided into a number of elements, not necessarily of equal length. In this case, however, the

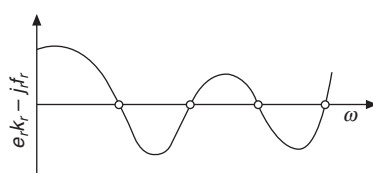


Fig. 7.13 Variation of boundary function with frequency

mass of an element is not concentrated at its ends but is imagined to be distributed uniformly along its length. The system of forces and moments acting along the element is as shown in Fig. 7.14, and its equilibrium in harmonic motion leads to the following equations

$$G_{n+1} = G_n + \int_{r_{n+1}}^{r_n} \Omega^2 rm dr = G_n + \frac{1}{2} m\Omega^2 (r_n^2 - r_{n+1}^2) \quad (7.34)$$

$$S_{n+1} = S_n - \int_{r_{n+1}}^{r_n} \omega^2 Zm dr = S_n - \frac{1}{2} m\omega^2 l_n (Z_n + Z_{n+1}) \quad (7.35)$$

$$\begin{aligned} M_{n+1} &= M_n - G_n (Z_n - Z_{n+1}) - S_n l_n + \int_{r_{n+1}}^{r_n} (r - r_{n+1}) \omega^2 m Z dr \\ &\quad - \int_{r_{n+1}}^{r_n} (Z_n - Z_{n+1}) \Omega^2 rm dr \\ &= M_n - G_n (Z_n - Z_{n+1}) - S_n l_n + \omega^2 l_n^2 m (2Z_n + Z_{n+1})/6 \\ &\quad - \Omega^2 l_n m (2r_n + r_{n+1})(Z_n - Z_{n+1})/6 \end{aligned} \quad (7.36)$$

These three equations are analogous to eqns 7.23, 7.24, and 7.25 of Myklestad's method. Inspection of the above equations shows that the bending moments $M_0, M_1, \dots, M_n, \dots$ along the blade can be expressed in matrix form as

$$M = \omega^2 aZ + \Omega^2 bZ \quad (7.37)$$

where a and b are square matrices, and functions of r and m , Z is the column vector of the element displacements, and M is the column vector of bending moments.

The deformation of the blade represented by Z may be split into two components

$$Z = Z_E + Z_R$$

where Z_E is the elastic deformation of blade bending and Z_R is the rigid-body rotation about the flapping hinge. If there is no flapping hinge, $Z_R = 0$.

To obtain a relationship expressing the blade deformation as a function of the applied moment distribution, we use the unit load method¹⁰. This states that, if M_1 is the bending moment distribution due to the application of a *unit* load at a point at which we wish to calculate the deflection, and if M is the actual moment distribution then the required deflection δ is given by

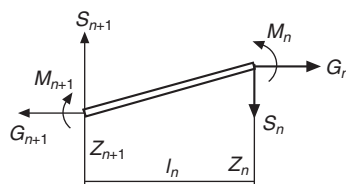


Fig. 7.14 Forces on blade element

$$\delta = \int_0^R (MM_1/EI) dr$$

Let us consider the contribution to this deflection due to *one* of the blade elements. Let M_A and M_B be the moments at the ends of the element due to the applied loading, and let M_{A1} and M_{B1} be the moments due to the unit load, Fig. 7.15, at which it is required to know the deflection. If we suppose that these bending moments vary linearly across the element, the contribution δ_{AB} to the deflection can easily be calculated and expressed conveniently in matrix form as

$$\begin{aligned} \delta_{AB} &= \int_{AB} (MM_1/EI) dr \\ &= [M_{A1}, M_{B1}] \begin{bmatrix} \frac{l}{3EI} & \frac{l}{6EI} \\ \frac{l}{6EI} & \frac{l}{3EI} \end{bmatrix} \begin{bmatrix} M_A \\ M_B \end{bmatrix} \end{aligned}$$

where l is the length of the element.

If a number of successive elements is now considered, with the corresponding moment distributions $M_{A1}, M_{B1}, \dots, M_{N1}, \dots$ and $M_A, M_B, \dots, M_N, \dots$, the deflection due to all these elements is

$$\delta = [M_{A1}, M_{B1}; \dots, M_{N1}, \dots]$$

$$\cdot \begin{bmatrix} \frac{l}{3EI} & \frac{l}{6EI} & 0 & 0 & \cdots & 0 \\ \frac{l}{6EI} & \frac{l}{3EI} + \frac{l}{3EI} & \frac{l}{6EI} & 0 & \cdots & 0 \\ 0 & \frac{l}{6EI} & \frac{l}{3EI} + \frac{l}{3EI} & \frac{l}{6EI} & \cdots & 0 \\ \cdots & \cdots & \cdots & \cdots & \cdots & \cdots \\ 0 & 0 & 0 & & & \vdots \end{bmatrix} \begin{bmatrix} M_A \\ M_B \\ \vdots \\ M_N \\ \vdots \end{bmatrix} \quad (7.38)$$

To define the deformation of the complete blade, we need to know the deflections

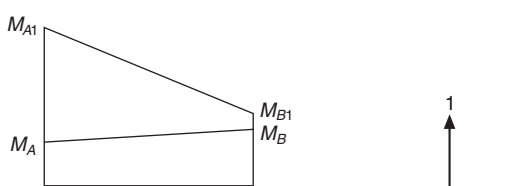


Fig. 7.15 Moment due to application of unit load

at the ends of each of the elements. This will require repeating the above calculations using the bending moment distributions corresponding to unit loads applied at each station. When this is done, the row matrix $[M_{A1}, M_{B1}, \dots]$ then becomes a square matrix M_1 , say, the columns of which give the bending moment distributions due to each of the applied unit loads. The centre matrix of eqn 7.38 is called a *flexibility* matrix and will be denoted by f . The total set of deflections is then given by

$$Z_E = M_1^T f M \quad (7.39)$$

where Z_E is the matrix of the values of δ . Eliminating M between eqns 7.37 and 7.39 gives

$$Z_E = \omega^2 a^*(Z_E + Z_R) + \Omega^2 b^*(Z_E + Z_R) \quad (7.40)$$

where a^* and b^* are matrices resulting from the addition and multiplication of previously defined matrices. Rearranging eqn 7.40 gives

$$(I - \Omega^2 b^*)Z_E = \omega^2 a^*(Z_E + Z_R) + \Omega^2 b^* Z_R$$

giving $Z_E = \omega^2 [I - \Omega^2 b^*]^{-1} a^*(Z_E + Z_R) + \Omega^2 [I - \Omega^2 b^*]^{-1} b^* Z_R$

or $Z_E = \omega^2 c(Z_E + Z_R) + \Omega^2 d Z_R \quad (7.41)$

where c and d are square matrices.

The hingeless rotor

If no flapping hinge is present, $Z_R = 0$, giving

$$Z_E = \omega^2 c Z_E$$

or $(c - I/\omega^2)Z_E = 0 \quad (7.42)$

The eigenvalues and eigenvectors of eqn 7.42 give the required frequencies and mode shapes.

The hinged rotor

When there is a flapping hinge, the moment at the hinge line must be zero and from eqn 7.37 we have

$$M_h = \omega^2 a_h(Z_E + Z_R) + \Omega^2 b_h(Z_E + Z_R) = 0 \quad (7.43)$$

the suffix h indicating that the row of the matrix corresponding to the hinge line is used. Substituting the value of Z_E given by eqn 7.41 into the second bracket of eqn 7.43 gives

$$\omega^2 a_h(Z_E + Z_R) + \Omega^2 b_h[\omega^2 c(Z_E + Z_R) + d Z_R + Z_R] = 0$$

or, on rearranging,

$$\omega^2(a_h + \Omega^2 b_h c)(Z_E + Z_R) + \Omega^2 b_h(I + d)Z_R = 0 \quad (7.44)$$

Now the unknowns in Z_R are linearly related through an unknown rotation α about the flapping hinge, i.e.,

$$Z_R = e\alpha \quad (7.45)$$

where e is a column matrix giving the distances of the ends of the blade elements from the flapping hinge. Then substituting eqn 7.45 into eqn 7.44 gives

$$\Omega^2 b_h(I + d)e\alpha = -\omega^2(a_h + \Omega^2 b_h c)(Z_E + Z_R)$$

or

$$\alpha = -\omega^2[\Omega^2 b_h(I + d)e]^{-1}(a_h + \Omega^2 b_h c)(Z_E + Z_R)$$

so that eqn 7.45 can be written

$$Z_R = -\omega^2 e[\Omega^2 b_h(I + d)e]^{-1}(a_h + \Omega^2 b_h c)(Z_E + Z_R) \quad (7.46)$$

Substituting for Z_R in eqn 7.41 gives

$$Z_E = \omega^2[c - de\{\Omega^2 b_h(I + d)e\}^{-1}(a_h + \Omega^2 b_h c)](Z_E + Z_R) \quad (7.47)$$

and on adding eqns 7.46 and 7.47 we get

$$(Z_E + Z_R) = \omega^2[c - (I + d)e\{\Omega^2 b_h(I + d)\}^{-1}(a_h + \Omega^2 b_h c)](Z_E + Z_R) \quad (7.48)$$

Defining c^* to be the matrix in the square brackets, we have

$$Z_E + Z_R = \omega^2 c^*(Z_E + Z_R)$$

or

$$[c^* - I/\omega^2](Z_E + Z_R) = 0 \quad (7.49)$$

The eigen values and eigen vectors of c^* yield the required frequencies and mode shapes of the hinged blade.

The above method need not be confined to straight elements. For a given number of elements, the accuracy can be greatly improved by taking curved elements – for example, a cubic variation – the curvature being determined by the deformation of neighbouring elements. The relationships eqns 7.37 and 7.39 have to be modified accordingly, but the net result is a considerable increase of accuracy for only a slight increase of computer time.

7.2.2 Lagwise bending

When considering motion of the blade in the lagging plane*, i.e. in the plane of rotation, we have to note that the centrifugal force on a blade element is directed radially outwards from the hub and therefore, unlike the flapping case, the direction, as well as the magnitude of the force, varies along the blade. Consider the forces, inertial and aerodynamic, acting on a given element of the blade and their moment about another point P of the blade, Fig. 7.16. If r_1 is the radial distance of the element and r the radial distance of the point P from the hub, the moment of all the forces about P is

*Lagging and chordwise motion are the same only if the blade chord is parallel to the plane of rotation, i.e. when the pitch angle is zero.

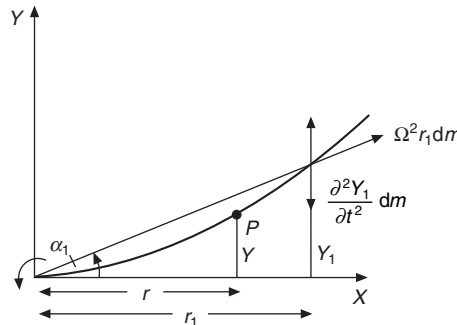


Fig. 7.16 Lagwise forces acting on blade

$$\begin{aligned}
 M = EI \frac{\partial^2 Y}{\partial r^2} &= \int_r^R m \Omega^2 r_1 (r_1 - r) \sin \alpha_1 dr_1 - \int_r^R m \Omega^2 r_1 (Y_1 - Y) \cos \alpha_1 dr_1 \\
 &\quad - \int_r^R m \frac{\partial^2 Y_1}{\partial t^2} (r_1 - r) dr_1
 \end{aligned} \tag{7.50}$$

Differentiating with respect to r we have, after cancelling certain terms,

$$\begin{aligned}
 \frac{\partial M}{\partial r} &= - \int_r^R m \Omega^2 Y_1 dr_1 + \frac{\partial Y}{\partial r} \int_r^R m \Omega^2 r_1 dr_1 + \int_r^R m \frac{\partial^2 Y_1}{\partial t^2} dr_1 \\
 &= - \int_r^R m \Omega^2 Y_1 dr_1 + \frac{\partial Y}{\partial r} G(r) + \int_r^R m \frac{\partial^2 Y_1}{\partial t^2} dr_1
 \end{aligned}$$

Differentiating again gives

$$\frac{\partial^2 M}{\partial r^2} = \frac{\partial^2}{\partial r^2} \left[EI \frac{\partial^2 Y}{\partial r^2} \right] = \frac{\partial}{\partial r} \left[G \frac{\partial Y}{\partial r} \right] - m \left(\frac{\partial^2 Y}{\partial r^2} - \Omega^2 Y \right)$$

or

$$\frac{\partial^2}{\partial r^2} \left[EI \frac{\partial^2 Y}{\partial r^2} \right] - \frac{\partial}{\partial r} \left[G \frac{\partial Y}{\partial r} \right] + m \left(\frac{\partial^2 Y}{\partial r^2} - \Omega^2 Y \right) = 0 \tag{7.51}$$

where it is understood that the value of EI refers to lagwise bending.

To discuss the free lagging motion of the blade, assume a solution

$$Y = RT(x)\chi(t)$$

where $T(x)$ is a function of x alone and $\chi(t)$ is a function of t alone. By the same argument as that used for the flapping equation, we arrive at the mode shape equation

$$\frac{d^2}{dx^2} \left[EI \frac{dT}{dx^2} \right] - R^2 \frac{d}{dx} \left(G \frac{dT}{dx} \right) - m(\nu^2 + 1)\Omega^2 R^4 T = 0 \tag{7.52}$$

and the frequency equation

$$d^2\chi/d\psi^2 + v^2\chi = 0 \quad (7.53)$$

The boundary conditions relating to eqn 7.52 are the same as those of flapping motion:

(a) *Hinged blade (including lag hinge offset)*

$$\begin{array}{lll} \text{At } x = e, & y = 0, & d^2y/dx^2 = 0 \\ \text{At } x = 1, & d^2y/dx^2 = 0, & d^3y/dx^3 = 0 \end{array} \quad (\text{where } y = Y/R)$$

(b) *Hingeless blade*

$$\begin{array}{lll} \text{At } x = 0, & y = 0, & dy/dx = 0 \\ \text{At } x = 1, & d^2y/dx^2 = 0, & d^3y/dx^3 = 0 \end{array}$$

The lagging mode shape equation, eqn 7.52, is identical in form to the flapping equation except that the frequency ratio v appears as $v^2 + 1$ in the mode equation. This is explained physically by the fact that the centrifugal force field in the lagging plane is radial instead of parallel as in the flapping plane, and the relationship between the mode shape and the frequency is different.

The only exact solution of eqn 7.52 is $T(x) = x$ for $e = 0$, which gives $v^2 + 1 = 1$ or $v = 0$. Thus, the first mode shape is a straight line from the hub associated with zero lagging frequency. When the lag hinge offset is not zero there is no exact solution to the lag equation but we would expect a close approximation to be a straight line moving about the hinge point, i.e. like a rigid blade, with a frequency of approximately $\sqrt{(3/2e)\Omega}$, e being the non-dimensional lag hinge offset. As we mentioned in Chapter 1, a typical value of e is about 0.05, in which case $v_1 = 0.274$.

The calculation of the lag mode shapes and frequencies generally can be achieved by the methods described for the flapping equation.

For hingeless blades the first mode shape is determined largely by the stiffness near the root; in fact, the structural element at the root is designed to give suitable flap and lag frequencies. Since the stiffening effect of the centrifugal field is much less than in the flapping motion, the first lag frequency is much more sensitive to changes of root stiffness. The lagging and flapping stiffnesses are ‘matched’ in such a way as to minimize torsional moments when lagging and flapping motion occurs. This point will be discussed in more detail in Chapter 9 on aeroelastic coupling, but the typical first mode frequencies arising from such a choice of stiffnesses are usually in the region of 0.55 Ω to 0.7 Ω , i.e. much higher than for the hinged blade.

When considering the higher modes, it will be appreciated that the lag stiffness will be much greater than the flapping stiffness; typically, over most of the blade the lagwise stiffness is about ten times greater. Calculations show that the shapes of the lagging modes have the same general appearance as those of the flapping motion but, whereas the first lag frequency is usually much smaller than the first flap frequency, the reverse is true for all the corresponding higher modes since the curvature of the blades invokes the much greater stiffness.

7.2.3 Torsional deflections

Consider a portion of the blade of span dr under the action of torsional moments. If C is the torsional moment of inertia per unit length of span, the inertia moment due to angular acceleration $\ddot{\theta}$ is $-C\ddot{\theta} dr$ and that due to the 'propeller moment' section 1.10, is $-C\Omega^2\theta dr$.

Then the elementary moment dL tending to twist the blade in the nose-up sense is

$$dL = -C\ddot{\theta} dr - C\Omega^2\theta dr \quad (7.54)$$

Now consider the torques acting on the sides of the element and let us define the positive value of the torque when its sense agrees with the positive direction of r . If W is the torque on the element, Fig. 7.17, the value is $-W$ on the left-hand side and $W + (\partial W/\partial r) dr$ on the right-hand side. For equilibrium we must have

$$-W + \frac{\partial L}{\partial r} dr + W + \frac{\partial W}{\partial r} dr = 0$$

or

$$\partial W/\partial r + \partial L/\partial r = 0 \quad (7.55)$$

Now the relationship between the angle of twist θ and the torque on the element is

$$W = E_s J \frac{\partial \theta}{\partial r}$$

where $E_s J$ is the torsional rigidity of the element, E_s being the modulus of rigidity or shear modulus and J being the polar second moment of area.

Hence, from eqns 7.54 and 7.55, the blade torsion equation is

$$\frac{\partial}{\partial r} \left(E_s J \frac{\partial \theta}{\partial r} \right) - C\ddot{\theta} - C\Omega^2\theta = 0 \quad (7.56)$$

Assuming solutions of the form

$$\theta = Q(x)\zeta(t)$$

we obtain the mode-shape equation

$$\frac{d}{dr} \left(E_s J \frac{dQ}{dr} \right) + C(\omega_\theta^2 - \Omega^2)Q = 0 \quad (7.57)$$

and

$$d^2\zeta/dt^2 + \omega_\theta^2\zeta = 0$$

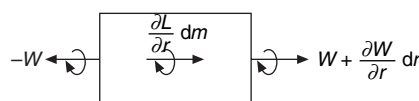


Fig. 7.17 Torsional moments acting on element

where ω_θ is a natural frequency of the free motion of the rotating blade.

Now the pitch control usually has a considerable degree of flexibility, so that the boundary condition to be satisfied at the root is given by

$$[E_s J \frac{d\theta}{dr}] = k_\theta \theta_0 \quad (7.58)$$

where θ_0 is the change of blade pitch at the feathering hinge and k_θ is the stiffness of the control system. Actually, the flexibility of the control system may be such as to allow as much as 70 to 80 per cent of the deflection at the tip to occur at the feathering hinge. The boundary condition at the tip is

$$\frac{d\theta}{dr} = 0 \quad \text{at} \quad r = R \quad (7.59)$$

which expresses the fact that the moment vanishes at the tip.

Consideration of eqn 7.57 shows that, since the torsional stiffness $E_s J$ is unaffected by rotor speed, the torsional *mode shapes* are also independent of the rotor speed, i.e. the mode shapes of a blade are the same whether it is rotating or not. It therefore follows that

$$\omega_\theta^2 - \Omega^2 = \text{constant}$$

When $\Omega = 0$, ω_θ is equal to the non-rotating torsional frequency, ω_0 say; hence

$$\omega_\theta^2 = \omega_0^2 + \Omega^2$$

i.e. the square of the torsional frequency is simply the sum of the squares of the non-rotating frequency and of the rotor speed.

Unlike the mode shape equations of flapping and lagging, the simpler form of the torsional equation, eqn 7.57, enables some exact solutions to be obtained.

Consider the case of constant torsional stiffness (except for flexibility at the root) and zero rotor rotational speed. Equation 7.57 can be written

$$\frac{d^2 Q}{dx^2} + \alpha^2 Q = 0 \quad (7.60)$$

where

$$\alpha^2 = \omega_0^2 CR^2 / E_s J \quad (7.61)$$

The solution of eqn 7.60 is

$$Q = A \cos \alpha x + B \sin \alpha x \quad (7.62)$$

The boundary conditions, eqns 7.58 and 7.59, give

$$B\alpha = (Rk_\theta / E_s J)A \quad (7.63)$$

and

$$\tan \alpha = B/A = Rk_\theta / E_s J \alpha \quad (7.64)$$

or

$$\alpha \tan \alpha = Rk_\theta / E_s J \quad (7.65)$$

Solutions of eqn 7.64 in conjunction with eqn 7.61 give the frequencies of the non-rotating blade for given values of k_θ and $E_s J$.

The displacement at the blade tip is given by

$$\begin{aligned} Q(1) &= A \cos \alpha + B \sin \alpha \\ &= A[\cos \alpha + (B/A) \sin \alpha] \\ &= A \sec \alpha, \text{ from eqn 7.64} \end{aligned}$$

The displacement at the root due to control flexibility is

$$Q(0) = A$$

Thus the ratio of the root deflection to that at the tip is

$$Q(0)/Q(1) = \cos \alpha \quad (7.66)$$

Let us suppose that in the first mode of motion the control stiffness is such that the root deflection is half that at the tip. Then, for this case, we see from eqn 7.66 that $\cos \alpha = \frac{1}{2}$ or $\alpha = \pi/3$. Then, if we take $E_s J/CR = 4000$ as a typical value, we have from eqn 7.61 that

$$\omega_0 = 10.5 \text{ Hz}$$

which is about two and a half times the typical rotor frequency. Thus, at normal rotor speed (4 Hz), the torsional frequency of our rotor blade is about 3.35Ω .

The choice of α for the first mode fixes the value of $Rk_\theta/E_s J$ in eqn 7.65, and the values of α for the higher modes are given by the solutions of

$$\alpha \tan \alpha = (\pi/3) \tan (\pi/3) = \pi/\sqrt{3} = 1.82$$

The next two solutions are easily found to be $\alpha = 3.62$ and 6.54 , giving $\omega_0 = 36.2$ and 65.4 Hz respectively. The corresponding mode shape outboard of the feathering hinge and normalised with respect to the tip deflection is

$$\begin{aligned} Q(x) &= A[\cos \alpha x + (B/A) \sin \alpha x] \\ &= \cos \alpha \cos \alpha x + \sin \alpha \sin \alpha x \\ &= \cos [\alpha(1 - x)] \end{aligned} \quad (7.67)$$

The mode shapes are found by giving α its appropriate values. The first shapes are shown in Fig. 7.18.

It is usual that the first mode frequency is several times the rotor frequency and may be as high as 6Ω or even more.

7.2.4 Intermodal coupling

In the previous sections we have examined the flapping and lagging and torsional mode shapes and frequencies on the assumptions that the motions are independent of one another. In general, however, a certain amount of elastic and inertial coupling exists when there is built-in twist and if the elastic and mass axes do not coincide. The complete coupled equations have been given by Houbolt and Brooks¹¹ and, more recently, by Sobey¹².

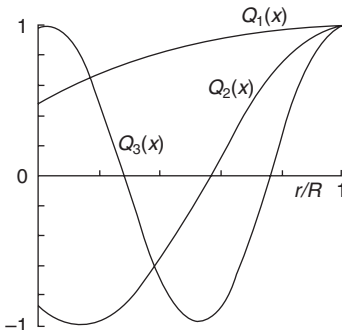


Fig. 7.18 Torsional mode shapes of a uniform blade

Aerodynamic and inertia coupling of the first-mode motions relating to classical blade flutter will be considered in Chapter 9.

To give an indication of how the torsional motion of the blade modifies the flapping equation, consider a blade with zero built-in twist. Referring to Figs 7.19 and 7.20 we see that twist introduces the following flapping moments and shears.

- (i) A component $Ge_A \sin \theta$ of the moment Ge_A , Ge_A being the moment of the blade tension about the elastic axis when the latter is displaced from the section centroid.
- (ii) The moment of the centrifugal force due to the displacement of the centre of gravity of the blade section relative to the elastic axis. The moment is easily

$$\text{seen to be equal to } \int_r^R \Omega^2 m r_l (e_1 \theta_1) dr_l.$$

- (iii) The change of shear force dS due to the inertia loading $-m e \ddot{\theta} dx$ resulting from the twisting motion.

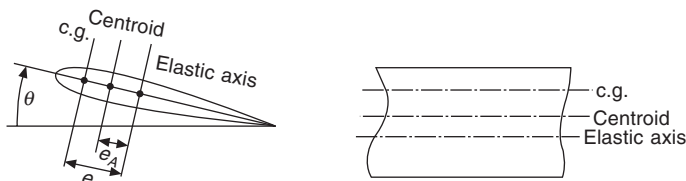


Fig. 7.19 Blade section geometry

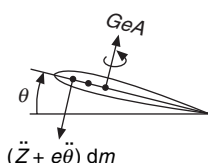


Fig. 7.20 Blade section forces and moments

Then, if M' is the sum of the moments due to the effects of twist, we have, for small θ ,

$$\frac{\partial^2 M'}{\partial r^2} = \frac{\partial S}{\partial r} = \frac{\partial^2}{\partial r^2} (Ge_A \theta) + \frac{\partial}{\partial r} (\Omega^2 rme \theta) - me \ddot{\theta}$$

Adding these terms to the uncoupled flap-bending equation, eqn 7.6 we get

$$\frac{\partial^2}{\partial r^2} \left(EI \frac{\partial^2 Z}{\partial r^2} - Ge_A \theta \right) - \frac{\partial}{\partial r} \left(G \frac{\partial Z}{\partial r} \right) - \frac{\partial}{\partial r} (\Omega^2 rme \theta) + m(\ddot{Z} + e \ddot{\theta}) = 0$$

This agrees with the equation of flapwise bending given by Houbolt and Brooks for the special case of zero built-in twist. By similar arguments we could derive the coupled lag and torsional equations of motion.

When the blade also has built-in twist, there is elastic coupling between the flapping and lagging motion. The full equations are given by Houbolt and Brooks, but a simple model used by Ormiston and Hodges¹³ to investigate flap-Jag instability will serve here to give a simple illustration of the effects of elastic coupling on the flapping and lagging motion. The flexibility of the blade is represented in the diagram of Fig. 7.21. Part of the flexibility is contained in the hub springs, which have flapping and lagging stiffnesses of K_{β_H} and K_{ξ_H} respectively. The remaining part of the blade flexibility lies just outboard of the feathering hinge so that the associated spring system, with stiffnesses K_{β_B} and K_{ξ_B} , rotates when blade pitch is applied.

It is clear that, when pitch is applied (i.e. $\theta \neq 0$), flapping motion, i.e displacements of the blade perpendicular to the plane of rotation, causes moments in the plane of rotation, and vice versa. It is not difficult to show that for flap and lag displacements β and ξ the elastic moments M_e and L_e in the flap and lag planes are given by

$$M_e = -\frac{\beta}{\Delta} [\kappa_\beta + \rho_e(\kappa_\xi - \kappa_\beta) \sin^2 \theta] - \frac{\xi \rho_e}{2\Delta} (\kappa_\xi - \kappa_\beta) \sin 2\theta \quad (7.68)$$

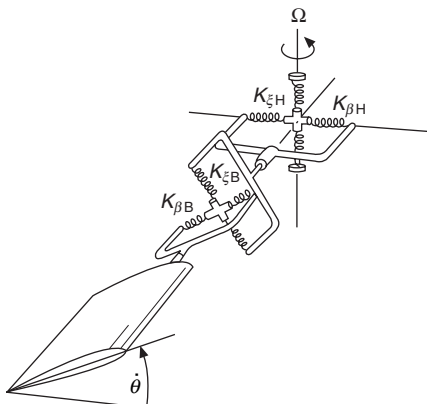


Fig. 7.21 Representation of stiffness coupling

$$L_e = -\frac{\xi}{\Delta} [\kappa_\xi - \rho_e (\kappa_\xi - \kappa_\beta) \sin^2 \theta] - \frac{\beta \rho_e}{2\Delta} (\kappa_\xi - \kappa_\beta) \sin 2\theta \quad (7.69)$$

where

$$\Delta = 1 + \rho_e (1 - \rho_e) \frac{\kappa_\xi + \kappa_\beta}{\kappa_\xi \kappa_\beta} \sin^2 \theta \quad (7.70)$$

$$\kappa_\beta = \frac{\kappa_{\beta_B} \kappa_{\beta_H}}{(\kappa_{\beta_B} + \kappa_{\beta_H})}, \quad \kappa_\xi = \frac{\kappa_{\beta_B} \kappa_{\xi_H}}{(\kappa_{\xi_B} + \kappa_{\xi_H})}$$

and ρ_e is the degree of elastic coupling defined by

$$\rho_e = \kappa_\beta / \kappa_{\beta_B} = \kappa_\xi / \kappa_{\xi_B} \quad (7.71)$$

When $\rho_e = 0$, the hinge system is contained entirely at the hub, i.e. the outboard springs are infinitely stiff, and no elastic coupling is possible. When $\rho_e = 1$, all the blade flexibility exists outboard of the feathering hinge and there is full elastic coupling.

To illustrate the effect of elastic coupling using the above model, let us consider a fully coupled hingeless blade ($\rho_e = 1$) with a given flapping stiffness but whose lag stiffness is to be varied. Let the collective-pitch angle be 15° .

Suppose that the uncoupled flapping and lagging frequencies ω_β and ω_ξ are given by the following Southwell formulae:

$$\omega_\beta^2 = (\kappa_\beta / I) \beta + 1.12 \Omega^2 \quad (7.72)$$

$$\omega_\xi^2 = (\kappa_\xi / I) \xi + 0.23 \Omega^2 \quad (7.73)$$

where I is the (same) moment of inertia in flapping and lagging and Ω is the rotor angular velocity. Let κ_β / I be fixed and equal to $0.13 \Omega^2$. If, for simplicity, we suppose that the coning angle is zero, so that the Coriolis moments can be ignored, and also that the change of lag stiffness κ_ξ does not alter the constant in eqn 7.73 then, using eqns 7.68 and 7.69, the flapping and lagging equations are

$$\frac{d^2 \beta}{d\psi^2} + \left(1.185 + 0.067 \frac{\kappa_\xi}{I\Omega^2} \right) \beta + \frac{1}{4} \left(\frac{\kappa_\xi}{I\Omega^2} - 0.13 \right) \xi = 0 \quad (7.74)$$

and

$$\frac{d^2 \xi}{d\psi^2} + \left(0.239 + 0.933 \frac{\kappa_\xi}{I\Omega^2} \right) \xi + \frac{1}{4} \left(\frac{\kappa_\xi}{I\Omega^2} - 0.13 \right) \beta = 0 \quad (7.75)$$

Substituting the assumed solutions $\beta = \beta_0 e^{\lambda \psi}$ and $\xi = \xi_0 e^{\lambda \psi}$ leads to the characteristic equation

$$\begin{aligned} & \left[\lambda^2 + \left(1.185 + 0.067 \frac{\kappa_\xi}{I\Omega^2} \right) \right] \left[\lambda^2 + \left(0.239 + 0.933 \frac{\kappa_\xi}{I\Omega^2} \right) \right] \\ & - \frac{1}{16} \left(\frac{\kappa_\xi}{I\Omega^2} - 0.13 \right)^2 = 0 \end{aligned} \quad (7.76)$$

Solution of this equation for a range of lag stiffnesses κ_ξ gives the flap and lag frequencies shown in Fig. 7.22. The figure shows an interesting phenomenon. When the blades are elastically uncoupled, the curves of flap and lag frequencies cross over as the lag stiffness is increased. However, when elastic coupling exists, the frequencies lie close to the uncoupled values when the frequencies are fairly widely separated, but as the cross-over point is approached the curves begin to diverge from one another and each becomes asymptotic to the frequency curve of the other mode.

It is instructive to examine the flap-lag ratio of each mode as the lag stiffness is varied. The flap-lag ratio can be obtained from either of eqns 7.74 and 7.75. Thus, from eqn 7.74, after substituting $\beta = \beta_0 e^{\lambda\psi}$ and $\xi = \xi_0 e^{\lambda\psi}$, we get

$$\frac{\beta_0}{\xi_0} = \frac{(\kappa_\xi/I\Omega^2 - 0.13)^2}{16[\lambda^2 + (1.185 + 0.067 \kappa_\xi/I\Omega^2)]}$$

Inserting values of λ corresponding to the lower curve shows that β_0/ξ_0 is very small for low values of κ_ξ , indicating that the motion consists almost entirely of lag, agreeing with the corresponding uncoupled motion, but that for large values of κ_ξ we find that β_0/ξ_0 is also large, indicating that the motion now consists mainly of flapping, in agreement with the uncoupled frequency curve which lies close to it. Thus, along either of the frequency curves of coupled motion the mode changes its character in the region of the uncoupled cross-over point.

A similar situation arises when flap and lag stiffness are kept constant but the frequencies change with rotor speed such that there is an intersection of a flap and a lag mode. For example, the second lag frequency might intersect the frequency curve of the fourth flap mode, as indicated in Fig. 7.23. Again, we would find that the lagging motion at low speeds would become mainly flapping motion after passing the uncoupled cross-over point, and vice versa.

It appears, therefore, that the coupling is important in the region where the frequency curves of two uncoupled modes would intersect one another.

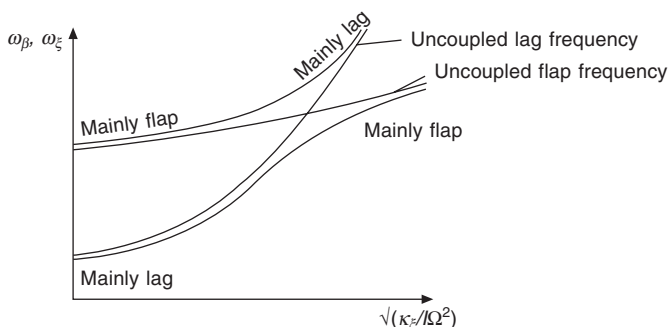


Fig. 7.22 Effect of stiffness coupling on flap and lag frequencies

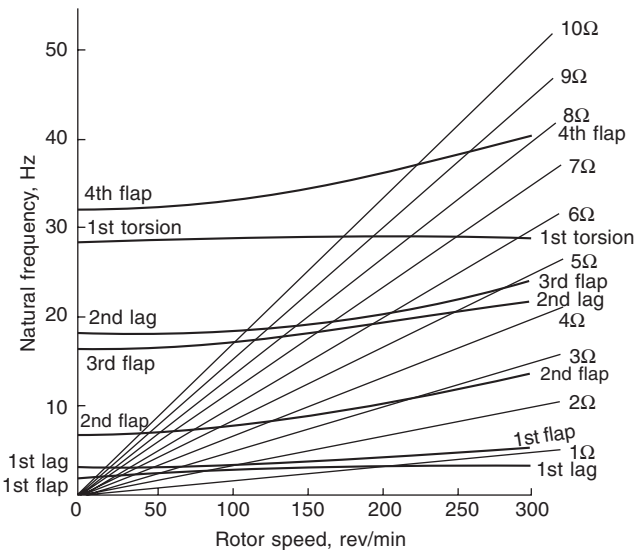


Fig. 7.23 Variation of blade bending frequencies with rotor speed

7.3 Forced response of rotor blades

7.3.1 Orthogonal property of the normal modes

The mode shapes possess a very important orthogonal property which can be deduced from the flapwise bending equation, eqn 7.11. Let $S_m(x)$ and $S_n(x)$ be two different solutions of eqn 7.11, with their associated frequency ratios λ_m and λ_n .

Thus, we have

$$\frac{d^2}{dx^2} \left(EI \frac{d^2 S_m}{dx^2} \right) - R^2 \frac{d}{dx} \left(G \frac{dS_m}{dx} \right) - m\lambda_m^2 \Omega^2 R^4 S_m = 0 \quad (7.77)$$

and
$$\frac{d^2}{dx^2} \left(EI \frac{d^2 S_n}{dx^2} \right) - R^2 \frac{d}{dx} \left(G \frac{dS_n}{dx} \right) - m\lambda_n^2 \Omega^2 R^4 S_n = 0 \quad (7.78)$$

Now multiply eqn 7.77 by S_n and eqn 7.78 by S_m . Consider the first equation:

$$S_n \frac{d^2}{dx^2} \left(EI \frac{d^2 S_m}{dx^2} \right) - R^2 S_n \frac{d}{dx} \left(G \frac{dS_m}{dx} \right) - m\lambda_m^2 \Omega^2 R^4 S_m S_n = 0 \quad (7.79)$$

Integrating the first term by parts from $x = 0$ to $x = 1$ gives

$$\begin{aligned} \int_0^1 S_n \frac{d^2}{dx^2} \left(EI \frac{d^2 S_m}{dx^2} \right) dx &= \left[S_n \frac{d}{dx} \left(EI \frac{d^2 S_m}{dx^2} \right) \right]_0^1 \\ &\quad - \int_0^1 \frac{dS_n}{dx} \frac{d}{dx} \left(EI \frac{d^2 S_m}{dx^2} \right) dx \end{aligned}$$

The term in the square brackets vanishes on account of the boundary conditions for both the hinged and hingeless blade. Further,

$$\begin{aligned} \int_0^1 \frac{dS_n}{dx} \frac{d}{dx} \left(EI \frac{d^2 S_m}{dx^2} \right) dx &= \left[\frac{dS_n}{dx} EI \frac{d^2 S_m}{dx^2} \right]_0^1 - \int_0^1 EI \frac{d^2 S_m}{dx^2} \frac{d^2 S_n}{dx^2} dx \\ &= - \int_0^1 EI \frac{d^2 S_m}{dx^2} \frac{d^2 S_n}{dx^2} dx \end{aligned}$$

on applying the boundary conditions again.

Similarly integrating the second term of eqn 7.79

$$\int_0^1 S_m \frac{d}{dx} \left(G \frac{dS_n}{dx} \right) dx = - \int_0^1 G \frac{dS_m}{dx} \frac{dS_n}{dx} dx$$

Thus, the term by term integration of eqn 7.79 yields

$$\int_0^1 EI \frac{d^2 S_m}{dx^2} \frac{d^2 S_n}{dx^2} dx + R^2 \int_0^1 G \frac{dS_m}{dx} \frac{dS_n}{dx} dx - \lambda_m^2 \Omega^2 R^4 \int_0^1 mS_m S_n dx = 0 \quad (7.80)$$

Treating eqn 7.78 in the same way gives

$$\int_0^1 EI \frac{d^2 S_m}{dx^2} \frac{d^2 S_n}{dx^2} dx + R^2 \int_0^1 G \frac{dS_m}{dx} \frac{dS_n}{dx} dx - \lambda_n^2 \Omega^2 R^4 \int_0^1 mS_m S_n dx = 0 \quad (7.81)$$

Subtracting eqn 7.81 from eqn 7.80 gives

$$(\lambda_n^2 - \lambda_m^2) \int_0^1 mS_m S_n dx = 0$$

We conclude that, since $\lambda_n \neq \lambda_m$ when $m \neq n$,

$$\begin{aligned} \int_0^1 mS_m S_n dx &= 0, \quad m \neq n \\ &= f(n), \quad \text{say, when } m = n \end{aligned} \quad (7.82)$$

Equation 7.82 expresses the *orthogonal* properties of the modes in relation to the weighting function $m(x)$ (mass distribution). This means, for example, that if we integrate the product of any two dissimilar mode shapes together with the mass distribution $m(x)$, the result is zero. This fact serves as a useful check on the accuracy of computed mode shapes.

The orthogonal properties do not hold for a hingeless blade with a built-in coning angle β_0 , say, for in this case the boundary conditions are $dS/dx = \tan \beta_0$ at $x = 0$ and some of the terms in the integration of eqn 7.79 do not vanish at the limits. However, this is not really a restriction since the reference axes can be tilted so that the new dS/dx becomes zero at the blade root. There will then be a component of centrifugal

force $-m\Omega^2 r \tan \beta_0$ normal to the undeflected blade which can be treated as a spanwise loading to be added to $\partial F/\partial r$. Thus, the orthogonal properties can be made to apply to the blade with built-in coning by using the boundary conditions (b) and applying an extra spanwise loading $-m\Omega^2 r \tan \beta_0$.

We should also note the rather interesting fact that the teetering rotor satisfies both sets of boundary conditions. Figures 7.24(a) and 7.24(b) show two examples of the way the blade can bend. In Fig. 7.24(a) the shape of the blade is anti-symmetric about the hinge, so that there is a point of inflection there; i.e. $d^2S/dx^2 = 0$ at $x = 0$ and the boundary conditions are those of the hinged blade. In Fig. 9.4(b) the bending is symmetrical and each half behaves as if the root were rigidly fixed to the shaft; the boundary conditions therefore are those of the hingeless blade. Thus, the teetering rotor has twice as many mode shapes and frequencies as a single hinged or hingeless blade.

7.3.2 Forced response equations

Equation 7.6 refers to the free vibration of the rotor blade in the flapwise sense. The corresponding equation, taking into account the presence of external loading F , is

$$\frac{\partial^2}{\partial r^2} \left(EI \frac{\partial^2 Z}{\partial r^2} \right) - \frac{\partial}{\partial r} \left(G \frac{\partial Z}{\partial r} \right) + m \frac{\partial^2 Z}{\partial t^2} = \frac{\partial F}{\partial r} \quad (7.83)$$

We now make use of the orthogonal properties of the normal mode shapes to simplify the problem of determining the blade motion under the action of applied forces.

Let us suppose that the solution of eqn 7.83 to a known blade loading can be expressed as

$$Z = R \sum_{n=1}^{\infty} S_n(x) \phi_n(\psi) \quad (7.84)$$

where the terms $S_n(x)$ are the blade mode shapes calculated from solving eqn 7.11 but the terms $\phi_n(\psi)$ have yet to be determined. Substituting eqn 7.84 into eqn 7.83 gives

$$\begin{aligned} \sum_{n=1}^{\infty} \phi_n(\psi) \left[\frac{d^2}{dx^2} \left(EI \frac{d^2 S_n}{dx^2} \right) - R^2 \frac{d}{dx} \left(G \frac{d S_n}{dx} \right) \right] \\ + m\Omega^2 R^4 \sum_{n=1}^{\infty} S_n \frac{d^2 \phi}{d\psi^2} = R^2 \frac{\partial F}{\partial x} \end{aligned}$$

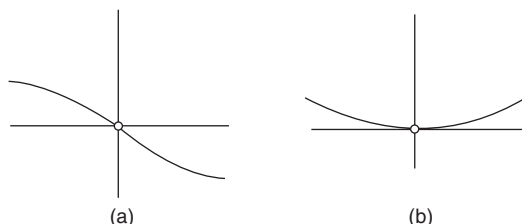


Fig. 7.24 Possible deflections of the teetering rotor

But from eqn 7.77 the terms in the large bracket can be replaced by

$$m\Omega^2 R^4 \sum_{n=1}^{\infty} \lambda_n^2 S_n$$

giving

$$\sum_{n=1}^{\infty} \left[\frac{d^2 \phi_n}{d\psi^2} + \lambda_n^2 \phi_n(\psi) \right] S_n(x) = \frac{1}{m\Omega^2 R^4} \frac{\partial F}{\partial x} \quad (7.85)$$

Multiplying eqn 7.85 through by $mS_m(x)$, integrating from 0 to 1, and applying the orthogonal properties as defined by eqn 7.82, gives

$$\frac{d^2 \phi_n}{d\psi^2} + \lambda_n^2 \phi_n = \frac{1}{\Omega^2 R^2 f(n)} \int_0^1 \frac{\partial F}{\partial x} S_n(x) dx \quad (7.86)$$

where $f(n) = \int_0^1 mS_n^2(x) dx$ is the generalised mass or inertia term for the n th mode.

Thus, the terms ϕ_n of eqn 7.84 are determined from the solutions of eqn 7.86. Unfortunately, although the orthogonal properties 'decouple' the inertia and elastic terms, represented by the left-hand side of eqn 7.83, the blade loading $\partial F/\partial r$ depends on the blade deflections which will, in general, contain all the blade modes of motion. Otherwise, each azimuth co-ordinate ϕ_n could be calculated individually from eqn 7.86. We shall discuss means of solving eqn 7.86 later in the chapter.

We may also derive the forced response equation from energy considerations.

It is convenient to express the energy forms in terms of the blade axes, which are non-Newtonian due to the rotation present. However, energy forms relative to these axes may be used in the same way as those for absolute energy forms, provided the inertia forces resulting from the rotation are treated as normal external forces^{14,15} in developing energy forms. In the present case, the inertia forces acting on a mass element in the blade are the centrifugal force and the Coriolis force. The former is normally considered to provide a potential energy term arising from the centrifugal effect, which can then be added to the potential or strain energy from elastic forces; the latter is usually removed to the right-hand side of the equations of motion, together with the other external, i.e. aerodynamic, forces.

The *kinetic energy* T of the mass elements of the blade relative to axes rotating with the blade is

$$\begin{aligned} T &= \frac{1}{2} \int_0^R m \left(\frac{\partial Z}{\partial t} \right)^2 dr \\ &= \frac{1}{2} \Omega^2 R^3 \int_0^1 m \left(\frac{\partial z}{\partial \psi} \right)^2 dx \end{aligned} \quad (7.87)$$

m being, as usual, the mass per unit length of the blade.

Assuming as before

$$z = \sum_{n=1}^{\infty} S_n(x) \phi_n(\psi)$$

we have

$$\frac{\partial z}{\partial \psi} = \sum_{n=1}^{\infty} S_n(x) \frac{d\phi_n}{d\psi}$$

so that substitution in eqn 7.87 we find

$$\begin{aligned} T &= \frac{1}{2} \Omega^2 R^3 \sum_{m=1}^{\infty} \sum_{n=1}^{\infty} \frac{d\phi_m}{d\psi} \frac{d\phi_n}{d\psi} \int_0^1 m S_m S_n dx \\ &= \frac{1}{2} \Omega^2 R^3 \sum_{n=1}^{\infty} \left(\frac{d\phi_n}{d\psi} \right)^2 f(n) \end{aligned} \quad (7.88)$$

from the orthogonal relations eqn 7.82

The *strain energy* U_B due to bending is¹⁰

$$\begin{aligned} U_B &= \frac{1}{2} \int_0^R EI \left(\frac{\partial^2 Z}{\partial r^2} \right)^2 dr \\ &= \frac{1}{2R} \int_0^1 EI \left(\frac{\partial^2 z}{\partial x^2} \right)^2 dx \end{aligned} \quad (7.89)$$

$$= \frac{1}{2R} \sum_{m=1}^{\infty} \sum_{n=1}^{\infty} \phi_m \phi_n \int_0^1 EI \frac{d^2 S_m}{dx^2} \frac{d^2 S_n}{dx^2} dx \quad (7.90)$$

The potential energy U_G due to the centrifugal stiffening effect arises from the centrifugal force G acting on a mass element doing negative work when the radius of its point of application decreases as a result of blade bending (the ‘shortening effect’). Then

$$\begin{aligned} U_G &= \int_0^R G \{r - r[1 - (\partial Z / \partial r)^2]^{1/2}\} dr \\ &= \frac{1}{2} R \int_0^1 G \left(\frac{\partial z}{\partial x} \right)^2 dx \end{aligned} \quad (7.91)$$

for small deflections. Substituting for $\partial z / \partial x$ we have

$$U_G = \frac{1}{2} R \sum_{m=1}^{\infty} \sum_{n=1}^{\infty} \phi_m \phi_n \int_0^1 G \frac{dS_m}{dx} \frac{dS_n}{dx} dx$$

The total strain and potential energy is

$$U = U_B + U_G = \frac{1}{2R} \sum_{m=1}^{\infty} \sum_{n=1}^{\infty} \phi_m \phi_n \int_0^1 \left(EI \frac{d^2 S_m}{dx^2} \frac{d^2 S_n}{dx^2} + R^2 G \frac{dS_m}{dx} \frac{dS_n}{dx} \right) dx$$

$$= \frac{1}{2} \lambda_n^2 \Omega^2 R^3 \sum_{m=1}^{\infty} \sum_{n=1}^{\infty} \phi_n^2 \int_0^1 m S_m S_n dx \quad (7.92)$$

from eqn 7.81, so that

$$U = \frac{1}{2} \lambda_n^2 \Omega^2 R^3 \sum_{n=1}^{\infty} f(n) \phi_n^2 \quad (7.93)$$

on using the orthogonal properties again.

The *external work* done by the elementary force $(\partial F / \partial r)dr$ in an arbitrary displacement is

$$\delta(\delta W) = R \frac{\partial F}{\partial x} dx \sum_{n=1}^{\infty} S_n(x) \delta \phi_n$$

and for the whole blade

$$\delta W = R \sum_{n=1}^{\infty} \delta \phi_n \int_0^1 \frac{\partial F}{\partial x} S_n dx$$

so that

$$\frac{\partial W}{\partial \phi_n} = R \int_0^1 \frac{\partial F}{\partial x} S_n dx \quad (7.94)$$

Note that since only blade bending is being considered, the Coriolis force, which acts in the lead-lag sense, does not contribute to this work form.

Now, Lagrange's equations for small displacements are

$$\frac{d}{dt} \left(\frac{\partial T}{\partial \dot{\phi}_n} \right) - \frac{\partial T}{\partial \phi_n} + \frac{\partial U}{\partial \phi_n} = \frac{\partial W}{\partial \phi_n}$$

or, with $\psi = \Omega t$,

$$\frac{d}{d\psi} \left(\frac{\partial T}{\partial \dot{\phi}_n} \right) - \frac{\partial T}{\partial \phi_n} + \frac{\partial U}{\partial \phi_n} = \frac{\partial W}{\partial \phi_n} \quad (7.95)$$

Then, using eqns 7.88, 7.93, and 7.94, Lagrange's equations give

$$\frac{d^2 \phi_n}{d\psi^2} + \lambda_n^2 \phi_n = \frac{1}{\Omega^2 R^2 f(n)} \int_0^1 \frac{\partial F}{\partial x} S_n(x) dx \quad \text{as before} \quad (7.96)$$

The response equations of the blade in lagging motion are of the same form as for the flapping motion, i.e. they take the form

$$\frac{d^2 \chi_n}{d\psi^2} + v_n^2 \chi = \frac{1}{\Omega^2 R^2 g(n)} \int_0^1 \frac{\partial F_y}{\partial x} T_n(x) dx$$

where

$$g(n) = \int_0^1 m T_n^2(x) dx$$

is the generalised inertia for the n th lag bending mode, and F_g is the lagwise external (aerodynamic) loading.

7.3.3 Solution of the forced response equation

We shall now consider the solution of the forced response equation, eqn 7.86 above.

For a rigid blade, ϕ_1 can be identified with the flapping angle β and the right hand side with the aerodynamic moment M_A . As mentioned before, the orthogonal properties of the normal modes decouple the inertia and stiffness terms so that the terms on the left hand side of eqn 7.86 are independent of the other modes. Unfortunately, the aerodynamic loading contains all the modes, since the complete blade motion is required to determine the aerodynamic incidence. This means that the right hand side is a function of ϕ_1, ϕ_2, \dots , etc., so that the mode equations cannot be solved independently. We are therefore faced with the problem of integrating these equations in the most efficient way.

The usual procedure is to assume a starting value for the blade motion – for example, we may take the classical rigid blade flapping – and compute the aerodynamic loading and the integral on the right hand side of eqn 7.86 for the modes being considered. The value of the integral is then imagined to remain constant over a small azimuth variation $\Delta\psi$ and the corresponding changes of ϕ_n and $d\phi_n/d\psi$ are computed from eqn 7.86. The loading integral is then re-calculated and ϕ_n and $d\phi_n/d\psi$ are computed for the next azimuth step $\Delta\psi$. These stepwise integrations are continued until the required values of ϕ_n converge to within an acceptable limit. The integrations may extend over several resolutions before satisfactory convergence has been achieved. Part of the process of convergence concerns the transient blade motion, because of the inevitability of some error between the assumed blade motion, taken as the starting value, and the true motion; and part will be due to the inherent features in the integration process. There must, of course, be as many integrations as there are modes taken to represent the blade motion.

Of the methods of integration, the most common is probably the fourth order Runge-Kutta, but it appears that convergence difficulties arise if the step lengths are too small, particularly for the higher modes.

A simpler and yet more accurate method is to take advantage of the fact that, if the right hand side of eqn 7.86 is kept constant, the equation can be solved exactly over the step length. Let us denote the right hand side of eqn 7.86 by f_i , where f_i is the constant value corresponding to the i th step. Then eqn 7.86 can be written as

$$\frac{d^2\phi_n}{d\psi^2} + \lambda_n^2 \phi_n = \phi_{in} \quad (7.96)$$

To avoid confusion, we shall drop the suffix n from ϕ_n and let ϕ represent any mode displacement. Let ϕ_i and ϕ'_i be the values of ϕ and $d\phi/d\psi$ at the start of the i th step; then eqn 7.96 can be written as

$$\frac{d^2\phi}{d\psi^2} + \lambda^2 \phi = f_i$$

whose solution is easily found to be

$$\phi = \frac{f_i}{\lambda^2} (1 - \cos \lambda\psi) + \phi_i \cos \lambda\psi + \frac{\phi'_i}{\lambda} \sin \lambda\psi$$

If $\Delta\psi$ is the step change of ψ , the values of ϕ and $d\phi/d\psi$ at the start of the $(i+1)$ th step are

$$\phi'_{i+1} = \frac{f_i}{\lambda^2} (1 - \cos \lambda\Delta\psi) + \phi_i \cos \lambda\Delta\psi + \frac{\phi'_i}{\lambda} \sin \lambda\Delta\psi \quad (7.97)$$

and

$$\phi'_{i+1} = \frac{f_i}{\lambda} \sin \lambda\Delta\psi - \lambda\phi_i \sin \lambda\Delta\psi + \phi'_i \cos \lambda\Delta\psi \quad (7.98)$$

These are the initial values at the start of the next interval, at the end of which

$$\phi_{i+2} = \frac{f_{i+1}}{\lambda^2} (1 - \cos \lambda\Delta\psi) + \phi'_{i+1} \cos \lambda\Delta\psi + \frac{\phi'_{i+1}}{\lambda} \sin \lambda\Delta\psi \quad (7.99)$$

Eliminating ϕ'_{i+1} and ϕ'_i by means of eqns 7.97 and 7.98 leads to the recurrence relationship

$$\phi_{i+2} = 2\phi'_{i+1} \cos \lambda\Delta\psi - \phi_i - \frac{1 - \cos \lambda\Delta\psi}{\lambda^2} (f_{i+1} + f_i) \quad (7.100)$$

connecting the mode displacement with the values at the two previous intervals and the corresponding loading integrals.

Wilkinson and Shilladay¹⁶ have obtained the same result by appealing to sampled data theory and using the Z-transform. The values of f_i can be represented as discrete input functions occurring at regular intervals, as in Fig. 7.25.

The use of constant values of f_i over the interval is referred to as a zero-order hold, Fig. 7.26. Improved accuracy can be obtained by assuming that f_i varies linearly over an interval according to the slope of the straight line connecting the values of f_{i-2} and f_{i-1} , Fig. 7.27. This is called a first-order hold. The differential equation for this case is

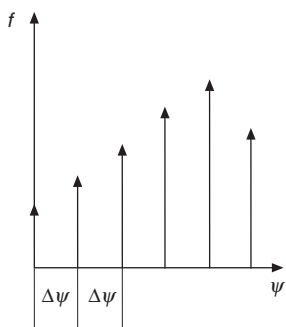


Fig. 7.25 Discrete input frequency

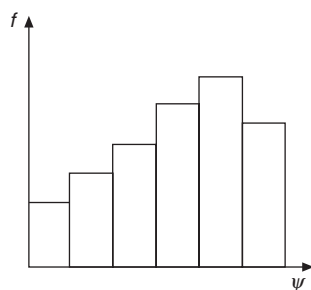


Fig. 7.26 Zero-order hold forcing

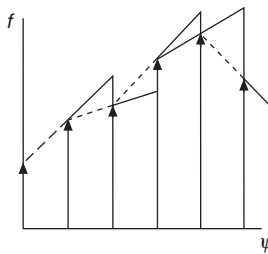


Fig. 7.27 First-order hold forcing

$$\frac{d^2\phi}{d\psi^2} + \lambda^2\phi = f_i + \frac{f_i - f_{i-1}}{\Delta\psi} \psi \quad (7.101)$$

with the solution

$$\phi = \frac{f_i}{\lambda^2} (1 - \cos \lambda \Delta\psi) + \frac{f_i - f_{i-1}}{\lambda^2 \Delta\psi} - \frac{f_i - f_{i-1}}{\lambda^3 \Delta\psi} \sin \lambda \psi + \phi_i \cos \lambda \psi + \frac{\phi'_i}{\lambda} \sin \lambda \psi \quad (7.102)$$

By proceeding as before, we obtain the recurrence relationship

$$\begin{aligned} \phi_{i+2} &= 2\phi_{i+1} \cos \lambda \Delta\psi - \phi_i + \\ \frac{1}{\lambda^2} \left[(f_{i-1} - 2f_i + f_{i+1}) \left(\cos \lambda \Delta\psi - \frac{\sin \lambda \Delta\psi}{\lambda \Delta\psi} \right) + 2f_{i+1} (1 - \cos \lambda \Delta\psi) \right] \end{aligned} \quad (7.103)$$

Wilkinson and Shilladay have tested the recurrence relationships eqns 7.100 and 7.103 for cases with known exact solutions and have found that they are more accurate and allow faster computation than the Runge–Kutta method.

We can also take advantage of the fact that in steady flight the aerodynamic loading, and the consequent blade motion, is periodic so that the right hand side of the modal equation 7.86 is expressible in the form of a Fourier series. If this is done, the complete solution of eqn 7.86 can be written down at once, since it represents the well known response of a second-order system forced by a series of harmonic functions, Appendix A.4. Of course, the loading integral on the right hand side of eqn 7.86 will not, initially, be known exactly, since it depends in a complicated way on the motion being calculated. An integrative solution must be adopted, and the classical rigid blade flapping can be used as a first approximation. The loading integral is then calculated, expressed as a Fourier series, and the values of the mode displacements ϕ_n are obtained. The values of ϕ_n and $d\phi_n/d\psi$ are then used to obtain a second approximation to the loading $\partial F/\partial x$, and the process is repeated until satisfactory convergence has been achieved. There are, of course, a number of numerical methods for calculating the Fourier series of a set of periodic values.

If, in the method just described, the modal equation is used as it appears in

eqn 7.86, we shall encounter the difficulty of resonance¹⁶ for those modes with a natural frequency equal or close to the rotor frequency. This can be avoided by noting that the aerodynamic loading contains damping which, although non-linear on account of the non-linear aerodynamic data which will undoubtedly be used, will nevertheless be roughly proportional to $d\phi_n/d\psi$.

If such a term is removed from the loading integral of eqn 7.86 and is transferred to the left hand side of the equation, we shall have the case of a harmonically forced system with quite high linear damping, and the large amplitudes near resonant frequency will not occur. Since $d\phi_n/d\psi$ will not be known when transferred, the calculation of the damping terms remaining in the integral must be based on the blade motion of the previous approximation, as has been described for the case earlier.

7.4 Blade deflections in flight

The deflection of the rotor blade in flight can be calculated by the method of the previous section in conjunction with the estimated blade mode shapes and frequencies and the aerodynamic loading. These calculations can also be used to obtain the stresses in the blade and at the hub. For illustration, however, we give below examples of the measurement of blade deflection obtained by photographing the blade in flight. In this experiment, a 16 mm camera taking 240 frames per second (about 60 frames per rotor revolution) was mounted on the hub of an experimental Westland 'Scout' with a hingeless rotor, and was directed to look along the span of one of the blades. A typical photograph ($\psi = 290^\circ$, 54 m/s, level flight) is shown in Fig. 7.28. It was assumed that the contributions of the first three modes were sufficient to account for the measured blade deflection. The calculated mode shapes and their associated frequencies are shown in Fig. 7.29.

The flapping deflection of any part of the blade would then be expressible in the form

$$Z(x, \psi) = R[S_1(x)\phi_1(\psi) + S_2(x)\phi_2(\psi) + S_3(x)\phi_3(\psi)]$$

With S_1 , S_2 and S_3 known, the generalised co-ordinates ϕ_1 , ϕ_2 , ϕ_3 in terms of azimuth could be determined from analysis of the photographs. The results, expressed in terms of the displacement of the blade tip, are shown in Fig. 7.30.

It should be emphasised that the displacements are measured relative to the hub axis. The amount of first-mode displacement which occurs, is of course, directly dependent on the amount of cyclic pitch applied and will be such as to trim the longitudinal and lateral moments about the hub, including the hub moments due to blade deflection in the second and third modes.

It can be seen that the contributions of the second and third modes to the blade deflection are quite small and would be still smaller if the first mode deflection were measured relative to the no-feathering axis. This justifies the assumption of the rigid blade which is used in much of helicopter analysis. Calculations show that, for the flight case considered, neglect of the second and third modes results in only about a 7 per cent error in the hub moment.



Fig. 7.28 Typical photograph of blade in flight (hingeless Westland 'Scout', 53.5 m/s, $\psi = 290^\circ$)

7.5 Basic features of the hingeless rotor

Many helicopters now employ hingeless rotor systems. The design of such systems has become possible due to two main factors: the increased understanding of the aeroelastic and dynamic behaviour of rotor systems and the application of composite material to critical components in the aeronautical field.

The initial development was the replacement of the conventional flapping and lagging hinges by flexible structural elements. Such a system is normally referred to as the semi-rigid rotor. Subsequent developments led to the totally bearingless rotor where, in addition to the elimination of the flapping and lagging hinges, blade feathering is accommodated by the torsional flexibility of the hub elements.

The main advantages claimed for hingeless rotors are:

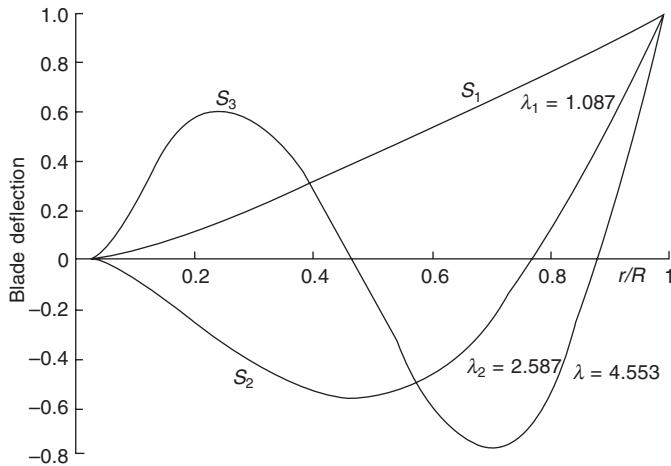


Fig. 7.29 Blade-flapping mode shapes

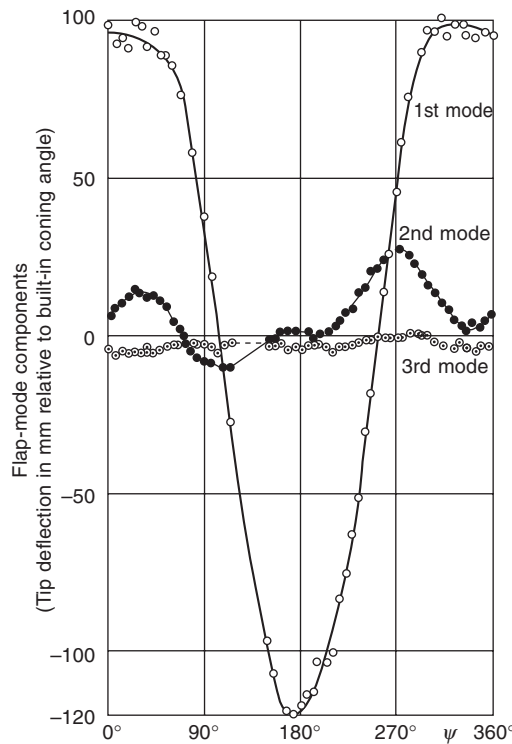


Fig. 7.30 Modal content of blade flapwise deflection

- (i) the elimination of hinges leads to a great simplification of hub design, with consequent reduction of manufacture and maintenance costs, and also reduced aerodynamic drag;
- (ii) much greater hub moments, leading to improved control power which is virtually independent of the level of rotor thrust, and increased angular rate damping. Both these features contribute to an improvement in handling qualities.

In this section we shall consider only the flapping mode shapes and frequencies of the hingeless blade and the hub moments exerted when the blade is deflected. The problems of the various forms of intermodal coupling and the particular problem of air resonance are considered in Chapter 9. A comprehensive review of the benefits and problems associated with hingeless rotors has been given by Hohenemser¹⁷.

The mode shape analysis of the hingeless blade can be dealt with by the methods described earlier in this chapter, noting that the root boundary conditions are $z = 0$ and $dz/dx = 0$, or perhaps some fixed value ('built-in' coning).

Typical lower mode shapes and frequencies are given in Fig. 7.31.

The first flapping frequency ratio of hingeless rotors usually lies within the range 1.08 to 1.17 and, as can be seen from Fig. 7.31, the curvature of the blade is confined mainly to the root region, most of the outer part of the blade being almost straight. It is this local curvature, however, when combined with a typical distribution of bending stiffness in this region, which produces the large hub moments characteristic of the hingeless blade.

In order to investigate the second of the benefits of the hingeless rotor listed above, a method is needed for calculating the moments transmitted to the hub due to

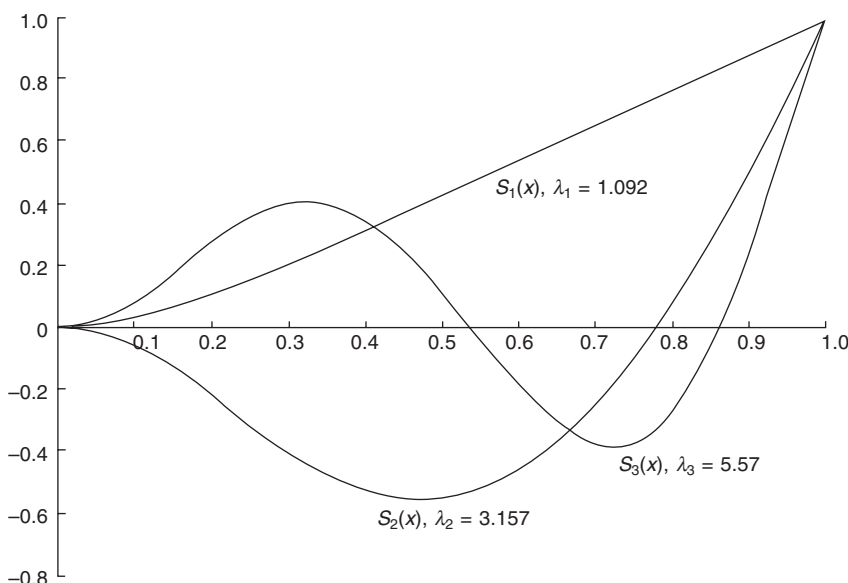


Fig. 7.31 Typical flapping mode shapes for hingeless blade

the deflection of the blades. The first analysis for such calculations was made by Young¹⁸ who produced a very simple expression for the hub moment. Fig. 7.32 refers.

Young calculated the moment at the blade root $M(0, t)$ of the aerodynamic, centrifugal, and inertia loadings as

$$M(0, t) = \int_0^R \left(\frac{\partial F}{\partial r} - m\Omega^2 Z - m \frac{\partial^2 Z}{\partial t^2} \right) r \, dr \quad (7.104)$$

By means of the blade bending equation

$$\frac{\partial^2}{\partial r^2} \left(EI \frac{\partial^2 Z}{\partial r^2} \right) - \frac{\partial}{\partial r} \left(G \frac{\partial Z}{\partial r} \right) + m \frac{\partial^2 Z}{\partial t^2} = \frac{\partial F}{\partial r}$$

the terms $\partial F/\partial r - m\partial^2 Z/\partial t^2$ can be eliminated from eqn 7.104 giving

$$M(0, t) = \int_0^R \left[\frac{\partial^2}{\partial r^2} \left(EI \frac{\partial^2 Z}{\partial r^2} \right) - \frac{\partial}{\partial r} \left(G \frac{\partial Z}{\partial r} \right) - m\Omega^2 Z \right] r \, dr$$

Writing the blade deflection as

$$Z = R \sum_{n=1}^{\infty} S_n(r) \phi_n(t)$$

the root moment can be written

$$M(0, t) = \int_0^R \sum_{n=1}^{\infty} \phi_n R \left[\frac{d^2}{dr^2} \left(EI \frac{d^2 S_n}{dr^2} \right) - \frac{d}{dr} \left(G \frac{d S_n}{dr} \right) - m \Omega^2 S_n \right] r \, dr$$

But the blade mode shapes satisfy the equation

$$\frac{d^2}{dr^2} \left(EI \frac{d^2 S_n}{dr^2} \right) - \frac{d}{dr} \left(G \frac{d S_n}{dr} \right) - m \lambda_n^2 \Omega S_n = 0$$

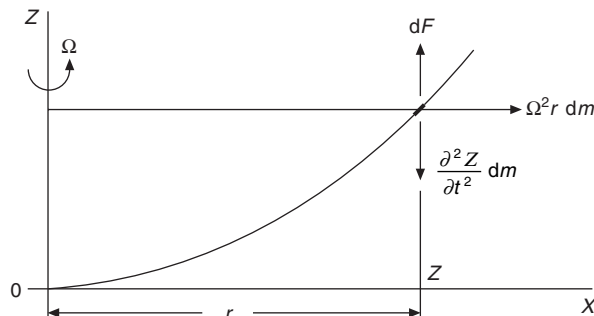


Fig. 7.32 Flapwise forces acting on blade

so that the root moment finally becomes

$$M(0, t) = \Omega^2 R \sum_{n=1}^{\infty} \phi_n (\lambda_n^2 - 1) \int_0^R mr S_n dr \quad (7.105)$$

Since, in the case of the rotor with a flapping hinge we only need to use the first rigid blade mode for considerations of performance and stability and central, let us assume that we need only consider the first bending mode of the hingeless rotor for the same purposes.

Then if only the first mode is considered, the moment is

$$M(0, t) = (\lambda^2 - 1) R^3 \phi_1(t) \int_0^1 mx S_i dx \quad (7.106)$$

This is a slightly more general form of the equation given by Young, who calculated only the increment due to a cyclic pitch change in hovering flight.

It has been shown by Simons¹⁹ and by Curtiss and Shupe²⁰ that the derivation of eqn 7.106 implies that the aerodynamic loading distribution has the same shape as the first bending mode, i.e. that

$$\frac{\partial F}{\partial x} \propto S_1(x) \cdot m(x)$$

This implicit assumption may not be seriously in error at low values of μ , but one might expect that at high values the loading might depart considerably from the first mode shape and throw doubt on the validity of eqn 7.106.

To avoid this difficulty, another expression for the root moment can be derived.

References to eqn. 7.104, the root moment can be written as

$$M(0, t) = \int_0^R r \frac{\partial F}{\partial r} dr - \Omega^2 \int_0^R mt \left(\frac{\partial^2 Z}{\partial \psi^2} + Z \right) dr \quad (7.107)$$

Writing, as before

$$Z = R \sum_{n=1}^{\infty} S_n(x) \phi_n(\psi)$$

eqn 9.110 becomes

$$M(0, t) = \int_0^R r \frac{\partial F}{\partial r} dr - R^3 \sum_{n=1}^{\infty} \left(\frac{d^2 \phi_n}{d \psi^2} + \phi_n \right) \int_0^1 Mx S_n dx$$

Equation 7.106 has been used by Bramwell² to obtain stability derivatives of a hingeless rotor.

Defining a root moment coefficient by

$$M_c = M/\rho b_c \Omega^2 R^4$$

eqn 7.106 can be written in non-dimensional form as

$$M_c = \frac{a(\lambda_1^2 - 1)}{b\gamma_1} \phi_1(\psi) \quad (7.108)$$

$$\text{where } \gamma_1 = \frac{\rho acR}{\int_0^1 mx S_1 dx}$$

which is equivalent to the lock number for the hinged rigid blade.

Since, for considerations of performance and stability and control, we may consider only the 1st harmonic response, the flapping of the hingeless blade can be written in the form

$$\phi_1(\psi) = \beta = \bar{a}_0 - \bar{a}_1 \cos \psi - \bar{b}_1 \sin \psi$$

when $\bar{\beta}, \bar{a}_0, \bar{a}_1, \bar{b}_1$, are analogous to the rigid blade flapping angle and flapping coefficients. Then the pitching and rolling moment coefficients C_m and C_l of a hingeless rotor with b blades are

$$C_m = \frac{a(\lambda_1^2 - 1)\bar{a}_1}{z\gamma_1} \quad (7.109)$$

$$C_l = \frac{a(\lambda_1^2 - 1)\bar{b}_1}{2\gamma_1} \quad (7.110)$$

The flapping coefficients $\bar{a}_0, \bar{a}_1, \bar{b}_1$ can be calculated by a similar analysis to that for the hinged rigid blade. The equations, although quite straight forward, are rather cumbersome because unlike those of the centrally hinged blade, the integrals involving the mode shapes do not lend to simple fractions and the equations do not give the coefficients explicitly. The equations have been given by Bramwell²¹ and Curtiss and Shupe²⁰. The calculations show that the amplitude of flapping is only a little less than that if the blade were hinged.

Returning to the determination of the hub moment, and since we are interested only in the pitching and rolling moments on the helicopter, only the first harmonic motion need be considered, in which case, for the n th mode

$$\phi_n = (\bar{a}_0)_n - (\bar{a}_1)_n \cos \psi - (\bar{b}_1)_n \sin \psi$$

$$\text{so that } \frac{d^2\phi_n}{d\psi^2} + \phi_n = (\bar{a}_\omega)_n$$

hence, substituting in the modified version of eqn 7.110, we have

$$M(0, \psi) = r \frac{\partial F}{\partial r} dr + \Omega^2 R^3 \sum_{n=1}^{\infty} (\bar{\phi}_0)_n \int_0^1 mx S_n dx$$

When all the blades are taken together to form the total pitching and rolling moments, the last term on the right-hand side vanishes, so that the hub moment reduces to

$$M(0, \psi) = \int_{\partial}^R r \frac{\partial F}{\partial r} dr \quad (7.111)$$

In this equation, given by Simons and by Curtiss and Shupe, no restriction need be placed on the loading, although, in practice, the loading will depend on the number of modes chosen to represent the blade motion. According to Curtiss and Shupe, only one mode is necessary over a well range of conditions, but for high values of μ two modes ought to be used for better accuracy. On the other hand, if the general equation in terms of blade flapping is used, eqn 7.106, we have to include that number of modes which, in superposition, approximate to the true loading shape. In general, this is longer than that for eqn 7.111.

Let us now consider modelling the hingeless rotor by defining an equivalent hinged rigid blade system.

Although Young derived eqn 7.106 for the particular case of a cyclic pitch application in hovering flight, instead of proceeding with the calculations in terms of mode shape, as has been discussed above, he replaced the hingeless blade with a rigid blade with an offset hinge and a torsional spring. The amount of offset and the torsional spring strength were chosen to match the rotating and non-rotating natural frequencies of the actual blade. This model of the hingeless blade has received general acceptance and serves very well for calculating the flapping motion and hub moment; indeed it is quite usual to express the moment of a hingeless blade in terms of an ‘equivalent hinge offset’.

An interesting point is that, if the offset blade and torsional spring are taken as a mechanical equivalent to the hingeless blade, the hub moment of the hingeless blade, when calculated from first principles, approximates more closely to that given by eqn 7.111 than to that given by eqn 7.106. For, taking the spring strength as k_s per unit flapping angle, Fig. 7.33, the equations of motion of the blade are

$$\Omega^2 R^3 \frac{d^2 \beta}{d\psi^2} \int_e^1 m(x - e)^2 dx + \Omega^2 R^3 \beta \int_e^1 mx(x - e) dx + k_s \beta = M_A \quad (7.112)$$

and

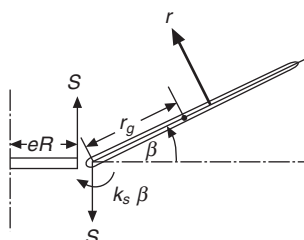


Fig. 7.33 Equivalent offset hinge

$$M_b \Omega^2 r_g \frac{d^2 \beta}{d\psi^2} = F - S \quad (7.113)$$

where M_A is the moment of the aerodynamic force about the hinge M_b is the blade mass. F is the aerodynamic force on the blade, and S is the shear force at the hinge. β , as usual, is assumed to be a small angle. The moment at the root is clearly

$$M(0, \psi) = SeR + k_s \beta + \int_0^{eR} r \frac{\partial F}{\partial r} dr \quad (7.114)$$

Now, for simple harmonic motion, and omitting the constant coning angle, we have

$$\frac{d^2 \beta}{d\psi^2} = -\beta$$

so that eqn 7.112 can be written

$$\begin{aligned} M_A &= \Omega^2 R^3 \beta \left\{ \int_e^1 mx(x - e) dx - \int_e^1 m(x - e)^2 dx \right\} xk_s \beta \\ &= \Omega^2 R^3 \beta e \int_e^1 m(x - e) dx + k_s \beta \end{aligned} \quad (7.115)$$

Similarly eqn 7.113,

$$F - S = M_b \Omega^2 r_g \frac{d^2 \beta}{d\psi^2}$$

can be written

$$\begin{aligned} F - S &= -\Omega^2 \beta \int_{eR}^R m(r - eR) dr \\ &= -\Omega^2 R^2 \beta \int_e^1 m(x - e) dx \end{aligned} \quad (7.116)$$

Eliminating the integral between eqns 7.116 and 7.115 gives

$$SeR + k_s \beta = FeR + M_A$$

so that substituting in eqn 7.114 gives for the hub moment,

$$\begin{aligned} M(0, \psi) &= FeR + M_A + \int_e^{eR} r \frac{\partial F}{\partial r} dr \\ &= eR \int_{eR}^R \frac{\partial F}{\partial r} dr + \int_{eR}^R (r - eR) \frac{\partial F}{\partial r} dr + \int_0^{eR} r \frac{\partial F}{\partial r} dr \\ &= \int_0^R r \frac{\partial F}{\partial r} dr \end{aligned} \quad (7.117)$$

which is identical to eqn 7.111, except, of course, that in the evaluation of $\frac{\partial F}{\partial r}$ the incidence would be determined by the rigid blade flapping.

If now, we ignore the aerodynamic shear force at the hinge, i.e. we put $F = 0$, then we have from eqn 7.116

$$\delta = \Omega^2 R^2 \beta \int_e^1 m(x - e) dx$$

and, if we ignore the moment at the root due to aerodynamic forces between the hinge and the root, then we have from eqn. 7.114

$$M(0, \psi) = S e R + k_s \beta$$

giving

$$M(0, \psi) = e \Omega^2 R^3 \beta \int_e^1 M(x - e) dx + k_s \beta \quad (7.118)$$

If we ignore the aerodynamic shear force at the hinge and the moment of aerodynamic forces about the hinge i.e. we put $M_A = 0$ in addition, then the blade flapping motion is unforced and the motion will take place at the natural frequency of rigid blade flapping.

This implies

$$\frac{d^2 \beta}{d\psi^2} + \lambda_1^2 \beta = 0$$

Substituting for $\frac{d^2 \beta}{d\psi^2}$ into eqn 7.112 gives

$$-\Omega^2 R^3 \lambda_1^2 \beta \int_e^1 m(x - e)^2 dx + \Omega^2 R^3 \beta \int_e^1 Mx(x - e) dx + k_s \beta = 0$$

$$\text{hence, } \lambda_1^2 = \frac{R^3 \int_e^1 Mx(x - e) dx + k_s / \Omega^2}{R^3 \int_e^1 m(x - e)^2 dx}$$

$$\text{giving } \lambda_1^2 - 1 = \frac{e R^3 \int_e^1 M(x - e) dx + k_s / \Omega^2}{R^3 \int_e^1 M(x - e)^2 dx}$$

Substituting the numerator of this expression with eqn. 7.118 finally gives

$$M(0, \psi) = \Omega^2 R^3 (\lambda_1^2 - 1) \beta \int_e^1 m(x - e)^2 dx \quad (7.119)$$

This expression is equivalent to eqn 7.106 with the flapping angle β in place of ϕ_1 , with the integral term corresponding to the mode shape integral.

In fact, the integral $R^3 \int_e^1 m(x - e)^2 dx$ is the moment of inertia of the blade about the flapping hinge. If we denote this by T_β , we can write eqn. 7.119 as

$$M(0, \psi) = \Omega^2 I_\beta (\lambda_1^2 - 1)\beta \quad (7.120)$$

Thus, Young's model of the hingeless blade is seen, by comparison of eqns 7.106 and 7.119, to be equivalent to the model utilising the modal approach (and considering only the first mode of bending), providing that the effect of the aerodynamic forces are ignored.

It might appear that the offset hinge rigid blade model, as depend by eqn 7.119, might be a very convenient way of handling the rigid blade problem. However, it is easily seen that calculation will involve integrals whose lower limit is e and, as this gives rise to a large number of terms in powers of e up to e^4 , the algebra becomes rather unwieldy. In practice, an analysis based directly on the true mode shapes is no less convenient, and will be followed in order to determine the pitching and rolling moment coefficients in terms of rotor and aerodynamic parameters. It is the case that, although eqn 7.107 is formally very simple and appears to require no more than two modes for its accurate evaluation, it has some disadvantages compared with eqn 7.106. When eqn 7.110 is evaluated in terms of the aerodynamic parameters θ_0 , λ , and the flapping and central coefficients, the expressions are found to be quite lengthening. Defining the integrals

$$C_1 = \int_0^1 x^2 S_1 dx, \quad F_1 = \int_0^1 x S_1 dx, \quad G_1 = \int_0^1 S_1 dx$$

we find for the pitching and rolling coefficients

$$C_M = \left(-\frac{a}{4} \right) \left[\left\{ C_1 + \frac{1}{4} \mu^2 (1 - G) \right\} \bar{b}_1 - \mu \bar{a}_0 \left\{ (1 - G) - \frac{1}{2} F_1 \right\} \right. \\ \left. - \frac{1}{4} A_1 \left(1 + \frac{1}{2} \mu^2 \right) - \frac{1}{4} \kappa_i \lambda_i + \frac{1}{4} \hat{q} + 4' \hat{\rho} / \gamma_1 \right] \quad (7.121)$$

and

$$C_l = \left(-\frac{a}{4} \right) \left[-\frac{1}{4} \left(\frac{1 + 3\mu^2}{2} \right) B_1 - \left\{ C_1 - \frac{1}{4} \mu^2 (1 - G) \right\} \bar{a}_1 + \frac{2\mu\theta_0}{3} \right. \\ \left. + \frac{1}{2} \mu b_1 + \frac{1}{2} \mu \lambda + \frac{1}{4} \hat{p} - \frac{4\hat{q}}{\gamma_1} \right] \quad (7.122)$$

where A_1 and B_1 are the cyclic control angles, λ_i is the mean induced velocity ratio, κ the induced velocity gradient, θ_1 the blade twist workout, and \hat{p} and \hat{q} one the non-dimensional pitching and rolling velocities. Similar equations have been given by Curtiss and Shupe²⁰.

Equations 7.121 and 7.122 should be compared with the particularly simple results indicated by eqns 7.109 and 7.110. Further, numerical examples show that the ‘coupling’ moments, e.g. the rolling moment arising from a longitudinal central displacement, appear as the small difference between two nearly equal quantities, i.e. they are ‘ill-conditioned’ and the results could be husbandry²². If we denote by $(M_c)_a$ the hub moment coefficient based on the aerodynamic loading, eqn 7.111, and if $(M_c)_f$ is the coefficient based on the flapping displacement eqn 7.106, Simons¹⁹ has shown that when one mode is considered

$$(M_c)_a = (M_c)_f + (a/2b) \int_0^1 (x - \bar{F}S_1)x^2\alpha \, dx \quad (7.123)$$

where α is the local blade incidence, $\bar{F} = \gamma_2/\gamma_1$, and the equivalent Lock’s number for the hingeless blade, $\gamma_2 = \rho acR/E_1$, where $E_1 = \int_0^1 mS_1^2 \, dx$ is the generalised mass or inertia of the blade first flapping mode.

Thus, the hub moment of eqn 7.111 can be found in terms of eqn 7.106, together with a ‘correction’ term represented by the integral of eqn 7.123. Then to a very good approximation²² it is found that

$$(C_m)_a = (a/2\gamma_1)(\lambda_1^2 - 1)\bar{a}_i + j_1 \mu \bar{a}_0$$

and

$$(C_l)_a = (a/2\gamma_1)(\lambda_1^2 - 1)\bar{b}_1 + j_2 \left(B_i - \frac{1}{2} \mu \theta_1 \right) - j_3 \mu \theta_0 - j_4 \mu \lambda \quad (7.125)$$

$$\text{where } j_1 = (a/2) \left[1 - G_1 - \frac{1}{2} F_1 - \frac{1}{2} \bar{F}(1 - D_1) \right]$$

$$j_2 = \frac{1}{4} - \bar{F}C_1$$

$$j_3 = \frac{2}{3} - 2\bar{F}F_1$$

$$j_4 = \frac{1}{2} - \bar{F}G_1$$

$$\text{and } D_1 = \int_0^1 S_1^2 \, dx$$

Equations 7.124 and 7.125 are only a little more complicated than eqns 7.109 and 7.110 but, for an analysis based on one mode, are just as accurate as eqns 7.121 and 7.122 and avoid the ‘ill-conditioning’ feature.

The stability and control derivatives for a hingeless rotor have been given by Bramwell^{21,22}. Generally speaking, it is found that the force derivatives are only slightly different from those calculated for the hinged rotor and presented in Chapter 5. The flapping motion of the blade, in spite of the elastic moment at the root, is also very slightly different from that of the rigid hinged blade under similar conditions, so

that the principal difference between the two rotors is the moment they exert on the hub. For the centrally hinged rotor, the pitching moment coefficient for a unit of the rotor has already been shown to be $t_e h$ and, of course, the same thrust moment applies to the hingeless rotor.

Let us use eqn. 7.108 to find the additional elastic moment coefficient for a typical case.

For unit flapping we have

$$M_c = (a/2\gamma_1)(\lambda_1^2 - 1)$$

Typical values for a hingeless rotor are $a = 5.7$, $\gamma_1 = 7.5$, $\lambda_1^2 = 1.24$, so that $C_m = 0.091$. For $t_e h$ we have already used the value 0.0214 (Chapter 4), so that the total coefficient for the hingeless rotor is 0.1124, giving a ratio of 5.26 to 1 when compared to the value for the centrally hinged rotor.

Thus quite a good approximation to the derivatives of a hingeless rotor helicopter is to take the force derivatives calculated in Chapter 5 and increase the flapping moments in some ratio determined from a calculation similar to that above.

References

1. Hildebrand, F. B., *Methods of applied mathematics*, Englewood Cliffs NJ, Prentice-Hall, 1956.
2. Temple, G. and Bickley, W. G., *Rayleigh's principle*, New York, Dover Publications, 1956.
3. Southwell, R. V. and Gough, Barbara S., 'On the free transverse vibrations of airscrew blades', *Rep. Memo. aeronaut. Res. Coun.* 766, 1921.
4. Bishop, R. E. D. and Johnson, D. C., *The mechanics of vibration*, London, Camb. Univ. Press, 1960.
5. Duncan, W. J., 'Galerkin's method in mechanics and differential equations', *Rep. Memo. aeronaut. Res. Coun.* 1798, 1937.
6. Duncan, W. J., 'Principles of the Galerkin method', *Rep. Memo. aeronaut. Res. Coun.* 1948, 1938.
7. Holzer, H., *Die Berechnung der Drehschwingungen*, Berlin, Springer Verlag, 1921.
8. Isakson, G. and Eisley, J. G., 'Natural frequencies in coupled bending and torsion of twisted rotating and non-rotating blades', *NASA CR-65*, July, 1964.
9. Williams, R. F., Unpublished material, City Univ. London.
10. Scanlan, Robert H. and Rosenbaum, Robert, *Introduction to aircraft vibration and flutter*, New York, Macmillan, 1960.
11. Houbolt, John C. and Brooks, George W., 'Differential equations of motion for combined flapwise bending, chordwise bending and torsion of twisted non-uniform rotor blades', *NACA Rep. 1346*, 1958.
12. Sobey, A. J., 'Dynamical analysis of the shaft-fixed blade', *R. Aircr. Establ. tech. Rep.* 73175, 1974.
13. Ormiston, Robert A. and Hodges, Dewey, H. 'Linear flap-lag dynamics of hingeless rotor blades in hover', *J. Am. Helicopter Soc.*, April 1972.
14. Done, G. T. S. and Simpson, A., 'Dynamic instability of certain conservative and non-conservative systems', *J. Mech. Eng. Sci.*, **19**(6), 1977.
15. Done, G. T. S., 'Relative energy concepts in rotating system dynamics', 2nd Int. Conf. on Vibrations in Rotating Machinery, Cambridge, UK, 2–4 Sept. 1980.

16. Wilkinson, R. and Shilladay, J. D., 'A comparison of the azimuthwise integration methods used in the rotor performance computer programs', *Westland Helicopters Res. Memo.* 55, 1969.
17. Hohenemser, K. H., 'Hingeless rotorcraft flight dynamics', *AGAR Dograph* 197, 1974.
18. Young, M. I., 'A simplified theory of hingeless rotors with application to tandem helicopters', *Proc. 18th Annual natn. Forum Am. Helicopter Soc.*, 1962.
19. Simons, I. A., 'Some thoughts on a stability and control research programme with special reference to hingeless rotor helicopter', *Westland Helicopters Res. Memo.* 79, 1970.
20. Curtiss, H. C., jnr and Shupe, N. K., 'A stability and control theory for hingeless rotors', *27th Annual natn. Forum Am. Helicopter Soc.*, Preprint 541, 1971.
21. Bramwell, A. R. S., 'A method for calculating the stability and control derivatives of helicopters with hingeless rotors', *Res. Memo. City Univ. Lond. Aero.* 694, 1969.
22. Bramwell, A. R. S., 'Further note on the calculation of the hub moments of a hingeless helicopter rotor', *Res. Memo. City Univ. Lond. Aero.* 71/2, 1971.

Rotor induced vibration

8.1 Introduction

We have seen in Chapter 3 that the aerodynamic loads on a helicopter rotor blade vary considerably as it moves round the rotor disc, and in steady flight these loads are periodic. The rotor forces and moments causing fuselage vibration are transmitted from the blades to the rotor hub and then by means of the main rotor drive shaft into the main rotor gearbox bearings and hence into the gearbox casing, and finally into the fuselage at the gearbox attachment points.

Again, as we saw in Chapter 3, these loads arise from the aerodynamic forces on the rotor blades, together with the inertia forces produced by the flapping and lagging motions of the blade.

In addition to the main rotor loads, tail rotor force fluctuations may also be of concern but in the vast majority of cases the main rotor forcing is the prime cause of unwanted vibration.

The control of vibration is important for four main reasons:

- (i) to improve crew efficiency, and hence safety of operation;
- (ii) to improve the comfort of passengers;
- (iii) to improve the reliability of avionic and mechanical equipment;
- (iv) to improve the fatigue lives of airframe structural components.

Hence it is very important to control vibration throughout the design, development and in-service stages of a helicopter project.

It may be appreciated from section 3.11 that the generation of oscillatory aerodynamic loads at frequencies which are integral multiples of the rotational speed is fundamental to the edgewise operation of the rotor in forward flight, and hence forced vibrations of the helicopter cannot be entirely eliminated. Therefore the efforts of the design and development organisations must be devoted to the minimisation of the vibratory loads and to the minimisation of the fuselage response.

Subsequent sections of this chapter will indicate how this is achieved, although it

should be recognised that it is not yet possible to predict accurately the vibration level of a helicopter in a specific flight condition. However, much valuable information can be generated which can lead to an acceptable standard of vibration.

8.2 The exciting forces

The hub forces and moments from each blade can be resolved into force components X , Y , Z , and moment components L , M , N relative to fixed axes in the helicopter, Fig. 8.1. The axes are taken to conform with standard stability notation, i.e. with the Z axis pointing downwards along the hub axis and the Y axis pointing to starboard. The moment N can be disregarded since it forms part of the rotor torque.

In Chapter 1, section 1.11, we defined the rotating reaction forces along and perpendicular to the hub axes as R_1 , R_2 , R_3 , Fig. 8.2.

If ψ is the azimuth angle of the zeroth (reference) blade, the azimuth angle of the k th blade is $\psi_k = \psi + 2\pi k/b$. The corresponding components in the fixed X , Y , Z directions are given by

$$X_k = -R_{1k} \cos \psi_k + R_{2k} \sin \psi_k$$

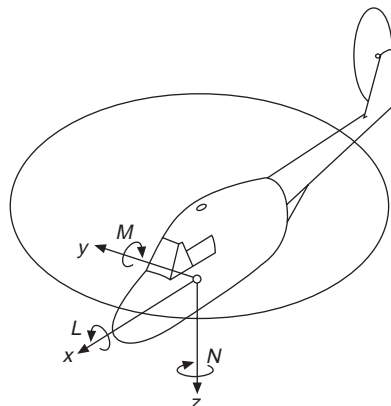


Fig. 8.1 Force components resolved along helicopter body axes

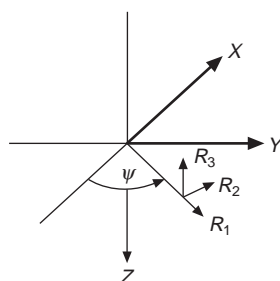


Fig. 8.2 Reactions at blade hinge

$$Y_k = R_{1k} \sin \psi_k + R_{2k} \cos \psi_k$$

$$Z_k = -R_{3k}$$

Now, in steady flight the forces R_{1k}, R_{2k}, R_{3k} will be periodic and therefore expressible in the form of a Fourier series as

$$\begin{aligned} R_{1k} &= P_0 + P_1 \cos \psi_k + P_2 \cos 2\psi_k + P_3 \cos 3\psi_k + \dots \\ &\quad + Q_1 \sin \psi_k + Q_2 \sin 2\psi_k + Q_3 \sin 3\psi_k + \dots \end{aligned} \quad (8.1)$$

$$\begin{aligned} R_{2k} &= S_0 + S_1 \cos \psi_k + S_2 \cos 2\psi_k + S_3 \cos 3\psi_k + \dots \\ &\quad + T_1 \sin \psi_k + T_2 \sin 2\psi_k + T_3 \sin 3\psi_k + \dots \end{aligned} \quad (8.2)$$

$$\begin{aligned} R_{3k} &= U_0 + U_1 \cos \psi_k + U_2 \cos 2\psi_k + U_3 \cos 3\psi_k + \dots \\ &\quad + V_1 \sin \psi_k + V_2 \sin 2\psi_k + V_3 \sin 3\psi_k + \dots \end{aligned} \quad (8.3)$$

Considering the force components along the shaft first, the total force in the Z direction is

$$Z = - \sum_{k=0}^{b-1} R_{3k} = -bU_0 - \sum_{n=1}^{\infty} \sum_{k=0}^{b-1} U_n \cos n\psi_k - \sum_{n=1}^{\infty} \sum_{k=0}^{b-1} V_n \sin n\psi_k$$

From the results of Appendix A.3, the summations can be simplified to give

$$\begin{aligned} Z &= -b[U_0 + U_b \cos b\psi + U_{2b} \cos 2b\psi + \dots \\ &\quad + V_b \sin b\psi + V_{2b} \sin 2b\psi + \dots] \end{aligned} \quad (8.4)$$

Thus, the only harmonics which remain are those which are multiples of the number of blades. If, for example, the rotor has four blades, only harmonics of frequency 4Ω , 8Ω , ..., etc. contribute to the total vertical force, apart from the steady load bU_0 . This result assumes, of course, that all the blades are perfectly matched (track and balance). If one or more blades are not matched, other frequencies Ω , 2Ω , ..., etc. may arise.

Considering now the force components in the plane of the hub, the X force is of the form

$$\begin{aligned} X &= - \sum_{k=0}^{b-1} P_0 \cos \psi_k + \sum_{k=0}^{b-1} S_0 \sin \psi_k \\ &\quad - \sum_{n=1}^{\infty} \sum_{k=0}^{b-1} P_n \cos n\psi_k \cos \psi_k - \sum_{n=1}^{\infty} \sum_{k=0}^{b-1} Q_n \sin n\psi_k \cos \psi_k \\ &\quad + \sum_{n=1}^{\infty} \sum_{k=0}^{b-1} S_n \cos n\psi_k \sin \psi_k + \sum_{n=1}^{\infty} \sum_{k=0}^{b-1} T_n \sin n\psi_k \sin \psi_k \end{aligned} \quad (8.5)$$

If the blades are perfectly matched, P_0 and S_0 are the same for all blades and the first two terms vanish. Using the well known formulae for the products of sines and cosines, the remaining sums can be written as

$$\begin{aligned}
X = & -\frac{1}{2} \sum_{n=1}^{\infty} \sum_{k=0}^{b-1} (P_n + T_n) \cos(n+1)\psi_k - \frac{1}{2} \sum_{n=1}^{\infty} \sum_{k=0}^{b-1} (P_n - T_n) \cos(n-1)\psi_k \\
& - \frac{1}{2} \sum_{n=1}^{\infty} \sum_{k=0}^{b-1} (Q_n - S_n) \sin(n+1)\psi_k - \frac{1}{2} \sum_{n=1}^{\infty} \sum_{k=0}^{b-1} (Q_n + S_n) \sin(n-1)\psi_k
\end{aligned} \tag{8.6}$$

Using the results of Appendix A.3, the first and third sums reduce to $b \cos mb\psi$ and $b \sin mb\psi$, respectively, when $n+1=mb$, i.e. when $n=mb-1$, ($m=1, 2, 3, \dots$), and the second and fourth sums to $b \cos mb\psi$ and $b \sin mb\psi$ when $n=mb+1$. Therefore, X becomes

$$\begin{aligned}
X = & -\frac{1}{2}b \sum_{m=1}^{\infty} [P_{mb-1} + T_{mb-1} + P_{mb+1} - T_{mb+1}] \cos mb\psi \\
& - \frac{1}{2}b \sum_{m=1}^{\infty} [Q_{mb-1} - S_{mb-1} + Q_{mb+1} + S_{mb+1}] \sin mb\psi
\end{aligned} \tag{8.7}$$

Similarly

$$\begin{aligned}
Y = & \frac{1}{2}b \sum_{m=1}^{\infty} [S_{mb-1} - Q_{mb-1} + S_{mb+1} + Q_{mb+1}] \cos mb\psi \\
& + \frac{1}{2}b \sum_{m=1}^{\infty} [P_{mb-1} + T_{mb-1} - P_{mb+1} + T_{mb+1}] \sin mb\psi
\end{aligned} \tag{8.8}$$

Thus, if a blade of a three-bladed rotor produces a force $F=R_2 \cos 2\psi$ on the hub, the corresponding X and Y force components are $-R_2 \cos 2\psi \cos \psi$ and $R_2 \cos 2\psi \sin \psi$ respectively. By expressing the trigonometrical products as the sums of sines and cosines, these components are $-\frac{1}{2}R_2 \cos 3\psi$ and $-\frac{1}{2}R_2 \cos \psi$ in the X direction and $\frac{1}{2}R_2 \sin 3\psi$ and $-\frac{1}{2}R_2 \sin \psi$ in the Y direction. But since $n+1=b$, for this case, the terms in 3ψ add, whereas the terms in ψ cancel. If, however, $F=R_3 \cos 3\psi$, the X and Y components for the individual blade would consist of terms in 2ψ and 4ψ , but for the complete three-bladed rotor these terms would vanish since neither $(n+1)$ nor $(n-1)$ is equal to b .

The type of hub influences the vibratory loading systems applied to the fuselage. The vibratory pitch and roll moments generated by an articulated rotor are significantly smaller than those produced by a semi-rigid or hingeless rotor.

The choice of the number of blades is also important. This is primarily due to two effects. First, the level of aerodynamic oscillatory loading tends to decrease as the harmonic order increases, and since the $b\Omega$ forcing is the prime cause of fuselage vibration, the larger the number of blades, the smaller will be the basic aerodynamic vibratory input.

Figure 8.3 shows the predicted rotor head loadings for a typical medium weight helicopter with a semi-rigid hub and four or five blades through the forward speed range. It indicates a very significant reduction in hub vibratory moments when five blades are used, which is primarily due to the fact that the 3Ω aerodynamic loading is not transmitted to the fuselage with a five bladed rotor.

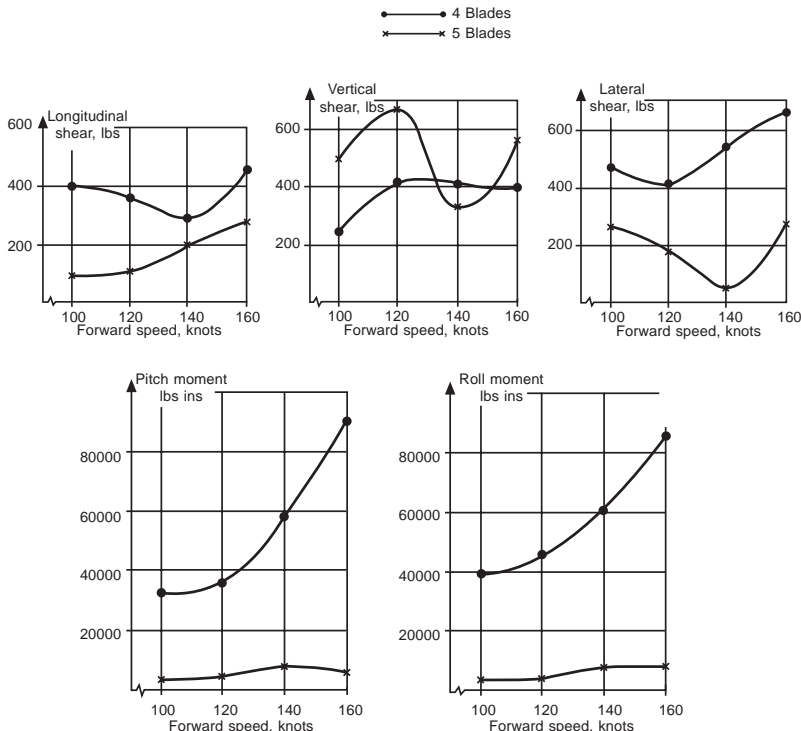


Fig. 8.3 Comparison of four and five blade hub loads

8.3 The dynamic design of rotor blades

The successful design of a helicopter rotor system is concerned with meeting the exacting dynamic requirements which it is necessary to satisfy if acceptable behaviour is to be achieved in the areas of handling qualities, fuselage vibration levels, acceptable airframe and rotor blade fatigue lives, and rotor system aeroelastic stability. The trend towards increasing mechanical simplification combined with increased aerodynamic and structural efficiency has intensified the difficulties experienced in achieving the optimum dynamic characteristics. However, the particular properties of composite materials, often used in a hybrid glass and carbon form of construction, have more readily enabled the design aims to be met.

The correct dynamic design of rotor blades is essential for two main reasons:

- the minimisation of the amplification of the rotor blade aerodynamic vibratory loading which is transmitted to the fuselage; and
- the minimisation of the total vibratory loading of the blade to provide an acceptable fatigue life.

For many years, helicopters utilised rotor blades of essentially constant radial

distributions of mass and stiffness, and their dynamic characteristics, when associated with a rotor hub having a low offset of flapping hinge, and a modest helicopter cruise speed, led to a not very satisfactory but acceptable situation. However, the advent of rotor systems with higher actual or effective offsets of flapping hinge, together with helicopter cruise speeds in excess of 150 knots, has led to the necessity for refining the structural design of the rotor blade to offset the increase in vibratory loading due to the above effects.

Figure 8.4 indicates the unsatisfactory positioning of natural frequencies which occurs if rotor blades of constant radial structural properties are associated with a rotor hub having a significant effective offset of flapping hinge.

The proximity of the second and third flapping mode frequencies to the 3Ω and 5Ω aerodynamic forcing loads will lead to high vibratory fatigue loading of the blades and, for the case of a four-bladed rotor, large 4Ω pitch and roll moments transmitted to the airframe.

Figure 8.5 indicates the situation that could be achieved utilising the design flexibility

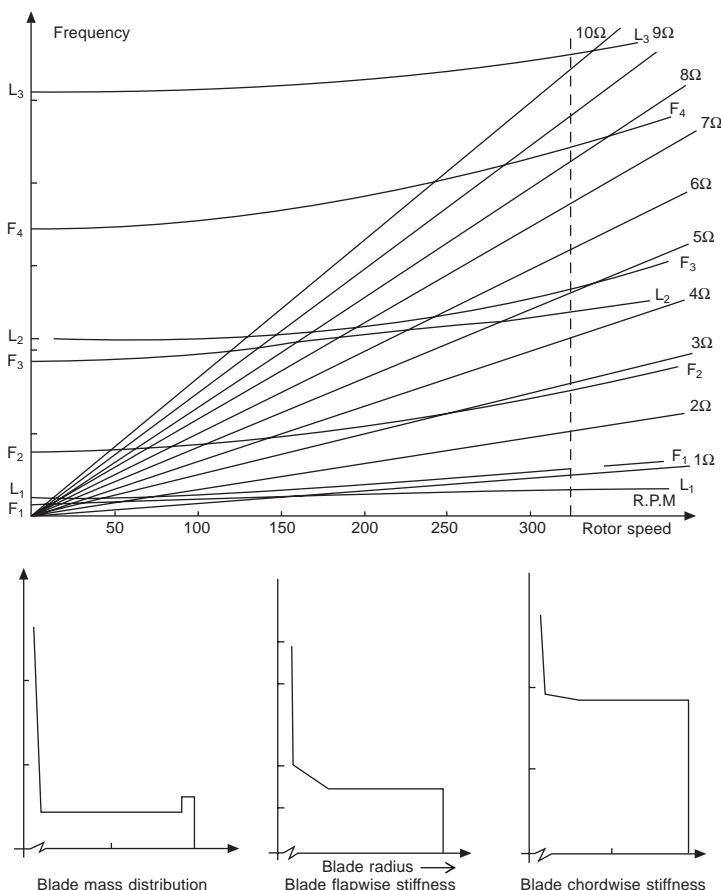


Fig. 8.4 Frequency spectrum for blade with constant radial properties

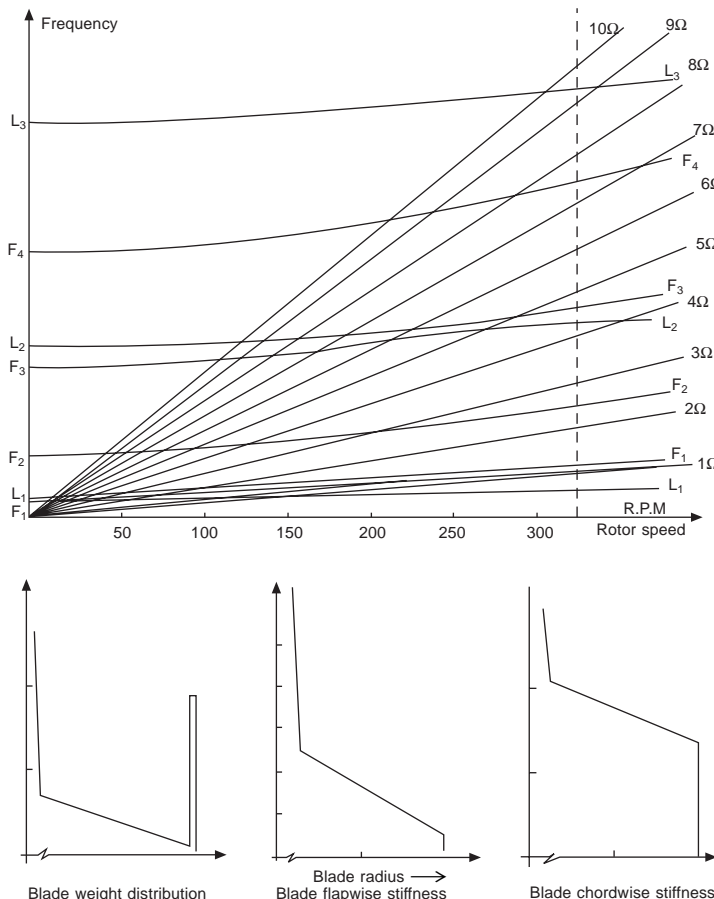


Fig. 8.5 Frequency spectrum for blade with tapered radial properties

possible using a hybrid combination of composite materials to produce a significant degree of mass and stiffness taper along the blade span. This improvement is characterised by the separation of the second and third flapping mode frequencies from the 3Ω and 5Ω aerodynamic forcing frequencies respectively. Calculations indicate that the 4Ω moment applied to the fuselage is reduced by 47 per cent for the improved design.

The ratio of material properties that strongly influences the dynamic characteristics of a blade is the modulus of the material divided by the density, i.e. E/ρ and E_s/ρ . As the values of these are essentially constant for all normally used metals, the scope for the dynamic tuning of metal blades is severely limited.

However, for fibre reinforced composite materials, the values of E/ρ can vary from 50 per cent to 250 per cent of the typical metal values, and the value of E_s/ρ can vary from 20 per cent to 200 per cent of the metal values, dependent upon fibre type and orientation.

Modern composite blades can use a mixture of glass and carbon fibre, and the

required values of flapwise, lagwise and torsional stiffnesses can be achieved almost independently.

Figure 8.6 indicates a possible method of achieving satisfactory dynamic characteristics.

Flapwise stiffness can be adjusted without affecting lagwise or torsional stiffness by introducing discrete layers of carbon fibre on the upper and lower surfaces of the glass fibre D-spar. The lagwise stiffness can be adjusted by introducing carbon fibre in a spanwise sense at the extreme trailing edge of the blade without affecting flapwise or torsional stiffness. Control of torsional stiffness is best achieved by selecting the appropriate fibre type and orientation for the trailing edge skins.

The desirable characteristics of spanwise taper of mass and stiffness can be readily obtained by the selective introduction of unidirectional carbon fibre in the spanwise sense on the upper and lower walls of the main spar section.

8.4 Main rotor gearbox mounting systems

In order to minimise the vibratory forces fed into the fuselage, various methods of mounting the main rotor gearbox have been used.

The following descriptions form a representative selection of the main passive systems which have been used with varying degrees of success.

- (i) Simple soft mounting of the rotor/gearbox/engine system (Fig. 8.7). Soft suspension systems derive from the principle illustrated by the simple single degree of freedom sprung mass undergoing forced vibration that may be found in student textbooks on vibrations, e.g. Thomson¹. The force transmitted through the spring to the support is seen to be reduced the lower the ratio of natural frequency to excitation frequency becomes.

Since the quasi-static deflections of the suspended system would be unacceptably large if conventional soft mountings are placed at the gearbox

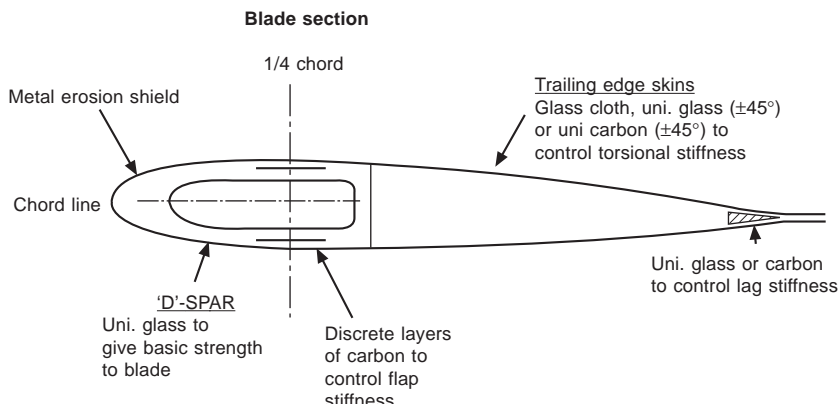


Fig. 8.6 Composite blade construction

feet, it becomes necessary to isolate as large a mass as possible. Hence it is attractive to mount the gearbox and engines on a raft, and then attach the raft to the fuselage using the chosen mountings. By this means, an adequately low natural frequency of the isolated system can be achieved without unacceptably large displacements of the rotor, gearbox, engines and controls under trim and manoeuvre loads. However, attenuation of the vibratory forces by this means is only modest and certain loadings may be transmitted without any reduction.

- (ii) A rotor/gearbox/engine mounting system designed to respond to the $b\Omega$ forcing frequency in such a manner that the spring and inertia forces generated by the response cancel, as far as possible, the effects of the rotor generated forcing (Fig. 8.8).

For example, a possible design criterion for such a system could be the minimisation of the total $b\Omega$ frequency pitching moment at the helicopter centre of gravity. The attenuation efficiency of such a system would only be optimal for a specific flight condition having a particular relationship between the rotor hub forces and moments.

- (iii) Systems employing the Dynamic Anti-Resonant Vibration Isolator (DAVI)¹. Originally developed for the isolation of crew seats by the Kaman company, this principle has been applied very successfully to the mounting of the gearbox².

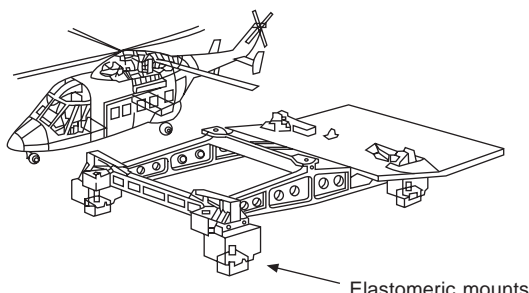


Fig. 8.7 Westland W-30 raft mounting system

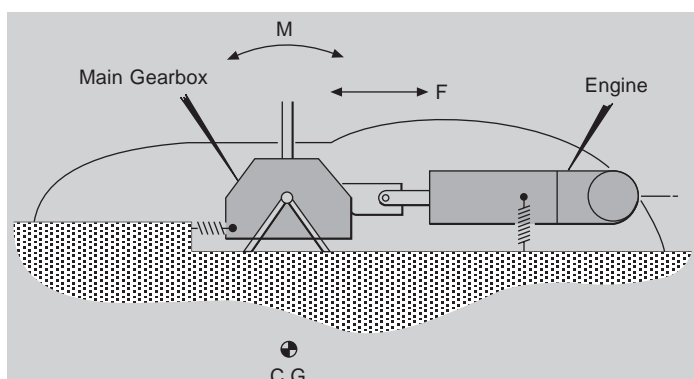


Fig. 8.8 Flexibly mounted gearbox and engine system

Figure 8.9 illustrates its use and response characteristics. An appreciation of how the vibration reduction is achieved may be obtained by study of the simplified but equivalent model shown in Fig. 8.10. In this, the upper mass M_1 represents the gearbox and rotor, and M_2 the helicopter fuselage, and between them is mounted a rigid arm, which carries a small mass m_{bob} (the ‘bobweight’) at its tip.

The equations of motion when there is no damping are easily obtained as

$$\begin{bmatrix} -\omega^2 [M_1 + m_{\text{bob}}(1 + \Lambda_b)^2] + K & \omega^2 m_{\text{bob}} \Lambda_b (1 + \Lambda_b) - K \\ \omega^2 m_{\text{bob}} \Lambda_b (1 + \Lambda_b) - K & -\omega^2 [M_2 + m_{\text{bob}}(1 + \Lambda_b)^2] + K \end{bmatrix} \begin{bmatrix} x_1 \\ x_2 \end{bmatrix} = \begin{bmatrix} F_0 e^{i\omega t} \\ 0 \end{bmatrix}$$

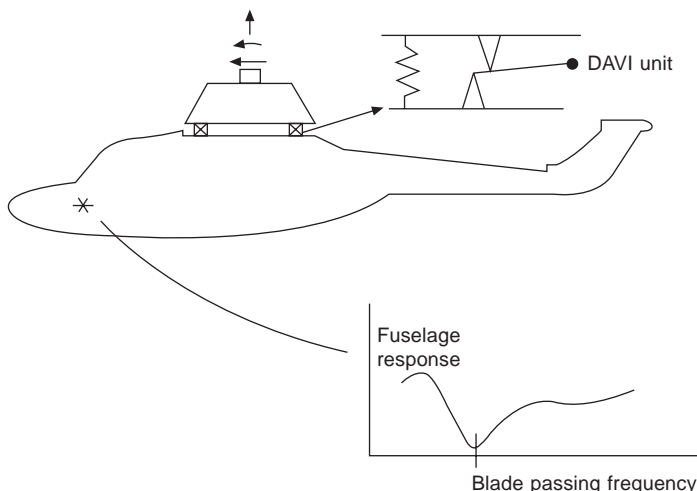


Fig. 8.9 The DAVI gearbox mounting system

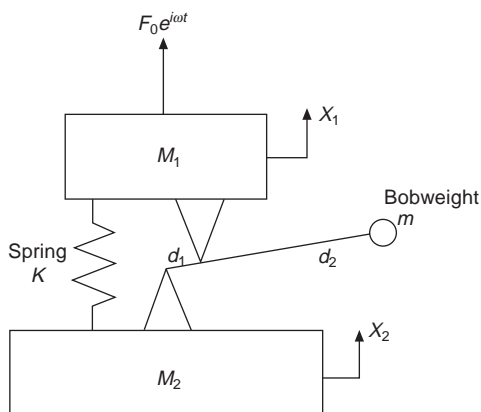


Fig. 8.10 Simplified DAVI model

where F_0 is the amplitude of the exciting force and $\Lambda_b = d_2/d_1$ is the ratio of lengths of the rigid arm either side of the mounting point on M_1 . The system is seen to be ‘free-free’ so the net linear momentum is zero at all instants of time. This leads to a relationship between x_1 and x_2 which is used to eliminate x_1 from one of the equations, allowing the following expression for x_2K/F_0 (the normalised fuselage response) to be formed.

$$\frac{x_2 K}{F_0} = \frac{[\tilde{\omega}^2 \mu_b \Lambda_b (1 + \Lambda_b) - 1]}{[\tilde{\omega}^2 \mu_b \Lambda_b (1 + \Lambda_b) - 1]^2 - [1 - \tilde{\omega}^2 (1 + \mu_b \Lambda_b^2)] [1 - \tilde{\omega}^2 (\rho_m + \mu_b (1 + \Lambda_b)^2)]}$$

The main parameters of the system are the fuselage to gearbox and rotor mass ratio $\rho_m = M_2/M_1$, the bobweight mass ratio $\mu_b = m_{\text{bob}}/M_1$, the bobweight arm length ratio Λ_b , and the normalised excitation frequency $\tilde{\omega} = \omega(K/M_1)^{-1/2}$. The denominator of the response expression is the characteristic equation for the system, the roots of which provide the natural frequencies (one of which is zero, since the system is ‘free-free’), and the numerator similarly provides the zero response frequency. The latter shows that the bobweight mass is reduced as Λ_b is increased. However, there is a practical upper limit, since the greater the ratio is, the stiffer, and hence the heavier, the arm becomes. Figure 8.11 shows the variation of the response amplitude with excitation frequency for the simple undamped DAVI model for a particular set of chosen parameters.

The DAVI unit can provide a very high attenuation over a narrow frequency range, whilst utilising a value of spring stiffness which overcomes the problem of excessive quasi-static deflections. The system is also relatively insensitive to variations in the isolated mass. The balance between the degree of attenuation

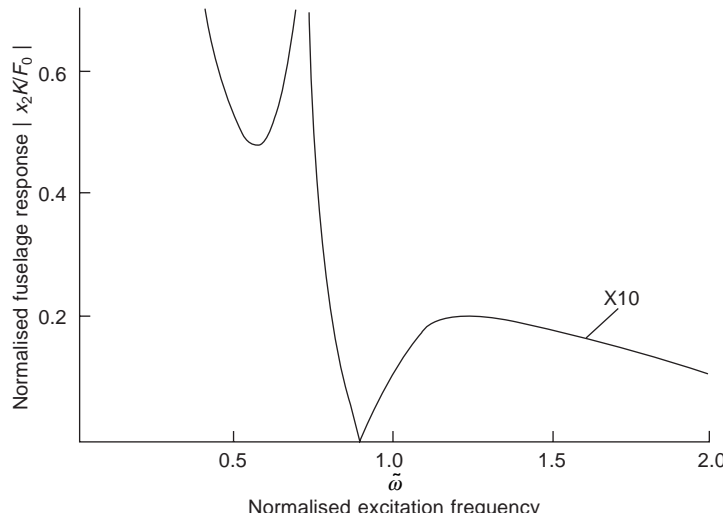


Fig. 8.11 Response amplitude of simplified DAVI model as a function of excitation frequency ($\Lambda_b = \rho_m = 10$, $\mu_b = 0.01$). Note: amplitudes on right-hand section of curve are multiplied by ten.

and the ability to cater for variations in rotor speed can be controlled by the amount of damping built into the DAVI units.

(iv) The Bell 'Nodamatic' gearbox mounting system³

This method (Fig. 8.12) interposes a beam mounting arrangement between the gearbox and the fuselage and is configured such that the fuselage is effectively suspended from the node points of the beam system when it is vibrating in response to the rotor hub forcing loads and moments. In fact, the system is mathematically equivalent to the DAVI principle, with the beam system providing the stiffness and inertia properties of the DAVI units.

8.5 Dynamic response of the fuselage

Due to the fundamental design requirements of the helicopter primarily in terms of the requirements of crew and equipment, and aerodynamic drag, the basic shape of the fuselage will be determined by considerations other than its vibrational characteristics. In the early stages of design, the fuselage can be represented by an assemblage of beams of defined bending and torsional stiffness properties (Fig. 8.13) together with the appropriate mass distribution.

Calculations can then be performed which will:

- (i) indicate the rough proximity of any major beam bending mode frequency to the $b\Omega$ rotor forcing frequency; and
- (ii) indicate the sensitivity of the forced response to changes in the stiffness of structural components which may be amenable to significant alteration, e.g.

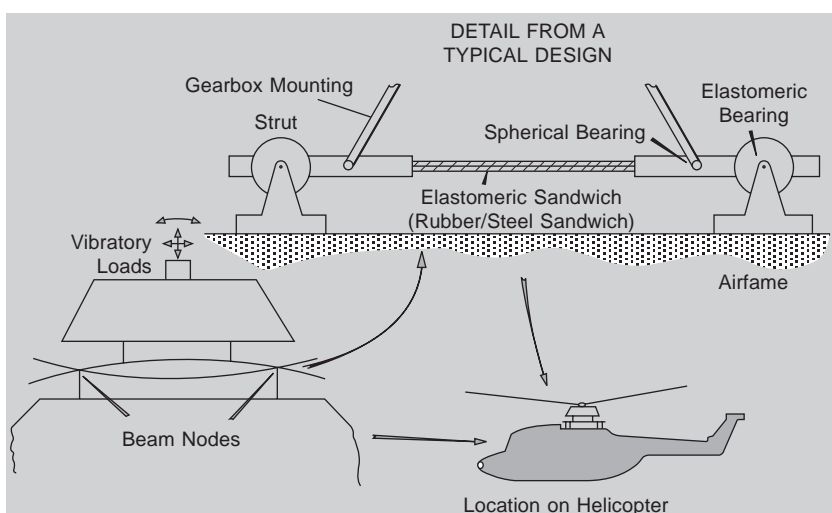


Fig. 8.12 Principle of the nodal beam mounting system

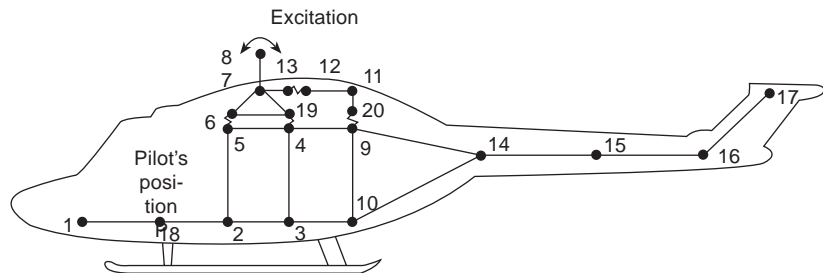


Fig. 8.13 Fuselage beam (stick) model

main rotor head stiffness relative to the fuselage, and tail boom stiffness. Thus, if ground vibration or flight tests indicate evidence of a major forced response problem, it may be possible to significantly reduce the response by making an acceptable change to the structural stiffness in a particular area (Figs 8.14 and 8.15).



Fig. 8.14 Army Lynx with struts on tailcone

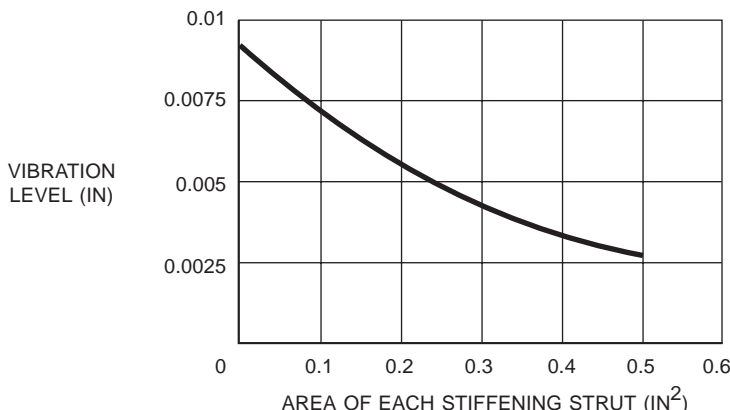


Fig. 8.15 Lynx cockpit 4R vibration as a function of strut stiffness

An extension of this approach referred to as ‘structural manipulation’ has been developed whereby an order of ranking of areas of structural sensitivity is determined (Fig. 8.16). The method⁴ then optimises the values of stiffness changes required in a chosen number of structural elements to minimise a defined ‘index of performance’ which could be in the form of the vibrational response in a designated area of the fuselage due to specified forcing components applied at a defined location.

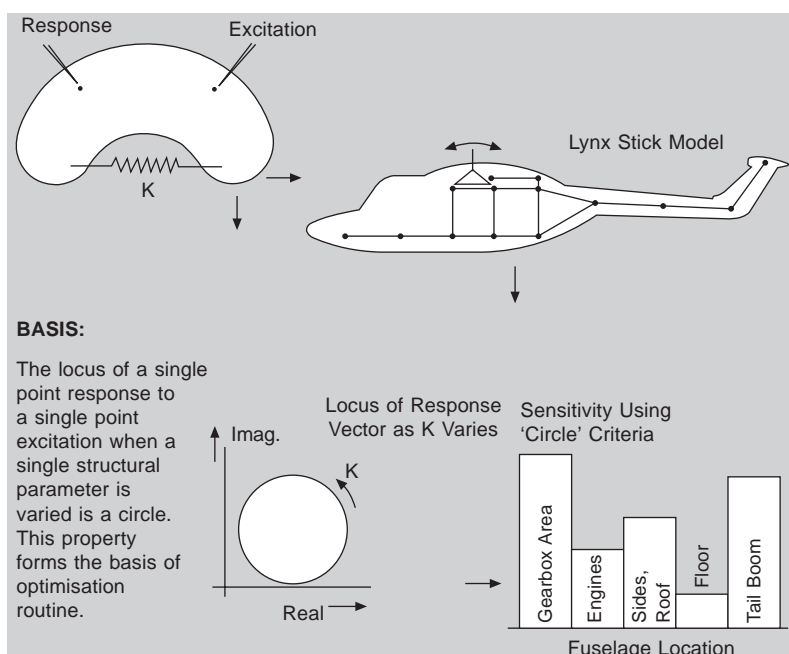


Fig. 8.16 Structural manipulation

When the structural design of the fuselage is at a more advanced stage, a finite element method of dynamic analysis such as NASTRAN⁵ will be used to predict more accurately the dynamic response characteristics of the airframe. Figure 8.17 indicates a typical finite element model.

Due to difficulties in assessing the stiffness properties of structural joints, the results of such calculations will be used to predict trends in the dynamic behaviour of the fuselage as a result of possible changes in stiffness and mass distribution. Following manufacture and vibration test of a prototype airframe, the finite element model would be empirically adjusted to match the test results. The use of the adjusted model will increase confidence in subsequent analytical predictions, from which beneficial design changes may result.

8.6 Vibration absorbers

Having made all the beneficial stiffness and mass distribution changes which are possible without major redesign, it may still be the case that the levels of vibration experienced in flight at crew stations or passenger locations are unacceptable.

In this case, it will be necessary to have recourse to additional methods of vibration reduction which can be incorporated with minimum disturbance to the existing design.

The absorbers described in this section are all based on the principle of the simple sprung mass vibration absorber described and analysed in vibration text-books¹. This shows that by attaching an extra small mass by means of a spring or elastic mount to a body undergoing forced vibration, the amplitude of vibration can be reduced to zero (if the system is undamped, as in the ideal case), or nearly zero for small damping, if the natural frequency of the sprung mass by itself is made to coincide with that of the forcing frequency.

The available absorbers may be conveniently divided into two categories:

- (i) those designed to reduce overall levels of vibration throughout the fuselage;
- (ii) those designed to produce a reduction in vibration in a local area of the fuselage.

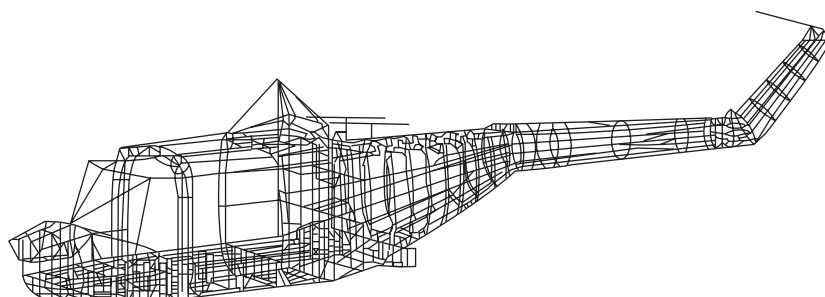


Fig. 8.17 Fuselage finite element model

Passive methods which fall into the first category are:

- (a) The rotor head mounted vibration absorber, of which two distinct types have been successfully employed:
- (i) The centrifugal pendulum (bifilar) absorber⁶ as developed by Sikorsky (Fig. 8.18.)

In the bifilar type, the required spring stiffness is provided by centrifugal force and hence the natural frequency of the device varies with rotor speed, as does the forcing frequency. Thus the bifilar absorber exhibits a degree of self-tuning with respect to changes in rotor speed.

Since the natural frequency also depends on the square root of the ratio of mounting radius to pendulum length, the small value of the latter which the bifilar geometry confers allows a practical design which can be mounted close in to the centre of the hub.

Figure 8.19 illustrates the basic geometry of the bifilar absorber, and also the model from which the following equation of motion can be derived:

$$b \ddot{\gamma} + (a + c) \Omega^2 \gamma = 0$$

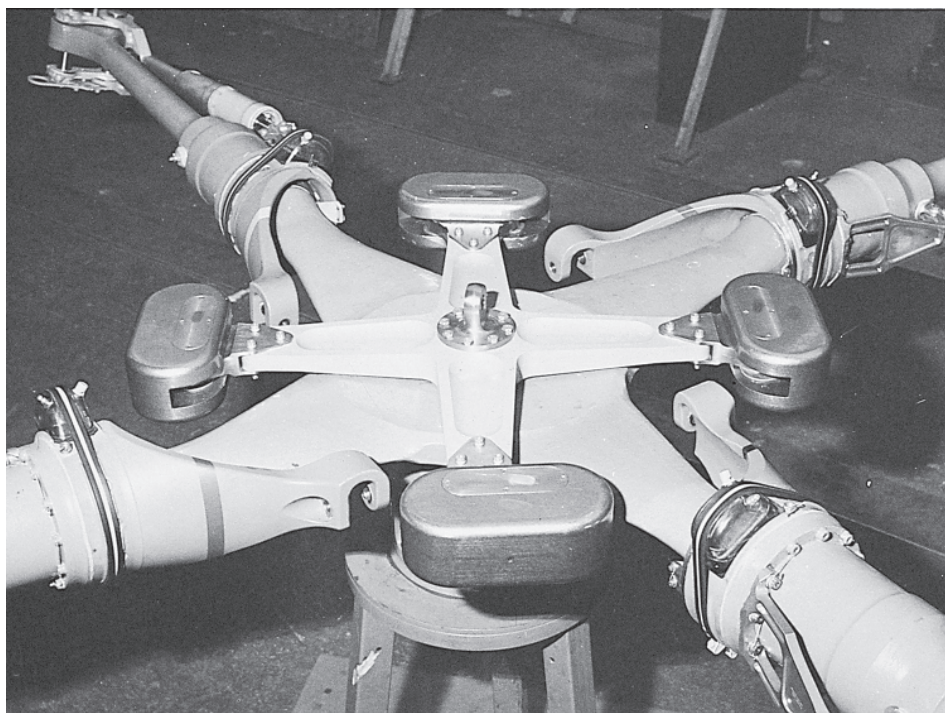
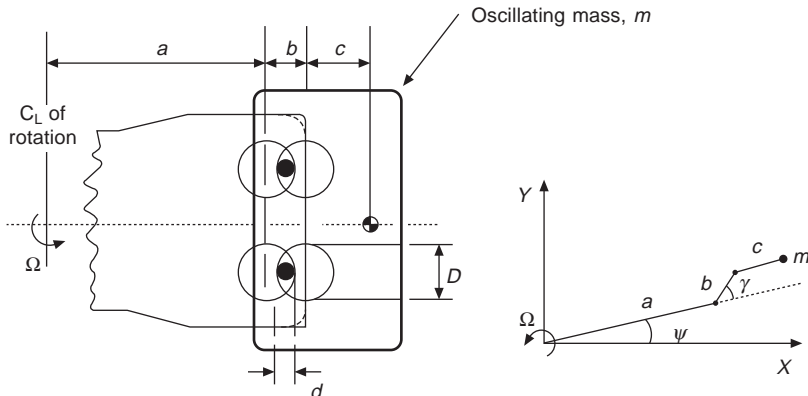


Fig. 8.18 Bifilar absorber fitted to Lynx rotor head

**Fig. 8.19** Geometry and model of the bifilar

where γ is the angular motion of the pendulum arm

a is the offset of the fixed pendulum point from the rotor centre of rotation

b is the effective length of the pendulum

c is the offset of the centre of gravity of the oscillating mass from its pivot point

d is the diameter of the pin connecting the fixed arm and the oscillating mass

D is the diameter of the holes in the fixed arm and the oscillating mass
Thus $b = D - d$

It should be noted that in the model, the arm of length c always remains parallel to the arm of length a .

For the case of small amplitudes of oscillation of the moving mass, we may write $\ddot{\gamma} = \omega_n^2 \gamma$, where ω_n is the natural frequency of oscillation of the moving mass, giving

$$\left(\frac{\omega_n}{\Omega} \right)^2 = \frac{a + c}{D - d}$$

Assuming some typical values of absorber geometry

$$a = 75 \text{ cm} \quad c = 6 \text{ cm} \quad D = 10 \text{ cm}$$

then, for an absorber tuned to 3Ω forcing frequency, the pin diameter, d , is equal to 1 cm. The equivalent pendulum length, $(D - d)$, is equal to 9 cm, thus confirming its very small value.

However, due to the large oscillatory amplitude necessary to provide adequate force from a device of acceptable mass, the absorber exhibits a tuning non-linearity with respect to amplitude and hence flight condition. Other features of this type of absorber include the fact that a single bifilar can only reduce the

magnitude of either the $(b - 1)\Omega$ or the $(b + 1)\Omega$ components in the rotating system, the relatively low ratio of mass producing the cancelling force to the total installed mass, and the significant maintenance requirements necessary to maintain minimum damping of the moving mass.

Applications include the S-61 series, the Black Hawk and the S-76 Sikorsky helicopters. The S-76 uses two bifilars tuned to 3Ω and 5Ω forcing frequencies.

- (ii) The fixed frequency 'flexispring' absorber⁷ as developed by Westland (Fig. 8.20). This type of absorber utilises glass fibre reinforced plastic for the spring material, and operates efficiently over the small variation of rotor speed about the governed datum typical of the modern rotor speed control system. The rate of force-cancelling mass to total installed mass is high, it responds to the total $b\Omega$ frequency forcing, and requires no maintenance. Applications include the Westland Lynx and W.30 helicopters.

Figure 8.21 indicates the effect of the Flexispring absorber on the cockpit vibration levels of the Westland 30 as a function of forward speed.

It should be noted that, although both the above types of absorber can only generate oscillatory forces in the plane of the rotor system, they will respond beneficially to any forced response mode which involves in-plane motion of the rotor head, resulting from the total applied rotor forcing system.

- (b) A centrifugal pendulum type of absorber mounted on the rotor blade⁸. This type of absorber has been used on the Bolkow Bo 105 and Hughes 500 helicopters. Figure 8.22 shows the Hughes installation which consists of

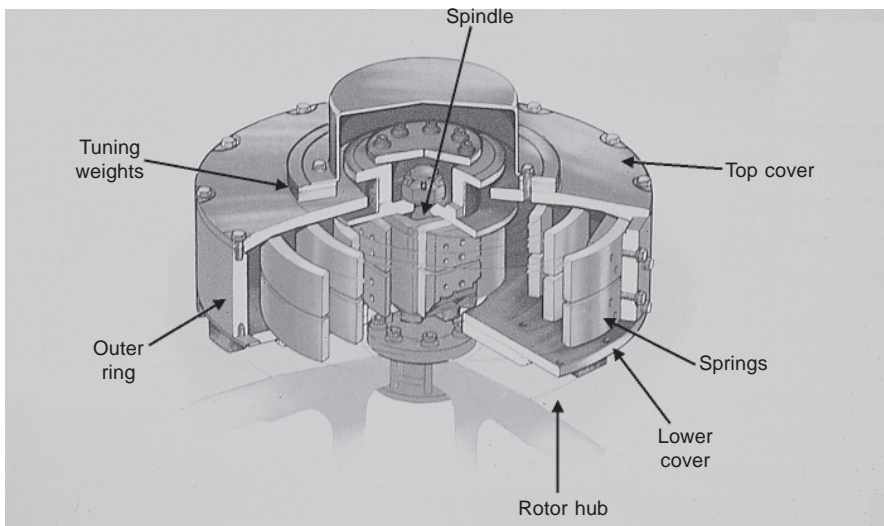


Fig. 8.20 Flexispring absorber

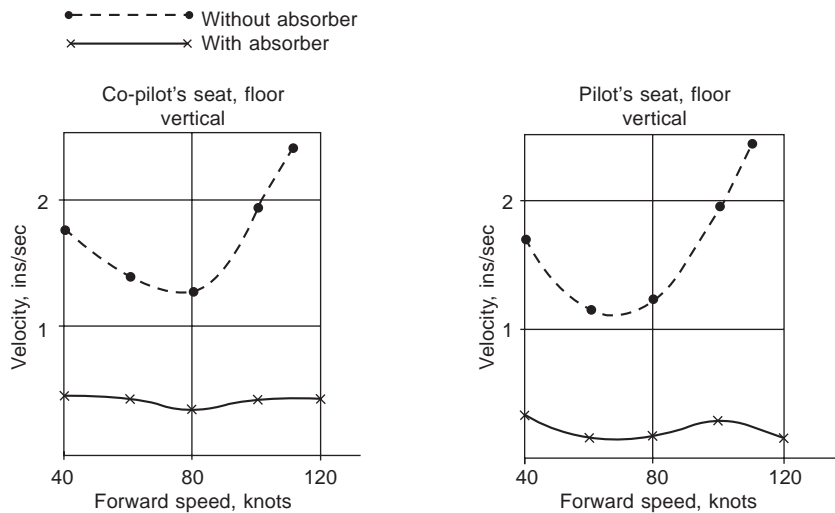


Fig. 8.21 Effect of the vibration absorber on Westland 30 4R vibration

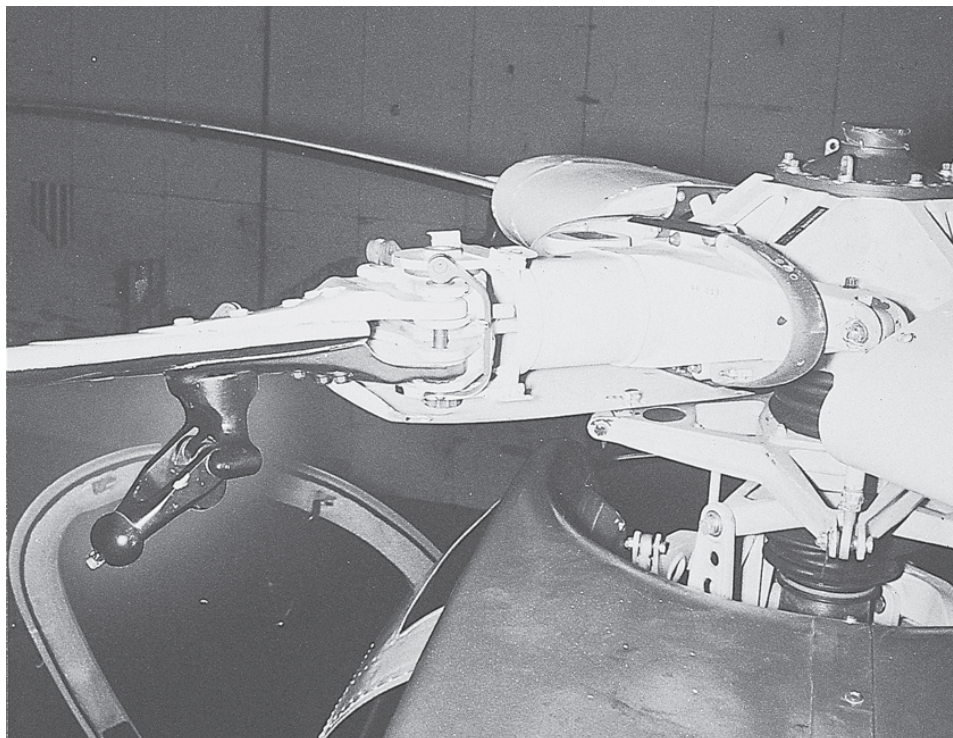


Fig. 8.22 Hughes blade mounted pendulum absorber

absorbers tuned to the 3Ω and 5Ω excitation frequencies for the four-bladed rotor version, where their purpose is to reduce the response of the second and third flapwise bending modes of the blade to the 3Ω and 5Ω frequency oscillatory air loads in the rotating system.

Passive methods which fall into the second category are:

- (a) The fuselage mounted classical mass-spring absorber.

This involves the mounting of a suitably heavy mass, usually situated in the local region of the operating crew and passengers, tuned to the $b\Omega$ forcing frequency. Use may be made of an existing heavy item such as the aircraft battery, as in the Sea-King helicopter (Fig. 8.23 shows the installation), or the mass may be parasitic, as in certain models of the Boeing Vertol Chinook helicopter. In the former case, the natural frequency of the absorber is constant, and to be effective the inherent damping of the moving mass must be minimal so that the amplification at resonance is large. However, under such circumstances the efficiency of the absorber will decline with excursions of rotor speed away from the nominal governed value. This particular disadvantage is overcome in the case of the Chinook helicopter by the use of an electrically actuated system which changes the effective value of the sprung mass in accordance with changes in rotor speed.

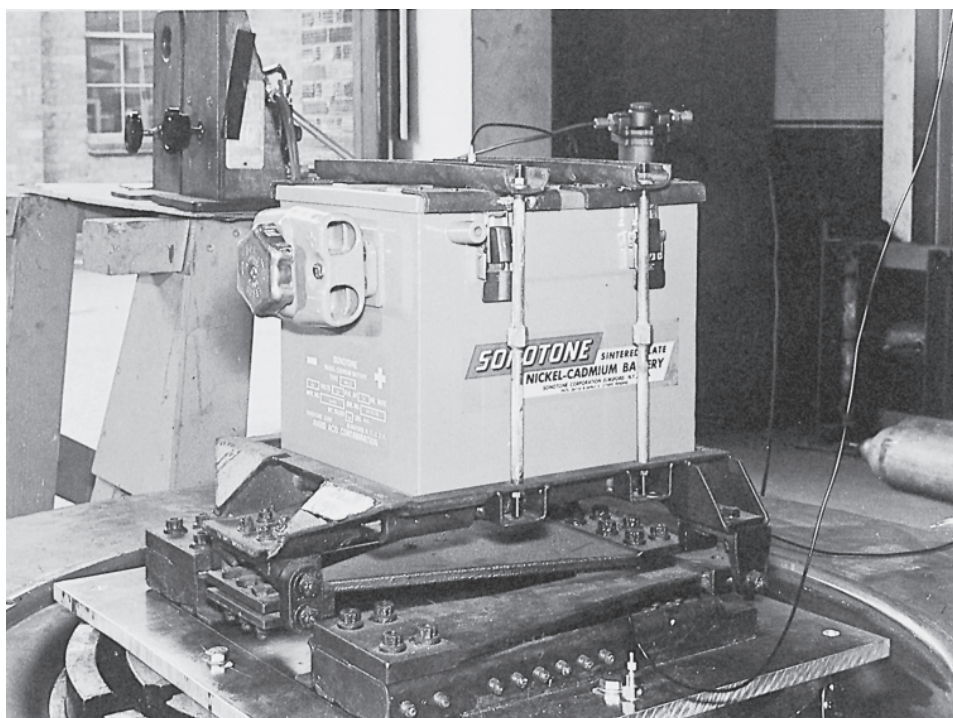


Fig. 8.23 Sea King battery vibration absorber

8.7 Active control of vibration

Recent developments in the reduction of helicopter vibration by the use of active control systems have produced encouraging results. These developments have taken place along two quite different approaches.

8.7.1 The application of higher harmonic pitch control to the rotor blades (HHC)⁹

Since airframe vibration originates with the rotor blade oscillatory air loads, a potentially attractive method of vibration control is the application of blade pitch at frequencies greater than the rotor rotational frequency, in order to produce a forcing system generating an airframe response which would oppose that arising from the basic rotor forcing.

Figure 8.24 shows diagrammatically the concept of HHC. The rotor generates oscillatory forces which cause the fuselage to vibrate. Transducers mounted at key locations in the fuselage measure the vibration, and this data is analysed by an onboard computer. Based upon this data, the computer generates, using optimal control techniques, signals which are transmitted to a set of actuators which, typically, vary the blade pitch at frequencies of $(b - 1)\Omega$, $b\Omega$, and $(b + 1)\Omega$. Oscillatory aerodynamic loads are thus produced which modify the total $b\Omega$ frequency response of the fuselage, and the whole cycle of measurement of the modified vibration, data analysis and resultant actuator response is repeated.

Using the appropriate control strategy, the process can be made to converge to minimise the fuselage vibration. Key elements in the successful implementation of HHC are hydraulic actuators with an adequate high-frequency response characteristic and a successful control algorithm.

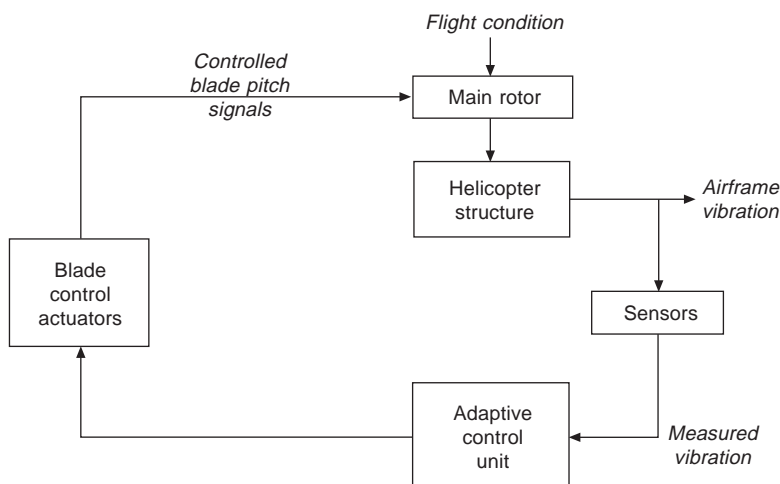


Fig. 8.24 Concept of HHC

The oscillatory blade pitch motions can be applied either through a conventional swashplate or spider control system, or by means of individual blade actuation in the rotating system (Fig. 8.25). In the latter case, the input can be applied near the root of the blade, or by the use of an outboard aerodynamic servo tab.

In defining the control algorithm, self-adaptive techniques are used in order to cater for change in fuselage dynamics (due to loading changes, for example) and rotor behaviour with flight condition.

The control algorithm depends on the assumption of a linear relationship between measured vibration at $b\Omega$ frequency and the higher harmonic rotor forcing of the form

$$\mathbf{Y} = \mathbf{T}\mathbf{X} + \mathbf{B}$$

where \mathbf{Y} is a vector consisting of the $b\Omega$ sine and cosine Fourier components of the measured vibration at a number of fuselage locations. The HHC input \mathbf{X} is a vector consisting of Fourier sine and cosine components of blade pitch at $(b - 1)\Omega$, $b\Omega$ and $(b + 1)\Omega$ frequencies. \mathbf{T} denotes the rotor/fuselage transfer matrix, and \mathbf{B} is the background uncontrolled vibration. Since these parameters vary with flight condition, a statistical estimator (Kalman filter) is used to track them during flight.

The final part of the control system is an optimal controller which uses the estimated \mathbf{T} and \mathbf{B} parameters to minimise the index of performance J , where

$$J = \sum_{i=1}^m W_i Y_i^2 + \sum_{j=1}^n A_j X_j^2$$

where W_i are the relative weightings of the m vibration measurements Y_i and A_j are the relative weightings of the n HHC blade pitch inputs X_j . This index allows for the weighting of the various vibration measuring positions according to helicopter role,

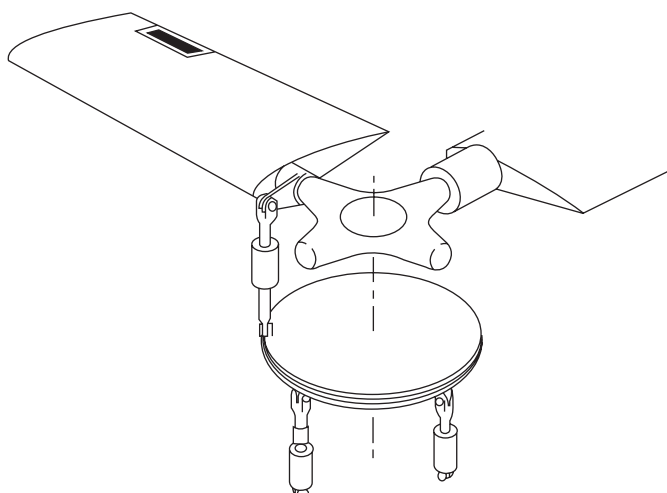


Fig. 8.25 HHC blade pitch actuation

and the ability to limit the authority of the HHC inputs when constrained by the proximity of rotor aerodynamic limits.

The estimates of the \mathbf{T} and \mathbf{B} parameters are continuously updated, which allows the system to adapt to changes in rotor aerodynamic and fuselage dynamic states. Figure 8.26 indicates a typical blade pitch waveform with and without HHC. A feature of some concern is the increase in blade pitch at the 270° retreating blade azimuth position. This could, near the flight envelope boundary, have the effect of introducing a premature onset of blade stall.

It is possible that additional blade area may have to be provided to prevent this.

8.7.2 The active control of structural response (ACSR)¹⁰

Subsequent to the development of HHC, an alternative approach to the active control of helicopter vibration has evolved. This consists of connecting a number of actuators between convenient points on the airframe to apply oscillatory forces to the structure. The magnitude and phase of the loads generated by the actuators are determined by a control algorithm which minimises the vibrational response of the fuselage at a number of key positions. Figure 8.27 shows the basic concept of ACSR.

The basis of ACSR is that, if a force F is applied to a structure at a point P and an equal and opposite force (the reaction) is applied at a point Q, then the effect will be to excite all the modes of vibration of the structure which possess relative motion between points P and Q. This requirement for relative motion in the modal response between the points where the actuator forces are applied is an essential feature of ACSR.

Experience to date has indicated that positioning actuators across the main rotor

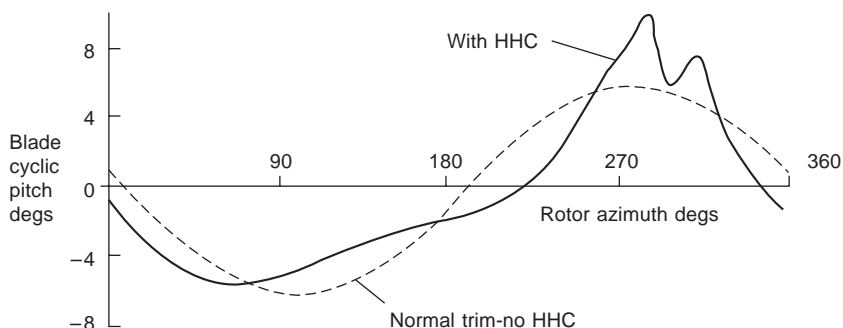


Fig. 8.26 HHC blade pitch waveform

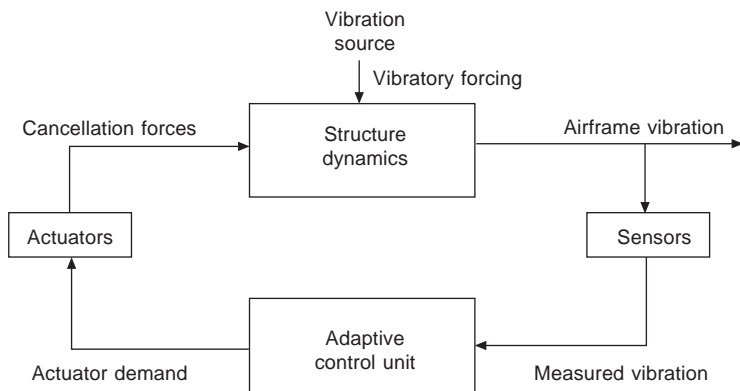


Fig. 8.27 Concept of ACSR

gearbox and fuselage interface is very effective, and Fig. 8.28 shows a method of gearbox attachment which combines the mounting struts with the actuators.

The basic equation relating the various parameters is identical in form to that for HHC,

i.e.

$$\mathbf{Y} = \mathbf{T}\mathbf{X} + \mathbf{B}$$

where \mathbf{Y} is the measured fuselage vibration

\mathbf{X} is the vector of actuator forces

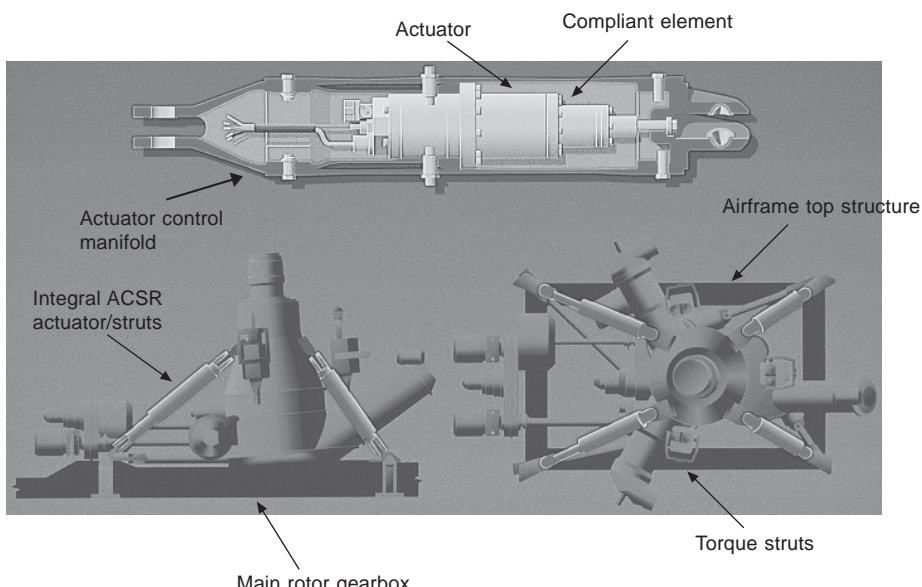


Fig. 8.28 ACSR gear box mounting struts with integral actuators

T is the transfer matrix relating the actuator forces to the fuselage vibration
 B is the background, uncontrolled, vibration

In general, with N control forces, the response at N locations in the fuselage can be reduced to zero, provided that the T matrix is non-singular. However, it is considered preferable to attempt to reduce the vibration at a larger number of locations to acceptably low levels rather than to attempt to achieve zero vibration at a few positions.

Two categories of control algorithm are applicable to the implementation of ACSR. These may be classified as either frequency or time domain in nature. Emphasis has been placed on the frequency domain approach in the early applications of this technique.

The general arrangement for the frequency domain control strategy is shown in Fig. 8.29. This indicates that the primary functions of the controller are signal processing, parameter estimation and control.

As a very broad statement, it appears that active control techniques can produce vibration levels which are in the region of about one-half of the levels achieved by passive methods, and this has indicated that the long-term goal of the 'jet smooth ride' helicopter may at last be a possibility.

Figure 8.30 shows a comparison of the vibration levels of the Westland W30 helicopter without a vibration reduction system, and when fitted with a Flexispring rotor head absorber, and an ACSR system.

8.8 Vibration at frequencies other than $b\Omega$

The minimisation of forcing frequency components from the rotor system which are

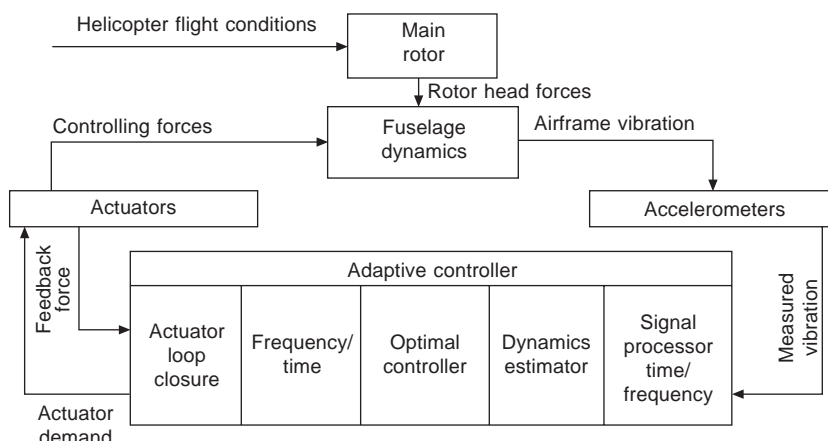


Fig. 8.29 ACSR frequency domain control strategy

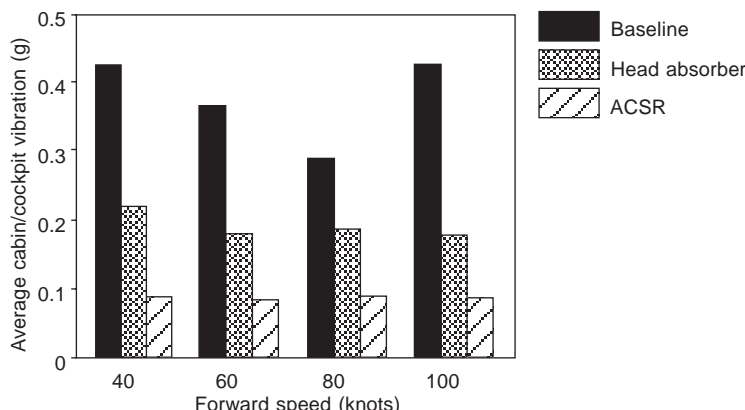


Fig. 8.30 Comparison of Westland W30 vibration levels

normally self-cancelling within the rotor is very much related to the ability to manufacture identical blades and lag dampers. The major residual is usually at 1Ω frequency, and this is minimised by blade balancing and tracking procedures on a whirl tower and on the helicopter during ground running, and if necessary also in hovering and high-speed forward flight.

Reasonably identical lag plane damper performance characteristics are required so that undesirable vibration under conditions of 1Ω blade flapping (which results in large lag plane oscillations) can be avoided.

A quite distinct type of vibration problem which is of aerodynamic origin is due to the effects of vortices shed from the region near the main rotor head which can, under certain flight conditions, strike the tail rotor and the fixed vertical and horizontal tail surfaces. This phenomenon has been observed mainly as a response at the fuselage fundamental lateral bending frequency and is particularly dependent on the sideslip angle in flight. This problem may be intensified by the addition of excrescences such as a radome to the upper surface of the fuselage aft of the rotor.

This problem is often referred to as the 'lateral shakes' or the 'shuffle'. Solutions to this problem have been found by the addition of suitable fairings to the main rotor head and to the airframe aft of the head. Figures 8.31 and 8.32 indicate the origin of

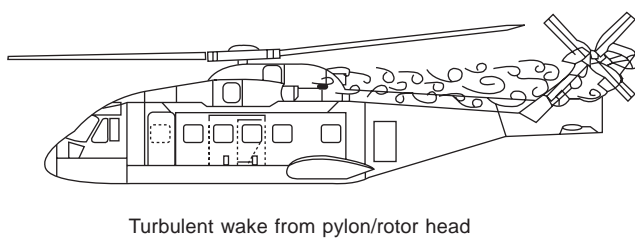


Fig. 8.31 Origin of the 'shuffle' problem

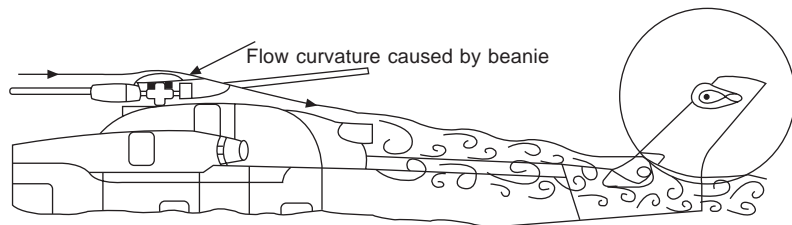


Fig. 8.32 Effect of 'beanie' on the turbulent wake

the problem, and the beneficial effect of the rotor head fairing (often referred to as the 'beanie').

There can also be vibration problems due to mechanical excitation arising from the transmission system. The effects of these sources of vibration can be held to acceptable limits by the correct positioning of shaft whirling speeds, an adequate standard of static and dynamic balancing of main and tail rotor hubs and transmission shafts, and the accurate machining of gear teeth profiles.

8.9 Measurement of vibration in flight

As an example of the vibration amplitudes and forces occurring on a helicopter in

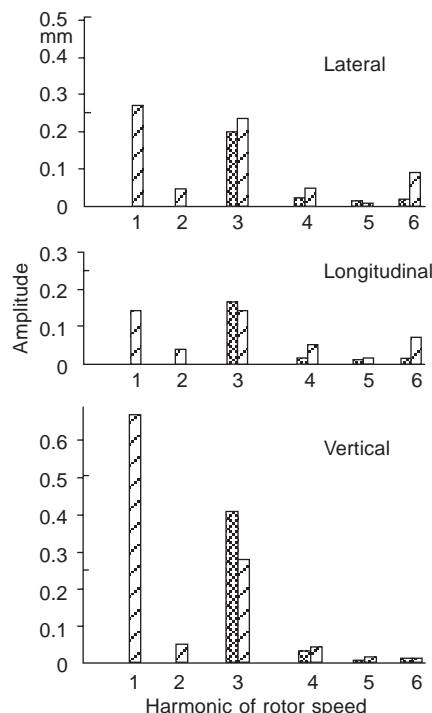


Fig. 8.33 Spectra of vibration amplitudes

flight, we discuss below some results from measurements made at the Royal Aircraft Establishment.* The measurements of the amplitudes and forces in three perpendicular directions were made near the hub of a three-bladed single rotor helicopter over the full range of flight speeds.

The results showed that the amplitude of the first-harmonic vibrations were quite large, as can be seen from the harmonic spectrum, Fig. 8.33. However, the first harmonic measurements showed a large amount of scatter, particularly from flight to flight, and this indicates that the vibration was probably due to a variable amount of rotor blade imbalance. The next largest component of vibration was that of the third harmonic, but the amount of scatter in this case was very small, Fig. 8.34, indicating excitation from aerodynamic and inertia forces of the complete three-bladed rotor, as discussed in section 8.2.

The results shown in Fig. 8.34 show two features in common with those of other helicopter vibration measurements. The first is that the level of vibration generally increases with speed. This is to be attributed, of course, to the increasing asymmetry of the rotor thrust loading and the corresponding increase of the harmonic content in

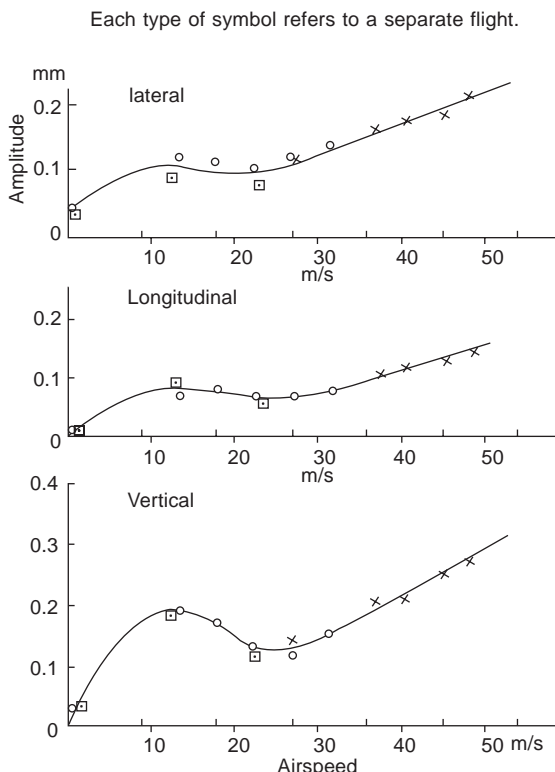


Fig. 8.34 Vibration amplitude as a function of airspeed

*Now the Defence Evaluation and Research Agency (DERA).

the blade flapping. The other feature is the pronounced ‘hump’ at about 13 m/s ($\mu \approx 0.07$). It is in this region that the influence of the trailing vortices from the blades is greatest. As was discussed in Chapter 6, at low speeds the upwash at the front of the rotor is quite large in relation to the forward speed, and this has the effect of keeping the trailing vortices close to the rotor. Consequently, there will be large velocity gradients near the front part of the rotor, giving rise to large higher harmonics in the flapping motion. It is of interest to note that large lateral blade flapping also occurs in this range of flight speeds, and this was found to be due to the asymmetry of the induced-velocity distribution with respect to the lateral axis.

References

1. Thomson, W. T., *Theory of vibrations with applications*, New Jersey, Prentice-Hall Inc., 1981.
2. Flannelly, W. G., ‘The Dynamic Anti-Resonant Vibration Isolator’, 22nd Annual Forum of the American Helicopter Society, Washington, May 1976.
3. Gaffey, T. M. and Balke, R. W., ‘Isolation of Rotor Induced Vibration with the Bell Focal Pylon Nodal Beam System’, Paper 760892, SAENAEM Meeting, November 1976.
4. Done, G. T. S. and Hughes, A. D., ‘Reducing vibration by structural modification’, *Vertica*, **1**, 31–38, 1976.
5. McCormick, C. W., ‘NASTRAN users’ manual’, *NASA SP-22*, 1969.
6. Paul, W. F. ‘The Main Rotor Bifilar Pendulum Vibration Absorber’, *Vertiflite*, February 1970.
7. White, R. W. ‘A Fixed Frequency Rotor Head Vibration Absorber Based upon GFRP Springs’, Fifth European Rotorcraft Forum, Amsterdam, 1979.
8. Amer, K. B. and Neff, J. R., ‘Vertical-Plane Pendulum Absorbers for Minimising Helicopter Vibratory Loads’, AHS/NASA Specialists Meeting on Rotorcraft Dynamics, Moffett Field, Calif., February 1974.
9. Wood, E. R., Powers, R. W., Cline, J. H. and Hammond, C. E., ‘On Developing and Flight Testing a Higher Harmonic Control System’, 39th Annual Forum of the American Helicopter Society, St Louis, Mo., May 1983.
10. Staple, A. E., ‘An Evaluation of Active Control of Structural Response as a Means of Reducing Helicopter Vibration’, Fifteenth European Rotorcraft Forum, Amsterdam, September 1989.

Aeroelastic and aeromechanical behaviour

9.1 Introduction

In previous chapters, the effect on the motion of the blade of coupling between its degrees of freedom has been ignored. For performance and stability and control aspects, this neglect is, in general, entirely justified, but possible blade and rotor system instabilities due to coupling must be considered.

There are also important instabilities involving coupling of rotor blade and airframe motion, and these must also be taken into account.

Rotor blade instabilities to be considered are:

- (i) main rotor pitch-lag instability;
- (ii) main rotor pitch-flap flutter;
- (iii) main rotor stall flutter;
- (iv) main rotor blade weaving;
- (v) tail rotor pitch-flap ('umbrella mode') instability;
- (vi) main and tail rotor flap-lag instability;
- (vii) tail rotor pitch-flap-lag instability.

A review of the aeroelastic problems of helicopter and V/STOL aircraft has been given by Loewy¹.

The coupled rotor blade and airframe instabilities to be considered are:

- (i) ground resonance;
- (ii) air resonance.

9.2 Main rotor pitch-lag instability

Although referred to as pitch-lag instability, the degrees of freedom participating in the motion are flap and lag, with the instability arising from the presence of a kinematic coupling between pitch and lag, or a torsional moment which twists the blade when it is deflected in the flapping and lagging senses.

The effect of these couplings is to induce aerodynamic lift loads in response to blade lag deflections which cause the blade to flap and the resulting Coriolis loads induce more lag motion.

One aspect which can cause a degradation in pitch-lag stability in certain flight conditions is the change in kinematic pitch-lag coupling as a function of steady coning angle, steady lag deflection and impressed blade pitch due to changes in the orientation of the pitch control system track rods. This problem will be exacerbated by the use of short track rods.

With semi-rigid and bearingless rotors the steady flap and lag deflections tend to be much smaller than those for articulated rotors, hence this type of instability is less likely to occur for these types of rotor system.

Pitch-lag instability is generally experienced as a limit cycle oscillation of the rotor blades phased in a manner which transmits a stirring motion to the airframe, due to the oscillatory shear forces generated by the blades in the plane of rotation.

On some helicopters, this type of instability occurs only under conditions of large amplitude forced oscillation of the blades in the lag plane (due to the Coriolis forces generated by large amplitude cyclic flapping), so that the effectiveness of any lag plane damper which may be present is reduced. The frequency of the oscillation of the blades relative to the rotating hub is that of the fundamental lag plane mode.

The first cause of coupling referred to in the first paragraph of this section may be regarded as the α_2 effect (see section 1.2), and the relationship between the blade pitch and lagging angle is, for small angles,

$$\Delta\theta = -\alpha_2\xi$$

The second cause of coupling can be understood with reference to Fig. 9.1. Forces dF_y and dF_z are capable of exerting torques about the blade span axes when the blade

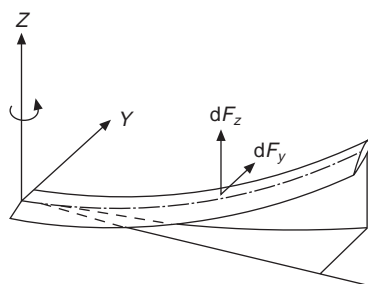


Fig. 9.1 Blade bending deformation

is deformed in bending. To calculate these torques, consider the moments exerted by these force components, with reference to the projections of the deformed blade onto the XY and XZ axes, Figs 9.2 and 9.3. The torque exerted by the sum of the elementary forces dF_y and dF_z about a point P at a distance r from the axis of rotation is

$$\begin{aligned} L(r) = & - \int_r^n \left[(Z_1 - Z) - (r_1 - r) \frac{dZ}{dr} \right] \frac{dF_y}{dr_1} dr_1 \\ & + \int_r^n \left[(Y_1 - Y) - (r_1 - r) \frac{dY}{dr} \right] \frac{dF_z}{dr_1} dr_1 \end{aligned} \quad (9.1)$$

Differentiating eqn 9.1 with respect to r and cancelling terms results in

$$\begin{aligned} \frac{dL}{dr} = & - \frac{d^2Z}{dr^2} \int_r^n (r_1 - r) dF_y + \frac{d^2Y}{dr^2} \int_r^n (r_1 - r) dF_z \\ = & - \frac{d^2Z}{dr^2} N_A + \frac{d^2Y}{dr^2} M_A \end{aligned} \quad (9.2)$$

since the integrals are the external lagging and flapping moments respectively. But, if EI_y and EI_z are the lagwise and flapwise blade stiffnesses, we also have

$$d^2Z/dr^2 = M_A/EI_z \quad \text{and} \quad d^2Y/dr^2 = N_A/EI_y$$

so that eqn 9.2 can be written

$$\frac{dL}{dr} = M_A N_A \left(\frac{1}{EI_y} - \frac{1}{EI_z} \right) \quad (9.3)$$

It is clear that the torque due to blade deflection will be zero if $EI_y = EI_z$ at every point of the blade. If this is satisfied the blade is called a ‘matched-stiffness’ blade. For a hingeless blade the structural element near the root, which allows most of the lag bending of the blade, can be ‘matched’ relatively easily to achieve almost zero

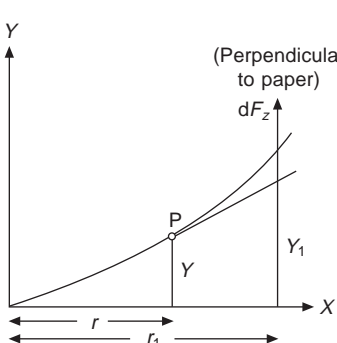


Fig. 9.2 Projection of the deformed blade onto the XY plane

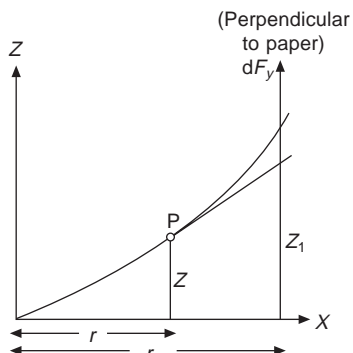


Fig. 9.3 Projection of the deformed blade onto the XZ plane

torsional moment along the entire blade. It is obvious that the torque exerted on a hinged blade will also be zero if the *feathering* hinge lies outboard of the lagging and flapping hinges, Fig. 9.4, for then the axis about which the torque is calculated follows the blade when it lags and flaps.

Hansford and Simons² have shown that by neglecting the pitching inertia of the blade, which is justifiable because of the high torsional stiffness, it is possible to write the torsional deflection θ as

$$\theta(\psi) = \beta(\psi)\xi(\psi) \frac{1 - \lambda_1^2 + \kappa_1^2}{v_1^2} \frac{I_\beta}{I_\theta} \quad (9.4)$$

where I_β and I_θ are the blade flapping and pitching moments of inertia, and $\lambda_1\Omega$, $\kappa_1\Omega$ and $v_1\Omega$ are the rotating blade uncoupled natural frequencies in flap, lag and torsion respectively.

If, for example, the flapping frequency is 1.1Ω , the required lagging frequency for zero twist is found to be 0.458Ω . Thus, a condition of zero or very small blade twist can be achieved by suitably choosing the flapping and lagging frequencies. It can be seen from eqn 9.4 that the relationship is non-linear in β and ξ , but for small variations about steady flapping and lagging angles β_0 and ξ_0 the twist can be expressed as

$$\Delta\theta = \frac{1 - \lambda_1^2 + \kappa_1^2}{v_1^2} \cdot \frac{I_\beta}{I_\theta} (\beta_0\xi + \xi_0\beta) \quad (9.5)$$

This relationship between the pitch angle $\Delta\theta$ and the flapping and lagging angles can be expressed as

$$\Delta\theta = k_\beta\beta + k_\xi\xi \quad (9.6)$$

The same relationship applies to the hinged blade. The coefficient k_β represents the δ_3 hinge effect and k_ξ the α_2 hinge effect, as mentioned at the beginning of this section. The inclusion of these terms merely adds $-\gamma(k_\beta\beta + k_\xi\xi)/8$ to the left-hand side of the appropriate equation of motion (see eqn 9.25). The usual solution procedure leading to a quartic characteristic equation may be followed, and the stability can be discussed in terms of the roots of the equation. This has been done by Pei³, who finds for an approximate stability criterion that

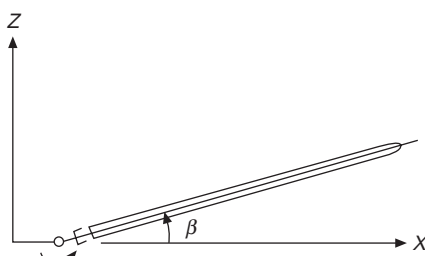


Fig. 9.4 Outboard position of feathering hinge

$$F_{\dot{\xi}} + \frac{2k_{\xi}}{1 - (\beta_0/\theta_0)k_{\beta}} \cdot \frac{\beta_0^2}{\theta_0} \Omega C > 0 \quad (9.7)$$

where $F_{\dot{\xi}}$ is the lag damping coefficient in the equation of motion involving lagging motion (see, for example eqn 9.26) and C is the moment of inertia in lagging motion. However, Pei also shows that the above criterion can be deduced from simple physical arguments. Since the lagging motion is generally of much lower frequency than that of the natural flapping motion, the flapping response can be calculated as if the lagging excitation at any instant were being steadily applied. Therefore, the change of lift moment due to the lagging and flapping motion can be written as

$$\Delta M = \frac{\partial M}{\partial \theta} \Delta \theta = \frac{\partial M}{\partial \theta} (k_{\xi}\dot{\xi} + k_{\beta}\beta)$$

The change in flapping angle β , if $\dot{\xi}$ is at sufficiently low frequency, can be expressed as (change of lift moment)/(centrifugal moment) or,

$$\beta = \frac{(k_{\xi}\dot{\xi} + k_{\beta}\beta) \partial M / \partial \theta}{B\Omega^2}$$

But in steady motion, with lift moment ΔM , the coning angle β_0 is given by

$$\beta_0 = \frac{\theta_0 \partial M / \partial \theta}{B\Omega^2}$$

so that

$$\beta = (\beta_0/\theta_0) (k_{\xi}\dot{\xi} + k_{\beta}\beta)$$

$$\text{or } \beta = \frac{(\beta_0/\theta_0)k_{\xi}\dot{\xi}}{1 - (\beta_0/\theta_0)k_{\beta}} \quad (9.8)$$

As a result of the flapping motion, the Coriolis moment N causing lagging is, for small disturbances,

$$N = 2C\Omega\beta_0\dot{\beta} = 2C\Omega \frac{\beta_0^2}{\theta_0} \cdot \frac{k_{\xi}\dot{\xi}}{1 - (\beta_0/\theta_0)k_{\beta}}$$

from eqn 9.8. Since this moment is proportional to $\dot{\xi}$, it may be regarded as a viscous damping moment. Then, including the damping of the lag damper and the drag moment, represented by $F_{\dot{\xi}}$, the total damping will be positive if

$$F_{\dot{\xi}} + \frac{2k_{\xi}}{1 - (\beta_0/\theta_0)k_{\beta}} \cdot \frac{\beta_0^2}{\theta_0} \Omega C > 0$$

as given by eqn 9.7.

For the helicopter with hinged blades, the criterion can be expressed in terms of the α_2 and δ_3 hinges as

$$F_{\dot{\xi}} + \frac{2 \tan \alpha_2}{1 - (\beta_0/\theta_0) \tan \delta_3} \cdot \frac{\beta_0^2}{\theta_0} \Omega C > 0$$

Since $F_{\dot{\xi}}$ represents the lag damping, and is therefore positive, instability can occur only if the second term is a sufficiently large negative number. The sign of this term can be regarded as depending only on α_2 , since δ_3 would have to be unusually large and positive to change the sign of the denominator. Thus, instability is possible when α_2 is negative, i.e. when the blade pitch increases as the blade moves forward in lagging motion.

9.3 Main rotor pitch-flap flutter

Essential for this form of instability is a mechanism coupling blade pitch and flap. The type of coupling normally encountered is due to adverse offsets of the chordwise centre of gravity of the blade section from the blade feathering axis which is normally coincident with the $\frac{1}{4}$ -chord point. This instability is very similar in nature to the fixed wing bending torsion flutter problem, and has been avoided on almost all helicopter rotor blades by mass balancing the blade so that the chordwise position of the centre of gravity of each spanwise element is forward of the blade section $\frac{1}{4}$ -chord point. This is usually accomplished by the use of non-load-carrying mass balance weights along the full length of the blade.

In the region of the blade root end attachment, local reinforcing usually has the effect of moving the centre of gravity well aft of the $\frac{1}{4}$ -chord point. However, analysis indicates that for a blade which is reasonably stiff in flatwise bending and torsion, the product of inertia of the blade about axes coincident with the flapping and feathering hinge lines is the significant parameter. Therefore, the effect of an aft movement of the centre of gravity in the root region can be counteracted by the addition of a relatively small mass positioned near the leading edge of the blade close to the tip.

For the case where complete decoupling is not achieved by mass balancing, then the blade flatwise and torsional stiffnesses, and the effective torsional stiffness of the pitch control circuit at the blade root, are important parameters.

The presence of blade flutter would normally be detected by the presence of high oscillatory loads in the blade pitch control circuit.

Since on a conventional rotor blade the amount of mass balance material is of the order of 9 to 12 per cent of total blade mass, then considerable weight saving could be achieved if it were possible to relax the mass balance requirements. However, a reduction in blade mass implies an increase in blade coning angle for a given value of lift, and this can lead to problems involving increased lag plane loading, and more severe damping requirements in lag to suppress certain types of instability. A reduction in blade mass would decrease the rotational moment of inertia of the total rotor system, thus adversely influencing the autorotational characteristics of the rotor and, in the case of partial power failure, the 'fly-away' manoeuvre.

Compared to the classical bending torsion flutter of aircraft wings, the motion of

the helicopter blade is modified by the powerful centrifugal action which effectively increases the stiffness of the flapping motion.

The mechanism of pitch-flap flutter is that, as the blade flaps, inertial and aerodynamic moments arise which twist the blade and, in turn, modify the aerodynamic flapping moment. The inertial effect of pitching on the flapping motion is very small.

Let us derive the flapping and torsional equations of motion. It will be sufficient to consider a rigid blade hinged at the root but with arbitrary flapping and torsional frequencies. We shall take the elastic axis of the blade as one of our reference axes which, since it will not in general be a principal axis of the blade, requires the equations of motion to be derived with a little care. If the axes are fixed in the blade, Fig. 9.5 the angular velocity components about these axes when the blade flaps and twists are found to be

$$\omega_1 = \dot{\theta} + \Omega \sin \beta \approx \dot{\theta} + \Omega \beta$$

$$\omega_2 = -\beta \cos \theta + \Omega \sin \theta \cos \beta \approx \dot{\beta} + \Omega \theta$$

$$\omega_3 = \beta \sin \theta + \Omega \cos \theta \cos \beta \approx \Omega$$

Since the blade is very thin in relation to its chord and span, the products of inertia D and E are negligible, but F , which represents the chordwise distribution of mass relative to the elastic axis, should be retained. Then, from eqn A.1.7 the components of angular momentum are

$$h_1 = A\omega_1 - F\omega_2$$

$$h_2 = B\omega_2 - F\omega_1$$

$$h_3 = C\omega_3$$

Differentiating with respect to time and retaining only first-order terms, we obtain

$$\dot{h}_1 = A\ddot{\theta} + A\Omega^2\theta + F\ddot{\beta} + F\Omega^2\beta$$

$$\dot{h}_2 = -B\ddot{\beta} - B\Omega^2\theta - F\ddot{\theta} - F\Omega^2\theta$$

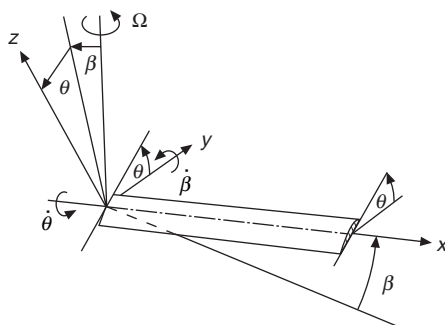


Fig. 9.5 Blade deflection in combined flapping and torsion

The above expressions represent the inertia terms of the torsional and flapping motion. If the elastic stiffnesses about these axes are included, the equations of motion can be written

$$\frac{d^2\theta}{d\psi^2} + v_1^2 \theta + \frac{F}{A} \left(\frac{d^2\beta}{d\psi^2} + \beta \right) = \frac{L_A}{A\Omega^2} \quad (9.9)$$

$$\frac{d^2\beta}{d\psi^2} + \lambda_1^2 \beta + \frac{F}{B} \left(\frac{d^2\theta}{d\psi^2} + \theta \right) = \frac{M_A}{B\Omega^2} \quad (9.10)$$

where $v_1\Omega$ and $\lambda_1\Omega$ are the uncoupled torsional and flapping frequencies and L_A and M_A are the aerodynamic torsional and flapping moments.

In calculating the flapping and feathering moments, we should consider the unsteady aerodynamic coefficients discussed in Chapter 6 and represented by the function $C(k)$. It will be assumed that the flexural axis coincides with the aerodynamic centre. Then, from eqn 6.26, with $\bar{x} = -\frac{1}{2}$ and replacing the theoretical lift slope 2π by a general value a , the spanwise thrust distribution is

$$\frac{dT}{dr} = \frac{1}{2} \rho ac\Omega^2 r^2 \left[\alpha - \frac{\dot{\beta}}{\Omega} + \frac{1}{2} \frac{c}{r} \frac{\dot{\alpha}}{\Omega} \right] C(k) + \frac{1}{8} \rho ac^2 \left[\Omega r \dot{\alpha} - r \ddot{\beta} + \frac{1}{4} c \ddot{\alpha} \right]$$

where $\dot{\alpha}$ is the component of angular velocity about the blade span, which includes the component of shaft angular velocity due to flapping, i.e. $\dot{\alpha} = \dot{\theta} + \Omega\beta$ and $z = -r\beta$. The flapping moment M_A is found by integrating $r dT/dr$ over the span, which gives

$$M_A = \frac{1}{8} \rho ac\Omega^2 R^4 \left[\alpha - \frac{\dot{\beta}}{\Omega} + \frac{2}{3} \frac{c}{R} \frac{\dot{\alpha}}{\Omega} \right] C(k) \\ + \frac{1}{8} \rho ac\Omega^2 R^4 \left[\frac{1}{3} \frac{c}{R} \frac{\dot{\alpha}}{\Omega} - \frac{1}{3} \frac{c}{R} \frac{\ddot{\beta}}{\Omega^2} + \frac{1}{8} \frac{c}{R} \frac{\ddot{\alpha}}{\Omega^2} \right]$$

The term c/R is the reciprocal of the aspect ratio of the blade and is typically about 1/20. Since the terms in $\ddot{\alpha}$ and $\ddot{\beta}$ are usually negligible, the expression for M_A reduces approximately to

$$M_A = \frac{1}{8} \rho ac\Omega^2 R^4 \left[\alpha - \frac{d\beta}{d\psi} \right] C(k) = \frac{\gamma}{8} B\Omega^2 \left[\alpha - \frac{d\beta}{d\psi} \right] C(k)$$

Similarly, the aerodynamic pitching moment about the flexural axis is approximately

$$L_A = \frac{1}{32} \rho ac^3 \Omega^2 R^2 \frac{d\alpha}{d\psi} = \frac{1}{32} \rho ac^3 \Omega^2 R^2 \left(\frac{d\theta}{d\psi} + \beta \right) \\ = \frac{1}{32} \frac{\gamma B\Omega^2}{A^2} \left(\frac{d\theta}{d\psi} + \beta \right)$$

where A is the blade aspect ratio R/c . The equations of coupled pitch-flapping motion are therefore

$$\frac{d^2\theta}{d\psi^2} + v_1^2\theta + \frac{F}{A} \left(\frac{d^2\beta}{d\psi^2} + \beta \right) = -\frac{1}{32} \frac{\gamma}{A^2} \frac{B}{A} \left(\frac{d\theta}{d\psi} + \beta \right)$$

and

$$\frac{d^2\beta}{d\psi^2} + \lambda_1^2\beta + \frac{F}{B} \left(\frac{d^2\theta}{d\psi^2} + \theta \right) = \frac{\gamma}{8} \left[\theta - \frac{d\beta}{d\psi} \right] C(k)$$

where θ represents changes of α from the steady state.

If the displacement of the c.g. of a blade elemental strip $\sigma_g c$ (positive when the c.g. is behind the flexural axis) is constant along the span, it is easy to show that $F = -\sigma_g c r_g M$, where r_g is the spanwise position of the c.g. of the blade; and, if we also write $A = Mk_A^2 c^2$, the equations above become

$$\frac{d^2\theta}{d\psi^2} + \frac{1}{32} \frac{\gamma B}{A^2 A} \frac{d\theta}{d\psi} + v_1^2\theta - \frac{\sigma_g r_g}{ck_A^2} \left(\frac{d^2\beta}{d\psi^2} + \beta \right) + \frac{1}{32} \frac{\gamma B}{A^2 A} \beta = 0$$

$$\frac{d^2\beta}{d\psi^2} + \frac{\gamma}{8} C(k) \frac{d\beta}{d\psi} + \lambda_1^2\beta + \frac{F}{B} \left(\frac{d^2\theta}{d\psi^2} + \theta \right) - \frac{\gamma}{8} C(k)\theta = 0$$

The term proportional to F/B in the flapping equation and the second term involving the aspect ratio in the pitching equation can be ignored. Then, writing for the flapping moment of inertia $B = Mk_B^2 R^2$, the final equations in hovering flight are

$$\frac{d^2\theta}{d\psi^2} + \frac{\gamma}{8} \cdot \frac{1}{4} \left(\frac{k_B}{k_A} \right)^2 \frac{d\theta}{d\psi} + v_1^2\theta - \frac{\sigma_g r_g}{ck_A^2} \left(\frac{d^2\beta}{d\psi^2} + \beta \right) = 0 \quad (9.11)$$

$$\frac{d^2\beta}{d\psi^2} + \frac{\gamma}{8} C(k) \frac{d\beta}{d\psi} + \lambda_1^2\beta - \frac{\gamma}{8} C(k)\theta = 0 \quad (9.12)$$

The frequency equation corresponding to the equations of motion 9.11 and 9.12 is easily found to be

$$\begin{aligned} & \lambda^4 + \frac{\gamma}{8} \left[C(k) + \frac{1}{4} \left(\frac{k_B}{k_A} \right)^2 \right] \lambda^3 \\ & + \left[\lambda_1^2 + v_1^2 - \frac{\gamma}{8} \frac{\sigma_g r_g}{ck^2} C(k) + \frac{\gamma^2}{252} \left(\frac{k_B}{k_A} \right)^2 C(k) \right] \lambda^2 \\ & + \frac{\gamma}{8} \left[v_1^2 C(k) + \frac{1}{4} \left(\frac{k_B}{k_A} \right)^2 \right] \lambda + v_1^2 \lambda_1^2 - \frac{\gamma}{8} \frac{\sigma_g r_g}{ck^2} C(k) = 0 \end{aligned} \quad (9.13)$$

Of the above constants, the only two which can readily be varied are the chordwise blade c.g. position and the non-rotating torsional frequency. Divergence occurs when the term independent of λ is equal to zero, i.e. when

$$v_1^2 = \frac{\gamma}{8} \frac{\sigma_g r_g}{ck^2} \frac{C(k)}{\lambda_1^2} \quad (9.14)$$

For $C(k) = 1$, i.e. when unsteady aerodynamic effects are neglected, eqn 9.14 defines a straight line relating the torsional frequency to the chordwise c.g. location. It is clear that the boundary exists for positive values of σ_g , i.e. a rearward location of the c.g. relative to the $\frac{1}{4}$ -chord point. The physical interpretation of divergence is simply that, if the c.g. of the blade is located sufficiently far behind the $\frac{1}{4}$ -chord point, the component of centrifugal force about the blade-span axis, which arises when the blade flaps, exerts a nose up moment which is greater than the torsional restoring moment.

To find the flutter boundary we put $\lambda = i\omega$, the condition for undamped oscillations, and equate the real and imaginary parts to zero. We then find

$$v_1^2 = \omega^2 + \frac{(\omega^2 - 1)(x_g/k)^2}{4C(k)} \quad (9.15)$$

and

$$\sigma_g = 2 \left(\frac{k_B}{k_A} \right)^2 \frac{ck_A^2}{\gamma r_g C^2(k)} \left[\omega^2 - \lambda_1^2 + \frac{\gamma^2 C^2(k) \omega^2 / 64}{\omega^2 - 1} \right] \quad (9.16)$$

Equations 9.15 and 9.16 provide the relationship between v_1 and σ_g for which undamped oscillations occur with ω^2 , the square of the flutter frequency ratio, as parameter. Thus, if v_1 is given, eqn 9.15 can be solved for ω^2 , which can then be inserted into eqn 9.16 to obtain σ_g .

A sketch of typical divergence and flutter boundaries as functions of σ_g and v_1^2 for $C(k) = 1$ is shown in Fig. 9.6. The two curves correspond to the four roots of the characteristic frequency quartic, eqn 9.14. If the torsional frequency is fixed at the value corresponding to the point A of Fig. 9.6 and the chordwise c.g. position is moved aft, the line AA' is traced. The motion is completely stable until the intersection with the divergence boundary is reached. At this point, A', one of the roots of the frequency quartic becomes zero, and just to the right of A' the root becomes positive, denoting the unstable divergence. The remaining roots between A' and A'' are a negative real root (stable) and a complex pair denoting a damped oscillation. To the right of the point A'' the oscillation becomes undamped also. Moving along BB'' the unstable flutter oscillation is met first, and then the divergence.

Analysis of the equations 9.13, 9.15 and 9.16 shows that the flutter and divergence boundaries exist only for positive values of σ_g , which shows that pitch-flap motion must be stable for $\sigma_g < 0$, i.e. when the centre of gravity of the blade is ahead of the flexural axis. Since the torsional frequency must have a positive value, Fig. 9.6 shows that stable motion is possible even when the centre of gravity is behind the

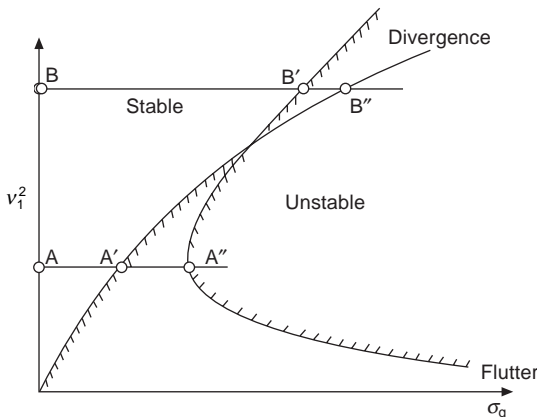


Fig. 9.6 Stability boundaries for torsional motion

flexural axis. Inspection of eqns 9.15 and 9.16 shows that for flapping frequencies greater than Ω , i.e. $\lambda_1 > 1$, the flutter boundary is shifted to the left. This suggests that offset or hingeless blades are rather less stable than centrally hinged blades.

The effect of taking unsteady aerodynamic coefficients ($C(k) \neq 1$) into account is quite small. The appropriate value of $C(k)$ must be obtained iteratively, since the flutter frequency ω must be known before $C(k)$ can be estimated. The flutter boundary is modified as sketched in Fig. 9.7.

Stammers⁴ has shown that forward flight has a stabilising influence on flutter which tends to occur at half-integer frequencies.

9.4 Main rotor stall flutter

This is a single degree of freedom flutter problem involving torsional oscillation of the blade. It normally takes the form of a limit cycle oscillation giving rise to high

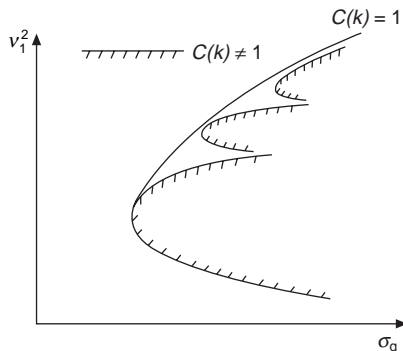


Fig. 9.7 Stability boundaries for torsional motion ($C(k) \neq 1$)

oscillatory loads in the blade pitch control circuit, and occurs over a stalled region of the retreating blade side of the rotor disc. This region must cover a sufficient proportion of the total disc area for the instability to allow one or more cycles of torsional oscillation before the blade moves into a stable (non-stalled) region of the rotor disc.

Consider an aerofoil oscillating periodically in pitch in an airstream of velocity V . The pitching moment coefficient can be expressed as

$$C_m = \frac{M(\alpha)}{\frac{1}{2}\rho V^2 c^2} = a_0 + a_1 \sin pt + a_2 \sin 2pt + \dots + b_1 \cos pt + \dots$$

where α is the instantaneous incidence, p is the angular frequency, and c is the chord. The work done in one cycle is

$$W = \oint M \, d\alpha$$

If the oscillations are harmonic, the incidence can be written as

$$\alpha = \alpha_0 + \alpha_1 \sin pt$$

where α_0 is the mean incidence and α_1 is the amplitude of the oscillations.

We then find that

$$\begin{aligned} W &= \frac{1}{2}\rho V^2 c^2 p \int_0^{2\pi/p} \alpha_1 b_1 \cos^2 pt \, dt \\ &= \frac{1}{2}\pi\rho V^2 c^2 \alpha_1 b_1 \end{aligned}$$

The work is therefore proportional to the coefficient b_1 ; if b_1 is negative, work is dissipated and the damping is positive. Thus, the damping depends on the out-of-phase component of the pitching moment.

The basic mechanism of the instability is negative damping in pitch due to aerodynamic pitching moment hysteresis caused by the periodic shedding of intense vorticity at a blade angle of attack instantaneously greater than the static stalling angle⁵.

Hovering rotor tests of these oscillations have been described by Ham and Young⁶. Explanation of the phenomenon has already been alluded to in Chapter 6. We saw there that at high incidence a suction peak occurs over the rear part of the aerofoil, resulting in a large nose down pitching moment, and this gives rise to a substantial out-of-phase moment of negative damping, particularly at the comparatively low values of the reduced frequency typical of helicopter operation. The variation of damping with incidence and reduced frequency is graphically displayed in the three-dimensional diagram taken from Carta's paper, Fig. 9.8. The 'hollow' indicates the region in which negative damping occurs.

Now, as we saw in Chapter 6, the aerofoil undergoes a large variation of incidence, and therefore of rate of change of incidence, at high tip speed ratios. It will be assumed that the rotor blade responds to the changing conditions at its fundamental torsional frequency ω_0 , which, in association with the local chordwise velocity $\Omega R(x + \mu \sin \psi)$,

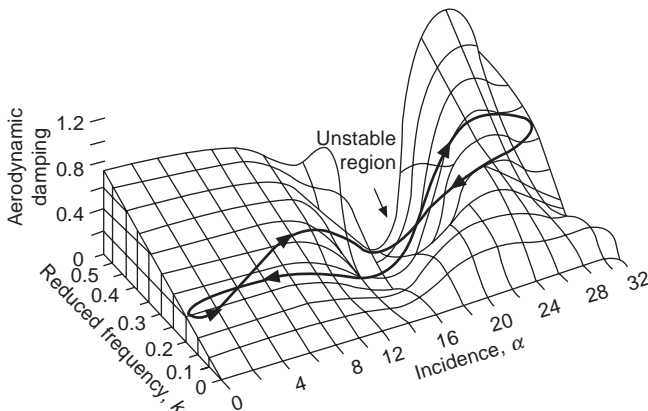


Fig. 9.8 Contours of blade torsional damping

enables us to define the instantaneous value of the reduced frequency k , i.e. we assume that the appropriate value of k is given by

$$k(x, \psi) = \omega_0 b / \Omega R (x + \mu \sin \psi)$$

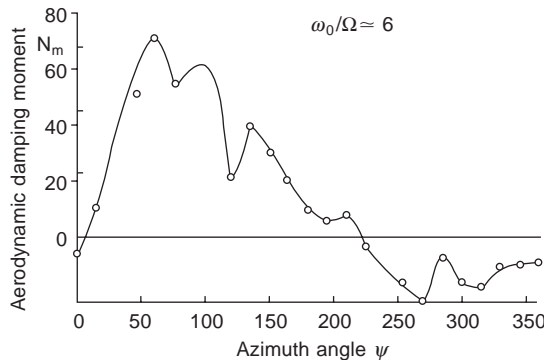
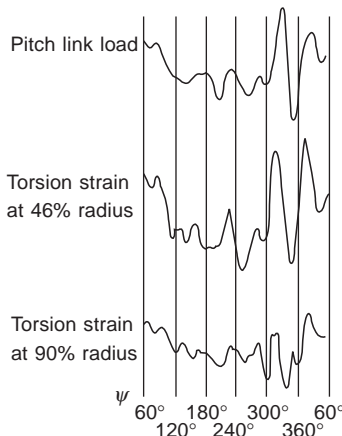
where b is the semi-chord. Thus, for a given radial position, the variations of incidence and reduced frequency trace out a closed path on the surface as shown in Fig. 9.8. In the range, or ranges, of azimuth angle which lie in the region of negative damping, torsional flutter can be expected to occur. It has been assumed that the damping at any azimuth angle is the same as if the incidence and reduced frequency were fixed, i.e. that the damping corresponding to given values of α and k applies instantaneously at the given azimuth angle. For the blade as a whole we can define a ‘weighted-mean’ damping by integrating the local two-dimensional values in association with the first torsional mode shape $Q_1(x)$ to obtain

$$\zeta_{\text{mean}} = \int_0^1 Q_1^2(x) \zeta(\alpha, k) dx$$

where the reduced frequency to be used is that defined above.

The torsional damping defined in this way has been calculated by Carta for a case in which $\mu = 0.17$ and $C_T/\sigma = 0.111$, and the result is shown in Fig. 9.9. We see that negative damping occurs in the region 225° to 10° , and in this region we can expect stall flutter to occur. To test the validity of this assumption, the torsional stress and pitch link loads for the same flight case, Fig. 9.10, have been examined. It can be seen that large values of torsional stress and pitch link loads occur in this region, demonstrating that the calculation of the damping gives a good indication of the possibility of stall flutter.

The high pitch link loads which occur in stall flutter may be a serious obstacle to increased flight speeds. According to Ham⁷, the most profitable way of reducing these loads is to use aerofoil sections which have high dynamic stall angles, so that they can operate in the retreating blade region below the stall angle as much as possible.

**Fig. 9.9** Aerodynamic torsional damping as a function of azimuth**Fig. 9.10** Variation of pitch link loads with azimuth angle

9.5 Main rotor blade weaving

Blade weaving is the name given to a form of instability which can affect two-bladed ‘teetering’ rotors, i.e. rotors with two blades rigidly connected together at their root ends with a built-in non-zero coning angle, and suspended on a central flapping or ‘teetering’ hinge. The phenomenon involves the same basic coupling mechanism as the main rotor pitch–flap flutter problem described in section 9.3, but since both blades move as a single entity, extra terms arise in addition to those of eqns 9.11 and 9.12.

Consider the two-bladed teetering rotor of Fig. 9.11. The blades are joined at angle $2\beta_0$ (twice the built-in coning angle) and are feathered so that the steady pitch angle between the blades is $2\theta_0$. The two blades are then imagined to move as a rigid body except that torsional flexibility of the control system will allow some mutual feathering. The latter motion will have a negligible effect on the moments of inertia of the whole

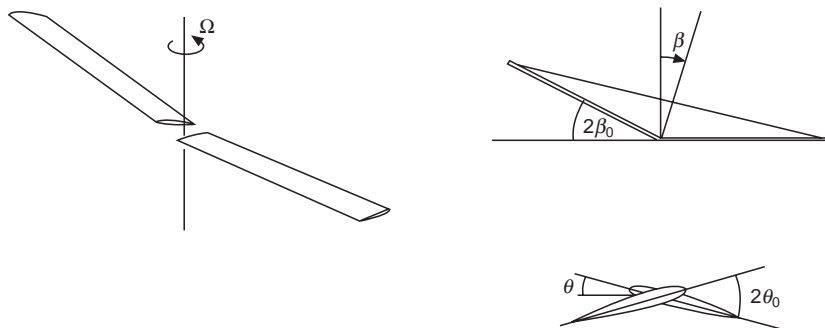


Fig. 9.11 Teetering rotor with combined flapping and feathering

rotor system, so the assumption of complete rigidity is justified. If the lines of the centre of mass intersect at the hub, Euler's equations, eqns A.1.11 to A.1.13 can be applied to the rotor as a whole. Coleman and Stempin⁸, who first investigated this motion, have shown that, if A , B , C are the principal moments of inertia of the individual blades, the corresponding moments of inertia of the rotor with coning angle β_0 and collective pitch setting θ_0 are

$$A' = 2A \cos^2\beta_0 + 2B \sin^2\theta_0 \sin^2\beta_0 + 2C \cos^2\theta_0 \sin^2\beta_0 \approx 2(A + B\beta_0^2)$$

$$B' = 2B \cos^2\theta_0 + 2C \sin^2\theta_0 \approx 2B$$

$$C' = 2A \sin^2\beta_0 + 2B \sin^2\theta_0 \cos^2\beta_0 + 2C \cos^2\theta_0 \cos^2\beta_0 \approx 2(C - B\beta_0^2)$$

assuming $A + B = C$ for the individual blades.

As might be expected, the flapping and lagging moments of inertia are very little different from those of the original blades, but the pitching moment of inertia is greatly increased by coning angle. The angular velocity components of the rotor are the same as those of the previous section, and the linearised Euler equations are found to be

$$\ddot{\theta} + \frac{C' - B'}{A'} \Omega^2 \theta + \left(\frac{A' + B' - C'}{A'} \right) \Omega \dot{\beta} = \frac{L_A}{A'} \\ \ddot{\beta} + \frac{C' - A'}{B'} \Omega^2 \beta - \frac{A' + B' - C'}{B'} \Omega \dot{\theta} = \frac{M_A}{B'}$$

The important difference between these equations and those of the pitch–flap coupling of section 9.3 is that, since the rotor can no longer be regarded as a lamina, $A' + B' - C' \neq 0$ so that the coefficients of $\Omega\dot{\theta}$ and $\Omega\dot{\beta}$ do not vanish as they did in the latter case. Let us write the equations in the non-dimensional form originally used by Coleman and Stempin. They are

$$\frac{d^2\theta}{d\psi^2} + H_D \frac{d\theta}{d\psi} + (I_A + K'_\theta)\theta - (1 - I_A) \frac{d\beta}{d\psi} - H_D\beta = 0 \quad (9.17)$$

$$\frac{d^2\beta}{d\psi^2} + H_B \frac{d\beta}{d\psi} + I_B \beta + (1 - I_A) \frac{d\theta}{d\psi} + H_B \theta = 0 \quad (9.18)$$

In the above equations, H_B and H_D represent damping of the pitching and flapping motion; I_A and I_B are defined by

$$I_A = \frac{C' - B'}{A'} + \frac{H'_1}{A'}$$

and

$$I_B = \frac{C' - A'}{B'} - \frac{H'_5}{B'}$$

and we have approximately

$$1 - I_A = \frac{2B}{A} \beta_0^2 + \frac{H'_1}{A'}$$

and

$$1 - I_B = 2\beta_0^2 - \frac{H'_5}{B'}$$

where the terms in H'_1 and H'_5 represent aerodynamic damping. It can be seen that, since B/A is usually a very large ratio, $1 - I_A$ is strongly dependent on coning angle whereas $1 - I_B$ varies little. K'_θ is the stiffness of the pitch control. Coleman and Stempin state that H_D depends strongly on coning angle but that H_B is practically unaffected.

The equations of motion 9.17 and 9.18 are similar in form to those of section 9.3 (eqns 9.11 and 9.12) except for the presence here of the terms in $d\beta/d\psi$ and $d\theta/d\psi$. (Since the motion has been referred to principal axes through the centre of gravity of the blade, the term in $\ddot{\beta}$ is absent.) Coleman and Stempin's calculations show that these extra terms are destabilising and that the instability depends mainly on the coning angle and to a lesser extent on the pitch setting angle θ_0 . An important result of their investigations is that instability can occur even when the centre of mass of the blade is ahead of the $\frac{1}{4}$ -chord point. A sketch of the variation of the stability boundaries with control stiffness, coning angle, and chordwise c.g. location is given in Fig. 9.12. When instability occurs, the blade tips trace out a wavy or 'weaving' path which gives rise to the name of the phenomenon.

9.6 Tail rotor pitch-flap ('umbrella mode') instability⁹

This type of instability depends on the existence of some form of coupling between blade pitching and flapping motions, and is very similar to the main rotor blade pitch-flap flutter problem described in section 9.3.

In the case of the tail rotor, the coupling usually arises from the large δ_3 coupling introduced to reduce tail rotor blade flapping and stresses in forward flight. This

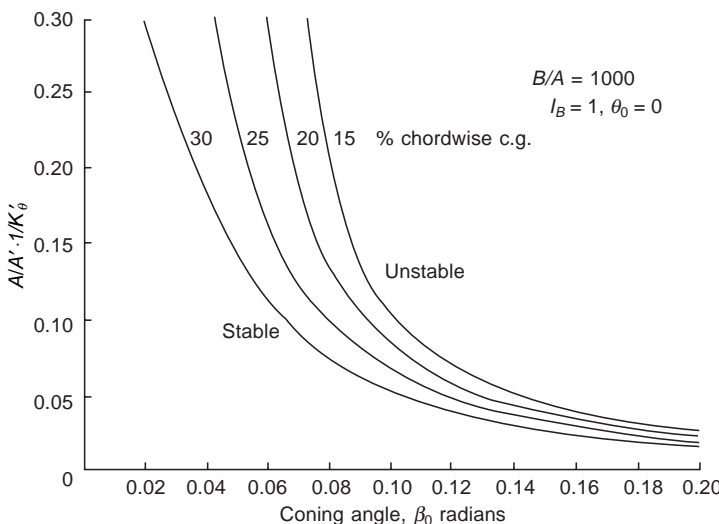


Fig. 9.12 Stability boundaries of blade weaving motion

coupling is normally of the order of one degree of reduction in blade pitch per degree of ('upward') blade flapping.

This form of instability is usually experienced as a limit cycle oscillation with all blades moving in phase. Hence the description 'umbrella mode' applied to this type of motion.

The stiffness and damping of the pitch control circuit between the blades and the pitch control actuator have a fundamental influence on this phenomenon.

In general, stable solutions can be found with both high and low pitching mode frequencies, in the absence of pitch circuit damping.

Where the possibility of instability arises, the onset of this is difficult to predict due to the presence of backlash and friction damping effects in the pitch control circuit, and in fact the occurrence in practice tends to be somewhat erratic. Disturbances below a certain threshold will subside, but beyond this divergence will occur, rapidly reaching a constant level.

The frequency of the oscillation is at or close to the fundamental flapping frequency of the tail rotor blade which is typically 1.2Ω . The reason that it is significantly greater than 1Ω is primarily due to the additional aerodynamic stiffness arising from the δ_3 coupling.

Figure 9.13 indicates a typical stability boundary as a function of pitch control circuit stiffness and damping.

9.7 Main and tail rotor flap-lag instability

We have already seen in Chapter 1 that blade flapping produces large Coriolis moments in the plane of the rotor. For the articulated rotor, a drag hinge is provided to relieve

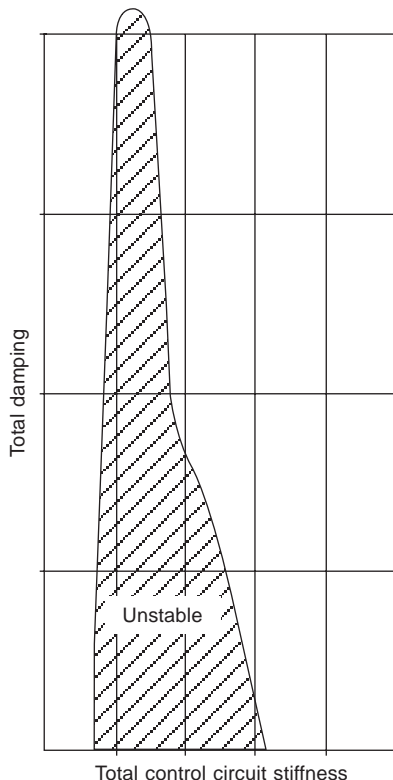


Fig. 9.13 Stability boundary for coupled pitch–flap motion

the blade of these moments and allow it to move in the plane of rotation (lagging). For semi-rigid and totally bearingless rotors, and for the majority of tail rotors, the lagwise flexibility provided at the root end of the blade permits the corresponding lagwise movement, and is designed to accommodate the resulting moments.

The lagging motion means that the instantaneous angular velocity of the blade in the plane of rotation is slightly different from the (assumed) constant angular velocity of the shaft, and this in turn means that the centrifugal flapping moment depends on the lagging motion. The variations of relative airspeed due to lagging also affect the aerodynamic flapping moment. Thus, the flapping and lagging motions are clearly coupled, but to investigate the stability of these motions we must derive the appropriate equations of motion. Referring to Fig. 9.14, if the lagging angular velocity is $\dot{\xi}$, then the instantaneous angular velocity is $\Omega + \dot{\xi}$ and, by the arguments of Chapter 1, the centrifugal flapping moment is $-B(\Omega + \dot{\xi})^2\beta$, tending to restore the blade to the plane of rotation. Neglecting the term in $\dot{\xi}^2$, the first-order flapping moment is $-B(\Omega^2 + 2\Omega\dot{\xi})\beta$ and the equations of flapping and lagging motion are

$$B\ddot{\beta} + B\lambda_1^2\Omega^2\beta + 2B\Omega\beta\dot{\xi} = M_A \quad (9.19)$$

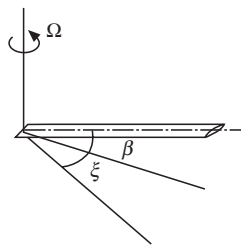


Fig. 9.14 Simple flap-lag blade model

$$C\ddot{\xi} + C\kappa_1^2 \Omega^2 \xi - 2C\Omega\beta\dot{\beta} = N_A \quad (9.20)$$

where we have written $\lambda_1\Omega$ and $\kappa_1\Omega$ for the undamped natural flapping and lagging frequencies which can apply to both hinged and hingeless blades. The aerodynamic moments M_A and N_A will contain aerodynamic coupling terms. To calculate them we consider the force on a blade element under conditions of flapping and lagging. For simplicity we consider only hovering flight. Referring to Fig. 9.15, the elementary flapping and lagging forces are, respectively,

$$dZ = dL \cos \phi + dD \sin \phi \approx dL$$

$$dY = dL \sin \phi \quad dD \cos \phi \approx dL\phi - dD$$

Now

$$dL = \frac{1}{2}\rho W^2 \ c a(\theta + \phi) dr$$

$$\approx \frac{1}{2}\rho U_T^2 \ c C_D \ dr$$

and

$$dD \approx \frac{1}{2}\rho U_T^2 \ c C_D \ dr$$

Also,

$$\tan \phi \approx \phi = U_P/U_T$$

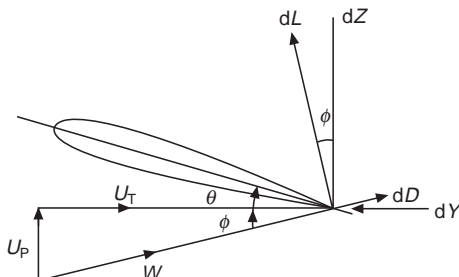


Fig. 9.15 Forces on blade element

therefore,

$$dZ = \frac{1}{2} \rho ac dr (\theta U_T^2 + U_P U_T) \quad (9.21)$$

and

$$dY = \frac{1}{2} \rho ac dr (\theta U_P U_T + U_P)^2 - \frac{1}{2} \rho U_T^2 C_D c dr \quad (9.22)$$

The velocity components U_P and U_T are

$$U_T = (\Omega + \dot{\xi})r; \quad U_P = -r\dot{\beta} - v_i$$

Expanding eqns 9.21 and 9.22 and neglecting squares and products of $\dot{\beta}$ and $\dot{\xi}$ gives

$$dZ = \frac{1}{2} \rho ac [\theta(\Omega^2 r^2 + 2\Omega\dot{\xi}r^2) - \Omega\dot{\beta}r^2 - \Omega rv_i - \Omega\dot{\xi}v_i] dr$$

$$dY = -\frac{1}{2} \rho c C_D (\Omega^2 r^2 + 2\Omega\dot{\xi}r^2) dr$$

$$-\frac{1}{2} \rho ac (\theta\Omega\dot{\beta}r^2 + \theta\Omega rv_i + \theta\dot{\xi}rv_i - v_i^2 - 2\dot{\beta}rv_i) dr$$

Integrating rdZ and rdY , assuming C_D , θ , and v_i to be constant, we obtain for the aerodynamic flapping and lagging moments

$$M_A = \frac{1}{8} \rho ac \Omega^2 R^4 \left[\theta - \frac{4}{3} \lambda_i - \frac{\dot{\beta}}{\Omega} + \left(2\theta - \frac{4}{3} \lambda_i \right) \frac{\dot{\xi}}{\Omega} \right] \quad (9.23)$$

$$N_A = -\frac{1}{8} \rho ac \Omega^2 R^4 \left[\left(\frac{C_D}{a} + \frac{4}{3} \theta \lambda_i - 2\lambda_i^2 \right) + \left(\theta - \frac{8}{3} \lambda_i \right) \frac{\dot{\beta}}{\Omega} \right. \\ \left. + \left(\frac{2C_D}{a} + \frac{4}{3} \theta \lambda_i \right) \frac{\dot{\xi}}{\Omega} \right] \quad (9.24)$$

The constant terms on the right-hand sides of eqns 9.23 and 9.24 give the steady state flapping and lagging angles β_0 and ξ_0 . Since we are concerned only with perturbations from the steady state, these terms can be omitted; but, since the last two terms of eqns 9.19 and 9.20 representing the Coriolis acceleration are products, they must be written in first order form as $2B\Omega\beta_0\dot{\xi}$ and $-2C\Omega\beta_0\dot{\beta}$.

Finally, if it is assumed that the flapping and lagging moments of inertia, B and C , are equal, the equations of disturbed motion become

$$\frac{d^2\beta}{d\psi^2} + \frac{\gamma}{8} \frac{d\beta}{d\psi} + \lambda_i^2 \beta + C_{\dot{\xi}} \frac{d\xi}{d\psi} = 0 \quad (9.25)$$

$$F_{\dot{\beta}} \frac{d\beta}{d\psi} + \frac{d^2\xi}{d\psi^2} + F_{\dot{\xi}} \frac{d\xi}{d\psi} + \kappa_i^2 \xi = 0 \quad (9.26)$$

where

$$C_{\dot{\xi}} = 2\beta_0 - \frac{\gamma}{8} \left(2\theta - \frac{4}{3} \lambda_i \right)$$

$$F_{\dot{\beta}} = \frac{\gamma}{8} \left(\theta - \frac{8}{3} \lambda_i \right) - 2\beta_0$$

$$F_{\dot{\xi}} = \frac{\gamma}{8} \left(k_{\dot{\xi}} + \frac{2C_D}{a} + \frac{4}{3} \theta \lambda_i \right)$$

and where $k_{\dot{\xi}}$ is the non-dimensional artificial lag damping, if any. The characteristic equation of this motion is

$$(\lambda^2 + \gamma\lambda/8 + \lambda_i^2)(\lambda^2 + F_{\dot{\xi}}\lambda + \kappa_i^2) - C_{\dot{\xi}}F_{\dot{\beta}}\lambda^2 = 0$$

which is of the form

$$A\lambda^4 + B\lambda^3 + C\lambda^2 + D\lambda + E = 0$$

where

$$A = 1$$

$$B = \gamma/8 + F_{\dot{\xi}}$$

$$C = \lambda_i^2 + \kappa_i^2 + \gamma F_{\dot{\xi}}/8 - C_{\dot{\xi}}F_{\dot{\beta}}$$

$$D = \gamma \kappa_i^2/8 + F_{\dot{\xi}}\lambda_i^2$$

$$E = \lambda_i^2 \kappa_i^2$$

To find the neutral stability boundaries we equate Routh's discriminant to zero, i.e. we put

$$R = BCD - D^2 - B^2E = 0$$

It has been shown by Ormiston and Hodges¹⁰ that this expression can be put into the form

$$(\theta - 4\lambda_i/3)^2 = \frac{\lambda_i^4}{2(\lambda_i^2 - 1)(2 - \lambda_i^2)} \left[\frac{2C_D}{a} + k_{\dot{\xi}} + \frac{64\alpha(\lambda_i^2 - \kappa_i^2)}{\gamma^2(1 + \alpha)(\kappa_i^2 + \alpha\lambda_i^2)} \right] \quad (9.27)$$

where

$$\alpha = k_{\dot{\xi}} + 2C_D/a + 4\theta\lambda_i/3$$

Equation 9.27 includes artificial damping omitted by Ormiston and Hodges.

The relationship, eqn 9.27 shows clearly that instability, if it occurs at all, does so only if $1 < \lambda_i^2 < 2$, i.e. when the flapping frequency is between Ω and $\Omega\sqrt{2}$. Further, for a given value of λ_i , the lowest possible value of θ for instability occurs when $\kappa_i = \lambda_i$, i.e. when the lagging and flapping frequencies are identical, in which case the corresponding value of θ is given by

$$(\theta - 4\lambda_i/3)^2 = \frac{(2C_D/a k_{\dot{\xi}})\lambda_i^4}{2(\lambda_i^2 - 1)(2 - \lambda_i^2)}$$

The absolute minimum value of collective pitch occurs when $\lambda_1 = \kappa_1 = \sqrt{(4/3)} = 1.153$, from which we easily find that

$$\theta = 4\lambda_i/3 + 2\sqrt{(2C_D/a + k_{\dot{\xi}})} \quad (9.28)$$

The stability boundaries for a case in which $k_{\dot{\xi}} = 0$, taken from Ormiston and Hodge's paper, is shown in Fig. 9.16. It is clear that, unless the lag frequency is higher than about 0.95Ω , instability would not be expected to occur.

The vast majority of rotor systems, both articulated and hingeless, with more than two blades have fundamental lag frequencies significantly below this value and are therefore not likely to be susceptible to this form of instability. (The case of the two-bladed teetering rotor with built-in coning angle is treated separately in section 9.5.)

An exception to the general rule was the gyro-controlled 'rigid' rotor developed by Lockheed, where the fundamental lag frequency was greater than 1Ω and the design of such a system would have to include consideration of this type of instability.

However, the fundamental lag frequency of tail rotors is normally greater than 1Ω (but significantly less than 2Ω in order to avoid excessive blade and hub vibratory loading), and tail rotors must be designed to avoid this form of instability, which is generally referred to as tail rotor 'buzz' and is usually of a mild 'limit cycle' nature.

Since the tendency to instability increases as the fundamental flap and lag frequencies approach the same value, it is instructive to examine the factors which influence these frequencies. It is usually the case that the elastic stiffness of the root region of the blade is significantly less in the flatwise direction compared to the chordwise direction. Hence, as blade pitch is increased, the lower flatwise stiffness reduces the lag frequency from its value at zero pitch. Furthermore, due to the large value of

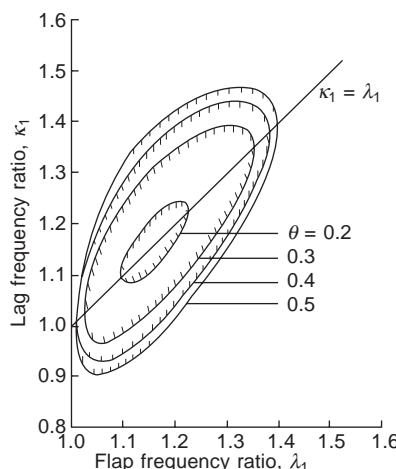


Fig. 9.16 Stability boundaries for coupled flap-lag motion

pitch-flap (δ_3) coupling typically employed on tail rotors (in order to reduce flapping in forward flight), the fundamental flapping frequency will be well above 1Ω . Consequently it is very probable that the flap and lag frequencies will coalesce at high values of blade pitch.

Figure 9.16 clearly indicates the increasing area of instability as blade pitch is increased.

9.8 Tail rotor pitch-flap-lag instability⁹

The analysis describing the tail rotor ‘buzz’ phenomenon referred to in section 9.7 does not require the inclusion of the torsion, or pitch, degree of freedom, and hence may be considered to represent the case of a torsionally stiff blade and pitch control circuit.

If this additional degree of freedom is included in the analysis, an additional region of instability appears which represents the much more severe instability known as tail rotor ‘bang’.

This form of instability is associated with the coalescence of the flap, lag and torsion mode frequencies.

Figure 9.17 illustrates the position of the stability boundaries as a function of the

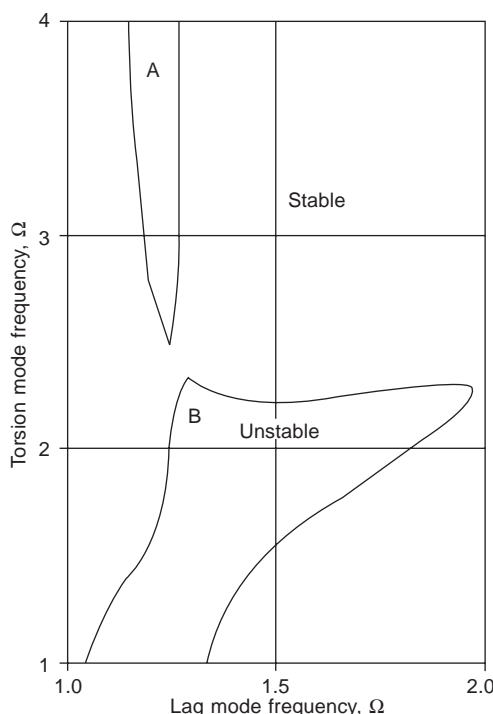


Fig. 9.17 Stability boundaries for coupled pitch–flap–lag motion

frequencies of the torsion and lag modes, for typical values of uncoupled flap frequency, δ_3 coupling, and pitch angle setting.

Region A of the figure represents the ‘buzz’ instability appropriate to high values of torsional stiffness, and Region B represents the ‘bang’ instability.

One aspect which has to be given careful consideration is the placement of the torsion mode frequency. Because the blades will experience different stiffnesses at the pitch change track rod depending upon the phase relationship between the torsional motion of each blade, a number of torsion mode frequencies will exist.

Each of these frequencies must be chosen so as to avoid the unstable region.

This is an example of a case where the behaviour of the tail rotor and control system must be considered in combination in order to define the correct data for the appropriate single blade analysis.

In practice, increasing the bending stiffness of the pitch change ‘spider’ arms, and of the pitch change rod attached to the centre of the ‘spider’, has produced freedom from both the ‘buzz’ and ‘bang’ instabilities.

9.9 Ground resonance

Any helicopter with a main rotor blade fundamental lag mode frequency less than 1Ω is susceptible in principle to the instability known as ground resonance.

The degrees of freedom involved are the lead–lag motion of the rotor blades and any fuselage mode containing motion of the rotor hub in the rotor plane.

If the blades lag in phase, the centre of gravity of the rotor system remains on the axis of rotation, but out-of-phase oscillatory motion of the blades will cause the rotor system centre of gravity to move off the axis of rotation and describe a circle, giving rise to inertia forces which will subject the fuselage and its chassis to an oscillatory force.

The mode of blade motion in which the direction of rotation of the centre of gravity of the rotor system is in the opposite sense to the direction of rotation of the rotor system is known as the ‘regressive’ lag mode, whereas the ‘progressive’ lag mode refers to the case where the centre of gravity moves in the same direction as the direction of rotor rotation.

The potential for instability occurs in the vicinity of a frequency coalescence between the ‘regressive’ lag mode and a fuselage mode, provided that the fundamental lag frequency is less than the rotational speed of the rotor. The phase relationships between the couplings are such that a frequency coalescence when the lag mode frequency is greater than the rotor speed does not produce an instability, neither does a coalescence with the ‘progressive’ lag mode.

The important parameters with respect to ground resonance are blade lag mode frequency and damping, fuselage frequency and damping, and fuselage mode shape. Of lesser significance are flap mode stiffness and aerodynamic loads. Ground resonance is basically a purely mechanical instability which could exist *in vacuo*.

In practice, a stability augmentation system can influence ground resonance, and if a significant response of such a system can be anticipated at the frequencies

associated with ground resonance, then its characteristics must be included in the analysis. An alternative approach is to ensure that the feedback systems are filtered in such a way so as not to respond at the frequencies of potential ground resonance oscillations.

Let us calculate the displacement of the rotor centre of gravity for an arbitrary motion of the blades. Let x_{k_g} and y_{k_g} be the co-ordinates of the centre of gravity of the k th blade relative to the centre of the hub, Fig. 9.18. This figure can represent either a hinged blade or a hingeless blade (as an offset rigid blade with hinge restraint, Chapter 7).

We easily find that

$$x_{k_g} = -eR \cos \psi_k - r_g \cos (\psi_k + \xi_k)$$

$$y_{k_g} = eR \sin \psi_k + r_g \sin (\psi_k + \xi_k)$$

Since ξ_k is a small angle, these relationships can be written approximately as

$$x_{k_g} = -(eR + r_g) \cos \psi_k + r_g \xi_k \sin \psi_k$$

$$y_{k_g} = (eR + r_g) \sin \psi_k + r_g \xi_k \cos \psi_k$$

Summing over the b blades of the rotor the co-ordinates of the centre of gravity of the rotor are

$$x_{r_g} = -\frac{eR + r_g}{b} \sum_{k=0}^{b-1} \cos \psi_k + \frac{r_g}{b} \sum_{k=1}^{b-1} \xi_k \sin \psi_k$$

or

$$x_{r_g} = (r_g/b) \sum_{k=0}^{b-1} \xi_k \sin \psi_k \quad (9.29)$$

and, similarly,

$$y_{r_g} = (r_g/b) \sum_{k=0}^{b-1} \xi_k \cos \psi_k \quad (9.30)$$

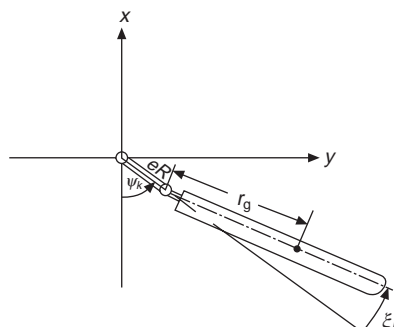


Fig. 9.18 Blade displacement in lagging motion

Now, suppose that the blades oscillate in lagging motion with frequency $\kappa\Omega$ such that

$$\xi_k = \xi_0 \cos \kappa\psi_k$$

Then substituting in eqn 9.29

$$\begin{aligned} x_{r_g} &= (r_g \xi_0 / b) \sum_{k=0}^{b-1} \cos \kappa\psi_k \sin \psi_k \\ &= (r_g \xi_0 / 2b) \sum_{k=0}^{b-1} [\sin(\kappa+1)\psi_k - \sin(\kappa-1)\psi_k] \end{aligned}$$

Since κ is arbitrary we find from eqn 9.29 that

$$x_{r_g} = \frac{r_g \xi_0}{2b} \left[\sigma_1 \sin(\kappa+1) \left(\psi + \frac{b-1}{b} \pi \right) - \sigma_{-1} \sin(\kappa-1) \left(\psi + \frac{b-1}{b} \pi \right) \right] \quad (9.31)$$

$$\text{where } \sigma_1 = \frac{\sin(\kappa+1)\pi}{\sin[(\kappa+1)\pi/b]} \text{ and } \sigma_{-1} = \frac{\sin(\kappa-1)\pi}{\sin[(\kappa-1)\pi/b]}$$

Similarly we find that

$$y_{r_g} = \frac{r_g \xi_0}{2b} \left[\sigma_1 \cos(\kappa+1) \left(\psi + \frac{b-1}{b} \pi \right) + \sigma_{-1} \cos(\kappa-1) \left(\psi + \frac{b-1}{b} \pi \right) \right] \quad (9.32)$$

The interpretation of eqns 9.31 and 9.32 is that the centre of gravity of the rotor whirls round the hub with a displacement consisting of two modes, one with frequency $(\kappa+1)\Omega$ and amplitude $r_g \xi_0 \sigma_1 / 2b$ and the other with frequency $(\kappa-1)\Omega$ and amplitude $r_g \xi_0 \sigma_{-1} / 2b$. The motion corresponding to the upper frequency $(\kappa+1)\Omega$ is in the same direction as the rotor rotation and is described as a 'progressive' motion; the motion corresponding to the lower frequency $(\kappa-1)\Omega$ is in the same or opposite direction to the rotor rotation according to whether $\kappa-1$ is positive or negative. When negative, the motion is described as 'regressive'.

The whirling centre of gravity produces periodic inertia forces which excite motion of the whole airframe on its undercarriage ('chassis' mode). If one of the frequencies of the oscillating inertia forces coincides with a chassis frequency, the potential for the occurrence of ground resonance exists.

This coincidence of frequencies can be represented in diagrammatic form, Fig. 9.19, which applies to an articulated rotor with no lag hinge restraint. The comparable diagram for a rotor with hinge restraint, or utilising an elastic hub element is shown in Fig. 9.20.

For a blade without hinge restraint, i.e. without a drag-hinge spring or elastic element, the lag frequency will always be less than the rotor speed and, therefore, $\kappa-1$ will always be negative. In Figs 9.19 and 9.20 the horizontal line represents the (constant) chassis frequency ω_c .

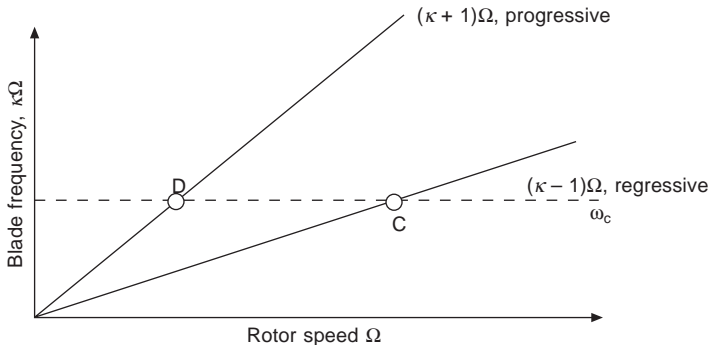


Fig. 9.19 Uncoupled chassis and rotor frequencies – articulated rotor, no hinge restraint

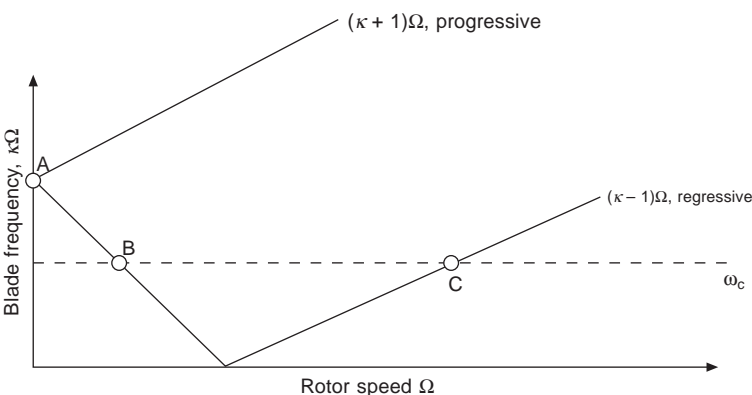


Fig. 9.20 Uncoupled chassis and rotor frequencies – rotor with drag hinge spring or elastic element

In Fig. 9.20 the point A represents the blade frequency when the rotor hub is stationary and is assumed here to be higher than the chassis frequency.

As the rotor speed increases, the branch corresponding to the whirl frequency $(\kappa - 1)\Omega$ intersects the chassis line at B and again at C when $(\kappa - 1) < 0$.

If the chassis frequency were higher than the frequency of the non-rotating blade there would have been an intersection with the $(\kappa + 1)\Omega$ branch.

The corresponding intersection for the case of the articulated rotor is point D on Fig. 9.19. It will be shown later that this intersection and the one corresponding to the point B cannot lead to instability. Ground resonance, if it occurs, is associated only with intersection C.

Let us now derive the equations of motion of the chassis–rotor system. It will be assumed that the chassis motion is confined to a single degree of freedom in the plane of the rotor – say, the lateral direction. The extension to two degrees of chassis motion is quite straightforward, but the analysis becomes rather too involved for simple results to be obtained. In practice, however, the chassis frequencies in the two directions are often far enough apart for the single-degree-of-freedom analysis to be applied with reasonable approximation to either direction separately.

The equations of blade lagging motion, relative to an unaccelerated hub, have already been obtained in Chapters 1 and 7. We must now include the inertia moment acting on the blade due to lateral oscillations of the chassis mode. Referring to Fig. 9.21 the inertia force on a blade element due to hub acceleration is $\ddot{y} dm$ in the negative y direction. Hence, the inertia lagging moment N_i about the real or virtual hinge is

$$N_i = - \int_{eR}^R r \ddot{y} \cos(\psi_k + \xi_k) dm$$

For small lagging angle ξ_k , and neglecting the product $\ddot{y}\xi_k$, we have, approximately,

$$\begin{aligned} N_i &= - \ddot{y} \cos \psi_k \int_{eR}^R r dm \\ &= - M_b r_g \ddot{y} \cos \psi_k \end{aligned} \quad (9.33)$$

where M_b is the mass of the blade. The equation of motion of the k th blade can then be written

$$\begin{aligned} \ddot{\xi}_k + 2\kappa\Omega\delta\xi_k + \kappa^2\Omega^2\xi_k &= -M_b r_g \ddot{y} \cos \psi_k / I \\ &= -(\ddot{y}/l_b) \cos \psi_k \end{aligned} \quad (9.34)$$

where δ is the damping coefficient, which may include both aerodynamic and artificial damping, $\kappa\Omega$ is the natural undamped frequency, and $l_b = I/M_b r_g$.

The displacement of the centre of gravity of the rotor in the y direction has already been found to be

$$y_{rg} = (r_g/b) \sum_{k=0}^{b-1} \xi_k \cos \psi_k \quad (9.30)$$

so that the equation of motion of the airframe and chassis is

$$\begin{aligned} (M + bM_b)\ddot{y} &= -bM_b\ddot{y}_{rg} - (M + bM_b)\kappa_c^2 \Omega^2 y - 2\kappa_c\Omega\delta_c(M + bM_b)y \\ &= r_g M_b \sum_{k=0}^{b-1} \xi_k \cos \psi_k - (M + bM_b)\kappa_c^2 \Omega^2 y \\ &\quad - 2\kappa_c\Omega\delta_c(M + bM_b)\dot{y} \end{aligned} \quad (9.35)$$

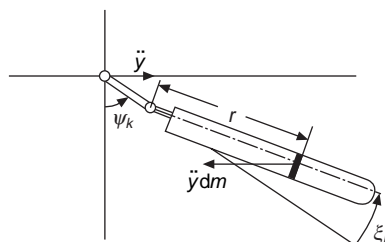


Fig. 9.21 Inertial force on blade due to fuselage motion

where δ_c is the damping coefficient of the chassis and $\kappa_c\Omega$ is its undamped natural frequency, M being the effective mass of the fuselage in the chassis mode.

The periodic terms in eqns 9.34 and 9.35 can be removed by using the Coleman co-ordinates, Appendix A.3. Let

$$\eta = - (2/b) \sum_{k=0}^{b-1} \xi_k \sin \psi_k$$

and

$$\zeta = - (2/b) \sum_{k=0}^{b-1} \xi_k \cos \psi_k$$

from which we get

$$\begin{aligned} \sum_{k=0}^{b-1} \dot{\xi}_k \sin \psi_k &= \frac{1}{2}b(\Omega\zeta - \dot{\eta}); \quad \sum_{k=0}^{b-1} \dot{\xi}_k \cos \psi_k = - \frac{1}{2}b(\Omega\eta - \dot{\zeta}) \\ \sum_{k=0}^{b-1} \ddot{\xi}_k \sin \psi_k &= - \frac{1}{2}b(\ddot{\eta} - 2\Omega\dot{\zeta} - \Omega^2\eta) \\ \sum_{k=0}^{b-1} \ddot{\xi}_k \cos \psi_k &= - \frac{1}{2}(\ddot{\zeta} + 2\Omega\eta - \Omega^2\zeta) \end{aligned}$$

Then, multiplying eqn 9.34 by $\sin \psi_k$ and summing over all the blades, we get

$$\ddot{\eta} + 2\Omega\delta\dot{\eta} + (\kappa^2 - 1)\Omega^2\eta - 2\Omega\dot{\zeta} - 2\Omega^2\delta\zeta = 0 \quad (9.36)$$

Repeating the process with $\cos \psi_k$ gives

$$\ddot{\zeta} + 2\Omega\delta\dot{\zeta} + (\kappa^2 - 1)\Omega^2\zeta + 2\Omega\dot{\eta} + 2\Omega^2\delta\eta - \ddot{\eta}/l_b = 0 \quad (9.37)$$

and eqn 9.35 can be written

$$\ddot{\eta} + 2\Omega\delta_c\dot{\eta} + \kappa_c^2\Omega^2\eta - \mu r_g \ddot{\zeta} = 0 \quad (9.38)$$

where $\mu = \frac{1}{2}bM_b/(M + bM_b)$ is the ‘mass ratio’, i.e. the ratio of half the blade mass to the total mass.

Equations 9.36, 9.37 and 9.38 are three simultaneous differential equations with constant coefficients in the variables η , ζ , and y . The solutions of these equations can be obtained in the same way as the stability equations of Chapter 5 by assuming that

$$\eta = \eta_0 e^{\lambda t}, \quad \zeta = \zeta_0 e^{\lambda t}, \quad y = y_0 e^{\lambda t}$$

Substituting in the equations and expanding the determinant of the co-efficients leads to a frequency equation of the form

$$A\lambda^6 + B\lambda^5 + C\lambda^4 + D\lambda^3 + E\lambda^2 + F\lambda + G = 0 \quad (9.39)$$

where the coefficients are functions of the non-dimensional chassis and blade natural frequencies $\kappa_c\Omega$ and $\kappa\Omega$. Unfortunately, the above sextic cannot be solved in general terms and, even when solved numerically, the many parameters involved make

interpretation difficult. One method of obtaining useful results is to note that the regions of instability will be bounded by curves representing undamped (neutral) oscillations. These can be found by assuming a solution to eqn 9.39 in the form $\lambda = i\omega$, where ω is real. Inserting this solution into the sextic and equating real and imaginary parts leads to the equations

$$A\omega^6 - C\omega^4 + E\omega^2 - G = 0 \quad (9.40)$$

$$B\omega^4 - D\omega^2 + F = 0 \quad (9.41)$$

in which

$$A = 1.$$

To solve these equations we take a range of values of κ_c , calculate the values of a , c , and e (which are functions of κ_c) and solve the biquadratic equation 9.41 for ω . These values of ω are inserted into the left-hand side of eqn 9.40 which is then plotted against ω . The values of ω which give zero values to the left-hand side of eqn 9.40 are solutions of eqns 9.40 and 9.41. We therefore have the values of the chassis frequency at which undamped oscillations occur. Coleman and Feingold¹¹ and Price¹² have presented these boundaries in the form of charts which enable the ranges of rotor speed, if any, for which the oscillations are unstable to be found.

Although the method described above gives a complete solution to the equations, it is possible to derive some valuable conclusions by simpler approaches. We shall describe first an approach given by Mil¹³.

Let us suppose that the chassis mode consists of lateral oscillations of amplitude y_0 and frequency p in the form

$$y = y_0 \sin pt \quad (9.42)$$

Then, according to eqn 9.34 the motion of the blade is given by

$$\begin{aligned} \ddot{\xi}_k + 2\kappa\Omega\delta\dot{\xi}_k + \kappa^2\Omega^2\xi_k &= \frac{y_0}{l_b} p^2 \sin pt \cos \psi_k \\ &= \frac{1}{2} \frac{y_0}{l} p \left[\sin \left\{ (p + \Omega)t + \frac{2\pi k}{b} \right\} + \sin \left\{ (p - \Omega)t - \frac{2\pi k}{b} \right\} \right] \end{aligned} \quad (9.43)$$

Equation 9.43 represents a second order system excited by a pair of simple-harmonic forcing functions. The solution must therefore be of the form

$$\xi_k = \xi_1 \sin [(p + \Omega)t + \psi_1] + \xi_2 \sin [(p - \Omega)t + \psi_2] \quad (9.44)$$

where ξ_1 , ξ_2 , ψ_1 , ψ_2 are amplitudes and phase angles which can be determined from the known response of such systems, Appendix A.4. Now, the blade motion would be expected to reach large amplitudes if one of the forcing frequencies lies close to the natural frequency of the lagging motion of the blade. Let us first consider resonance in the case

$$\kappa\Omega = |p - \Omega|$$

The amplitude of the blade oscillations will then be determined almost entirely by the second of the forcing terms on the right-hand side of eqn 9.43 and the response can be written approximately as

$$\xi_k = \xi_0 \cos [(p - \Omega)t - 2\pi k/b] \quad (9.45)$$

where

$$\xi_0 = -y_0 p^2 / 4\delta\kappa\Omega(p - \Omega)$$

Now, from eqn 9.30 the centre of gravity of the blades when the chassis mode consists of oscillations in the form given by eqn 9.41 is

$$y_{rg} = y + (r_g/b) \sum_{k=0}^{b-1} \xi_k \cos (\Omega t + 2\pi k/b)$$

Substituting for ξ_k from eqn 9.45 and expressing the products of the cosine terms as sums gives

$$y_{rg} = y + (r_g \xi_0 / 2b) \sum_{k=0}^{b-1} [\cos pt + \cos \{(2\Omega - p)t + 4\pi k/b\}]$$

From an analysis similar to that of Appendix A.3, we can easily show that

$$\sum_{k=0}^{b-1} \cos \{(2\Omega - p)t + 4\pi k/b\} = 0$$

so that

$$y_{rg} = \frac{1}{2} r_g \xi_0 \cos pt$$

The inertia force P_{in} acting on the chassis due to the oscillating centre of gravity of the blades is given by

$$\begin{aligned} P_{in} &= -bM_b \ddot{y}_{rg} \\ &= -bM_b \ddot{y} - \frac{bM_b y_0 p^4 r_g}{8\delta l_b \kappa \Omega (p - \Omega)} \cos pt \end{aligned}$$

and from eqn 9.35 the equation of motion of the chassis is

$$\begin{aligned} (M + bM_b) \ddot{y} + 2\delta_c \kappa_c \Omega (M + bM_b) \dot{y} + (M + bM_b) \kappa_c^2 \Omega^2 y \\ = -\frac{bM_b y_0 p^4 r_g}{8\delta l_b \kappa \Omega (p - \Omega)} \cos pt \end{aligned}$$

or

$$\ddot{y} + 2\delta_c \kappa_c \Omega \dot{y} + \kappa_c^2 \Omega^2 y = -\frac{\mu y_0 p^4 r_g}{8\delta l_b \kappa \Omega (p - \Omega)} \cos pt$$

But the solution to this equation must correspond to the motion assumed originally, eqn 9.41 and this requires that

$$p = \kappa_c \Omega$$

and

$$\delta\delta_c = \frac{\mu \kappa_c^2}{8\kappa(1 - \kappa_c)} \cdot \frac{r_g}{l_b} \quad (9.46)$$

remembering also that

$$\kappa\Omega = |\kappa_c - 1| \Omega$$

From these three relationships the critical rotor speed may be calculated. To ensure that the oscillations at resonance will be no worse than neutrally damped, the *product* of the dampings of the chassis and of the blade should satisfy the relationship eqn 9.46.

If we now consider the other possible resonant state represented by

$$\kappa\Omega = |p + \Omega|$$

we find that the above formulae remain the same but that Ω is everywhere replaced by $-\Omega$. Then, according to eqn 9.46 it appears that for undamped oscillations $\delta\delta_c$ would have to be negative, i.e. that either δ and δ_c would have to be negative. Since this is impossible, we conclude that ground resonance does not occur for $\kappa\Omega = |p + \Omega|$.

Referring to eqn 9.46 again, and since $\delta\delta_c$ cannot be negative, undamped vibrations can only occur if $\Omega > p$. In Figs 9.19 and 9.20 this is satisfied only by point C, i.e. the intersection of the branch of negative (regressive) values of $\kappa - 1$ with the chassis frequency.

An interesting method of simplifying the ground resonance problem has been given by Done¹⁴. In this method, details of which can be found in the original paper, it has been assumed that, by a suitable choice of co-ordinates, the higher frequency (progressive) mode branching from the point A in Fig. 9.20 can be neglected, so that the simplified equations relate only to the chassis mode and to the lower frequency rotor mode.

By means of this approximation and using eqns 9.36 to 9.38 Done arrives at a characteristic quartic equation of the form

$$\begin{aligned} (\lambda^2 + 2\delta_c\kappa_c\Omega\lambda + \kappa_c^2\Omega^2)[\lambda^2 + 2\delta_c\kappa_c\Omega + (\Omega - \Gamma)^2] + \frac{\mu(\Omega - \Gamma)}{2\Gamma} \lambda^4 \\ + \frac{\mu(\Omega - \Gamma)}{2\Gamma^2} \delta_c\kappa_c\Omega^2\lambda^3 = 0 \end{aligned} \quad (9.47)$$

where Γ is the blade rotating lag frequency in the absence of Coriolis force coupling.

The roots $\lambda = \lambda_{re} \pm i\lambda_{im}$, where $\lambda_{im} \equiv \kappa$, of eqn 9.47 can be plotted as shown in Fig. 9.22. The lower diagram, showing the imaginary parts of the roots, corresponds to the diagram of Fig. 9.20 but with the degrees of freedom coupled. As can be seen the effect of coupling is to modify the shape of the diagram in the neighbourhood of the (uncoupled) crossing points. If unstable oscillations occur, the branches fail to meet at C since real roots occur in this region, as is shown by the small loop in the λ_{re} diagram. The extent of the instability is indicated by the size of the gap between the branches.

The amount of damping required which just gives harmonic oscillations can be found by substituting $\lambda = \pm i\kappa_c\Omega = \pm i(\Omega - \Gamma)$ into eqn 9.47. Done shows that this leads to

$$\delta\delta_c = \mu\kappa_c^2/8\kappa(1 - \kappa_c)$$

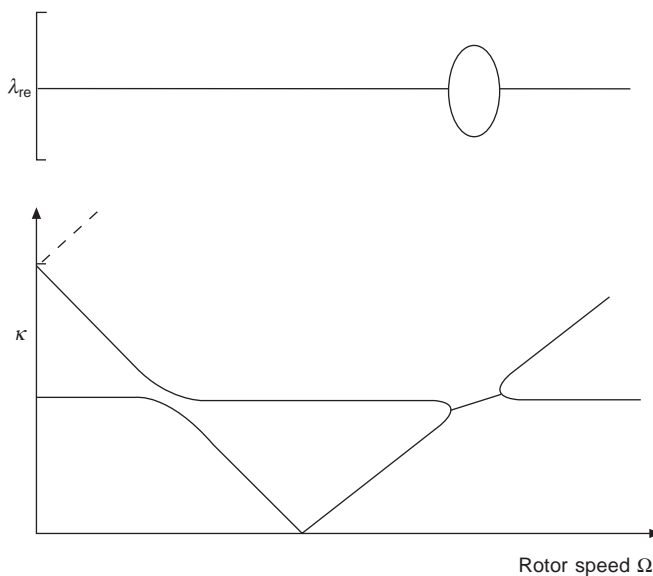


Fig. 9.22 Effect of coupling on fuselage and whirling frequencies

as given before in eqn 9.45 except that, since in Done's analysis the blade is represented by a point mass, the value of r_g/l_b is equal to unity.

The damping requirement to suppress ground resonance is strongly influenced by the lag mode frequency.

Figure 9.23 indicates the variation of the damping requirement for a range of lag mode frequencies. The closer the lag mode frequency is to 1Ω , the smaller the amount of damping that is required to ensure stability.

As previously indicated, ground resonance is completely eliminated if the blade lag frequency is greater than 1Ω . A rotor with this characteristic is termed 'supercritical'. This solution is found in the two-bladed teetering rotor and the Lockheed gyro-controlled multi-blade 'rigid rotor' design.

However, unless the lag mode frequency is sufficiently greater than 1Ω , e.g. 1.5Ω , there may be fatigue strength problems due to high amplification of the first harmonic air and Coriolis loads. Flap-lag instability is also a possibility for a rotor with a 'supercritical' lag frequency, as described in section 9.7.

A significant point to note when designing for, and demonstrating in practice, freedom from ground resonance is that the full available range of rotor lift must be considered. This is because chassis geometry, oleo stiffness, tyre stiffness, and damping rates are all functions of the reaction at the ground contact position. The non-linear effects of oleo stiffness are very significant, and due to oleo 'sticking' when the load becomes less than the 'break-out' load in the high lift condition, the oleo cannot dissipate any energy. Hence, apart from the effects of stiffness change, the only significant contribution to chassis mode damping in this condition is provided by the hysteresis effects of the tyres.

Also to be considered are the full range of tyre pressures (deflated to overinflated),

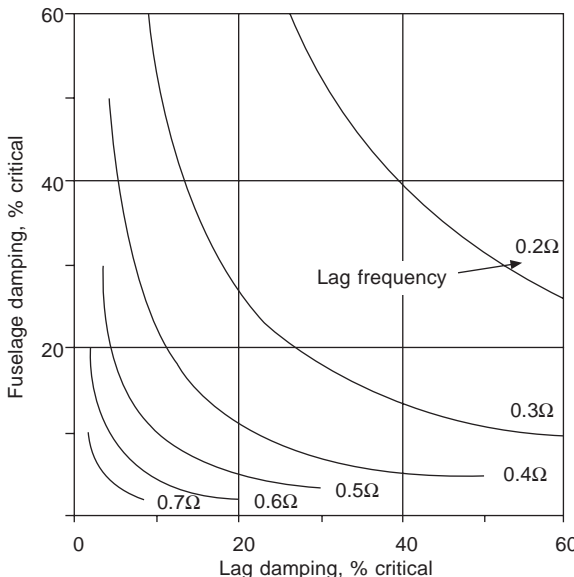


Fig. 9.23 Damping requirement as a function of lag mode frequency

tie-down situation and wheel orientation (particularly relevant to Naval helicopters), wheel brake situation, and surface contact conditions.

The various defined loading states of the helicopter will also have to be considered, since these will influence the chassis mode frequencies and shapes, e.g. the roll/lateral mode frequency will be reduced by the presence of external stores.

Viscous damping in both the airframe and rotor is normally assumed in the analysis, and once stability boundaries have been established, a conversion to the particular form of damping employed in the rotor can be made. For example, a common design of blade hydraulic damper utilises a very high rate of ' V^2 ' damping followed by a constant force cut-off. The conversion of the viscous damping requirement to another form of damping is based on equating the energy dissipation per cycle of oscillation. This leads to the concept of an allowable blade 'swing angle' in the ground resonance mode, above which the motion of the helicopter will be divergent. Disturbances of the helicopter producing blade 'swing angles' below this value will subside.

This situation implies that it is necessary to know the levels of hub acceleration in the plane of the rotor which will be experienced in service, and which may force the blades to oscillate in the ground resonance mode.

In order to ensure stability over the full range of the many variables involved, it has become the practice to define a chassis mode case (which may be realistic or artificial) that will lead to the worst possible instability.

It can be shown that more blade lag damping is required as the chassis mode frequency increases (provided that the frequency coalescence still occurs below the maximum possible rotor speed). Thus an assumption is often made in the design stage that the frequency coalescence occurs at the maximum operating rotor speed, and sufficient

damping is then provided to ensure stability in this worst case. Thus, freedom from ground resonance will be established for the full range of operating conditions.

9.10 Air resonance

In Chapter 5, the dynamic stability of the helicopter was discussed on the assumption that the motion was ‘quasi-steady’, i.e. the acceleration of the helicopter could be ignored and the response of the rotor depended only in the instantaneous translational and angular velocities of the helicopter. As we shall see, in making this assumption a certain mode of motion is suppressed which is of little significance as a conventional stability mode, but may, in the case of hingeless rotors, couple with the blade ‘regressive’ lag mode to produce an instability in flight which is closely related to ground resonance.

For such rotor systems, the regressive cyclic flapping mode can couple with the fuselage roll and pitch motions to produce ‘slow gyroscopic’ modes (sometimes also referred to as ‘pendulum’ modes) of the helicopter at frequencies which are close to the ‘regressive’ lag mode frequency at normal operating rotor speed.

Let us suppose that the hingeless helicopter is pitching and rolling with a frequency high enough to prevent significant translational velocities. As we shall be concerned only with the first flapping mode, let the displacement of a point of the blade be given by

$$Z = RS_1(x)\bar{\beta}(\psi)$$

where we write $\bar{\beta}(\psi)$ as the azimuth co-ordinate of the blade by analogy with the flapping angle β of the rigid blade, as in section 7.5. The mode response equation is, by eqn 7.86.

$$\frac{d^2\bar{\beta}}{d\psi^2} + \lambda_1^2 \bar{\beta} = \frac{1}{\Omega^2 R^2 f(1)} \int_0^1 \frac{\partial F}{\partial x} S_1(x) dx$$

where $\lambda_1 \Omega$ is the flapping frequency and $S_1(x)$ is the first mode bending shape.

For pitching and rolling motion only, the blade loading $\partial F/\partial x$ can easily be shown to be

$$\begin{aligned} \frac{\partial F}{\partial x} &= \frac{1}{2} \rho a c \Omega^2 R^3 \left(-x S_1 \frac{d\bar{\beta}}{d\psi} + x \hat{p} \sin \psi + x \hat{q} \cos \psi \right) \\ &+ 2m\Omega^2 R^2 (x \hat{p} \cos \psi - x \hat{q} \sin \psi) + m\Omega^2 R^2 \left(x \frac{d\hat{p}}{d\psi} \sin \psi + x \frac{d\hat{q}}{d\psi} \cos \psi \right) \end{aligned}$$

The first bracket represents the change of aerodynamic incidence due to the angular motion and flapping; the second and third brackets denote the gyroscopic and angular acceleration inertia forces. The flapping equation of the k th blade can then be written

$$\begin{aligned} \frac{d^2\beta_k}{d\psi^2} + \frac{\gamma_2 E_1}{2} \frac{d\beta_k}{d\psi} + \lambda_1^2 \beta_k &= \frac{\gamma_2}{2} (F_1 \hat{p} \sin \psi + F_1 \hat{q} \cos \psi) \\ &+ \frac{\gamma_2}{\gamma_1} \left(2 \hat{p} \cos \psi - 2 \hat{q} \sin \psi + \frac{d\hat{p}}{d\psi} \sin \psi + \frac{d\hat{q}}{d\psi} \cos \psi \right) \end{aligned} \quad (9.48)$$

where E_1 , F_1 , γ_1 and γ_2 have been defined in section 7.5.

We now define the Coleman co-ordinates of flapping motion by

$$\bar{a}_1 = -\frac{2}{b} \sum_{k=0}^{b-1} \bar{\beta}_k \cos \psi_k; \quad \bar{b}_1 = -\frac{2}{b} \sum_{k=0}^{b-1} \bar{\beta}_k \sin \psi_k \quad (9.49)$$

Then, adopting the same procedure as for the lagging equations, the result of summing eqn 9.48 over all the blades leads to

$$\bar{a}_1'' + \bar{v}\bar{a}_1' + (\lambda_1^2 - 1)\bar{a}_1 + 2\bar{b}_1' + \bar{v}\bar{b}_1 = -\frac{\gamma_2 F_1}{2} \hat{q} - \bar{F} \left(2\hat{p} + \frac{d\hat{q}}{d\psi} \right) \quad (9.50)$$

$$\bar{b}_1'' + \bar{v}\bar{b}_1' + (\lambda_1^2 - 1)\bar{b}_1 - 2\bar{a}_1' - \bar{v}\bar{a}_1 = -\frac{\gamma_2 F_1}{2} \hat{p} + \bar{F} \left(2\hat{q} + \frac{d\hat{p}}{d\psi} \right) \quad (9.51)$$

where $\bar{v} = \gamma_2 E_1 / 2$, $\bar{F} = \gamma_2 / \gamma_1$, and the dashes denote differentiation with respect to ψ .

From eqn 7.106 of Chapter 7, the moment exerted on the hub by the flapping deflection of the k th blade is

$$M_k = (\lambda_1^2 - 1) \Omega^2 R^3 \bar{\beta}_k \int_0^1 mx S_1(x) dx$$

Resolving about the rolling and pitching axes and summing over all the blades gives for the rolling and pitching moments

$$L = b\rho ac\Omega^2 R^4 (\lambda_1^2 - 1) \bar{b}_1 / 2\gamma_1$$

$$M = b\rho ac\Omega^2 R^4 (\lambda_1^2 - 1) \bar{a}_1 / 2\gamma_1$$

Including the thrust moment, the rolling and pitching equations of the helicopter are

$$A \frac{dp}{dt} = \frac{b\rho ac\Omega^2 R^4 (\lambda_1^2 - 1)}{2\gamma_1} \bar{b}_1 + Th\bar{b}_1 \quad (9.52)$$

$$B \frac{dq}{dt} = \frac{b\rho ac\Omega^2 R^4 (\lambda_1^2 - 1)}{2\gamma_1} \bar{a}_1 + Th\bar{a}_1 \quad (9.53)$$

Non-dimensionalising eqns 9.52 and 9.53 by dividing by $\rho s A \Omega^2 R^3$ gives

$$\frac{d\hat{p}}{d\psi} = \frac{a(\lambda_1^2 - 1)}{2\mu^* i_A \gamma_1} \bar{b}_1 + \frac{t_c h}{i_A \mu^*} \bar{b}_1 \quad (9.54)$$

$$\frac{d\hat{q}}{d\psi} = \frac{a(\lambda_1^2 - 1)}{2\mu^* i_B \gamma_1} \bar{a}_1 + \frac{t_c h}{i_B \mu^*} \bar{a}_1 \quad (9.55)$$

where μ^* , i_A , and i_B are the mass parameter and inertia coefficients defined in Chapter 5.

The rolling and pitching motions when the blade flapping acceleration is included are represented by the four equations

$$\bar{a}_1'' + \bar{v}\bar{a}_1' + \bar{\chi}\bar{a}_1 + 2\bar{b}_1' + \bar{v}\bar{b}_1 + 2\bar{F}\hat{p} + \bar{F} \frac{d\hat{q}}{d\psi} + K\hat{q} = 0 \quad (9.56)$$

$$-2\bar{a}_1' - \bar{v}\bar{a}_1 + \bar{b}_1'' + \bar{v}\bar{b}_1' + \bar{\chi}\bar{b}_1 + \bar{F} \frac{d\hat{p}}{d\psi} + K\hat{p} - 2\bar{F}\hat{q} = 0 \quad (9.57)$$

$$\bar{k}_A\bar{b}_1 - \frac{d\hat{p}}{d\psi} = 0 \quad (9.58)$$

$$\bar{k}_B\bar{a}_1 - \frac{d\hat{q}}{d\psi} = 0 \quad (9.59)$$

where

$$\bar{k}_A = \frac{a(\lambda_1^2 - 1)}{2\mu^*i_A\gamma_1} + \frac{t_c h}{\mu^*i_A}; \quad \bar{k}_B = \frac{a(\lambda_1^2 - 1)}{2\mu^*i_B\gamma_1} + \frac{t_c h}{\mu^*i_B}$$

$$\bar{K} = \gamma_2 F_1/2, \quad \bar{\chi} = \lambda_1^2 - 1$$

The usual form for the solution, $\hat{p} = \hat{p}_0 e^{\lambda\tau} \dots$ etc., leads to a sextic characteristic equation

$$A\lambda^6 + B\lambda^5 + C\lambda^4 + D\lambda^3 + E\lambda^2 + F\lambda + G = 0$$

where

$$A = 1$$

$$B = 2\bar{v}$$

$$C = 4 + 2\bar{\chi} + \bar{v}^2 + \bar{F}(\bar{k}_A + \bar{k}_B)$$

$$D = 2\bar{v}(2 + \bar{\chi}) + (\bar{k}_A + \bar{k}_B)(\bar{K} + \bar{F}\bar{v})$$

$$E = \bar{\chi}^2 + \bar{v}^2 + (\bar{k}_A + \bar{k}_B)[\bar{F}(4 + \bar{\chi}) + \bar{K}\bar{v}] + \bar{k}_A\bar{k}_B\bar{F}^2$$

$$F = (\bar{k}_A + \bar{k}_B)(\bar{\chi}\bar{K} + 2\bar{F}\bar{v}) + 2\bar{F}\bar{K}\bar{k}_A\bar{k}_B$$

$$G = \bar{k}_A\bar{k}_B(\bar{K}^2 + 4\bar{F}^2)$$

Taking as typical values

$$\bar{v} = 0.836, \quad \bar{\chi} = 0.245, \quad \bar{F} = 1.08, \quad \bar{K} = 1.146$$

$$\bar{k}_A = 0.102, \quad \bar{k}_B = 0.0204,$$

the roots of the sextic are found to be

$$\lambda_{1,2} = -0.408 \pm 2.03i$$

$$\lambda_{3,4} = -0.215 \pm 0.246$$

$$\lambda_5 = -0.356, \quad \lambda_6 = -0.07$$

If the complex roots are substituted back into the equations of motion and the

ratios of the variables are examined, as was done in Chapter 5, it is found that the first complex pair corresponds to a tilt of the rotor disc whose axis moves in the same direction as the rotor with a frequency just over twice that of the rotor; the second pair of roots corresponds to a rotor tilt which is a retrograde, or backward, motion, with a frequency about a quarter that of the rotor. It is this latter mode of motion whose frequency is likely to lie close to the lagging frequency of the blade.

Let us suppose that the shaft is fixed, i.e. that the pitching and rolling motion is now absent. This assumption can be expressed mathematically by making \bar{k}_A and \bar{k}_B infinitely large. The sextic is found to degenerate into a quartic which, with the other constants having the same values as before, has the roots

$$\lambda_{1,2} = -0.42 \pm 2.03i$$

$$\lambda_{3,4} = -0.42 \pm 0.21i$$

It can be seen that the fast, forward, motion is hardly affected by constraining the angular motion of the fuselage and that only the damping of the slow, backward, mode is changed significantly. It can easily be shown¹⁵ that the motion described above is exactly the same as that of a damped spring-restrained gyroscope whose polar moment of inertia is the same as that of the rotor, and the spring stiffness is the same as the hub moment due to the rotor tilt.

The motion of the helicopter consists, therefore, of a fast rotor precession, which is practically independent of the motion of the fuselage, and a slow precession in which the fuselage motion, mainly rolling, has some influence on the damping and frequency. Because the fuselage moves considerably in this latter mode, and appears to rock under the rotor, it is often referred to as the 'pendulum' mode, but this is an incorrect description since, as we have seen, the mode is still present even when the fuselage is fixed. The 'slow gyroscopic mode' is suggested as a more apt description.

The two real roots of the sextic correspond to the damping in pitch and roll, as already discussed in Chapter 5.

We now have to investigate the interaction of this blade flapping and fuselage motion with the lagging motion of the blades. Due to the rolling and pitching of the fuselage, the associated acceleration of the hub contributes inertia terms to the lagging equations as in the case of ground resonance. However, blade flapping also occurs in this motion, and the corresponding Coriolis inertia terms must be included. Also, the inertia of the lagging blades causes further pitching and rolling moments on the helicopter.

The Coriolis terms due to blade flapping are proportional to $\bar{\beta} d\bar{\beta}/d\psi$, which, for small perturbations, can be linearised to $\bar{a}_0 d\bar{\beta}/d\psi$, \bar{a}_0 being assumed constant at the value for steady hovering flight. There is also a lagwise aerodynamic force due to the change of direction of the local flow when the blade flaps, and this is clearly proportional to the local induced velocity and to the flapping rate $d\bar{\beta}/d\psi$. Thus, both the coning angle and the induced velocity are parameters of the motion.

If the co-ordinate of a point of the lagging blade is expressed as

$$Y = RT_1(x) \xi(\psi)$$

the following non-dimensional quantities may be defined¹⁵, as

$$\hat{H} = \frac{bgR}{2W} \int_0^1 mT_1(x)dx; \quad \bar{J} = \frac{\int_0^1 mS_1 T_1(dS_1/dx)dx}{\int_0^1 mT_1^2 dx}$$

$$\bar{L} = 2\bar{a}_0 \bar{J}; \quad \bar{H} = \frac{\int_0^1 mT_1 dx}{\int_0^1 mT_1^2 dx}$$

and in addition to eqns 9.50 and 9.51 we have the roll, pitch, and lagging equations in the form

$$\frac{h\hat{H}}{i_A} \zeta'' + \bar{k}_A \bar{b}_1 - \frac{d\hat{p}}{d\psi} = 0 \quad (9.60)$$

$$-\frac{h\hat{H}}{i_B} \eta'' + \bar{k}_B \bar{a}_1 - \frac{d\hat{q}}{d\psi} = 0 \quad (9.61)$$

$$\zeta'' + 2\delta\zeta' + (\kappa^2 - 1)\zeta + 2\eta' + 2\delta\eta + \bar{L}\bar{a}'_1 - \bar{L}\bar{b}_1 - \bar{H}h \frac{d\hat{p}}{d\psi} = 0 \quad (9.62)$$

$$\eta'' + 2\delta\eta' + (\kappa^2 - 1)\eta - 2\zeta' - 2\delta\zeta + \bar{L}\bar{a}_1 + \bar{L}\bar{b}'_1 + \bar{H}h \frac{d\hat{q}}{d\psi} = 0 \quad (9.63)$$

The derivation of these equations is given in Bramwell's paper¹⁵. As can be seen, we now have six second order differential equations which lead to a polynomial characteristic equation of the tenth degree when the usual method of solution is adopted. Lytwyn *et al.*¹⁶ have considered a mathematical model with eighteen degrees of freedom which includes flexibility of the fuselage and of the feathering mechanism. The problem is too complicated for simple results to be obtained as was found possible with ground resonance. Numerical methods have to be used for calculating the roots of the equations for ranges of values of the parameters occurring in a particular case.

The results of such calculations, though, have been rather inconsistent. There appears to be no 'resonance' of the kind occurring in the ground resonance problem, i.e. there is no sudden deterioration of damping near the coincidence of blade lagging and fuselage rolling mode frequencies. There may be an unstable lagging motion¹⁷ when only the natural air damping (about 2 per cent of critical) and structural damping are present, and this instability remains fairly constant over a wide range of rotor speeds. This may be due to the fact that the flap damping is very high, which would tend to 'flatten out' the response curve so that resonance is not apparent. Increasing the lag damping to about 5 per cent of critical seems to place this mode in the stable region. Typical roots from such calculations for the case of 2 per cent damping are

$$\lambda_{1,2} = +0.008 \pm 0.37i \quad (\text{slow})$$

$$\lambda_{3,4} = -0.03 \pm 1.7i \quad (\text{fast})$$

the unit of time being that corresponding to one radian of rotor revolution.

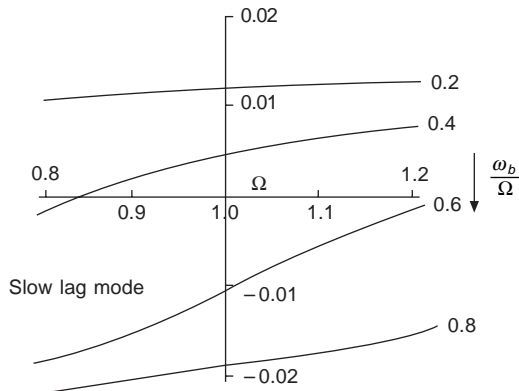


Fig. 9.24 Real part of slow lag mode root, 2 per cent critical lag damping

Figure 9.24 indicates the real part of the slow lag mode root as a function of rotor speed for a range of values of fundamental lag mode frequency and 2 per cent critical lag damping.

Since the lag natural frequency for semi-rigid and hingeless rotor systems is typically greater than 0.6Ω , it is seen that stability is ensured for values of rotor speed throughout the normal range and well beyond.

Because the fuselage ‘stiffness’ term arises from blade flapping, which is aerodynamically heavily damped, the effective damping in the ‘slow gyroscopic’ modes is high. However, we have noted that the important parameter in the suppression of ground resonance is the product of the blade lag mode and chassis mode dampings. Indeed, analysis shows that with high fuselage damping and low lag damping the width of the unstable region is large¹⁷.

Thus, the possibility of air resonance remains if the lag damping is very low. On the other hand, analysis shows that the amount of lag damping required to suppress the instability is quite small. Consequently air resonance will only be a potential problem for rotors with relatively high flap stiffness and low lag damping, a possible combination for both semi-rigid and hingeless rotor systems.

However, the amount of lag damping required is much less than is typically required to suppress ground resonance. Therefore, a helicopter which is stable under the conditions most likely to give rise to ground resonance is unlikely to be subject to an air resonance problem.

Reference 19 provides useful additional information on aspects of air resonance.

References

1. Loewy, R. G., ‘Review of rotary-wing V/STOL dynamic and aeroelastic problems’, *J. Amer. Helicopter Soc.*, July 1969.
2. Hansford, R. E., and Simons, I. A., ‘Torsion–flap–lag coupling on helicopter rotor blades’, *J. Amer. Helicopter Soc.*, October 1973.

3. Pei, Chi Chou, 'Pitch-lag instability of helicopter rotor blades', *J. Amer. Helicopter Soc.*, July 1958.
4. Stammers, C. W., 'The flutter of a helicopter rotor blade in forward flight', *Aeronaut. Q.*, February 1970.
5. Carta, F. O., 'An analysis of the stall flutter instability of helicopter rotor blades', *J. Amer. Helicopter Soc.*, October 1967.
6. Ham, N. D. and Young, M. I., 'Torsional oscillations of rotor blades due to stall', *J. Aircraft*, May to June 1966.
7. Ham, N. D. 'Helicopter blade flutter', *AGARD Rep. 607*, January 1973.
8. Coleman, Robert P., and Stempin, Carl W., 'A preliminary theoretical study of aerodynamic instability of a two-bladed helicopter rotor', *NACA Res. Memo. L6H 23*, 1946.
9. Balmford, D. E. H., Hansford, R. E. and King, S. P. 'Helicopter dynamics'. Westland Helicopters Ltd. Report, March 1985.
10. Ormiston, Robert A. and Hodges, Dewey H., 'Linear flap-lag dynamics of hingeless rotor blades in hover', *J. Amer. Helicopter Soc.*, April 1972.
11. Coleman, R. P. and Feingold, A. M., 'Theory of self-excited mechanical oscillations of helicopter rotors with hinged blades', *NACA Rep. 1351*, 1958.
12. Price, H. L., 'Simplified helicopter ground resonance stability boundaries', *Aircraft Engineering*, October and November 1962.
13. Mil, M. L., et al., *Helicopters – calculation and design*, vol. II, 'Vibrations and dynamic stability', *NASA Tech. Transl. NASA TT F-519*, 1968.
14. Done, G. T. S., 'A simplified approach to helicopter ground resonance', *Aeronaut. J.*, May 1974.
15. Bramwell, A. R. S., 'An introduction to helicopter air resonance', *Aeronautical Research Council R & M. 3777*, 1975.
16. Lytwyn, R. T., Miao, W., and Woitsch, W., 'Airborne and ground resonance of hingeless rotors' *J. Amer. Helicopter Soc.*, April 1971.
17. Ballock, J. C. A., 'Some calculations for air resonance of a helicopter with non-articulated rotor blades', *Aeronautical Research Council R & M 3743*, 1974.
18. Ormiston, R. A., 'Aeromechanical stability of soft in-plane hingeless rotor helicopters,' Paper 25, 3rd European Rotorcraft Forum, Aix-en-Provence, September 1977.
19. King, S. P. 'Theoretical and experimental investigations into helicopter air resonance,' 39th Annual Forum of American Helicopter Society, St Louis, MO, May 1983.

Appendices

A.1 Euler's equations

A.1.1 Angular momentum and the equations of angular motion

We define the *relative angular momentum*, \mathbf{h} , of a system of particles comprising a body by

$$\mathbf{h} = \sum \mathbf{r} \times (m\mathbf{v}_r) \quad (\text{A.1.1})$$

where \mathbf{r} is the position vector of a particle of mass m and \mathbf{v}_{rel} is the velocity of the particle *relative to the origin*, which may be that of a moving frame. The summation is taken over all the particles of the system. Then

$$d\mathbf{h}/dt = \sum (d\mathbf{r}/dt) \times (m\mathbf{v}_{\text{rel}}) + \sum \mathbf{r} \times (md\mathbf{v}_{\text{rel}}/dt) \quad (\text{A.1.2})$$

Now, if \mathbf{v} is the *absolute* velocity of the particle and \mathbf{v}_0 the velocity of the origin of the moving frame,

$$\mathbf{v}_{\text{rel}} = d\mathbf{r}/dt = \mathbf{v} - \mathbf{v}_0$$

and

$$d\mathbf{v}_{\text{rel}}/dt = d\mathbf{v}/dt - d\mathbf{v}_0/dt$$

Since

$$(d\mathbf{r}/dt) \times \mathbf{v}_{\text{rel}} = (d\mathbf{r}/dt) \times (d\mathbf{r}/dt)$$

the first term of eqn A.1.2 is zero; therefore,

$$d\mathbf{h}/dt = \sum \mathbf{r} \times (md\mathbf{v}/dt) - \sum \mathbf{r} \times (md\mathbf{v}_0/dt)$$

But $md\mathbf{v}/dt = \mathbf{F}$, where \mathbf{F} is the resultant external force acting on the particle.

Hence

$$\sum \mathbf{r} \times (md\mathbf{v}/dt) = \sum \mathbf{r} \times \mathbf{F} = \mathbf{T}$$

where \mathbf{T} is the moment of the external forces about the origin.

Also, since $d\mathbf{v}_0/dt$ is constant over the system of particles,

$$\sum \mathbf{r} \times (m\mathbf{v}_0/dt) = M\mathbf{r}_g \times \mathbf{a}_0$$

since $\sum m\mathbf{r}$ is the mass moment of the system relative to the origin, M being the total system mass, \mathbf{r}_g the position vector of the centre of gravity of the system, and \mathbf{a}_0 the acceleration of the origin of the moving frame. Thus, finally,

$$d\mathbf{h}/dt = \mathbf{T} - M\mathbf{r}_g \times \mathbf{a}_0 \quad (\text{A.1.3})$$

We can obtain an alternative formula by defining the *absolute* angular momentum by

$$\mathbf{H} = \sum \mathbf{r} \times (m\mathbf{v}) \quad (\text{A.1.4})$$

where, as above, \mathbf{v} is the *absolute* velocity of the particle. By an argument similar to that above we obtain the equation

$$d\mathbf{H}/dt = \mathbf{T} - \mathbf{v}_0 \times M\mathbf{v}_g \quad (\text{A.1.5})$$

where \mathbf{v}_g is the velocity of the centre of gravity of the system of particles.

We now expand the general vector eqns A.1.3 and A.1.5 in terms of components measured in the chosen frame of reference.

From the defining equations A.1.1 and A.1.2 we find that

$$\mathbf{H} = \mathbf{h} + \sum \mathbf{r} \times m\mathbf{v}_0 = \mathbf{h} + M\mathbf{r}_g \times \mathbf{v}_0$$

For subsequent applications we shall choose axes which are fixed in the body, as it is clearly convenient that the inertial properties of the body should remain constant with time. We can then write for the particle velocity \mathbf{v}_r

$$\mathbf{v}_r = \boldsymbol{\Omega} \times \mathbf{r}$$

where $\boldsymbol{\Omega}$ is the angular velocity of the body and axes, so that, from eqn A.1.1

$$\begin{aligned} \mathbf{h} &= \sum \mathbf{r} \times (m\boldsymbol{\Omega} \times \mathbf{r}) \\ &= \sum m\boldsymbol{\Omega}(\mathbf{r} \cdot \mathbf{r}) - \sum m\mathbf{r}(\boldsymbol{\Omega} \cdot \mathbf{r}) \end{aligned} \quad (\text{A.1.6})$$

Now let us write

$$\mathbf{r} = xi + yj + zk$$

$$\boldsymbol{\Omega} = \omega_1 i + \omega_2 j + \omega_3 k$$

where i, j, k are a set of orthogonal unit vectors fixed in the body. If we also write

$$\mathbf{h} = h_1 i + h_2 j + h_3 k$$

we find on expanding eqn A.1.6 that the the components of angular momentum are given by

$$\left. \begin{aligned} h_1 &= A\omega_1 - F\omega_2 - E\omega_3 \\ h_2 &= B\omega_2 - D\omega_3 - F\omega_1 \\ h_3 &= C\omega_3 - E\omega_1 - D\omega_2 \end{aligned} \right\} \quad (\text{A.1.7})$$

where A, B, C, D, E, F are the moments and products of inertia defined by

$$\begin{aligned} A &= \sum m(y^2 + z^2), & B &= \sum m(x^2 + z^2), & C &= \sum m(x^2 + y^2) \\ D &= \sum myz, & E &= \sum mxz, & F &= \sum mxy \end{aligned}$$

The relations given by eqn 1.12 can be expressed conveniently in matrix form as

$$\begin{bmatrix} h_1 \\ h_2 \\ h_3 \end{bmatrix} = \begin{bmatrix} A & -F & -E \\ -F & B & -D \\ -E & -D & C \end{bmatrix} \begin{bmatrix} \omega_1 \\ \omega_2 \\ \omega_3 \end{bmatrix}$$

where the square matrix is sometimes referred to as the *inertia tensor*.

The inertia tensor can be regarded as an operator which transforms the angular velocity vector into the angular-momentum vector.

It is always possible to choose axes through any point in the body such that the products of inertia D, E, F vanish. These axes are called *principal axes*, in which case

$$\mathbf{h} = A\omega_1\mathbf{i} + B\omega_2\mathbf{j} + C\omega_3\mathbf{k} \quad (\text{A.1.8})$$

If the origin of the axes is a *fixed point* or the *centre of gravity*, we find that

$$\mathbf{d}\mathbf{h}/dt = \mathbf{d}\mathbf{H}/dt = \mathbf{T} \quad (\text{A.1.9})$$

since, in both cases, $\mathbf{r}_g \times \mathbf{a}_0 = 0$ and either $\mathbf{v}_0 = 0$ or $\mathbf{v}_0 = \mathbf{v}_g$ so that $\mathbf{v}_0 \times \mathbf{v}_g = 0$.

Since, in general, the axes will be moving

$$\mathbf{d}\mathbf{h}/dt = \partial\mathbf{h}/\partial t + \boldsymbol{\Omega} \times \mathbf{h} \quad (\text{A.1.10})$$

and taking the special case of rotation about a fixed point and referring the motion to principal axes, eqns A.1.8, A.1.9 and A.1.10 give

$$A\dot{\omega}_1 - (B - C)\omega_2\omega_3 = L \quad (\text{A.1.11})$$

$$B\dot{\omega}_2 - (C - A)\omega_3\omega_1 = M \quad (\text{A.1.12})$$

$$C\dot{\omega}_3 - (A - B)\omega_1\omega_2 = N \quad (\text{A.1.13})$$

where L, M, N are the components of the torque \mathbf{T} .

Equations A.1.11, A.1.12 and A.1.13 are known as *Euler's dynamical equations* and can easily be remembered from their cyclic form.

A.1.2. Euler's equations for a rigid blade

In dealing with blade motion, however, we often wish to regard the blade as a rigid body moving about a hinge system which is offset from the rotor axis. To simplify matters we can assume that the hinge system is effectively concentrated at a point. Thus, the blade moves about a point which is not fixed, Fig. A.1.1, and Euler's equations no longer apply.

On the other hand, it would be inconvenient to take the centre of gravity as origin for, in calculating the torque, we would have to consider the unknown reactions at the hinge. We can, however, extend Euler's equations by making use of eqn A.1.3. Let us write the position vector of the c.g. relative to the hinge as

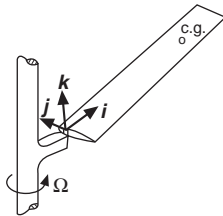


Fig. A.1.1 Blade pivot point

$$\mathbf{r}_g = x_g \mathbf{i} + y_g \mathbf{j} + z_g \mathbf{k}$$

and the absolute acceleration of the hinge as

$$\mathbf{a}_0 = a_x \mathbf{i} + a_y \mathbf{j} + a_z \mathbf{k}$$

Then the term $\mathbf{r}_g \times \mathbf{a}_0$ in eqn A.1.3 becomes

$$\mathbf{r}_g \times \mathbf{a}_0 = (y_g a_z - z_g a_y) \mathbf{i} + (z_g a_x - x_g a_z) \mathbf{j} + (x_g a_y - y_g a_x) \mathbf{k}$$

and, taking principal axes as before, eqn A.1.3 can be expanded to give

$$A \dot{\omega}_1 - (B - C)\omega_2\omega_3 - M_b(y_g a_z - z_g a_y) = L \quad (\text{A.1.14})$$

$$B \dot{\omega}_2 - (C - A)\omega_3\omega_1 - M_b(z_g a_x - x_g a_z) = M \quad (\text{A.1.15})$$

$$C \dot{\omega}_3 - (A - B)\omega_1\omega_2 - M_b(x_g a_y - y_g a_x) = N \quad (\text{A.1.16})$$

in which M_b is the blade mass. Equations A.1.14, A.1.15 and A.1.16 are referred to as the ‘extended’ Euler equations. Actually, the centre of gravity of the blade can be considered to lie practically on the i axis, so that we can write $\mathbf{r}_g = x_g \mathbf{i}$ and the above equations can be simplified to

$$A \dot{\omega}_1 - (B - C)\omega_2\omega_3 = L \quad (\text{A.1.17})$$

$$B \dot{\omega}_2 - (C - A)\omega_3\omega_1 + M_b x_g a_z = M \quad (\text{A.1.18})$$

$$C \dot{\omega}_3 - (A - B)\omega_1\omega_2 - M_b x_g a_y = N \quad (\text{A.1.19})$$

If the hinge offset distance is eR and the rotor shaft rotates with angular velocity Ω , then \mathbf{a}_0 is clearly of magnitude $\Omega^2 eR$ and is directed from the hinge to the shaft axis.

A.2 The stability equations

The theory of Appendix A.1 can be applied to obtain the stability equations which are discussed in detail in Chapter 5. We take an orthogonal set of axes, fixed in the helicopter and whose origin is located at the helicopter’s centre of gravity. It can be supposed, as is usual with the fixed wing aircraft, that the helicopter has a longitudinal plane of symmetry, although this is rather less true of the single rotor helicopter

because of its tailrotor. The axes will be chosen so that the x and z directions lie in the longitudinal plane with the y axis pointing to starboard, Fig. A.1.2.

The equations of motion of the helicopter, treating it as a rigid body, are

$$\mathbf{F} = m d\mathbf{v}/dt \quad (\text{A.2.1})$$

and

$$\mathbf{T} = d\mathbf{h}/dt \quad (\text{A.2.2})$$

where \mathbf{F} is the resultant external force on the helicopter and m its mass, and \mathbf{T} is the moment of this force.

We shall suppose that in trimmed flight there is no sideslip, so that the initial flight velocity components along the x , y , z axes are U , 0, W . During disturbed flight the increments of velocity will be denoted by u , v , w , so that the velocity vector \mathbf{v} can be written as

$$\mathbf{v} = (U + u)\mathbf{i} + v\mathbf{j} + (W + w)\mathbf{k} \quad (\text{A.2.3})$$

It will be supposed that the disturbance velocity components are small compared with the steady components U and W . In trimmed flight the angular velocity of the helicopter can be written as

$$\boldsymbol{\Omega} = p\mathbf{i} + q\mathbf{j} + r\mathbf{k} \quad (\text{A.2.4})$$

Then if X , Y , Z are the components of the force \mathbf{F} , the force equations, from eqn A.2.1 are

$$m[\dot{u} + q(W + w) - vr] = X \quad (\text{A.2.5})$$

$$m[\dot{v} + r(U + u) - p(W + w)] = Y \quad (\text{A.2.6})$$

$$m[\dot{w} + pv - q(U + u)] = Z \quad (\text{A.2.7})$$

The angular momentum equation (eqn A.2.2) can be written

$$\mathbf{T} = \partial\mathbf{h}/\partial t + \boldsymbol{\Omega} \times \mathbf{h} \quad (\text{A.2.8})$$

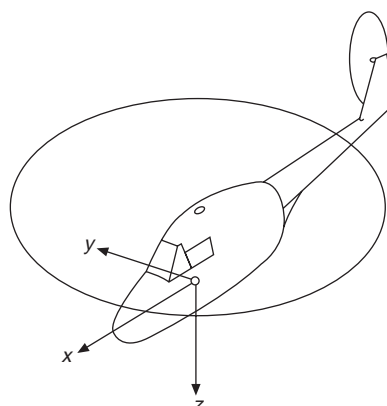


Fig. A.1.2 Axis system for the helicopter

and the components of momentum are, from eqn A.1.7,

$$h_1 = Ap - Fq - Er$$

$$h_2 = Bq - Dr - Fp$$

$$h_3 = Cr - Ep - Dq$$

With $\mathbf{T} = Li + Mj + Nk$, the expansion of eqn A.2.8 gives

$$A\dot{p} - (B - C)qr + D(r^2 - q^2) - E(pq + \dot{r}) + F(pr - \dot{q}) = L \quad (\text{A.2.9})$$

$$B\dot{q} - (C - A)rp + E(p^2 - r^2) - F(qr + \dot{p}) + D(qp - \dot{r}) = M \quad (\text{A.2.10})$$

$$C\dot{r} - (A - B)pq + F(q^2 - p^2) - D(rp + \dot{q}) + E(rq - \dot{p}) = N \quad (\text{A.2.11})$$

The two sets of equations A.2.5 to A.2.7 and A.2.9 to A.2.11 can be simplified considerably by assuming that the disturbance velocity and angular velocity components are so small that squares and products of them can be neglected. Further, if we assume that the helicopter has a plane of symmetry, the products of inertia D and F both vanish.

Then the force and moment equations simplify to

$$m\dot{u} + qW = X \quad (\text{A.2.12})$$

$$m\dot{v} + rU - pW = Y \quad (\text{A.2.13})$$

$$m\dot{w} - qU = Z \quad (\text{A.2.14})$$

and

$$A\dot{p} - E\dot{r} = L \quad (\text{A.2.15})$$

$$B\dot{q} = M \quad (\text{A.2.16})$$

$$C\dot{r} - E\dot{p} = N \quad (\text{A.2.17})$$

In particular, if ‘wind axes’ are chosen, i.e. if the x axis is initially taken to lie parallel to the flight direction, then $W = 0$ and the terms containing W vanish in eqns A.2.12 and A.2.13.

A.3 Multiblade summations

In some helicopter problems it is necessary to calculate the total force or moment on the helicopter by adding the contributions of the individual blades. In steady motion these blade contributions are periodic, and a typical term for a given blade would be $A_n \cos n\psi$. If there are b equally spaced blades, the contribution of the neighbouring blades will be $A_n \cos n(\psi \pm 2\pi/b)$ and the total effect of all the blades is therefore

$$A_n \cos n\psi + A_n \cos n(\psi + 2\pi/b) + \dots + A_n \cos n[\psi + 2\pi(b-1)/b]$$

$$= A_n \sum_{k=0}^{b-1} \cos n(\psi + 2\pi k/b)$$

Let

$$C = \sum_{k=0}^{b-1} \cos n(\psi + 2\pi k/b)$$

and

$$S = \sum_{k=0}^{b-1} \sin n(\psi + 2\pi k/b)$$

so that

$$C + iS = \sum_{k=0}^{b-1} e^{in(\psi + 2\pi k/b)} = e^{in\psi} \sum_{k=0}^{b-1} e^{2\pi kni/b}$$

The terms in the summation are a geometric series, and we easily find that

$$C + iS = \frac{e^{in\psi} (e^{2\pi ni} - 1)}{e^{2\pi ni/b} - 1}$$

If n is not an integer, $C + iS$ can be written

$$\begin{aligned} C + iS &= \frac{e^{in\psi} e^{in\pi} (e^{in\pi} - e^{-in\pi})}{e^{in\pi/b} (e^{in\pi/b} - e^{-in\pi/b})} \\ &= \frac{\sin \pi n}{\sin (\pi n/b)} \left\{ \cos n \left[\psi + \frac{b-1}{b} \pi \right] + i \sin n \left[\psi + \frac{b-1}{b} \pi \right] \right\} \end{aligned}$$

giving

$$C = \frac{\sin \pi n}{\sin (\pi n/b)} \cos n \left(\psi + \frac{b-1}{b} \pi \right) \quad (\text{A.3.1})$$

and

$$S = \frac{\sin \pi n}{\sin (\pi n/b)} \sin n \left(\psi + \frac{b-1}{b} \pi \right) \quad (\text{A.3.2})$$

If n is an integer but *not* a multiple of the number of blades b , we see that $C + iS = 0$. If n is a multiple of b

$$C + iS = 0/0$$

By L'Hospital's theorem,

$$\begin{aligned} C + iS &= e^{in\psi} \left[\frac{d(e^{2\pi ni} - 1)/dn}{d(e^{2\pi ni/b} - 1)/dn} \right]_{n = \text{multiple of } b} \\ &= \frac{b e^{ni\psi} [2\pi i e^{2\pi ni}]}{2\pi i e^{2\pi ni/b}} \\ &= b e^{in\psi} \end{aligned}$$

giving

$$C = b \cos n\psi \quad \text{and} \quad S = b \sin n\psi \quad (\text{A.3.3})$$

Thus

$$C = \frac{\sin \pi n}{\sin (\pi n/b)} \cos n \left(\psi + \frac{b-1}{b} \pi \right), \text{ if } n \text{ is not an integer}$$

$$= 0, \text{ if } n \text{ is not a multiple of } b$$

$$= b \cos n\psi, \text{ if } n \text{ is a multiple of } b$$

$$S = \frac{\sin \pi n}{\sin (\pi n/b)} \sin n \left(\psi + \frac{b-1}{b} \pi \right), \text{ if } n \text{ is not an integer}$$

$$= 0, \text{ if } n \text{ is not a multiple of } b$$

$$= b \sin n\psi, \text{ if } n \text{ is a multiple of } b$$

The Coleman co-ordinates

In ground and air resonance problems (Chapter 9) there are equations of the form

$$\ddot{x}_k + 2\Omega k \dot{x}_k + \Omega^2 x_k = p(t) \sin \psi_k + q(t) \cos \psi_k + \dots \quad (\text{A.3.4})$$

where $p(t)$ and $q(t)$ are functions of time.

The equation can be taken to represent a variable quantity x_k which is measured with respect to the rotating k th blade. We wish to find the total effect of all the blades. To do this we define new co-ordinates u and v , say, such that

$$u = -(2/b) \sum_{k=0}^{b-1} x_k \cos \psi_k \quad (\text{A.3.5})$$

$$v = -(2/b) \sum_{k=0}^{b-1} x_k \sin \psi_k \quad (\text{A.3.6})$$

where, as in the previous section, ψ_k takes the values $\psi, \psi + 2\pi/b, \dots, \psi + 2\pi(b-1)/b$. Differentiating eqns A.3.5 and A.3.6, we easily find, remembering $d\psi/dt = \Omega$,

$$\sum_{k=0}^{b-1} \dot{x}_k \sin \psi_k = b(\Omega u - \dot{v})/2; \quad \sum_{k=0}^{b-1} \dot{x}_k \cos \psi_k = -b(\Omega v + \dot{u})/2$$

$$\sum_{k=0}^{b-1} \ddot{x}_k \sin \psi_k = -b(\ddot{v} - 2\Omega \dot{u} - \Omega^2 v)/2$$

$$\sum_{k=0}^{b-1} \ddot{x}_k \cos \psi_k = -b(\ddot{u} + 2\Omega \dot{v} - \Omega^2 u)/2$$

Also, we can show that

$$\sum_{k=0}^{b-1} \sin^2 \psi_k = \sum_{k=0}^{b-1} \cos^2 \psi_k = b/2$$

and

$$\sum_{k=0}^{b-1} \sin \psi_k \cos \psi_k = 0$$

Then, multiplying eqn A.3.4 by $\cos \psi_k$, summing over the blades, and using the above relationships, we get

$$\ddot{u} + 2\Omega k u + 2\Omega \dot{v} + 2\Omega^2 k v = -q(t)$$

Similarly, performing the same procedure with $\sin \psi_k$,

$$\ddot{v} + 2\Omega k \dot{u} - 2\Omega \ddot{u} - 2\Omega^2 k u = -p(t)$$

The transformations represented by eqns A.3.5 and A.3.6, called the Coleman transformations, have removed the periodic terms from eqn A.3.4. They effectively resolve a rotating quantity into components along axes fixed in the helicopter body.

A.4 The frequency response of a second order system

It has been seen that the rotor blade, whether supposed rigid or flexible, can be treated as a spring–mass–dashpot, or second order, system when the blade displacement from equilibrium is small. Further, in steady flight, the loads forcing the blade are periodic and can be expressed in the form of a Fourier series. The blade motion can therefore be derived from the response of a second order system to a harmonic forcing function and it is useful to present the main results in this Appendix.

The differential equation of the motion can be represented typically as

$$m\ddot{x} + c\dot{x} + kx = F_0 \cos \omega t \quad (\text{A.4.1})$$

where m is the mass of the system, c is the viscous damping coefficient, k is the spring stiffness, and F_0 is the amplitude of the applied force.

When $F_0 = 0$ we have the case of free motion; when the damping is zero the free motion is sinusoidal with natural angular frequency ω_n given by $\omega_n = \sqrt{(k/m)}$.

Let us write the critical damping coefficient (just suppresses oscillatory motion) $c_{\text{crit}} = 2\sqrt{(k/m)} = 2k/\omega_n$ and define a non-dimensional damping factor ζ by $\zeta = c/c_{\text{crit}}$. The equation of motion, eqn A.4.1, can then be written

$$\ddot{x} + 2\zeta\omega_n \dot{x} + \omega_n^2 x = (F_0/m) \cos \omega t$$

The solution of this equation is known to be

$$x = x_0 \cos(\omega t - \varepsilon) \quad (\text{A.4.2})$$

where

$$x_0 = F_0 / \sqrt{[(k - m\omega^2)^2 + c^2\omega^2]}$$

and

$$\varepsilon = \tan^{-1} [c\omega/(k - m\omega^2)]$$

Defining a frequency ratio $\tilde{\omega}$ by $\tilde{\omega} = \omega/\omega_n$, x_0 and ε can be written

$$x_0 = F_0 / [k \sqrt{(1 - \tilde{\omega}^2)^2 + 4\zeta^2\tilde{\omega}^2}] \quad (\text{A.4.3})$$

and

$$\varepsilon = \tan^{-1} [2\zeta\tilde{\omega}/(1 - \tilde{\omega}^2)]$$

Now F_0/k is the static deflection, i.e. the displacement of the system under a steady load F_0 . Denoting this deflection by x_{st} we can represent the amplitude x_0 of the oscillating displacement as the static deflection multiplied by a magnification factor $\bar{\mu}$, where

$$\bar{\mu} = x_0/x_{st} = 1/\sqrt{[(1 - \tilde{\omega}^2)^2 + 4\zeta^2 \tilde{\omega}^2]} \quad (\text{A.4.4})$$

Thus the response of the system can be completely expressed by the quantities $\bar{\mu}$ and ε as functions of the frequency ratio $\tilde{\omega}$ and the damping ratio ζ , these quantities being shown plotted in Figs A.4.1 and A.4.2.

It can be seen from the solution of eqn A.4.2 that the response frequency is always

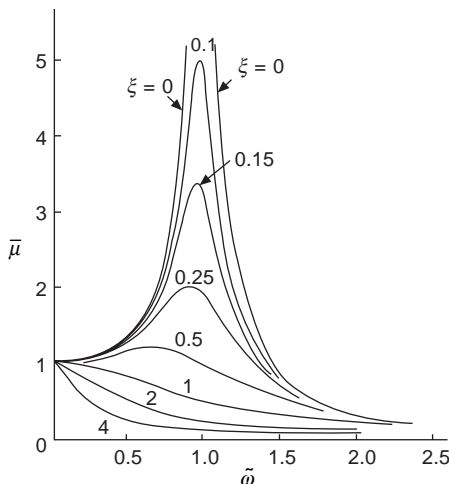


Fig. A.4.1 Amplitude of second order system to harmonic forcing function

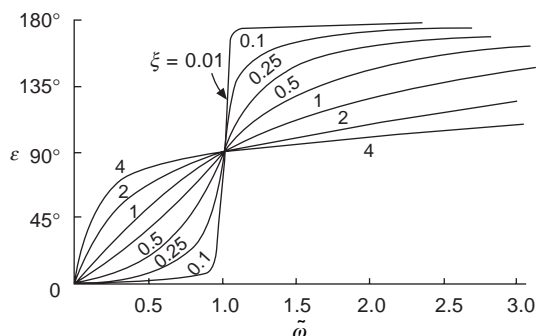


Fig. A.4.2 Phase relationship between response of second order system and forcing function

the same as the forcing frequency. When $\tilde{\omega} = 1$, i.e. when $\omega = \omega_n$, the system is said to be forced at its resonant frequency. It might be thought that the response amplitude is greatest at this frequency, but examination of Fig. A.4.1 shows that the maximum amplitude occurs at rather less than the resonant frequency. In fact, the aerodynamic damping factor of a flapping blade is typically of the order $\zeta = 0.4$, from which we see that the maximum amplitude occurs at $\tilde{\omega} = 0.85$. However, at resonance the phase angle is always 90° however great the damping.

Index

- Absorbers, *see* vibration
Actuator disc, 34, 37
Aeroelastic behaviour:
 main rotor
 blade weaving, 332
 flap-lag instability, 335
 pitch-flap flutter, 324
 pitch-lag instability, 320
 stall flutter, 329
 tail rotor
 flap-lag instability, 335
 pitch-flap-lag instability, 341
 pitch-flap (umbrella mode) instability, 334
Aerofoil characteristics:
 in forward flight, 221–232
 effect of Mach number, 222
 oscillating at low incidence, 204–212
 oscillating at high incidence, 225–232
Aeromechanical behaviour:
 air resonance, 352
 ground resonance, 342
Air resonance, 352
Angular momentum, 360
Attitude of helicopter:
 lateral, 30
 longitudinal, 28, 116
Autorotation, 132
Autostabilization, 175–179
- Bell stabilising bar, 176
Bending of blades, 238–289
 calculation of modes and frequencies, 242
 finite-element method, 253
 Galerkin method, 249
 Lagrange's equations, 243
 Myklestad method, 251
Rayleigh–Ritz method, 246
Southwell formula, 248
flapwise bending modes and frequencies, 238
intermodal coupling, 262
lagwise bending modes and frequencies, 257
forced response equation, 269
torsional modes and frequencies, 260
Biot–Savart law, 198
Blade deflections measured in flight, 276
Blade element theory:
 forward flight, 92
 vertical flight, 46
Blades, bending, *see* bending of blades
Blades, dynamic design, 294
Blade–vortex interactions (BVI), 219–221
Boundary layer on rotating blade:
 forward flight, 235
 hovering flight, 233
- Circulation:
 effect of finite number of blades, 62
Coleman co-ordinates, 367
Coleman *et al*:
 ground resonance, 342
 induced velocity distribution, 79
Coning angle, equation for, 107
Control derivatives, 180–183
Control response, 180–192
 to cyclic pitch, 185
 to vertical gusts, 190
 to lateral cyclic pitch, 188
 to longitudinal cyclic pitch, 183
Cyclic pitch:
 helicopter response to, 183

- Cyclic pitch (*continued*)
 lateral cyclic pitch to trim, 30
 longitudinal cyclic pitch to trim, 28
- Damping in pitch and roll, 139
- Downwash velocity:
 forward flight, 77
 hovering flight, 39
- Dynamic stability, 137–195
 equations, 363
 lateral, 166–175
 longitudinal, 140–166
- Eigenvalues and eigenvectors of flapping blade, 241
- Euler's equations, 362
 extended equations, 363
- Feathering:
 equation of motion, 10
 torsional vibrations, 260
- Figure of merit, 55
- Flapping:
 coefficients, 106
 in terms of disc axes, 108
 equation, 7
 forward flight, 105
 at high μ , 105
 in hovering flight, 10
 response to pitching and rolling, 15
- Flutter, 324
 stall, 329
- Free wake model 74, 216
- Fuselage drag, 130
 variation with weight, 130
- Goldstein circulation factors, 63
- Goldstein–Lock theory, 59
- Ground effect, 57
- Ground resonance, 342
- H*-force:
 definition, 27
 forward flight, 98
- Hingeless rotor:
 basic features, 277
 hub moment, 279
 effect on stability, 165, 174, 189
- Hovering flight:
 actuator disc theory, 34
 blade element theory, 46
 figure of merit, 55
 induced velocity in, 39
 inflow angle, 52
 optimum rotor, 54
 performance in, 50
- Induced power:
 forward flight, 90
 hovering flight, 40
- Induced velocity:
 flight and wind tunnel tests, 84
 forward flight, 77
 hovering flight, 39
 vertical climb and descent, 43
- Inflow angle:
 forward flight, 95
 vertical flight, 52
- In-plane motion:
 equation of motion for, 9
 effect of drag hinge distance on, 9
 geometric interpretation, 19
- Lagging:
 equation of motion, 9
 motion due to flapping, 19
- Lateral trim equations, 30
 solution of, 125
- Lift coefficient:
 contours of, 228
 in terms of thrust coefficient, 49
- Longitudinal trim equations, 28, 116
 solution of, 1, 117–123
 stability, 140
- Mangler and Squire induced velocity distribution, 81
- Manoeuvrability, 186
 pull-up manoeuvre, 194
- Multiblade summations, 365
- Offset hinges:
 effect on flapping frequency, 7
 effect on lag frequency, 9
 moment due to, 25
- Optimum rotor, 54
 figure of merit, 55

- Orthogonal property of normal modes, 267
- Performance:
- autorotation, 132
 - calculation of, 128
 - forward flight, 127–136
 - hovering flight, 51
- Power calculations:
- forward flight, 128
 - hovering flight, 51
 - induced power, 51
- Prandtl wake theory, 60
- Prescribed wake model, 69, 202
- Response to vertical, gust, 190
- Reverse flow area, 106
- Rotating frame of reference:
- angular momentum in, 360
- Rotor:
- axes systems, 26
 - forces and moments, 21
 - hinge system, 1
 - response to pitching and rolling, 15
- Rotor wake, *see* vortex wake
- Second order system, frequency response, 368
- Solidity, definition, 48, 55
- Stability characteristics:
- forward flight, 163, 173
 - effect of hingeless rotor on, 165
 - hovering flight, 160, 173
 - effect of tailplane on, 164
- Stability derivatives:
- lateral, 168–172
 - longitudinal, 143–147
- Stability equations, 363
- lateral, 166–168
 - longitudinal, 140–143
- Stall flutter, 329
- Stall of oscillating aerofoil, 228
- Static stability, 193
- Swash plate, 17
- Swirl velocity, 44
- Tailplane:
- effect on control response, 187
 - effect on dynamic stability, 164
 - effect on gust response, 190
 - effect on longitudinal trim, 123
- Tailrotor loss in forward flight, 128
- Theodorsen's wake theory, 67
- Thrust:
- coefficient:
 - definition, 48
 - forward flight, 96
 - hovering flight, 47
 - definition, 27
 - equations:
 - forward flight, 97
 - hovering, 48
 - effect on high incidence on, 225
- Tip loss factor, 65
- Tip shapes, 223
- Tip vortex, 70
- Torque coefficient, 50
- forward flight, 102
 - vertical flight, 50
- Turbulent wake state, 43
- Velocity components at blade, 92–96
- Vibration:
- active control of vibration, 310–314
 - active control of structural response (ACSR), 312
 - higher harmonic control (HHC), 310
 - dynamic design of rotor blades, 294
 - exciting forces, 291
 - frequencies other than $h\Omega$, 314
 - fuselage response, 301
 - main rotor gearbox mounting systems, 297
 - DAVI mounting system, 298
 - measurement in flight, 316
 - vibration absorbers, 304
 - battery, 309
 - bifilar, 305
 - Flexispring, 307
 - pendulum, 307
- Vortex ring state, 42
- Vortex wake:
- forward flight, 196–221
 - prescribed wake, 202–216
 - free wake, 216–221
 - hovering flight, 59–75
 - rigid wake, 59–69
 - prescribed wake, 69–74
 - free wake analysis, 74–75
- Vortices
- shed, 196
 - trailing, 196
- Weaving, blade, 332
- Wind axes, 365
- Windmill brake state, 42